ISSN 1520-295X

Experimental, Numerical and Analytical Studies on the Seismic Response of Steel-Plate Concrete (SC) Composite Shear Walls

by

Siamak Epackachi and Andrew S. Whittaker



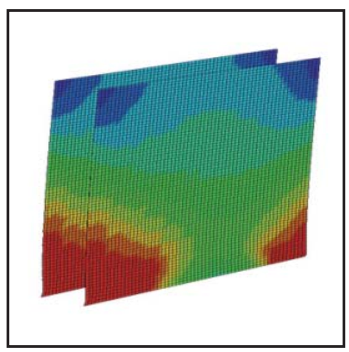
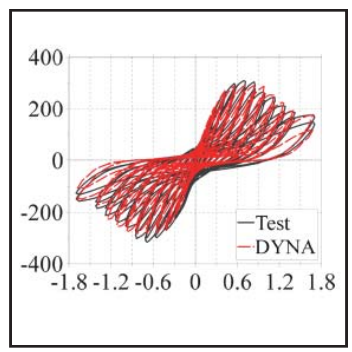

Technical Report MCEER-16-0001

June 15, 2016

This research was conducted at the University at Buffalo, State University of New York, and was supported primarily by the National Science Foundation under Grant Number 0829978.

NOTICE

Experimental, Numerical and Analytical Studies on the Seismic Response of Steel-Plate Concrete (SC) Composite Shear Walls

by

Siamak Epackachi[1] and Andrew S. Whittaker[2]

Publication Date: June 15, 2016
Submittal Date: September 10, 2015

Technical Report MCEER-16-0001

National Science Foundation Grant Number: 0829978

1 Teaching Assistant Professor, Department of Civil, Structural and Environmental Engineering, University at Buffalo, State University of New York
2 Professor, Chair, and MCEER Director, Department of Civil, Structural and Environmental Engineering, University at Buffalo, State University of New York

MCEER
University at Buffalo, State University of New York
212 Ketter Hall, Buffalo, NY 14260
E-mail: *mceer@buffalo.edu*; Website: *http://mceer.buffalo.edu*

Preface

MCEER is a national center of excellence dedicated to the discovery and development of new knowledge, tools and technologies that equip communities to become more disaster resilient in the face of earthquakes and other extreme events. MCEER accomplishes this through a system of multidisciplinary, multi-hazard research, in tandem with complimentary education and outreach initiatives.

Headquartered at the University at Buffalo, The State University of New York, MCEER was originally established by the National Science Foundation in 1986, as the first National Center for Earthquake Engineering Research (NCEER). In 1998, it became known as the Multidisciplinary Center for Earthquake Engineering Research (MCEER), from which the current name, MCEER, evolved.

Comprising a consortium of researchers and industry partners from numerous disciplines and institutions throughout the United States, MCEER's mission has expanded from its original focus on earthquake engineering to one which addresses the technical and socio-economic impacts of a variety of hazards, both natural and man-made, on critical infrastructure, facilities, and society.

The Center derives support from several Federal agencies, including the National Science Foundation, Federal Highway Administration, Department of Energy, Nuclear Regulatory Commission, and the State of New York, foreign governments and private industry.

This report presents the results of experimental, numerical, and analytical studies on the in-plane cyclic behavior of rectangular steel-plate concrete (SC) composite shear walls. The SC walls considered in this study were composed of steel faceplates, infill concrete, headed steel studs anchoring the faceplates to the infill, and tie rods connecting the two faceplates through the infill. Four large-size specimens with an aspect ratio of 1.0 were tested under displacement-controlled, in-plane cyclic loading in the laboratory at the University at Buffalo. The design variables considered in the testing program included wall thickness, reinforcement ratio, and slenderness ratio. The walls were identified to be flexure- and flexure-shear critical. The progression of damage in the four walls was identical, namely, cracking and crushing of the infill concrete at the toes of the walls, outward buckling and yielding of the steel faceplates near the base of the wall, and tearing of the faceplates at their junctions with the baseplate. A robust finite element model was developed in LS-DYNA for nonlinear cyclic analysis of the SC walls. The LS-DYNA model was validated using the results of the cyclic tests of the four SC walls. The validated LS-DYNA model was used to conduct a comprehensive parametric study to investigate the effects of wall aspect ratio, reinforcement ratio, wall thickness, and uniaxial concrete compressive strength on the in-plane response of SC walls. Simplified analytical models, suitable for preliminary analysis and design of SC walls, were developed, validated, and implemented in MATLAB. Analytical models were proposed for monotonic and cyclic simulations of the in-plane response of flexure- and flexure-shear-critical SC wall piers. The model for cyclic analysis was developed by modifying the Ibarra-Krawinkler Pinching model. The analytical models were verified using the results of the parametric study and validated using the test data.

ABSTRACT

The seismic performance of rectangular steel-plate concrete (SC) composite shear walls is assessed for application to buildings and mission-critical infrastructure. The SC walls considered in this study were composed of two steel faceplates and infill concrete. The steel faceplates were connected together and to the infill concrete using tie rods and headed studs, respectively. The research focused on the in-plane behavior of flexure- and flexure-shear-critical SC walls.

An experimental program was executed in the NEES laboratory at the University at Buffalo and was followed by numerical and analytical studies. In the experimental program, four large-size specimens were tested under displacement-controlled cyclic loading. The design variables considered in the testing program included wall thickness, reinforcement ratio, and slenderness ratio. The aspect ratio (height-to-length) of the four walls was 1.0. Each SC wall was installed on top of a re-usable foundation block. A bolted baseplate to RC foundation connection was used for all four walls. The walls were identified to be flexure- and flexure-shear critical. The progression of damage in the four walls was identical, namely, cracking and crushing of the infill concrete at the toes of the walls, outward buckling and yielding of the steel faceplates near the base of the wall, and tearing of the faceplates at their junctions with the baseplate.

A robust finite element model was developed in LS-DYNA for nonlinear cyclic analysis of the flexure- and flexure-shear-critical SC walls. The DYNA model was validated using the results of the cyclic tests of the four SC walls. The validated and benchmarked models were then used to conduct a parametric study, which investigated the effects of wall aspect ratio, reinforcement and slenderness ratios, axial load, and steel and concrete strengths on the in-plane response of SC walls.

Simplified analytical models, suitable for preliminary analysis and design of SC walls, were developed, validated, and implemented in MATLAB. Analytical models were proposed for monotonic and cyclic simulations of the in-plane response of flexure- and flexure-shear-critical SC wall piers. The model for cyclic analysis was developed by modifying the Ibarra-Krawinler Pinching (IKP) model. The analytical models were verified using the results of the parametric study and validated using the test data.

ACKNOWLEDGMENTS

This research project was conducted as part of a National Science Foundation-funded NEES research project on conventional reinforced concrete and steel-plate concrete composite shear walls with low aspect ratios. The project was funded by the U.S. National Science Foundation under Grant No. 0829978. This financial support is gratefully acknowledged.

Many individuals and organizations contributed to this research project. The steel shells for the composite walls were fabricated in the Bowen Laboratory at Purdue University. Professor Amit Varma and Dr. Efe Kurt of Purdue University played important roles in the design of the test articles, the execution of the experiments in the Structural Engineering and Earthquake Simulation Laboratory at the University at Buffalo, and the preliminary interpretation of results reported herein. Dr. Nam H. Nguyen, formerly a graduate student at the University at Buffalo, collaborated with the lead author and Dr. Kurt on the execution of the experiments. The technicians and staff of the Structural Engineering and Earthquake Simulation Laboratory at the University at Buffalo executed the experiments. LPCiminelli Inc. cast the test specimens and the reusable foundation. The research product described in this MCEER report would not have been possible without these contributions. The authors are extremely grateful for this support.

The opinions, findings, conclusions or recommendations expressed in this report are those of the authors and do not necessarily reflect the views of MCEER, the State of New York, Purdue University, or the project collaborators.

TABLE OF CONTENTS

TABLE OF CONTENTS (CONT'D)

TABLE OF CONTENTS (CONT'D)

TABLE OF CONTENTS (CONT'D)

TABLE OF CONTENTS (CONT'D)

LIST OF FIGURES

LIST OF FIGURES (CONT'D)

LIST OF FIGURES (CONT'D)

LIST OF FIGURES (CONT'D)

LIST OF FIGURES (CONT'D)

LIST OF FIGURES (CONT'D)

LIST OF TABLES

LIST OF TABLES (CONT'D)

GLOSSARY

The following definitions are used in Chapter 8 of this report.

A_c	Cross-sectional area of infill concrete
A_r	Cross-sectional area of threaded bar
A_s	Cross-sectional area of steel faceplates
A_{sb}	Effective cross-sectional area of baseplate for a section cut parallel to the width of baseplate
A'_{sb}	Effective cross-sectional area of baseplate for a section cut between two threaded bars parallel to the length of baseplate
a	Ratio of the hardening modulus to the elastic modulus of the steel faceplates
B	Width of baseplate
c	Depth to the neutral axis
d	Rate parameter in IKP model
d'_i	Distance between the center of ith row of threaded bars and the neutral axis
d_i	Distance between the center of ith row of threaded bars and the wall centerline
d_{unl}	Unloading stiffness rate parameter
d_{rel}	Reloading stiffness rate parameter
d_a	Accelerated stiffness rate parameter
E_c	Elastic modulus of concrete (ksi)
E_s	Elastic modulus of steel (ksi)
E_c^{cr}	Elastic modulus of cracked concrete = $0.7E_c$
E_i	Hysteretic energy dissipated in ith cycle
E_t	Hysteretic energy dissipation capacity
F'_c	Compressive force on infill concrete
F_c	Peak force
F_s	Compressive and tensile forces in the steel faceplates
F_y	Yield force in the IKP model
F_y^+	Yield force in the first quadrant
F_y^-	Yield force in the third quadrant
F_y^t	Force corresponding to yielding of steel faceplates at the tension end of the wall

F_y^c	Force corresponding to yielding of steel faceplates at the compression end of the wall
F_r	Residual force
$F_{\max}^{+}$	Maximum force achieved in previous cycles in first quadrant
$F_{\max}^{-}$	Maximum force achieved in previous cycles in third quadrant
f_b	Maximum bearing stress on foundation
f_c	Concrete stress
f_s	Steel stress
f_c'	Uniaxial compressive stress of concrete (ksi)
f_y	Yield stress of steel faceplates (ksi)
f_u	Ultimate stress of steel faceplates (ksi)
f_y^e	Effective yield stress of steel faceplates (ksi)
f_y'	Average of yield and ultimate stress of steel (ksi)
f_r	Modulus of rupture of concrete (ksi)
f_{sx}	Horizontal stress in steel faceplates
f_{sy}	Vertical stress in steel faceplates
f_{sxy}	Shear stress in steel faceplates
f_{cx}	Horizontal stress in infill concrete
f_{cy}	Vertical stress in infill concrete
f_{cxy}	Shear stress in infill concrete
G_c	Elastic shear modulus of concrete (ksi)
G_s	Elastic shear modulus of steel (ksi)
H	Height of wall panel
h_r	Level of the resultant of the lateral loads applied above an SC panel in multi-story SC walls
I_c	Moment of inertia of infill concrete
I_s	Moment of inertia of steel faceplates
I_{sb}	Moment of inertia of baseplate about an axis parallel to the width of baseplate
I_{sb}'	Moment of inertia of part of baseplate between two threaded bars about an axis parallel to the length of baseplate
k	Ratio of the yield strain of the steel faceplates to the concrete strain corresponding to the peak stress
k_f	Pinching parameter in MIKP model

k_d Pinching parameter in the MIKP model

ξ Pinching parameter in the MIKP model

K_b Lateral stiffness of the wall connection (kips/in)

K_f Flexural stiffness of the wall panel (kips/in)

K_s Shear stiffness of the wall panel (kips/in)

K_t Lateral stiffness of the wall panel (kips/in)

K_e Elastic shear stiffness of the SC wall (kips/rad)

K_{cr} Shear stiffness of the SC wall after concrete cracking (kips/rad)

K_y Shear stiffness of the SC wall after yielding of steel faceplates (kips/rad)

K_e^p Effective stiffness of the wall panel (kips)

K_α Shear stiffness of the steel faceplates (kips/rad)

K_β Shear stiffness of the diagonally cracked infill concrete (kips/rad)

K_θ Rotational stiffness of the spring (kip-in/rad)

K_{unl} Unloading stiffness in the IKP model

K_{rel} Reloading stiffness in the IKP model

K'_{unl} Unloading stiffness in the MIKP model

K'_{rel} Reloading stiffness in the MIKP model

L Length of wall

L_b Length of baseplate

L_c Distance between the edge of the baseplate and end of the wall

L_r Total length of threaded bar from top of the baseplate to the nut-washer assembly at the bottom

L_t Longitudinal spacing between the center of the first row of threaded bars at the tension end of the wall and the end of the wall

L'_t Lateral spacing between the center of threaded bars on sides of the wall and face of the wall

M Bending moment applied to the SC wall cross-section

M_i Bending moment in the ith sub element

M_{cr} Flexural strength of the SC wall at concrete cracking

M_y^t Flexural strength of the SC wall at yielding of steel faceplates at the tension end of the wall

M_y^c Flexural strength of the SC wall at yielding of steel faceplates at the compression end of the wall

M_c Flexural strength of the SC wall at the maximum concrete compressive strain equal to ε_{c0}

M_u	Flexural strength of the SC wall at concrete crushing
N_x	Normal force along the length of the wall applied to the SC wall cross-section
N_y	Normal force along the height of the wall applied to the SC wall cross-section
m	Number of sub-elements along the height of a panel
m_r	Number of rows of threaded bars within the length of the wall
n	Modular ratio
n_r	Number of threaded bars at the first row at the tension end of the wall
n'	Coefficient of concrete stress-strain relationship
r	Coefficient of concrete stress-strain relationship
S	Longitudinal spacing of threaded bars
t_c	Thickness of the infill concrete
t_s	Thickness of each steel faceplate
t_p	Thickness of the baseplate
T_1	Tensile force in each threaded bar at the first row of the bars at the tension end of the wall
T_i	Tensile force in each threaded bar at the i^{th} row
V	Shearing force applied to the SC wall cross-section
V_{cr}	Shearing strength of the SC wall at concrete cracking
V_y	Shearing strength of the SC wall at yielding of the steel faceplates
V_u	Shearing strength of the SC wall at concrete crushing
V_{ni}	In-plane shear strength of the SC wall specified by AISC N690s1
V_i	Shearing force in the i^{th} sub element
x	Ratio of the concrete strain to strain corresponding to peak stress
y_i	Distance between the center of the i^{th} sub element and the top of the wall
Δy_i	Height of the i^{th} sub element
Δ_1	Uplift of the baseplate at the first row of threaded bars at the tension end of the wall
Δ_b	Lateral displacement due to base rotation
Δ_f	Flexural displacement at the top of the panel
Δ_{fj}	Flexural displacement at the top of the j^{th} panel
Δ_i	Uplift of the baseplate at the i^{th} row of threaded bars

Δ_s	Shear displacement at the top of the panel
Δ_{s1}	Downward deflection of the baseplate at the first row of threaded bars at the tension end of the wall
Δ_{si}	Downward deflection of the baseplate at the ith row of threaded bars
Δ_{sj}	Shear displacement at the top of the jth panel
Δ_t	Total displacement at the top of the panel
θ^{cr}	Angle of the inclination of the diagonal cracking in infill concrete
γ_i	Shear strain in the ith sub-element
γ_{cr}	Shear strain of the SC wall at concrete cracking
γ_y	Shear strain of the SC wall at yielding of the steel faceplates
γ_{xy}^{sc}	Shear strain of the SC wall
γ_u	Shear strain in the SC wall at concrete crushing
$\gamma_{unl,1}$	Deterioration parameter for the first unloading branch
$\gamma_{unl,2}$	Deterioration parameter for the second unloading branch
$\gamma_{rel,1}$	Deterioration parameter for the first reloading branch
γ_a	Accelerated stiffness deterioration parameter
τ	Average shear stress in the steel faceplates
ν_s	Poisson's ratio for steel
η	Strength-adjusted reinforcement ratio
ρ	Reinforcement ratio
$\bar{\rho}$	Strength-adjusted reinforcement ratio
ρ'	Modulus-adjusted reinforcement ratio
λ	Aspect ratio of a wall panel
ε_{cr}	Concrete cracking strain
ε_c	Concrete strain
ε_s	Steel strain
ε_{c0}	Strain at peak stress of concrete
ε_{sh}	Steel strain at hardening
ε_x^{sc}	Normal strain along the length of the wall
ε_y^{sc}	Normal strain along the height of the wall

ε_y	Steel strain at yielding
ε_u	Steel strain at peak stress
α	Ratio of neutral axis depth to length of the wall
α_s	Ratio of post-yield stiffness to elastic stiffness in the IKP model
α_{s1}	Ratio of wall stiffness after yielding of steel faceplates at the tension end of wall to effective stiffness in the MIKP model
α_{s2}	Ratio of wall stiffness after yielding of steel faceplates at the compression end of wall to effective stiffness in the MIKP model
α_c	Ratio of post-capping stiffness to elastic stiffness
ϕ_{cr}	Curvature of the SC wall cross-section at concrete cracking
$\phi_y{}^t$	Curvature of the SC wall cross-section at yielding of steel faceplates at the tension end of wall
$\phi_y{}^c$	Curvature of the SC wall cross-section at yielding of steel faceplates at the compression end of wall
ϕ_c	Curvature of the SC wall cross-section at maximum concrete compressive strain equals to ε_{c0}
ϕ_u	Curvature of the SC wall cross-section at concrete crushing
ϕ_i	Curvature in the i^{th} sub-element
θ	Rotation of the baseplate
β	Deterioration parameter
β_1	Stress block coefficient
β_2	Stress block coefficient
δ_y	Yield displacement in the IKP model
δ_c	Displacement corresponding to the peak force in the IKP model
δ_r	Displacement corresponding to the residual force in the IKP model
δ_y^t	Yield displacement corresponding to the yielding of steel faceplates at the tension end of the wall
δ_y^c	Yield displacement corresponding to the yielding of steel faceplates at the compression end of the wall
δ_{perl}	Maximum residual displacement in the previous cycle, same quadrant

CHAPTER 1

INTRODUCTION

1.1 General

Steel-plate concrete (SC) composite walls consisting of steel faceplates, infill concrete, and connectors used to anchor the steel faceplates together and to the infill concrete, have potential advantages over conventional reinforced concrete and steel plate shear walls in terms of constructability and seismic performance.

SC panels enable modular construction leading to potential time and cost savings over conventional reinforced concrete walls. Double skin SC wall shells can be fabricated offsite, assembled on site, and filled on-site with concrete to create a monolithic structure. The use of steel faceplates eliminates the need for on-site formwork, and the faceplates serve as primary reinforcement.

SC wall construction has received attention from the research and design professional communities but the number of applications to date is limited. Most proposals for SC wall construction have involved two steel faceplates with infill concrete. Fukumuto et al. (1987) proposed SC construction in the form of modular box units, as reproduced in Figure 1-1. Another proposal from 1987 used SC panels for submerged tunnels [Tomlinson (1989),Wright (1991b)], as shown in Figure 1-2.

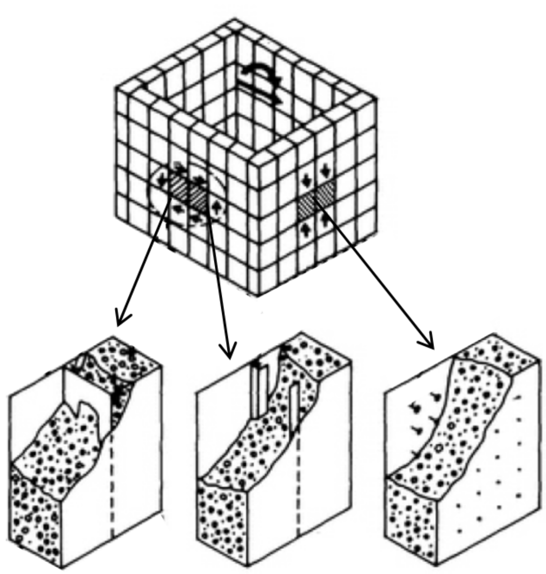

Figure 1-1 Modular box units [Fukumuto et al. (1987)]

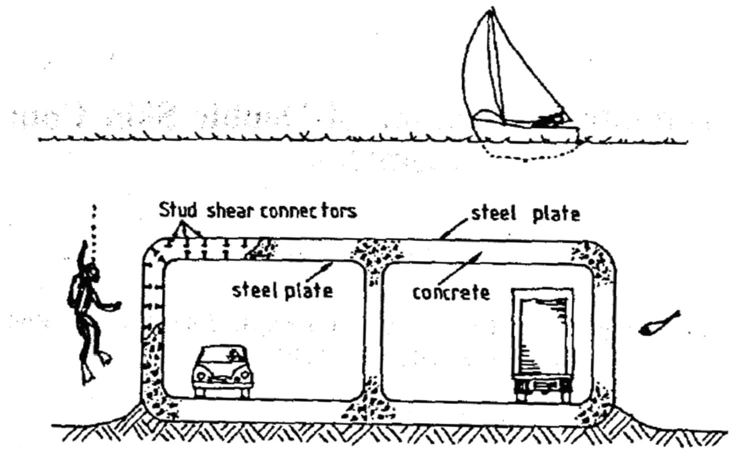

Figure 1-2 Submerged tunnel application of SC panels [Wright et al. (1991b)]

Another proposal from the late 1980s was an SC shear wall, composed of two corrugated steel faceplates and infill concrete [Wright (1995), and Wright et al. (1992,1994)]. The corrugated steel faceplates of Figure 1-3 were to be connected to steel beams and columns by fasteners.

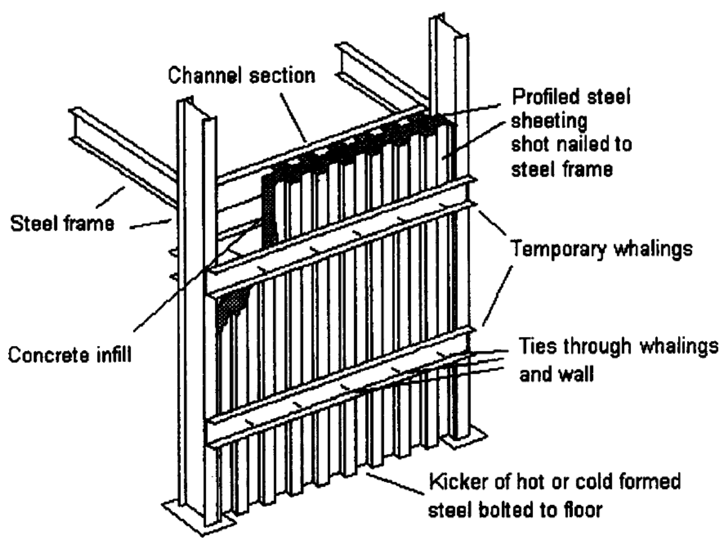

Figure 1-3 SC wall panels with corrugated steel faceplates wall [Wright et al. (1995)]

Other variations on SC wall construction have included those shown in Figure 1-4 below, with SC faceplates with infill *reinforced* concrete, where the role of the reinforced concrete was to prevent out-of-plane *elastic* buckling of the steel plate (shear wall).

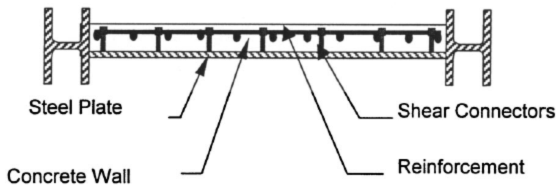

(a) RC wall on one side of the steel plate

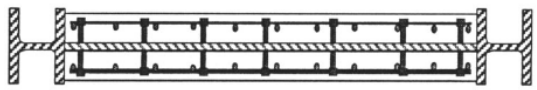

(b) RC walls on both sides of the steel plate

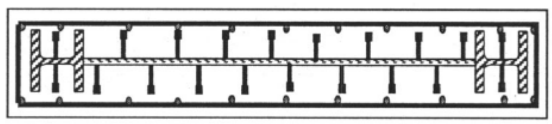

(c) Steel plate wall encased in RC wall

Figure 1-4 SC wall alternatives with reinforced concrete infill [Zhao et al. (132)]

The proposed applications of SC walls seen in Figure 1-3 and Figure 1-4 provide possible incremental advances over more conventional framing systems. The proposal of Figure 1-3 attaches the SC wall panels to an existing steel frame, and duplicates gravity load resistance, which is not economical. The alternatives of Figure 1-4 seek to overcome the known challenges with steel plate shear walls, which require stiffening to prevent elastic buckling, and capacity-protected vertical (column) and horizontal (beam) steel boundary elements. The cost associated with overcoming these challenges has precluded their use in the building and nuclear industries.

A proprietary composite product, Bi-Steel, was proposed by British Steel (later Corus) (2002) for flooring systems, beams and columns, fire resisting systems and building cores. A Bi-Steel panel consists of two steel faceplates and steel bars that are friction welded to the faceplates at both ends. Bi-Steel panels are welded together and filled with concrete on site. Figure 1-5 presents Bi-Steel construction details.

(a) Internal construction

(b) Shear walls

Figure 1-5 Bi-Steel construction [Tata Steel Inc. (96)]

The use of SC wall construction in nuclear power plants has been studied for nearly 20 years, with an emphasis on elastic response in design basis shaking. Safety-related nuclear applications have involved steel faceplates and infill (unreinforced) concrete, where the faceplates provide formwork and reinforcement, and the SC walls provide both gravity and earthquake resistance, without the introduction of internal steel framing for gravity-load resistance. Application of SC walls to containment internal structures and shield buildings in nuclear power plants has begun in the United States and China, with US applications based substantially on the work of Varma and his co-workers at Purdue University [e.g., Varma et al. (2009,2011a,2011b,2011c,2012,2013a)]. SC walls have not been used for earthquake-resistant building construction, in part because there is little data on the seismic performance of these walls at deformation levels expected in buildings subjected to maximum earthquake shaking.

To date, design of SC walls (for nuclear applications) has been based in part on proprietary test data and the limited data available in the literature. Most of the experiments were conducted at small scales and focused on the essentially elastic range of response. The small-scale tests can not represent reality well because construction materials and conditions are generally very different from those used for field applications. Prior numerical studies have primarily focused on response in the elastic range. The simulation of cyclic nonlinear response, and the loss of stiffness and strength due to damage, have not been thoroughly investigated. The available physics-based equations address only the pure shear response of SC walls, and flexural and shear-flexure responses have not been studied.

1.2 Research Objectives

The focus of the research project presented in this report is flexure- and flexure-shear critical SC wall piers. The SC wall piers studied in this report consist of two steel faceplates, infill concrete, headed steel studs anchoring the faceplates to the infill, and tie rods connecting the two faceplates through the infill. Figure 1-6 presents a cut-away view of such a SC wall pier. Shear-critical walls, namely, those walls with boundary columns and flanges and those rectangular walls with very low aspect ratios are not addressed. Only loading in the plane of the wall is considered.

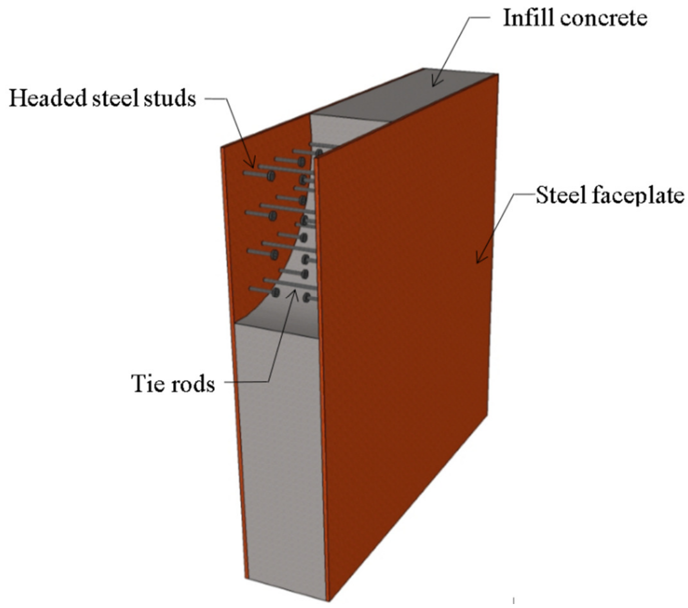

Figure 1-6 SC wall pier construction studied herein

The objectives of the research project are:

1. To generate a large-scale test data for rectangular SC walls subjected to in-plane cyclic lateral loading.
2. To provide knowledge on the cyclic response, failure modes, effects on response of design parameters, and dynamic properties such as energy dissipation and viscous damping of SC wall piers.
3. To develop a reliable finite element model for the nonlinear cyclic analysis of flexure- and flexure-shear-critical SC walls.
4. To investigate the effects on response of key design parameters, including aspect ratio, reinforcement ratio, wall thickness, and compressive strength of concrete.
5. To develop reliable analytical models for monotonic and cyclic analyses of single- and multi-story SC walls, suitable for preliminary analysis and design.

1.3 Research Outline

This report is organized in nine chapters, a list of references, and four appendices. Chapter 2 presents a literature review. Chapter 3 provides information on the pre-test analysis and preliminary design of the SC wall specimens. The details of the experimental program including descriptions of the four specimens, the construction of the foundation block and the wall panels, material testing, test setup, loading protocol, and instrumentation are presented in Chapter 4.

Results of the tests are provided in Chapter 5. In Chapter 6, a finite element model for nonlinear cyclic analysis of flexure- and flexure-shear-critical SC walls is developed and validated. Chapter 7 presents the results of a parametric study that investigates the effects of aspect ratio, reinforcement ratio, faceplate slenderness ratio, axial load, and steel and concrete strengths on the response of SC walls. Simplified models for the monotonic and cyclic analyses of flexure- and flexure-shear-critical single- and multi-story SC walls, and for the prediction of initial stiffness of an SC wall with a baseplate connection, are developed in Chapter 8. Chapter 9 summarizes the research and identifies the key conclusions. A list of references follows Chapter 9. Appendix A includes CAD drawings of the SC specimens, foundation block, and the SC wall connection to the block. Photographs of the specimens at different drift ratios and of the damage to the infill concrete of SC2 and SC4 at the end of testing are presented in Appendix B. Specifications for the rosette gages used to measure strains in the steel faceplates are provided in Appendix C. The MATLAB code for the Modified-Ibarra-Krawinkler-Pinching (MIKP) model for the cyclic analysis of SC walls is provided in Appendix D.

CHAPTER 2

LITERATURE REVIEW

2.1 Overview

This chapter reviews the literature on experimental and numerical studies on steel-plate concrete (SC) composite shear walls. Section 2.2 summarizes the experimental and analytical studies. Section 2.3 reviews finite element (numerical) studies of the behavior of SC walls.

2.2 Review of Experimental Studies on SC walls

Suzuki et al. (1984) proposed an analytical method to predict the peak strength of rectangular SC panels under combined bending, axial, and shear loads. These SC panels were equipped with flange plates. They assumed that the load was resisted at peak strength by a diagonal tension field in the steel faceplates and diagonal compression field in the infill concrete, as cartooned in Figure 2-1. Figure 2-1(a) shows the compression field in the infill concrete; α is the angle of the compression field to the horizontal. The tension field of Figure 2-1(d) is characterized by two parameters β and ξ, where β is the angle of the tension field to the horizontal and $\xi\mathrm{h}$ is the height of the faceplate over which the tension field is developed. The resultant load in the tension field is decomposed into two forces T and $\tilde{\mathrm{T}}$, where T is the tensile force resisted by the steel faceplates and the two components of $\tilde{\mathrm{T}}$ along the height ($\tilde{\mathrm{T}}_y$ in Figure 2-1(b)) and length ($\tilde{\mathrm{T}}_x$ in Figure 2-1(c)) of the panel are resisted by the infill concrete and the steel flange plates, respectively. Figure 2-1(b) shows the force $\tilde{\mathrm{T}}_y$ resisted by the infill concrete and the reaction force F generated at the corners of the infill concrete. Figure 2-1(c) shows the force $\tilde{\mathrm{T}}_x$ resisted by one of the flange plates and the tensile and compressive reactions K and J, respectively. Figure 2-1(f) illustrates the equilibrium of the internal forces in the steel faceplates and flange plates, K, J, F, and T, and the external forces in the steel faceplates and flange plates, $\mathrm{N_s}$, $\mathrm{Q_s}$, and $\mathrm{M_s}$. Figure 2-1(e) presents the equilibrium of the internal force in the infill concrete, C, with the external forces in the concrete, $\mathrm{N_c}$, $\mathrm{Q_c}$, and $\mathrm{M_c}$.

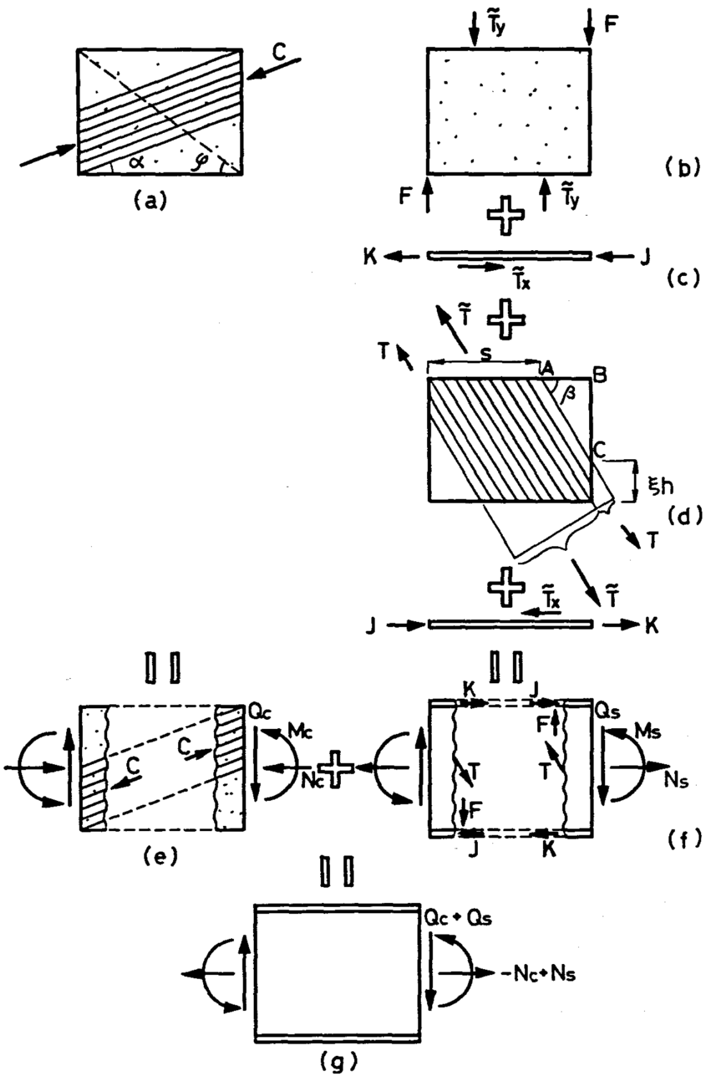

Figure 2-1 Load transfer mechanisms at peak strength [Suzuki et al. (1984)]

Suzuki et al. tested four SC walls to validate the proposed method. The ratio of predicted to measured peak shear strengths varied from 0.7 to 1. More accurate predictions were obtained for the shear-critical SC panels. The proposed method underestimated the peak shear strength of the flexure-critical panels.

Fukumoto et al. (1987) tested 1/4-scale steel plate, plain concrete, and composite shear walls under axial and shear loads to study the effects of composite action between the steel faceplates and the infill concrete, slenderness ratio, and stiffening methods for the steel faceplates, on the response of SC walls. The composite walls were constructed by assembling welded steel boxes and infilling them with concrete. Figure 2-2 presents the three types of connectors considered in that study, namely, vertical steel insert plates, steel angles, and headed studs.

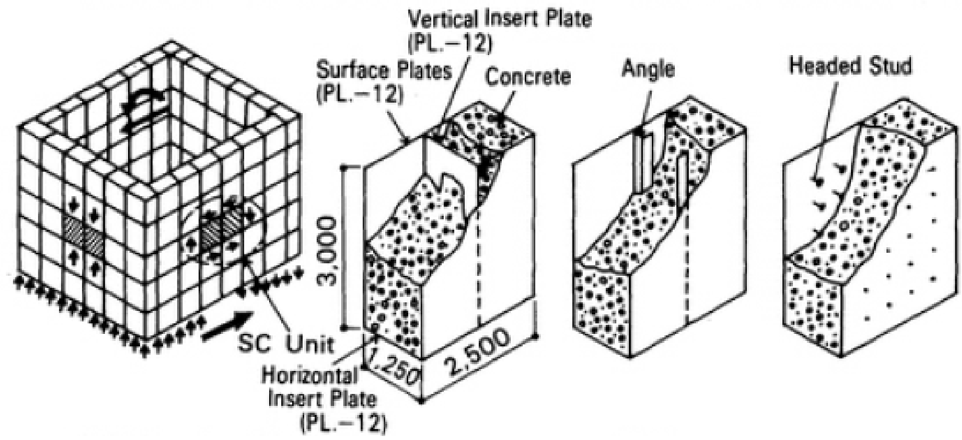

Figure 2-2 Types of connectors used in experimental study [Fukumoto et al. (1987)]

The experimental studies showed that the axial and shear responses of SC walls are substantially affected by composite action of the steel faceplate and the infill concrete; the axial and shear strengths of the composite wall were 14% and 40% greater than the corresponding superposed strengths of the steel plate and plain concrete walls, respectively.

The initial stiffness of the SC walls under axial compression was not affected by the presence of the vertical insert plates. The tangent stiffness beyond the elastic range decreased as the spacing of the insert plates increased. Using a smaller spacing for the insert plates increased the axial strength but did not have a significant effect on the shear strength. The shear load-displacement relationships of SC walls was affected by the type of connector used.

Fukumoto et al. proposed an analytical model to predict the monotonic response of SC walls. The proposed method (Figure 2-3) assumed that the shear load was resisted by tensile ties in the steel faceplates oriented at 45° to the horizontal and diagonally inclined compression struts in the infill concrete.

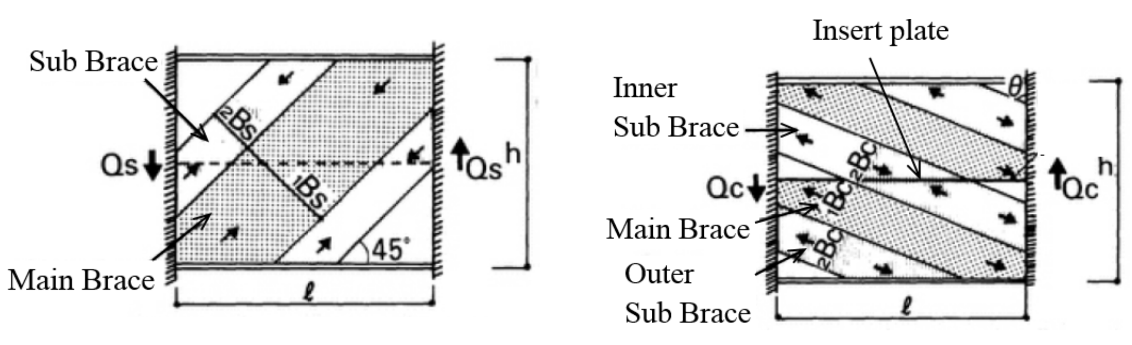

(a) Tensile ties in the steel faceplate (b) Compression struts in the infill concrete

Figure 2-3 Analytical model proposed by Fukumoto et al. (1987)

They calculated the shear strength of an SC wall as:

$$Q_{sc} = Q_s + Q_c$$

$$Q_s = t_s[{}_1B_s\sigma_s(\varepsilon_s) + {}_2B_s\sigma_s(\varepsilon_s')]\cos 45^\circ \tag{2-1}$$

$$Q_c = t_c[(n+1)_1B_c\sigma_c(\varepsilon_c) + n_2B_c\sigma_c(\varepsilon_c) + {}_2B_c\sigma_c(\varepsilon_c')]\cos\theta$$

where θ is the inclination angle of the compression struts; ${}_1B_s$ and ${}_2B_s$ are the effective widths of the main tie and the sub ties in the steel faceplates, respectively (see Figure 2-3); and ${}_1B_c$, and ${}_2B_c$ are the effective widths of the main strut and sub struts in the infill concrete, respectively. As seen in Figure 2-3, the main tie in the steel faceplate is a single diagonal connecting two opposite corners of the SC panel and the sub ties are parallel to the main tie. The main strut in the infill concrete is assumed to form between the vertical insert plates, as presented in Figure 2-3. The modeling parameters θ, ${}_1B_s$, ${}_2B_s$, ${}_1B_c$, and ${}_2B_c$ are calculated as:

$$\theta = \tan^{-1}[(n+1)l/h] \tag{2-2}$$

$${}_1B_s = (h - l/4)\cos 45^\circ \tag{2-3}$$

$${}_2B_s = l/4\cos 45^\circ \tag{2-4}$$

$${}_1B_c = {}_2B_c = \frac{h\sin\theta}{2(n+1)} \tag{2-5}$$

where t_s is the sum of the steel faceplate thicknesses; t_c is the thickness of the infill concrete; h and l are the height and length of SC wall, respectively; σ_s and σ_c are the stresses in the steel faceplates and infill concrete, respectively; ε_s and ε_c are the axial strain in the main steel tie and the axial strains in the main and inner sub struts of the infill concrete, respectively; and ε_s' and ε_c' are the axial strains in the sub ties and outer sub struts of the steel faceplates and infill concrete, respectively. The outer and inner sub struts (braces in Figure 2-3) in the infill concrete are located in Figure 2-3. There was a good agreement between the measured and predicted shear strengths but the displacement corresponding to the peak shear load was underestimated.

Akiayama et al. (1989) tested a 1/10-scale model of a pressurized water reactor containment internal structure (CIS) consisting of primary and secondary shield SC walls, a reinforced concrete base mat, upper and lower loading slabs, steam generator compartments, pressurizer compartment, and a number of partition walls. The thickness of the SC walls and steel faceplates were 4.3 in. and 0.06 in., respectively. The experimental program included two types of tests, namely, cyclic quasi-static horizontal loading and vibration tests. The ratio of the cyclic horizontal load applied to the upper slab to that applied to the lower slab was fixed at 2.6. The CIS specimen is presented in Figure 2-4.

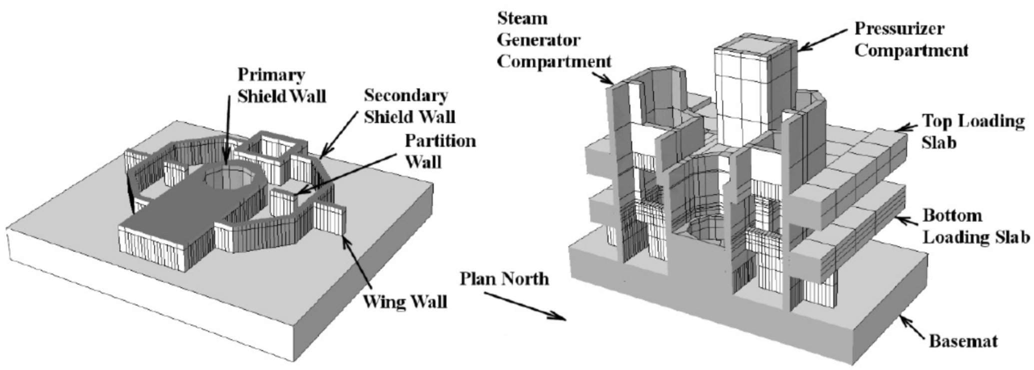

Figure 2-4 Overview of the 1/10-scale CIS specimen [Varma et al. (2013a)]

On the basis of their test results, they proposed empirical equations to predict the resistance of an SC wall at the onset of concrete cracking, steel faceplate yielding, and peak strength. Their equation to predict the peak shear strength is:

$$V_u = 0.57 f_y A_s + 4.5\sqrt{f_c'} A_c \tag{2-6}$$

where A_s and A_c are the cross-sectional areas of the steel faceplates and infill concrete, respectively; and f_y and f_c' are the yield strength of the steel faceplates and the compressive strength of the infill concrete, respectively. The equivalent viscous damping of the specimen, calculated using hysteresis loops from the cyclic test, was 5% prior to the yielding of the steel faceplates and up to 20% after the yielding of the steel faceplates.

Wright et al. (1991b) conducted 53 tests on 1/3-scale double skin composite beam, column, and beam-column specimens to investigate the effects on response of connector spacing, thickness of the steel faceplates, concrete strength, length of the connectors, load eccentricity, and axial load variation. A 5.9 × 5.9 in. cross-section was used for all specimens. The length of the specimens varied between 60 in. and 90 in. The specimens were simply supported at their ends and subjected to two concentrated out-of-plane loads, 7 in. away from the mid-span of the specimen. Wright et al. suggested the results of those beam and column tests could be indicative of composite wall behavior assuming a plane strain state. The peak shear and axial strengths, and damage were reported. Wright et al. (1991a) used the experimental results to develop a design guideline for composite elements. Empirical equations were provided to characterize the strength and stiffness of composite sections. The proposed empirical equations were validated using results of tests of eleven large-scale beam, column and beam-column specimens. Recommendations were made for the construction and detailing of the double skin composite structures.

Takeda et al. (1995) tested seven composite wall panels subjected to cyclic, in-plane, pure shear loading to investigate the effects of thickness of the steel faceplates, partitioning webs, and the use of studs, on the shear response of the SC panels. The length and height of the panels were 47 in. and the thickness of all specimens was 7.8 in. The specimens were composed of two steel faceplates, infill concrete, headed steel studs anchoring the faceplates to the infill, and the partitioning webs connecting the steel faceplates together. The test specimens are shown in Figure 2-5.

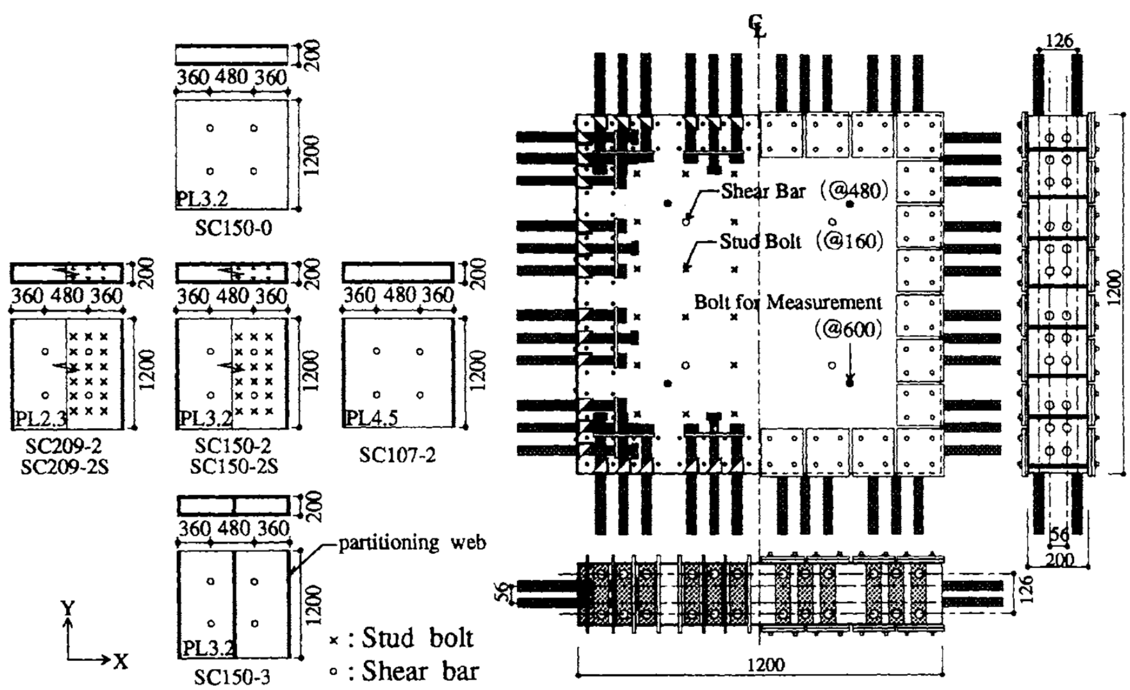

Figure 2-5 Test specimens [Takeda et al. (1995)]

The typical failure mode was concrete cracking, followed by buckling of the steel faceplates, following faceplate yielding. The authors reported that the studs had no effect on the strength, ductility and hysteretic behavior of the test specimens. Takeda et al. parsed the pre-peak-strength response into four regions, namely 1) elastic, 2) post-concrete cracking, 3) post-buckling of the steel faceplates, and 4) post-yielding of the steel faceplates. The shear response of SC panels was idealized as a perfectly-plastic force-displacement relationship since the shear strength of these SC panels did not deteriorate at shear strains greater than 2%. Damage included concrete cracking, and buckling and local tearing of the steel faceplates. An ultimate shear strain of 8% was proposed for SC panels subjected to pure shear loading on the basis of the test results

Takeuchi et al. (1995) summarized the results of a feasibility study on SC wall construction and compared the time and cost to build RC and SC walls, as presented in Figure 2-6.

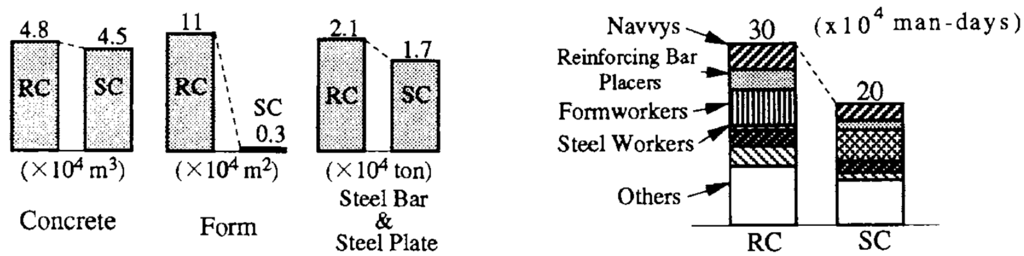

(a) Material quantities (b) Manpower requirements

Figure 2-6 Results of the feasibility study [Takeuchi et al. (1995)]

They synthesized the results of tests on SC walls performed in Japan: 1) compression tests to investigate the optimum spacing of the headed studs, 2) shear and bending tests to investigate the in-plane shear and flexural responses of H-shaped (flanged) SC walls with web reinforcement ratios ranging between 0.7% and 2%, and 3) tests to study the effect on response of the connection of an SC wall to its foundation. The test specimens are described in Figure 2-7.

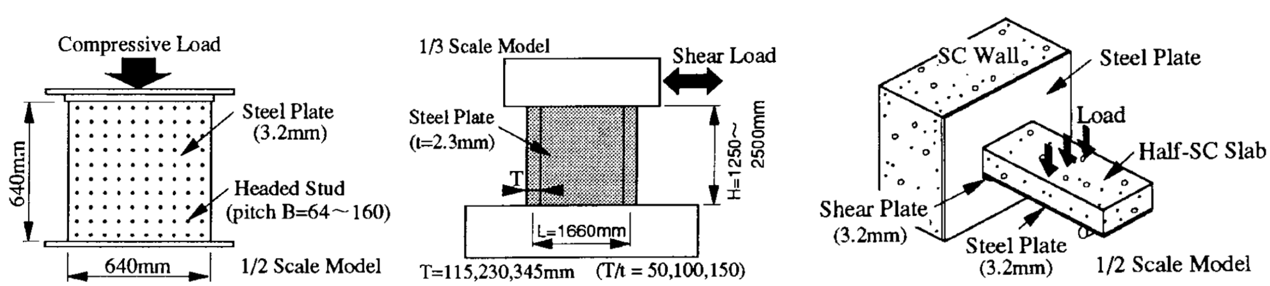

(a) Compression test (b) Shear and bending test (c) Wall-foundation joint test

Figure 2-7 Three types of SC wall experiments [Takeuchi et al. (1995)]

Four 1/5-scale SC walls were subjected to cyclic compressive loading by Usami et al. (1995) with particular attention being paid to the buckling characteristics of the steel faceplates. The specimens were composed of two steel faceplates, two steel flange plates, infill concrete, and headed studs. The faceplate slenderness ratio varied between 20 and 50. Drawings of the test specimens are reproduced in Figure 2-8.

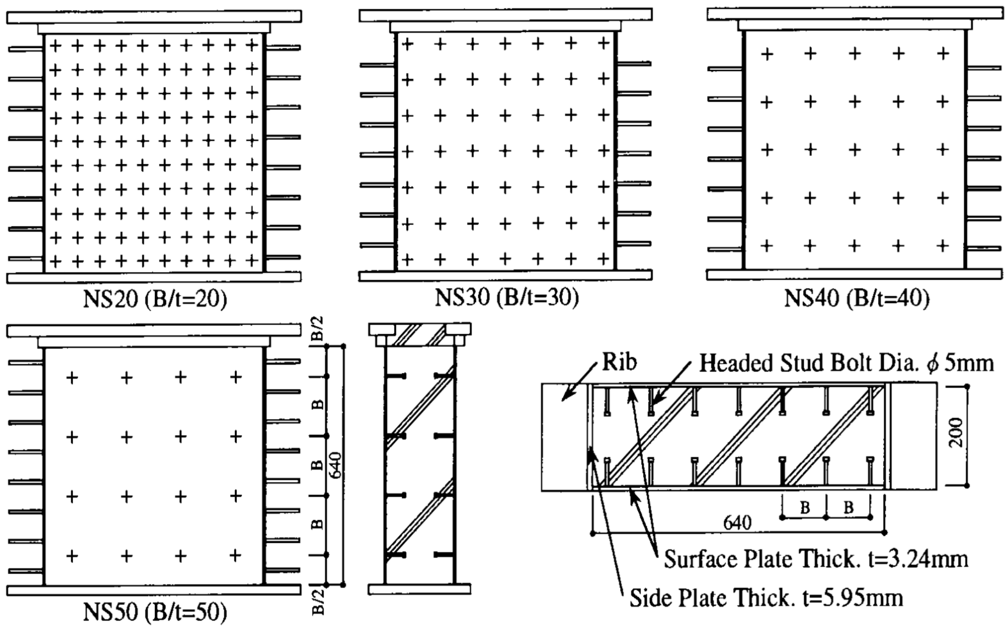

Figure 2-8 SC wall specimens [Usami et al. (1995)]

Usami's study indicated that the axial load-displacement relationship of an SC wall did not change abruptly at the onset of buckling and yielding of the steel faceplates. They proposed that the Euler equation for elastic buckling of a column with a fixed-pinned boundary condition would accurately predict the buckling stress of the steel faceplates using B/t_s as the slenderness ratio for cases with buckling stress less than $0.6f_y$, where B is the spacing between the studs, t_s is the thickness of each steel faceplate, and f_y is the yield stress of the steel faceplates. The Euler equation over-predicted buckling stress when it exceeded $0.6f_y$. Test results and the proposed relationship between buckling stress of the steel faceplates and slenderness ratio are presented in Figure 2-9.

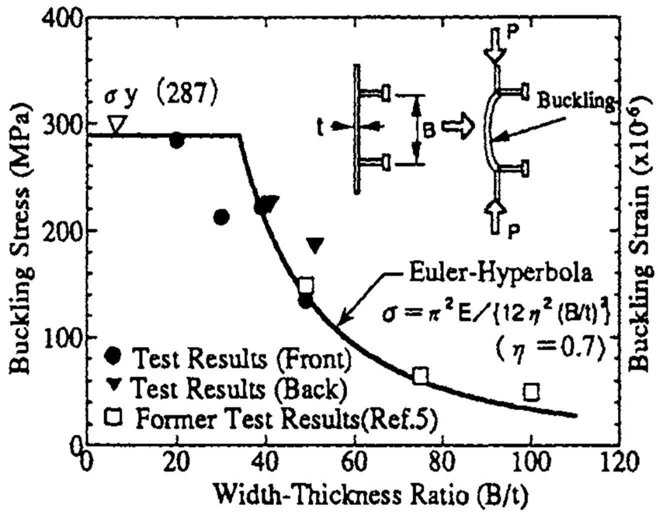

Figure 2-9 Buckling stress of the steel faceplates [Usami et al. (1995)]

Sasaki et al. (1995) tested seven flanged SC wall specimens with aspect ratios ranging between 1/3 and 1/2 to investigate the effects of aspect ratio, reinforcement ratio, axial load, and the use of headed studs attached to the end plates of the web wall (see the plan view of the SC wall in Figure 2-10) on the flexural-shear response of SC walls. A faceplate slenderness ratio of 33 was used. Damage to the SC walls included concrete cracking, yielding and buckling of the steel faceplates, and concrete crushing. On the basis of the test data, the lateral stiffness and peak shear strength of an SC wall increases with decreasing shear span-to-depth ratio and increasing reinforcement ratio. The peak shear strength increased, but the initial stiffness did not, as the axial load was increased. The use of headed studs at the connection of the flange walls and the web wall had no effect on response. A comparison of the responses of SC and RC walls with a shear span-to-depth ratio of 0.8 and a reinforcement ratio of 1.7% indicated that the peak shear strength and the displacement at peak strength were substantially greater for the SC wall than for the RC wall.

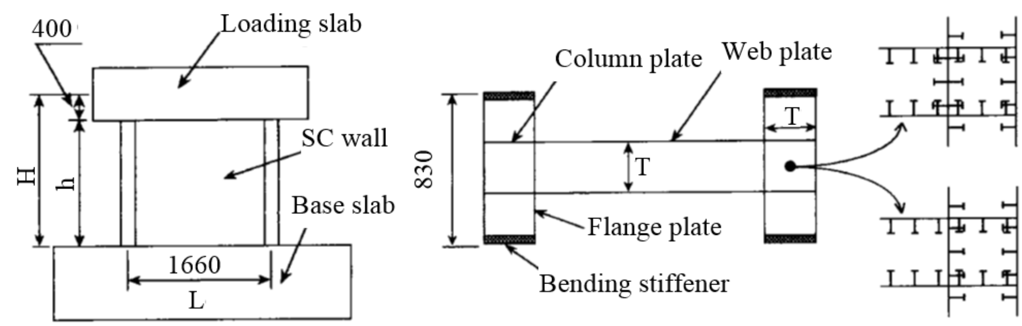

Figure 2-10 SC wall specimen [Sasaki et al. (1995)]

Suzuki et al. (1995) proposed an analytical method to predict the peak shear strength of H-shaped (flanged) SC walls by assuming that the shear load was resisted by a combination of arch and truss mechanisms as presented in Figure 2-11. The study indicated that the orientation of the concrete strut affected the contributions of the truss- and arch-action mechanisms to the peak shear strength but that the peak shear strength of SC wall was not significantly influenced. The concrete strut, shown in Figure 2-11(b), is oriented at 45° to the horizontal.

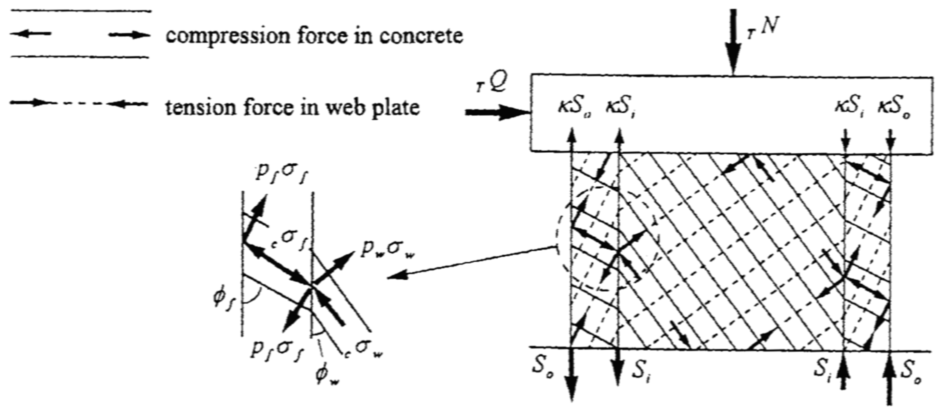

(a) Truss mechanism

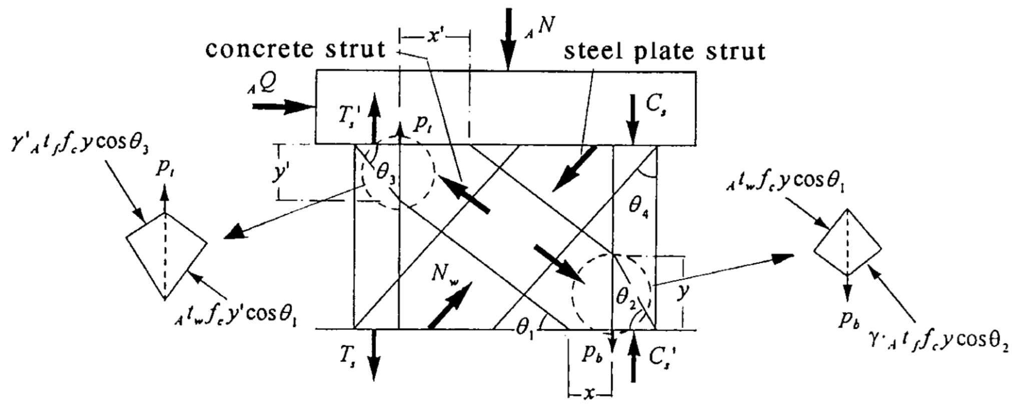

(b) Arch mechanism

Figure 2-11 Load transfer mechanisms in flanged SC walls [Suzuki et al. (1995)]

Takeuchi et al. (1995) proposed an analytical method to simulate the pure shear behavior of SC walls in three regions, namely, 1) elastic, 2) post-concrete cracking, and 3) post-steel buckling. Figure 2-12 presents the load transfer mechanism in an SC panel subjected to a lateral loading. Takeuchi et al. proposed an ultimate shear strain of 0.06% for the analysis of SC panels on the basis of available results on pure shear testing of SC panels. Figure 2-13 presents the SC construction considered by Takeuchi et al. (1998).

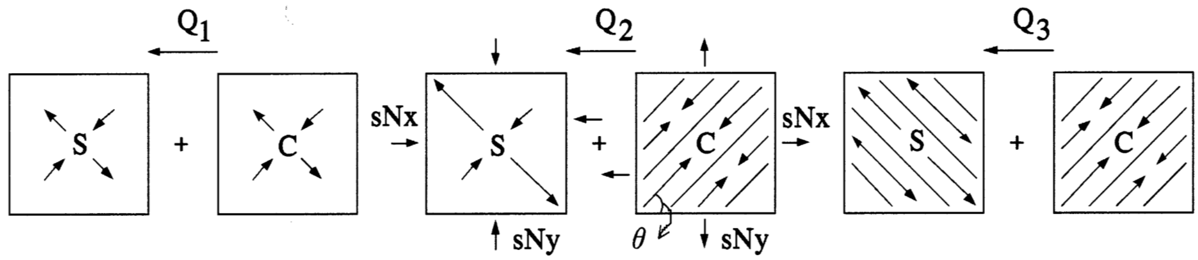

(a) Elastic (b) Post-concrete cracking (c) Post-steel faceplate yielding

Figure 2-12 Load transfer mechanism of an SC panel under pure shear loading [Takeuchi et al. (1995)]

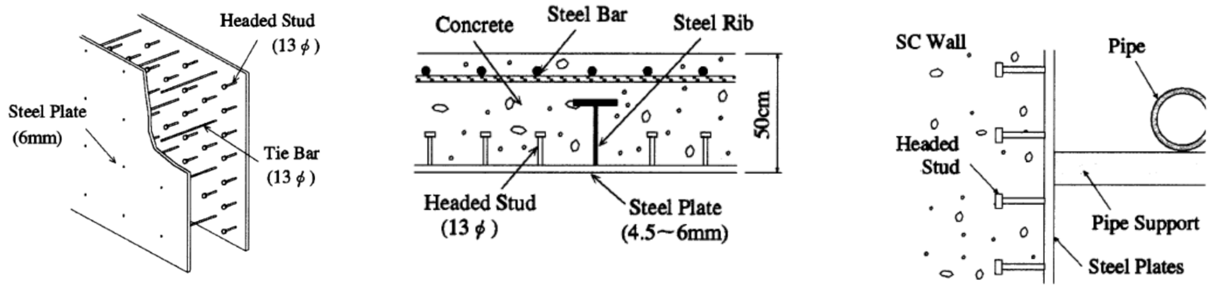

(a) SC wall panel (b) SC floor (c) Pipe supports

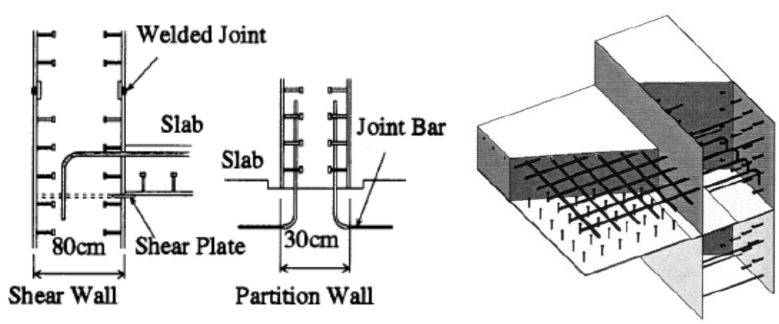

(d) SC wall joints

Figure 2-13 Proposed details for SC construction [Takeuchi et al. (1998)]

A tri-linear shear force-shear strain relationship, similar to that proposed by Takeuchi et al. (1995), was proposed by Akita et al. (2001) considering concrete cracking, faceplate yielding, and concrete crushing. The ultimate shear strain was assumed to be 6000 micro strain, corresponding to a concrete diagonal compressive strain of 3000 micro strain. They proposed that the moment-curvature relationship of an SC wall could be calculated using the moment-curvature relationship of an equivalent RC wall having a cross-section with identical dimensions to those of the infill concrete cross-section and a reinforcement ratio equal to the ratio of the cross-sectional area of the steel faceplates to the total cross-sectional area of the SC wall. The ultimate bending moment was calculated using the results of a plastic analysis of the SC wall cross-section.

Tsuda et al. (2001) conducted an experimental study to investigate the behavior of connections of an SC wall to an RC foundation. Figure 2-14 identifies the alternatives considered, which included joint bars. The shear load was assumed to be transferred from the steel faceplates to the infill concrete by shear studs and from the infill concrete to the base slab by joint bars. The joint-bar connection included horizontal tie bars enclosing the joint bars over a limited height above the foundation to avoid a bond failure of the connection.

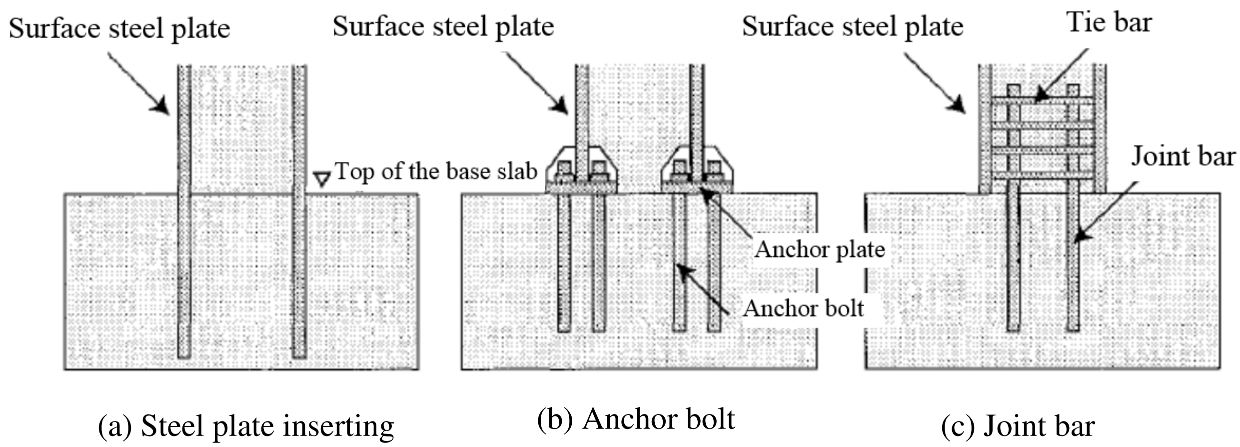

Figure 2-14 Types of connection of an SC wall to its foundation [Tsuda et al. (2001)]

Figure 2-15 shows a base connection using joint bars, and steel web plates instead of tie bars. Tsuda et al. conducted a series of pull-out tests to investigate the effects of embedment depth of the joint bars, length of the partitioning steel web, number of joint bars, and number of layers of joint bars on the tensile strength of the connection. They developed an equation to predict the tensile strength of the connection on the basis of the test results.

The global response of SC walls equipped with the proposed joint-bar connection was investigated by testing four walls under cyclic lateral loading. The aspect ratio of the walls varied from 0.62 to 1.23. The test results were used to develop an analytical method to predict the shear and flexural responses of SC walls.

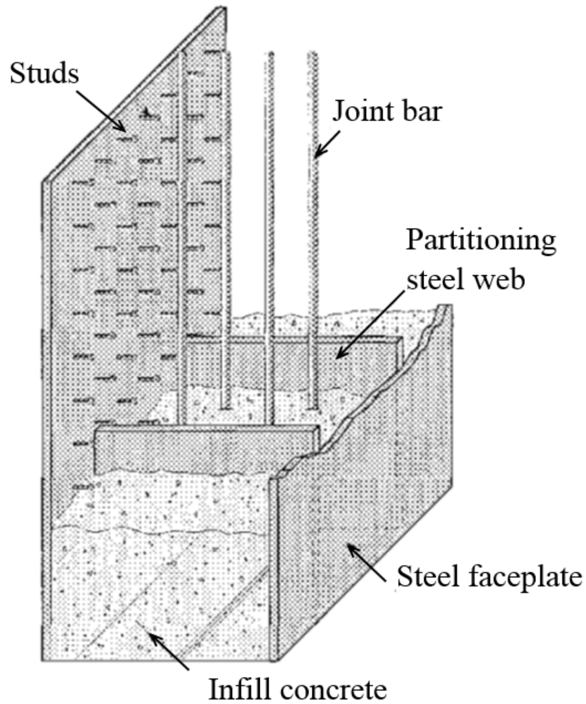

Figure 2-15 Proposed joint-bar connection [Tsuda et al. (2001)]

Ozaki et al. (2001b) investigated the effect of web openings on the cyclic shear response of SC walls by testing six SC panels with through-thickness circular and square openings at the center of the web, and one solid SC panel. The ratio of the surface area of the opening to the surface area of the SC panel was 0.15. The presence of the opening had no effect on the shear strain of the SC panels at the onset of concrete cracking and steel faceplate yielding. The shear strain at the peak shear resistance of the SC walls with openings was a factor of 2 to 3 than that of the solid SC wall. On the basis of the test data, Ozaki et al. developed an analytical method to predict the response of SC panels with openings by applying reduction factors on the stiffness and strength of solid SC panels, where the reductions factors were derived as a function of the dimensions of the opening. Finite element analyses were conducted to convert the proposed reduction factors for the effect of reinforcement around the opening.

Ozaki et al. (2001a) tested flanged SC walls with different aspect and reinforcement ratios under lateral loading to investigate the in-plane response of shear-critical and flexure-critical SC walls. Five shear-critical SC specimens with aspect ratios ranging from 0.5 to 0.85 and reinforcement ratios ranging from 0.7% to 2% were tested. The SC specimens were connected to their foundation by extending the steel faceplates and the infill concrete into the foundation concrete. The reinforcement ratio had a small effect on the initial stiffness and cracking strength of the shear-critical SC walls but it significantly affected the yield and the peak shear strengths. The displacements corresponding to the yield and peak shear strengths were not affected by the reinforcement ratio. Ozaki et al. proposed that the tensile and shear stresses in the concrete at the onset of cracking were $1.2\sqrt{f_c'}$ and $\sqrt{f_c'}$ (units in kg and cm), respectively. Four flexure-critical SC walls with aspect ratios of 0.7 and 0.85, and a reinforcement ratio of 2%, were tested. The flexure-critical SC walls were connected to their foundations using baseplates and anchor bars. The design parameters considered in this part of the study were aspect ratio, axial force, and SC wall connection to the foundation block. Ozaki et al. proposed that the flexural strength of flexure-critical SC walls be calculated using the results of a plastic analysis of the SC wall cross-section. Drawing of the test specimens are reproduced in Figure 2-16.

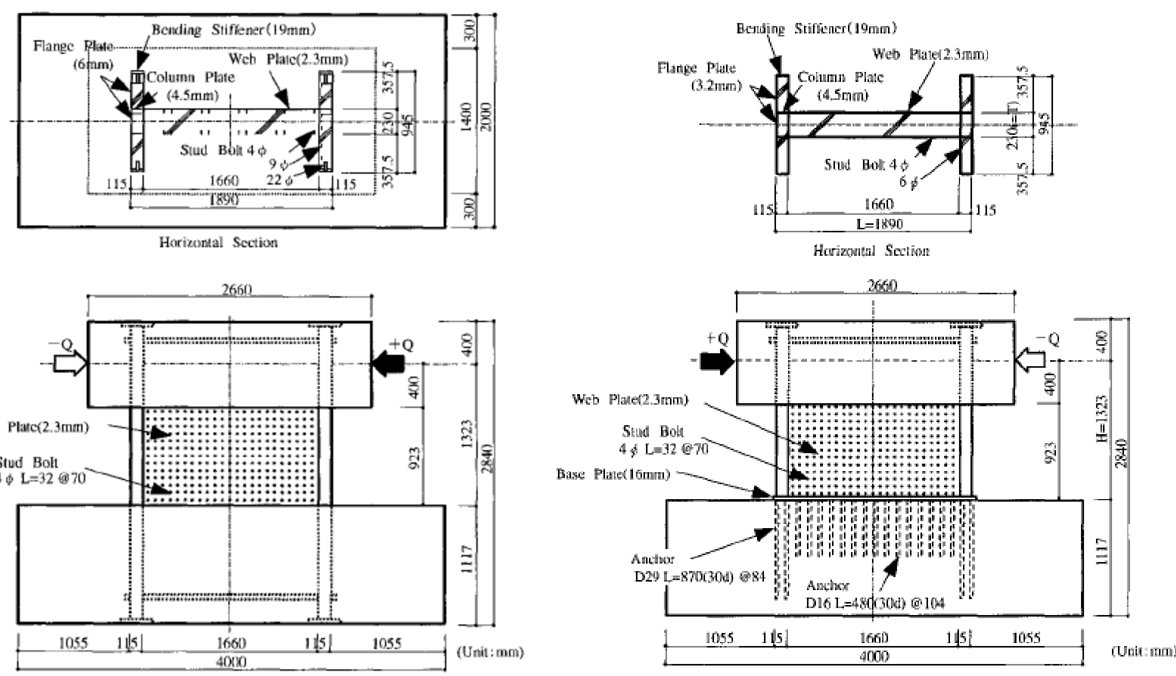

(a) Shear-critical specimen (b) Flexure-critical specimen

Figure 2-16 Test specimens [Ozaki et al. (2001a)]

Emori (2002) tested three 1/4-scale SC wall box units (specimens 200K, 100K, and 67K in Table 2-1) under shear and axial compressive loads. The SC wall box units were constructed by assembling and welding the prefabricated steel box units consisting of two steel faceplates and vertical and horizontal partition plates, and filling the boxes with concrete. Headed studs and tie rods were not used. To investigate the effect of composite action on the response of the SC wall boxes, one steel plate box specimen (100S in Table 2-1) and two concrete solid specimens (0C and

1C in Table 2-1) were included in the test program. In Table 2-1, the width-to-thickness ratio is the spacing between the partition plates divided by the thickness of each steel faceplate.

Results of the shear and axial compression tests are presented in Figure 2-17. The width-to-thickness ratio, b/t_s, had a significant effect on the axial strength but only a minor effect on the shear strength. The pre-peak shear response and the displacement corresponding to the peak shear strength were significantly affected by the width-to-thickness ratio.

Table 2-1 Test specimens [Emori (2002)]

Width-to-thickness ratio (b/t_s)	Cross-sections		
	(SC)	(S)	(C)
200	(200K) 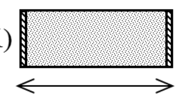 b=640 mm	-	For compression test (0C)  For shear test (1C) 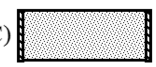
100	(100K) 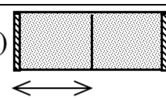 b=320 mm	(100S) 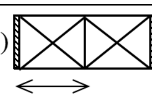 b=320 mm	
67	(67K) 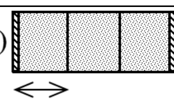 b=213 mm	-	-

The results of the axial and shear tests of the composite panels, steel plate boxes, and concrete panel were used to study the effect of composite action on the shear and axial responses of SC walls. Figure 2-18 shows that the shear and axial compressive responses of the SC walls were affected by composite action. The axial and shear strengths of the SC walls were 15% and 43% greater than the corresponding superposed strengths of the steel boxes and concrete panels, respectively. These results showed that composite action, which delayed local buckling of the steel faceplates and confined the infill concrete, had significant effect on the behavior of the composite panels.

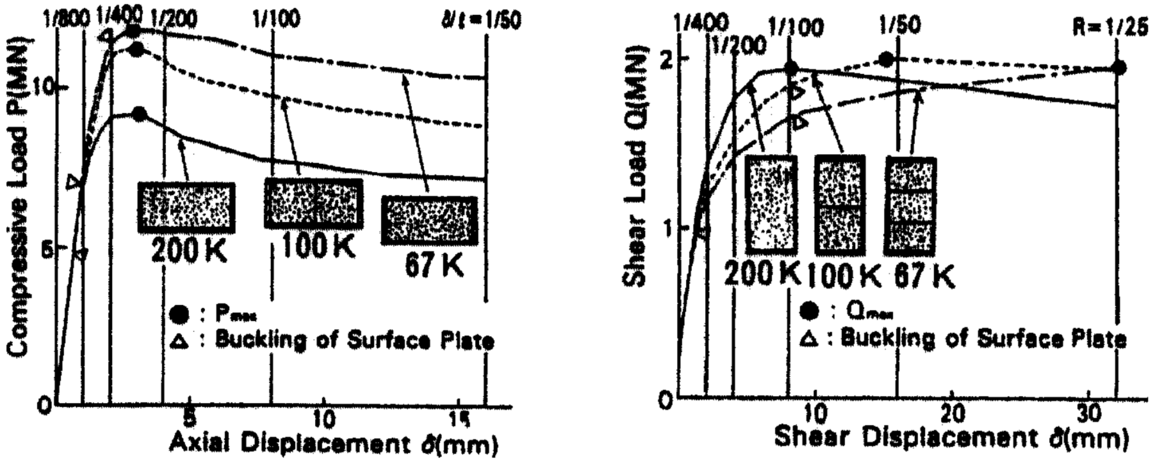

(a) Compression test (b) Shear test

Figure 2-17 Axial and shear responses of SC wall box units [Emori (2002)]

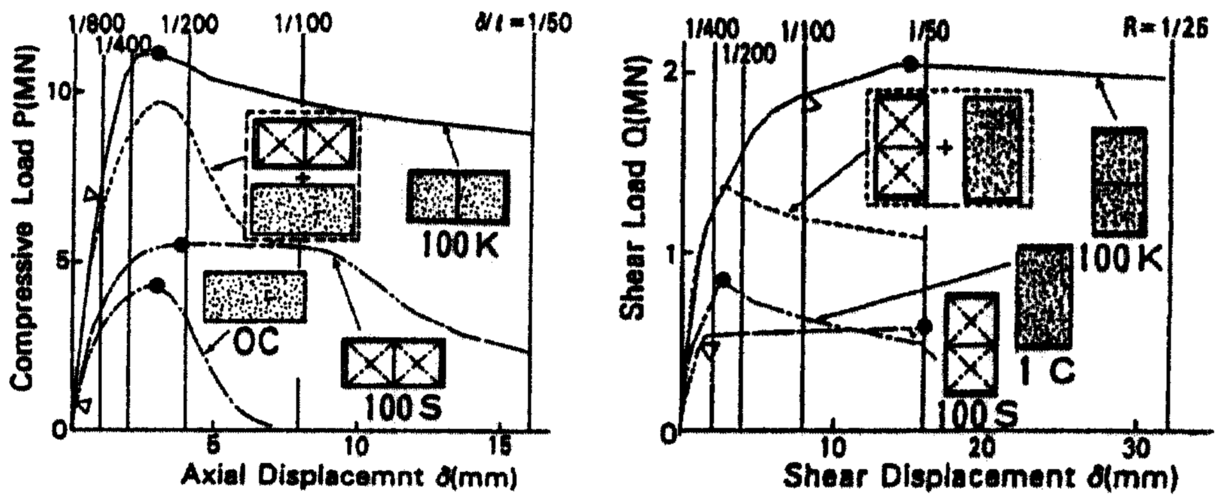

(a) Compression test (b) Shear test

Figure 2-18 Effects of composite action on axial and shear responses [Emori (2002)]

Zhao et al. (2004) tested two 1/2-scale three-story composite shear walls consisting of a single steel faceplate welded to the surrounding steel frame and a precast reinforced concrete panel bolted to the steel faceplate. In one specimen, termed a *traditional composite wall*, the reinforced concrete panel was in direct contact with the boundary steel beams and columns. In the second, termed an *innovative composite wall*, a 1.25 in. gap between the reinforced concrete panel and the surrounding steel frame was maintained to avoid early cracking and crushing of the concrete. The innovative composite wall exhibited similar responses to that of a stiffened steel plate shear wall at small lateral displacements. Upon closing the gap between the reinforced concrete panel and the boundary steel framing, the reinforced concrete panel contributed to the lateral resistance of the composite wall. Schematic drawings of the test specimens are reproduced in Figure 2-19. Both specimens resisted lateral loading greater than 80% of the peak strength up to a drift ratio of 5%. The rate of the post-peak strength deterioration of the traditional composite wall was greater than that of the innovative composite wall because the gap between the reinforced concrete panel and the boundary columns and beams delayed severe damage to the concrete wall. Importantly, the lateral stiffness and peak shear strength were not significantly affected by the presence of the gap since the contribution of the concrete panel to the total strength and lateral stiffness was estimated to be less than 20%. Zhao et al. proposed that the shear strength of the reinforced concrete panel could be ignored in the calculation of the peak shear strength of the composite wall but that its stiffness should be included in calculations of force-displacement response.

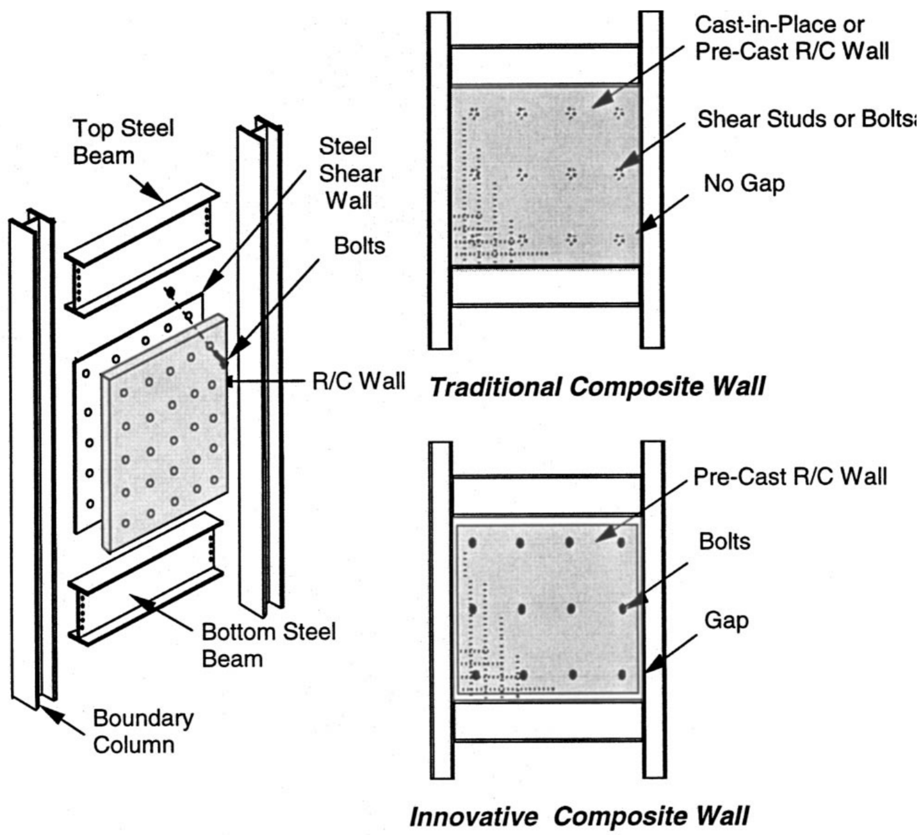

Figure 2-19 Composite shear walls [Zhao et al. (2004)]

Ozaki et al. (2004) tested nine SC panels subjected to cyclic in-plane shear loading to investigate the effects of steel faceplate thickness, axial compressive loading, and partitioning webs on the shear response of SC panels. Figure 2-20 presents a cut-away view of the SC panel.

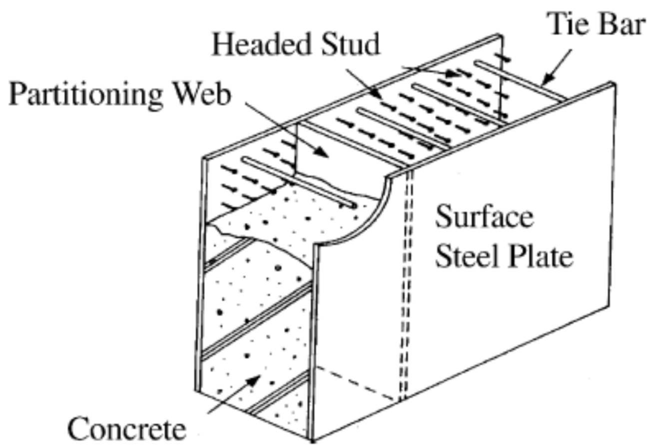

Figure 2-20 SC panel [Ozaki et al. (2004)]

On the basis of the test results, the greater the steel faceplate thickness, the greater the elastic shear stiffness, the post-cracking shear stiffness, and the yield and peak strengths of SC wall but the lower the shear strain at peak strength. The elastic shear stiffness was not influenced by the axial compressive force. However, as the axial compressive force increased, the post-cracking shear stiffness decreased slightly. An increase in the axial compressive force increased the shear strength at the onset of concrete cracking but it had no effect on the yield and peak shear strengths for the range of axial loads applied (0 to $0.07 A_c f_c'$, where A_c is the cross-sectional area of the infill concrete and f_c' is the compressive strength of the concrete). The partitioning webs in the specimens tested by Ozaki et al. had no impact on the yield and peak shear strengths of the SC panels.

Ozaki et al. parsed the in-plane response of SC walls in shear into three regions: 1) elastic, 2) concrete cracking, and 3) steel faceplate yielding. In the elastic range, the infill concrete and the steel faceplates were modeled using an isotropic elastic and isotropic elastic plane-stress behaviors, respectively. They proposed that the shear stress, τ_c, in an SC wall at the onset of concrete cracking could be calculated as:

$$\tau_c^2 = \sigma_t^2 + \sigma_t \sigma_a \tag{2-7}$$

where σ_a is the axial compressive stress on the infill concrete and σ_t is the tensile strength of the infill concrete. Substituting $\sigma_t = 0.33\sqrt{f_c'}$ (unit:MPa), as proposed by Collins et al. (1991), into (2-7) results the shear stress of SC walls at the onset of concrete cracking as:

$$\tau_c = \sqrt{0.33\sqrt{f_c'}(0.33\sqrt{f_c'} + \sigma_a)} \tag{2-8}$$

The shear strength of SC wall at the onset of steel faceplate yielding and the peak shear strength were calculated as:

$$Q_y = \frac{k(G_c + G_s)}{\sqrt{G_c^{\ 2} + 3k^2 G_s^{\ 2}}} \frac{f_y A_w}{2} \tag{2-9}$$

$$Q_u = (A_w + A_p) f_y \tag{2-10}$$

where G_c and G_s are the elastic shear moduli of the infill concrete and steel faceplates, respectively; f_y is the yield stress of the steel faceplates; A_w is the cross-sectional area of the steel faceplates; and k is calculated as:

$$k = 1 + (1 - \nu_s) p_{dx} \tag{2-11}$$

where p_{dx} is the ratio of the cross-sectional area of the horizontal partitioning webs to the cross-sectional area of the steel faceplates and ν_s is Poisson's ratio for the steel faceplates.

Booth et al. (2007) tested two full-scale, simply supported, 22-ft long beams to study the out-of-plane behavior of composite walls. The specimens were subjected to thermal and mechanical loadings. The mechanical loading included two concentrated loads applied at third points of the beam. The effect of thermal loading on the shear and flexural responses was studied. The concrete cracking patterns at different thermal and mechanical loading conditions were documented. Exposure of the beams to an elevated temperature leaded to severe concrete cracking; the out-of-plane flexural stiffness of the cracked specimens was reduced to 14% of that of the un-cracked specimens. Booth et al. developed a 2D fiber-based finite element model assuming 1) 2D plane stress behavior for the steel faceplates and infill concrete, 2) plane section remains plane, and 3) perfect bond between the steel faceplates and the infill concrete. Booth's model successfully predicted the flexural stiffness of the SC walls at ambient conditions but the temperature-induced deformations could not be predicted accurately due to the simplified modeling assumptions. Booth et al. then conducted further research [Varma et al. (2009)] to improve the analytical approach for predicting the behavior of SC walls subjected to combined thermal and mechanical loadings.

Eom et al. (2009) tested three 1/3-scale solid SC walls and two 1/4-scale coupled SC walls under cyclic lateral loading. The walls had rectangular and T-shaped (flanged) cross sections. The SC walls were flexure-critical with aspect ratios of 3.7 and 2.7 for the solid and coupled walls, respectively. The spacing of the tie rods connecting the two steel faceplates, divided by the thickness of each steel faceplate was 30 and 50 for the solid and coupled walls, respectively. The steel faceplates were CJP-welded to a baseplate in one solid SC wall: specimen DSCW1N presented in Figure 2-21. Due to the premature fracture of the welded connection of the faceplates to the baseplate at 1.5% drift ratio, and prior to flexural yielding of the steel faceplates, triangular rib plates were welded to the both ends of the SC wall cross section (specimen DSCW1H in Figure 2-21) and specimen was re-tested. The addition of the rib plates did not significantly improve the response of the SC wall and so the rib-plates were removed and the specimen was strengthened by fillet welding cover plates to the steel faceplates, flange plates, and the baseplate (specimen DSCW1C in Figure 2-21) and re-tested. The coupled wall specimens DSCW4 and DSCW5 were strengthened to avoid the premature failure seen in the solid walls through the addition of cover plates, which are identified in Figure 2-22.

The test results indicated that the addition of cover plates at the base of the SC walls significantly improved the shear response and avoided the premature fracture of the welded connection of the faceplates to the baseplate. The SC walls failed due to the steel faceplate buckling and crushing of the infill concrete above the cover plates. Eom et al. proposed an analytical method to predict the shear strength of rectangular and T-shaped SC walls on the basis of a plastic analysis of an SC wall cross-section. Perfect bond between the steel faceplates and infill concrete was assumed and the effect of axial load was considered.

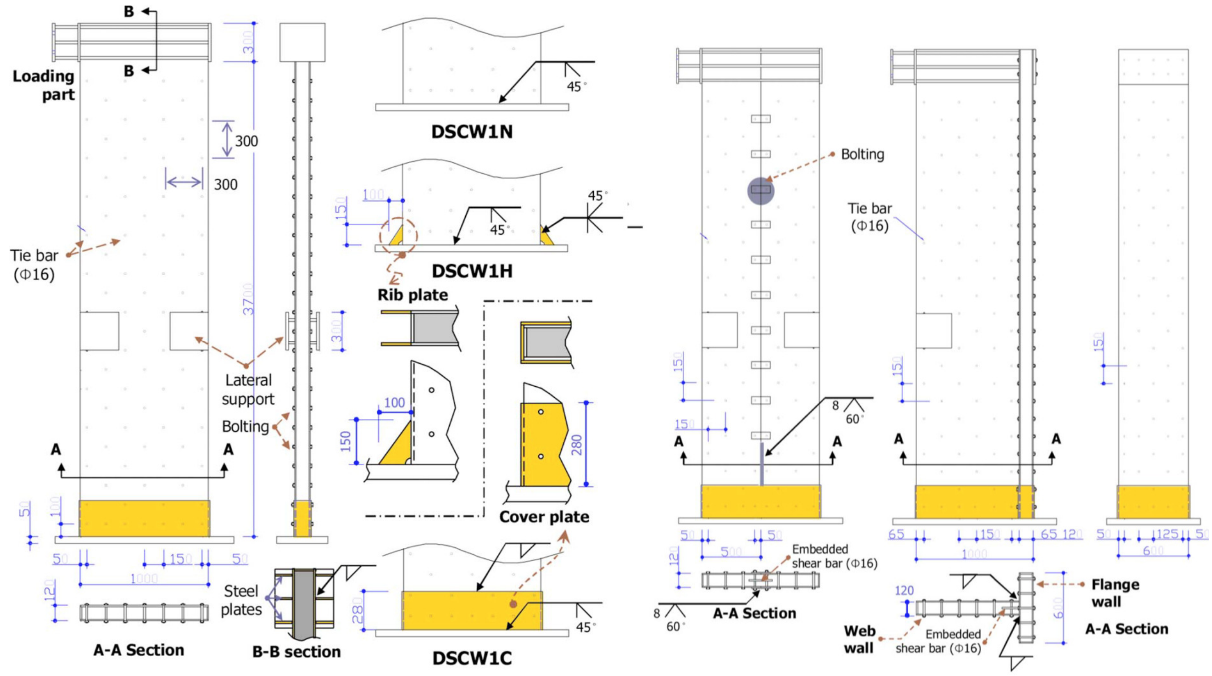

(a) DSCW1 (b) DSCW2 (c) DSCW3

Figure 2-21 Isolated SC wall specimens [Eom et al. (2009)]

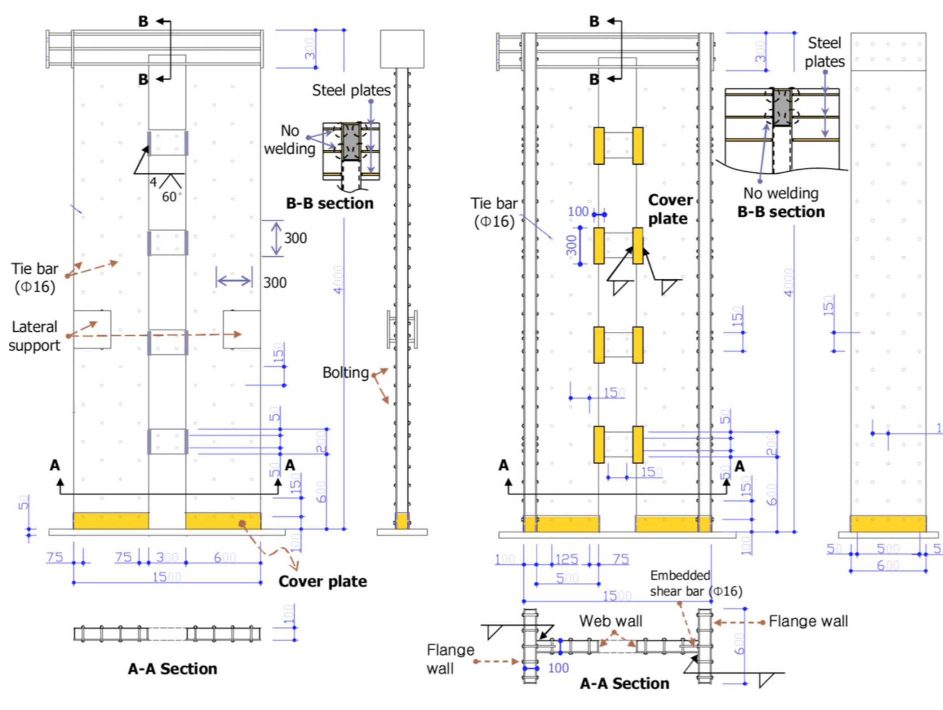

(a) DSCW4 (b) DSCW5

Figure 2-22 Coupled SC wall specimens [Eom et al. (2009)]

Hong et al. (2010) tested nine SC beams subjected to concentrated out-of-plane loads at different locations along the beam span to investigate the out-of-plane behavior of SC walls. The design parameters considered in the investigation were shear-to-span ratio, steel faceplate thickness, and shear reinforcement ratio, A_{sv}/sb, where A_{sv} is the cross-sectional area of the shear reinforcement, s is the spacing of the reinforcement, and b is the width of the beam. Shear reinforcement consisted of two #5-leg ties at 15 in. on center. Headed studs, tie rods, and H-shaped steel profiles were used as connectors. Load-deflection curves for the beams, cracking patterns in the infill concrete, and strain distributions in the steel faceplates were documented.

Similar to the analytical approach proposed by Ozaki et al. (2004), Varma et al. (2011c) developed mechanics-based equations to predict the in-plane shear response of SC walls. Concrete cracking was assumed to occur when the shear force exceeded the cracking threshold corresponding to a principal tensile stress of $2\sqrt{f_c'}$ (psi), which indirectly accounted for the effects of restrained shrinkage in the infill concrete. The infill concrete was assumed to behave as an orthotropic elastic material with a) no stiffness perpendicular to the direction of cracking and b) 70% of the elastic compression modulus (E_c) in the orthogonal direction. The stiffness of the cracked SC wall was calculated assuming orthotropic behavior of the infill concrete and isotropic elastic plane stress behavior of the steel faceplates. Varma et al. assumed that the peak shear strength of SC walls corresponded to the onset of the yielding of the steel faceplates.

The proposed method was used to predict the in-plane shear response of the SC walls tested by Ozaki et al. (2004). The method successfully predicted the initial stiffness of the SC walls but the peak shear strength was underestimated because the peak shear strength was associated with the onset of steel faceplate yielding.

Varma et al. (2011c) tested a large-scale flanged SC wall subjected to lateral loading to validate the proposed analytical method. The web and flanges of the SC wall were designed to resist shear force and bending moments, respectively. The reinforcement ratio $(=2t_s/T)$ and the slenderness ratio (s/t_s) of the SC wall were 4.2% and 11.3, respectively, where t_s is the thickness of each steel faceplate, T is the thickness of the web of the SC wall, and s is the spacing of the studs. Good agreement was obtained between the analytical and test results. A photograph of the specimen is shown in Figure 2-23.

Figure 2-23 Test specimen [Varma et al. (2011c)]

Varma et al. (2011a) tested an SC beam, similar to those tested by Booth et al. (2007), but subjected to larger displacements. The beam was subjected to thermal and mechanical loading. Varma et al. proposed that the out-of-plane flexural stiffness of the composite section away from the heated region could be reasonably predicted using cracked transformed section properties (see Figure 2-24(a)). At the center of the heated region, the thermal gradient through the specimen depth caused significant cracking in the infill concrete. Varma et al. assumed that the fully cracked infill concrete did not contribute to the out-of-plane flexural stiffness and the initial slope of the moment-curvature relationship of the heated composite beam could be reasonably predicted using the out-of-plane flexural stiffness of the steel faceplates alone. As seen in Figure 2-24(b), the thermal gradient through the specimen depth shifted the origin of the moment-curvature relationship to a negative curvature, ϕ_{th}, as a thermal-induced curvature for zero moment. The curvature ϕ_{th}, generated due the thermal gradient through the specimen depth in the absence of mechanical loading, was calculated as:

$$\phi_{th} = \frac{\alpha_s \Delta T}{T - t_s} \tag{2-12}$$

where α_s is the thermal expansion coefficient of the steel faceplates; ΔT is the increment of the temperature; and T and t_s are the thicknesses of the SC section and each steel faceplate, respectively. The moment at zero curvature, M_{th}, was calculated as:

$$M_{th} = E_s I_s \phi_{th} \tag{2-13}$$

where $E_s I_s$ is the flexural rigidity of the steel faceplates.

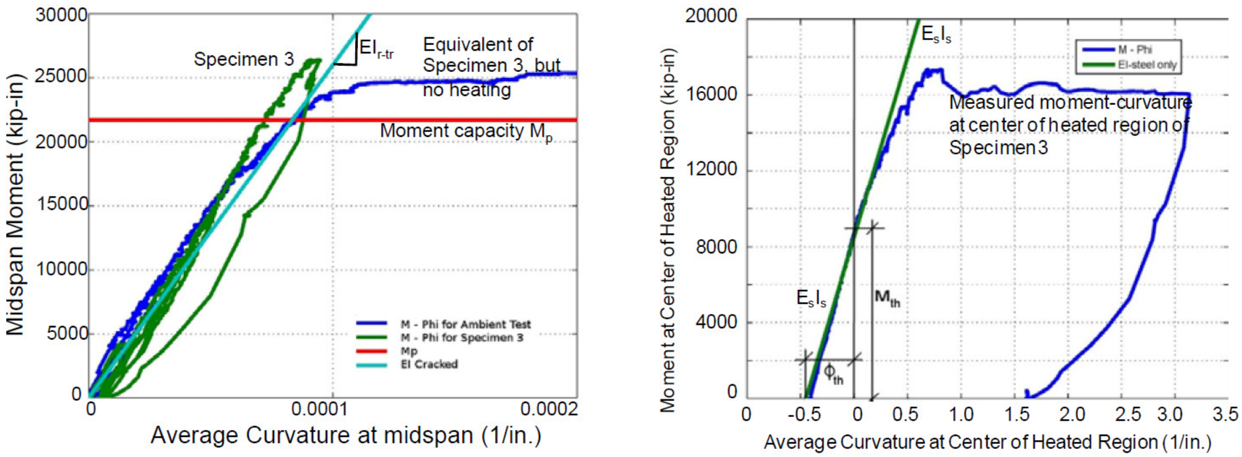

(a) Away from heating region (b) At center of heated region

Figure 2-24 Moment-curvature relationship of a composite beam section [Varma et al. (2011a)]

Varma et al. derived an equation to predict the out-of-plane flexural stiffness of SC section using the cracked transformed composite section properties. The simplest form of the derived equation [Varma et al. (2011a)] is:

$$EI_{cr-tr} = E_s I_s + \beta E_c I_c \tag{2-14}$$

where $E_c I_c$ is the flexural rigidity of the infill concrete; and β is $0.48\rho' + 0.1$, where ρ' is the stiffness normalized reinforcement ratio and was calculated as:

$$\rho' = \frac{2t_s}{T}\frac{E_s}{E_c} \tag{2-15}$$

They proposed Equation (2-16) to predict the out-of-plane flexural stiffness of SC walls taking into account the reduction of stiffness due to concrete cracking and thermal effects.

$$EI_{eff} = (E_s I_s + \beta E_c I_c)(1 - \frac{\Delta T}{150^\circ F}) \geq E_s I_s \tag{2-16}$$

Equation (2-16) calculates the out-of-plane flexural stiffness of the composite section at temperatures greater than 150°F to be that of the steel faceplates only.

Nie et al. (2014) tested twelve SC walls subjected to high axial and cyclic lateral loads to investigate the effects of reinforcement ratio, concrete strength, thicknesses of the steel face and flange plates, concrete reinforcement, and wall aspect ratio on the in-plane response of SC walls. The reinforcement and aspect ratios varied from 4.6% to 7.1% and from 1 to 2, respectively. A photograph of the test setup is presented in Figure 2-25.

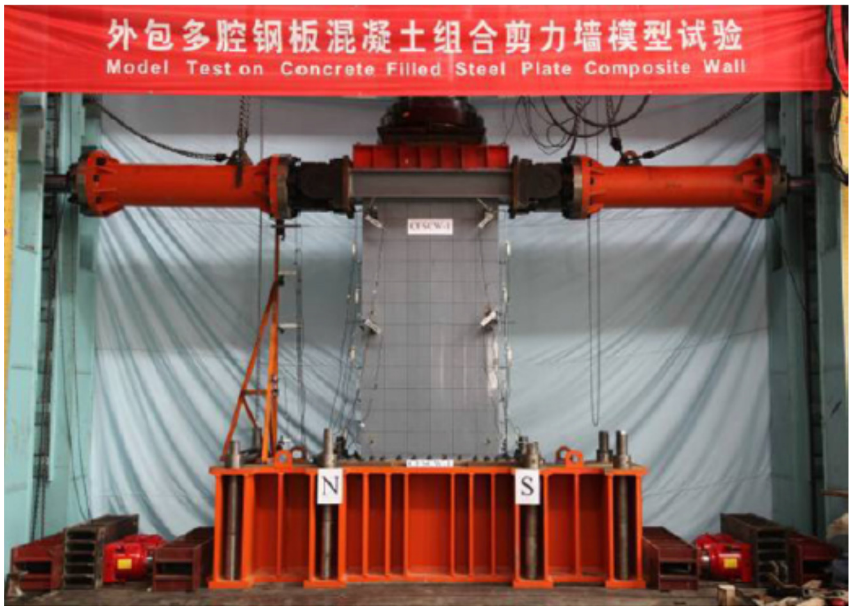

Figure 2-25 SC wall test setup [Nie et al. (2014)]

The failure modes, lateral force-displacement relationships, contributions of the shear and flexural displacements to the total lateral displacement were reported. The results of a cross-section analysis were used to predict the shear strength of flexure-critical SC walls assuming 1) plane section remains plane, and 2) perfect bond between the steel faceplates and the infill concrete. Nie et al. proposed that the ACI or Eurocode specifications for the maximum width-to-thickness ratio of CFT columns could be used as an upper limit value for the slenderness ratio of the steel faceplates to prevent steel faceplate buckling prior to yielding. Using their test data, Nie et al. proposed an equation to predict the effective stiffness of SC walls [Nie et al. (2014)]. The proposed equation was derived based on the effective shear and flexural stiffnesses of SC walls, where the effective shear and flexural stiffness were calculated using a fixed angle truss method and the results of a fiber analysis of SC wall cross-section, respectively. The details of the fixed angle truss theory are available in Nie et al. (2014). The effective stiffness was calculated as:

$$K_{eff} = \frac{K_{e,f} K_{e,v}}{K_{e,f} + K_{e,v}} \tag{2-17}$$

where $K_{e,f}$ and $K_{e,v}$ are the effective flexural and shear stiffnesses of SC walls and were expressed as:

$$K_{e,f} = 3(0.5E_s I_s + \beta E_c I_c) / H^3 \tag{2-18}$$

$$K_{e,v} = \frac{2\gamma t_s E_s \sin\theta_c \cos\theta_c}{(2t_s n + T \sin^4\theta_c)H} \tag{2-19}$$

where $E_s I_s$ and $E_c I_c$ are the flexural rigidities of the steel faceplates and infill concrete, respectively; H is the height of the SC wall; t_s and T are the thicknesses of each steel faceplate and the SC wall, respectively; θ_c is the angle of concrete cracking; and n is the modular ratio. Parameters γ and β are calculated using equations available in Nie et al. (2014).

Sener et al. (2013,2014) summarized available test data on the out-of-plane shear and flexural behaviors of SC beams provided by Japanese, Korean, and US researchers for the purpose of characterizing the out-of-plane response of SC walls. Design variables included loading configuration, width of the beams, steel faceplate thickness, reinforcement ratio and faceplate slenderness ratios, shear span-to-depth ratio, inclusion of shear reinforcement, and spacing of shear studs. The measured out-of-plane shear and the flexural strengths of 48 SC beam specimens were compared with the predictions provided by the design codes in Japan for SC [JEAC 4618 (2009)], South Korea for SC [KEPIC SNG (2010)], and US for RC [ACI 349 (2006)]. The shear and flexural strengths were overestimated using the Japanese and Korean SC specifications. Sener et al. showed that the ACI specifications for reinforced concrete beams could be used to estimate the out-of-plane monotonic shear and flexural strengths of SC beams, by equating SC beams to a doubly reinforced concrete beams.

Zhang et al. (2013,2014) and Varma et al. (2013b) investigated the effect of the use of shear studs on local buckling of steel faceplates and composite action in SC walls. On the basis of the available test data and the results of finite element analyses, they proposed that stud spacing should be selected to 1) prevent the elastic local bulking of steel faceplates, and 2) provide adequate development length for steel faceplates, where the development length was defined as the length over which the steel faceplate could develop its yield strength under the axial tensile loading. Based on these two criteria, the maximum stud spacing was proposed to be:

$$s = \min\left(1.0\sqrt{\frac{E}{f_y}}\ ,\ \sqrt{\frac{\phi Q_n L_d}{t_s f_y}}\right) \tag{2-20}$$

where E and f_y are the elastic modulus and yield stress of the steel faceplates, respectively; ϕ is a reduction factor, taken as 0.65 for stud shank failure; Q_n is the shear capacity of a single stud; and L_d is the development length taken at least three times the wall thickness to provide 75% to 90% partial composite action. The finite element analyses conducted by Zhang et al. (2013,2014) indicated that the partial composite action was affected by the reinforcement and faceplate slenderness ratios. As the reinforcement ratio and stud spacing were decreased, the degree of composite action increased.

Hong et al. (2014) summarized analytical studies on the in-plane shear behavior of SC walls and proposed two analytical models to predict the shear force and deformation capacities of SC walls having vertical ribs. Seven SC panels subjected to pure shear load were tested to validate the accuracy of the proposed model. Four of the seven specimens were reinforced with vertical ribs. A photograph of the test setup is presented in Figure 2-26. A comparison of the analytical and experimental results indicated that the proposed model could not predict the shear response of SC walls. The ratio of the measured to the predicted peak shear strengths of SC panels varied from 0.4 to 1.35. In that study, they tested six low aspect ratio flanged SC walls under lateral loading. Four walls were reinforced with vertical ribs. The predicted and measured pre-peak shear responses of two specimens compared favorably and measured peak shear strengths were slightly under-predicted.

Figure 2-26 Test setup for pure shear loading [Hong et al. (2014)]

2.3 Review of Studies on Finite Element (Micro) Modeling of SC Walls

Link et al. (1995) developed a finite element model to simulate the out-of-plane behavior of SC walls used in offshore structures. An orthotropic constitutive model and an elastic-plastic model were used to model the infill concrete and the steel faceplates, respectively. Friction between the steel faceplates and the infill concrete was modeled using Lagrangian multiplier gap elements presented in Figure 2-27. Results of the in-plane and out-of-plane shear responses of SC beams tested by Stephens et al. (1990) and Hassinen et al. (1989) were used to validate the finite element model. The pre- and post-peak out-of-plane responses of the SC beams were successfully predicted using the model.

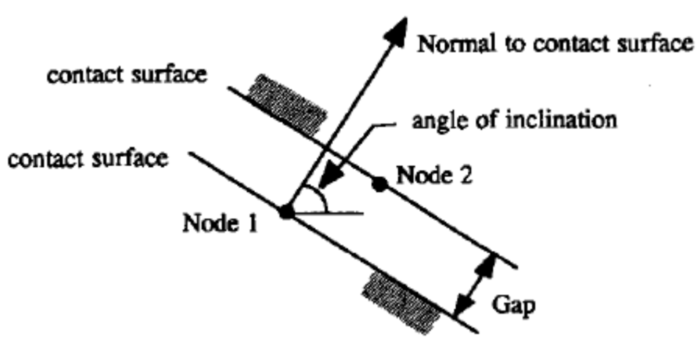

Figure 2-27 Schematic drawing of the gap element [Link et al. (1995)]

Uy et al. (1996) developed a finite strip model to simulate elastic local buckling of steel faceplates in composite members, where the finite strip model was developed as a special form of the finite element model. Finite element models simulate plate buckling using polynomials in the longitudinal and transverse directions whereas the finite strip model uses a harmonic series in the longitudinal direction and a polynomial in the transverse direction to describe the buckling displacements. The proposed model was validated using available analytical solutions in the literature. Design curves for buckling coefficients and slenderness ratios of the steel faceplates used in profiled composite beams, slabs, walls and composite beams and columns with different boundary conditions were provided.

Emori (2002) proposed a 2D finite element model to simulate the shear response of SC wall box units using two laminated steel and concrete plates. Friction between the steel faceplates and the infill concrete and steel partition plates was modeled using axial and shear springs. The compressive stress in cracked concrete at a given compressive strain was assumed to be 70% of that of un-cracked concrete to account for the effect of concrete cracking on the compressive stress-strain relationship of concrete. The shear responses of the SC wall tested by these authors, presented in Section 2.2, were used to validate the proposed finite element model. Good agreement was achieved between the measured and predicted shear responses of the SC walls. The developed finite element model is presented in Figure 2-28.

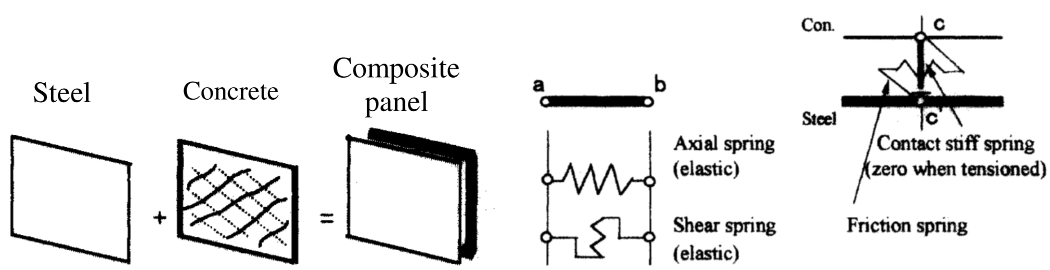

(a) Finite element layered model (b) Modeling of the partition plates and friction

Figure 2-28 Finite element modeling of SC wall box units [Emori (2002)]

Zhou et al. (2010) developed a 2D finite element model in OpenSees to simulate the cyclic response of SC walls. Membrane elements with plane stress behavior were used to model the infill concrete and the steel faceplates. The finite element model did not include the connectors, and the steel faceplates were tied to the infill concrete where the studs were attached to the steel faceplates. The Cyclic-Softened-Membrane-Model (CSMM) developed by Mansour et al. (2005a, 2005b) was used to model the infill concrete and a J2 plasticity model was used to model the steel faceplates. The CSMM model used to simulate the response of the infill concrete was validated using data for test of an RC shear wall [Zhong (2005)]. The SC wall model was not validated. Zhou et al. conducted a parametric study to investigate the effects of wall thickness and faceplate slenderness ratio on the in-plane shear response of SC walls.

Ali et al. (2013) developed an ABAQUS model to simulate the cyclic behavior of I-shaped (flanged) SC walls. The concrete damage plasticity (CDP) and bilinear kinematic hardening models were used to model the infill concrete and the steel faceplates, respectively. The flange wall was tied to the web. Contact between the steel faceplates and the infill concrete was considered. The infill concrete and the steel faceplates were modeled using solid elements. The model was validated using the data from cyclic loading test of four I-shaped SC walls. The model accurately predicted the backbone curve of the measured cyclic force-displacement relationship. The pinched behavior seen in the experiments was not captured because the bilinear kinematic model could not recover the nonlinear buckled response of the steel faceplates. The ABAQUS-predicted post-peak response was not presented. The ABAQUS model is presented in Figure 2-29.

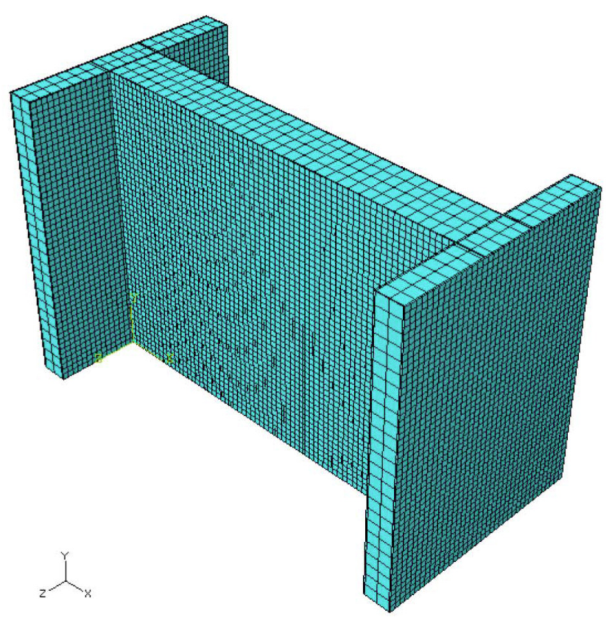

Figure 2-29 ABAQUS model of I-shaped SC walls [Ali et al. (2013)]

Vecchio et al. (2011) applied the Distributed-Stress-Field-Model (DSFM) to SC walls subjected to axial and in-plane monotonic and cyclic shear loads using the two-dimensional nonlinear finite element analysis program, VecTor2 [Vecchio (1989,1990)]. The strains in the steel faceplates were calculated assuming perfect bond between the steel faceplates and the infill concrete. The steel faceplates was assumed to buckle when the principal compressive stress in the faceplate elements exceeded the critical buckling stress proposed by Usami et al. (1995). The adequacy of the model was investigated by simulating the monotonic and cyclic responses of the SC walls tested by Sasaki et al. (1995), Usami et al. (1995), and Ozaki et al. (2001a,2004) The DFSM predicted the reported shear strengths to within 5% but the stiffness at displacements less than those associated with peak strength was significantly overestimated [Vecchio et al. (2011)].

The dynamic response of RC and the SC walls were investigated by Chaudhary et al. (2011) using modal and response-history analyses by ABAQUS. The infill concrete and the steel faceplates were modeled using 3D solid elements. A smeared crack model and a J2 plasticity model were used to model the infill concrete and the steel faceplates, respectively. The elastic dynamic response of the RC model was validated using the measured natural frequency of a flanged RC shear wall tested by Nuclear Power Engineering Corporation [NPEC (1994)]. The SC wall model was not validated. Three types of shear walls were analyzed, namely, a RC shear wall, and two SC walls with a web reinforcement ratio equal to that used in RC wall. Two SC wall models were studied to investigate the effect of the connection between the steel faceplates and infill concrete on dynamic response: models with flexible and rigid connections between the steel faceplates and infill concrete.

Varma et al. (2011b) developed an ABAQUS model to simulate the out-of-plane shear behavior of SC walls. The Brittle-Cracking (BC) model and an elastic-plastic model with isotropic hardening were used to simulate the behavior of the infill concrete and the steel faceplates, respectively. The BC model was used because of its advanced cracking features and element deletion option. This material model assumes linear elastic behavior for concrete in compression. The model was validated using the results of eight large-scale simply-supported SC beams under monotonic out-of-plane loading [Varma et al. (2011b)]. Shear studs were not used in five of the specimens. The effects of reinforcement ratio, beam width, steel faceplate thickness, and shear span-to-depth ratio, on out-of-plane shear response were investigated. There was good agreement between the analysis and the test results for one specimen without shear studs. The peak shear strengths of the SC beams with shear studs were underestimated by a factor of 1.2. On the basis of the analysis and test results, Varma et al. concluded that the ACI equations for the shear strength of RC beams could be reasonably used to predict the out-of-plane monotonic shear strength of SC beams.

Danay (2012) developed an analytical solution to predict the strain and stress fields in the steel faceplate and the infill concrete, the shear forces resisted by the studs, crack spacing, and crack opening in SC walls under in-plane, bi-axial, tensile and in-plane tensile-compressive loadings. The connectors between the steel faceplates and the infill concrete were modeled using shear springs distributed uniformly over the surface area of the steel faceplates. The proposed analytical model was validated using data from the pure shear loading tests of Ozaki et al. (2004). The post-cracking behavior of SC walls under tensile and shear loadings are presented in Figure 2-30.

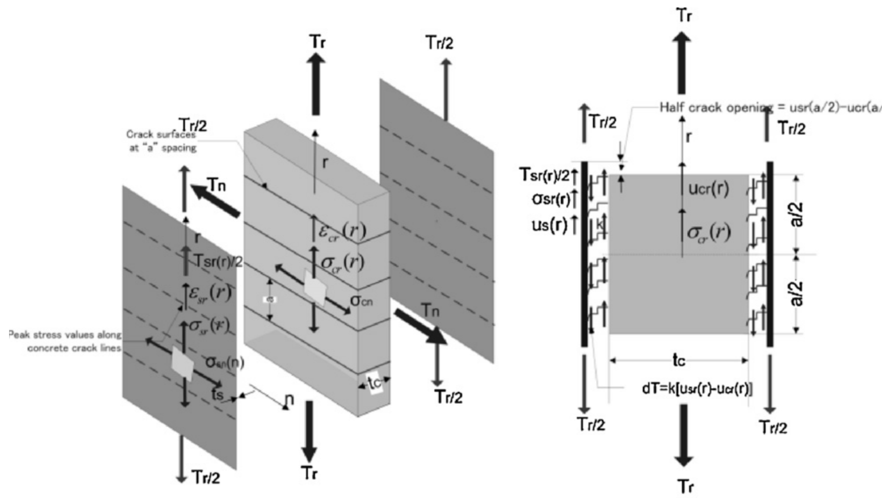

(a) Pure tension loading

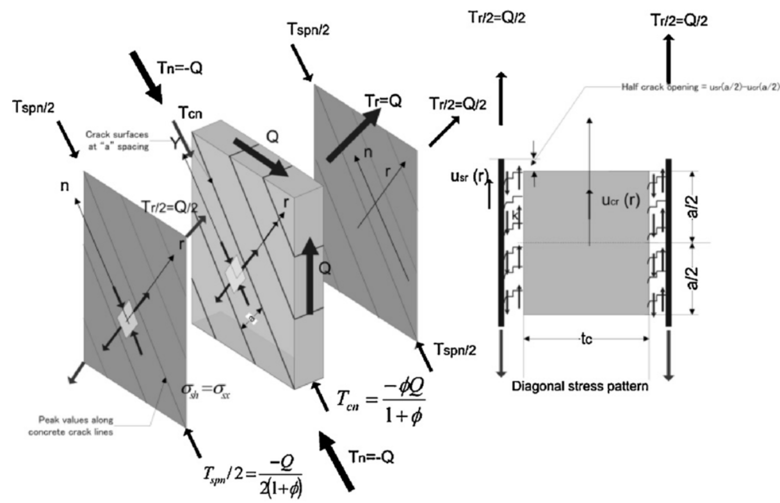

(b) Pure shear loading

Figure 2-30 Post cracking mechanisms [Danay (2012)]

Xiaowei et al. (2013) conducted a numerical study on SC walls under axial compressive and cyclic lateral loadings to investigate the influences of axial compressive force and steel faceplate thickness on the global response of SC walls. Smeared-crack solid elements and piece-wise-linear plastic shell elements with isotopic hardening were used to model the infill concrete and the steel faceplates, respectively. Hard contact between the steel faceplates and the infill concrete was assumed to avoid penetration of the steel faceplates into the infill concrete. Friction between the steel faceplates and the infill concrete was modeled using spring elements in the tangential direction. The stiffness of the springs was estimated using an experimental load-slip relationship for shear studs embedded in concrete.

The predicted hysteretic behavior of SC walls was parsed into three regions, namely 1) elastic, 2) elastic-plastic, and 3) hardening. Cracking of the infill concrete and yielding of the steel faceplates were assumed to occur in stage 2, and the faceplates were assumed to buckle in stage 3. Post-peak-strength response, where pinching and stiffness and strength deteriorations are expected, was not considered. Data from tests of four SC walls under axial and lateral loadings were used to validate the model. The proposed model successfully predicted the shear strengths of the walls but underestimated the displacements at peak force. Xiaowei et al. generated bending moment-axial force interaction curves for SC walls using the results of the finite element analysis.

Varma et al. (2011c) proposed a mechanics-Based-Model (MBM) to predict the in-plane response of SC panels under shear forces, as presented in Section 2.2. This simplified model: 1) assumed linear elastic behavior for concrete in compression, and 2) did not consider the post-cracking and the post-faceplate yielding regimes of response. To address these limitations, Varma et al. (2014) developed a layered composite shell finite element model using ABAQUS to extend the simplified model and to predict the response of SC walls under monotonic loading. Multi-axial plasticity with Von-Mises yield surface and kinematic hardening was used to model the steel faceplates. A smeared crack model was used for the infill concrete. The experimental data of Ozaki et al. (2004) were used to validate the numerical model. Both the MBM and ABAQUS model under-predicted the peak shear strength of SC walls. Analytical and numerical models were used to generate in-plane force, and in-plane force and out-of-plane moment interaction curves. Based on the analysis and test results, a simple design approach was proposed for SC walls subjected to a combined in-plane forces and out-of-plane bending moments.

Varma et al. (2013a) developed a finite element model to simulate the monotonic and cyclic responses of the 1/10-scale model of a pressurized water reactor containment internal structure (CIS) tested by Akiayama et al. (1989). The CIS structure consisting of primary and secondary shield walls, two reinforced concrete slabs, stream generator compartments, pressurizer compartment, and a number of partition and wing walls was modeled in ABAQUS. The CDP model was used for concrete and steel elements were modeled using the multi-axial plasticity model with combined hardening. The shear studs and tie rods were modeled using beam and connector elements. The components of the finite element model are presented in Figure 2-31.

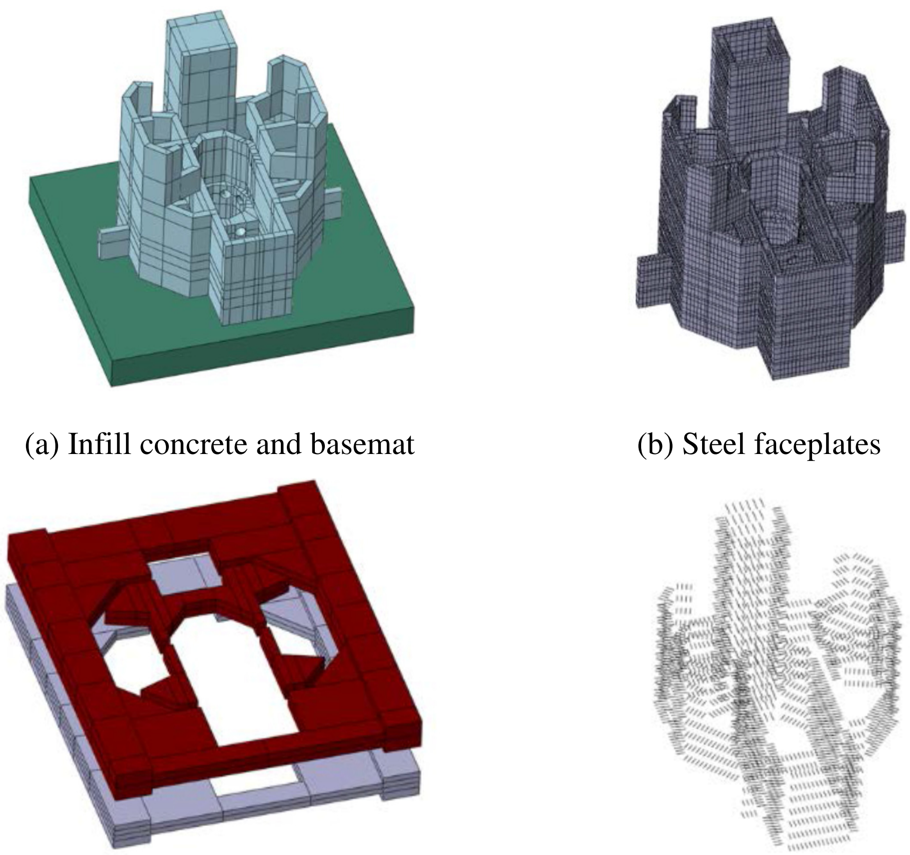

(a) Infill concrete and basemat (b) Steel faceplates

(c) Reinforced concrete slabs (d) Tie bars

Figure 2-31 Finite element model of CIS structure [Varma et al. (2013)]

To investigate the effect of shear connectors on the lateral load response of the CIS structure, two ABAQUS models were analyzed assuming: 1) perfect bond between the steel faceplates and the infill concrete, and 2) partial bond by explicitly modeling the shear connectors. The predicted monotonic force-displacement relationships were most similar, indicating that shear connectors had no significant effect on the monotonic response of the CIS structure noting that the faceplate slenderness ratio was 40. The models successfully predicted the peak shear strength but the pre-peak stiffness was slightly underestimated. Cyclic analysis was conducted assuming perfect bond between the steel faceplates and infill concrete, based on the results of the monotonic analysis. The monotonic analysis model was updated to include cyclic damage and deterioration rules in the concrete material model and ductile damage and fracture criteria in the steel material model. The updated ABAQUS model successfully predicted the peak shear strength but the pinched response and stiffness deterioration were not captured.

Kurt et al. (2013) conducted LS-DYNA analyses of rectangular and flanged SC walls subjected to a monotonic in-plane shear loading. The DYNA-predicted force-displacement relationship matched the measured monotonic response up to peak strength. A parametric study was conducted to investigate the effect of wall thickness and aspect ratio on the behavior of SC walls. This study showed that the shear strength of a rectangular SC wall with an aspect ratio (i.e., height-to-length) greater than 1.0 is governed by the moment capacity of the cross-section at the base of the wall. For SC walls with an aspect ratio of less than 1.0, Kurt et al. concluded that the smaller the aspect ratio, the greater the shear strength, with a maximum strength less than the pure in-plane shear strength calculated as $A_s f_y$, where A_s and f_y are the cross-sectional area and the yield stress of the steel faceplates, respectively. Guidelines for connecting SC walls to RC foundation were proposed.

CHAPTER 3

PRELIMINARY DESIGN AND ANALYSIS OF SC WALLS

3.1 Introduction

The experimental program was developed assuming a maximum of four steel-plate concrete (SC) composite shear walls were to be tested as part of a research project on conventional and innovative structural walls with a low aspect ratio. Given that the focus was low aspect ratio, rectangular walls that were flexure- and flexure-shear critical, an aspect ratio (height/length) of 1.0 was chosen for the walls.

Choosing an aspect ratio of 1.0 for all four specimens, SC1, SC2, SC3 and SC4, allowed other important design parameters to be varied. Ranges on key design parameters were identified, considering the capacities of the equipment and facilities in the laboratory at the University at Buffalo. After examining many alternatives, one steel faceplate thickness and two total thicknesses (steel faceplates and infill concrete) were selected. Studs and tie rods were used in SC1 and SC3 but only tie rods were used in SC2 and SC4, in part to permit the removal of the faceplates from SC2 and SC4, to allow examination of the damage to the infill concrete.

Section 3.2 provides the design basis for the test specimens. Section 3.3 presents the cross-sectional analysis of the walls. Section 3.4 presents the results of a preliminary finite element analysis conducted to predict the force-displacement relationships for the SC walls under monotonic loading. Section 3.5 presents the designs of the SC wall connection to the foundation and of the re-usable foundation block.

3.2 Preliminary Design of Test Specimens

The test specimens were designed with considerations of a draft version of AISC N690s1 (2014). Section N9.1.1c of AISC N690s1 limits the reinforcement ratio to the range of 1.5% to 5%, where the reinforcement ratio is defined as the cross-sectional area of the faceplates divided by the cross-sectional area of the SC wall web. Using 3/16 in. thick steel faceplates and total wall thicknesses of 12 inches and 9 inches, the reinforcement ratios of SC1/SC2 and SC3/SC4 were 3.1% and 4.2%, respectively.

Sections N9.3 and N9.4b of AISC N690s1 determine the maximum stud spacing to be the smaller of the spacing required to a) limit the width-to-thickness ratio to $1.0\sqrt{E_s / f_y}$ to prevent local buckling of the steel faceplates before yielding, and b) develop the yield strength of the steel faceplates over a development length, L_d, where the development length of steel faceplates is considered to be no more than three times the wall thickness. Grade 36 ASTM A572 steel with a yield stress of 36 ksi was assumed for the design of the steel faceplates. The expected yield stress ($= 1.4 \times 36 \text{ ksi} = 50.4 \text{ ksi}$) of the steel faceplates was used to calculate the stud spacing, where the factor of 1.4 was taken from the AISC Seismic Provisions 2005 (2005). The maximum spacing of the studs according to the width-to-thickness ratio criterion is:

$$s_1 \le t_s \sqrt{\frac{E_s}{f_y}} = 3/16 \sqrt{\frac{29000}{50}} = 4.5 \text{ in.} \text{ for SC1, SC2, SC3, and SC4}$$

Assuming that the development length equals to three times the wall thickness, the maximum spacing of the studs according to the development length criterion is:

$$s_2 \le \sqrt{\frac{L_d Q_n}{t_s f_y}} = \sqrt{\frac{3 \times 12 \times 5}{3/16 \times 50}} = 4.4 \text{ in.} \text{ for SC1 and SC2, and}$$

$$s_2 \le \sqrt{\frac{L_d Q_n}{t_s f_y}} = \sqrt{\frac{3 \times 9 \times 5}{3/16 \times 50}} = 3.8 \text{ in.} \text{ for SC3 and SC4}$$

where Q_n is the shear capacity of a headed stud. For a 3/8 in. diameter headed stud, the shear capacity per the Appendix D of ACI 349-06 (2006), is:

$$Q_n = 0.7 A_{sc} F_u^{stud} = 0.7 \times \frac{\pi}{4} (3/8)^2 \times 65 = 5 \text{ kips}$$

The stud spacing, calculated as a smaller of s_1 and s_2, equaled 4.4 in. and 3.8 in. for SC1 and SC2, and SC3 and SC4, respectively. Only tie rods (i.e., no studs) were used in SC2 and SC4. The studs were spaced 4 in. on center in SC1. A stud spacing of 4.5 in. was used for SC3 to investigate the effect on response of using a spacing greater than that specified by the AISC N690s1.

Tie rods are used to connect the two steel faceplates and provide structural integrity and the out-of-plane shear reinforcement. AISC N690s1 specifies a maximum tie rod spacing equal to the wall thickness. A tie rod spacing equal to one half of the AISC-specified maximum spacing was used for SC2 and SC4 because no studs were used in these walls, although out-of-plane loads were not imposed. In the other two specimens, the tie rod spacing was set equal to the thickness of the wall. The tie rods were spaced at 12in., 6 in., 9 in., and 4.5 in. for SC1, SC2, SC3, and SC4, respectively. A schematic of the walls is presented in Figure 3-1.

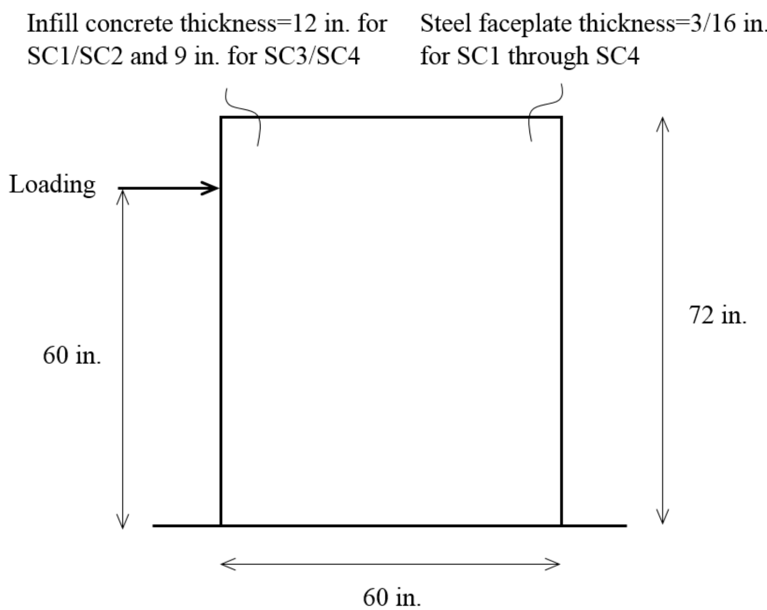

Figure 3-1 Elevation of SC walls

3.3 Cross-Sectional Analysis of SC Walls

3.3.1 Introduction

The flexural strengths of the SC walls were estimated using the cross-section program XTRACT (2002), which is a fiber-based cross-sectional analysis software. This calculation was made to establish the lateral strength of the walls, assuming they were flexure-critical. Moment-curvature relationships and axial force-bending moment interaction diagrams of a concrete, steel, reinforced concrete, and composite sections can be calculated using XTRACT. Two concrete material models can be accommodated: unconfined and confined. The input parameters for unconfined concrete are uniaxial compressive and tensile strengths; post-crushing strength; concrete strains corresponding to yield, crushing, spalling, and failure; and Young's modulus. The yield strain is typically taken as the strain corresponding to $0.4f_c'$, where f_c' is the uniaxial compressive strength of the concrete. Typical values of the crushing and spalling strains are 0.003 and 0.006, respectively, per Section R10.2.3 of ACI 318-11 (2011). The properties of confined concrete, including the concrete strength and crushing strain, are calculated automatically using the Mander model [Mander et al. (1988)] and information on the detailing of the cross section. The stress-strain relationship of the rebar is characterized in three regions: 1) elastic, 2) the yield plateau, and 3) strain hardening. A parabolic curve is used for the strain hardening branch. The input parameters for the steel material are yield and ultimate stresses, strains at the onset of hardening and ultimate stress, and Young's modulus.

XTRACT discretizes a cross-section into a series of fibers. Finer meshes lead to more accurate analysis. Each fiber within the discretized cross section is associated with a uniaxial steel or concrete material. There are two types of analyses available in XTRACT: displacement-controlled and force-controlled. In displacement-controlled analysis, the curvature is incremented and the fiber strains relative to the strain at the centroid of the cross section (an arbitrary strain) at each value of the curvature are calculated assuming plane section remains plane. The stress in each fiber is calculated using the calculated fiber strain and its uniaxial stress-strain material model. The resisting axial force and bending moment are calculated by integrating the fiber stresses across the cross section. The absolute value of the strain at the centroid of the cross section is calculated by solving the equilibrium equations. The curvature is incremented until the concrete or steel strain reaches a specified failure strain. In force-controlled analysis, the force or moment is incremented. The force-controlled analysis of the cross section in each load step is based on a Newton-Raphson iteration process.

3.3.2 XTRACT Analysis of SC walls

3.3.2.1 Material Properties

Trial designs of specimens SC1 and SC3 were modeled in XTRACT. The flexural strengths were calculated for two of the four SC walls, SC1 and SC3, since the geometrical properties of SC1 and SC2, and SC3 and SC4, were nominally identical. Nominal material properties were used. Element sizes of 2 in. and 1 in. were used for infill concrete and steel faceplates, respectively, on the basis of preliminary analysis. The XTRACT model of SC1 is presented in Figure 3-2.

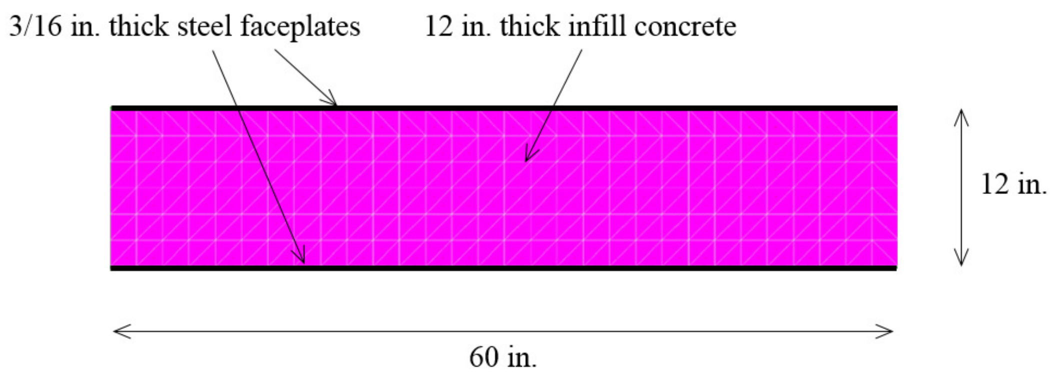

Figure 3-2 XTRACT model of SC1

Table 3-1 and Table 3-2 presents the concrete and steel material properties input to the XTRACT model, respectively. In Table 3-1, E_c is the Young's modulus of the infill concrete; f_c' is the uniaxial concrete compressive strength; f_r is the concrete stress corresponding to the spalling; ε_{yc} is the strain at $0.4f_c'$; ε_{uc} is the strain corresponding to peak stress; and ε_{sp} and ε_f are the spalling and failure strains, respectively. In Table 3-2, E_s is Young's modulus of the steel faceplates; f_y and f_u are the yield and ultimate stresses of the steel faceplates, respectively; ε_{sh} is the strain at the onset of hardening; and ε_{us} is the strain at the ultimate stress.

Table 3-1 Concrete material properties for XTRACT analysis

E_c (ksi)	f_c' (ksi)	f_r (ksi)	ε_{yc} (%)	ε_{uc} (%)	ε_{sp} (%)	ε_f (%)
3605	4	0.4	0.04	0.2	1.0	1.0

Table 3-2 Steel material properties for XTRACT analysis

E_s (ksi)	f_y (ksi)	f_u (ksi)	ε_{sh} (%)	ε_{us} (%)
29000	36	55	1.5	15.0

Young's modulus of the infill concrete was calculated using (3-1), according to Section 8.5.1 of ACI 318-11 (2011):

$$E_c = 57000\sqrt{f_c'} \tag{3-1}$$

The strain corresponding to peak stress was calculated using (3-2) proposed by Chang et al. (1994):

$$\varepsilon_{uc} = \frac{(f_c')^{1/4}}{4000} \tag{3-2}$$

The concrete stress corresponding to spalling was calculated using the concrete stress-strain relationship proposed by Tsai (1988) :

$$f_c = f_c'\left(\frac{nx}{1+(n-\frac{r}{r-1})x+\frac{x^r}{r-1}}\right) \tag{3-3}$$

where x is the concrete strain normalized by ε_{uc}, and n and r are the coefficients of the concrete stress-strain relationship and calculated using (3-4) and (3-5), proposed by Chang et al. (1994):

$$n = \frac{46}{(f_c')^{3/8}} \tag{3-4}$$

$$r = \frac{f_c'}{750} - 1.9 \tag{3-5}$$

where ε_{yc} corresponds to a concrete stress of $0.4f_c'$. The spalling and failure strains were assumed to be 1%, noting that the flexural strength is not affected by concrete spalling and failure since it is achieved when the concrete strain reaches ε_{c0}: the concrete strain at f_c'. The properties for ASTM A36 steel were taken from Brockenbrough et al. (1999).

3.3.2.2 Flexural Strengths of SC Walls

The assumptions made to calculate the flexural strength of the SC walls were: (1) plane sections remain plane after bending; (2) flexure-shear interaction is ignored; (3) the effect of confinement on the behavior of the infill concrete is not considered; and (4) the steel faceplates and the infill concrete are perfectly bonded.

Figure 3-3 presents the moment-curvature relationships for SC1 and SC3. The XTRACT-predicted flexural strengths of SC1 and SC3 were 20610 kips-in. and 19650 kips-in., respectively. The shear strengths of SC1 and SC3 corresponding to these flexural strengths were 344 kips and 328 kips, respectively.

To determine whether the specimens were likely to be flexure-critical or shear-critical, the maximum shear resistance of the walls was calculated using (3-6) to (3-8) that are based on the draft Appendix N9 to AISC N690s1 (2014), Ozaki et al. (2004), and Varma et al. (2011c):

$$V_{n1} = kf_y A_s \tag{3-6}$$

$$V_{n2} = A_s f_y \tag{3-7}$$

$$V_{n3} = \alpha A_s f_y \tag{3-8}$$

where k is $1.11 - 5.16\bar{\rho}$, and $\bar{\rho}$ is the strength-adjusted reinforcement ratio and calculated as:

$$\bar{\rho} = \frac{A_s f_y}{31.6 A_c \sqrt{f_c'}} \tag{3-9}$$

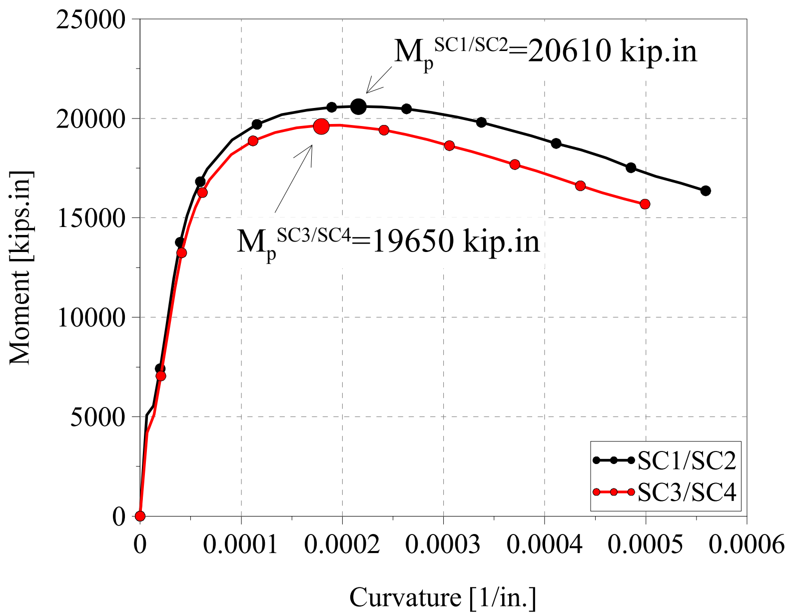

Figure 3-3 Moment-curvature relationships for the SC walls

where A_s and A_c are the cross-sectional areas of the steel faceplates and the infill concrete, respectively. In (3-8), α is calculated as:

$$\alpha = \frac{K_\alpha + K_\beta}{\sqrt{3K^2_{\ \alpha} + K_\beta}} \tag{3-10}$$

where

$$K_{\alpha} = G_s A_s \tag{3-11}$$

$$K_{\beta} = \frac{1}{\dfrac{2(1-\nu_s)}{A_s E_s} + \dfrac{4}{A_c E_c^{cr}}} \tag{3-12}$$

where G_s is the elastic shear modulus of the steel faceplates, ν_s is Poisson's ratio of the steel faceplates, and E_c^{cr} is Young's modulus of the cracked infill concrete and taken as $0.7E_c$.

The maximum shear resistance of the walls per the draft Appendix N9 to AISC N690s1 (2014), Ozaki et al. (2004), and Varma et al. (2011c) is 870/855/815 kips for SC1/SC2 and 840/855/780 kips for SC3/SC4. The SC walls were identified to be flexure-critical since the shear strength associated to the flexural strength of the walls was less than their maximum shear resistance.

3.4 Pre-Test Finite Element Analysis of SC Walls

The general-purpose finite element code ABAQUS [SIMULIA (2012a,2012b)] was used to verify the XTRACT-predicted peak shear strengths and to estimate the shear force-lateral displacement relationships for the four walls. The ABAQUS model of SC1 is shown in Figure 3-4.

The model took advantage of symmetry to reduce the computational effort. As seen in Figure 3-4, the model included one steel faceplate, infill concrete, a baseplate attached to the steel faceplate, a steel plate embedded in the foundation, studs and tie rods, a loading plate attached to the actuator, and threaded bars used to secure the baseplate to the foundation. The foundation was not included in the model since preliminary analyses indicated that the foundation block was effectively rigid and had no effect on the response of the SC walls.

The Concrete-Damage-Plasticity (CDP) model was used for the infill concrete and the J2 plasticity model with isotropic hardening was used for the steel faceplates. Friction between the infill concrete and the steel faceplate, and buckling of the steel faceplate were considered. Beam elements were used to represent the studs and tie rods. Solid elements were used to model the infill concrete, baseplate, steel plate, loading plate, and post-tensioning bars. Shell elements were used for the steel faceplate. The infill concrete was modeled with 1 × 1 × 1 in. elements and the steel faceplate was modeled with 0.5 × 0.5 in. elements. Nominal material properties were used for the pre-test ABAQUS calculations.

The predicted shear force-lateral displacement relationships of SC1 through SC4 are presented in Figure 3-5. In this figure, drift ratio is defined the lateral displacement devided by the vertical distance between the line of loading and the top of the foundation block (= 60 inches). The peak resistances of 300 kips for SC1/SC2 and 250 kips for SC3/SC4 agreed reasonably well with the estimate of shear corresponding to flexural strengths (= 344 kips for SC1/SC2 and 328 kips for SC3/SC4), which ignored flexure-shear interaction.

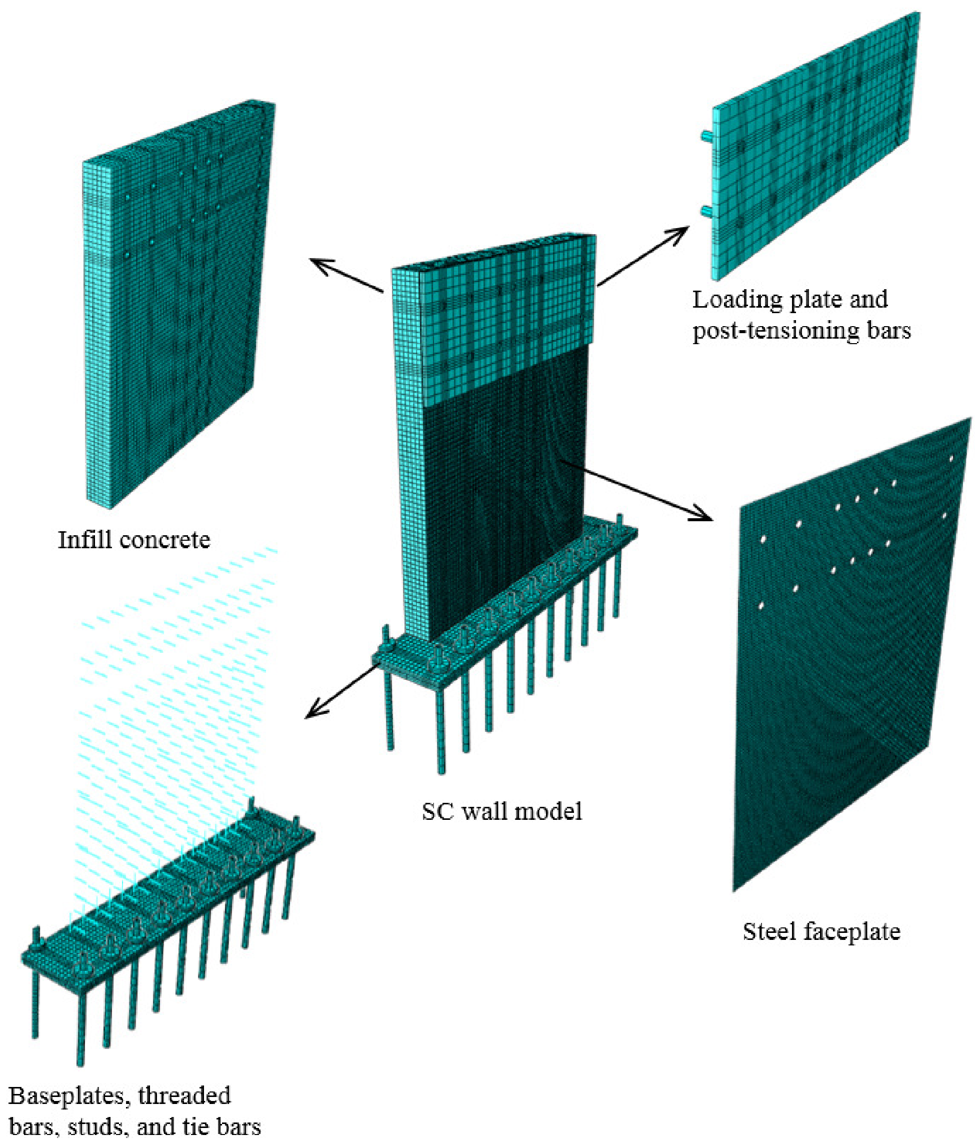

Figure 3-4 ABAQUS modeling of SC1

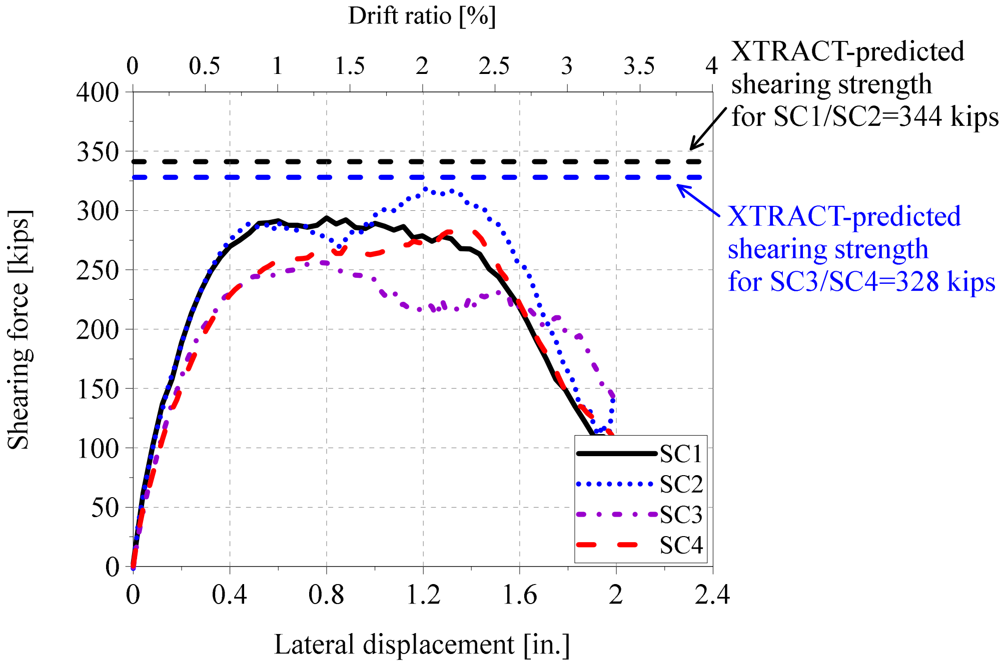

Figure 3-5 ABAQUS-predicted force-displacement relationships of SC walls

Figure 3-6 presents the distributions of vertical stress (S22) and shear stress (S12) in SC1 at peak shear resistance, in units of ksi. It is evident from these distributions that yielding of the faceplates (and their subsequent buckling and fracture) is affected more by normal stress (S22) than shear stress, which is an expected result because the walls were calculated to be flexure-critical, per section 3.3.2.2.

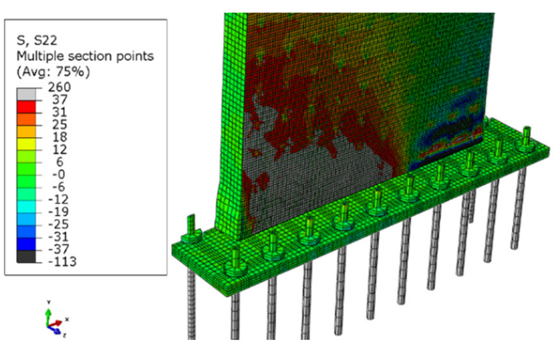

(a) Vertical normal stress (S22) distribution

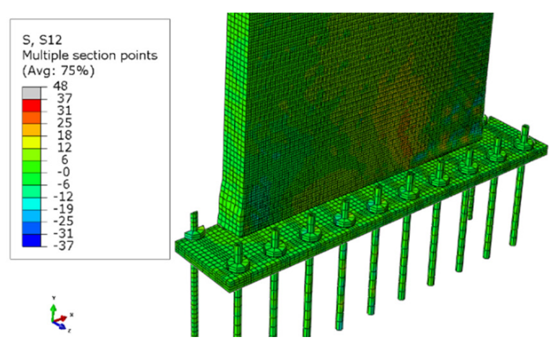

(b) Shear stress (S12) distribution

Figure 3-6 Stresses in the steel faceplate of SC1 at the point of maximum resistance

3.5 Design of the SC Wall Base Connection and the Foundation Block

A pre-tensioned bolted connection was used to anchor the SC specimens to a foundation block. Figure 3-7 presents the details of the SC wall connection. The connection consisted of a steel plate embedded in the foundation block, a baseplate attached to the steel faceplates, threaded bars securing the baseplate to the foundation block, headed studs attached to the baseplate, shear lugs attached to the steel plate embedded in the foundation block, and a steel anchorage securing the threaded bars to the foundation block. Post-tensioned Dwyidag bars were used to anchor the foundation block to the strong floor. The baseplate, threaded bars, and the Dwyidag bars were sized to remain elastic, with a margin, under the maximum predicted shear force of 350 kips (Section 3.3.2.2).

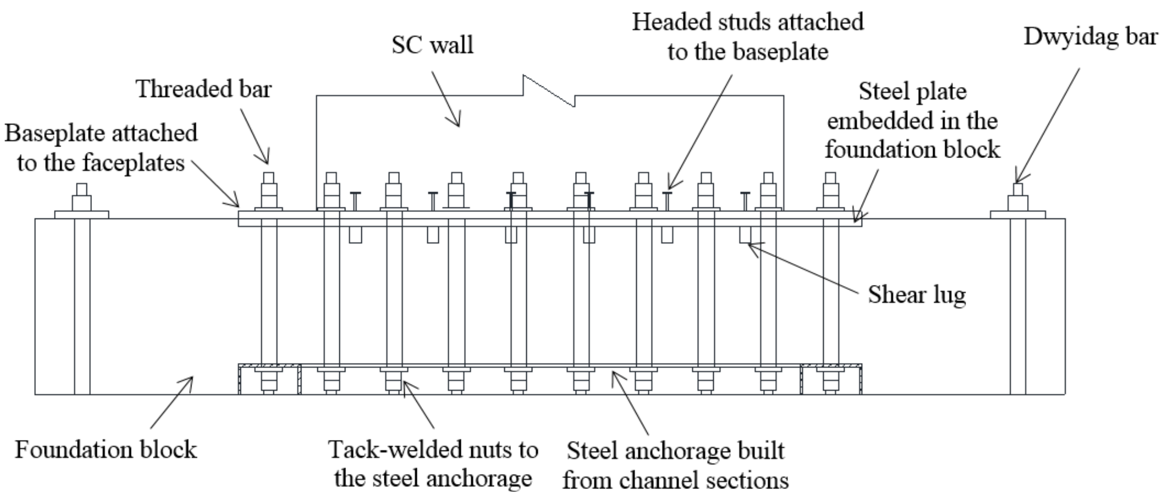

Figure 3-7 SC wall connection to the foundation block

The dimensions and detailing of the SC wall connection and the foundation block were based on the results of the finite element analysis of the SC walls and analysis of strut-and-tie models, respectively, as described in Nguyen (2016). The CAD drawings of the details of the foundation block and the SC wall connection are provided in Appendix A.

The design of the studs that attached the infill concrete to the baseplate followed the steps enumerated below:

1. The contribution of the steel faceplates and the infill concrete to the total shear load (from Section 3.3.2.2) was calculated using the elastic shear stiffness of the steel faceplates (3-13) and the post-cracked shear stiffness of the infill concrete (3-14), as proposed by Varma et al. (2011c).

$$K_{\alpha} = G_s A_s \tag{3-13}$$

$$K_{\beta} = \frac{1}{\frac{2(1-\nu_s)}{A_s E_s} + \frac{4}{A_c E_c^{cr}}} \tag{3-14}$$

where A_s and A_c are the cross-sectional areas of the steel faceplates and infill concrete, respectively; G_s is the elastic shear modulus of the steel faceplates; ν_s is Poisson's ratio of the steel faceplates; and E_c^{cr} is the Young's modulus of the cracked infill concrete, taken as $0.7E_c$. The shear stiffness of the steel faceplates and the infill concrete were 250960 kips/rad and 230040 kips/rad, respectively, using the nominal material properties of the steel faceplates and the infill concrete, as specified in Section 3.3.2.1.

2. The contributions of the steel faceplates and the infill concrete to the total shear load were calculated as:

$$V_S = \frac{K_\alpha}{K_\alpha + K_\beta} V_{SC} = \frac{250960}{250960+230040} 350 = 182 \text{ kips}$$

$$V_C = \frac{K_\beta}{K_\alpha + K_\beta} V_{SC} = \frac{230040}{250960+230040} 350 = 168 \text{ kips}$$

where V_S and V_C are the shear forces resisted by the steel faceplates and the infill concrete, respectively, and V_{SC} is the XTRACT-predicted peak shear force for SC1.

3. Using 5/8-in. diameter shear studs with a shear capacity [Appendix D of ACI 349-06 (2006)] of:

$$Q_n = 0.7 A_{sc} F_u^{stud} = 0.7 \times \frac{\pi}{4} (5/8)^2 \times 65 = 14 \text{ kips}$$

eighteen number 5/8-in. diameter studs were required to resist a shear force of 250 kips (equals to ~1.5×168 kips, where 1.5 provides a margin on capacity).

CHAPTER 4

EXPERIMENTAL PROGRAM

4.1 Introduction

This chapter describes the experimental program. The geometrical properties of the four SC wall specimens are described in Section 4.2. The construction of the foundation block and the SC walls are described in Section 4.3. Section 4.4 presents the concrete cylinder and steel coupon test results. The setup and loading protocol for testing the SC walls are presented in Sections 4.5 and 4.6, respectively. The instrumentation used to monitor the response of the walls is presented in Section 4.7.

4.2 Description of the SC Wall Specimens

The preliminary design of the test specimens was provided in Chapter 3. Table 4-1 summarizes the geometry of the walls: H is the height of the specimen; L is the length of the specimen; the overall thickness (two faceplates and the infill concrete) is T; the studs and tie rods are spaced at distance S; and the thickness of each faceplate is t_s. The reinforcement ratio, $2t_s / T$, is the cross-sectional area of the faceplates divided by the total cross-sectional area. The faceplate slenderness ratio, S / t_s, is the spacing of the connectors (studs or tie rods) divided by the steel faceplate thickness. The diameter of the studs and tie rods was 0.375 in. for all walls. The description of the test sepcimens is available as a part of the complete set of experimental data found on the NEES Project Warehouse (https://nees.org/warehouse/project/676) [Epackachi et al. (2014a, 2014b, 2014c, 2014d)].

Table 4-1 Test specimen configurations

Specimen	Wall dimension $H \times L \times T$ (in. × in. × in.)	Stud spacing (in.)	Tie rod spacing (in.)	Reinforcement ratio (%)	Faceplate slenderness ratio
SC1	60×60×12	4	12	3.1	21
SC2	60×60×12	-	6	3.1	32
SC3	60×60×9	4.5	9	4.2	24
SC4	60×60×9	-	4.5	4.2	24

The parameters considered in the design of the specimens were wall thickness, reinforcement ratio, and faceplate slenderness ratio. The locations of the studs and tie rods on the steel faceplates of the four SC walls are presented in Figure 4-1.

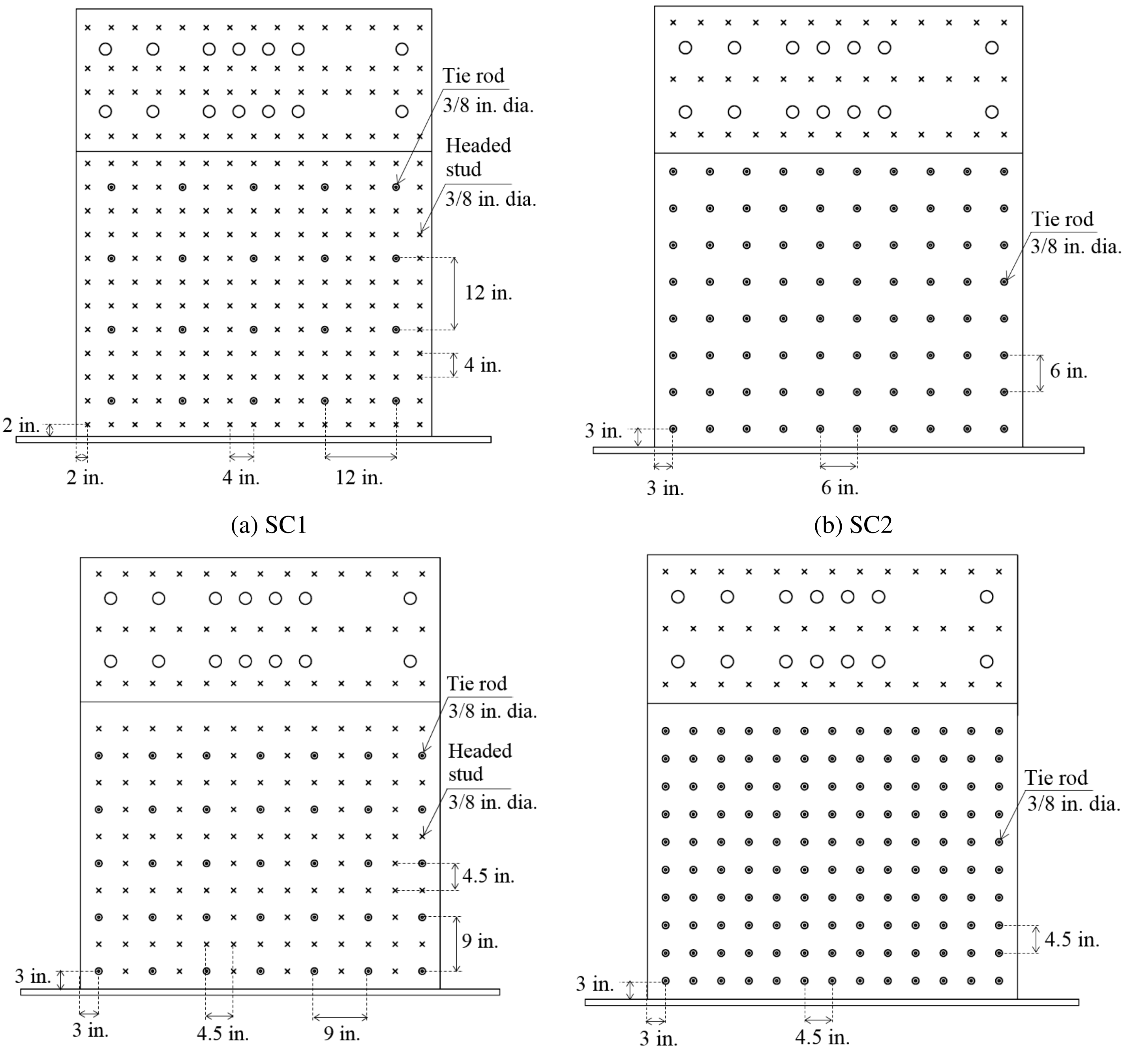

Figure 4-1 Locations of studs (×) and tie rods (⊙) attached to the steel faceplates

Each SC wall was installed on top of a re-usable foundation block. The base of each wall included a 1-in. thick A572 Gr.50 steel baseplate to which the faceplates were CJP groove welded. Two rows of thirteen 5/8-in. diameter headed steel studs were welded to the baseplate to anchor the concrete and improve the transfer of shear and tensile forces. The baseplate was installed atop a 1-in. thick baseplate embedded in the foundation block and was secured to the foundation block using twenty two 1.25-in. diameter threaded B7 bars that were post-tensioned to 100 kips per bar. The threaded bars were anchored to the foundation block using anchor nuts welded to a built-up steel anchorage placed at the bottom of the foundation. To improve the shear force transfer between the SC wall and the foundation block, eight 12×12×1.5 in. A36 shear lugs were fillet welded to the plate embedded into the foundation block. Figure 4-2 presents an elevation of and a cross-section through specimen SC1.

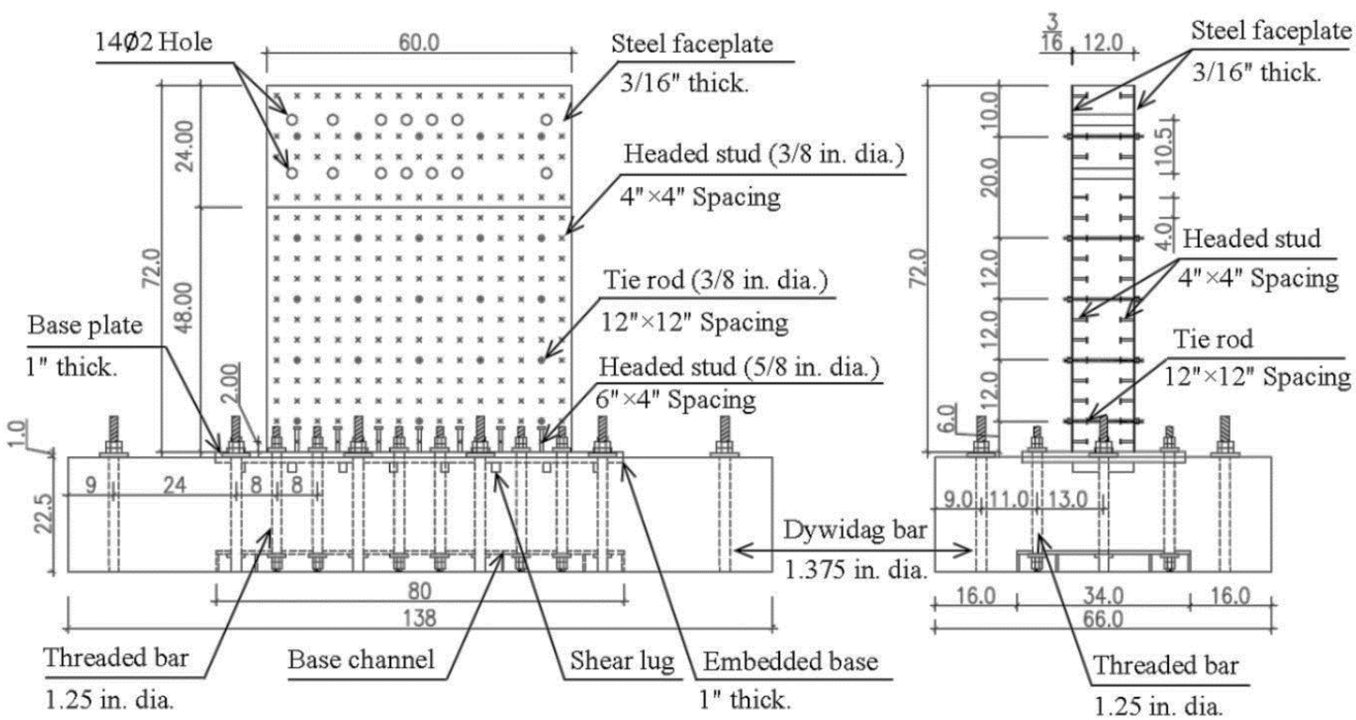

Figure 4-2 Elevation view and cross section through specimen SC1 [Epackachi et al. (2013b)]

4.3 Construction of the Test Specimens and the Foundation Block

Four steel shells, each composing two steel faceplates, a baseplate welded to the steel faceplates, headed studs attached to the steel faceplates and the baseplate, and tie rods bolted to the steel faceplates were fabricated at the Bowen Laboratory at Purdue University [Kurt (2015)] and shipped to the University at Buffalo. The steel-plate concrete (SC) composite walls were constructed by pouring the concrete into the steel shells in the NEES laboratory at the University at Buffalo.

4.3.1 Wall Specimen Construction

Two 3/16 × 60 × 72 in. steel faceplates were fabricated for each specimen as follows [Kurt (2015)]:

1. Drill fourteen 2-in. diameter holes at the top of the steel faceplates (Figure 4-2) to create sleeves through which threaded bars were to be passed (Figure 4-3(a)).
2. Draw a grid on the surface of the steel faceplates to locate the points of the attachments of the connectors to the steel faceplates (Figure 4-3(a)).
3. Use a center punch to mark the steel faceplates at the locations of the attachments of the studs/tie rods to the faceplates. These marks were used to locate studs/tie rods after grinding of the steel faceplate and to prevent movement of the stud when using the stud gun.
4. Grind the steel faceplates at the points of the attachments of the studs to create a smooth surface (Figure 4-3(a)).
5. Weld the studs to the steel faceplates using a stud gun (Figure 4-3(b)).
6. Check the quality of the stud welds by a 90-degree bend test on a single welded stud (Figure 4-3(c)).
7. Drill 7/16-in. diameter holes through the steel faceplates at the tie rod locations.
8. Insert the tie rods through the drilled holes, and install and tighten nuts on both sides of each faceplate (Figure 4-3(d)).
9. Weld two rows of fifteen 0.675-in. diameter headed studs to the baseplate (Figure 4-3(e)).
10. Bevel one edge of the steel faceplate in preparation for its CJP welding to the baseplate (Figure 4-3(f)).
11. CJP groove weld each steel faceplate to the baseplate (Figure 4-3(g)).

Figure 4-4 is a photograph of the assembled steel shells of SC1, SC3, and SC4.

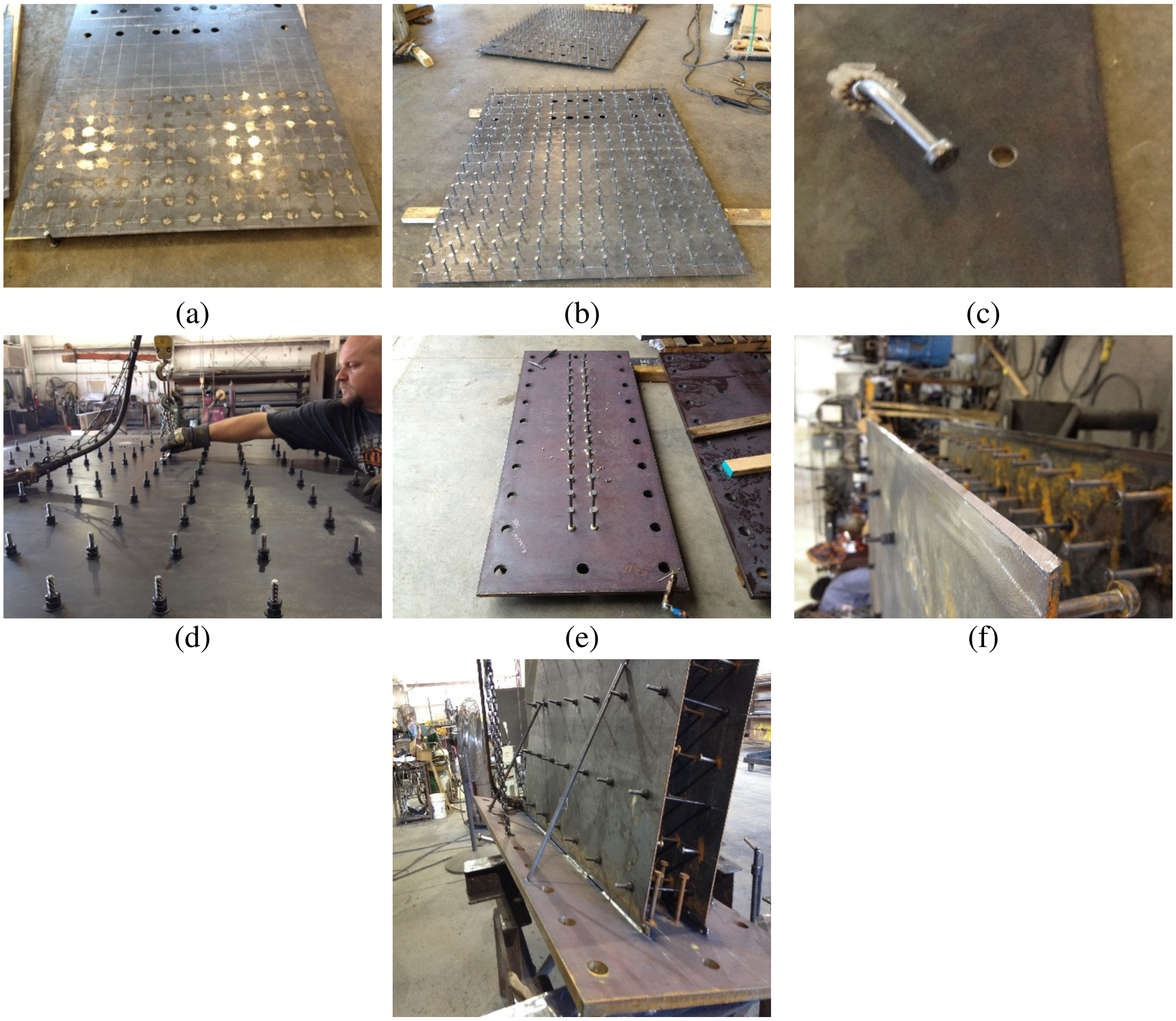

Figure 4-3 Construction of the steel shells [Kurt (2015)]

Figure 4-4 Assembled steel shells for SC wall construction [Kurt (2015)]

4.3.2 Foundation Construction

A steel anchorage built from channel sections was placed at the bottom of the foundation to anchor the threaded bars to the foundation block. The detailing of this element and its construction are described in Nguyen (2016). Figure 4-5 is a photograph of the anchor block in the formwork for the foundation. Nuts for 1.25-in. diameter B7 bars were tack welded to the underside of the channel (not seen in Figure 4-5) to permit tightening of the B7 anchor bolts from the top of the foundation. One of the bolts is seen in the figure. Each bolt was isolated from the surrounding concrete by a PVC sleeve.

Figure 4-5 Built-up steel anchorage and foundation formwork

Prior to placing the rebar cage into the foundation formwork, wooden plugs were attached at 24 inches on center to the soffit of the formwork at the location of the 2-in. diameter PVC sleeves to prevent movement of the sleeves during the installation of the rebar cage and the pouring of concrete. The rebar cage was then placed into the foundation formwork and the PVC sleeves were installed. The 1.25-in. diameter threaded B7 bars were passed through the (22) sleeves and screwed into the tack-welded nuts noted above. A steel plate was placed on the rebar cage, centered on the anchor block below, and over the B7 anchor bolts, and leveled. The concrete was poured into the formwork. The foundation block was water-cured for seven days after casting. Figure 4-6 shows steps in the construction of the foundation.

(a) Rebar cage

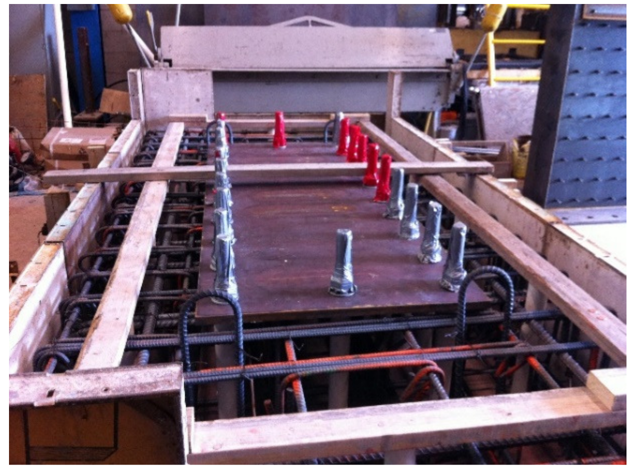

(b) Placing of the steel plate

(c) Concrete casting

(d) Cured foundation

Figure 4-6 Foundation construction.

4.4 Material Testing

4.4.1 Studs and Tie Rods

Based on information provided by the supplier, the 3/8-in. and 5/8-in. diameter Nelson studs and tie rods were fabricated from carbon steel with nominal yield and ultimate stresses of 50 and 75 ksi, respectively. The studs and tie rods were not tested.

4.4.2 Steel Faceplates

Three coupons were tested per ASTM A370 (1997) using a universal testing machine and a MTS electro-mechanical extensometer to determine the stress-strain relationship for the faceplate material. Coupons were cut from the top of one of the steel faceplates of SC1 after testing, where no yielding or damage were observed. The test fixture is shown in Figure 4-7.

(a) Universal testing machine

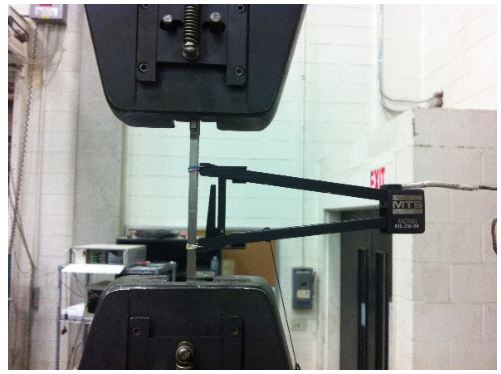

(b) MTS extensometer

Figure 4-7 Coupon test fixture

The measured stress-strain relationships of the coupons are presented in Figure 4-8. The yield and ultimate strengths of the steel faceplates were 38 and 55 ksi, respectively. The measured strain at the peak stress and the failure strain were 0.25 and 0.4, respectively.

4.4.3 Infill Concrete and Foundation

The uniaxial compressive strengths and Young's modulus of the infill concrete and the foundation concrete were calculated using the measured stress-strain relationships obtained from concrete cylinder tests. Testing followed ASTM C39-02 (2002). Cylinders were tested at 7, 14, 21, 28 days after concrete casting and on the days of the SC wall tests (=58, 75, 133, and 154 days after concrete casting, respectively, for SC1, SC2, SC3, and SC4). Cylinder tests were performed using a Forney compression testing machine, as shown in Figure 4-9.

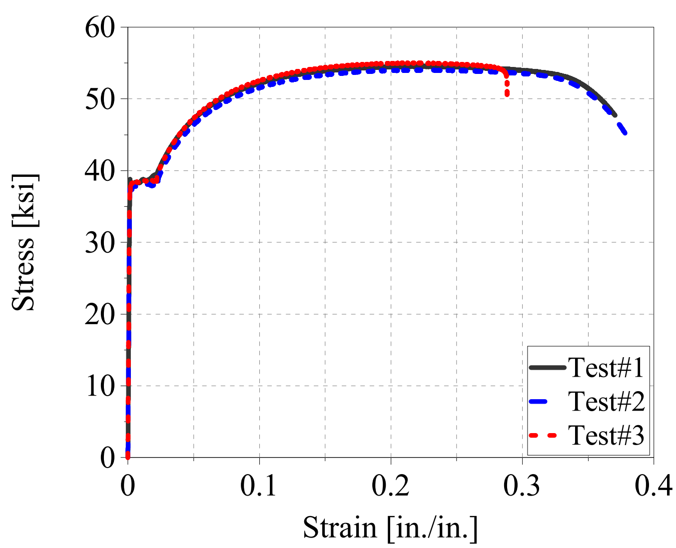

Figure 4-8 Stress-strain relationships of the faceplate coupons

Figure 4-9 Concrete cylinder test

Figure 4-10 presents a photograph of the instrumentation used for the cylinder tests. One steel ring and four steel supports were mounted on a cylinder, 5 in. from its ends, to support four equally spaced LVDTs that were used to measure the relative axial displacement along the 10 in. gage length.

Figure 4-10 Instrumentation of a concrete cylinder

The calculated Young's modulus and measured uniaxial compressive strengths of the concrete, calculated as averages from the concrete cylinders cracked on the day of testing, were 3000 ksi and 4.4 ksi for SC1/SC2, and 3300 ksi and 5.3 ksi for SC3/SC4. Figure 4-11 shows a concrete cylinder after testing.

Figure 4-11 Concrete cylinder after the test

4.5 Test Setup

4.5.1 Installation of the Foundation Block

A re-usable foundation block was used to test all four SC walls. The foundation block was placed on four shims to a) level the block, and b) provide a gap for grouting. The steel top plate was leveled using the shims. The gap between the block and the story floor was filled with a high-strength cementitious grout. After the grout had cured, 14 Dwyidag bars were installed to anchor the block to the strong floor, and tensioned to 100 kips per bar, for a total preload of the foundation block on the strong floor of 1400 kips.

4.5.2 Installation of the SC Wall Panels

Each SC wall panel was installed on the steel top plate of the foundation block. After plumbing the wall, the B7 threaded bars that joined the wall's baseplate to the steel top plate and reaction block were tensioned to 100 kips per bar, for a total preload of 2200 kips. The two loading brackets, one on each side of the wall, were installed and anchored to the wall using fourteen 1.25-in.

diameter B7 threaded bars that were then tensioned to 100 kips per bar. The loading brackets were then attached to the actuators.

The loading brackets were sized to remain elastic for the maximum loads that could be imposed by the actuators (approximately 450 kips per actuator). Finite element analysis was performed to confirm the adequacy of the loading apparatus; Nguyen (2016) provides details. The test set-up is shown in Figure 4-12. A plan view of the test fixture, showing the angle of inclination of the actuators to the plane of the wall (approximately 6 degrees), is shown in Figure 4-13, noting that the test fixture was not designed to prevent out-of-plane movement of the wall. A photograph of SC1 prior to testing is shown in Figure 4-14.

4.6 Loading Protocol

A displacement-controlled, reversed cyclic loading protocol, was used, loosely based on the recommendations of ACI 374.1-05 (2005). The loading history proposed for testing of reinforced concrete structural elements subjected to a unidirectional reversed cyclic loading is presented in Figure 4-15, where D_y is the yield drift ratio. Yielding is identified by a significant change in the rate of deformation under a small load increment, per Section 3.7.1 of ACI 374.1-05.

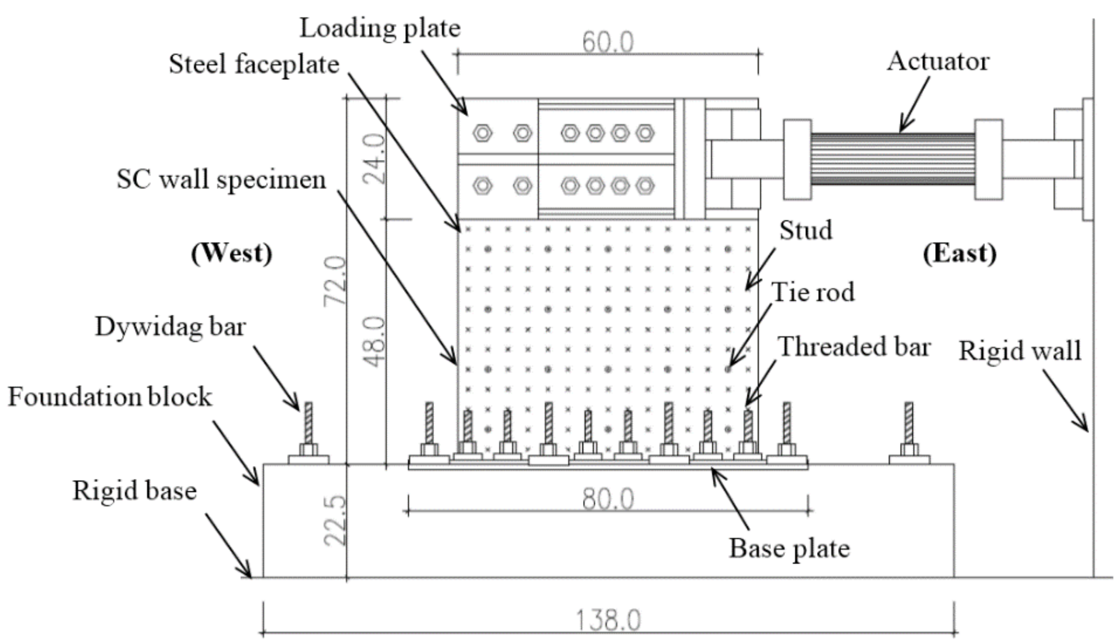

Figure 4-12 Test setup

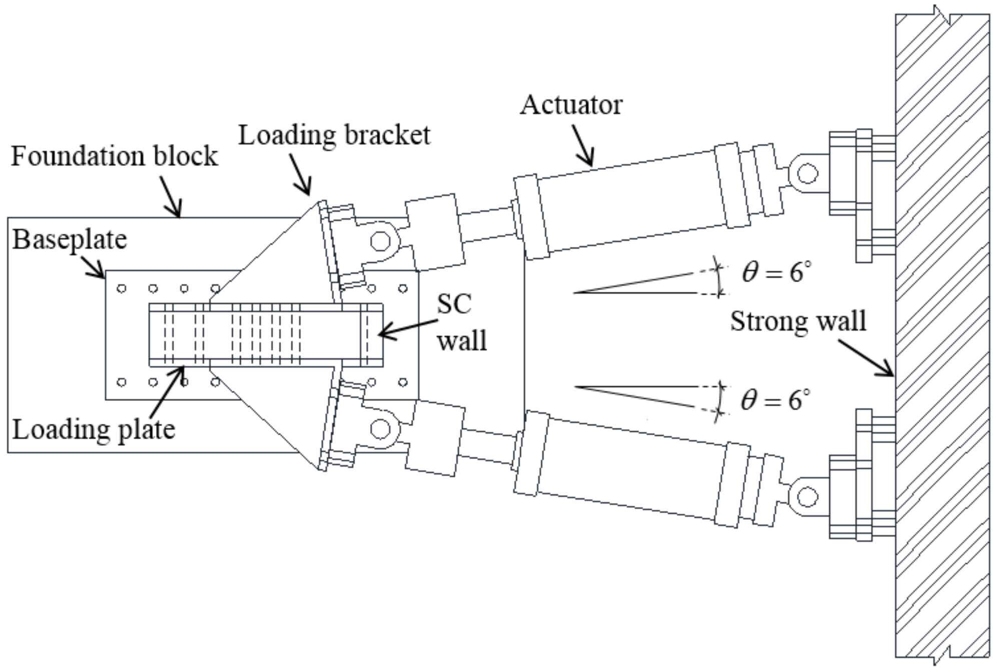

Figure 4-13 Plan view of the test fixture

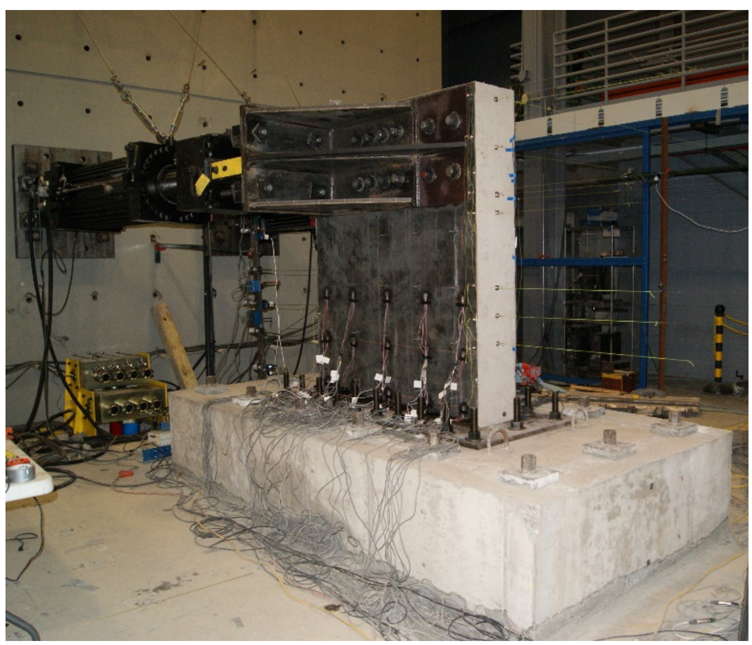

Figure 4-14 Specimen SC1

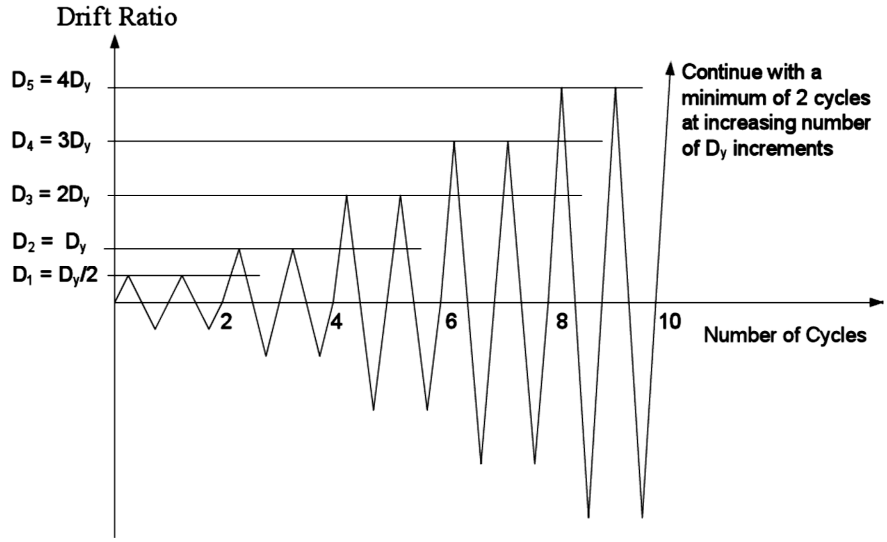

Figure 4-15 Deformation history for unidirectional cyclic loading of reinforced concrete structural elements [ACI 374.1-05 (2005)]

Figure 4-16 presents the approach proposed by ACI 374.1-05 to identify a yield (or reference) displacement. Analytical or experimental methods can be used to calculate the yield force, Q_y. The yield force, per ACI 374.1-05 (2005), is the measured or predicted force at the onset of 1) yielding of longitudinal reinforcement of flexure-critical members, 2) yielding of transverse reinforcement of shear-critical members, or 3) concrete crushing in columns subjected to high axial load. Per Figure 4-16, the yield displacement is calculated using a stiffness established at force $0.75Q_y$ and the yield force Q_y.

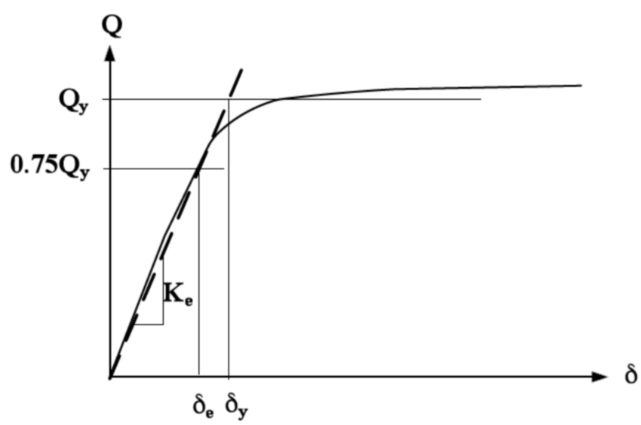

Figure 4-16 Determination of the yield displacement [ACI 374.1-05 (2005)]

The calculation of the yield (reference) displacement for SC1 is presented in Figure 4-17. The yield displacement was calculated using the ABAQUS-predicted force-displacement relationship (see Section 3.4). Assuming that yielding of the SC walls corresponded to the onset of the yielding of the steel faceplates, the yield displacement and its corresponding force for SC1 were estimated to be 0.14 in. and 150 kips, respectively. A yield (reference) displacement of 0.14 in. was used to generate the loading protocol for testing all four SC walls.

Two additional loading steps, at displacements of 10% and 75% of the reference displacement, were added to the deformation history of Figure 4-15 to capture SC wall response before and after cracking of the infill concrete.

Table 4-2 presents the loading protocol used to test the SC walls. The loading protocol consisted of 15 load steps with two cycles in each step. Two cycles of loading were imposed at displacements equal to fractions and multiples of the reference displacement (= 0.14 inch): 0.1, 0.5, 0.75, 1, 2 ... 12. In Table 4-2, drift ratio at any load step was calculated by dividing the peak displacement of that load step to the distance between the base of the wall and the centerline of horizontal loading (= 60 inches).

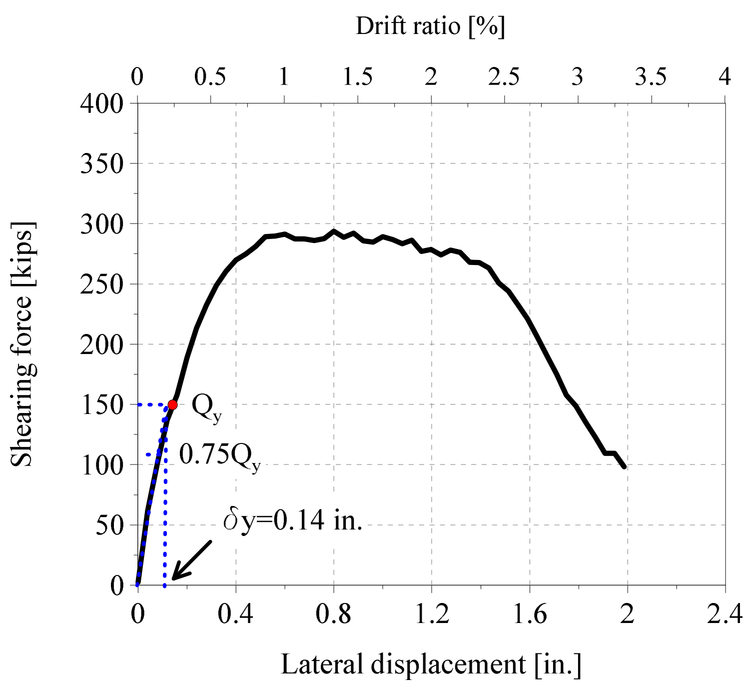

Figure 4-17 Yield or reference displacement calculation

In each loading cycle, a push was imposed first, followed by a pull, where push was defined as the loading in the positive direction, to the West (denoted as WL+), and pull was defined as the loading in the negative direction, to the East (denoted as EL-). The East and West directions are identified in Figure 4-12. Testing was terminated after steel faceplate fracture and crushing of the infill concrete at the toes of the walls. The loading speed was 0.01 in/sec. The loading protocol is presented in Figure 4-18.

Table 4-2 Loading protocol

Load step	Peak displacement (in.)	Drift ratio (%)	Number of cycles	Description
LS1	±0.014	0.02	2	$0.1\delta_y$
LS2	±0.070	0.12	2	$0.5\delta_y$
LS3	±0.105	0.18	2	$0.75\delta_y$
LS4	±0.142	0.23	2	δ_y
LS5	±0.283	0.47	2	$2\delta_y$
LS6	±0.425	0.70	2	$3\delta_y$
LS7	±0.567	0.93	2	$4\delta_y$
LS8	±0.709	1.17	2	$5\delta_y$
LS9	±0.850	1.40	2	$6\delta_y$
LS10	±0.992	1.63	2	$7\delta_y$
LS11	±1.134	1.87	2	$8\delta_y$
LS12	±1.276	2.10	2	$9\delta_y$
LS13	±1.417	2.33	2	$10\delta_y$
LS14	±1.701	2.80	2	$11\delta_y$
LS15	±1.984	3.27	2	$12\delta_y$

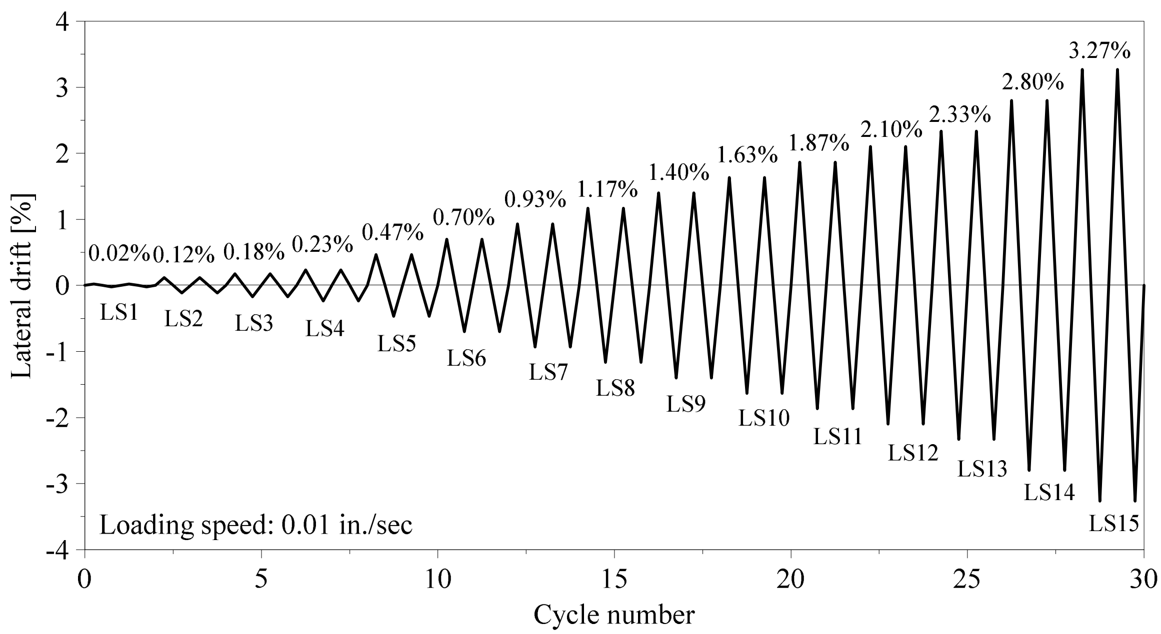

Figure 4-18 Deformation history for SC walls

4.7 Instrumentation of Test Specimens

Five types of instrumentation were used to monitor the response of the walls, namely, Krypton light-emitting diodes (LEDs), rosette strain gages, linear potentiometers, Temposonic displacement transducers, and linear variable displacement transducers. Two data acquisition systems (DAQ) were used to collect data. One DAQ was used to collect the data from the rosette strain gages, linear potentiometers, Temposonic displacement transducers, linear variable displacement transducers, actuator load cells and actuator Temposonic displacement transducers. The second DAQ collected the data from Krypton LEDs.

4.7.1 Krypton LEDs

The Krypton is a high-performance mobile coordinate measurement machine consisting of three linear cameras recording the infra-red light emitted by the LEDs (Figure 4-19). The 3D position of the LEDs is measured by combining the readings from three cameras with a single point accuracy ranging from 0.0024 in. to 0.005 in. and a volumetric accuracy ranging from 0.0035 in. to 0.007 in. depending on the distance between the LED and the cameras [SEESL (2008)].

Figure 4-19 Krypton cameras [SEESL (2008)]

To measure the in-plane and out-of-plane displacements of SC walls, 179, 158, 146, and 146 Krypton LEDs were attached to one steel faceplate of SC1, SC2, SC3, and SC4, respectively. The locations of the LEDs on the SC walls are presented in Figure 4-20.

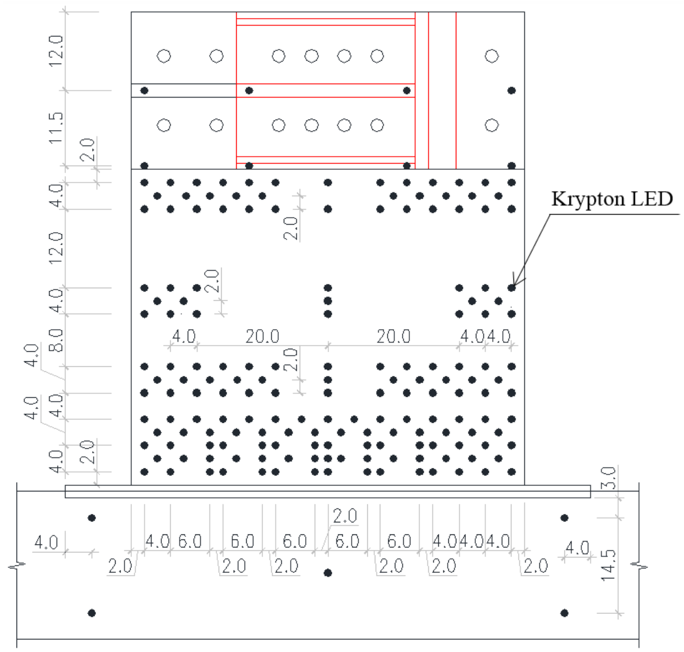

(a) SC1

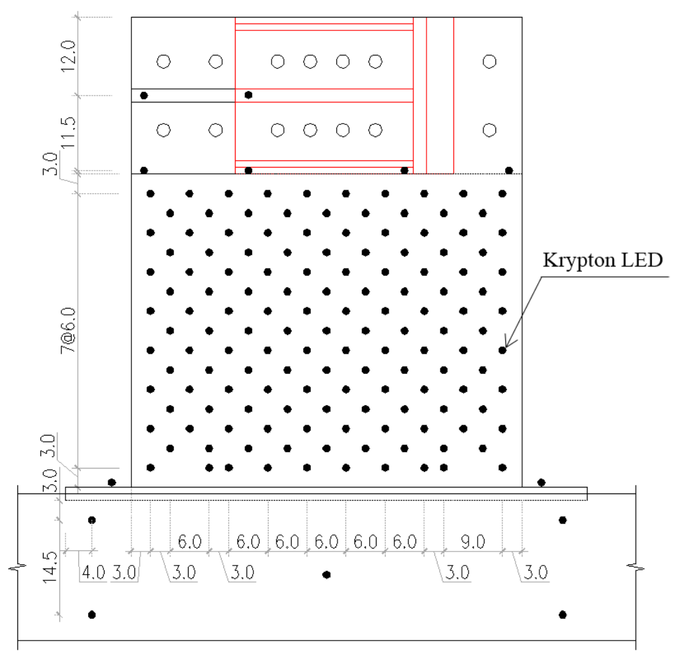

(b) SC2

Figure 4-20 Krypton LEDs on SC walls

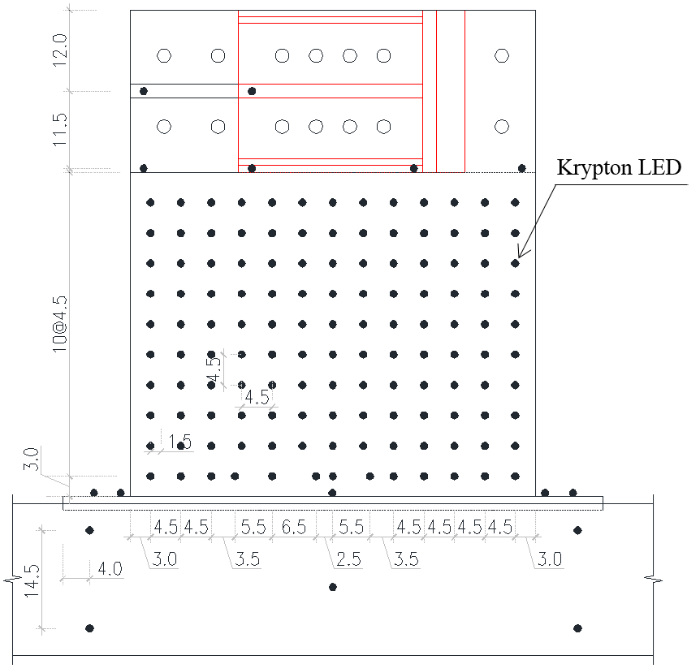

(c) SC3 and SC4

Figure 4-20 Krypton LEDs on SC walls (cont.)

4.7.2 Rosette Strain Gages

Three independent axial strains at different orientations at a point are required to determine the state of in-plane strain. The normal and shear strains are calculated using the three measured strains, the orientations of the uniaxial gages, and the strain transformation equations. Figure 4-21 presents the rosette strain gage, used for the experiments, manufactured by Vishay Precision Group Inc (2010). The specifications for the gage are provided in Appendix C.

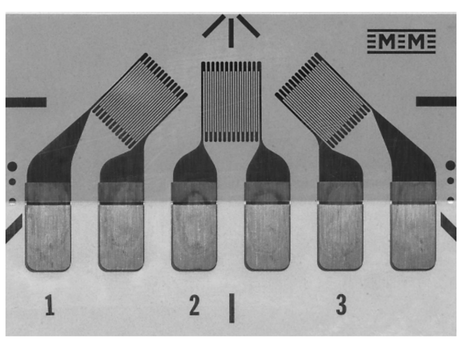

Figure 4-21 Rectangular rosette strain gage [Vishay Precision Group (2010)]

Fifteen, 11, 17, and 17 rosette strain gages were installed at three levels on one steel faceplate of SC1 through SC4, respectively, to measure strains at discrete locations. The rosette strain gages were mounted on the steel faceplate with the second gage vertical. The locations of the rosettes on the SC walls are presented in Figure 4-22.

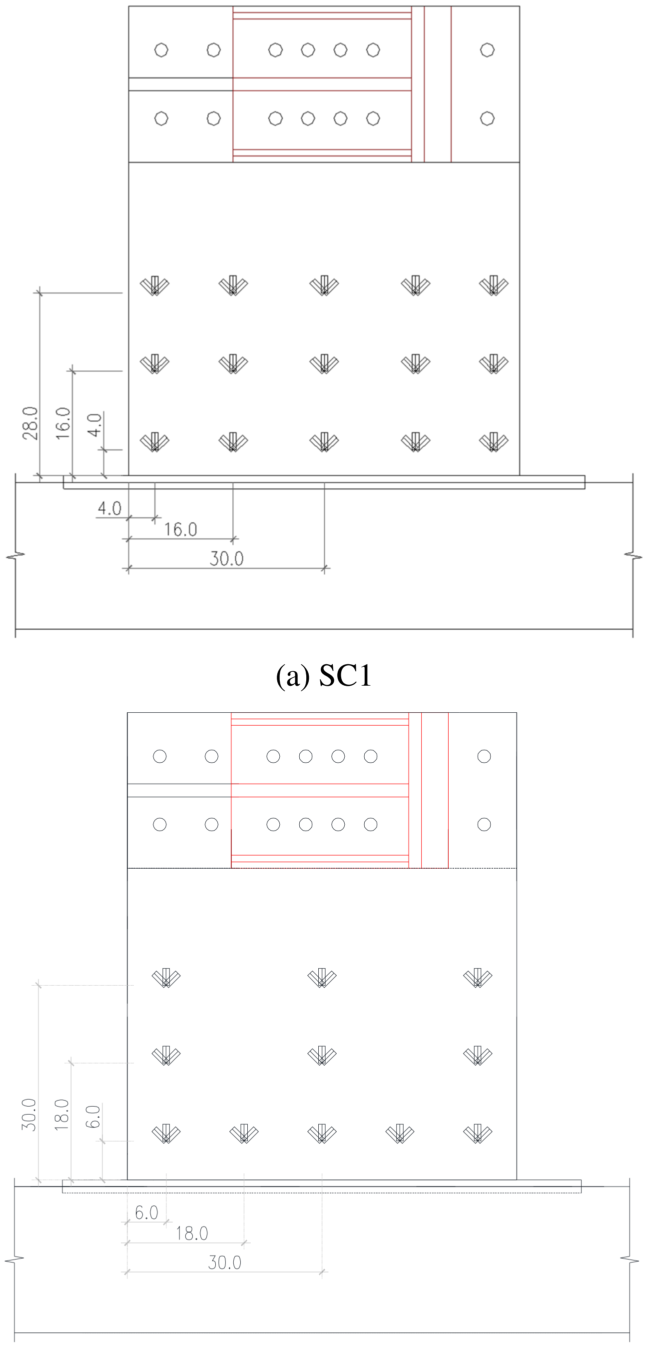

(a) SC1

(b) SC2

Figure 4-22 Rosette strain gages on SC walls

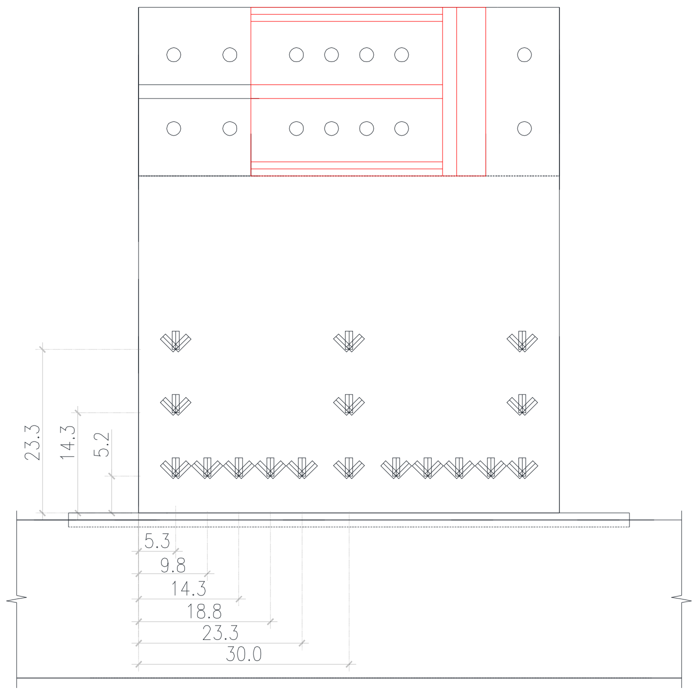

(c) SC3 and SC4

Figure 4-22 Rosette strain gages on SC walls (cont.)

4.7.3 LVDTs, Temposonic Displacement Transducers, and String Potentiometers

The horizontal and vertical movements of the foundation block relative to the strong floor were monitored using two horizontal linear variable displacement transducers (LVDTs) attached to the bottom corners of the foundation block and one vertical LVDT attached at the bottom center of the foundation block.

Nineteen string potentiometers and 7 Temposonic displacement transducers were attached to the ends of a wall to measure in-plane displacement along the height of the wall. Four string potentiometers were attached to the corners of one steel faceplate to measure the out-of-plane movement of the SC wall. Figure 4-23 presents the locations of the string potentiometers, Temposonic transducers, and LVDTs attached on the ends of the wall.

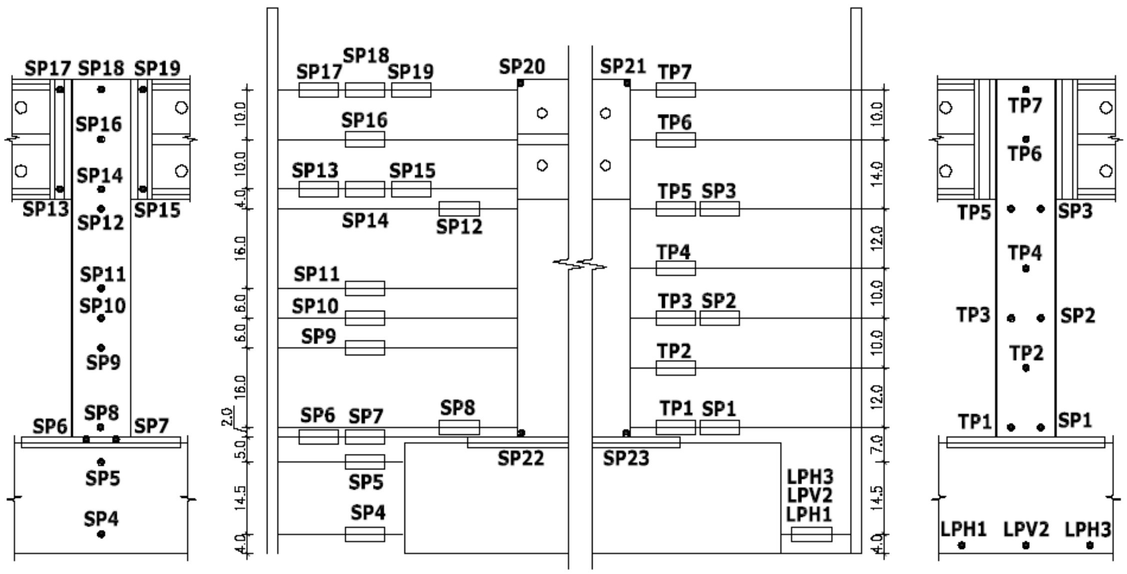

Figure 4-23 Layout of the linear potentiometers (SP), Temposonic displacement transducers (TP), and linear variable displacement transducers (LPH and LPV)

CHAPTER 5

EXPERIMENTAL RESULTS

5.1 Introduction

Information on the test specimens, materials, loading protocol, test setup, and instrumentation was provided in Chapter 4. This chapter summarizes the results of testing of the four SC walls in the NEES laboratory at the University at Buffalo [Epackachi et al. (2013a, 2013b, 2014e, 2015d), Chang et al. (2015), Kurt et al. (2015), Farhidzadeh et al. (2015), and Nguyen et al. (2013)].

The initial stiffness of the SC walls, the forces and displacements corresponding to the onset of buckling and yielding of the steel faceplates, to the peak load, and at the end of the tests are presented in Section 5.2. The progression of damage to the SC walls, including the cracking and crushing of the infill concrete, and buckling and fracture of the steel faceplates, are presented in Section 5.3. The cyclic force-displacement relationships are presented in Section 5.4. Section 5.5 discusses the post-peak response of the SC walls, focusing on the influence of stud spacing. Energy dissipation and equivalent viscous damping ratios are calculated in Section 5.6. Section 5.7 presents the strain and stress fields in the steel faceplates and the contribution of the steel faceplates to the total shear load. The variation of vertical strain in the steel faceplates along the length of the wall, near the base, at different drift ratios, is presented in Section 5.8. Section 5.9 discusses load transfer mechanisms in the SC walls. The lateral displacement profiles along the height of the SC walls are presented in Section 5.10. Section 5.11 identifies the contributions of shear, flexure, and base rotation to the total lateral displacement. The displacement ductility of the SC walls is established in Section 5.12. Cyclic secant stiffness is presented in Sections 5.13.

5.2 Test Results

Key test results are provided in Table 5-1. The initial stiffness of the SC walls, calculated at drift ratios less than 0.02%, are presented in the second column of the table. The values of the forces and displacements corresponding to the onset of faceplate buckling are listed in the third and fourth columns, respectively. The fifth and sixth columns in the table present computed data at the onset of faceplate yielding, where forces and displacements were calculated using rosette strain gage data and assuming a Von-Mises yield criterion. The seventh and eighth columns present peak loads and the corresponding drift ratios for both EL- and WL+ directions, where the EL- and WL+

directions were identified in Figure 4-12. The last column in the table lists the post-peak loads at a drift ratio of 3.3%, where the tests were terminated, for both EL- and WL+ directions. The test results are available as a part of the complete set of experimental data found on the NEES Project Warehouse (https://nees.org/warehouse/project/676) [Epackachi et al. (2014a, 2014b, 2014c, 2014d)].

Table 5-1 Results summary for SC1 through SC4

Specimen	Initial stiffness (kips/in.)	Data point						
		Onset of steel plate buckling		Onset of steel plate yielding		Peak load		Test termination at 3.3% drift ratio
	(kip/in.)	Load (kips)	Drift ratio (%)	Load (kips)	Drift ratio (%)	Load (kips) WL+/EL-	Drift ratio (%) WL+/EL-	Load (kips) WL+/EL-
(1)	(2)	(3)	(4)	(5)	(6)	(7)	(8)	(9)
SC1	1680	245	0.48	240	0.48	317/320	1.18/1.18	130/144
SC2	1420	200	0.48	200	0.48	314/319	1.18/1.18	134/126
SC3	1380	240	0.70	185	0.48	265/275	1.40/1.18	112/126
SC4	1310	240	0.70	200	0.48	270/275	1.18/1.18	120/141

The initial stiffness of SC3 and SC4 was less than that of the thicker wall SC1. The initial stiffness of SC2 was substantially less than SC1, which was not expected and is attributed to unknown flexibility at the base of the wall. The faceplates buckled at their vertical free edges prior to achieving peak load. Studs were not provided at the vertical free edges of the faceplates, as seen Figure 4-12. Plate buckling propagated towards the center of the wall during subsequent cycles of loading.

Yielding of the faceplates occurred prior to peak load. Peak load was observed at a drift ratio of 1.1+%. The peak loads developed in SC1 and SC2, and SC3 and SC4 are similar, which indicates that connector spacing, in the range provided, did not impact the peak shear resistance in these flexure-critical walls. The peak loads in SC1 and SC2 are greater than SC3 and SC4 because the infill concrete is 3 inches thicker in SC1 and SC2. The load in all four walls at a drift angle of 3.3% was approximately 130 kips.

5.3 Damage to SC Walls

Figure 5-1 provides photographs of damage to SC1 through SC4 at the end of testing. The progression of damage in the four SC walls was identical, sequentially 1) tensile cracking of the concrete at both ends of the wall, 2) outward buckling and yielding of the steel faceplates at the base of the wall, 3) crushing and spalling of concrete at the toes of the wall, and 4) tearing of the steel faceplates along their welded connection to the baseplate.

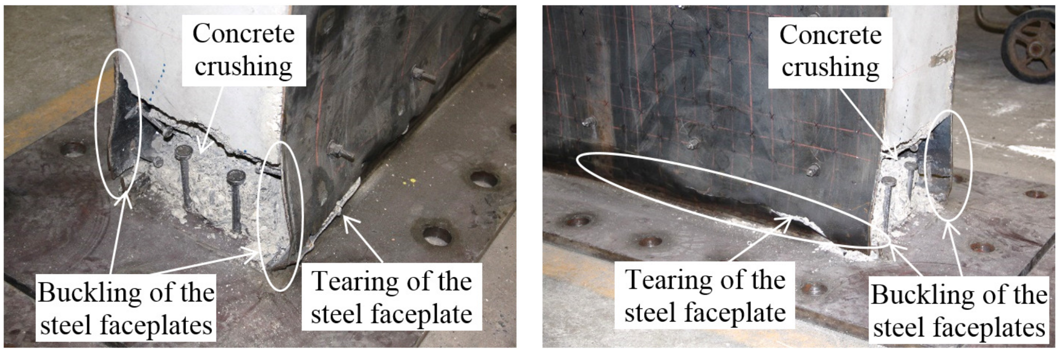

(a) SC1

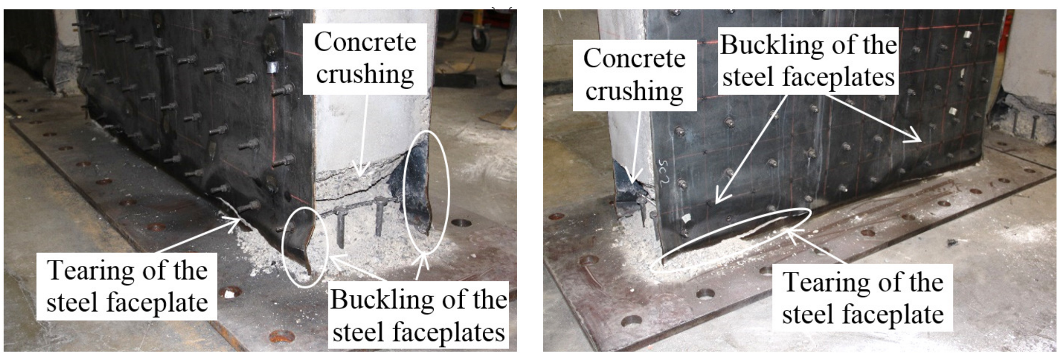

(b) SC2

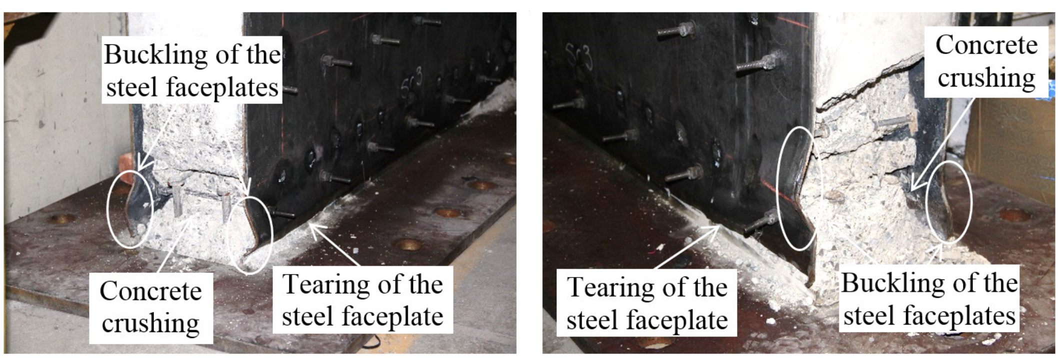

(c) SC3

Figure 5-1 Damage to SC walls at the end of testing

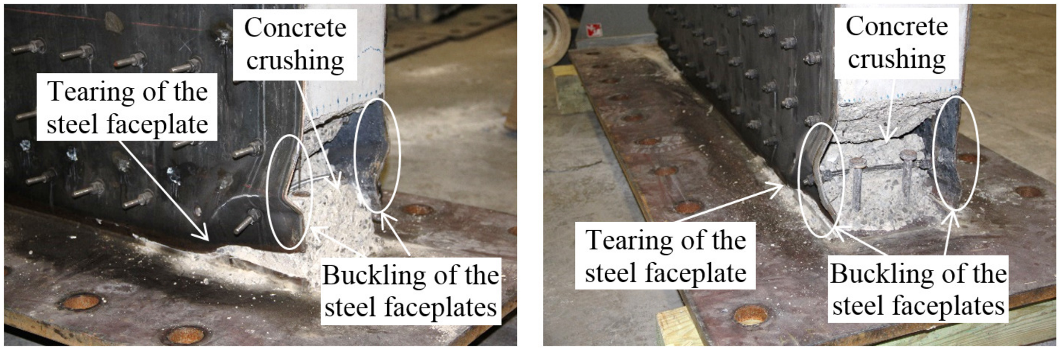

(c) SC4

Figure 5-1 Damage to SC walls at the end of testing (cont.)

A steel faceplate was removed from each of two specimens, SC2 and SC4, for the purpose of documenting damage to the infill concrete. As seen in Figure 5-2, one wide diagonal crack formed in the infill concrete of SC2 but no crack was observed at the web of the SC4. Most of the damage to the infill was concentrated immediately above the baseplate, at the level of the first row of tie rods.

(a) SC2

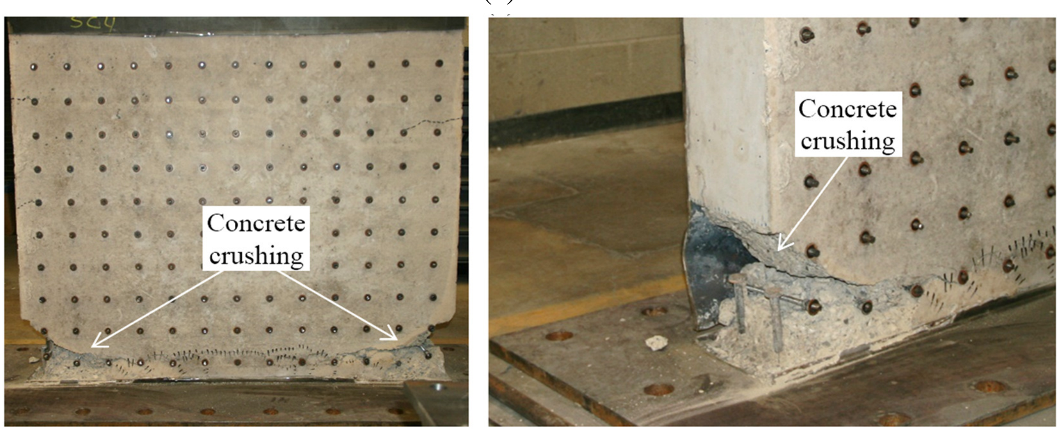

(b) SC4

Figure 5-2 Damage to the infill concrete of SC2 and SC4

Figure 5-3 presents the damage to SC1 through SC4 at different drift ratios. More photographs of damage to the SC walls and to the infill concrete of SC2 and SC4 at each loading step and at the end of the testing are provided in Appendix B. In Figure 5-3, LS denotes the load step, and CI and CII represent the first and second cycles in each load step, respectively. The sequence of the damage to the SC walls is presented in Table 5-2. Concrete cracking, steel faceplate buckling, and concrete crushing in the four SC walls occurred at drift ratios of 0.12%, 0.47%, and 1.17% respectively. Local tearing of the steel faceplates at their connection to the headed studs occurred at a drift ratio of 1.6% for SC1. Tearing of the faceplates along their welded connection to the baseplate begun at drift ratios of 1.4% for SC3 and SC4, 1.6% for SC2, and 2.3% for SC1. One tie rod in SC4 fractured at a drift ratio of 2.1%.

Tearing of the steel faceplates initiated immediately above the welded connection of the faceplates to the baseplate in SC2, SC3, and SC4. In SC1, the steel faceplates fractured first at connections to the headed studs. The lower corners of the steel faceplates, where the faceplates were expected to buckle, were restrained by headed studs in SC1 and tie rods in the other SC walls (see Figure 5-4). Headed studs anchor the faceplates to the infill concrete, enable composite action, and delay out-of-plane buckling of the faceplates. Crushed concrete around a stud cannot anchor a stud and local damage around the stud will affect the buckling resistance of the faceplate. (The use of tie rods near the base of the wall will significantly reduce the outward movement of the tie rod (and the faceplate) after concrete crushing, at the location of the tie rod, and consequently improve the response by delaying inelastic buckling of the faceplate).

5.4 Load-Displacement Cyclic Responses

The load-displacement relationships for SC1 through SC4 are presented in Figure 5-5. Points A, B, C, D, E, F, and G in Figure 5-5 represent the onset of concrete cracking, yielding of the steel faceplates, buckling of the steel faceplates, concrete crushing, fracture of the steel faceplates at their connection to the headed studs, tearing of the steel faceplate above the welded connection of the faceplates to the baseplate, and fracture of tie rod, respectively. The load was calculated by resolving the sum of the forces in the actuator load cells into the plane of the wall. The displacement was measured by a Temposonic displacement transducer attached to the side of the wall at the level of the actuators (60 in. above the base of the wall).

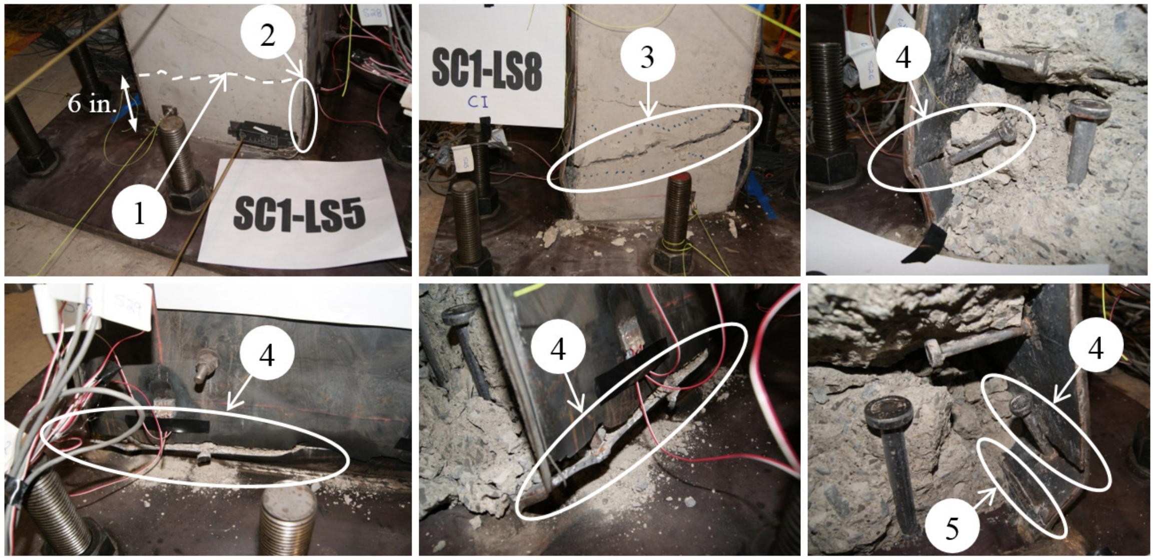

(a) SC1

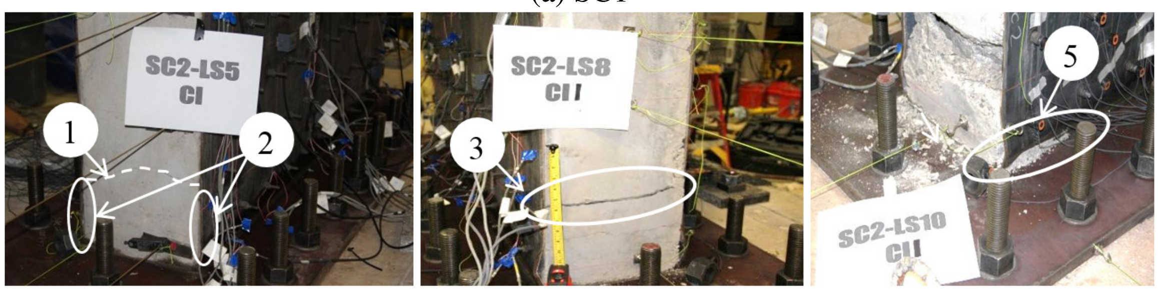

(b) SC2

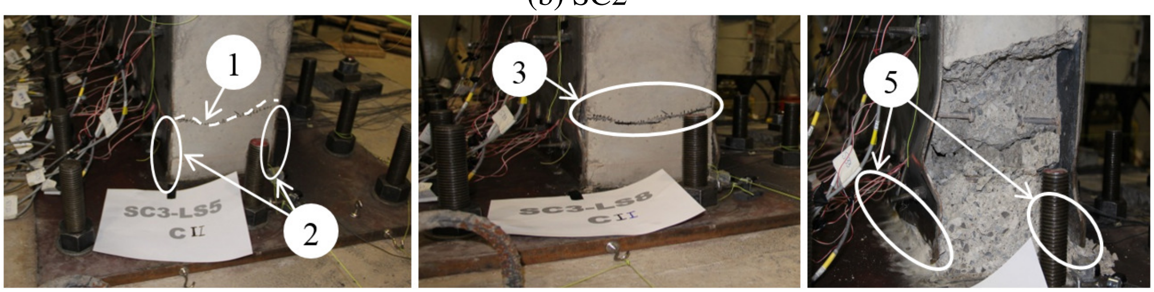

(c) SC3

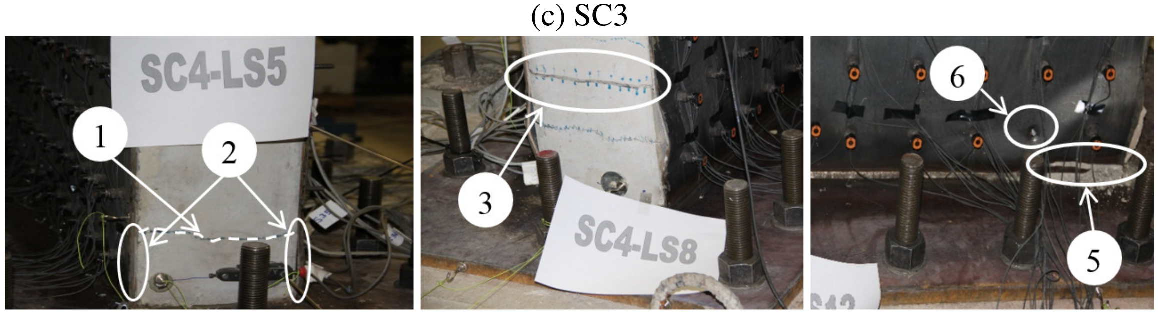

(d) SC4

1. Concrete cracking; 2. Steel faceplate buckling; 3. Concrete crushing; 4. Fracture of the steel faceplate at the level of the stud; 5. Fracture of the steel faceplate above the welded connection; 6. Fracture of the tie rod

Figure 5-3 Damage to SC walls

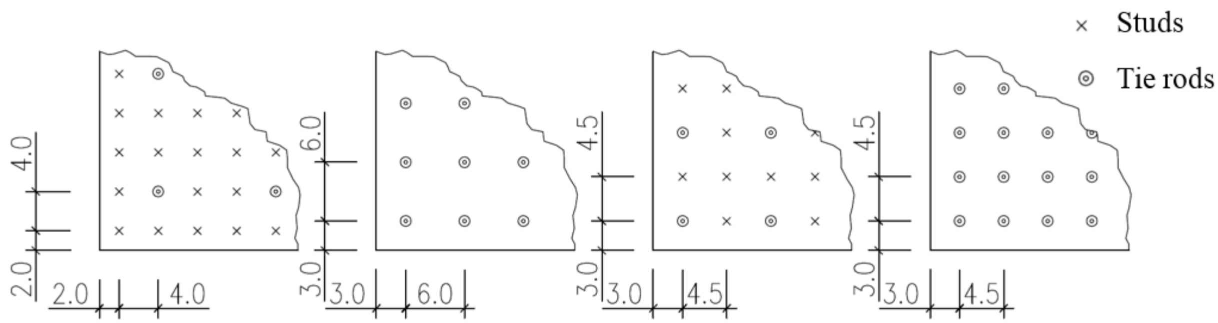

Figure 5-4 Location of the studs and tie rods attached to the steel faceplates

Table 5-2 Sequence of damage to SC walls

Load step	Drift ratio	Specimen	Damage
LS2	0.12%	SC1 through SC4	Concrete cracking at toes of the wall
LS5	0.47%	SC1 through SC4	Buckling of the steel faceplates
LS8	1.17%	SC1 through SC4	Concrete crushing at toes of the wall
LS9	1.40%	SC3 and SC4	Tearing of the steel faceplates immediately above the welded connection of the faceplates to the baseplate
LS10	1.63%	SC1	Local tearing of the steel faceplates at the connection point to the steel studs
		SC2	Horizontal tearing of the steel faceplates immediately above the welded connection of the faceplates to the baseplate
LS12	2.10%	SC4	Fracture of tie rod
LS13	2.33%	SC1	Horizontal tearing of the steel faceplates at the level of the steel studs and immediately above the welded connection of the faceplates to the baseplate

The peak load, observed at a relatively high drift ratio of 1.17+%, were 325 kips and 275 kips for SC1/SC2, and SC3/SC4, respectively. The pinched behavior was attributed to the damage to the infill concrete and steel faceplates, including concrete crushing and tearing of the steel faceplates, and flexibility at the base of the wall. The rates of the post-peak strength and stiffness deterioration were similar in SC2, SC3, and SC4. The rate of strength deterioration in SC1 post-peak-strength was much lower than in other walls up to point F in SC1 (2.33% drift ratio), where the steel faceplates fractured above their welded connection to the baseplate.

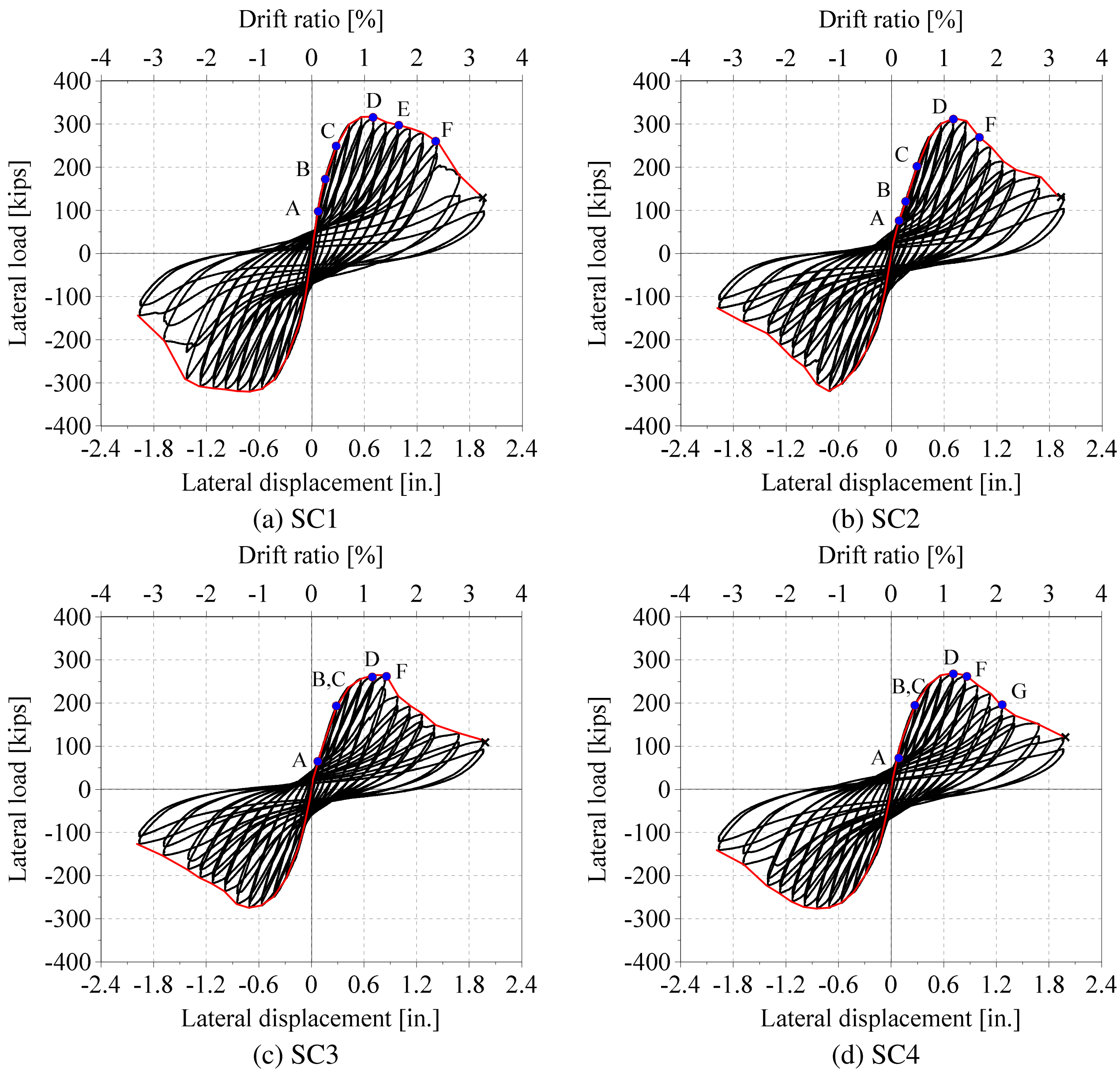

Figure 5-5 Cyclic force-displacement relationships and backbone curves for the SC walls

The onset of yielding of the steel faceplates was determined using the rosette strain gage data and assuming a Von-Mises yield criterion. As seen in Figure 5-5, yielding of the steel faceplates occurred prior to their buckling for SC1 and SC2. Buckling and yielding of the steel faceplates occurred at the same drift ratio for SC3 and SC4. Concrete crushing occurred at a drift ratio corresponding to the peak shear strength for the four SC walls. The pre-peak-strength response of SC walls could be approximated by a tri-linear force-displacement relationship to consider three stages of response, namely 1) elastic, 2) cracking of the infill concrete, and 3) buckling of the steel faceplates.

5.5 Post Peak Response of SC Walls

Inelastic behavior of the four SC walls was associated with yielding of the steel faceplates near the base of the walls and damage to the infill concrete at the ends of the walls. Local buckling of the steel faceplates in the region of high plastic strain near the base of the walls triggered plate fracture and tearing.

Figure 5-6 provides photographs of damage to the four walls at load step 10 (see Figure 4-17), which corresponds to a drift ratio of 1.63%. The first row of connectors was attached to the steel faceplates 2 in. (SC1) and 3 in. (SC2, SC3, and SC4) above the welded connection of the faceplates to the baseplate.

As seen in Figure 5-6, local buckling of the steel faceplates occurred above the first row of the connectors in SC1 and below the first row of connectors in SC2, SC3 and SC4. The use of a smaller distance (2 in.) between the baseplate and the first row of connectors in SC1 delayed the tearing of the faceplates and improved the response at displacements greater than those associated with peak strength (i.e., post peak) by forcing the inelastic buckling of the faceplates away from the CJP welded connection of the faceplates to the baseplate and into the panels defined by the first and second row of connectors.

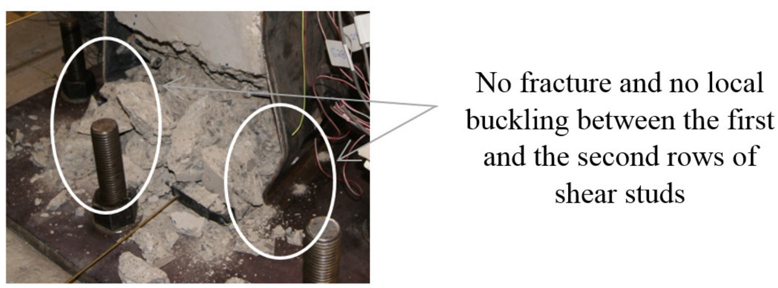

(a) SC1

(b) SC2

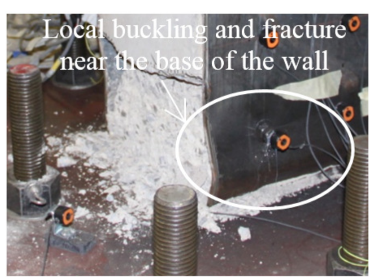

(c) SC3

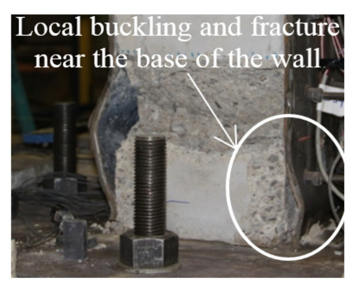

(d) SC4

Figure 5-6 Damage to SC walls

The cyclic backbone curves of Figure 5-7 provide further insight into the influence of the distance between the first row of the connectors and the base of the wall on the post-peak response of the SC walls. The rate of the post-peak strength deterioration of SC1 was much less than other specimens, which was due to the fracture of the steel faceplates in SC2, SC3 and SC4 at a lower drift ratio than in SC1. In SC4, the rate was slower in the EL- direction than in WL+ direction because the steel faceplate buckled and fractured first at the East toe of the wall. The faceplate buckled far from the baseplate at the western toe of SC4 (see Figure 5-8). The rate of the strength deterioration in SC2 and SC3 was almost identical in both the EL- and WL+ directions.

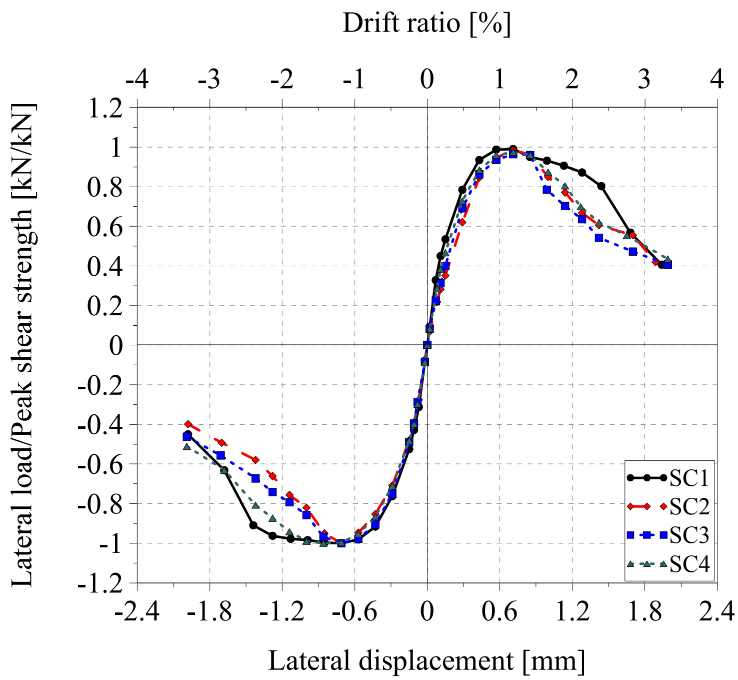

Figure 5-7 Cyclic backbone curves for the SC walls

5.6 Energy Dissipation and Viscous Damping

The cumulative energy dissipation in the SC walls is presented in Figure 5-9. The energy dissipated in each cycle was calculated as the area enclosed by the hysteresis loop in that cycle. The cumulative energy dissipation capacity of the thicker walls, with higher peak loads was expected to be greater than that of the thinner walls. The energy dissipation in SC4 was greater than that in SC2 due to a lower rate of post-peak strength deterioration in SC4 than in SC2, as discussed in Section 5.5.

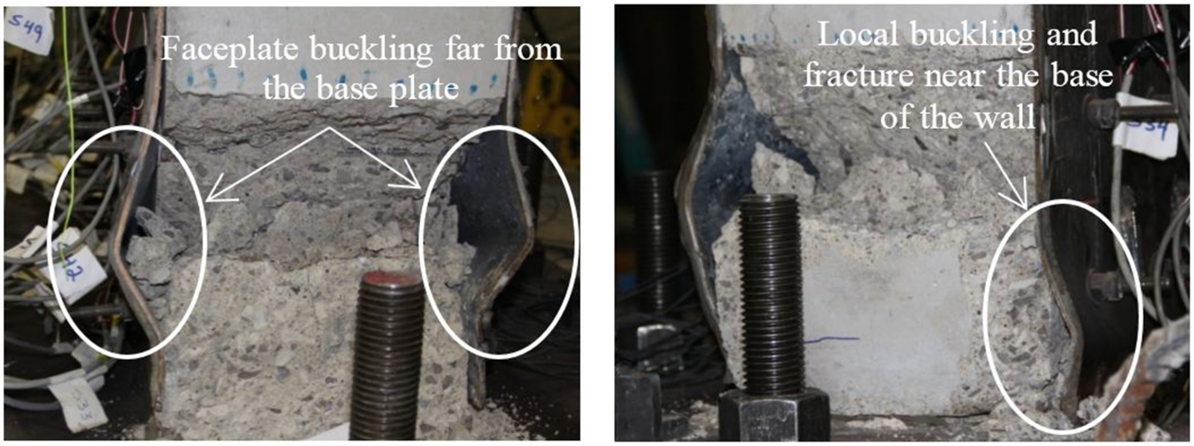

(a) West toe of the SC wall (b) East toe of the SC wall

Figure 5-8 Damage to SC4 at 1.6% drift angle

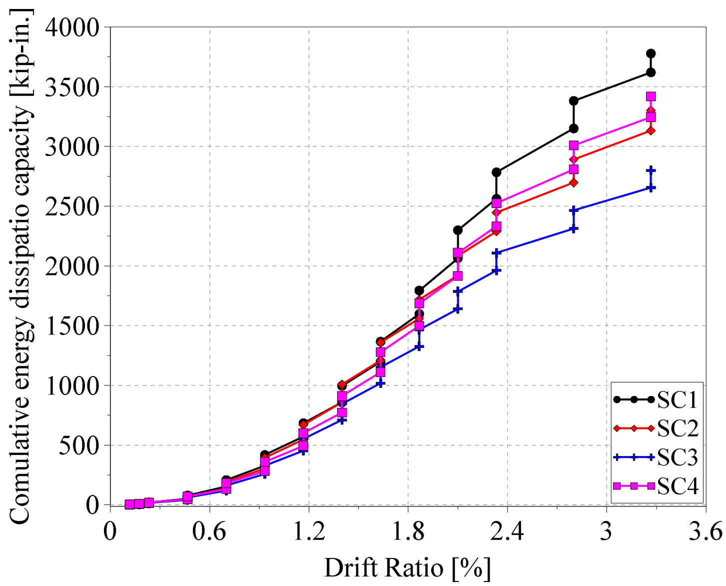

Figure 5-9 Cumulative energy dissipation capacities of SC walls

Equation (5-1) [Chopra (2012)] was used to calculate the equivalent viscous damping, ζ_{eq}, in the SC walls:

$$\xi_{eq} = \frac{1}{4\pi}\frac{E_D}{E_S} \tag{5-1}$$

where E_D is the energy dissipated in a vibration cycle and E_S is the corresponding strain energy. Figure 5-10 presents the equivalent viscous damping ratios calculated from experimental data for drift ratios up to 3.3%. The vertical dashed red line represents the drift ratio corresponding to peak strength. In the pre-peak-strength region, the equivalent viscous damping ratios for the walls are virtually identical. For drift ratios between 50% and 100% of those associated with peak strength, for which elastic dynamic analysis might be employed, the equivalent viscous damping ratios of flexure-critical SC walls varies from 7.5% to 10%. At drift ratios greater than those associated with peak strength, SC1 has the greatest viscous damping because its strength deteriorated more slowly than the other walls.

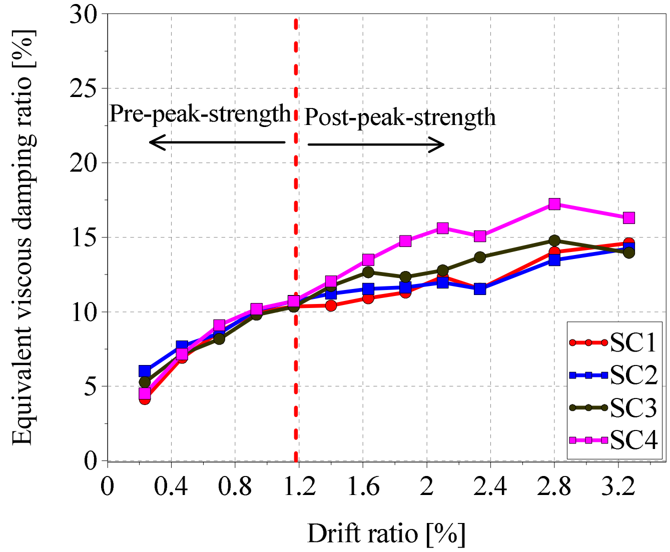

Figure 5-10 Equivalent viscous damping ratios

5.7 Strain and Stress Fields in the Steel Faceplates

A dense grid of Krypton LEDs attached to one steel faceplate was used to estimate the strain fields in the steel faceplates. The grid of the Krypton LEDs generated square panels on the surface of the faceplate (see Figure 4-20). Normal and shear strains in each square panel were calculated using the in-plane displacements measured by Krypton LEDs and an isoparametric quadrilateral formulation [e.g., Bathe (1982)] , as presented in (5-2):

$$\{\varepsilon\}=[B]\{u\} \Rightarrow \begin{Bmatrix} \varepsilon_x \\ \varepsilon_y \\ \gamma_{xy} \end{Bmatrix} = [B] \begin{Bmatrix} u_1 \\ v_1 \\ u_2 \\ v_2 \\ u_3 \\ v_3 \\ u_4 \\ v_4 \end{Bmatrix} \tag{5-2}$$

where $\{\varepsilon\}$ is a vector of the in-plane normal and shear strains; u_i and v_i are the measured horizontal and vertical nodal displacements at the four corners of each panel, respectively; and $[B]$ is the strain-displacement matrix and is derived using the shape functions presented in (5-3).

$$N_i = \frac{1}{4}(1 \pm s)(1 \pm t)\ , i = 1,...,4 \tag{5-3}$$

where (s, t) is the new coordinate system to which was mapped from the (x, y) coordinate system. The strains in the other steel faceplate were directly measured using rosette strain gages installed at three elevations, with the second gage vertical. The three strains measured by each rosette were transformed to normal and shear strains using (5-4) to (5-6).

$$\varepsilon_x = \varepsilon_a + \varepsilon_c - \varepsilon_b \tag{5-4}$$

$$\varepsilon_y = \varepsilon_b \tag{5-5}$$

$$\gamma_{xy} = \varepsilon_c - \varepsilon_a \tag{5-6}$$

where ε_a, ε_b, and ε_c are the strains measured by the first, second, and third strain gages, respectively; ε_x and ε_y are the transformed normal strains parallel to the length and height of the specimen, respectively; and γ_{xy} is the engineering shear strain.

The measured shear forces, corresponding to the level of the first row of strain gages and first row of LED panels above the baseplate, were calculated as the product of the average shear strain (calculated using either the rosettes strain gages or from the LED displacements), an assumed value of G (=11155 ksi) for the steel faceplates, and a total faceplate area of 22.5 inches, prior to the steel faceplate yielding.

Figure 5-11 presents the shear force-displacement relationships for the steel faceplates at small values of drift ratio, and prior to steel faceplate yielding, calculated using the displacements measured by the LEDs (solid blue line) and strains measured by rosettes (solid red line). Figure 5-11 shows that the LED- and rosette-measured shear force-displacement relationships are virtually identical.

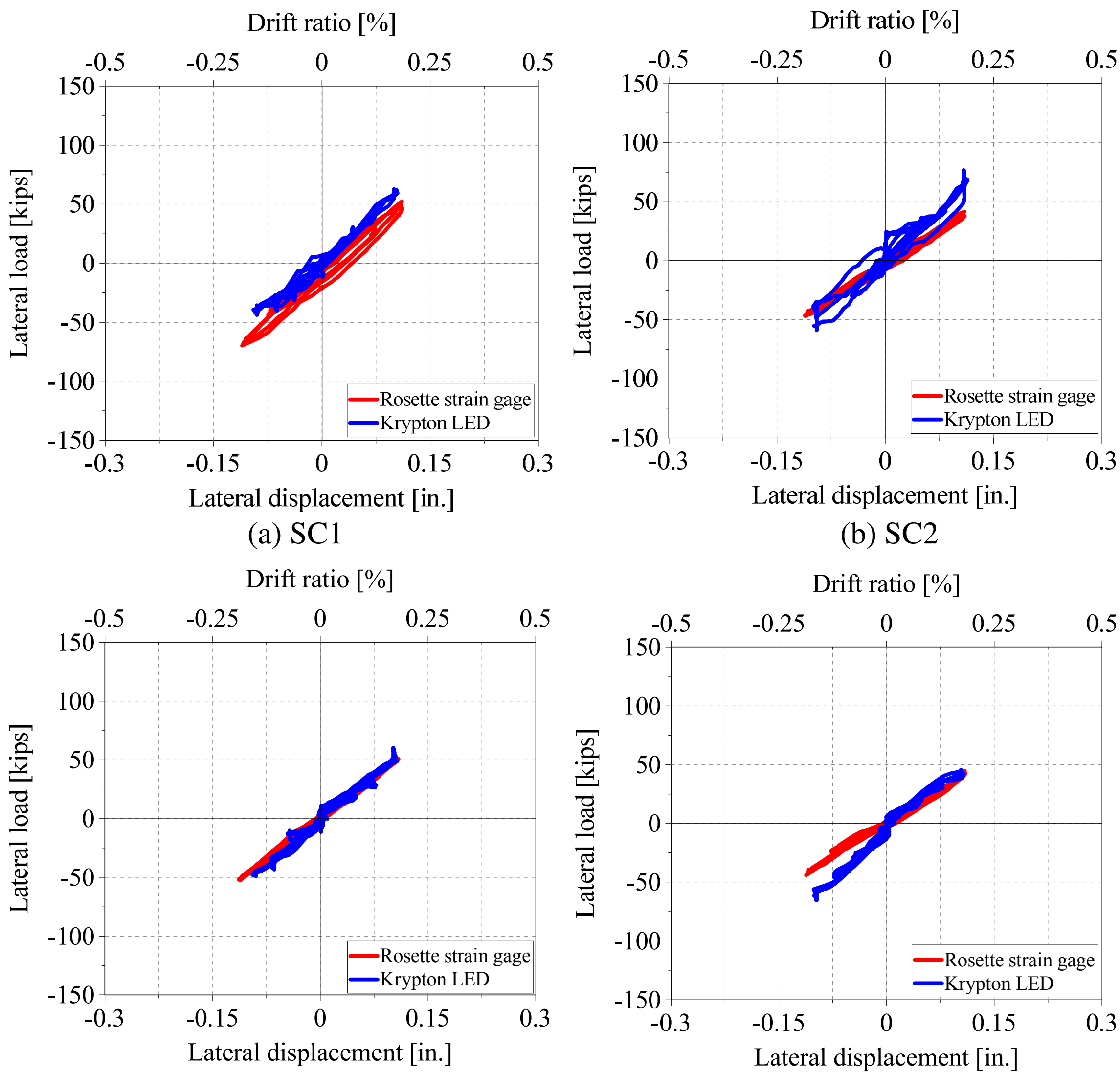

(a) SC1 (b) SC2

(c) SC3 (d) SC4

Figure 5-11 Measured shear force – displacement relationships in steel faceplates

Using the values of the normal and shear strains at the four corners of each panel generated by the grid of the Krypton LEDs, the values of the plane stress components were calculated using the elastic properties of the steel faceplates. At a node common to multiple panels, each stress component was calculated by assigning a weight to each panel, based on panel area. The distribution of the vertical, horizontal, and shear components of the strain and Von-Mises stress in a steel faceplate of SC1, at the displacements corresponding to 0.12%, 0.47%, 1.17%, and 1.87% drift ratios, are presented in Figure 5-12. The calculated strains and stresses are greatest at the bottom corners of the steel faceplate, where the out-of-plane buckling and tearing of the plate initiated. In Figure 5-12 (d), the regions colored red identify yielding of the steel faceplate.

The LED-measured in-plane displacements were used to calculate the displacement fields in the steel faceplates. Figure 5-13 presents the undeformed shape and deformed shapes (scaled by a factor of 10) in one steel faceplate of SC3 at displacements corresponding to ±0.47%, ±1.17%, ±1.42% , and ±1.87% drift ratio. The measured displacement field in the steel faceplates can be used to validate numerical models (see Section 6.4.6.3).

5.8 Vertical Strain in the Steel Faceplates

Figure 5-14 presents the measured vertical strain distribution in the steel faceplate of SC4 over the length of the wall at displacements corresponding to ±0.12%, ±0.18%, ±0.47%, ±0.95%, ±1.42%, ±1.89%, ±2.36%, and ±2.84% drift ratios. The vertical strains were measured using 11 rosette strain gages attached to the steel faceplate 5.2 in. above the baseplate. After the steel faceplates buckled, the attached strain gages attached to the buckled steel faceplate were over-ranged and so the vertical strains at these locations are not reported in Figure 5-14.

As seen in Figure 5-14, the assumption of plane sections remaining plane is not satisfied for drift ratios greater than 0.47%. The normalized depth to the neutral axis[1] from the compression toe varies from 0.35 at a drift ratio of 0.12%, to 0.25 at the drift ratio corresponding to the peak shear strength, to 0.45 at a drift ratio of 2.8%. In the pre-peak strength region, the neutral axis depth decreased as lateral displacement at top of the wall increased because as lateral displacement increased the horizontal cracks in the tension zone of the infill concrete propagated towards the mid-depth of the wall and more tensile force was transferred to the steel faceplates, which leaded to an increase to the depth of the tensile zone of the steel faceplates. However, in the post-peak strength region, buckling of the steel faceplates and crushing of the infill concrete on the compression side of the wall leaded an increase to the neutral axis depth in the faceplate.

[1] The normalized neutral axis depth is the ratio of the neutral axis depth to the length of the wall.

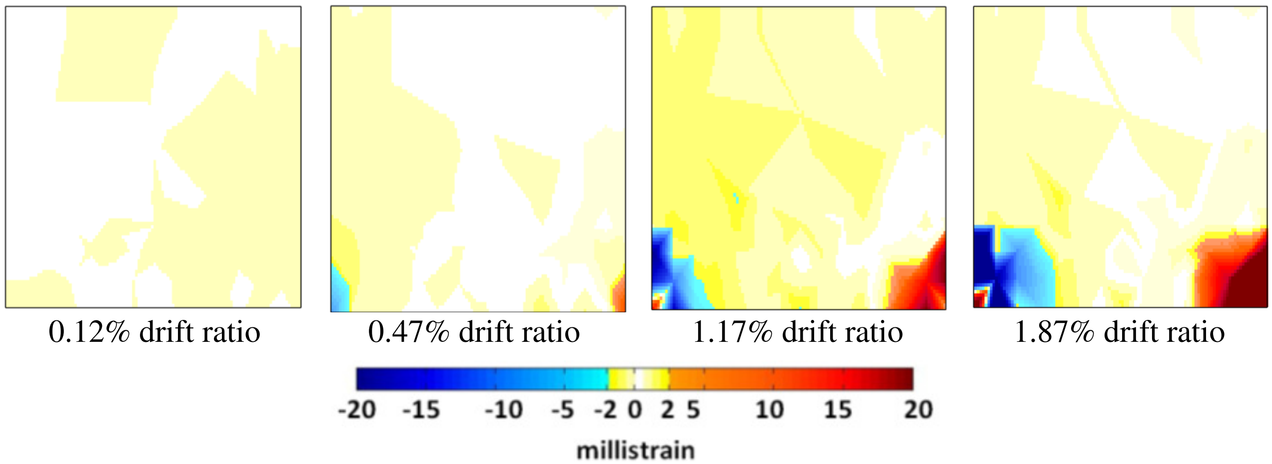

(a) Vertical strain

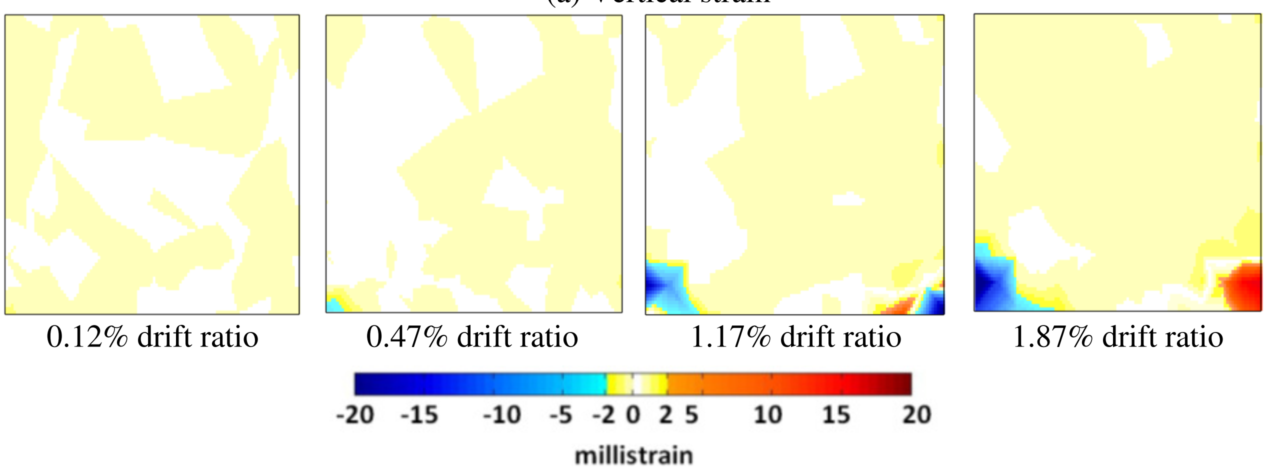

(b) Horizontal strain

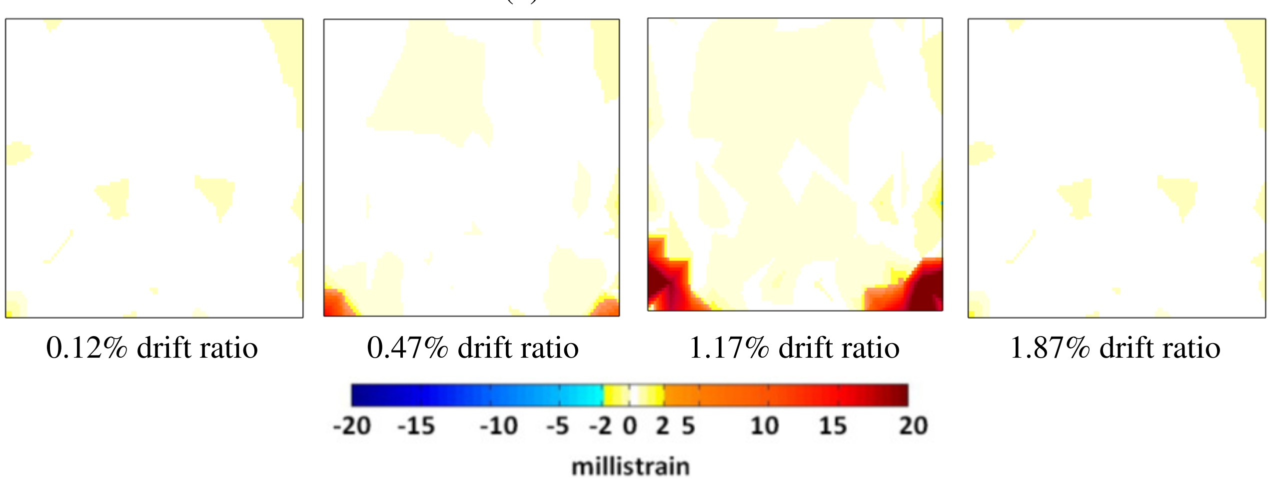

(c) Shear strain

Figure 5-12 Distribution of the strains and Von-Mises stress in steel faceplate of SC1

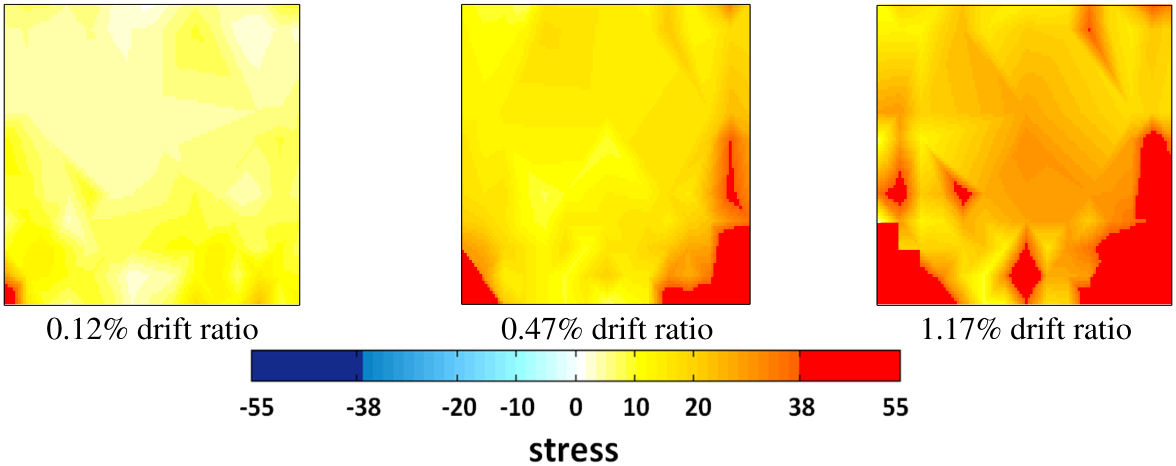

(d) Von-Mises stress

Figure 5-12 Distribution of the strains and Von-Mises stress in steel faceplate of SC1 (cont.)

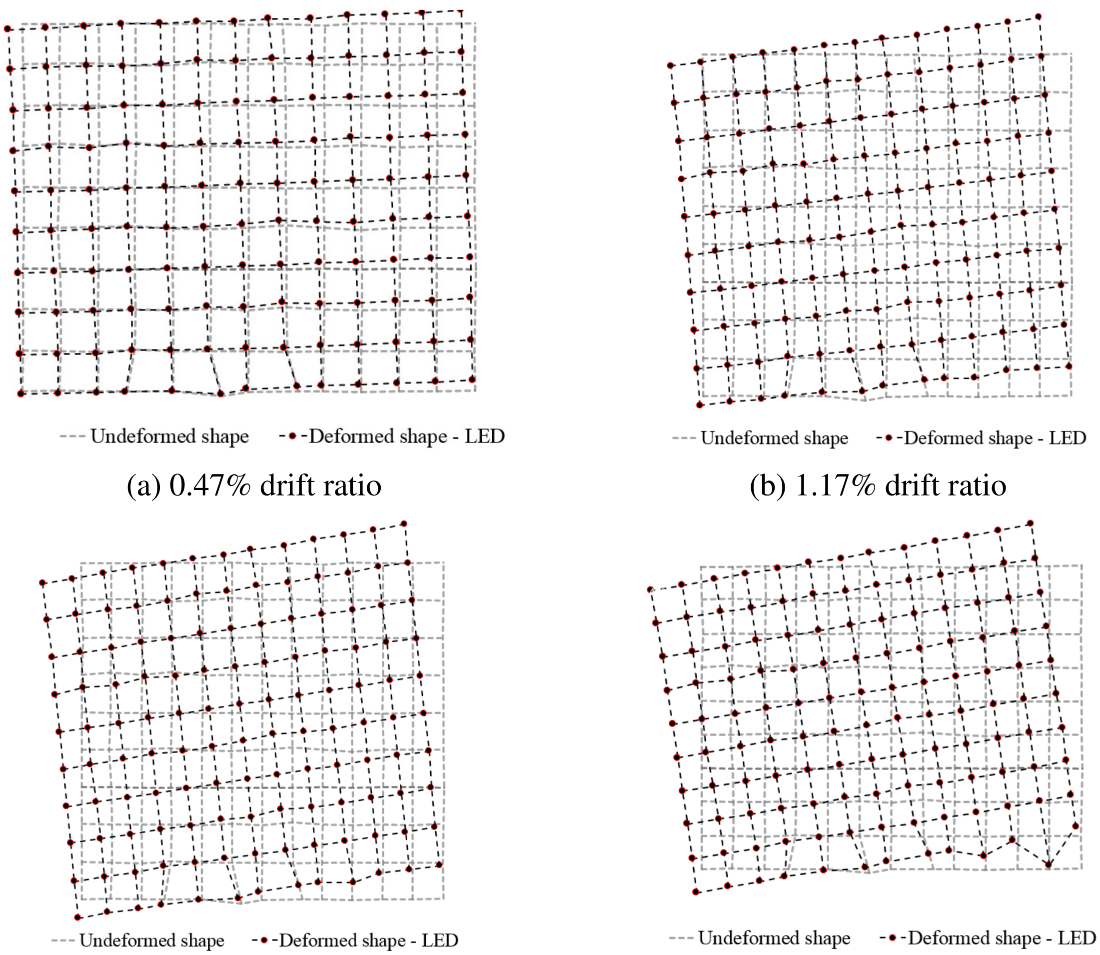

(a) 0.47% drift ratio

(b) 1.17% drift ratio

(c)1.42% drift ratio

(d) 1.87% drift ratio

Figure 5-13 Deformed shapes of the steel faceplate in SC3

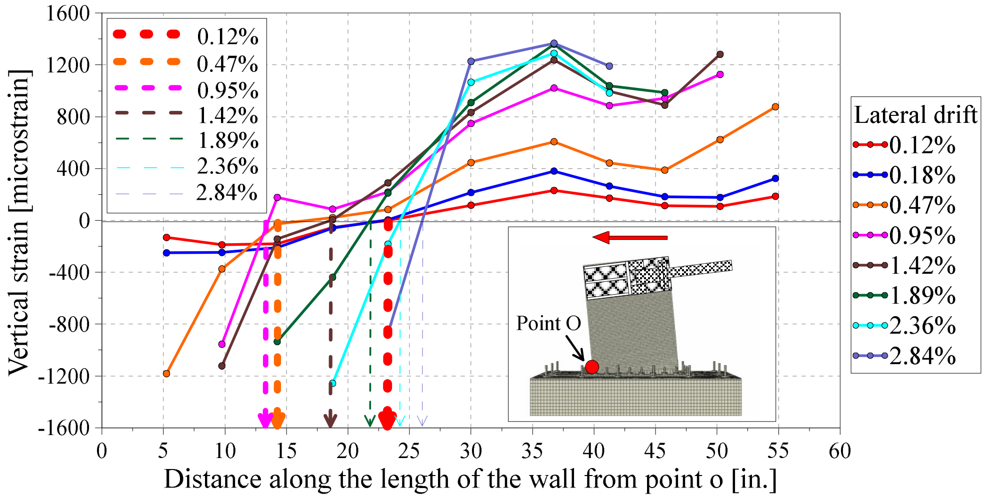

(a) Loading towards the West direction

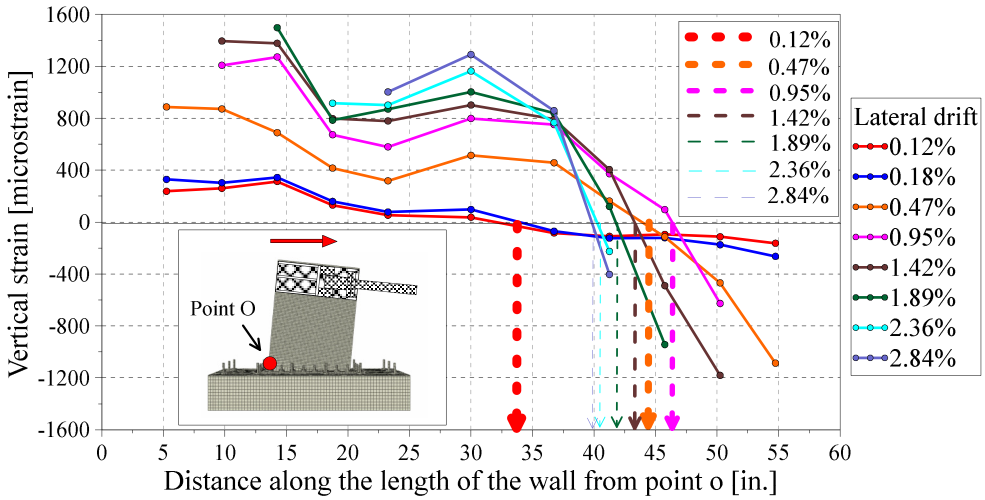

(b) Loading towards the East direction

Figure 5-14 Measured vertical strain distribution in the steel faceplate of SC4 over the length of the wall

5.9 Load Transfer in the SC Walls

To investigate load transfer between the steel faceplate and the infill concrete, the strain field in the steel faceplates and the horizontal shear force resisted by the steel faceplates were evaluated at different elevations over the height of the wall using nodal displacements measured by the LEDs.

The square grid of Krypton LEDs installed on one faceplate per wall enabled calculation of the strain field in the elastic range of response. The horizontal and vertical displacements from each LED were used to calculate the three in-plane strain components using an isoparametric quadrilateral formulation [e.g., Bathe (1982)]. The normal and shear stresses were then calculated using an elastic constitutive stress-strain relationship. The horizontal shear force resisted by the steel faceplates was calculated by integrating the shear stress along the length of the faceplate and multiplying by 2.

The horizontal shear forces resisted by the steel faceplates were calculated at the five levels along the height of the wall identified in Figure 5-15. Figure 5-16 presents results for cycles 3 through 8 and prior to faceplate yielding.

Force ratio is defined as the horizontal shear force resisted by the steel faceplates divided by the total applied lateral force (measured by the actuator load cells, resolved into the plane of the wall). The force ratio varies from 25% to 75%, and from 30% to 90%, for SC1/SC2 and SC3/SC4, respectively. The force ratios in SC3 and SC4 were greater than those in SC1 and SC3, supporting the intuitive statement that the higher the reinforcement ratio, the greater the steel faceplate contribution to the total shear force.

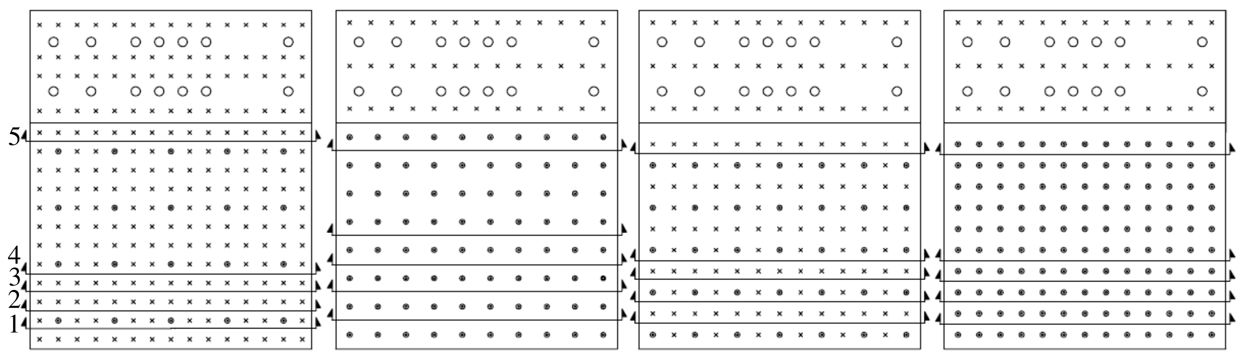

(a) SC1 (b) SC2 (c) SC3 (d) SC4

Figure 5-15 Reporting levels for the steel faceplates

The force ratios increased in SC1, SC3, and SC4 from the top of each specimen (level 5, see Figure 5-15) to the foundation. The shear force was transferred from the infill concrete to the steel faceplates through the connectors and interface friction between the infill concrete and steel faceplate, along the height of the wall. In SC2, the specimen with the highest plate slenderness ratio (=32), the greatest contribution of the steel faceplate to the total shear force before yielding of the faceplate was observed at level 3: the mid-height of the specimen.

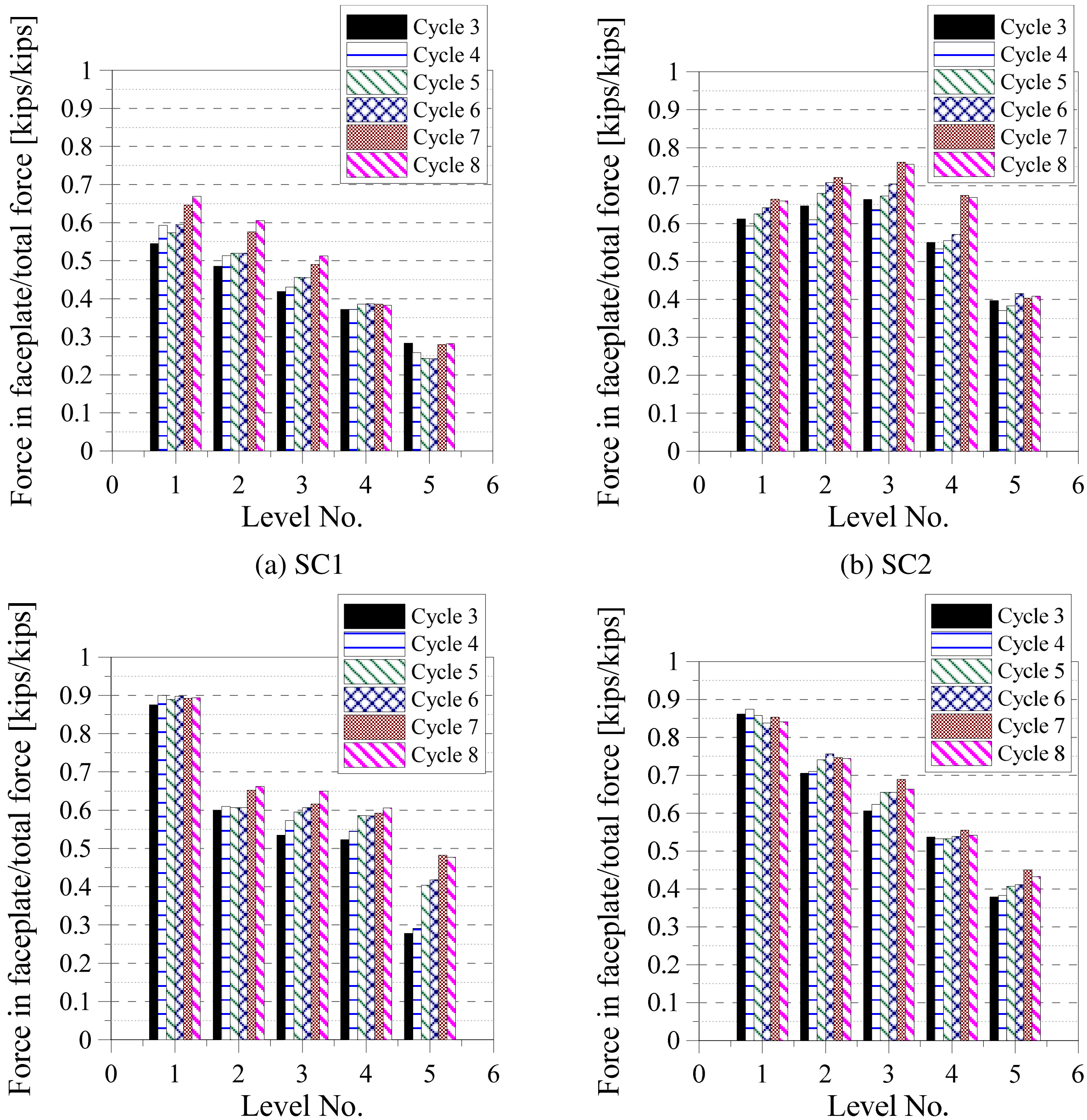

(a) SC1 (b) SC2

(c) SC3 (d) SC4

Figure 5-16 Ratio of the horizontal shear force resisted by the steel faceplates to the total applied load

The total horizontal shear force transferred by a row of connectors was calculated as the difference between the horizontal shear forces resisted by the steel faceplate above and below the row, which neglects interface friction. The shear forces resisted by the second, third, and fourth rows of the connectors were estimated to be 11/14/20 kips, 7/6/13 kips, 27/4/5 kips, and 13/10/16 kips for SC1 through SC4, respectively, in cycles 2 through 8. The shear strengths of one anchor were 4.3 kips and 16.5 kips for steel failure and concrete pryout, respectively, per Appendix D of ACI 318-11

(2011). Setting aside the vertical shear forces on the studs, the minimum nominal shear strength of a row of connectors is 65/43/56/56 kips, in SC1 through SC4, respectively, suggesting some margin against stud failure. No concrete crushing was observed around the tie rods in SC2 and SC4, which is not surprising given the calculated capacity of 16.5 kips per stud for concrete pryout.

5.10 Lateral Displacement Profile

Figure 5-17 presents the measured lateral displacement profile at different drift ratios. The lateral displacements were measured by Temposonic displacement transducers attached on one side of the wall specimen. Figure 5-17 shows that the measured profiles are almost linear over the height of the wall during the entire test. The lateral displacement profile is linear to a drift ratio of 3.3%, where upon significant damage had accrued to the steel faceplates and the infill concrete near the base of the wall. This result is attributed to the large contribution of the base rotation to the total lateral displacement (up to 85%, see Section 5.11).

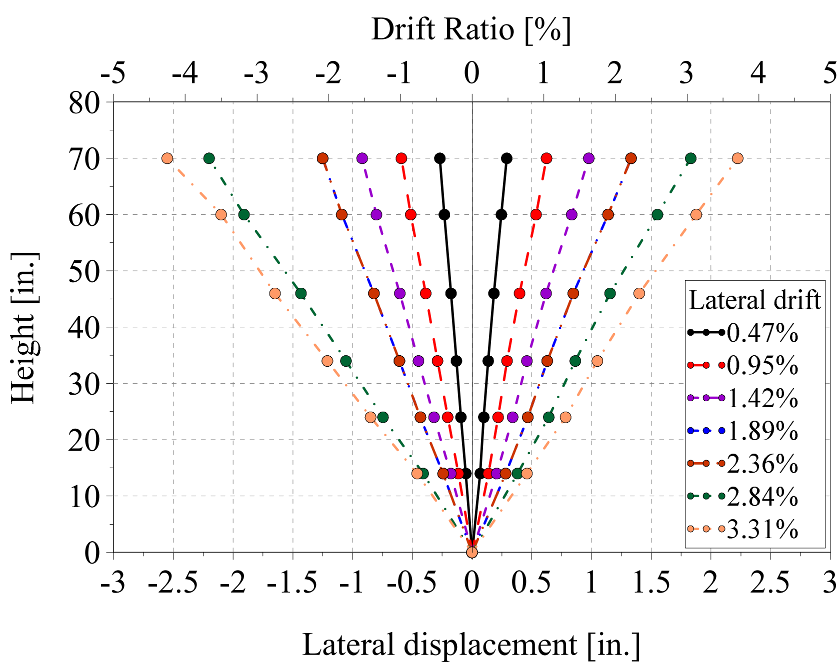

Figure 5-17 Lateral displacement profile along the height of the wall

5.11 Displacement Components

Figure 5-18 describes the three contributions to the lateral displacement at the top of the SC walls, namely, flexural displacement, Δ_f, shear displacement, Δ_s, and lateral displacement due to base rotation, Δ_r. The illustration is a section cut at a faceplate and not an elevation. The out-of-plane (vertical) deformation of the baseplate attached to the steel faceplates allowed rotation at the base of the wall.

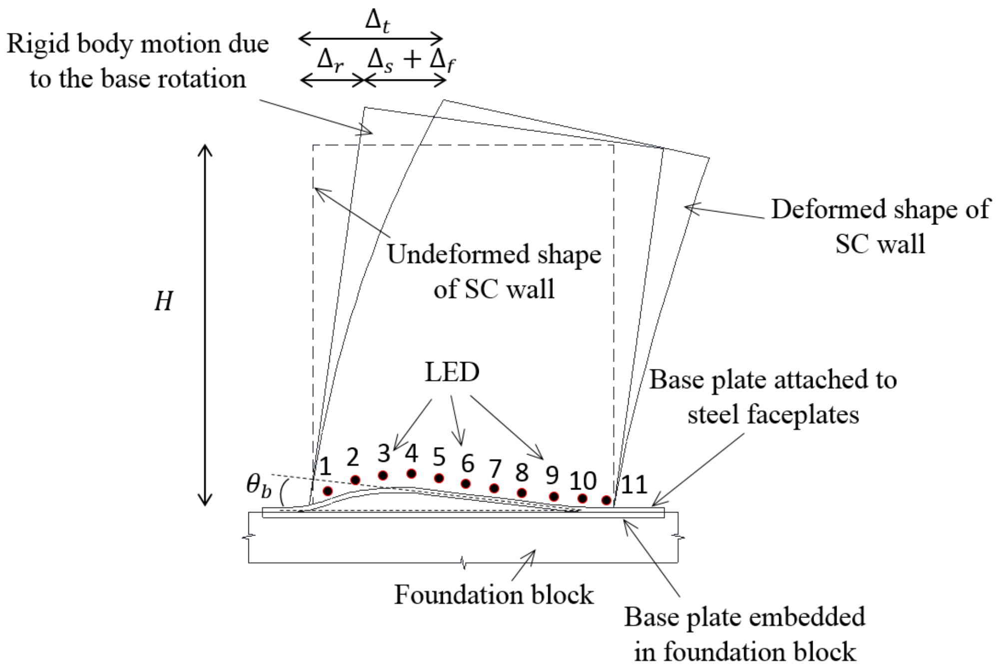

Figure 5-18 Components of the lateral displacement at top of the wall

The displacement at top of the wall due to the base rotation, Δ_r, was calculated using the vertical displacements measured by the first row of LEDs (see Figure 5-18):

$$\Delta_r = \theta_b H \tag{5-7}$$

where H is the height of the wall, and θ_b is the base rotation. The base rotation was calculated as the average of the angles between the horizontal axis and the lines connecting LEDs 4 to 9, 5 to 8, and 6 to 7.

The grid of Krypton LEDs generated horizontal strips across the surface of a faceplate as presented in Figure 5-19. The shear displacement in each strip was calculated as the product of the average shear strain, calculated using displacements measured by the LEDs, in the square panels comprising the strip, and the height of the strip, h_s. The shear component of the total lateral displacement at top of the wall was approximated as the product of the sum of the shear displacements of the horizontal strips (strips 1 to 9 in Figure 5-19) and the ratio of H_w / H_s, where the heights H_w and H_s are identified in Figure 5-19.

The flexural component of the total lateral displacement at top of the wall was calculated as the difference between the total lateral displacement and the sum of the shear displacement and the lateral displacement due to the base rotation.

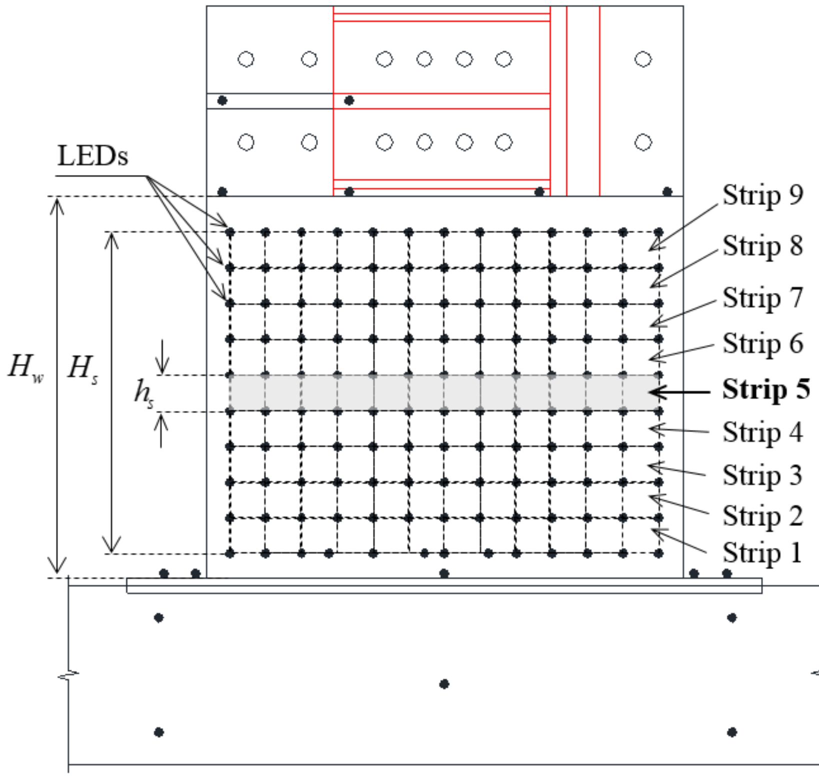

Figure 5-19 Definition of the horizontal strips for the shear displacement calculation

The contributions to the total lateral displacement of SC1 through SC4 are presented in Figure 5-20. As the lateral displacement increased, the percent contribution of the base rotation to the total displacement increased and the contributions of the shear and flexure displacements decreased. The contributions of the shear and flexural displacements to the total displacement varied from 35% at a drift ratio of 0.1% to 10% at a drift ratio of 2.5%. Figure 5-20 indicates that the displacement due to the base rotation governed the total lateral displacement at top of the SC walls. These results indicate that the baseplate connection between the SC wall and the foundation block was the major source of the flexibility in these walls and it needs to be carefully considered in the analysis, design, and detailing of SC walls with bolted baseplate to RC foundation connections.

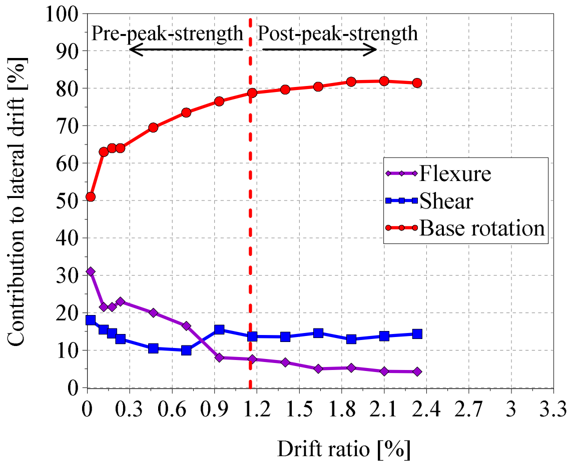

(a) SC1

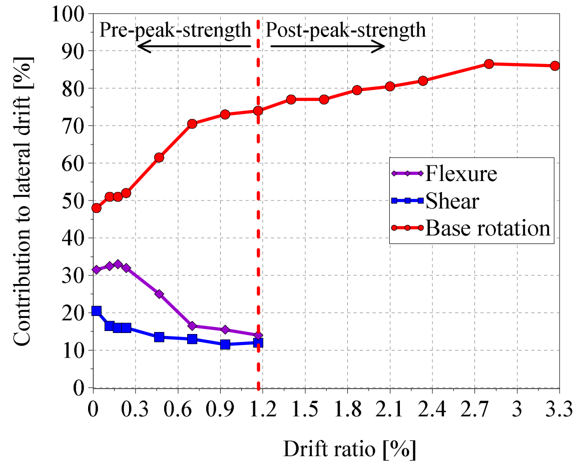

(b) SC2

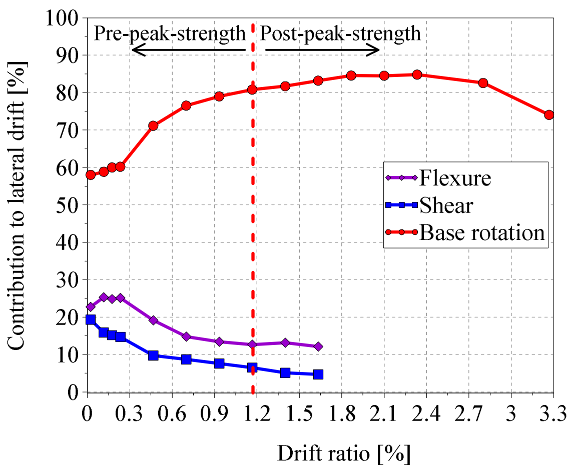

(c) SC3

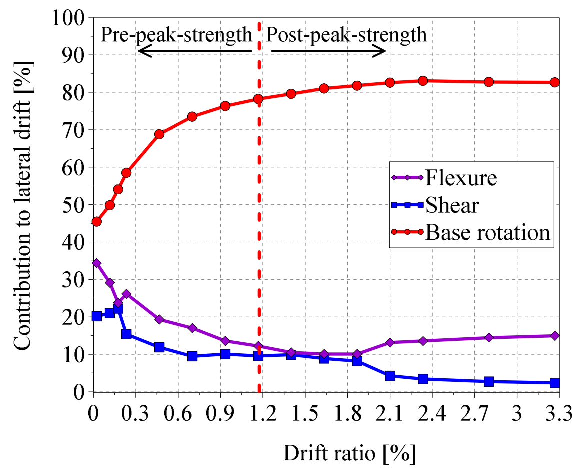

(d) SC4

Figure 5-20 Contribution of the lateral displacement components to the total displacement

5.12 Displacement Ductility of the SC Walls

Displacement ductility, defined as the ratio of the maximum displacement to the yield displacement, represents the ability of the structure to undergo large plastic deformation in the inelastic range without substantial loss of strength [Park (1988)]. There are a number of definitions of the yield and maximum displacements, both of which are needed to calculate displacement ductility. Figure 5-21 presents alternate definitions of the yield and maximum displacements per Park (1988), proposed for reinforced concrete elements. In this study, the yield displacement, δ_y, is defined as the yield displacement of an equivalent elastic-plastic system with the same peak resistance and energy absorption capacity as the real system: the third panel in Figure 5-21(a). Two definitions were considered for the maximum displacement, namely, the displacements corresponding to the peak load, $\delta_{\max,1}$, and 80% of the peak load, $\delta_{\max,2}$: the second and third panels in Figure 5-21(b). Table 5-3 presents the values of the yield and maximum displacements, and the displacement ductility for the four SC walls, with and without considering base rotation.

As seen in Table 5-3, there are significant differences between the values of the displacement ductility calculated using the two definitions of the maximum displacement. The values of the displacement ductility calculated considering base rotation were greater than those calculated after subtracting base rotation. The SC1 has the greatest displacement ductility due its highest tangent pre-peak-stiffness and lowest rate of the post-peak strength deterioration.

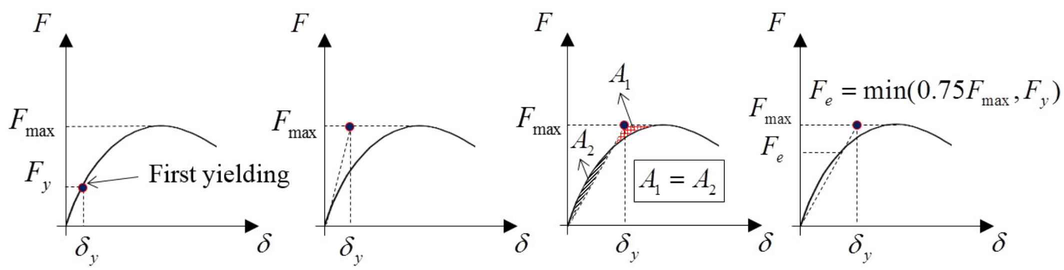

(a) Yield displacement

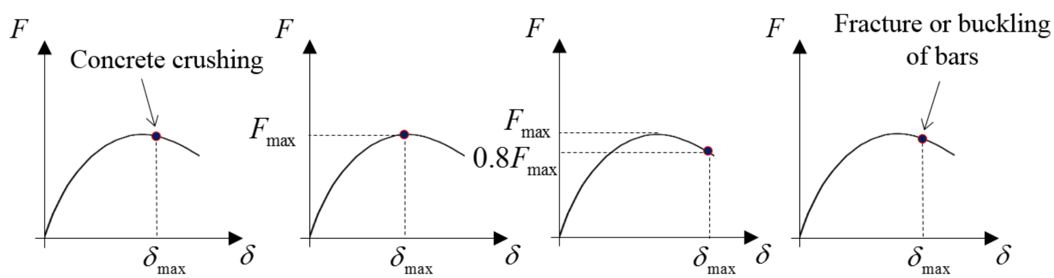

(b) Maximum displacement

Figure 5-21 Alternate definitions of the yield and maximum displacements

Table 5-3 Displacement ductility calculation

Specimen	Without base rotation					With base rotation				
	δ_y (in.)	$\delta_{\max,1}$ (in.)	$\delta_{\max,2}$ (in.)	$\frac{\delta_{\max,1}}{\delta_y}$ (in./in.)	$\frac{\delta_{\max,2}}{\delta_y}$ (in./in.)	δ_y (in.)	$\delta_{\max,1}$ (in.)	$\delta_{\max,2}$ (in.)	$\frac{\delta_{\max,1}}{\delta_y}$ (in./in.)	$\frac{\delta_{\max,2}}{\delta_y}$ (in./in.)
SC1	0.10	0.15	0.27	1.6	2.8	0.33	0.71	1.45	2.2	4.4
SC2	0.16	0.18	0.24	1.1	1.5	0.46	0.71	1.11	1.5	2.4
SC3	0.11	0.14	0.17	1.3	1.6	0.41	0.71	1.01	1.7	2.5
SC4	0.11	0.15	0.21	1.4	1.9	0.37	0.71	1.17	1.9	3.2

5.13 Averaged Secant Stiffness

Figure 5-22 presents the average secant stiffness of the specimens at different drift ratios. The vertical dashed red lines represent the drift ratio corresponding to the peak shear resistance of the SC walls. The average secant stiffness at ith load step, $K_{\mathrm{i}}^{\mathrm{sec}}$, was calculated as:

$$K_{\mathrm{i}}^{\mathrm{sec}} = \frac{V_{\mathrm{i}}^{1} + V_{\mathrm{i}}^{2}}{\Delta_{\mathrm{i}}^{1} + \Delta_{\mathrm{i}}^{2}} \;\; (\mathrm{i} = 1, 2, .., m) \tag{5-8}$$

where Δ_{i}^{1} and Δ_{i}^{2} represent the maximum lateral displacement at the first and second cycles of the ith load step, respectively; V_{i}^{1} and V_{i}^{2} are the corresponding shear forces for Δ_{i}^{1} and Δ_{i}^{2}, respectively; and m is the number of load steps. Figure 5-22 indicates that the SC1 had the greatest secant stiffness in the pre-peak-strength region, as the initial stiffness of this specimen was greater than the other specimens. The variation of the secant stiffness for other three specimens, SC2, SC3, and SC4, were virtually identical in pre- and post-peak strength regions.

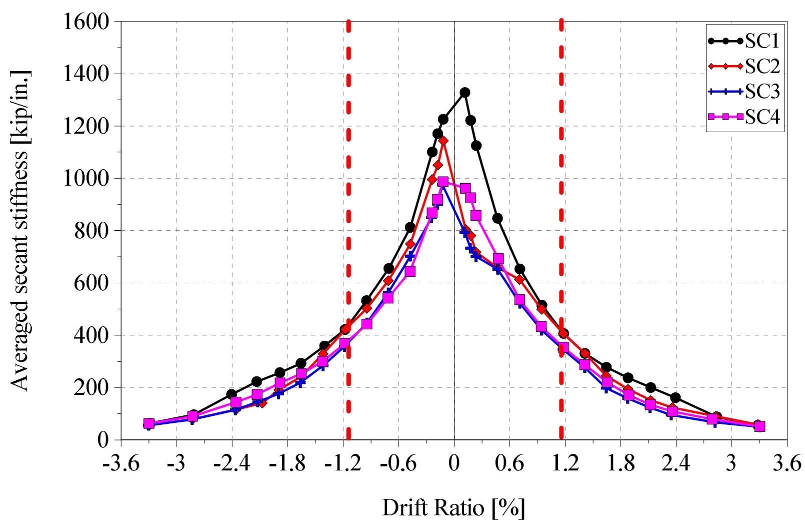

Figure 5-22 Averaged secant stiffness of the SC walls

CHAPTER 6

NUMERICAL ANALYSIS OF SC WALLS

6.1 Introduction

This chapter describes the nonlinear finite element modeling of flexure- and flexure-shear-critical rectangular SC walls using the general-purpose finite element codes ABAQUS [SIMULIA (2012a,2012b)], VecTor2 [Wong et al. (2013)], and LS-DYNA (2012a,2012b). Sections 6.2 and 6.3 describe the ABAQUS and VecTor2 modeling assumptions and analysis results, respectively. Section 6.4 includes information on the finite element model developed in LS-DYNA to simulate the nonlinear cyclic response of flexure- and flexure-shear critical SC walls. The developed finite element model was validated using data from testing of the four large-scale rectangular SC walls presented in Chapter 5. DYNA analysis results are presented, including global force-displacement responses, equivalent viscous damping ratio, strain and stress distributions in the steel faceplates, estimates of the contribution of the steel faceplates and infill concrete to the lateral resistance of the walls, and damage to the steel faceplates and infill concrete. Section 6.5 uses the validated DYNA model to investigate load transfer mechanisms in SC walls and axial and shear forces transferred by the connectors, and the effects on global response of a) the interface friction between the steel faceplates and the infill concrete, and b) the distribution of the shear studs attached to baseplate.

6.2 ABAQUS Analysis

This section discusses the numerical modeling of SC walls using the general-purpose finite element code ABAQUS [SIMULIA (2012a,2012b)]. The Concrete-Damage-Plasticity (CDP) model was used for the infill concrete and the J2 plasticity model with isotropic hardening was used for the steel faceplates. Friction between the infill concrete and the steel faceplates, and buckling of the steel faceplates were considered. The following subsections describe the modeling assumptions and the ABAQUS analysis results.

6.2.1 Concrete Material Model

The CDP model was used to simulate the behavior of the infill concrete. Although this material model was primarily developed for cyclic and dynamic analyses of concrete structures, it is also used for modeling of the quasi-brittle materials, such as rock, mortar, and ceramics. The CDP model cannot be used to simulate the response of concrete members under high confining pressure (e.g., greater than four or five times of uniaxial compressive strength of concrete [SIMULIA (2012b)]). Different yielding and stiffness degradations in tension and compression, softening behavior in tension and compression, stiffness recovery due to the closing of the cracks during cyclic loading, and strain rate are considered. The CDP model implemented in ABAQUS uses the yield function proposed by Lubliner et al. (1989) with the isotropic damage theory proposed by Lee et al. (1998).

6.2.1.1 Stress-Strain Relationship

The stress-strain relationship of the CDP material model is:

$$\{\sigma\} = (1-d)[C]\{\varepsilon - \varepsilon^{pl}\} \tag{6-1}$$

where $\{\sigma\}$ and $\{\varepsilon\}$ are the concrete stress and strain tensors, respectively; $\{\varepsilon^{pl}\}$ is the concrete plastic strain tensor; $[C]$ is the elastic stiffness matrix; and d is a scalar damage parameter representing stiffness degradation, and varies from zero to one for undamaged and damaged materials, respectively. Two independent scalar damage variables are defined to simulate damage in the tensile and compressive states of loading, where the state of loading is tensile if the sum of the concrete principal stresses is positive, and is compressive otherwise.

6.2.1.2 Yield Function

The CDP model uses the yield function proposed by Lubliner et al. (1989) with the modifications proposed by Lee et al. (1998) to account for different evolutions of strength in tension and compression. The yield function is calculated as:

$$F(\bar{\sigma}, \tilde{\varepsilon}^{pl}) = \frac{1}{1-\alpha}(\bar{q} - 3\alpha\bar{p} + \beta(\tilde{\varepsilon}^{pl})\left\langle \hat{\bar{\sigma}}_{\max} \right\rangle - \gamma\left\langle -\hat{\bar{\sigma}}_{\max} \right\rangle) - \bar{\sigma}_c(\tilde{\varepsilon}_c^{\ pl}) \leq 0 \tag{6-2}$$

where $\bar{\sigma}$ is the effective stress and is calculated using (6-1), where the scalar damage is set to zero ($d = 0$); $\bar{p}$ and $\bar{q}$ are the effective hydrostatic pressure and Mises equivalent effective stress, respectively; $\hat{\bar{\sigma}}_{\max}$ is the maximum principal stress; and coefficient α, as a function of equibiaxial stress (f_b') and uniaxial compressive stress of concrete (f_c'), is calculated as:

$$\alpha = \frac{f'_b - f'_c}{2f'_b - f'_c} \tag{6-3}$$

The value of α varies from 0.08 to 0.12 corresponding to typical ranges of f'_b / f'_c varying from 1.10 to 1.16. The coefficient β is a function of the plastic strain tensor and α :

$$\beta(\tilde{\varepsilon}^{pl}) = \frac{\bar{\sigma}_c(\tilde{\varepsilon}_c^{\ pl})}{\bar{\sigma}_t(\tilde{\varepsilon}_t^{\ pl})}(1-\alpha)-(1+\alpha) \tag{6-4}$$

where $\bar{\sigma}_c$ and $\bar{\sigma}_t$ are the effective compressive and tensile cohesion stresses, respectively. The coefficient γ is a function of the constant K_c that controls the shape of the yield surface in the deviatoric plane. Coefficient γ is used when $\hat{\bar{\sigma}}_{\max} < 0$ and is calculated as:

$$\gamma = \frac{3(1-K_c)}{2K_c - 1} \tag{6-5}$$

Figure 6-1 indicates that as K_c increases from 0.6 to 1.0, the shape of the deviatoric plane of the yield surface tends to a circle, as is assumed in the classical Drucker-Prager yield surface.

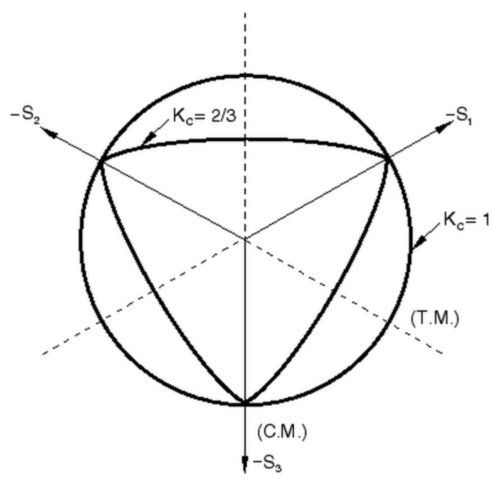

Figure 6-1 Deviatoric plane of the yield surface [SIMULIA (2012b)]

6.2.1.3 Flow Rule

The plastic strain orientation is defined using a non-associated flow rule in the CDP model. The Drucker-Prager hyperbolic function, $G(\bar{\sigma})$, is used as the potential function. The increment of plastic strain is a function of the derivative of the plastic function with respect to the effective stress. The plastic strain increment and the plastic function are calculated as:

$$\dot{\varepsilon}^{pl} = \dot{\lambda}\frac{\partial G(\bar{\sigma})}{\partial \bar{\sigma}} \tag{6-6}$$

$$G = \sqrt{(\chi f_t \tan\psi)^2 + \bar{q}^2} - \bar{p}\tan\psi \tag{6-7}$$

where χ is the eccentricity parameter defining the rate at which the potential function approaches the asymptote; ψ is the dilation angle; and f_t is the uniaxial tensile strength. As seen in Figure 6-2, the plastic potential function asymptotically approaches the linear Drucker-Prager flow potential at either high confining pressure or as χ tends to zero.

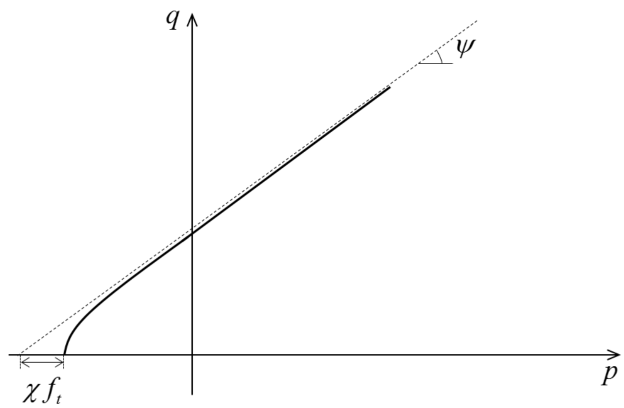

Figure 6-2 Plastic potential function [SIMULIA (2012b)]

6.2.1.4 Damage and Stiffness Degradation

The stiffness degradation (damage) in tension and compression are functions of the tensile and compressive hardening variables and vary from zero for undamaged material to one for fully damaged material. Figure 6-3 presents uniaxial (dashed line) and cyclic (solid line) stress-strain relationships for concrete. In Figure 6-3, d_t and d_c characterize the reduction in tensile and compressive stiffness, respectively. The tensile and compressive stiffness recovery factors, w_t and w_c, respectively, are used to capture the change in stiffness due to crack opening and closing during cyclic loading.

6.2.1.5 Modeling Parameters

The input parameters to the CDP concrete material model are: 1) uniaxial stress-strain relationships in compression and tension; 2) the ratio of the biaxial to uniaxial compressive stress of concrete, varying between 1.10 and 1.16; 3) a constant, K_c, varying between 0.67 and 1.0; 4) the dilation angle, ψ, varying between 15° and 45°; and 5) an eccentricity coefficient, χ, with a default value of 0.1.

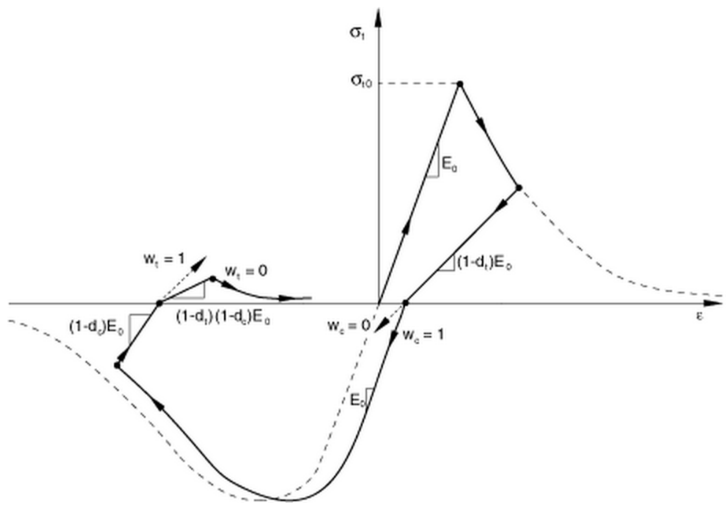

Figure 6-3 Uniaxial and cyclic stress-strain relationships of concrete [SIMULIA(2012b)]

The concrete stress-strain relationship proposed by Saenz (1964) was used to describe the compressive behavior of the infill concrete:

$$\sigma_c = f_c' \frac{K(\dfrac{\varepsilon_c}{\varepsilon_{c0}})}{1 + A(\dfrac{\varepsilon_c}{\varepsilon_{c0}}) + B(\dfrac{\varepsilon_c}{\varepsilon_{c0}})^2 + C(\dfrac{\varepsilon_c}{\varepsilon_{c0}})^3} \tag{6-8}$$

where the coefficients A, B, C, and K are:

$$A = C + K - 2 \tag{6-9}$$

$$B = 1 - 2C \tag{6-10}$$

$$C = K \frac{K_\sigma - 1}{(K_\varepsilon - 1)^2} - \frac{1}{K_\varepsilon} \tag{6-11}$$

$$K = E_0 \frac{\varepsilon_{c0}}{f_c'} \; K_\varepsilon = \frac{\varepsilon_r}{\varepsilon_{c0}} \; K_\sigma = \frac{f_c'}{f_r} \tag{6-12}$$

where ε_c and σ_c are the concrete strain and stress, respectively; ε_{c0} is the concrete strain at the peak stress; and ε_r and f_r are the ultimate concrete strain and stress, respectively.

The tensile stress-strain relationship of concrete was assumed to be linear up to the tensile strength. The post-cracked tensile response was linear. For the models described later in this chapter, the default values of ψ , χ , f_b' / f_c' , and K_c , 15°, 0.1, 1.16, and 0.67, respectively, were used. The damage parameters in tension and compression varied from 0.0 at peak stress to 1.0 at ultimate strain. Concrete stress-strain relationships derived from concrete cylinder tests were used to calculate uniaxial compressive strength and Young's modulus of the infill concrete for SC1 through SC4.

6.2.2 Steel Material Model

A J2 plasticity model with isotropic hardening was used to simulate the nonlinear behavior of the steel faceplates. The input parameters of this model are: 1) Young's modulus; 2) Poisson's ratio, and 3) the uniaxial stress-strain relationship. The average stress-strain relationship, obtained from coupon tests, was used to calculate the material properties of the steel faceplates.

6.2.3 Contact and Constraint Modeling

Contact between the infill concrete and the steel faceplates, the infill concrete and the baseplate, and the baseplate and the steel plate embedded in the foundation block was considered using a) hard contact in the normal direction to avoid penetration of slave nodes through master segments, and b) a Surface-To-Surface penalty-based formulation in the transverse direction to simulate interfacial friction. A Node-To-Surface constraint was used to tie the steel faceplates to the baseplate and to join the studs and tie rods to the steel faceplates. The studs and tie rods were coupled to the infill concrete elements using the Embedded-Constraint available in ABAQUS [SIMULIA (2012b)]. Slip between the connectors and the infill concrete was neglected.

6.2.4 Elements, Loading, and Boundary Conditions

Beam elements (B31) were used to represent the studs and tie rods. Eight-node solid elements with full integration (C3D8) were used to model the infill concrete. Four-node shell elements with full integration (S4) were used for the steel faceplates. Solid elements with reduced integration (C3D8R) were used to model the connection between the SC wall and its foundation block, including two 1-in. thick baseplates and the 22 1.25-in. diameter threaded B7 bars that secured the baseplate to the foundation block. The loading plates, post-tensioned threaded rods used to attach the loading plate to the SC walls, and the post-tensioning bars connecting the SC wall to the foundation block were modeled using eight-node solid elements with reduced integration (C3D8R). The infill concrete was modeled using 1 × 1 × 1 in. solid elements and the steel faceplates were modeled using 0.5 × 0.5 in. shell elements.

The SC walls were subjected to quasi-static cyclic loading (see Chapter 4) using two horizontally inclined actuators and loading plates that were attached to each specimen by 14 post-tensioned threaded rods. In the finite element model, the reversed cyclic loading was simulated by imposing horizontal nodal displacements at the center line of the loading plate, 60 in. above the baseplate. Since preliminary analysis indicated that the foundation block was effectively rigid, the block was not included in the finite element model. The model took advantage of symmetry to reduce the computational effort. The ABAQUS model of SC2 is presented in Figure 6-4.

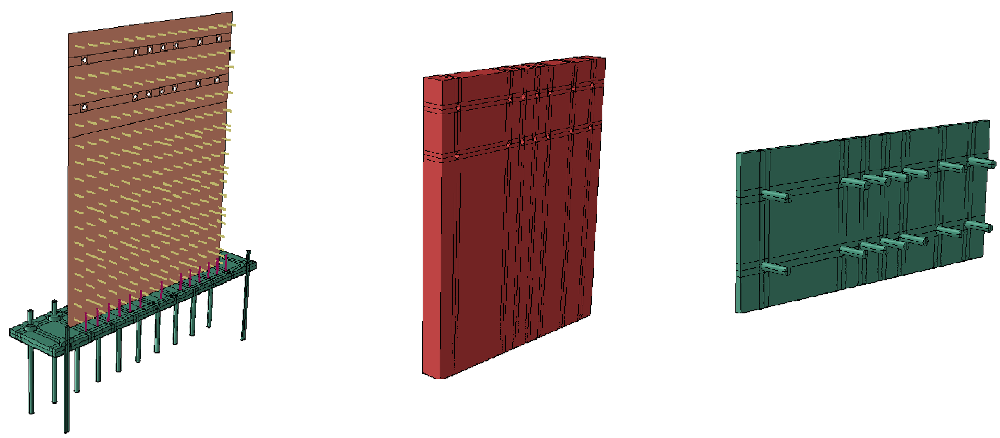

(a) Steel faceplate, connectors, baseplates, and threaded bars

(b) Infill concrete

(c) Loading plate and threaded bars

Figure 6-4 ABAQUS model of SC2

6.2.5 ABAQUS Analysis Results

Figure 6-5 presents the results of monotonic ABAQUS analysis together with the first quadrant of the measured cyclic force-displacement relationships of SC1 through SC4. ABAQUS successfully predicted the initial stiffness and peak shear strengths of the SC walls. As seen in Figure 6-5, the post-peak strength predicted by ABAUQS was greater than that measured in the tests for SC2, SC3, and SC4. This outcome was expected since monotonic response (ABAQUS-predicted response) is expected to overestimate cyclic response (test result) for a given post-peak displacements. The rate of strength deterioration in SC1 at displacements greater than that accounted with peak-strength was lower than that in the other walls due to the use of a smaller distance between the first row of connectors and the baseplate in SC1. However, the use of smaller distance between the first row of connector and the baseplate had no substantial effect on the ABAQUS-predicted response of SC1 and consequently the lower rate of the post-peak-strength deterioration in SC1 was not captured by ABAQUS.

Although ABAQUS reasonably predicted the monotonic response, the cyclic analysis of the SC walls terminated prematurely. The cyclic analyses terminated after a few cycles due to the distortion of some of infill concrete and steel faceplate elements. A number ABAQUS models were prepared and analyzed with different element sizes for the infill concrete and steel faceplate, boundary conditions, interactions between the connectors and the infill concrete, material models, and elements (2D or 3D) to investigate the source of the termination. The attempts were unsuccessful. Table 6-1 summarizes the modeling assumptions for selected ABAQUS models, including mesh size, element type, steel and concrete material models, and boundary conditions. The failed analyses are described in Figure 6-6.

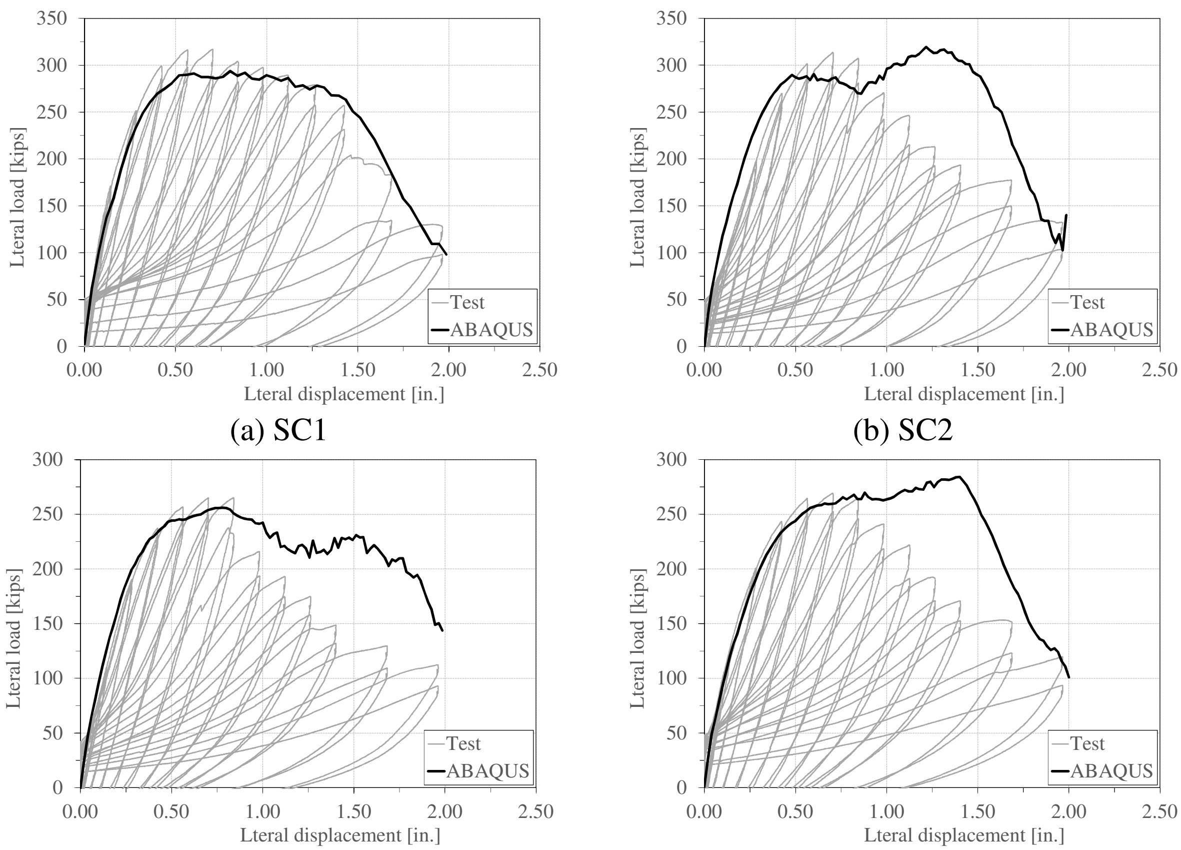

(a) SC1 (b) SC2

(c) SC3 (d) SC4

Figure 6-5 ABAQUS-predicted and measured force-displacement relationships

Table 6-1 Modeling assumptions for selected ABAQUS analyses of the SC walls

Model No.	Element				Material		Comments
	Infill concrete		Steel faceplate				
	Type	Mesh size (in.×in.×in.)	Type	Mesh size (in.×in.×in.)	Infill concrete	Steel faceplate	
Model 1	Solid (C3D8R)	1×2×2 and 2×2×2	Solid (C3D8R)	3/16×1×1	CDP	J2 plasticity with isotropic hardening	Foundation block, Dwyidag bars, loading plates, threaded bars and baseplates included.
Model 2	Solid (C3D8R)	1×2×2 and 2×2×2	Solid (C3D8R)	3/16×1×1	CDP	J2 plasticity with isotropic hardening	Foundation block, Dwyidag bars, threaded bars and baseplates included.
Model 3	Solid (C3D8R)	1×1×1	Solid (C3D8R)	3/16×1×1	CDP	J2 plasticity with isotropic hardening	Foundation block, Dwyidag bars, threaded bars and baseplates included.
Model 4	Solid (C3D8)	1×1×1	Solid (C3D8)	3/16×1×1	CDP	J2 plasticity with isotropic hardening	Foundation block, Dwyidag bars, and loading plates not modeled.
Model 5	Solid (C3D8)	1×1×1	Shell (S4)	1×1	CDP	J2 plasticity with isotropic hardening	Foundation block, Dwyidag bars, and loading plates not modeled.
Model 6	Solid (C3D8)	1×1×1	Shell (S4)	0.5×0.5	CDP	J2 plasticity with isotropic hardening	Foundation block, and Dwyidag bars not modeled; half of the SC wall modeled.
Model 7	Solid (C3D8)	1×1×1	Solid (C3D8)	3/16×0.5×0.5	CDP	J2 plasticity with isotropic hardening	Foundation block, and Dwyidag bars not modeled; half of the SC wall modeled.

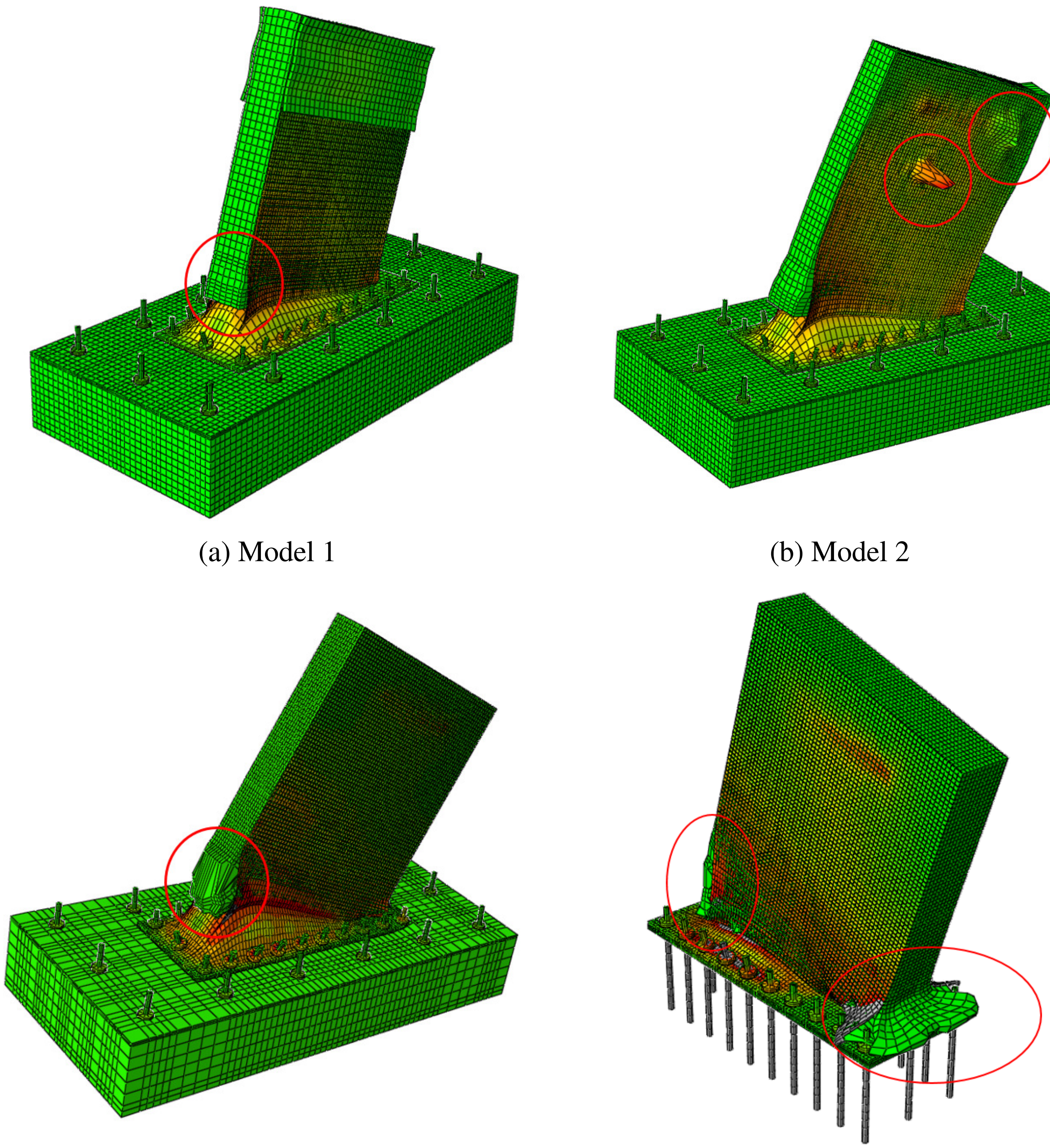

(a) Model 1 (b) Model 2

(c) Model 3 (d) Model 4

Figure 6-6 Failures of the ABAQUS analyses

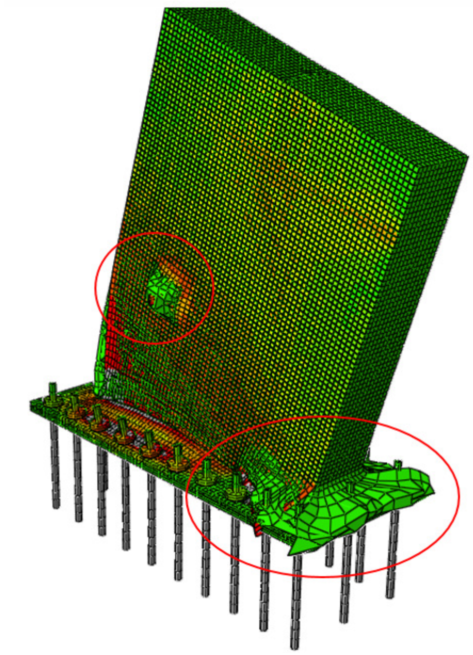

(e) Model 5

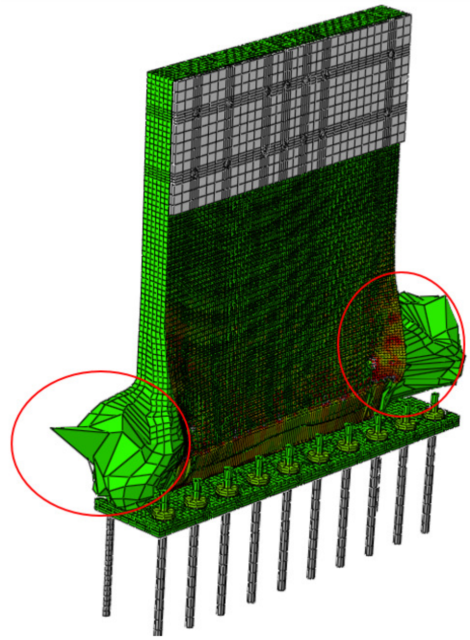

(f) Model 6

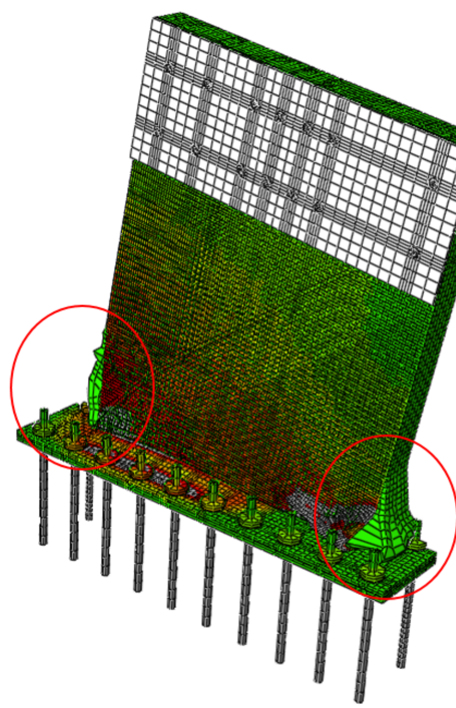

(g) Model 7

Figure 6-6 Failures of the ABAQUS analyses (cont.)

6.3 VecTor2 Analysis

VecTor2 is a two dimensional nonlinear finite element program used to simulate the in-plane response of reinforced concrete structures. VecTor2 is based on the Modified-Field- Compression-Theory (MCFT) [Vecchio et al. (1986)] and the Distributed-Stress-Field-Model (DSFM) [Vecchio (2000)]. The DSFM was proposed by Vecchio (2000) as an alternative to MCFT. It incorporates a smeared rotating crack model that considers slip deformations across crack surfaces and reorientation of the cracks during cyclic loading.

The material models available in VecTor2 consider the important behaviors of concrete and steel, such as compression softening, which is the effect on uniaxial concrete compressive strength of transverse tensile strains; tension stiffening, which captures the tensile stiffness of intact concrete between cracks; dowel action of reinforcing bars crossing cracks; the Bauschinger effect for reinforcement; buckling of reinforcement; concrete confinement; concrete dilation; bond slip; and deformations across cracks.

6.3.1 SC Wall Modeling

Vecchio et al. (2011) adopted the DSFM for the analysis of SC walls subjected to axial, and in-plane monotonic and cyclic shear loadings. They proposed the following relationship for the response of an SC element:

$$[\sigma]=[D][\varepsilon]-\left[\sigma^{0}\right] \tag{6-13}$$

where $[\varepsilon]$ and $[\sigma]$ are the strain and stress vectors; $\left[\sigma^{0}\right]$ is a prestress vector; $[D]$ is composite material stiffness matrix, calculated as the sum of the stiffness matrices of the infill concrete, the steel faceplates, and the steel reinforcement as:

$$[D]=\frac{t_c}{t_c+2t_s}[D_c]+\sum_{i=1}^{n}\frac{t_c}{t_c+2t_s}[D_{ri}]+\frac{2t_s}{t_c+2t_s}[D_s] \tag{6-14}$$

where $[D_c]$ is the stiffness matrix of the infill concrete, t_c and t_s are the thicknesses of the infill concrete and each steel faceplate, $[D_{ri}]$ is the stiffness matrix of each reinforcement component with angle α_i to the horizontal, and $[D_s]$ is the stiffness matrix for the steel faceplates. Matrices $[D_c]$ and $[D_{ri}]$ are calculated using equations available in Vecchio (2000). Compression softening, tension stiffening, dilation, and confinement are considered in the derivation of the concrete stiffness matrix. The Bauschinger effect and dowel action are considered in the calculation of the reinforcement stiffness matrix. The matrix $[D_s]$ is calculated as:

$$[D_s]=[T_s]^T\begin{bmatrix}\bar{E}_{s1} & 0 & 0\\ 0 & \bar{E}_{s2} & 0\\ 0 & 0 & \bar{G}_s\end{bmatrix}[T_s] \tag{6-15}$$

where $\bar{E}_{s1}$ and $\bar{E}_{s2}$ are the secant moduli of the steel faceplates in the principal stress directions, respectively; $\bar{G}_s$ is the shear modulus; and $[T_s]$ is a matrix that transforms the principal coordinate system back to the global coordinate system and calculated as:

$$[T_s]=\begin{bmatrix}\cos^2\theta_\varepsilon & \sin^2\theta_\varepsilon & \cos\theta_\varepsilon\sin\theta_\varepsilon\\ \sin^2\theta_\varepsilon & \cos^2\theta_\varepsilon & -\cos\theta_\varepsilon\sin\theta_\varepsilon\\ -2\cos\theta_\varepsilon\sin\theta_\varepsilon & 2\cos\theta_\varepsilon\sin\theta_\varepsilon & \cos^2\theta_\varepsilon-\sin^2\theta_\varepsilon\end{bmatrix} \tag{6-16}$$

The secant and shear moduli of the steel faceplates are calculated as:

$$\bar{E}_{s1}=\frac{f_{si}}{\varepsilon_{si}}\quad(i=1,2) \tag{6-17}$$

$$\bar{G}_s=\frac{\bar{E}_{s1}\bar{E}_{s2}}{\bar{E}_{s1}+\bar{E}_{s2}} \tag{6-18}$$

where ε_{si} and f_{si} $(i=1,2)$ are the principal strains and their corresponding stresses, respectively. The steel stresses are determined using the calculated principal strains and the uniaxial stress-strain relationship of the steel.

The prestress vector, $[\sigma^0]$, is defined as:

$$[\sigma^0]=[D_c]([\varepsilon_c^e]+[\varepsilon_c^p]+[\varepsilon_c^s])+\sum_{i=1}^{n}[D_{ri}]([\varepsilon_{ri}^e]+[\varepsilon_{ri}^p])+[D_s]([\varepsilon_s^e]+[\varepsilon_s^p]) \tag{6-19}$$

where $[\varepsilon_c^e]$, $[\varepsilon_{ri}^e]$, and $[\varepsilon_s^e]$ are the elastic offset strain vectors in the concrete, reinforcement, and the steel faceplates, respectively; $[\varepsilon_c^p]$, $[\varepsilon_{ri}^p]$, and $[\varepsilon_s^p]$ are the plastic offset strain vectors in the concrete, reinforcement, and the steel faceplates, respectively; and $\left[\varepsilon_c^s\right]$ is the concrete strain vector associated with slip across the cracks. The strain vectors are calculated using equations available in Vecchio (2000).

The Von-Mises yield criterion is used for the steel faceplates. The steel faceplates are assumed to be perfectly bonded to the infill concrete. Buckling of the steel faceplates is assumed to occur when the principal compressive stress exceeds the critical buckling stress [Sasaki et al. (1995)]. The proposed critical buckling stress, σ_{cr}, is:

$$\sigma_{cr} = \frac{\pi^2 E_s}{12(0.7\frac{s}{t_s})^2} \tag{6-20}$$

where s is the stud/tie rod spacing and s / t_s is the faceplate slenderness ratio.

The accuracy of the VecTor2 predictions was examined by simulating the monotonic and cyclic responses of SC walls tested by Sasaki et al. (1995), Usami et al. (1995), and Ozaki et al. (2004). The DFSM predicted the reported shear strengths to within 5% but the stiffness at displacements less than those associated with peak strength was significantly overestimated [Vecchio et al. (2011)], which was attributed to ignoring the interfacial slip between the steel faceplates and the infill concrete.

6.3.2 VecTor2 Modeling of the SC Walls

6.3.2.1 Material Model

Default material models were used to simulate the behavior of the infill concrete and the steel faceplates. The *Hognestad parabola* and *Modified Park-Kent* (1982) models were used to simulate the pre- and post-peak regions of concrete in compression, respectively. A linear descending branch was used to simulate the post-cracking tensile response of concrete. The *Vecchio 1992-A* [Vecchio et al. (1993)] model was used to consider compression softening. Tension stiffening was modeled using *Modified Bentz 2003* [Vecchio (2000)]. The effect of confinement was captured using the *Kupfer-Richart* model [Vecchio (1992)]. Dilation was simulated using the *Variable-Kupfer* model [Vecchio (1992)]. Concrete cracking was based on a *Mohr-Coulomb stress* criterion and the cracking stress was calculated using *DSFM* model [Vecchio (2000)]. The default value of the maximum crack of 40% of the aggregate size was used. The strains associated with slip across the cracks were calculated using *Walraven (Monotonic)* [Walraven (1981)] model. The *Nonlinear w/Plastic Offsets* model [Vecchio (2000)] was used to simulate the hysteretic response of concrete.

Table 6-2 presents the concrete material properties used as input to the VecTor2 model, where f_t is the tensile stress of the infill concrete, ε_{c0} is the concrete strain at peak stress, ν_c is Poisson's ratio, and γ_c is the concrete density.

Table 6-2 Concrete material properties input to VecTor2 model

f'_c (ksi)	f_t (ksi)	E_c (ksi)	ε_{c0} (in./in.)	ν_c	γ_c (lb/ft^3)
4.4	0.4	3000	0.0025	0.2	150

Table 6-3 presents the steel material properties input to VecTor2 model, where f_y and f_u are the yield and tensile stresses of the steel faceplates, respectively; ε_{sh} and ε_u are the steel strains at the onset of the strain hardening and peak stress, respectively; ν_s is Poisson's ratio; and s/t_s is the faceplate slenderness ratio.

Table 6-3 Steel material properties input to VecTor2 model

f_y (ksi)	f_u (ksi)	E_s (ksi)	ε_{sh} (in/in)	ε_u (in/in)	ν_s	s/t_s (in/in)
38	55	29000	0.003	0.03	0.3	30

6.3.2.2 Elements, Loading, and Boundary Conditions

The monotonic and reversed cyclic loading of the test specimens were simulated by imposing nodal horizontal displacements 60 in. above the base of the wall.

Three sets of VecTor2 models were analyzed: A) including the foundation, B) a rigid connection of the walls to an infinitely stiff base, and C) including the foundation flexibility by using four-node membrane elements to represent the steel baseplate, and truss elements with tension- and compression-only behaviors to represent the post-tensioned threaded bars used to secure the baseplate to the foundation block. The VecTor2 models are presented Figure 6-7.

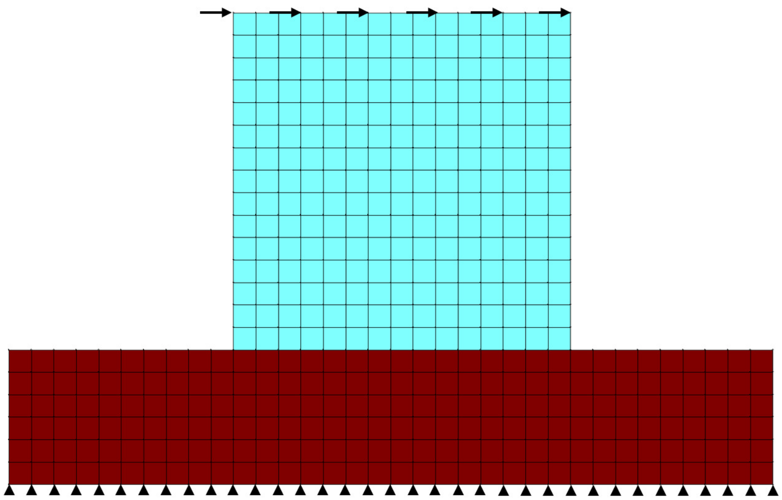

(a) Model A

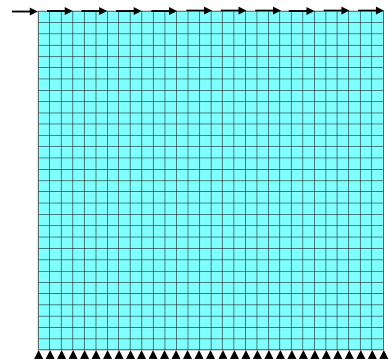

(b) Model B

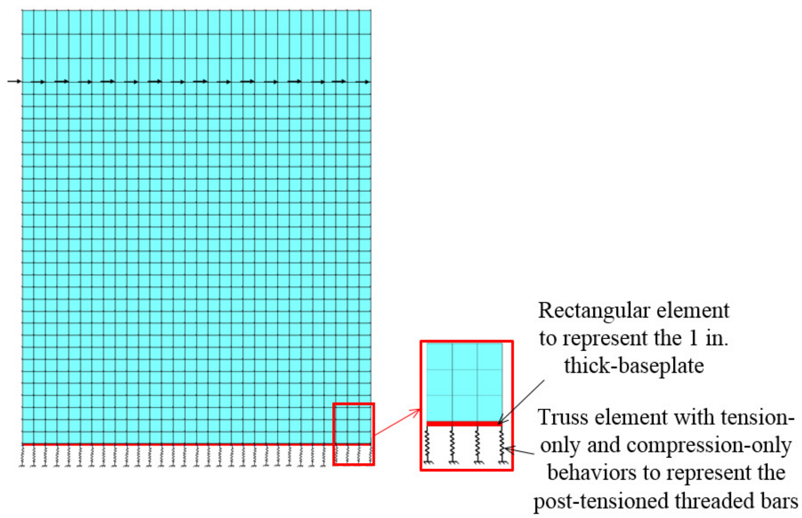

(b) Model C

Figure 6-7 VecTor2 models

Two axial behaviors were assigned to each truss element connecting the SC wall to the base: compression-only and tension-only. To prevent the penetration of wall elements into the stiff base, a compression-only behavior with very large stiffness and strength was used. The properties of the tension-only behavior, including cross-sectional area ($=0.02\ \text{in}^2$) and elasticity modulus (=580 ksi), were back-calculated from the measured initial stiffness of SC1.

Two inch × 2 in. elements were used for Models B and C. The mesh size in model A which included the foundation block, was increased to 4 in. due to a limit on the number of available elements in VecTor2. The height of the Model C was set at 72 in., including 12 in. above the loading level, and identical to the constructed walls.

6.3.3 VecTor2 Analysis Results

6.3.3.1 Load-Displacement Monotonic Response

Figure 6-8 presents the VecTor2-predicted monotonic force-displacement relationships (solid black line for Model A, dashed blue line for Model B, and dashed red line for Model C) together with the measured cyclic force-displacement relationship (solid gray line) for SC1. The initial stiffness was substantially overestimated by Model A (including the foundation block) and Model B (rigid base) because these models did not include the baseplate connection between the SC wall and the foundation block. The peak strength was significantly overestimated by Model A due to the use of a coarse mesh, which delayed the onset of damage (cracking) to the infill concrete. However, both the rigid- and flexible-base models, B and C, respectively, successfully predicted the peak shear resistance of SC1. The rate of post-peak strength deterioration predicted by all three models was substantially greater than that observed in the test. The discrepancies between the numerically-predicted and experimentally-measured post peak responses might be attributed to: 1) the effect of concrete confinement is neglected by VecTor2 analysis, which uses 2D elements for the steel faceplates and the infill concrete, 2) VecTor2 assumes perfect bond between the steel faceplates and infill concrete, and 3) the SC wall connection including the baseplate and the threaded bars could not be explicitly modeled using VecTor2.

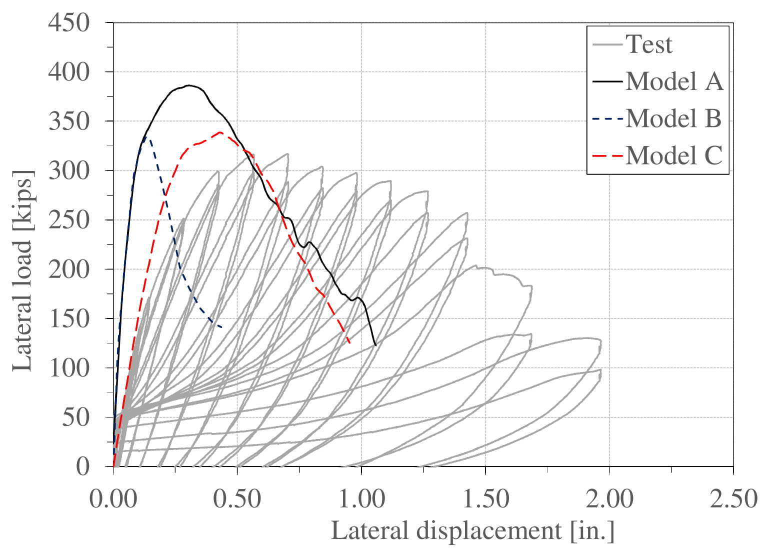

Figure 6-8 Analysis and test results for SC1

6.3.3.2 Crack Patterns in the Infill Concrete

Figure 6-9 presents the predicted deformed shape of SC1 (scaled by a factor of 7) and the crack patterns at peak load. The critical crack width was set to 0.0022, where the critical crack width is defined as the displacement at which the tensile normal stress across the crack is zero. The calculation of the crack width is presented in Section 6.4.1.2.

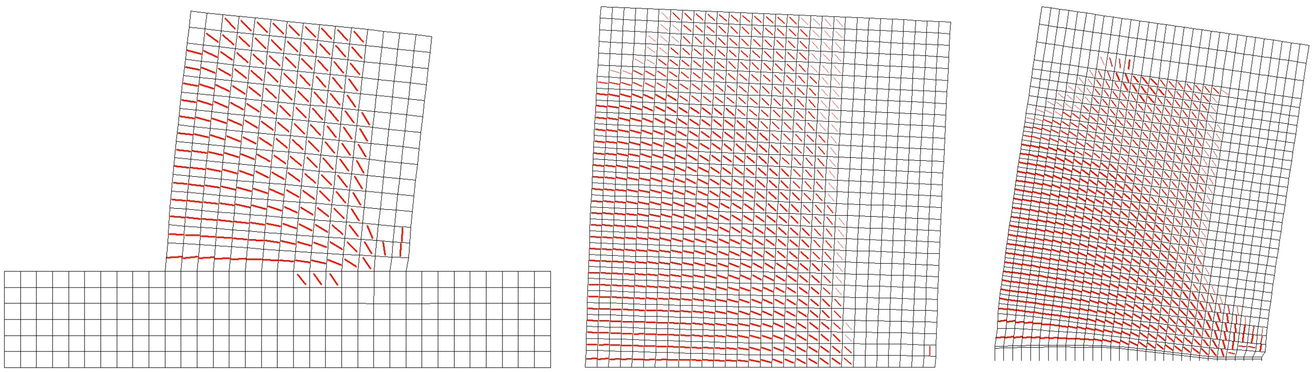

(a) Model A (b) Model B (c) Model C

Figure 6-9 VecTor2-predicted cracking pattern at peak load of SC1 under monotonic loading

6.3.3.3 Strain Distributions

The distributions of horizontal, vertical, and shear strains in SC1 at peak load are presented in Figure 6-10, Figure 6-11, and Figure 6-12, respectively. The high vertical and shear strains are concentrated near the base of the wall.

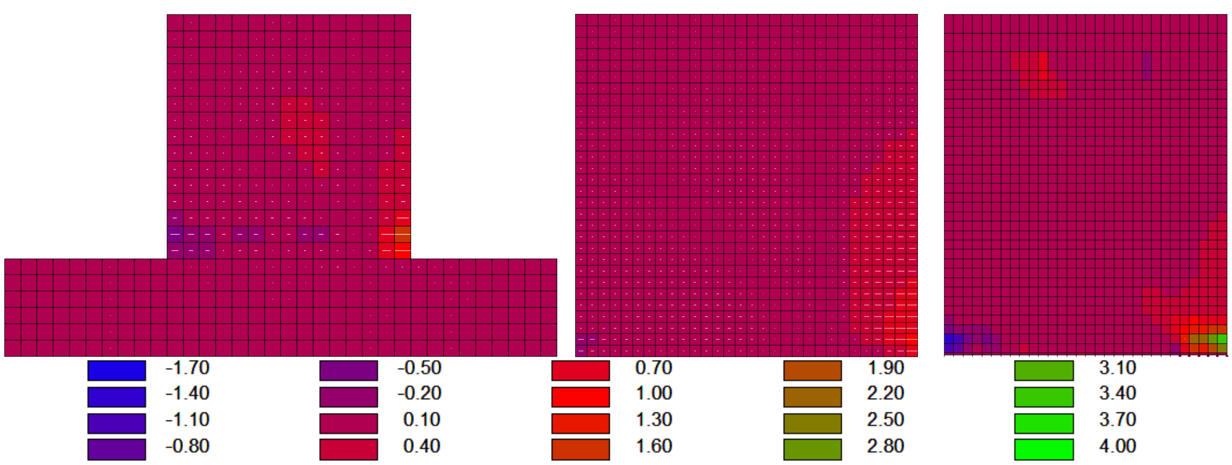

(a) Model A (b) Model B (c) Model C

Figure 6-10 Horizontal strain distribution at peak load (unit: millistrains)

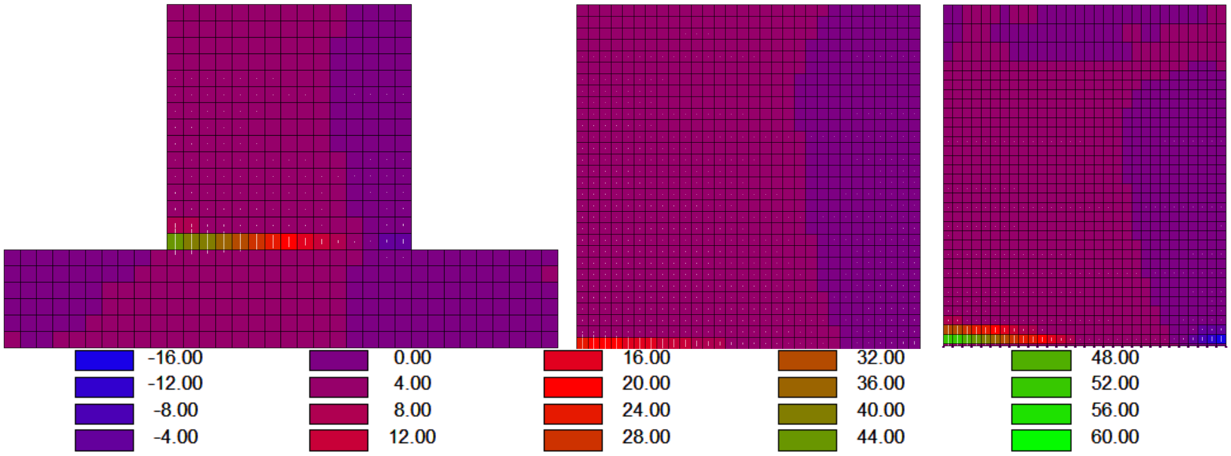

(a) Model A (b) Model B (c) Model C

Figure 6-11 Vertical strain distribution at peak load (unit: millistrains)

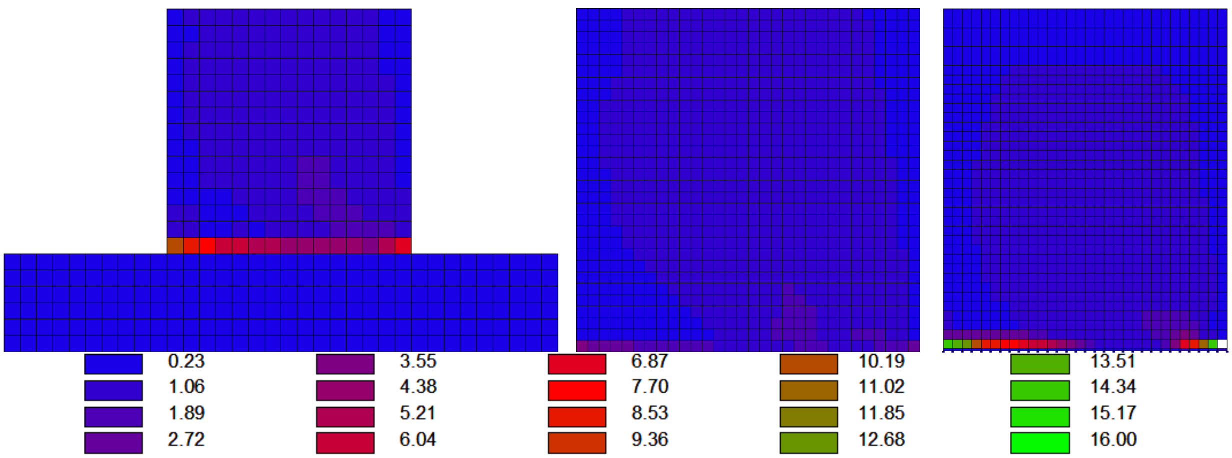

(a) Model A (b) Model B (c) Model C

Figure 6-12 Shear strain distribution at peak load (unit: millistrains)

6.3.3.4 Stress Distribution

The distributions of the horizontal, vertical, and shear stresses in the infill concrete of SC1 at peak load are presented in Figure 6-13, Figure 6-14, and Figure 6-15, respectively. Figure 6-14 provides an estimate of the depth of the compression zone in the infill concrete at the peak load ($=0.3L$, where L is the length of the wall). The stress distribution in the infill concrete of SC1, presented in Figure 6-15, indicates that the applied lateral load in the infill was transferred to the foundation by a diagonal compression strut.

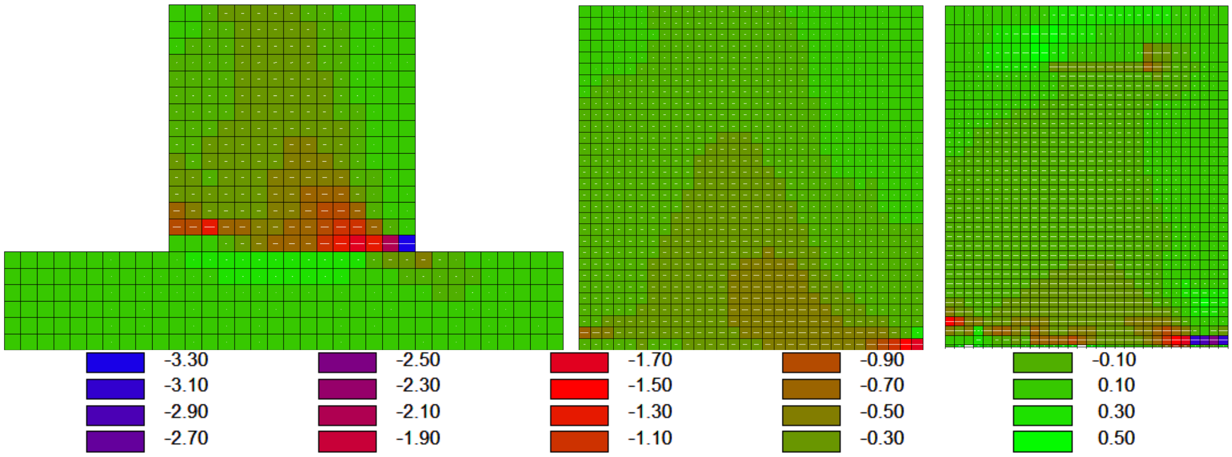

(a) Model A (b) Model B (c) Model C

Figure 6-13 Horizontal stress distribution at peak load in infill concrete (unit: ksi)

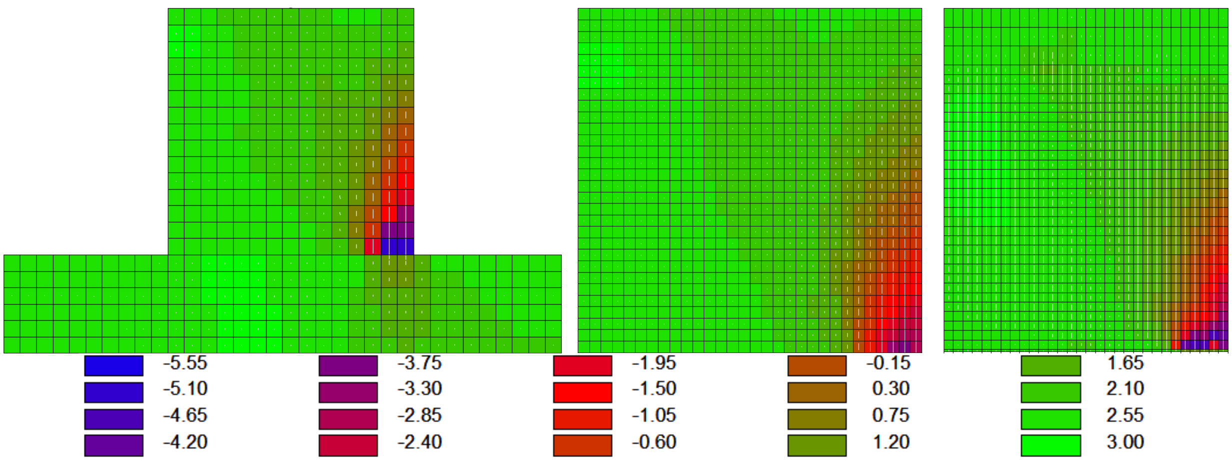

(a) Model A (b) Model B (c) Model C

Figure 6-14 Vertical stress distribution at peak load in infill oncrete (unit: ksi)

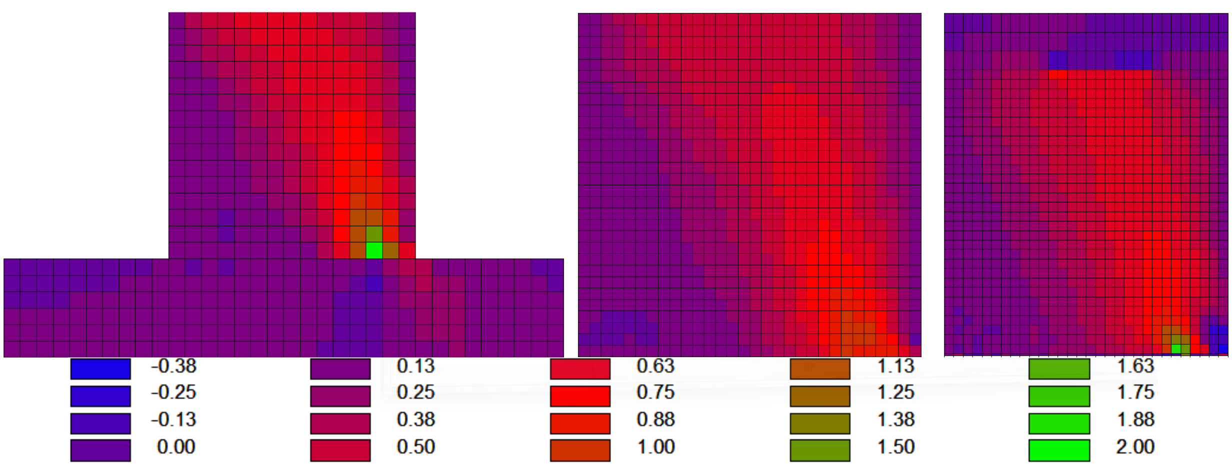

(a) Model A (b) Model B (c) Model C

Figure 6-15 Shear stress distribution at peak load in infill concrete (unit: ksi)

6.3.3.5 Load-Displacement Cyclic Response

Figure 6-16 presents the VecTor2-predicted and the measured cyclic force-displacement relationships for SC1. Similar to the predictions of monotonic response, Models A and B substantially overestimated the initial stiffness. The rate of post-peak strength deterioration in the predicted cyclic responses of the Models A and B is greater than that of the measured cyclic response. Models A and B predicted more damage than Model C because these models did not include the baseplate connection, and thus were stiffer, which led to premature concrete cracking, and buckling and yielding of the steel faceplates. As seen in Figure 6-16, the VecTor2 models captured the pinching behavior by considering opening, closing, and re-opening of cracks in the infill concrete caused by load reversals. Analysis of Model C terminated at the peak shear force due to the significant distortion of a number of the wall elements, as presented in Figure 6-16(c). Different mesh sizes, boundary conditions, and material models were analyzed but these attempts were unsuccessful.

6.4 LS-DYNA Analysis

This section describes a finite element model in LS-DYNA that simulates the nonlinear cyclic response of flexure- and flexure-shear-critical SC walls. LS-DYNA is a general-purpose finite element program for the static and dynamic analysis of structures. The finite element model is validated using data from testing of the four large-scale rectangular SC walls described in Chapters 4 and 5. The following subsections present the modeling assumptions and the finite element predictions, including global force-displacement responses, equivalent viscous damping ratio, damage to the steel faceplates and infill concrete, strain and stress distributions in the steel faceplates, estimates of the contribution of the steel faceplates and infill concrete to the lateral resistance of the walls, and axial and shear forces transferred by connectors. The impacts of interface friction between the steel faceplates and the infill concrete, and of the distribution of shear studs on the baseplate, to the global response of the SC walls are also presented [Epackachi et al. (2015b)].

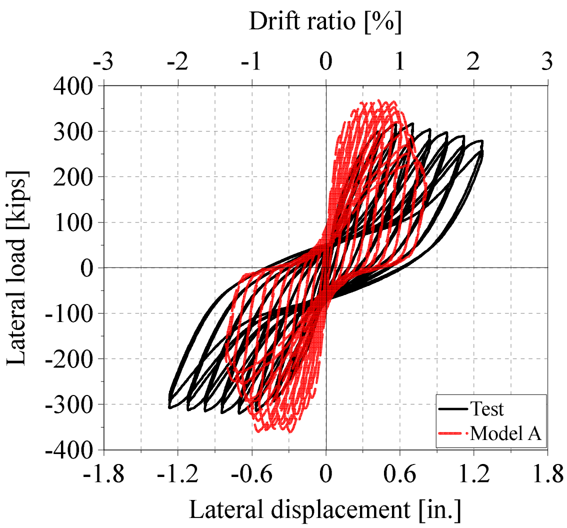

(a) Model A

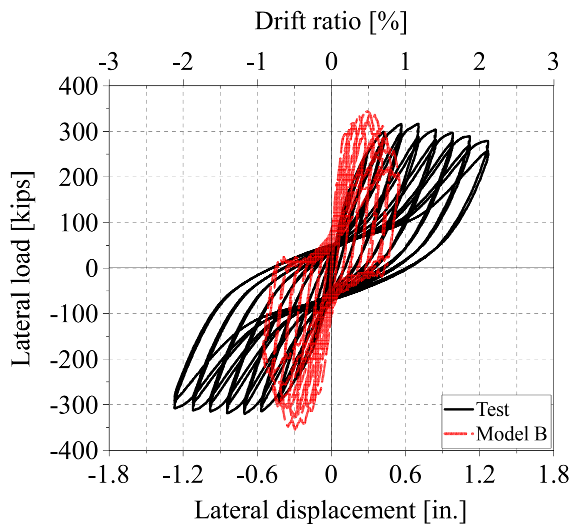

(b) Model B

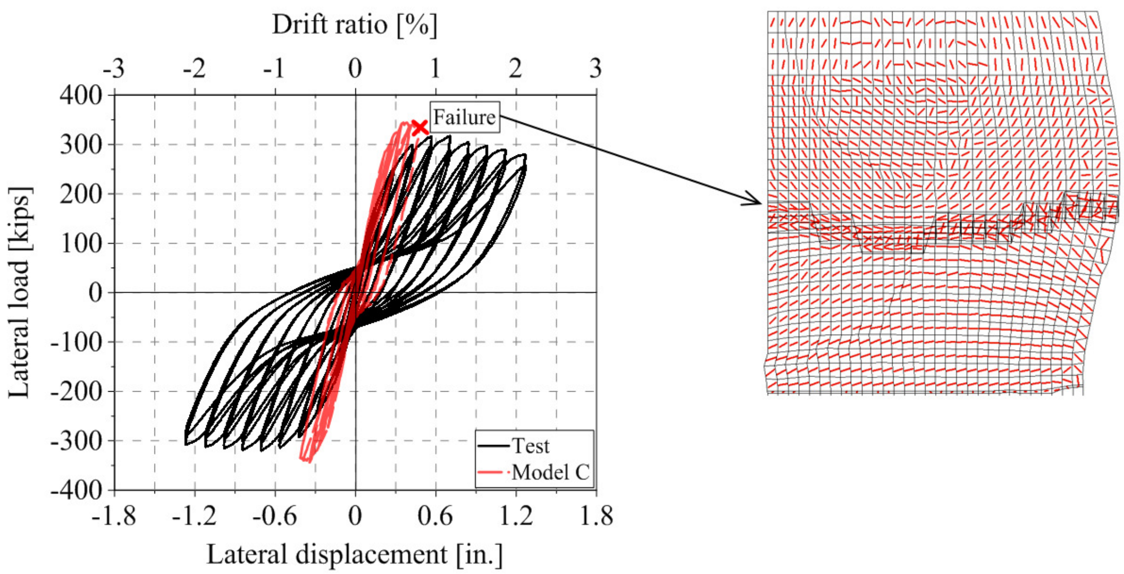

(c) Model C

Figure 6-16 VecTor2- predicted and measured cyclic force-displacement relationships

6.4.1 Concrete Material Model

Studies on the behavior of shear-critical reinforced concrete panels have identified the key features of concrete behavior to include shear force transfer across cracks due to aggregate interlock, opening and closing of cracks, loss of strength and stiffness in the direction parallel to cracks, slip along cracks, and tension stiffening. These behaviors can be explicitly addressed using smeared crack models, which describe a cracked solid by an equivalent anisotropic continuum with degraded material properties in the direction normal to the crack [e.g, Hu et al. (1990), Sittipunt et al. (1995), Vecchio (1999), Vecchio et al. (1995), Bessason et al. (2001), Hristovski et al. (2002), and Orakcal et al. (2012)].

The smeared crack Winfrith model (MAT085) in LS-DYNA, developed by Broadhouse (1986), was used to model the infill concrete. The Broadhouse model provides information on the orientation of the cracking planes (up to three orthogonal cracks for each element) and the width of the cracks [Schwer (2011)]. It assumes elastic-perfectly plastic behavior in compression (1986) and its yield surface is based on the four-parameter plastic surface of Ottosen model [Ottosen (1977)]. The yield surface expands as the hydrostatic pressure increases and its radii at the compressive and tensile meridia are determined using the compressive and tensile strengths of concrete (1986). The model considers shear stress across the crack due to the aggregate interlock. Tension stiffening is considered using a linear decay for the post-cracked tensile stress-strain relationship. Rather than using truss or beam elements to model reinforcement, the Winfrith model smears the rebar. The Winfrith model can incorporate strain-rate effects [LS-DYNA (2012b)].

6.4.1.1 Plasticity Model Definition in the Winfrith Model

The four-parameter plastic surface proposed by Ottosen (1977) is used as the failure surface in the Winfrith model. The Ottosen failure surface is expressed as:

$$F(I_1, J_2, \cos 3\theta) = a\frac{J_2}{(f_c')^2} + \lambda\frac{\sqrt{J_2}}{f_c'} + b\frac{I_1}{f_c'} - 1 \qquad (6\text{-}21)$$

where I_1 is the first invariant of the stress tensor; J_2 is the second invariant of the deviatoric stress tensor; $\cos 3\theta$ is an invariant as a function of the second and third invariants of the deviatoric stress tensor and θ is the Lodge angle, where the Lodge angle, varying between 0 and $\pi/3$, is used to represent the yield surface on the $\pi-\text{plane}$; λ is a function of $\cos 3\theta$; and f_c' is the uniaxial compressive strength of concrete.

The four parameters of the Ottosen model are a and b, which control the quadratic shape of the meridian curves of the failure surface, and k_1 and k_2, which control the noncircular shape of the failure surface on the deviatoric plane, from a nearly triangular shape to a circular shape with increasing the hydrostatic pressure [Chen et al. (2007)]. The parameter λ can be calculated as:

$$\lambda = \begin{cases} k_1 \cos\ [\frac{1}{3}\cos^{-1}(k_2 \cos 3\theta)] & \text{for } \cos 3\theta \geq 0 \\ k_1 \cos\ [\frac{\pi}{3} - \frac{1}{3}\cos^{-1}(-k_2 \cos 3\theta)] & \text{for } \cos 3\theta < 0 \end{cases} \tag{6-22}$$

The stress tensor and the deviatoric stress tensor are:

$$\sigma = \sigma_{ij} = \begin{bmatrix} \sigma_{11} & \sigma_{12} & \sigma_{13} \\ \sigma_{21} & \sigma_{22} & \sigma_{23} \\ \sigma_{31} & \sigma_{32} & \sigma_{33} \end{bmatrix} \tag{6-23}$$

$$S = S_{ij} = \begin{bmatrix} S_{11} & S_{12} & S_{13} \\ S_{21} & S_{22} & S_{23} \\ S_{31} & S_{32} & S_{33} \end{bmatrix} = \begin{bmatrix} \sigma_{11} - P & \sigma_{12} & \sigma_{13} \\ \sigma_{21} & \sigma_{22} - P & \sigma_{23} \\ \sigma_{31} & \sigma_{32} & \sigma_{33} - P \end{bmatrix} \tag{6-24}$$

where P is the hydrostatic stress and is calculated as $(\sigma_{11} + \sigma_{22} + \sigma_{33})/3$.

The first invariant of the stress tensor, and the second and third invariants of the deviatoric stress tensor are:

$$I_1 = \sigma_{ii} = \sigma_{11} + \sigma_{22} + \sigma_{33} \tag{6-25}$$

$$J_2 = 0.5 S_{ij} S_{ij} = (S_{11}^2 + S_{22}^2 + S_{33}^2 + 2S_{12}^2 + 2S_{13}^2 + 2S_{23}^2)/2 \tag{6-26}$$

$$J_3 = S_{ij} S_{jk} S_{ki} / 3 = \begin{vmatrix} S_{11} & S_{12} & S_{13} \\ S_{21} & S_{22} & S_{23} \\ S_{31} & S_{32} & S_{33} \end{vmatrix} \tag{6-27}$$

$\text{Cosine}3\theta$, which is a function of the second and third invariants of the deviatoric stress tensor, is calculated as:

$$\cos 3\theta = \frac{3\sqrt{3}}{2} \frac{J_3}{J_2^{3/2}} \tag{6-28}$$

The four parameters of the Ottosen model are calculated using the results of uniaxial tensile and compressive tests, and biaxial and triaxial tests as:

1. Uniaxial compressive stress of concrete, f_c' ($\theta = 60^\circ$ and $\cos 3\theta = -1$).

2. Uniaxial tensile stress of concrete, f_t ($\theta = 0^\circ$ and $\cos 3\theta = +1$).
3. Biaxial compressive stress of concrete, f'_{bc} ($\theta = 0^\circ$ and $\cos 3\theta = +1$); the Winfrith model uses the results of the biaxial tests of Kupfer et al. (1969); $\sigma_1 = \sigma_2 = 1.16 f'_c$ and and $\sigma_3 = 0$.
4. The triaxial stress state $((I_1 / \sqrt{3} f'_c, \sqrt{2J_2} / f'_c) = (-5, 4))$ on the compressive meridian ($\theta = 60^\circ$ and $\cos 3\theta = -1$) provides the best fit to the test results of Balmer (1949) and Richart et al. (1928).

In the Winfrith concrete model, the four parameters of the Ottosen model are internally calculated as (Schwer (2011)]:

$$a = \beta b + \gamma \tag{6-29}$$

$$b = \frac{1 + R\alpha\gamma / 3 - \alpha^2 \gamma / 3 - \alpha / R}{\alpha^2 \beta / 3 - 3\alpha - R\alpha\beta / 3} \tag{6-30}$$

$$K_1 = \frac{c}{\cos(\frac{1}{3} \cos^{-1}(k_2))} \tag{6-31}$$

$$k_2 = \cos(3 \tan^{-1}(\frac{1}{\sqrt{3}} - \frac{2d}{c\sqrt{3}})) \tag{6-32}$$

where α, β, and γ are non-dimensional constants and equal to 1.16, 0.59, and -0.61, respectively; R is the ratio of the uniaxial tensile to compressive stress of concrete; and the coefficients c and d are calculated as:

$$c = \frac{\sqrt{3}}{R}(1 - bR - R^2 a / 3) \tag{6-33}$$

$$d = \frac{3 + 3b - a}{\sqrt{3}} \tag{6-34}$$

6.4.1.2 Crack Analysis in the Winfrith Model

DYNA provides information on crack locations, orientations, and widths [LS-DYNA (2012a)]. The cracks can be displayed on the deformed shape of the concrete elements. A minimum crack width can be set to eliminate minor cracks. The post-cracking analysis of concrete is affected by whether strain-rate effects are included. If considered, the input parameter for crack analysis is the specific fracture energy; if not, the input parameter is the crack width. The specific fracture energy, G_f, is the energy required to propagate a tensile crack of unit area [CEB-FIP (1993)] and the crack width is the displacement at which the tensile stress normal to the crack is zero. The crack width or the crack opening displacement (COD) is presented in Figure 6-17, where L is the crack length.

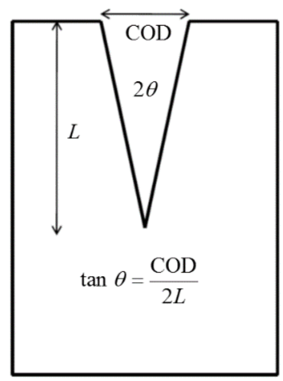

Figure 6-17 Crack opening displacement [Schwer (2011)]

The cracking formulation used in the Winfrith model is based on Wittmann et al. (1988). Wittman et al. tested a large number of concrete samples to provide a data base for the specific fracture energy, crack opening displacement, and peak load of the concrete samples as a function of aggregate size, concrete compressive stress, loading rate, water-to-cement ratio, and test specimen size.

Figure 6-18 presents the post-cracked tensile stress-displacement relationships of the concrete corresponding to two cases: 1) including the strain-rate effect (left figure) and 2) ignoring the strain-rate effect (right figure).

Fracture energy is calculated as the area under the tensile stress-displacement curve [Wittmann (1988)]. In the absence of experimental data, G_f, can be estimated using Equation 2.1-7 or Table 2.1.4 of the CEB-FIP Model Code (1993).

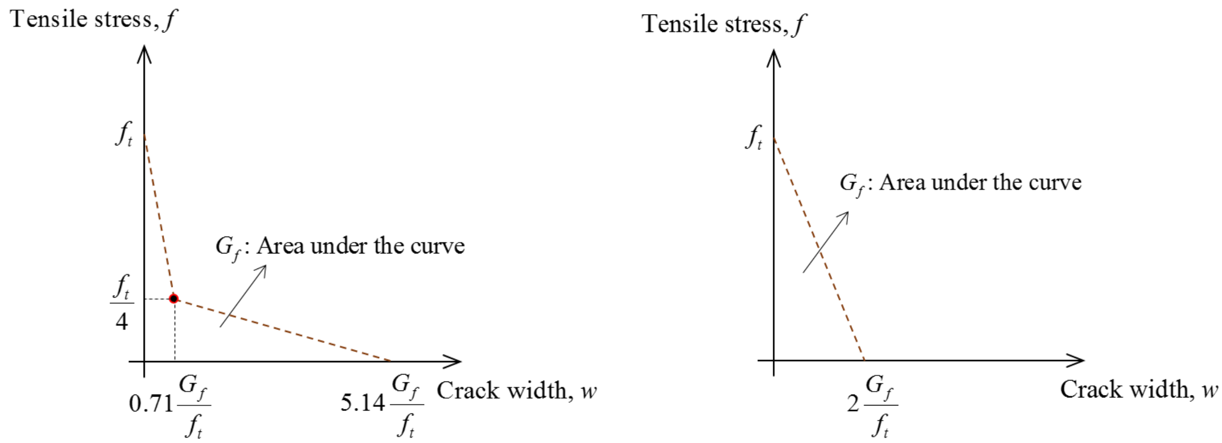

(a) with the strain-rate effect (b) without the strain-rate effect

Figure 6-18 Post-cracked tensile stress-displacement relationship [Schwer (2011)]

6.4.1.3 Values of Parameters Input to the Winfrith Model

The input parameters for the Winfrith model in LS-DYNA are: 1) mass density, 2) Young's modulus, 3) Poisson's ratio, 4) uniaxial compressive strength, 5) uniaxial tensile strength, 6) fracture energy or crack width depending on the choice of strain-rate option, and 7) aggregate size. Young's modulus and Poisson's ratio are used to predict elastic response. Uniaxial compressive and tensile strengths are used to define the failure surface. Fracture energy or crack width are used in the crack analysis, and aggregate size is used to calculate the shear capacity across the crack surface.

The input parameters for smeared reinforcement are: 1) Young's modulus, 2) hardening modulus, 3) ultimate strain, 4) yield stress, and 5) reinforcement ratio in the global X, Y, and Z directions, where the reinforcement ratio is calculated by dividing the area of the reinforcement by the total cross-sectional area of the element in the chosen direction.

The uniaxial compressive stress and Young's modulus for the infill concrete in SC1 through SC4 were calculated using the measured stress-strain relationships obtained from concrete cylinder tests conducted at the time of testing of each SC wall. The tensile stress and fracture properties of the concrete were calculated using CEB-FIP Model Code (1993), which calculates lower and upper bounds on the tensile strength (f_{tl} and f_{tu}) based on the uniaxial compressive strength as:

$$f_{tl} = 0.14\left(\frac{f'_c}{1.45}\right)^{2/3} \quad \text{(unit:ksi)} \tag{6-35}$$

$$f_{tu} = 0.27(\frac{f'_c}{1.45})^{2/3} \quad \text{(unit:ksi)} \tag{6-36}$$

The lower and upper bounds on the tensile strength of concrete were 290/560 psi and 330/640 psi, for SC1/SC2 and SC3/SC4, respectively. The tensile strength of concrete was assumed to be 350 psi and 400 psi for SC1/SC2 and SC3/SC4, respectively.

The fracture energies for the 0.75 in. maximum aggregate size used for the construction of SC1 through SC4, calculated using Table 2.1.4 of CEB-FIP Model Code, were 0.44 and 0.48 lbf/in. for SC1/SC2 and SC3/SC4, respectively. The strain-rate effect was not considered because the testing of the SC walls was quasi-static. As presented in Figure 6-18(b), the Winfrith model assumes a linear decay for the post-cracked tensile stress-displacement relationship of the concrete if the strain-rate effect is ignored. In this case, the crack width needs to be provided for the post-crack analysis. The crack width at zero stress, calculated using the equation provided in Figure 6-18(b), was 0.0025 in. for all walls. Table 6-4 presents the concrete material properties input to the DYNA model.

Table 6-4 Concrete material properties input to the DYNA model

Model	Mass density $(\frac{\text{lbf.sec}^2}{\text{in}^4})$	Young's modulus (ksi)	Poisson's ratio	Uniaxial compressive strength (ksi)	Uniaxial tensile strength (ksi)	Crack width (in.)	Agg. Size (in.)
SC1/SC2	2.25×10^{-4}	3000	0.18	4.40	0.35	0.0025	0.75
SC3/SC4	2.25×10^{-4}	3300	0.18	5.30	0.40	0.0025	0.75

6.4.2 Steel Material Model

A plastic-damage model, Mat-Plasticity-With-Damage (MAT081) with isotropic hardening, was used to simulate the nonlinear behavior of the steel faceplates and the connectors. Damage was assumed to begin after the equivalent plastic strain reached the strain corresponding to the peak stress of the stress-strain relationship. At fracture, the damage index equaled 1.0. The average stress-strain relationship, derived from coupon tests, was used to model the steel faceplates (see the coupon test results in Figure 4-8). Manufacturer-provided information on the yield and ultimate strengths of studs and tie rods were used. Fracture was ignored for the studs and the tie rods. Table 6-5 presents the steel material properties input to the DYNA model.

Table 6-5 Steel material properties input to the DYNA model

Material	Mass density $(\frac{\text{lbf.sec}^2}{\text{in}^4})$	Young's modulus (ksi)	Poisson's ratio	Yield strength (ksi)	Ultimate strength (ksi)	Failure strain (%)	Fracture strain (%)
Faceplate	7.34×10^{-4}	29000	0.30	38	55	30	40
Connectors	7.34×10^{-4}	29000	0.30	50	75	-	-

6.4.3 Contact and Constraint Modeling

Friction between the infill concrete and the steel faceplates, the infill concrete and the baseplate, and the baseplate and the steel plate embedded in the foundation block were considered using the Contact-Automatic-Surface-To-Surface formulation available in LS-DYNA (2012a). This contact avoids any penetration of a slave node through a master segment using a penalty-based approach [LS-DYNA (2012a)]. The coefficient of friction for steel on concrete was conservatively assumed to be 0.5 based on Rabbat et al. (1985) who showed that the coefficient of friction between a steel plate and cast-in-place concrete varied between 0.57 and 0.7. The impact of this assumption on response is identified later in this chapter. The contact formulation allowed for compression and tangential loads to be transferred between the contact surfaces: steel faceplates and infill concrete. A physical gap between the shell elements of the steel faceplate and solid elements of the infill concrete was considered because DYNA determines the contact surface of the shell element by normal projection of its mid-plane by a distance equal to half thickness of the shell. The steel faceplates were tied to the baseplate using the kinematic constraint Contact-Tied-Shell-Edge-To-Surface available in LS-DYNA (2012a). The studs and tie rods were coupled to the infill concrete elements using the Constrained-Lagrange-In-Solid formulation available in LS-DYNA (2012a) and slip between the connectors and the infill concrete was neglected. A schematic drawing of the connection between the steel faceplate and infill concrete is presented in Figure 6-19.

6.4.4 Elements

Beam elements were used to represent the studs and tie rods. Eight-node solid elements were used to model the infill concrete and the baseplates, and four-node shell elements were used for the steel faceplates. The post-tensioning bars connecting the SC wall to the foundation block were modeled using spring elements (see Figure 6-21). The constant stress formulation [ELFORM=1 in LS-DYNA (2012a)] and Belytschko-Tsay formulation [LS-DYNA (2012a)] were used for solid elements and shell elements, respectively. The cross section integrated beam element [Hughes-Liu beam in LS-DYNA (2012a)] was used for the shear studs and the tie rods. Springs were modeled using the discrete element formulation. The mesh sizes of the infill concrete and steel faceplates were selected based on the results of a mesh convergence study, described in the following subsection.

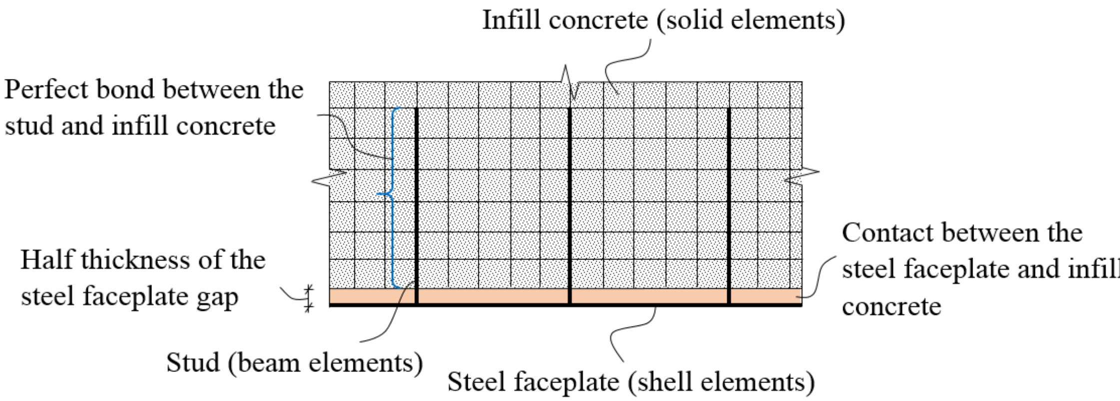

Figure 6-19 Schematic description of the connection between the steel faceplate and the infill concrete

6.4.4.1 Mesh Convergence Study

To determine a reasonable balance between solution accuracy and computation expense, five SC wall models, Models 1 through 5, with different mesh sizes (0.5, 1.0, and 2.0 in.) for the infill concrete and steel faceplates were analyzed. The mesh size of the concrete solid elements and steel shell elements for the five models are listed in Table 6-6.

Table 6-6 Mesh sizes for SC wall models

Model	Infill concrete (in.×in.×in.)	Steel faceplate (in.×in.)
Model 1	0.5×0.5×0.5	1.0×1.0
Model 2	2.0×2.0×2.0	1.0×1.0
Model 3	1.0×1.0×1.0	0.5×0.5
Model 4	1.0×1.0×1.0	2.0×2.0
Model 5	1.0×1.0×1.0	1.0×1.0

The effect of mesh size on the monotonic response is presented in Figure 6-20. The responses of Model 1 with 0.5 in. infill concrete elements and Model 3 with 0.5 in. steel faceplate elements were similar to the response of Model 5, indicating that the use of a mesh size less than 1.0 in. for the infill concrete and the steel faceplates had no effect on global response. Based on these results, the infill concrete was modeled using 1.0 × 1.0 × 1.0 in. solid elements and the steel faceplates were modeled using 1.0 × 1.0 in. shell elements.

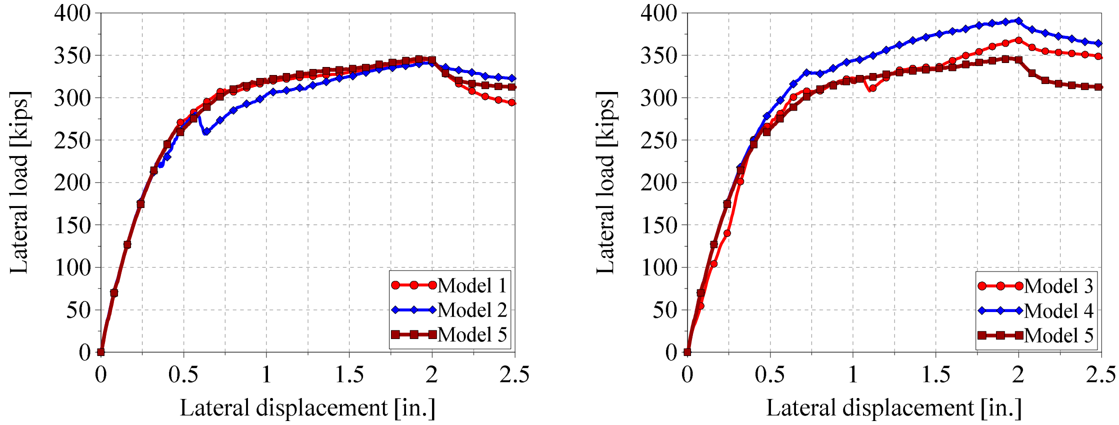

(a) Including infill concrete elements with 0.5, 1.0, and 2.0 in. mesh size

(b) Including steel faceplate elements with 0.5, 1.0, and 2.0 in. mesh size

Figure 6-20 Effect of mesh size on monotonic response

6.4.5 Loading and Boundary Conditions

The reversed cyclic loading of the test specimens was simulated by imposing horizontal displacements at the nodes of the infill concrete and steel faceplate elements, located at the level of the centerline of the loading plates, 60 in. above the baseplate.

Figure 6-21 presents the technique used for modeling the connection between an SC wall and its foundation using two 1-in. thick baseplates and 22 linear springs to represent the 1.25-in. diameter threaded B7 bars that secured the baseplate to the foundation block. The stiffness of the linear springs was back-calculated from the measured initial stiffness of the SC walls. Figure 6-22 presents the measured cyclic response of SC3 together with the DYNA-predicted monotonic responses corresponding to different spring stiffness at the base of the wall. Figure 6-22 indicates that the initial stiffness of SC3 was successfully predicted using a stiffness of 1×10^6 lbf/in per spring.

The effect of spring stiffness on the deformation of the SC walls is presented in Figure 6-23. The greater the stiffness of the linear springs, the smaller the vertical displacement of the SC walls and the smaller the gap opening between the baseplate attached to the faceplates and the steel plate tied to the stiff base. Similar analyses were conducted on the other SC walls to estimate the stiffness of the linear springs representing the post-tensioned threaded bars. The stiffness of each spring for SC1, SC2, and SC4, was 2×10^{7}, 1×10^{6}, 1.5×10^{6} lbf/in, respectively.

Since preliminary analysis indicated that the foundation block was effectively rigid, it was not included in the finite element model. The LS-DYNA model of SC2 is presented in Figure 6-24.

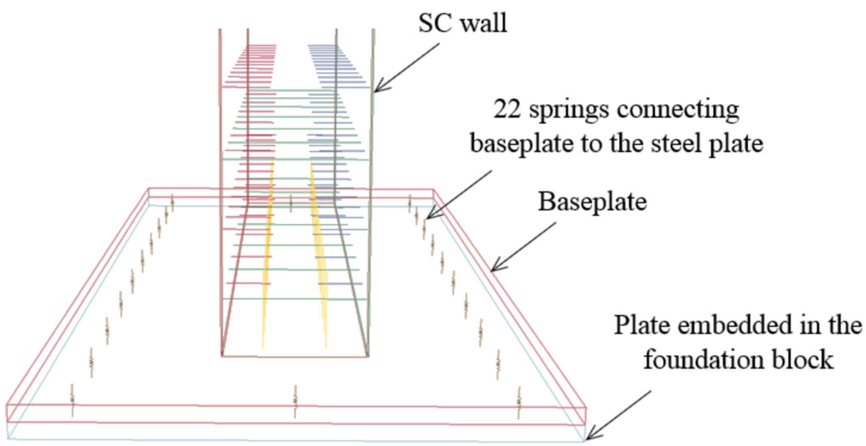

Figure 6-21 Modeling the connection between the SC wall and the foundation block

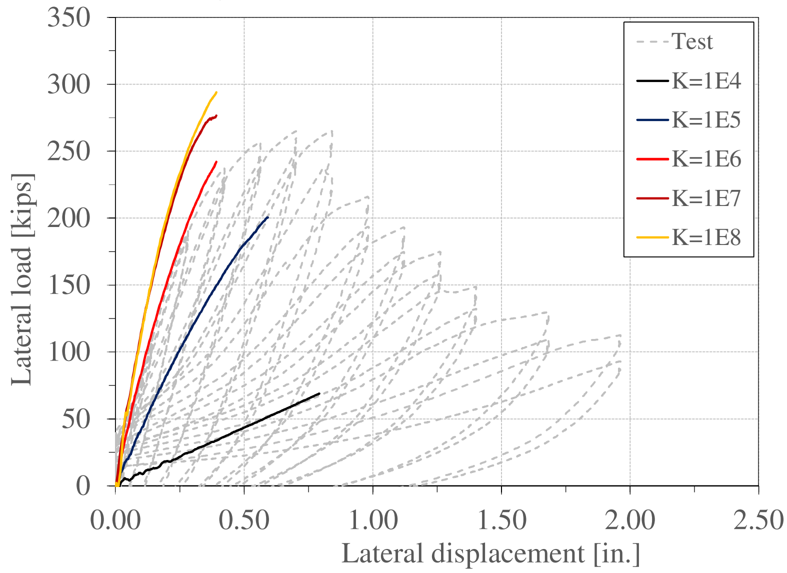

Figure 6-22 Initial stiffness (K) calculation

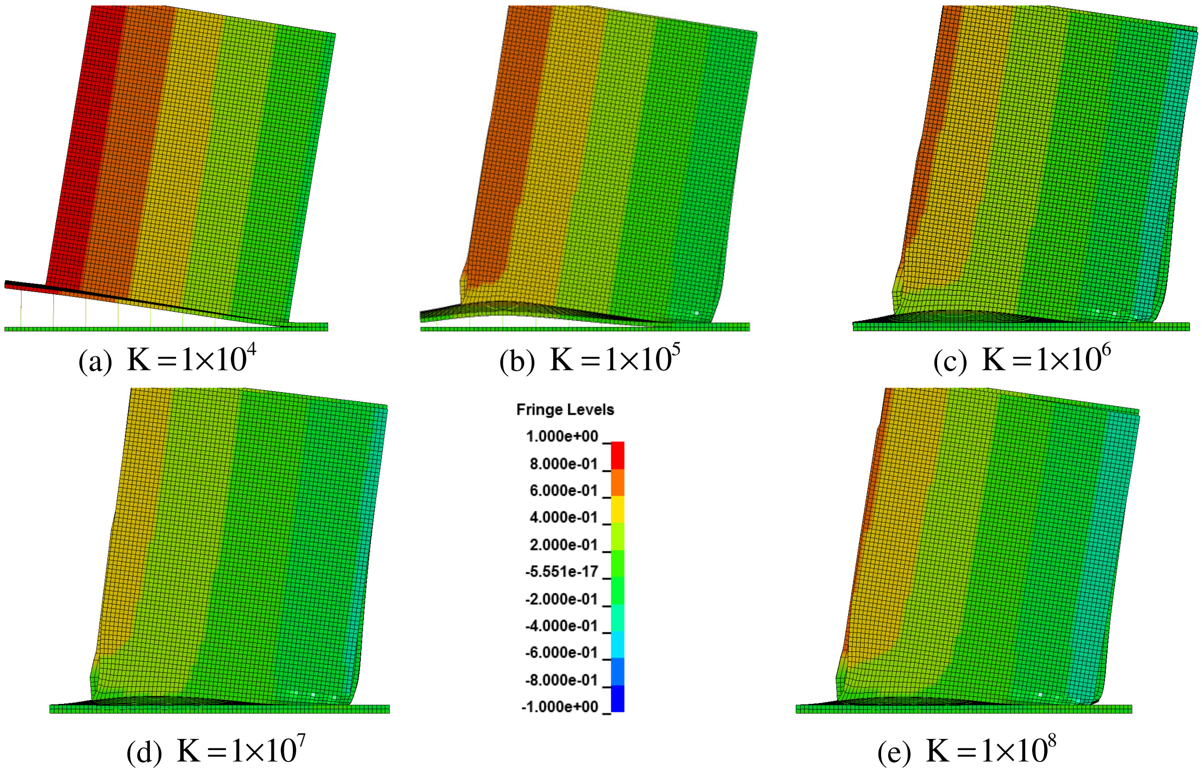

Figure 6-23 Contours of vertical displacement as a function of spring stiffness at 1.17% drift ratio (units: lb and inches)

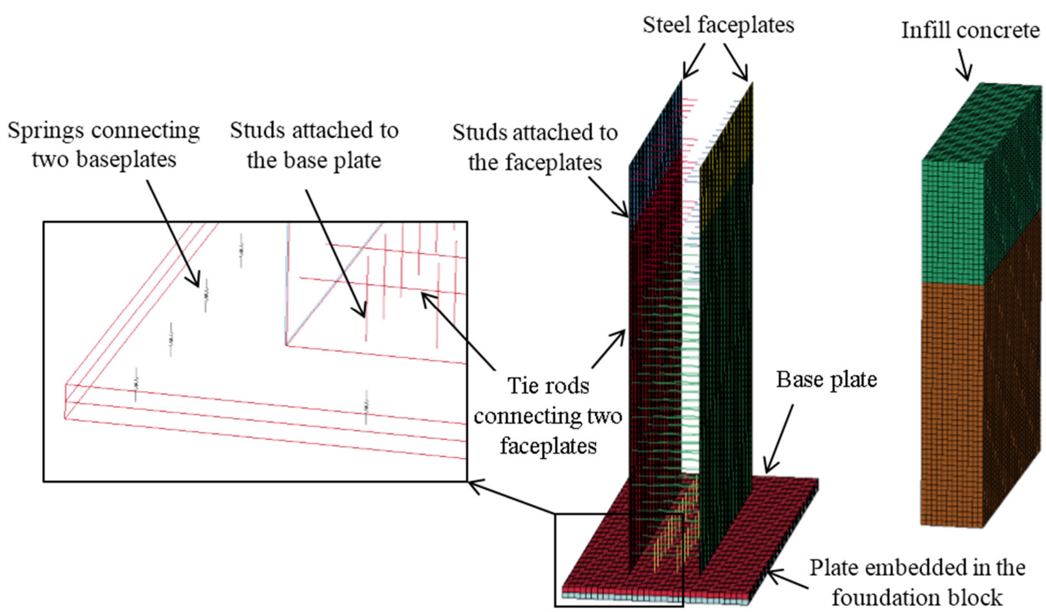

Figure 6-24 LS-DYNA model of SC2

6.4.6 LS-DYNA Analysis Results

The following sections describe the DYNA analysis results, including the global force-displacement responses, equivalent viscous damping ratio, damage to the steel faceplates and infill concrete, strain and stress distributions in the steel faceplates, and estimates of the contribution of the steel faceplates and infill concrete to the lateral resistance of the walls.

6.4.6.1 Load-Displacement Cyclic Response

The DYNA-predicted and measured force-displacement relationships for SC1 through SC4 are presented in Figure 6-25. In this figure, displacement is the horizontal movement of the wall in its plane at the level of the actuators; drift ratio is defined as the horizontal displacement divided by the distance between the base of the wall and the centerline of horizontal loading (= 60 inches). There was good agreement between the measured and predicted cyclic responses of SC walls, noting that initial stiffness was captured exactly through the choice of the axial stiffness of the springs at the base (see Section 6.4.5).

The predictions of the peak shear resistance and the rate of the reloading/unloading stiffness compared favorably with the test results. The predicted post-peak responses agreed well with the experimental results for SC2 and SC4 but were slightly under-estimated and over-estimated in SC1 and SC3, respectively. This outcome was attributed to damage to the infill concrete and its effect on the headed studs. Crushed concrete cannot anchor a stud and the buckling resistance of the faceplate is consequently reduced. If threaded (tie) rods are used to provide composite action and join the faceplates, outward movement of the tie rod (and the faceplate), at the location of the tie rod, is by-and-large prevented and faceplate buckling resistance is preserved. The local crushing of concrete was not addressed in the numerical model because beam elements were used to model the studs and these were coupled to the concrete elements. Pinching was successfully simulated using 1) the smeared crack concrete model that considers opening, closing and re-opening of the cracks induced by load reversals, and 2) the steel material model, which considers the out-of-plane buckling and fracture in the steel faceplates.

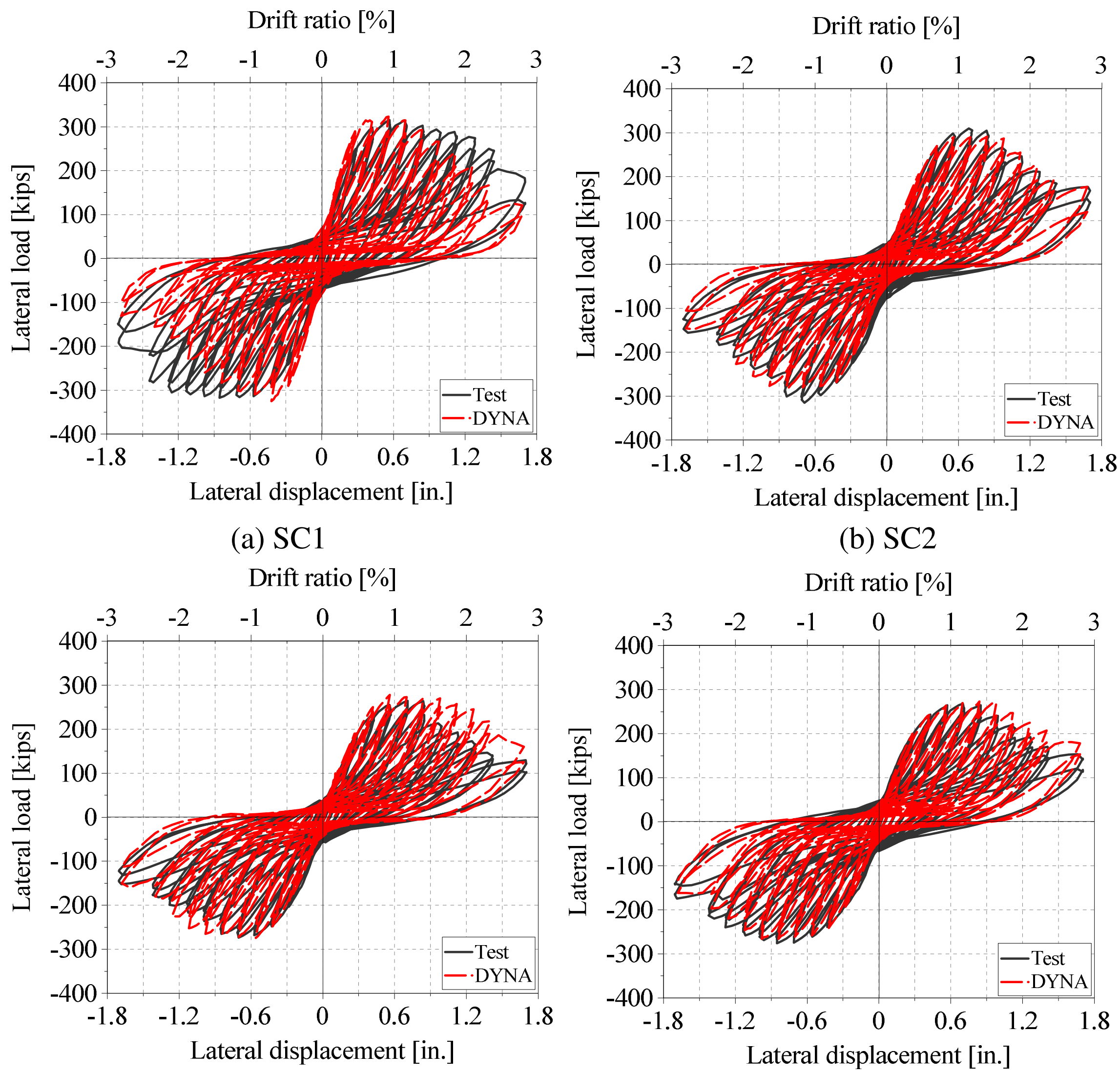

(a) SC1 (b) SC2

(c) SC3 (d) SC4

Figure 6-25 Predicted and measured lateral load-displacement relationships

6.4.6.2 Hysteretic Damping

Equivalent viscous damping is routinely used to model components and structures responding in the linearly elastic range [Chopra (2012)]. The measured hysteretic damping ratio at different drift ratios were presented at Chapter 5. The equivalent viscous damping ratio, calculated from experimental and numerical (DYNA) data for drift ratios up to 2% for SC1 through SC4, are presented in Figure 6-26. For drift ratios between 50 percent and 100% of those associated with peak strength, for which elastic dynamic analysis might be employed, the equivalent viscous damping ratios, calculated using the experimental and numerical data, were almost identical; the ratio exceeds 6% for both datasets. At drift ratios greater than those associated with peak strength, the DYNA simulations showed more pinching of the hysteresis loops for SC1 through SC4 than was measured and so underpredicted the dissipated energy in a given vibration cycle.

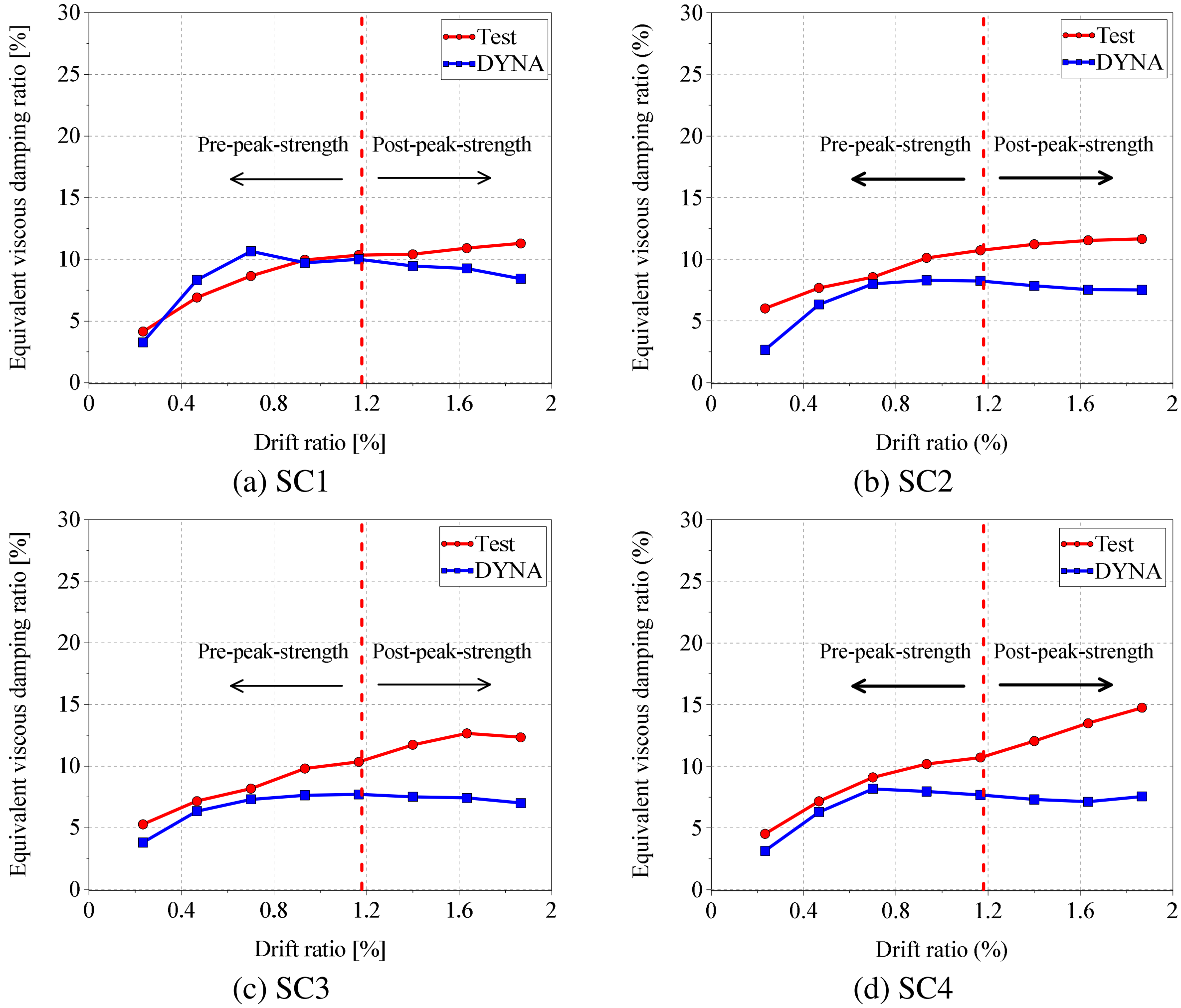

Figure 6-26 Equivalent viscous damping ratio

6.4.6.3 Steel Faceplate Contribution to the Total Load

A dense grid of Krypton LEDs was attached to one steel faceplate and rosette strain gages were installed at three elevations on the other faceplate to measure the strain fields in the steel faceplates. The grid of the Krypton LEDs generated square panels on the surface of the faceplate of the four walls. The rosette strain gages were mounted on the steel faceplate with the second gage vertical. In Section 5.7, the normal and shear strains in each panel were calculated using in-plane displacements measured by the Krypton LEDs and an isoparametric quadrilateral formulation. The three strains measured by each rosette were transformed to normal and shear strains.

Figure 6-27 presents information from the DYNA analyses and experiments for SC1 through SC4: the measured cyclic force-displacement relationship for the steel faceplates provided at small values of drift ratio prior to steel faceplate yielding using strains measured by rosettes (solid red line) and displacements measured by LEDs (solid blue line), the DYNA-predicted cyclic force-displacement relationship of SC wall (solid gray line), and the DYNA-predicted backbone curve of the force-displacement relationship for the steel faceplates (dashed black line). The predicted and measured shear forces resisted by the steel faceplates are at the level of the first row of strain gages above the baseplate. As presented in Chapter 6, the measured shear force in the steel faceplates was calculated as the product of the average shear strain (calculated using either the rosettes strain gages or from the LED displacements), an assumed value of G for the steel faceplates, and a total faceplate area of 22.5 inches, prior to steel faceplate yielding. Figure 6-27 indicates that the DYNA model successfully predicted the shear force in the steel faceplates.

The accuracy of the DYNA-predicted nonlinear response of the steel faceplates over the height of the wall was investigated further using 1) calculations of the Von-Mises stress distributions in the steel faceplates of SC1 and SC3, and 2) analysis of the deformed shape of the steel faceplates of SC3 at increasing levels of drift ratio.

For each square panel generated by the grid of the Krypton LEDs, the strains and stresses were calculated at its corners using an isoparametric quadrilateral formulation. At a node common to multiple panels, each stress component was calculated by assigning a weight to each panel, based on panel area. The DYNA-predicted Von-Mises stress distribution in one steel faceplate of SC1 and SC3 are presented in Figure 6-28 together with the Von-Mises stress distribution calculated using the LED-measured displacements.

There was reasonable agreement between the numerical and experimental results at the locations of greatest strain. The discrepancies between the numerical and experimental results were attributed in part to the use of polynomial functions to interpolate between the measured strains at the nodes of the grid (more accurate estimation of the strain fields in the steel faceplates could be obtained by using a smaller spacing for the LEDs and/or by adding one LED at the center of the panel.)

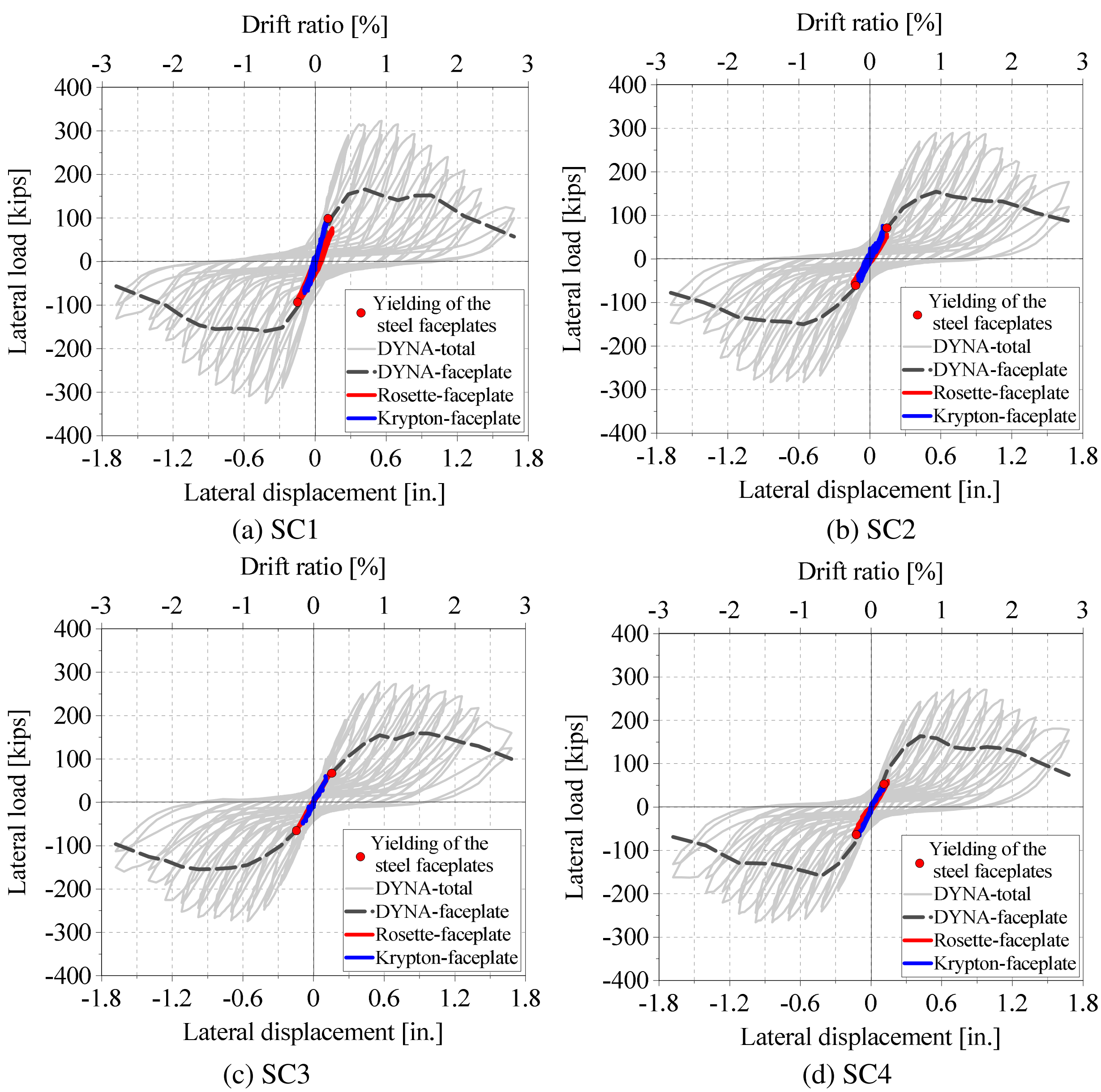

(a) SC1

(b) SC2

(c) SC3

(d) SC4

Figure 6-27 Predicted and measured cyclic force-displacement relationships in steel faceplates

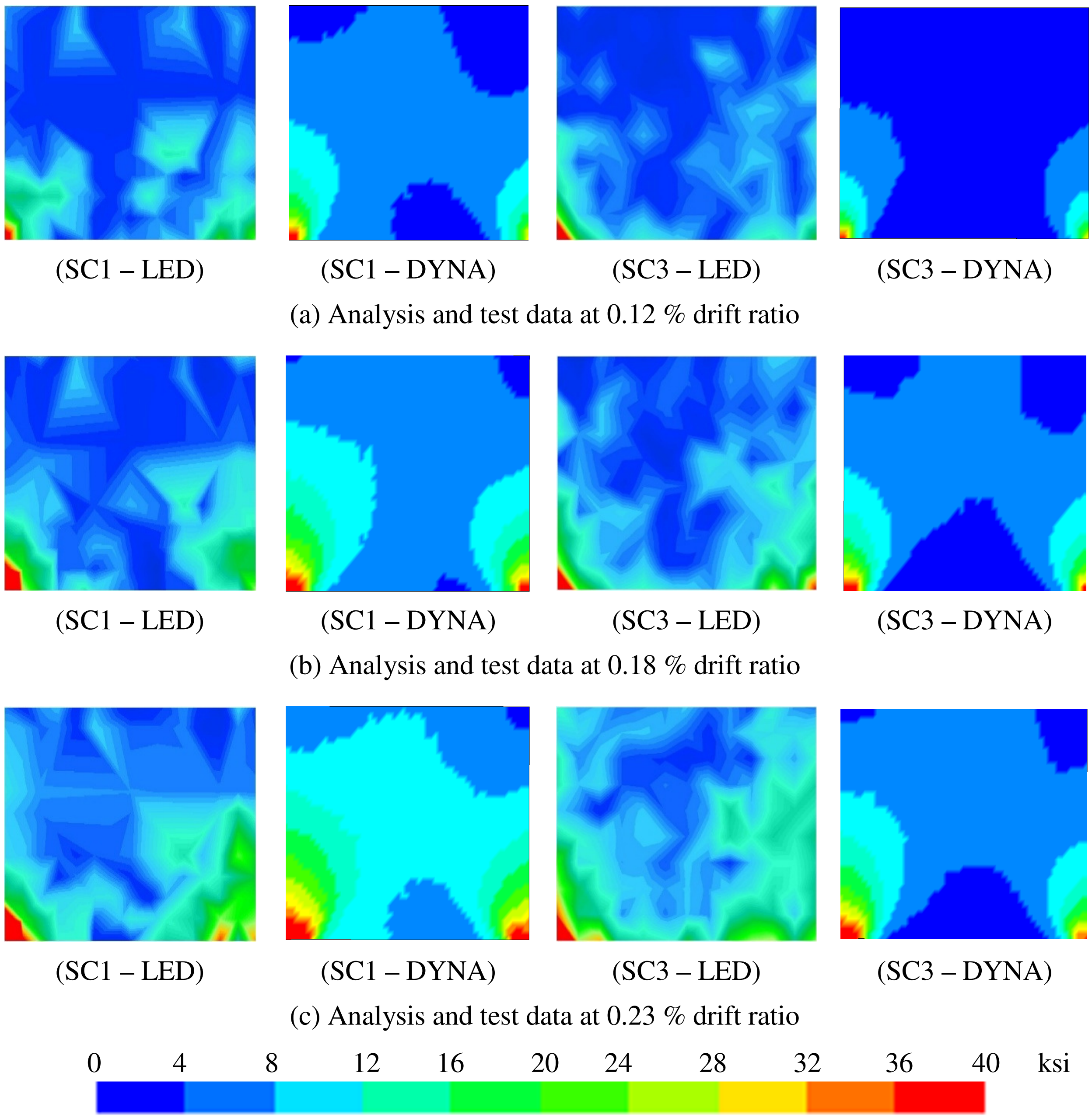

Figure 6-28 DYNA-predicted and measured Von-Mises stress distribution in steel faceplates

Figure 6-29 presents the undeformed shape and predicted and measured deformed shapes (scaled by a factor of 10) in one steel faceplate of SC3 at displacements corresponding to $\pm 0.23\%$, $\pm 0.47\%$, and $\pm 0.70\%$ drift ratio. The measured and DYNA-predicted displacement fields in the steel faceplate are very similar.

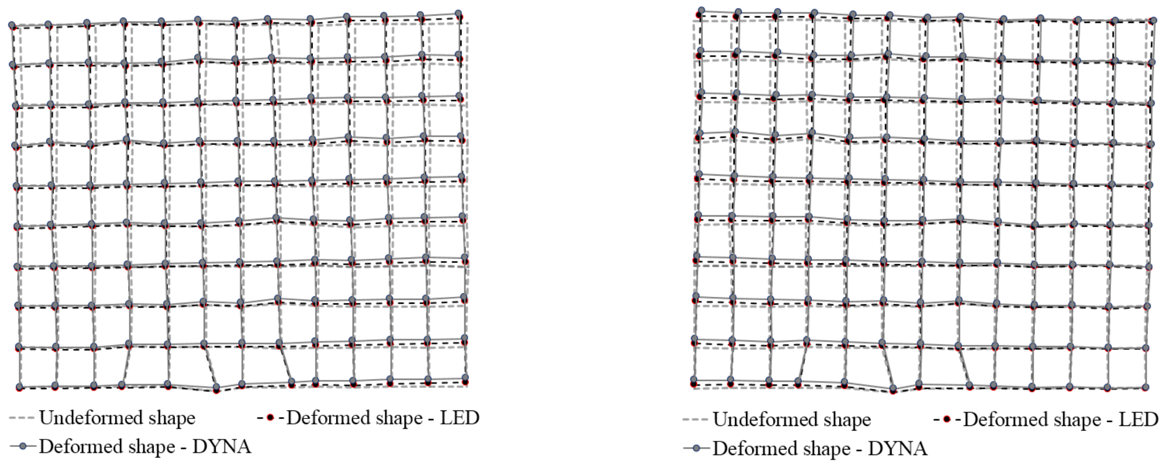

(a) at +0.23% (left panel) and -0.23% (right panel) drift ratio

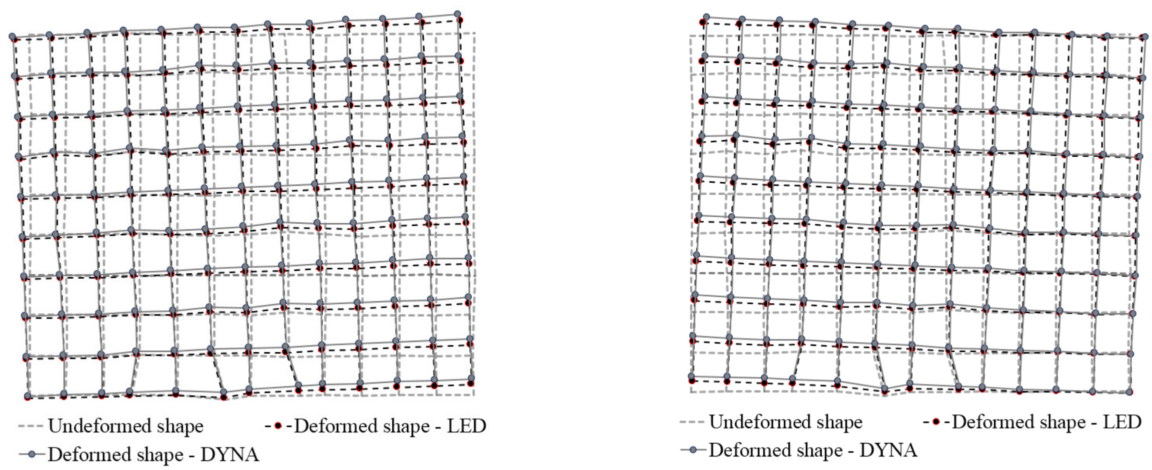

(b) at +0.47% (left panel) and -0.47% (right panel) drift ratio

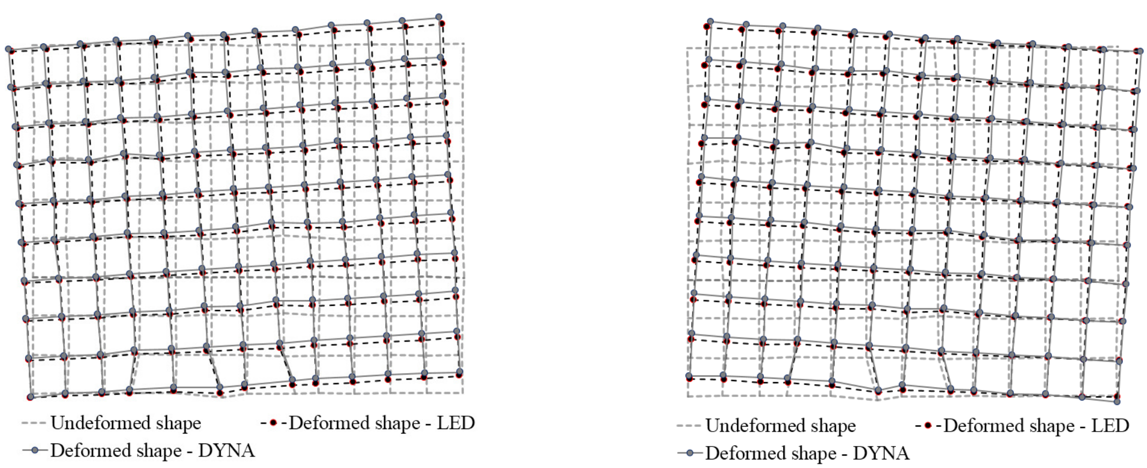

(c) at +0.70% (left panel) and -0.70% (right panel) drift ratio

Figure 6-29 DYNA-predicted and LED-measured deformed shapes of the steel faceplate in SC3

6.4.6.4 Damage to SC walls

Figure 6-30 and Figure 6-31 present the extent of damage to the steel faceplates and the infill concrete of SC1 through SC4, respectively, at 0.7%, 1.2%, and 2.8% drift ratios. The predicted damage and a photograph of the recorded damage to SC2 are presented in Figure 6-32(a). The damage to the SC walls, including the tensile cracking and crushing of the concrete at both ends of the wall, and outward buckling and tearing of the steel faceplates at the base of the wall were captured quite well by the finite element model.

The damage to the infill concrete of specimen SC2 is presented in Figure 6-32(b). Analysis of the DYNA model predicted damage to the infill concrete above the baseplate at the level of the heads of studs attached to the baseplate, which was observed in the experiment, as seen in the left panel.

Erosion of concrete was not considered in the DYNA analysis because the Winfrith model assumes an element to have failed, with no tensile strength and stiffness, when three orthogonal cracks have formed in it. The elements of the steel faceplates were eroded when the plastic strain reached the rupture strain measured in the coupon tests (=40%, see Section 4.4.2). This assumption was confirmed using numerical and experimental results. Preliminary analysis was conducted assuming no fracture in the steel faceplates and the history of the equivalent plastic strain of the steel faceplate elements near the vicinity of the tearing of the steel faceplates was monitored during the cyclic analysis. The fracture strain was then calculated as the value of the effective plastic strain of the critical steel faceplate elements corresponding to the cycle when the tearing of the steel faceplate occurred in the experiment.

Figure 6-32(a) and Figure 6-32(b) show that the extent of damage to the steel faceplate and the infill concrete predicted by DYNA was similar to that observed in the test.

6.4.7 Validation of the DYNA Model

The DYNA model of flexure-critical SC walls is considered to have been validated through comparisons of predictions and measurements at the global and local levels, including cyclic force-displacement relationships, equivalent damping ratios, shear forces in the steel faceplates, the deformed shapes of the steel faceplates, and the Von-Mises stress distributions in the steel faceplates.

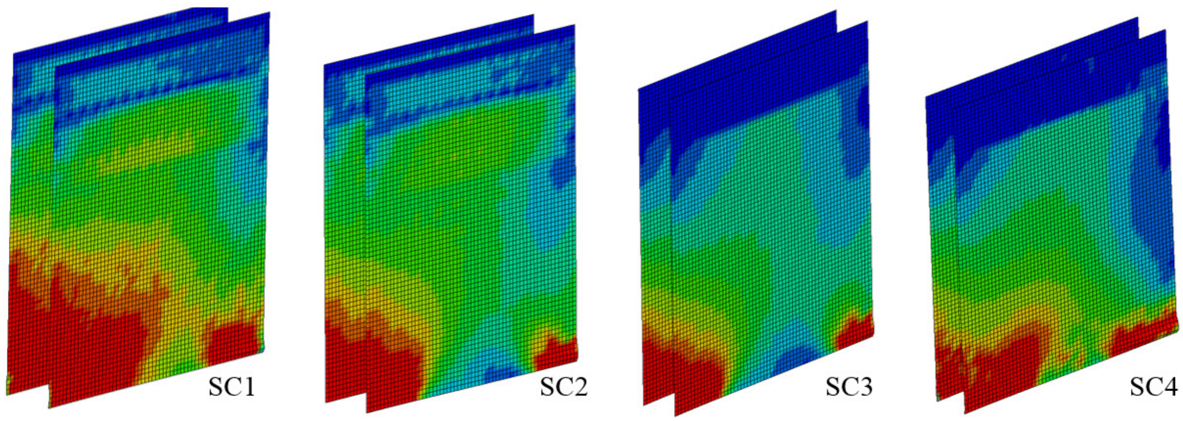

(a) at 0.7% drift ratio

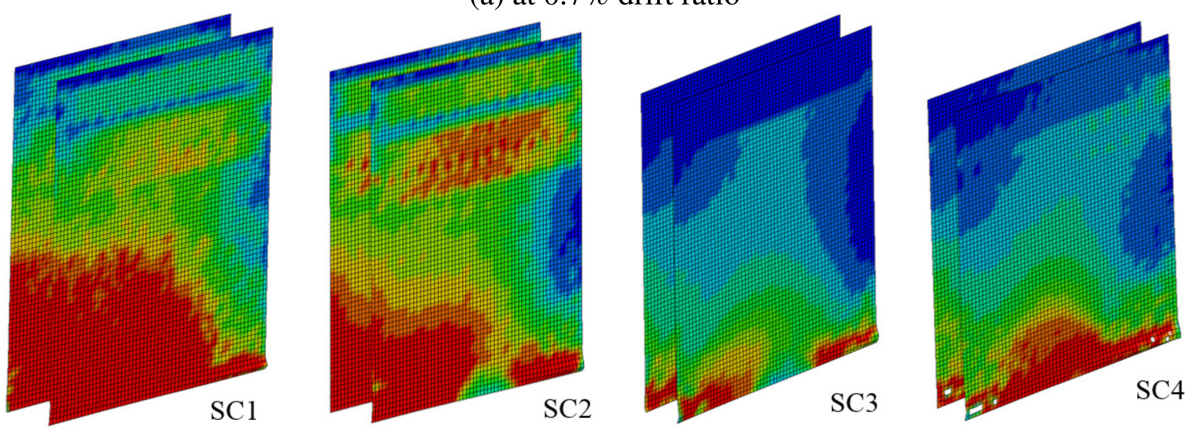

(b) at 1.2% drift ratio (corresponding to peak lateral strength)

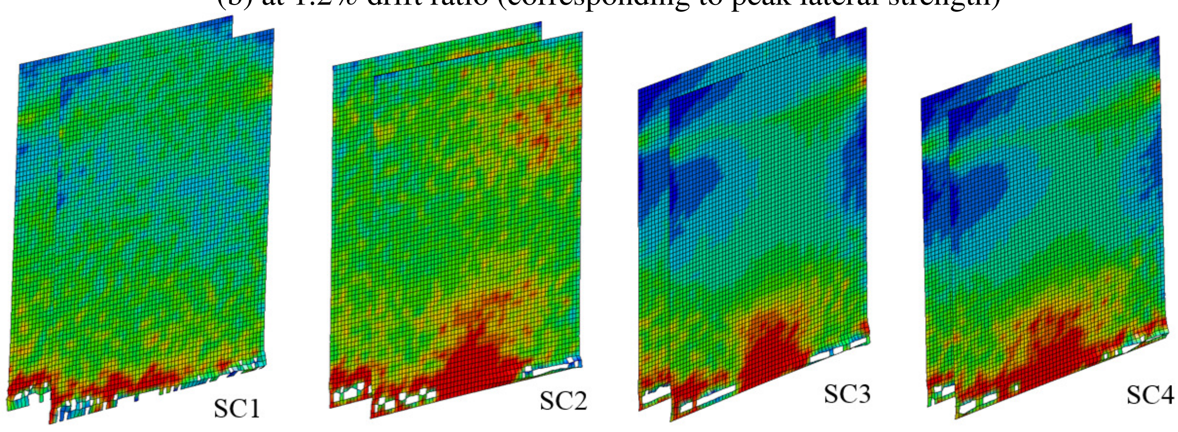

(c) at 2.8% drift ratio

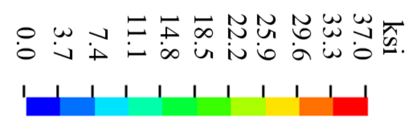

Figure 6-30 Damage and distribution of Von-Mises stress in the steel faceplates

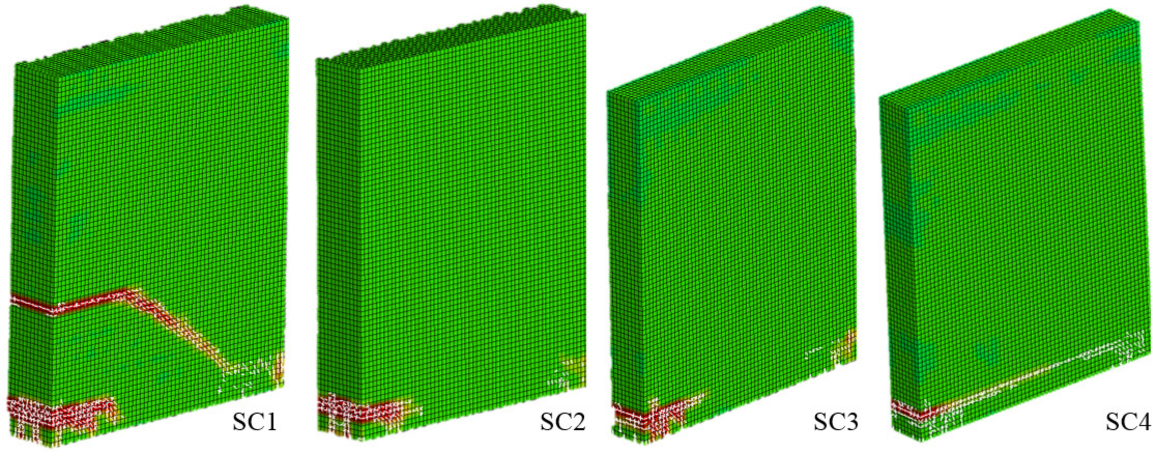

(a) at 0.7% drift ratio

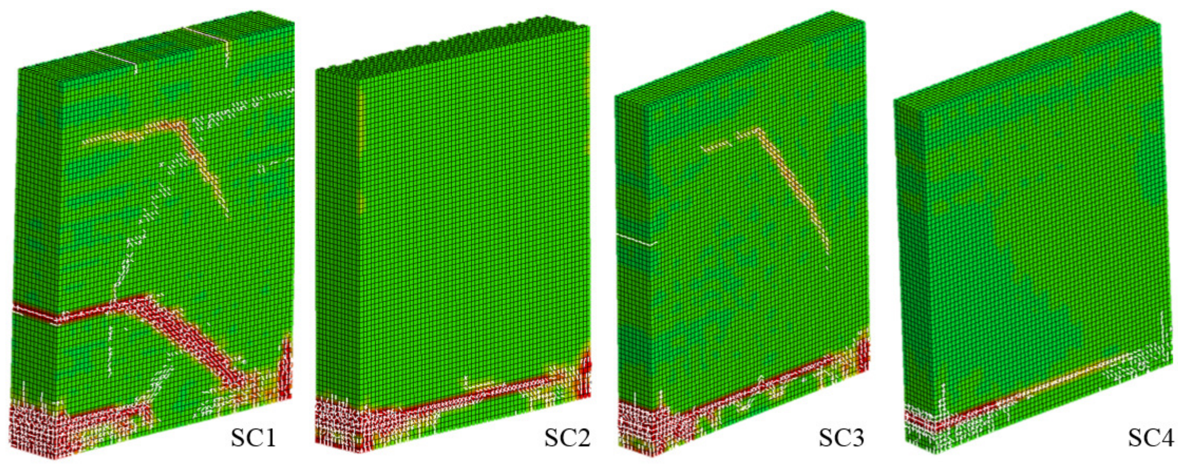

(b) at 1.2% drift ratio (corresponding to peak lateral strength)

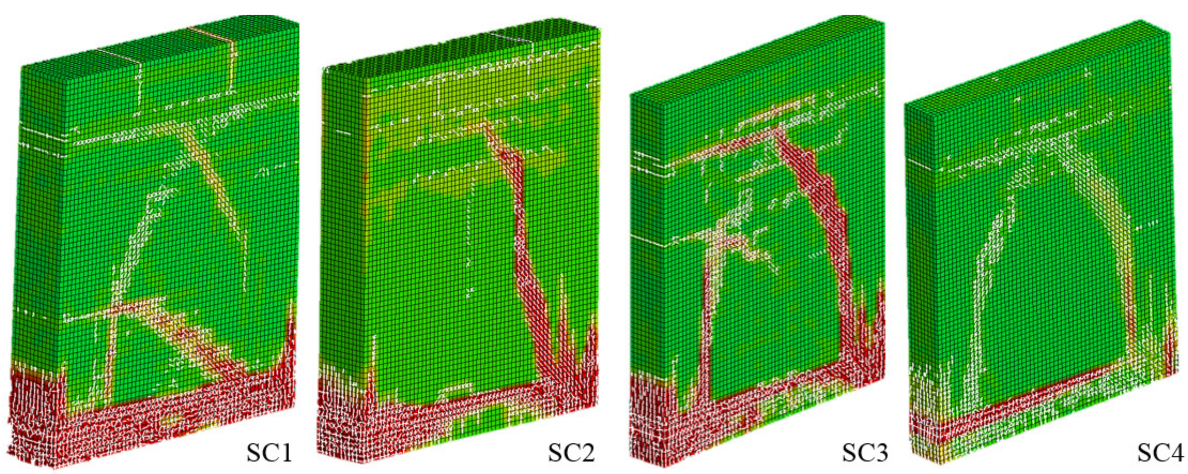

(c) at 2.8% drift ratio

Figure 6-31 Damage to the infill concrete

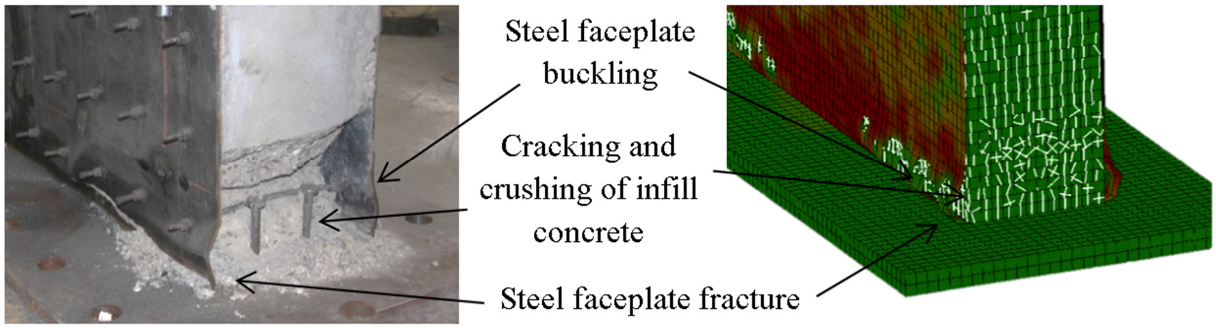

(a) Damage to specimen; test (left panel) and analysis (right panel)

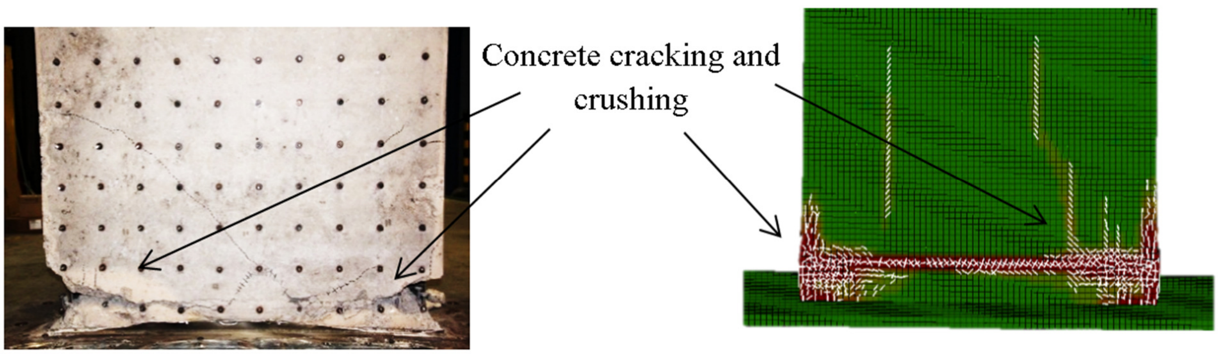

(b) Damage to infill concrete; test (left panel) and analysis (right panel)

Figure 6-32 Predicted and measured damage to SC2

6.5 Exploration of Modeling Assumptions and Design Decisions

A validated numerical model can be used to substantially expand an experimental dataset, to explore behaviors that cannot be readily measured, understand the impact of modeling assumptions, and explore design decisions. The validated DYNA model was used to investigate load transfer between the steel faceplates and the infill concrete, assumptions related to contact and constraint modeling, and the connection of the infill concrete to the baseplate.

6.5.1 Load Transfer Mechanism in SC Walls

The DYNA-predicted shear forces resisted by the steel faceplates of SC1 through SC4 were calculated at different elevations along the height of the wall and at some peak cyclic displacements. The contributions of the steel faceplates to the total shear load in SC1 through SC4 are presented in Figure 6-33.

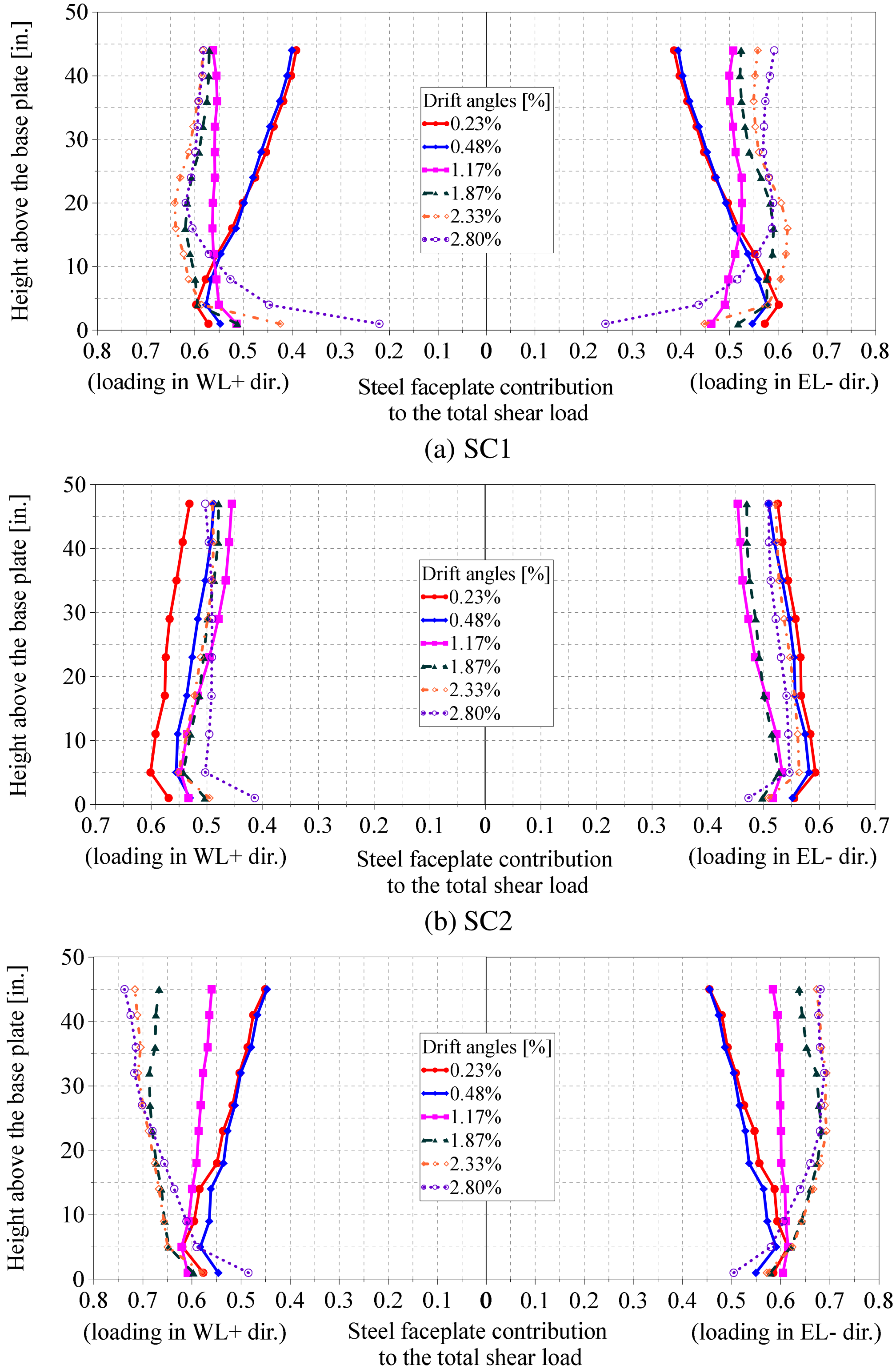

(a) SC1

(b) SC2

(c) SC3

Figure 6-33 Contribution of the steel faceplates to the total shear load

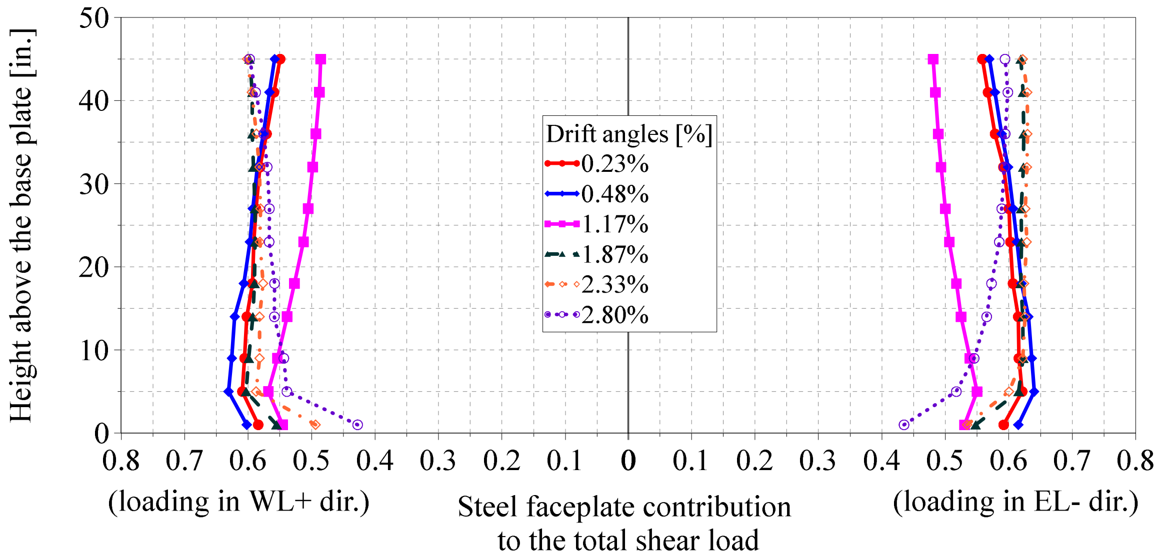

(d) SC4

Figure 6-33 Contribution of the steel faceplates to the total shear load (cont.)

The DYNA model assumed full composite action at the top of the SC wall because no slip was observed between the steel faceplates and infill concrete at the level of the loading plates. This was expected because a high normal pressure was applied to the steel faceplates and infill concrete by the post-tensioning of the loading plates to the specimen.

Figure 6-33 shows that at small drift ratios, and prior to peak load, the shear force resisted by the steel faceplates increased down the height of the wall due to the transfer of shear force from the infill concrete to the steel faceplates through the shear connectors. At peak load, the shear forces resisted by the steel faceplates at different levels along the height of the wall were approximately identical. In the post-peak strength region, the increasing damage to the steel faceplates, including out-of-plane buckling and tearing near the base of the wall, resulted in a significant reduction in the percentage contribution of the steel faceplates to the total resistance.

Figure 6-34 presents the DYNA-predicted cyclic force-displacement relationships of the infill concrete and steel faceplates in SC1. The horizontal shear forces resisted by the steel faceplates and the infill concrete were calculated 1 in. above the baseplate. The horizontal shear force resisted by the infill concrete 1 in. above the baseplate was calculated as the difference between the total shear force in the SC wall and the shear force resisted by the steel faceplates, calculated as the product of the average predicted shear stresses in the faceplates and a total faceplate area of 22.5 in^2.

The highly pinched hysteresis loops in the infill concrete was associated with damage to the infill concrete, including concrete cracking and crushing at the toes of the walls. The hysteresis loops for the steel faceplates were pinched due to tearing and buckling.

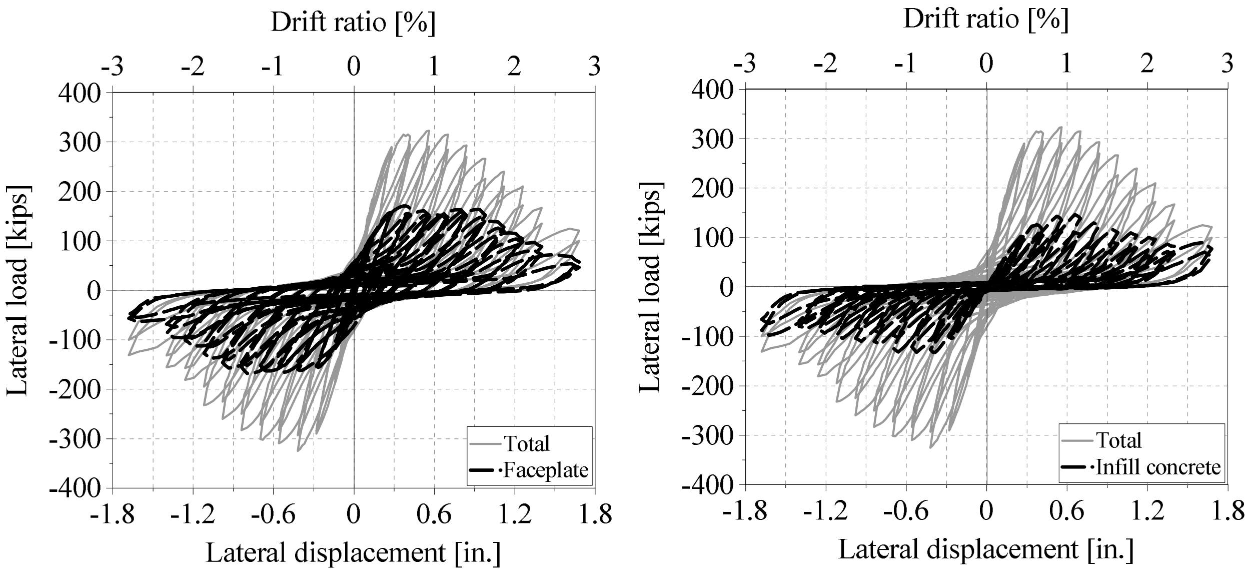

Figure 6-34 DYNA-predicted cyclic force-displacement relationships in SC1

6.5.2 Friction

To investigate the influence of friction between the steel faceplates and the infill concrete on in-plane response, the DYNA models of SC1 and SC3 were re-analyzed with the coefficient of friction set to zero. The global responses were essentially identical to those reported previously for a coefficient of friction of 0.5, and expected because the normal stresses acting on the faceplate-to-concrete interface were negligible.

Figure 6-35 reproduces the predicted cyclic response of the SC1 and SC3 of Figure 6-25 (Model 1) together with the results of analysis assuming perfect bond between the infill concrete and faceplates (Model 2). The pre-peak-strength response of these flexure-critical SC walls was not significantly affected by the assumption of perfect bond but counter-intuitive differences were evident in the post-peak behavior. Perfect bond did not allow the faceplates to buckle, concentrating inelastic deformation near the base of the wall, and leading to their premature fracture.

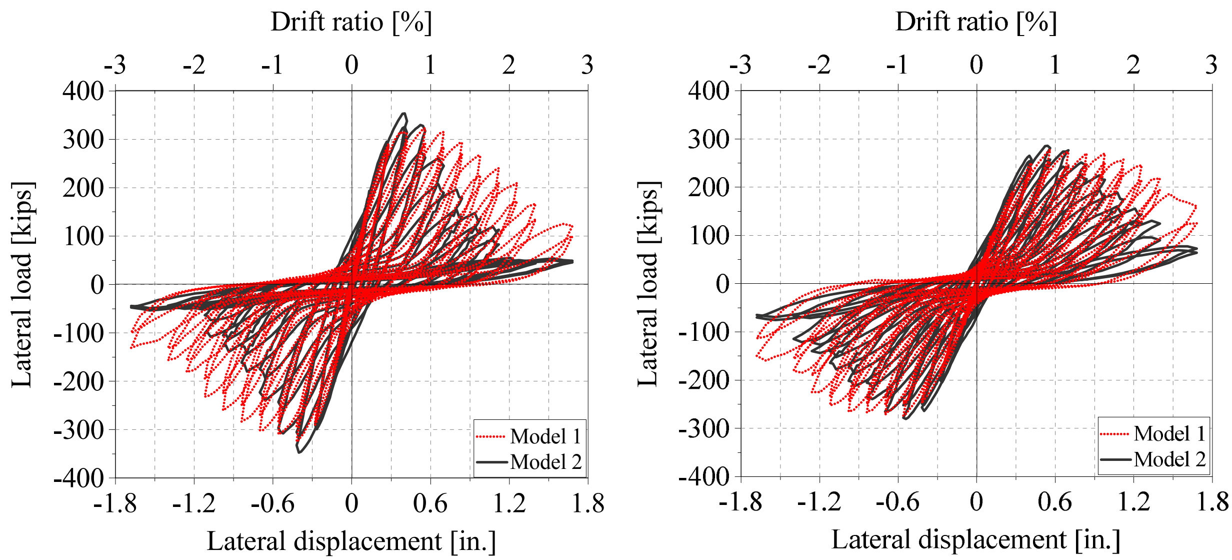

(a) SC1 (b) SC3

Figure 6-35 Influence of the assumption of perfect bond on in-plane response

Figure 6-36 presents fringes of plastic strain from the cyclic analysis of SC1 at a drift ratio of 1.5%: a drift ratio greater than that associated with peak strength. At 1.5% drift ratio, the plastic strain in some steel faceplate elements near the base of the wall in Model 2 exceeded the rupture strain whereas the plastic strains in the buckled steel faceplate of Model 1 were smaller than the rupture strain.

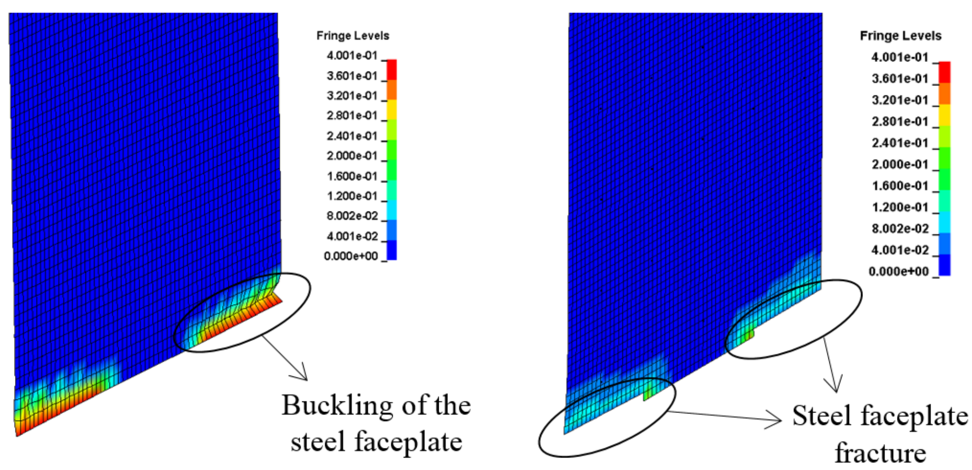

(a) Model 1 (a) Model 2

Figure 6-36 Plastic strain distribution in steel faceplates

6.5.3 Studs Attaching the Baseplate to the Infill Concrete

The tests of SC1 through SC4 revealed a failure plane at the level of the heads of the vertical studs that connected the infill concrete to the baseplate (see Figure 5-2). The heads of the studs occupied

5% and 7% of the shear area of the infill concrete in SC1/SC2 and SC3/SC4, respectively. Two DYNA models of SC2 (A and B), with different stud spacing, were prepared and analyzed to study the effect of stud spacing on the global and local responses of the flexure-critical walls. For Model A, studs were placed in 2 rows at 4 in on center (the as-tested condition); the studs were placed in 2 rows at 12 in on center for Model B. Finely meshed elements were used for the infill concrete surrounding the connectors; 3D solid elements were used to model the studs attached to the baseplate. Models A and B are presented in Figure 6-37.

Figure 6-38 presents the predicted tensile cracking of the infill concrete of the two DYNA models at drift ratios of 0.5% and 1.0%. Cracks formed in the horizontal plane defined by the heads of the studs in Model A at smaller drift ratios than in Model B. Figure 6-39 presents the predicted shear force-drift ratio relationships for the two models, which were identical up to a drift ratio of 0.5%, noting that baseplate flexibility contributes much of the total flexibility at this drift ratio.

As seen in Figure 6-39, the shear force in Model B is greater than that in Model at drift ratios greater than 0.5%, suggesting that an increase in stud spacing (Model B) may improve performance (and reduce cost), noting that this analysis did not determine the minimum number of studs or shear connectors required for adequate performance.

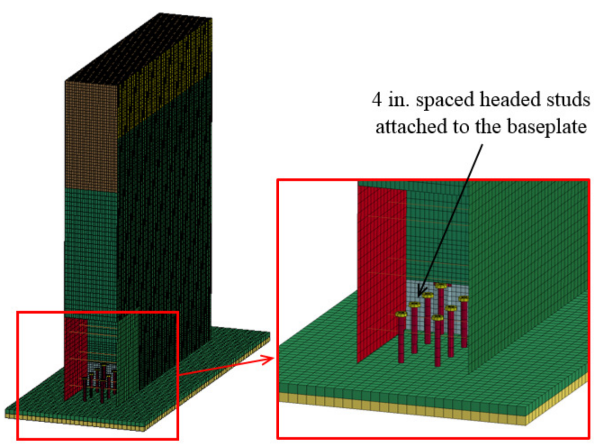

(a) Model A

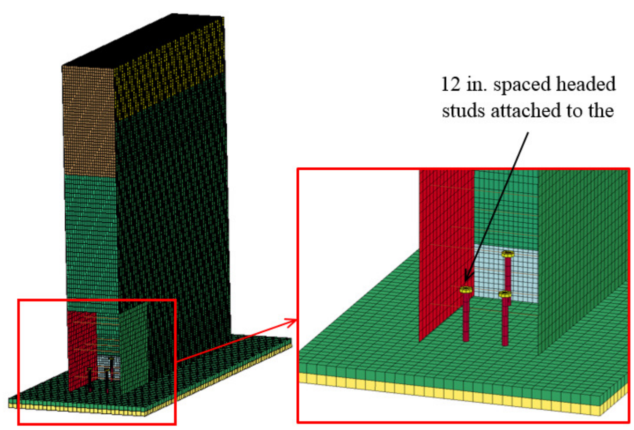

(b) Model B

Figure 6-37 DYNA models for studs attached to the baseplate

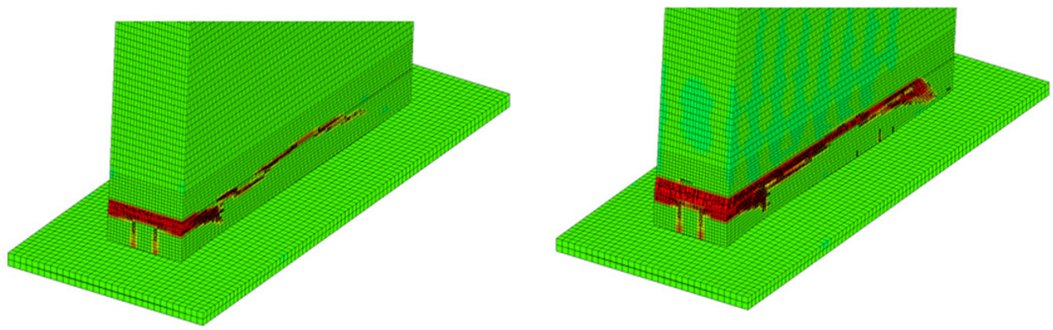

(a) Model A; 0.5% drift ratio (left panel) and 1.0% drift ratio (right panel)

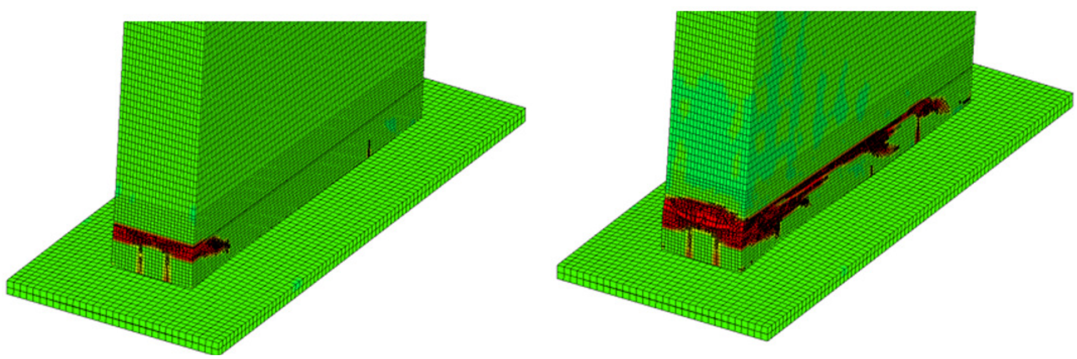

(b) Model B; 0.5% drift ratio (left panel) and 1.0% drift ratio (right panel)

Figure 6-38 Damage to infill concrete in Models A and B

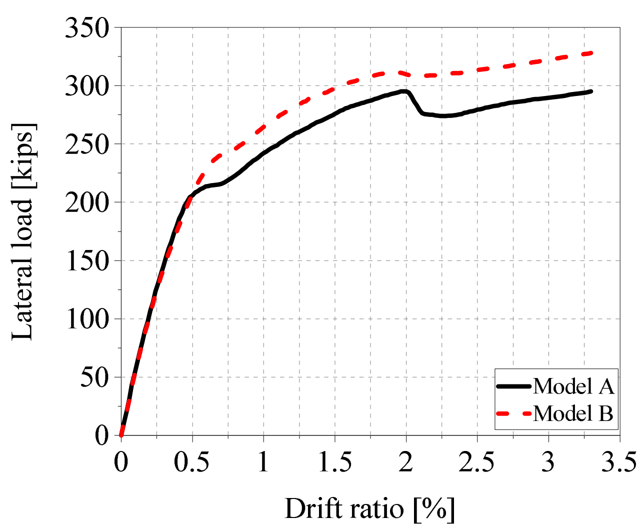

Figure 6-39 Lateral load-displacement relationships for Models A and B

6.5.4 Axial and Shearing Forces Transferred by Connectors

The maximum ratios of the axial and shear forces resisted by the connectors (calculated by DYNA analysis) to their corresponding nominal strengths are presented in Figure 6-40. For each connector, two ratios were calculated; the top and bottom values present the axial force (A) and shear force (S) ratios, respectively. The maximum axial and shear force ratios were not necessarily calculated at the same time instant.

The nominal axial and shear strengths of the connectors were calculated using Appendix D of ACI 318-11 (2011). Considering the steel and concrete breakout strengths of the connector in tension, and the steel and concrete pryout strengths of the connector in shear, the nominal tensile and shear strengths of the connector were calculated 8.3 kips.

The shear studs were designed using the approach proposed by Zhang et al. (2013), wherein the stud spacing selected to avoid local buckling in steel faceplates and to ensure good composite action in the SC wall: the sum of the shear stud capacities over the development length should be greater than the faceplate yield strength over the tributary area defined by the line connecting shear studs (see Figure 6-41). A development length, L_D, was defined as the length over which the steel faceplate developed its yield strength in axial tension: similar to the concept of rebar development length [ACI 318-11 (2011) and ACI 349 (2006)][Zhang et al. (2013)]. In Figure 6-41, the studs are spaced at distances s_l along the length of the wall and s_t over the height of the wall; Q_n is the shear capacity of a single anchor; ϕ is a reduction factor taken as 0.65 for studs in SC walls by Zhang et al. (2013); t_p is the thickness of each faceplate; and f_y is the nominal yield strength of the steel faceplate.

Zhang et al. (2013) observed that good composite action (75 to 90%) between the steel faceplates and infill concrete could be achieved if the stud spacing was selected based on a development length less than three times the wall thickness. They also recommended that the faceplate slenderness ratio be limited to $1.0\sqrt{E_s / f_y}$ to prevent elastic buckling, where E_s and f_y are the Young's modulus and yield stress of the steel faceplate, respectively.

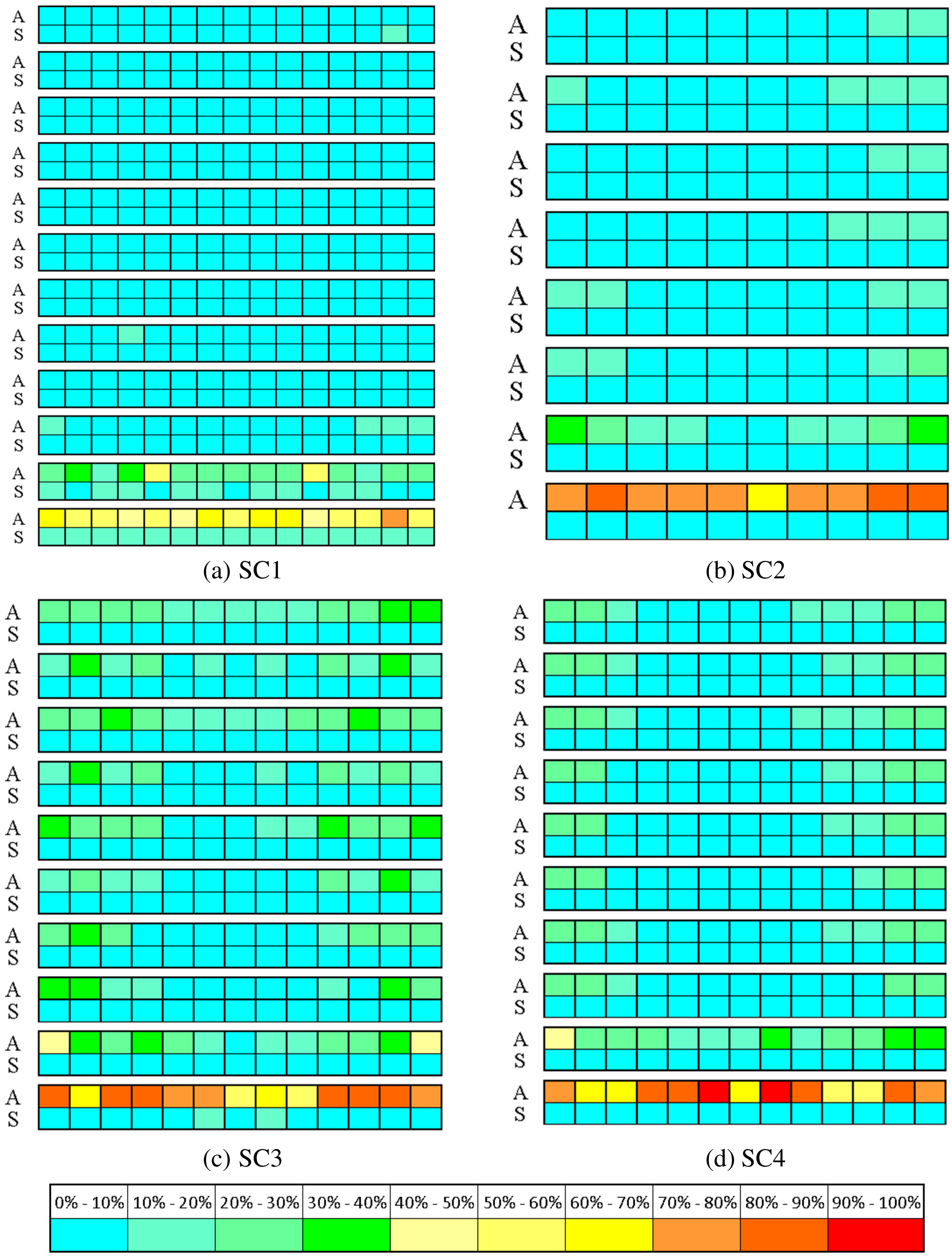

Figure 6-40 Maximum axial and shear force ratios for the connectors

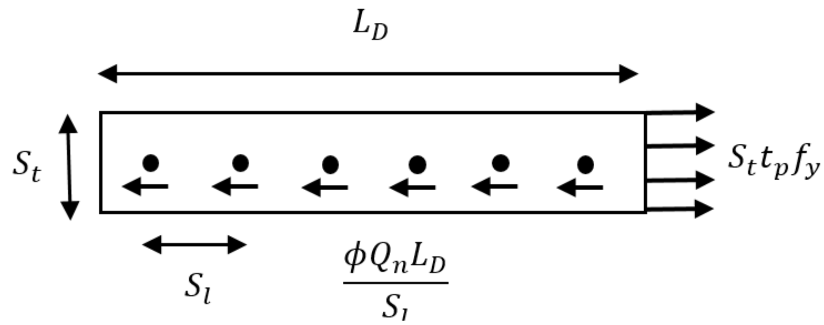

Figure 6-41 Schematic representation of development length [adapted from Zhang et al. (2014)]

The spacing and diameter of the shear studs used in SC1 through SC4 were based on these local buckling and composite action criteria. The development length, taken as three times of the wall thickness, was 36 in and 27 in for SC1/SC2, and SC3/SC4, respectively.

Post-test numerical analysis suggested that the design of these shear studs was conservative. In the two thicker walls, the axial force ratio was less than 0.2 except for the two rows of connectors closest to the base of the wall: see Figure 6-40. The high axial force ratio (=0.93) in the first row of connectors above the baseplate is attributed to the connectors resisting out-of-plane buckling of the steel faceplates.

CHAPTER 7

A PARAMETRIC STUDY: DESIGN OF SC WALLS

7.1 Introduction

This chapter summarizes results of a parametric study on the in-plane monotonic response of steel-plate concrete (SC) composite shear wall piers. The results of finite element analysis of 77 SC wall piers are used to investigate the effects of wall aspect ratio, reinforcement ratio, slenderness ratio, axial load, yield strength of the steel faceplates, and uniaxial compressive strength of concrete on the in-plane response of SC walls. The baseline model was validated and benchmarked in Chapter 6 using data from the tests of large-scale rectangular SC walls presented in Chapter 4.

Section 7.2 describes design variables considered in this study and Design of Experiments (DOE) used to explore the potential interactions of the design variables using a three-level six-factor fractional factorial design. Section 7.3 describes the DYNA modeling assumptions. DYNA analysis results are presented in Section 7.4. Section 7.5 presnts the results of the Analysis of Variance (ANOVA) including the interaction effects of the design variables on the shear force resisted by the infill concrete and steel faceplates and on the pre- and post-yield stiffness of SC walls. Section 7.6 presents a predictive model for the monotonic response of SC walls up to peak strength considering the effects of various design parameters. The adequacy of the predictive model is investigated in Section 7.7. The predictive model is validated using data from tests of four SC wall piers with an aspect ratio (height-to-length) of 0.5 in Section 7.8. Section 7.9 presents equations proposed to estimate the effective shear and flexural rigidities of SC wall piers for dynamic analysis. Sample calculations of the monotonic response and effective stiffness are provided in Section 7.10.

7.2 Parametric Study on SC Wall Piers

The general purpose finite element code LS-DYNA (2012a,2012b) was used to simulate the nonlinear response of 77 rectangular SC walls subjected to monotonic loading. Validation and benchmarking of the baseline model were presented in Chapter 6. The effects of design variables on the response are systematically investigated [Montgomery (1982)] by a statistical analysis. The details of the finite element analysis and Analysis of Variance (ANOVA) are described in the following sub-sections.

7.2.1 Design Variables

The design variables considered in this study are wall aspect ratio (AR), reinforcement ratio (RR), slenderness ratio of the steel faceplates (SR), axial force ratio (AL), yield strength of the steel faceplates (SS), and concrete compressive strength (CS). The reinforcement ratio is defined as the ratio of the cross-sectional area of the steel faceplates to the total cross-sectional area of SC wall. The faceplate slenderness ratio is the spacing of the connectors (studs or tie rods) divided by the steel faceplate thickness. The axial force ratio is the ratio of the applied axial compressive force to the product of the concrete compressive strength and the total wall area (i.e., $(2t_s + T)L_w$, where t_s and T are the thickness of each steel faceplate and infill concrete, respectively, and L_w is the length of the wall).

Three levels (i.e., low-, intermediate-, and high-levels) are considered for each design variable. The levels of the design parameters used in the numerical analysis are presented in Table 7-1. The values in parentheses show the coded values used in the analysis; the low, intermediate, and high levels of the factors are denoted by -1, 0, and +1, respectively.

Table 7-1 Levels of the design parameters

Variable	Low	Intermediate	High
Aspect ratio	0.5 (-1)	1.25 (0)	2.0 (+1)
Reinforcement ratio (%)	1.67 (-1)	3.33 (0)	5.0 (+1)
Slenderness ratio	10 (-1)	25 (0)	40 (+1)
Axial force ratio	0 (-1)	0.1 (0)	0.2 (+1)
Yield strength of the steel faceplates (ksi)	34 (-1)	50.5 (0)	67 (+1)
Concrete compressive strength (ksi)	4 (-1)	6 (0)	8 (+1)

Three aspect ratios (=0.5, 1.0, and 2.0) are considered to study the behavior of low-, intermediate- and high-aspect ratio walls, to address shear- and flexure-critical behaviors. The range for reinforcement ratio was based on Section N9.1.1c of AISC N690s1 (2014), which limits the reinforcement ratio to a minimum of 1.5% and a maximum of 5%. Section N9.3 of AISC N690s1 specifies a maximum slenderness ratio of $1.0\sqrt{E_s / f_y}$ to prevent local buckling of the steel faceplates before yielding, where E_s and f_y are the Young's modulus and nominal yield strength of the steel faceplate, respectively. For the range of the yield strength of the steel faceplates considered in this study (34 to 67 ksi), the AISC-specified maximum slenderness ratio varies between 21 and 29. This range was extended in the numerical study: 10 to 40. Plate steel of ASTM A36 ($f_y = 34$ ksi), A588 ($f_y = 50.5$ ksi), and A852 ($f_y = 67$ ksi) were used to represent low, intermediate, and high values of yield strength, respectively.

7.2.2 Design of Experiments (DOE)

Design of Experiments (DOE) concepts [Montgomery (1982)] were employed to explore the potential interactions of the design variables considered in this study and without bias. The DOE method represents an effective approach to assess the relationship between intrinsic factors that influence final output whether it is a design equation or behavioral response. Figure 7-1 is a geometrical representation of two- and three-level full factorial design together with a face-centered central composite design of three factors A, B, and C. Two-level full factorial design (Figure 7-1a) is widely used since it requires the smallest number of runs for a complete factorial design with many design variables [Montgomery (1982)]. However, the two-level factorial design assumes that the response is linear over the range of the design variables considered in the analysis. This assumption may not be applicable for the systems with nonlinear response [Montgomery (1982)]. In this study, a three-level, six-factor, fractional factorial design was selected to build different combinations of the design variables for the numerical analysis of SC walls. It was built using a face-centered central composite design (Figure 7-1b) by adding face-centered axial and center points to a two-level six-factor full factorial design. The central composite design, which consists of a two-level full factorial design with 2^k runs, where k is the number of factors, $2k$ axial runs, and n_c center runs, is the most commonly used approach to build second-order response surface models without a need to run a three-level full factorial experiment (Figure 7-1c). The central composite design method efficiently considers the effects of the first- (e.g., x_1, x_2, ..., x_n) and second-order terms (e.g., x_1^2, x_2^2, ..., x_n^2) on the response.

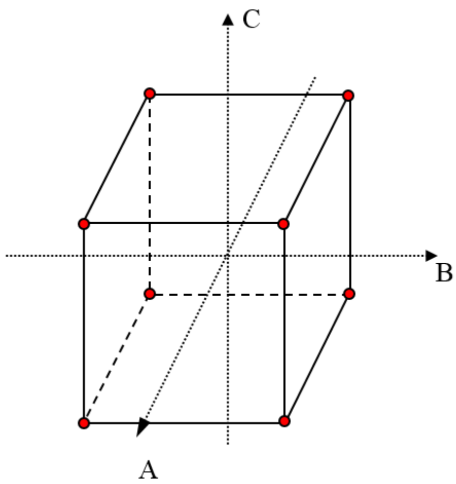

(a) Two level full factorial design

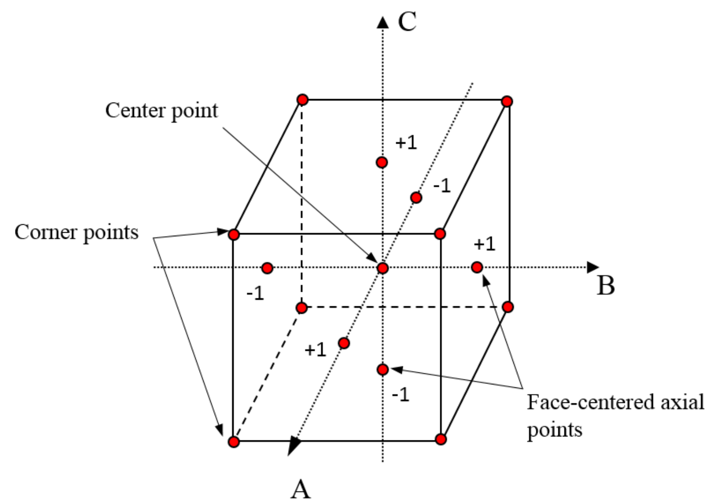

(b) Three level face-centered central composite design

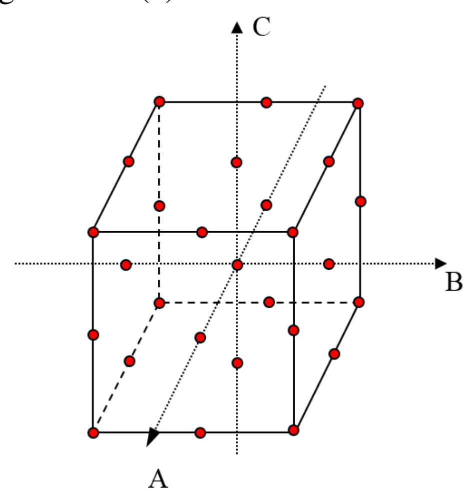

(c) Three level full factorial design

Figure 7-1 Three factor factorial design

7.3 Numerical Modeling of SC Walls

The general purpose finite element code LS-DYNA (2012a,2012b) was used to simulate the nonlinear response of 77 rectangular SC walls subjected to monotonic loading. Validation and benchmarking of the baseline model were presented in Chapter 6. The following subsections describe the modeling assumptions and the key analysis results.

7.3.1 Material Models

The smeared crack Winfrith model (MAT085) in LS-DYNA, developed by Broadhouse (1986), was used to model the infill concrete. Section 6.4.1 presents a detailed discussion on the properties of the Winfrith model. The material properties for the concrete compressive strengths input to the LS-DYNA model are presented in Table 7-2. Young's modulus for concrete was calculated using Equation 19.2.2.1(b) of ACI 318-14 (2014): $57000\sqrt{f_c'}$, where f_c' is the concrete compressive strength in units of psi. The tensile strength and fracture energy of the concrete were calculated per Sections 2.1.3.3.1 and 2.1.3.3.2 of [CEB-FIP (1993)], respectively, assuming an aggregate size of 0.75 in. for all concrete grades. The crack width was calculated as:

$$w = \frac{2G_f}{f_t} \tag{7-1}$$

where f_t is the nominal tensile strength of concrete, and G_f is the specific fracture energy: the energy required to propagate a tensile crack of unit area [CEB-FIP Model Code (1993)] that can be calculated as the area under the tensile stress-displacement curve [Wittmann et al. (1988)].

Table 7-2 Concrete material properties

Compressive strength level	Young's modulus (ksi)	Poisson's ratio	Uniaxial compressive strength (ksi)	Uniaxial tensile strength (ksi)	Crack width (in)	Agg. size (in)
Low	3605	0.20	4	0.40	0.002	0.75
Intermediate	4415	0.20	6	0.52	0.002	0.75
High	5100	0.20	8	0.64	0.002	0.75

The Piecewise-Linear-Plasticity model in LS-DYNA (MAT024) was used for the steel faceplates and connectors. Figure 7-2 presents the stress-strain relationships assumed for the ASTM A36, A588, A852 steels used for the steel faceplates. The nominal yield and ultimate strengths of the studs and tie rods were assumed to be 50 and 65 ksi, respectively, and not varied for the analysis. The material properties input to LS-DYNA for the different grades of steel are presented in Table 7-3.

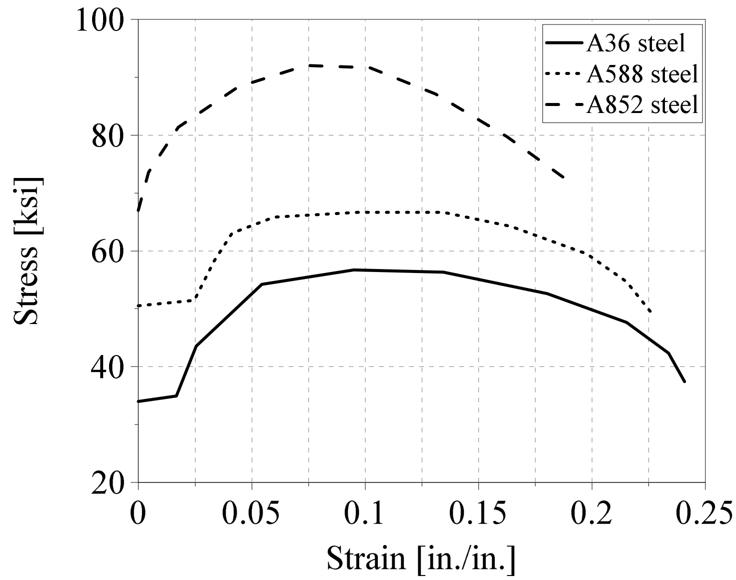

Figure 7-2 Stress-strain relationships for the steel material

Table 7-3 Steel material properties

Yield strength level	Young's modulus (ksi)	Poisson's ratio	Yield strength (ksi)	Ultimate strength (ksi)	Fracture strain (%)
Low	29000	0.30	34	57	24
Intermediate	29000	0.30	50.5	67	22
High	29000	0.30	67	92	19

7.3.2 Contact, Element, Loading, and Boundary Condition

The coefficient of friction between the steel faceplates and infill concrete was set equal to 0.57 based on Rabbat et al. (1985) and was not varied because the effect on response was known to be small.

The CONTACT-AUTOMATIC-SURFACE-TO-SURFACE formulation available in LS-DYNA (2012a) was used to model the friction between the infill concrete and the steel faceplates. The CONSTRAINED-LAGRANGE-IN-SOLID formulation available in LS-DYNA (2012a) was used to tie the studs and tie rods to the infill concrete elements.

The studs and tie rods were modeled using beam elements. The infill concrete and the steel faceplates were modeled using 1.0 × 1.0 × 1.0 in. eight-node solid elements and 1.0 × 1.0 in. four-node shell elements, respectively. The constant stress formulation [ELFORM=1 in LS-DYNA

(2012a)] and Belytschko-Tsay formulation are used for solid elements and shell elements, respectively. The cross-section integrated beam element [Hughes-Liu beam in LS-DYNA (2012a)] was used for the connectors. The LS-DYNA models of the low-, intermediate, and high-aspect ratio SC walls are presented in Figure 7-3. The length and the thickness of the walls were set to 60 in. and 12 in., respectively. The heights of the low-, intermediate- and high-aspect ratio SC walls were selected to achieve the desired aspect ratios of 0.5, 1.0, and 2.0, respectively. The 0.38-in. diameter of the studs and tie rods was based on the specifications proposed in AISC N690s1 (2014).

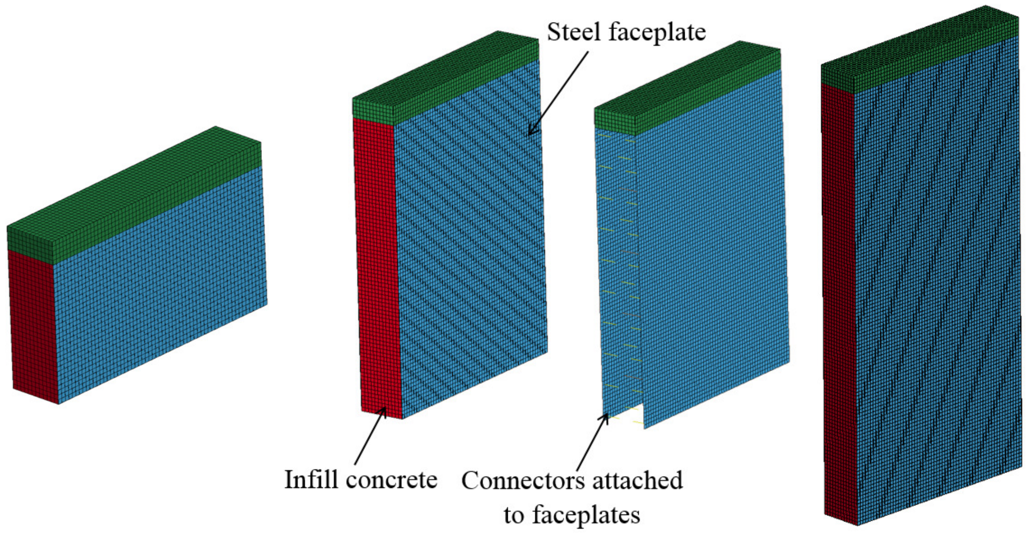

(a) Low-aspect ratio (b) Intermediate-aspect ratio (c) High-aspect ratio

Figure 7-3 LS-DYNA model of SC2

7.4 Analysis Results

Key analysis results are summarized in Table 7-4. The levels of the design variables for each run are listed in columns 2 to 7. Columns 8 to 10 present the shear force resisted by the infill concrete and the steel faceplates, and the pre-yield stiffness of the SC walls at the onset of the steel faceplate yielding. Columns 11 to 13 list the contributions of the infill concrete and the steel faceplates to the total peak shear strength and the post-yield stiffness of the SC walls. The pre-yield stiffness is the secant stiffness established at the force corresponding to the onset of the yielding of the steel faceplates. The post-yield stiffness is the slope of a line segment passing through the yield and reference points, where the reference point is established at the peak shear force and at a displacement calculated using an equal-energy-based tri-linear idealization of the LS-DYNA-predicted force-displacement relationship.

The shear force, V_{flex}, listed in column 14 of Table 7-4, is the shear force associated with the plastic moment of the SC wall cross-section estimated using the cross-section program XTRACT (2002). The calculations assumed perfect bond between the steel faceplates and the infill concrete, and nominal steel and concrete material properties. Column 15 lists the ratio of the LS-DYNA-predicted peak shear force, calculated as the sum of the shear force resisted by the infill concrete and the steel faceplates at the peak shear force, $V_c^p + V_s^p$, to the shear force associated with the plastic moment, V_{flex}. This ratio is greater than 1.0 for the low-, intermediate-, and high-aspect ratio SC walls indicating that SC wall piers will only be shear-critical if the aspect ratio is significantly less than 0.5.

Figure 7-4 presents the distribution of shear stress in the infill concrete of SC walls at peak shearing force, in units of ksi. Figure 7-4a, Figure 7-4b, and Figure 7-4c present analysis result for runs #1, #65, and #33 in Table 7-4: aspect ratios of 0.5, 1.0, and 2.0, respectively. As the aspect ratio increases, the depth to the neutral axis from the compression toe of the wall decreases. The inclined cracks in the tension zone of the low-aspect ratio SC wall indicate that there is a significant shear-flexure interaction in these walls. The behavior of the high-aspect ratio SC wall is dominated by flexure since the tensile cracks are horizontal.

Figure 7-5 presents the distributions of Von-Mises stress in the steel faceplates of the SC walls at peak shearing force, in units of ksi. Figure 7-5a, Figure 7-5b, and Figure 7-5c present analysis results for runs #1, #65, and #33 in Table 7-4. The yielded zones in the steel faceplates of the high-aspect ratio SC wall are concentrated in the bottom corners of the steel faceplates: flexure-controlled behavior. As the aspect ratio decreases, the yielded zone in the steel faceplates spreads across the web of the steel faceplates: shear-controlled behavior.

Table 7-4 LS-DYNA analysis results

Run	Factor levels						Data at yield point			Data at peak point			Cross-sectional analysis	
	AR	RR	SR	AL	SS	CS	V_c^y (kips)	V_s^y (kips)	K_y (kips /in)	V_c^p (kips)	V_s^p (kips)	K_p (kips /in)	V_{flex} (kips)	$\frac{V_c^p + V_s^p}{V_{flex}}$
(1)	(2)	(3)	(4)	(5)	(6)	(7)	(8)	(9)	(10)	(11)	(12)	(13)	(14)	(15)
1	-1	-1	-1	-1	-1	-1	217	51	17522	370	144	7751	360	1.43
2	-1	-1	-1	-1	-1	1	319	54	24328	500	141	10469	379	1.69
3	-1	-1	-1	-1	1	-1	349	145	10900	431	312	8999	644	1.15
4	-1	-1	-1	-1	1	1	478	133	15165	671	287	10940	707	1.36
5	-1	-1	-1	1	-1	-1	441	83	20724	570	180	12040	704	1.06
6	-1	-1	-1	1	-1	1	709	81	31240	1043	186	17738	1125	1.09
7	-1	-1	-1	1	1	-1	533	163	15367	574	363	11103	889	1.05
8	-1	-1	-1	1	1	1	907	143	26055	1009	358	17878	1331	1.03
9	-1	-1	1	-1	-1	-1	244	61	14992	362	136	5572	360	1.38
10	-1	-1	1	-1	-1	1	362	61	20854	490	108	3826	355	1.69
11	-1	-1	1	-1	1	-1	295	108	11415	421	301	5345	644	1.12
12	-1	-1	1	-1	1	1	436	108	15408	636	260	7544	707	1.27
13	-1	-1	1	1	-1	-1	476	91	18744	540	172	8158	704	1.01
14	-1	-1	1	1	-1	1	793	89	29120	988	175	9455	1125	1.03
15	-1	-1	1	1	1	-1	541	159	13921	509	353	5423	889	0.97
16	-1	-1	1	1	1	1	964	157	22302	989	291	9504	1331	0.96
17	-1	1	-1	-1	-1	-1	270	185	22392	495	455	13149	924	1.03
18	-1	1	-1	-1	-1	1	391	187	28490	787	424	13270	1020	1.19
19	-1	1	-1	-1	1	-1	388	364	18672	611	1012	10788	1567	1.04
20	-1	1	-1	-1	1	1	512	326	23742	921	930	14960	1740	1.06
21	-1	1	-1	1	-1	-1	459	278	24331	568	518	17717	1151	0.94
22	-1	1	-1	1	-1	1	765	274	34280	1020	514	20921	1586	0.97
23	-1	1	-1	1	1	-1	520	430	20983	624	1058	12254	1687	1.00
24	-1	1	-1	1	1	1	937	479	28156	1014	1077	14772	2065	1.01
25	-1	1	1	-1	-1	-1	303	216	20535	492	458	12073	924	1.03
26	-1	1	1	-1	-1	1	439	214	25813	741	432	12777	1020	1.15
27	-1	1	1	-1	1	-1	383	349	18162	571	993	11134	1567	1.00
28	-1	1	1	-1	1	1	546	346	22128	895	865	15881	1740	1.01
29	-1	1	1	1	-1	-1	465	264	24070	556	511	14862	1151	0.93
30	-1	1	1	1	-1	1	769	262	34021	1039	516	20377	1586	0.98
31	-1	1	1	1	1	-1	549	447	19796	568	1030	10800	1687	0.95
32	-1	1	1	1	1	1	949	445	27726	956	1034	16231	2065	0.96
33	1	-1	-1	-1	-1	-1	54	15	862	69	45	247	90	1.27
34	1	-1	-1	-1	-1	1	74	15	1260	87	40	242	89	1.43
35	1	-1	-1	-1	1	-1	56	41	540	125	92	323	161	1.35
36	1	-1	-1	-1	1	1	67	47	813	161	74	344	177	1.33
37	1	-1	-1	1	-1	-1	114	25	1110	149	56	463	176	1.17
38	1	-1	-1	1	-1	1	221	23	1546	289	55	591	281	1.22
39	1	-1	-1	1	1	-1	100	42	609	194	104	376	222	1.34
40	1	-1	-1	1	1	1	255	42	1276	319	108	488	333	1.28

Table 7-4 LS-DYNA analysis results (cont.)

Run	Factor levels						Data at yield point			Data at peak point			Cross-sectional analysis	
	AR	RR	SR	AL	SS	CS	V_c^y (kips)	V_s^y (kips)	K_y (kips /in)	V_c^p (kips)	V_s^p (kips)	K_p (kips /in)	V_{flex} (kips)	$\frac{V_c^p + V_s^p}{V_{flex}}$
(1)	(2)	(3)	(4)	(5)	(6)	(7)	(8)	(9)	(10)	(11)	(12)	(13)	(14)	(15)
41	1	-1	1	-1	-1	-1	53	21	688	62	53	195	90	1.28
42	1	-1	1	-1	-1	1	79	22	932	93	43	140	89	1.53
43	1	-1	1	-1	1	-1	39	50	487	104	97	267	161	1.25
44	1	-1	1	-1	1	1	53	57	620	132	92	263	177	1.27
45	1	-1	1	1	-1	-1	123	29	964	155	54	342	176	1.19
46	1	-1	1	1	-1	1	221	31	1415	286	53	434	281	1.21
47	1	-1	1	1	1	-1	125	54	755	151	123	293	222	1.23
48	1	-1	1	1	1	1	235	56	1133	289	117	482	333	1.22
49	1	1	-1	-1	-1	-1	71	57	1083	133	148	524	231	1.22
50	1	1	-1	-1	-1	1	97	57	1363	183	134	493	255	1.24
51	1	1	-1	-1	1	-1	98	111	914	195	309	536	392	1.29
52	1	1	-1	-1	1	1	117	110	1094	285	292	616	435	1.33
53	1	1	-1	1	-1	-1	122	75	1292	172	168	631	288	1.18
54	1	1	-1	1	-1	1	211	81	1740	325	156	756	396	1.21
55	1	1	-1	1	1	-1	143	137	1088	209	333	519	422	1.28
56	1	1	-1	1	1	1	242	144	1467	371	321	678	516	1.34
57	1	1	1	-1	-1	-1	55	65	936	95	169	440	231	1.14
58	1	1	1	-1	-1	1	72	74	1139	117	173	533	255	1.14
59	1	1	1	-1	1	-1	59	130	794	125	360	515	392	1.24
60	1	1	1	-1	1	1	58	148	903	177	365	571	435	1.25
61	1	1	1	1	-1	-1	108	89	1175	143	185	618	288	1.14
62	1	1	1	1	-1	1	203	97	1596	283	177	666	396	1.16
63	1	1	1	1	1	-1	107	166	967	122	403	509	422	1.24
64	1	1	1	1	1	1	216	173	1306	257	407	595	516	1.29
65	0	0	0	0	0	0	223	107	3565	325	260	1559	446	1.31
66	-1	0	0	0	0	0	560	226	20854	752	464	13740	1116	1.09
67	1	0	0	0	0	0	70	65	852	167	125	413	279	1.05
68	0	-1	0	0	0	0	228	53	3204	282	125	878	318	1.28
69	0	1	0	0	0	0	223	170	3824	399	356	1424	612	1.23
70	0	0	-1	0	0	0	226	110	3623	359	249	1416	446	1.36
71	0	0	1	0	0	0	224	115	3297	341	232	1102	446	1.29
72	0	0	0	-1	0	0	143	95	2879	269	218	914	373	1.30
73	0	0	0	1	0	0	304	123	3966	414	262	1666	540	1.25
74	0	0	0	0	-1	0	213	80	4033	295	179	1543	354	1.34
75	0	0	0	0	1	0	237	142	3221	368	375	1297	539	1.38
76	0	0	0	0	0	-1	167	107	2957	250	256	1371	387	1.31
77	0	0	0	0	0	1	279	114	4027	436	232	1251	500	1.34

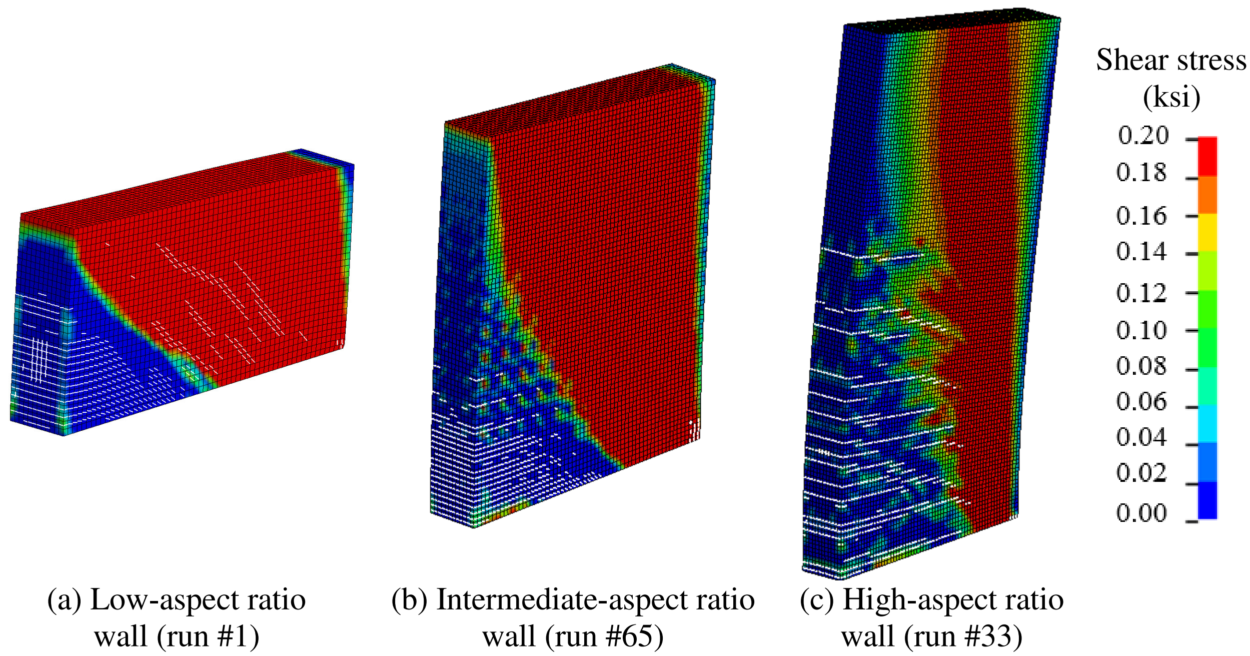

Figure 7-4 Shear stress distribution and cracking patterns in the infill concrete

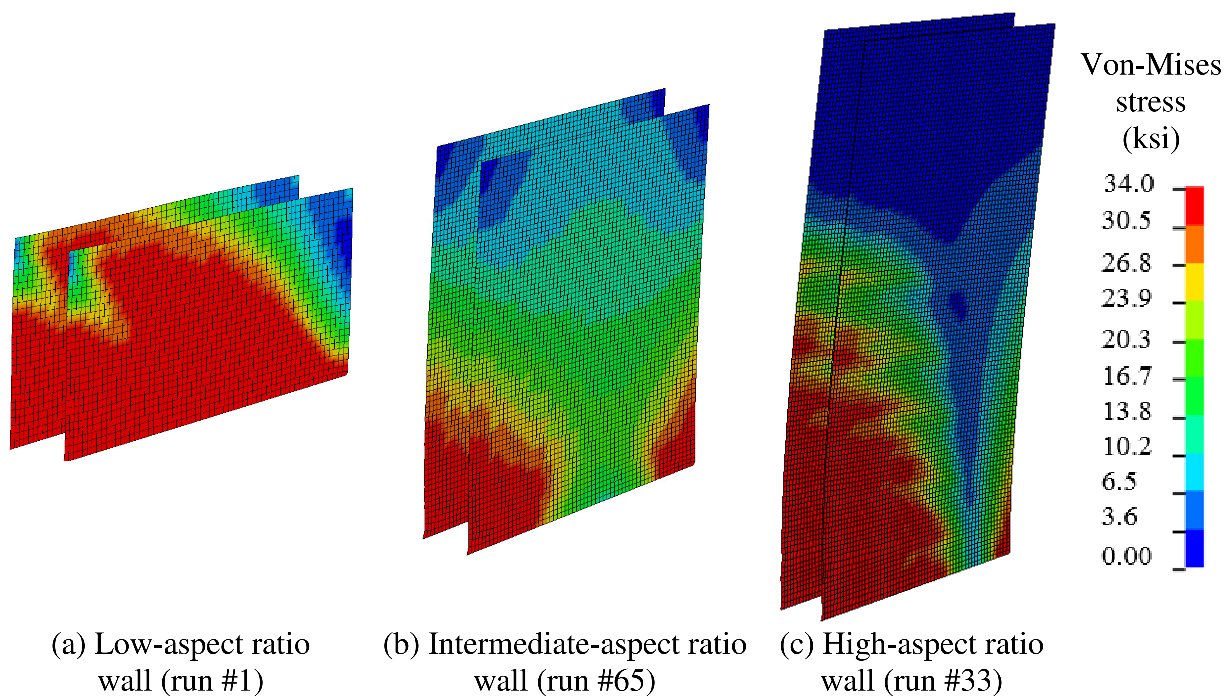

Figure 7-5 Von-Mises stress distribution in the steel faceplates of SC walls

7.5 Analysis of Variance

The Analysis of Variance (ANOVA) was conducted using the commercial software Minitab (2013). The results of the statistical analysis, including the main and interaction effects of the design variables on response, are presented in the following sections.

7.5.1 Main Effects

The average values of the response variables at the low and high levels of the design variables are presented in Figure 7-6. The plots identify the factors that have a significant effect on the response of SC walls: as the slope of the line increases, the main effect of the design variables increases [Montgomery (1982)].

Figure 7-6 shows that the aspect ratio (AR) has a significant effect on the yield and peak shear loads and on the pre- and post-yield lateral stiffness. The negative slope in these panels indicates that as the aspect ratio increases, the lateral strength and stiffness of SC walls decrease.

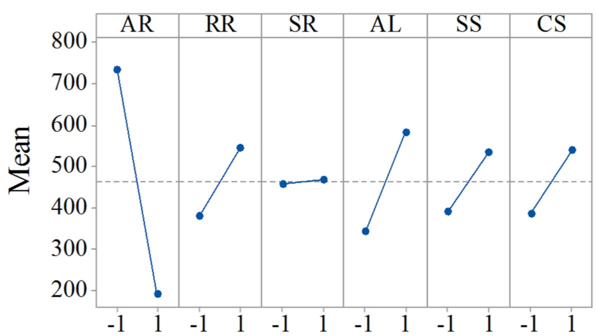

(a) V_y (kips)

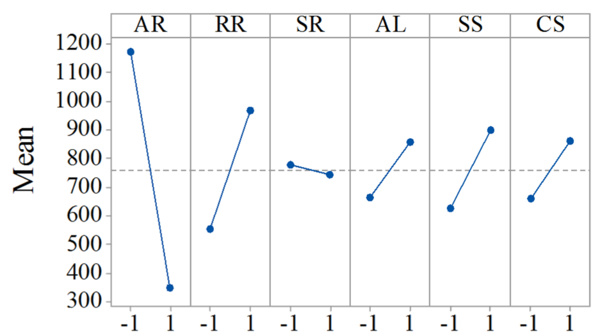

(b) V_p (kips)

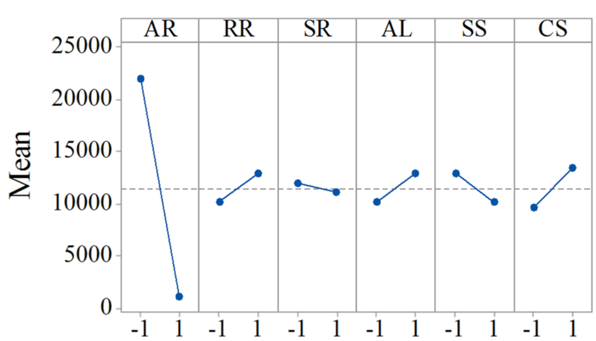

(c) K_y (kips/in)

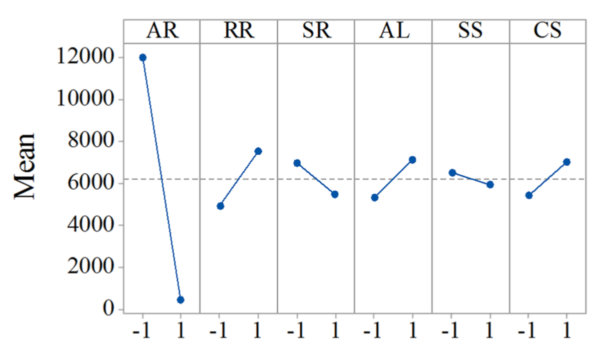

(d) K_p (kips/in)

Figure 7-6 Main effect plots of design variables

Figure 7-6 also indicates that reinforcement ratio (RR) has a greater effect on strength than stiffness because the slope of the RR line in the V_y and V_p plots is greater than in the K_y and K_p plots. The slenderness ratio (SR) has no effect on V_y but a small effect on V_p and K_y. The post-yield stiffness is affected by slenderness ratio: as the faceplate slenderness ratio increases, the post-yield stiffness decreases, which is an expected result because as the slenderness ratio increases, buckling of the steel faceplates and the onset of loss of stiffness occur earlier. Figure 7-6 also shows that the axial load ratio (AL), concrete compressive strength (CS), and steel yield strength (SS) have approximately the same effect on the yield and peak shear strengths of SC walls. However, an increase in the axial load and concrete compressive strength increase the pre- and post-yield stiffness but they decrease as the steel yield strength increases.

7.5.2 Interaction Effects

The interaction plots of the design variables for the response variable V_y are presented in Figure 7-7. The numbers in the second-to-last column are the values of V_y in kips. There is significant interaction between two variables if the effect of one variable on the response substantially changes for different values of another variable. Parallel lines in an interaction plot indicate that there is no interaction between the design variables. As the difference in the slopes of the lines increases, the degree of the interaction between the design variables increases [Montgomery (1982)]. The following paragraph explains how to interpret Figure 7-7 and Figure 7-8.

The panels in the first row of Figure 7-7 identify the significant interaction (i.e., different slopes of the solid and dashed lines) of aspect ratio (AR) and other design variables, except for slenderness ratio. The top left corner panel shows the interaction between aspect ratio and reinforcement ratio (RR). The solid and dashed lines present the change in the yield shear strength when the coded value of reinforcement ratio is changed from -1 to 1 for low and high aspect ratio SC walls, respectively. The greater slope of the solid line indicates that the reinforcement ratio affects the yield shear strength of low aspect ratio SC walls more than that of high aspect ratio walls. Indeed, an increase in the aspect ratio substantially decreases the effect of other design variables on the response of SC wall piers. The second row of panels in Figure 7-7 present the interaction between reinforcement ratio and other design variables. Except for the panel presenting the interaction between reinforcement ratio and steel strength (SS), the solid and dashed lines are parallel, indicating that reinforcement ratio does not interact with slenderness ratio, axial load, and concrete strength.

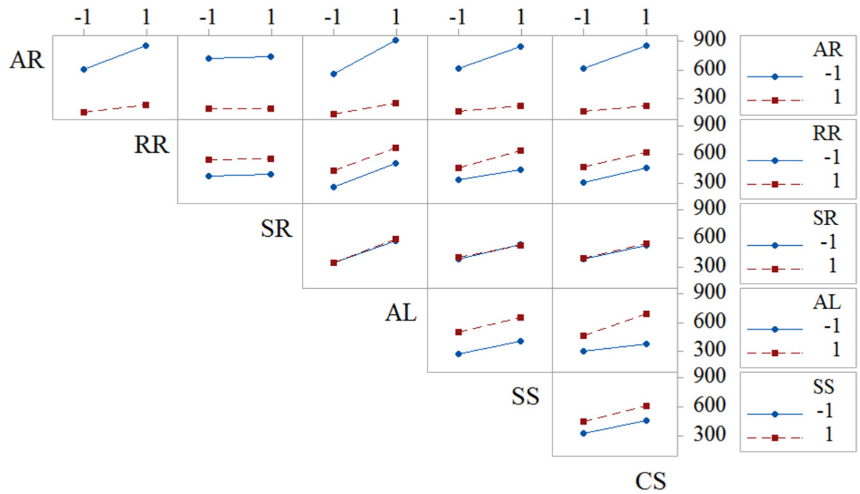

Figure 7-7 Interaction plots of design variables for V_y

Figure 7-8a, Figure 7-8b, and Figure 7-8c present the interaction plots for response variables V_p, K_y, and K_p, respectively.

7.6 Empirical Predictive Equations for the Monotonic Response of SC Wall Piers

The pre-peak-strength response of SC wall piers can be approximated by a tri-linear force-displacement relationship, as presented in Figure 7-9. Two stages of pre-peak response are assumed, namely, 1) pre- and 2) post-yielding of the steel faceplates.

The yield load, V_y, and the peak lateral strength, V_p, of a SC wall pier can be calculated as the sum of the factored strengths of the infill concrete, $A_c f_c'$, and the steel faceplates, $A_s f_y$, as follows:

$$V_y = \alpha_c^y A_c f_c' + \alpha_s^y A_s f_y \tag{7-2}$$

$$V_p = \alpha_c^p A_c f_c' + \alpha_s^p A_s f_y \tag{7-3}$$

where α_c^y, α_s^y, α_c^p, and α_s^p are factors that account for the design variables; A_c and A_s are the cross-sectional areas of the infill concrete and the steel faceplates, respectively; f_c' is the concrete compressive strength; and f_y is the yield strength of the steel faceplates.

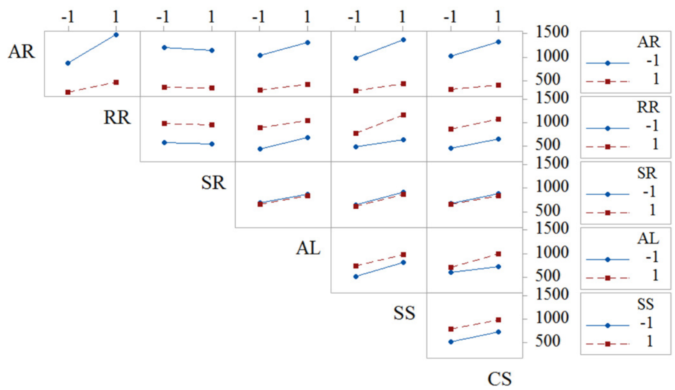

(a) V_p (kips)

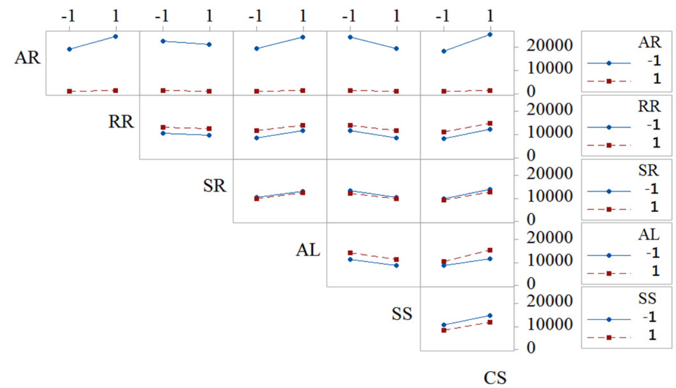

(b) K_y (kips / in)

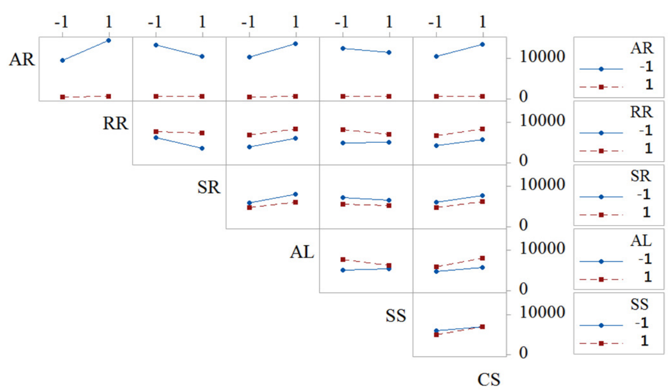

(c) K_p (kips / in)

Figure 7-8 Interaction plots of design variables

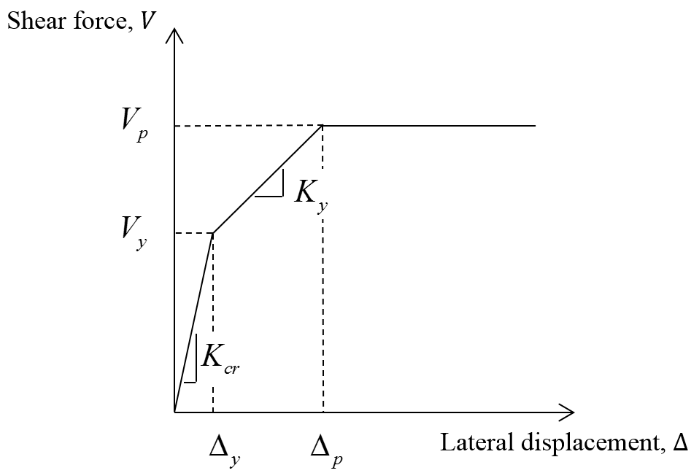

Figure 7-9 Tri-linear shear force-displacement relationship

The pre- and post-yield stiffness of an SC wall pier, in the absence of foundation flexibility, can be calculated as:

$$K_{cr} = \beta_y K_{el} \tag{7-4}$$

$$K_y = \beta_p K_{el} \tag{7-5}$$

where K_{el} is the theoretical initial stiffness of an SC wall and can be calculated as:

$$K_{el} = K_{el}^c + K_{el}^s = \frac{1}{\frac{1}{K_{fc}} + \frac{1}{K_{vc}}} + \frac{1}{\frac{1}{K_{fs}} + \frac{1}{K_{vs}}} \tag{7-6}$$

where K_{el}^c and K_{el}^s are the elastic stiffness of the infill concrete and the steel faceplates, respectively; K_{fc} and K_{vc} are the elastic flexural and shear stiffness of the infill concrete, respectively; and K_{fs} and K_{vs} are the elastic flexural and shear stiffness of the steel faceplates, respectively. The flexural and shear stiffness are calculated as:

$$K_{fc} = \frac{3E_c I_c}{h^3} \ , K_{fs} = \frac{3E_s I_s}{h^3} \tag{7-7}$$

$$K_{vc} = \frac{G_c A_c^{eff}}{h} \ , K_{vs} = \frac{G_s A_s^{eff}}{h} \tag{7-8}$$

where E_c and E_s are the elastic modulus of the concrete and steel, respectively; G_c and G_s are the shear modulus of the concrete and steel, respectively; I_c and I_s are the moment of inertia of the cross section of the infill concrete and the steel faceplates, respectively; A_c^{eff} and A_s^{eff} are the effective cross-sectional areas of the infill concrete and the steel faceplates, respectively, calculated as the total cross-sectional area divided by 1.2; and h is the height of the wall.

The results of the finite element analyses were used to develop empirical equations to calculate the strength and stiffness factors α_c^y, α_s^y, α_c^p, α_s^p, β_y, and β_p. The factors α_c^y and α_s^y were calculated as the LS-DYNA-predicted shear forces resisted by the infill concrete and steel faceplates, respectively, divided by the corresponding product of their compressive (yield) strengths and area. The factors α_c^p and α_s^p were calculated as the ratio of the contributions of the infill concrete and the steel faceplates to the peak shear strength, respectively, to the corresponding product of their compressive (yield) strengths and area. The factor β_y was calculated as the LS-DYNA-predicted normalized secant stiffness (i.e., secant stiffness divided by the theoretical initial stiffness) established at the force corresponding to the onset of the yielding of the steel faceplates. Factor β_p was estimated as the slope of a line segment passing through the yield and reference points of the LS-DYNA-predicted force-displacement relationship.

The calculated strength and stiffness factors were used as an input for the ANOVA. The results of the ANOVA for response factors α_s^y, α_c^y, β_y, α_c^p, α_s^p, and β_p are presented in Table 7-5 including the sum of squares, percentage contribution, mean squares, F- and P-values for each item of the full quadratic terms including linear, square, and 2-way interaction terms. The total sum of squares (SS) has N-1 degrees of freedom (DF), where N is the number of the analyses (=77). Considering full quadratic terms in the model, there are 27 terms with one degree of freedom for each term, where the degree of freedom for the main effect terms is the number of levels of the factor minus 1 and the degree of freedom of the interaction terms is calculated as the product of the degrees of freedom of the corresponding main effects. The percentage contribution, estimated as the ratio of the sum of squares for each term to the total sum of squares, shows the relative importance of each term used to predict the response variable. The mean squares calculated by dividing the sum of squares of each term to its corresponding degrees of freedom represents an estimate of the population variance. The F- and P-values in Table 7-5 represent the significance of each term on the response variable. The effects of the factors with a probability less than 5% (P-value less than 0.05) are considered to be significant on the response variable at the 95% confidence level. Table 7-5 indicates that all the design variables except the reinforcement ratio (RR), one square term AR^2, and a few of the interaction terms ($\mathrm{AR}\times\mathrm{SR}$, $\mathrm{AR}\times\mathrm{AL}$, $\mathrm{AR}\times\mathrm{SS}$, and $\mathrm{RR}\times\mathrm{SS}$) significantly affect α_s^y. The results presented in Table 7-5 help identify the terms with significant contributions (i.e., with a P-value less than 0.05) that need to be included in the regression model.

Table 7-5 ANOVA results

	Var.	DF	Response factor α_s^y					Response factor α_c^y				
			Seq SS	Contr.	MS	F-Val.	P-Val.	Seq SS	Contr.	MS	F-Val.	P-Val.
Linear	AR	1	0.2308	84.78%	0.2308	2584.5	0.00	0.1566	70.79%	0.1566	6548.7	0.00
	RR	1	0.0001	0.05%	0.0001	1.5	0.23	0.0005	0.22%	0.0005	20.0	0.00
	SR	1	0.0010	0.35%	0.0010	10.8	0.00	0.0000	0.00%	0.0000	0.1	0.76
	AL	1	0.0177	6.49%	0.0177	197.9	0.00	0.0346	15.63%	0.0346	1446.0	0.00
	SS	1	0.0007	0.26%	0.0007	7.9	0.01	0.0033	1.50%	0.0033	139.2	0.00
	CS	1	0.0000	0.00%	0.0000	0.0	0.91	0.0043	1.96%	0.0043	181.2	0.00
Square	AR^2	1	0.0065	2.38%	0.0019	20.8	0.00	0.0058	2.61%	0.0011	45.8	0.00
	RR^2	1	0.0000	0.00%	0.0000	0.1	0.82	0.0000	0.01%	0.0000	0.1	0.82
	SR^2	1	0.0000	0.00%	0.0000	0.0	0.94	0.0000	0.00%	0.0000	0.1	0.83
	AL^2	1	0.0000	0.00%	0.0000	0.1	0.75	0.0000	0.00%	0.0000	0.0	0.93
	SS^2	1	0.0000	0.00%	0.0000	0.0	0.83	0.0000	0.00%	0.0000	0.1	0.83
	CS^2	1	0.0000	0.00%	0.0000	0.0	0.92	0.0000	0.00%	0.0000	0.3	0.58
2-Way Interaction	AR×RR	1	0.0000	0.01%	0.0000	0.4	0.52	0.0002	0.08%	0.0002	7.4	0.01
	AR×SR	1	0.0004	0.16%	0.0004	5.0	0.03	0.0002	0.11%	0.0002	10.4	0.00
	AR×AL	1	0.0064	2.36%	0.0064	72.0	0.00	0.0086	3.89%	0.0086	360.2	0.00
	AR×SS	1	0.0009	0.35%	0.0009	10.6	0.00	0.0028	1.25%	0.0028	116.0	0.00
	AR×CS	1	0.0002	0.06%	0.0002	1.7	0.19	0.0022	0.99%	0.0022	91.5	0.00
	RR×SR	1	0.0000	0.00%	0.0000	0.1	0.79	0.0000	0.02%	0.0000	1.6	0.22
	RR×AL	1	0.0000	0.00%	0.0000	0.1	0.83	0.0004	0.20%	0.0004	18.7	0.00
	RR×SS	1	0.0011	0.40%	0.0011	12.3	0.00	0.0000	0.01%	0.0000	0.5	0.47
	RR×CS	1	0.0001	0.02%	0.0001	0.6	0.46	0.0001	0.02%	0.0001	2.2	0.15
	SR×AL	1	0.0000	0.00%	0.0000	0.1	0.77	0.0001	0.03%	0.0001	2.9	0.10
	SR×SS	1	0.0005	0.18%	0.0005	5.6	0.02	0.0001	0.06%	0.0001	5.8	0.02
	SR×CS	1	0.0000	0.02%	0.0000	0.6	0.46	0.0000	0.00%	0.0000	0.3	0.62
	AL×SS	1	0.0013	0.49%	0.0013	14.8	0.00	0.0000	0.01%	0.0000	0.7	0.40
	AL×CS	1	0.0000	0.00%	0.0000	0.0	0.87	0.0001	0.06%	0.0001	5.1	0.03
	SS×CS	1	0.0000	0.00%	0.0000	0.1	0.81	0.0000	0.01%	0.0000	0.6	0.46
Model		27	0.2678	98.39%	0.0099	111.1	0.00	0.2201	99.47%	0.0082	340.8	0.00
Error		49	0.0044	1.61%				0.0012	0.53%			
Total		76	0.2722	100.00%				0.2212	100.00%			

Table 7-5 ANOVA results (cont.)

	Var.	DF	Response factor α_s^p					Response factor α_c^p				
			Seq SS	Contr.	MS	F-Val.	P-Val.	Seq SS	Contr.	MS	F-Val.	P-Val.
Linear	AR	1	1.1472	91.37%	1.1472	5947.8	0.00	0.2403	82.46%	0.2403	5082.8	0.00
	RR	1	0.0037	0.29%	0.0037	19.1	0.00	0.0051	1.75%	0.0051	107.6	0.00
	SR	1	0.0001	0.01%	0.0001	0.6	0.43	0.0013	0.43%	0.0013	26.7	0.00
	AL	1	0.0323	2.58%	0.0323	167.7	0.00	0.0169	5.80%	0.0169	357.2	0.00
	SS	1	0.0026	0.21%	0.0026	13.4	0.00	0.0020	0.70%	0.0020	43.0	0.00
	CS	1	0.0033	0.26%	0.0033	17.0	0.00	0.0061	2.08%	0.0061	128.1	0.00
Square	AR^2	1	0.0302	2.41%	0.0042	21.5	0.00	0.0059	2.01%	0.0017	35.7	0.00
	RR^2	1	0.0002	0.02%	0.0000	0.0	0.99	0.0000	0.00%	0.0000	0.1	0.82
	SR^2	1	0.0001	0.00%	0.0000	0.1	0.79	0.0000	0.00%	0.0000	0.1	0.79
	AL^2	1	0.0000	0.00%	0.0000	0.2	0.70	0.0000	0.00%	0.0000	0.0	0.86
	SS^2	1	0.0015	0.12%	0.0015	7.7	0.01	0.0000	0.01%	0.0000	0.5	0.50
	CS^2	1	0.0000	0.00%	0.0000	0.0	1.00	0.0000	0.00%	0.0000	0.1	0.74
2-Way Interaction	AR×RR	1	0.0000	0.00%	0.0000	0.0	0.91	0.0015	0.50%	0.0015	30.7	0.00
	AR×SR	1	0.0061	0.49%	0.0061	31.6	0.00	0.0000	0.01%	0.0000	0.8	0.37
	AR×AL	1	0.0096	0.76%	0.0096	49.7	0.00	0.0018	0.63%	0.0018	38.9	0.00
	AR×SS	1	0.0005	0.04%	0.0005	2.4	0.13	0.0001	0.02%	0.0001	1.4	0.24
	AR×CS	1	0.0009	0.07%	0.0009	4.4	0.04	0.0020	0.69%	0.0020	42.6	0.00
	RR×SR	1	0.0019	0.15%	0.0019	9.6	0.00	0.0002	0.06%	0.0002	3.4	0.07
	RR×AL	1	0.0026	0.20%	0.0026	13.3	0.00	0.0032	1.09%	0.0032	67.0	0.00
	RR×SS	1	0.0004	0.03%	0.0004	1.9	0.18	0.0000	0.01%	0.0000	0.5	0.47
	RR×CS	1	0.0003	0.02%	0.0003	1.4	0.24	0.0001	0.03%	0.0001	1.6	0.21
	SR×AL	1	0.0000	0.00%	0.0000	0.1	0.77	0.0000	0.01%	0.0000	0.5	0.47
	SR×SS	1	0.0000	0.00%	0.0000	0.0	0.88	0.0003	0.10%	0.0003	5.9	0.02
	SR×CS	1	0.0003	0.03%	0.0003	1.7	0.20	0.0001	0.03%	0.0001	1.7	0.21
	AL×SS	1	0.0008	0.07%	0.0008	4.3	0.04	0.0015	0.50%	0.0015	30.9	0.00
	AL×CS	1	0.0013	0.11%	0.0013	6.9	0.01	0.0008	0.28%	0.0008	17.3	0.00
	SS×CS	1	0.0002	0.02%	0.0002	1.2	0.28	0.0001	0.02%	0.0001	1.5	0.23
Model		27	1.2461	99.25%	0.0462	239.3	0.00	27	0.2891	99.21%	0.2891	226.5
Error		49	0.0095	0.75%				49	0.0023	0.79%		
Total		76	1.2555	100.00%				76	0.2914	100.00%		

Table 7-5 ANOVA results (cont.)

	Var.	DF	Response factor β_y					Response factor β_p				
			Seq SS	Contr.	MS	F-Val.	P-Val.	Seq SS	Contr.	MS	F-Val.	P-Val.
Linear	AR	1	0.0065	0.63%	0.0065	7.5	0.01	0.0560	9.84%	0.0560	63.9	0.00
	RR	1	0.0235	2.29%	0.0235	27.3	0.00	0.1132	19.90%	0.1132	129.4	0.00
	SR	1	0.0576	5.62%	0.0576	66.8	0.00	0.0589	10.35%	0.0589	67.2	0.00
	AL	1	0.4016	39.18%	0.4016	466.3	0.00	0.1228	21.58%	0.1228	140.3	0.00
	SS	1	0.3730	36.39%	0.3730	433.2	0.00	0.0035	0.61%	0.0035	4.0	0.05
	CS	1	0.0123	1.20%	0.0123	14.3	0.00	0.0085	1.49%	0.0085	9.7	0.00
Square	AR^2	1	0.0001	0.01%	0.0071	8.3	0.01	0.0469	8.24%	0.0155	17.7	0.00
	RR^2	1	0.0061	0.60%	0.0006	0.7	0.42	0.0017	0.30%	0.0020	2.3	0.14
	SR^2	1	0.0014	0.14%	0.0001	0.1	0.74	0.0000	0.00%	0.0002	0.2	0.67
	AL^2	1	0.0004	0.04%	0.0000	0.0	1.00	0.0000	0.01%	0.0000	0.0	0.87
	SS^2	1	0.0035	0.34%	0.0028	3.3	0.08	0.0010	0.18%	0.0008	1.0	0.34
	CS^2	1	0.0008	0.07%	0.0008	0.9	0.36	0.0002	0.03%	0.0002	0.2	0.64
2-Way Interaction	AR×RR	1	0.0005	0.05%	0.0005	0.6	0.46	0.0002	0.03%	0.0002	0.2	0.64
	AR×SR	1	0.0059	0.58%	0.0059	6.9	0.01	0.0087	1.53%	0.0087	9.9	0.00
	AR×AL	1	0.0082	0.80%	0.0082	9.5	0.00	0.0005	0.09%	0.0005	0.6	0.45
	AR×SS	1	0.0019	0.19%	0.0019	2.2	0.14	0.0038	0.67%	0.0038	4.4	0.04
	AR×CS	1	0.0002	0.02%	0.0002	0.2	0.65	0.0029	0.51%	0.0029	3.3	0.07
	RR×SR	1	0.0004	0.04%	0.0004	0.5	0.48	0.0292	5.13%	0.0292	33.3	0.00
	RR×AL	1	0.0126	1.23%	0.0126	14.6	0.00	0.0098	1.72%	0.0098	11.2	0.00
	RR×SS	1	0.0244	2.38%	0.0244	28.3	0.00	0.0073	1.28%	0.0073	8.3	0.01
	RR×CS	1	0.0091	0.89%	0.0091	10.5	0.00	0.0003	0.06%	0.0003	0.4	0.54
	SR×AL	1	0.0021	0.20%	0.0021	2.4	0.13	0.0036	0.63%	0.0036	4.1	0.05
	SR×SS	1	0.0058	0.57%	0.0058	6.8	0.01	0.0010	0.17%	0.0010	1.1	0.30
	SR×CS	1	0.0018	0.18%	0.0018	2.1	0.15	0.0001	0.01%	0.0001	0.1	0.78
	AL×SS	1	0.0005	0.05%	0.0005	0.6	0.45	0.0340	5.97%	0.0340	38.8	0.00
	AL×CS	1	0.0225	2.19%	0.0225	26.1	0.00	0.0061	1.07%	0.0061	7.0	0.01
	SS×CS	1	0.0002	0.02%	0.0002	0.2	0.64	0.0060	1.05%	0.0060	6.8	0.01
Model		27	27	0.9828	95.88%	0.9828	42.3	27	0.5260	92.46%	0.5260	22.3
Error		49	49	0.0422	4.12%			49	0.0429	7.54%		
Total		76	76	1.0250	100.00%			76	0.5689	100.00%		

Table 7-6 lists the coefficients of the linear, square, and interaction terms of the regression equations for the response factors α_c^y, α_s^y, α_c^p, α_s^p, β_y, and β_p. The coefficient of each term estimates the change in the mean response per unit increase in that term when all other terms are held constant [Montgomery (1982)]. The regression equations also include a constant. The proposed equations are valid for the range of design variables presented in Table 7-1. Each term in Table 7-1 is a coded parameter ranging between -1 and 1. The relationship between the coded and actual terms is:

$$y_c = 2(\frac{y_a - A}{B - A}) - 1 \quad (7\text{-}9)$$

where y_c and y_a are the coded and actual values of the variable, respectively, and A and B are the actual lower and upper limits on the variable, respectively.

Section 7.10 includes the calculation of the monotonic response of a SC wall sample using the proposed strength and stiffness equations and coefficients of Table 7-6.

7.7 Adequacy of the Regression Models

In an analysis of variance, the regression model is developed assuming that the errors are normally and independently distributed with a mean of zero. The validity of this assumption and the model adequacy can be investigated by examining the residuals, where the residual is defined as the difference between the measured and model-predicted value of the response variable. The regression model is adequate if the residuals are structureless and normally distributed [Montgomery (1982)].

The normal probability of the residuals and the LS-DYNA-predicted response variables versus residuals are presented in Figure 7-10. The residuals of the response variables, presented in the left panels of Figure 7-10, are linear, indicating that the distribution of the residuals is normal. The plots of residuals versus response variables presented in the right panels of Figure 7-10 investigate the independence assumption in the analysis of variance. As seen in Figure 7-10, the plots of the residuals versus the response variables are random and structureless, indicating that the assumption of independence is valid.

Table 7-6 Coefficients of the regression models for the response variables

α_s^y		α_c^y		α_s^p		α_c^p		β_y		β_p	
Term	Coeff.	Term	Coeff.	Term	Coeff.	Term	Coeff.	Term	Coeff.	Term	Coeff.
Cons.	0.0914	Cons.	0.0522	Cons.	0.2018	Cons.	0.0790	Cons.	0.5909	Cons.	0.2215
AR	-0.0591	AR	-0.0487	AR	-0.1318	AR	-0.0603	AR	0.0099	AR	-0.0291
RR	0.0014	RR	0.0027	RR	0.0075	RR	0.0088	RR	0.0189	RR	0.0414
SR	0.0038	SR	0.0002	SR	-0.0014	SR	-0.0044	SR	-0.0295	SR	-0.0299
AL	0.0164	AL	0.0229	AL	0.0221	AL	0.0160	AL	0.0780	AL	0.0431
SS	-0.0033	SS	0.0071	SS	0.0063	SS	0.0055	SS	-0.0752	SS	-0.0073
AR^2	0.0262	CS	-0.0081	CS	-0.0071	CS	-0.0096	CS	0.0137	CS	-0.0113
AR×SR	0.0026	AR^2	0.0248	AR^2	0.0391	AR^2	0.0249	AR^2	0.0037	AR^2	0.0705
AR×AL	-0.0100	AR×RR	-0.0017	SS^2	0.0223	AR×RR	-0.0048	AR×SR	-0.0096	AR×SR	0.0117
AR×SS	0.0038	AR×SR	-0.0020	AR×SR	0.0098	AR×AL	-0.0054	AR×AL	0.0113	AR×SS	0.0077
RR×SS	-0.0042	AR×AL	-0.0116	AR×AL	-0.0122	AR×CS	0.0056	RR×AL	-0.0140	RR×SR	0.0214
SR×SS	-0.0028	AR×SS	-0.0066	AR×CS	0.0037	RR×AL	-0.0070	RR×SS	0.0195	RR×AL	-0.0124
AL×SS	-0.0046	AR×CS	0.0058	RR×SR	0.0054	SR×SS	-0.0021	RR×CS	-0.0119	RR×SS	-0.0107
		RR×AL	-0.0026	RR×AL	-0.0063	AL×SS	-0.0048	SR×SS	0.0095	SR×AL	-0.0075
		SR×SS	-0.0015	AL×SS	-0.0036	AL×CS	0.0036	AL×CS	0.0187	AL×SS	-0.0230
		AL×CS	0.0014	AL×CS	0.0046					AL×CS	0.0098
										SS×CS	0.0097

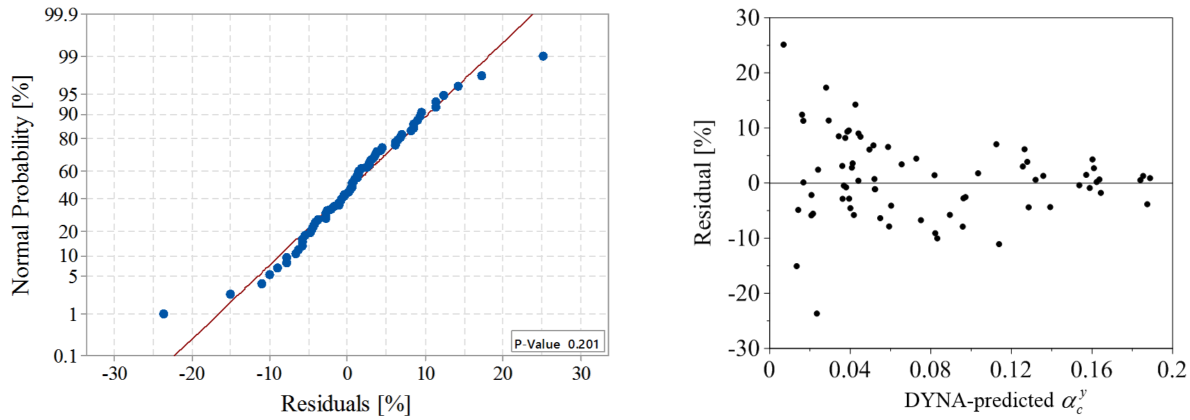

(a) Response factor α_c^y

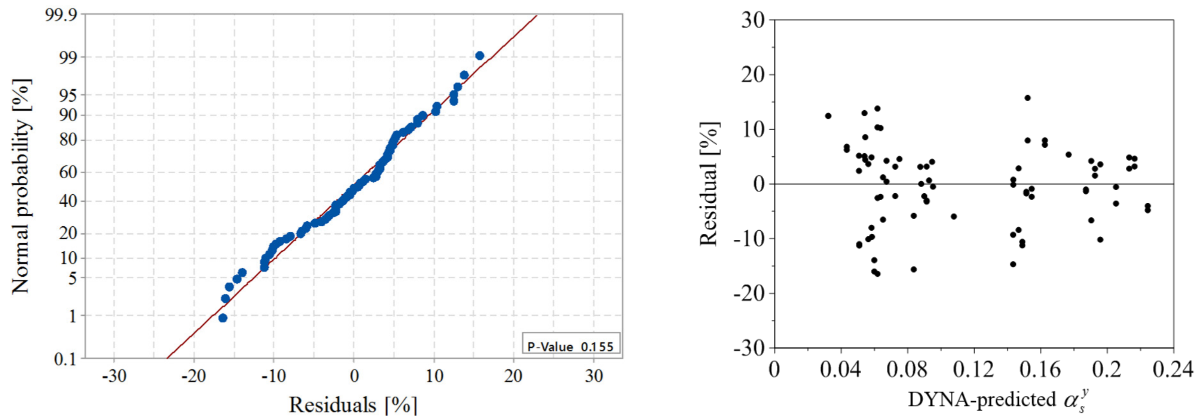

(b) Response factor α_s^y

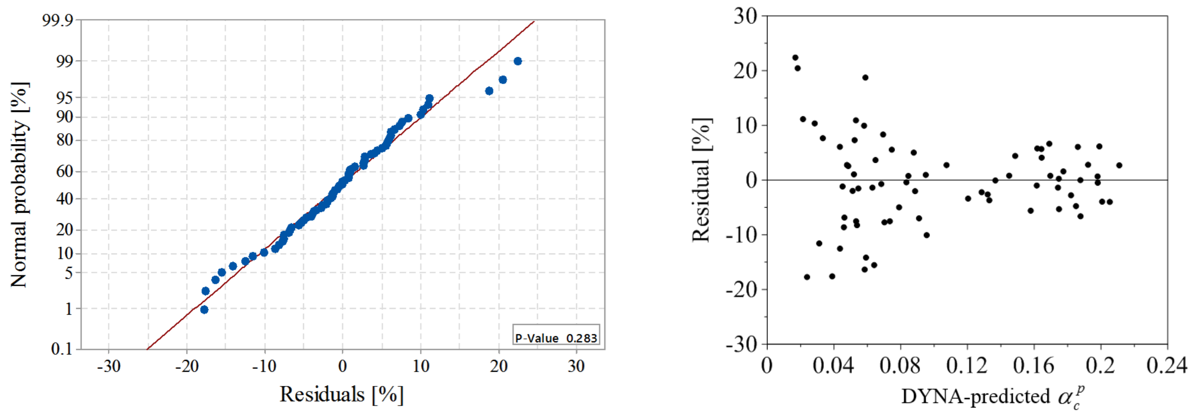

(c) Response factor α_c^p

Figure 7-10 Plots of normal probability versus residual (left) and residual versus LS-DYNA-predicted response variable (right)

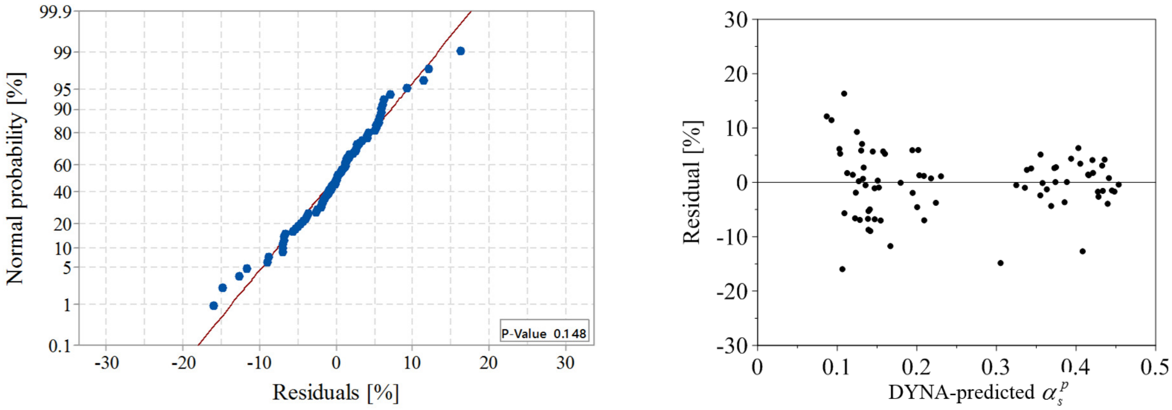

(d) Response factor α_s^p

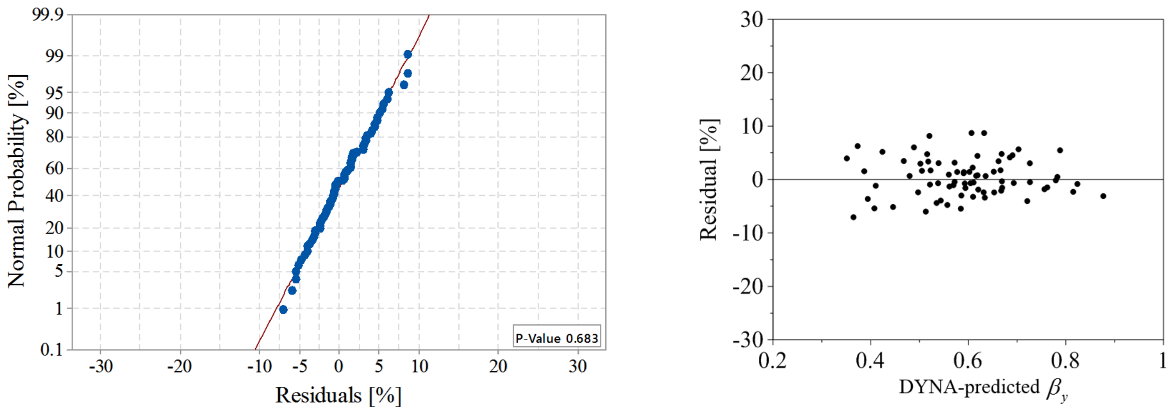

(e) Response factor β_y

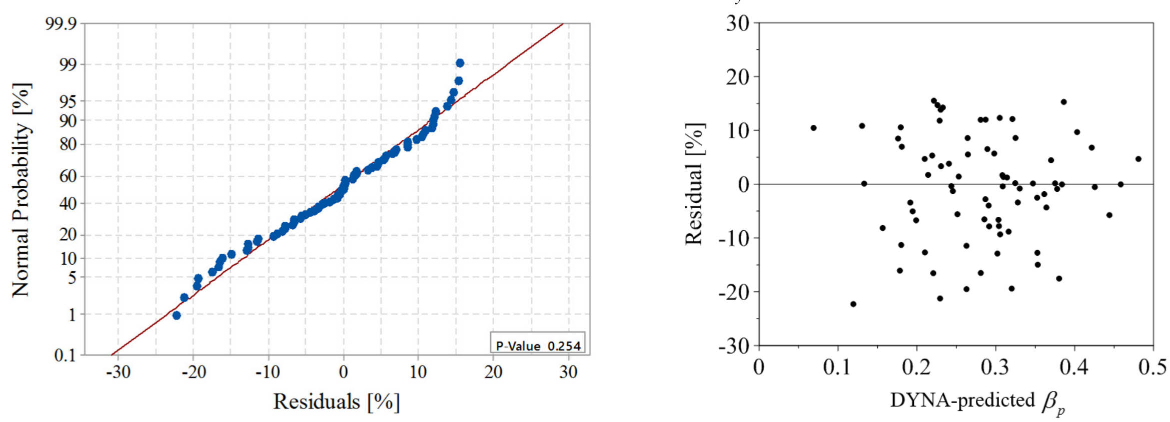

(f) Response factor β_p

Figure 7-10 Plots of normal probability versus residual (left) and residual versus LS-DYNA-predicted response variable (right), cont.

7.8 Validation of the Predictive Empirical Equations

Results of the in-plane shear response of SC walls tested by Chen (2016) were used to validate the proposed predictive equations. Data from the tests of SC walls at the University at Buffalo were not used for this validation study because they were used to validate the LS-DYNA model.

Chen (2016) tested four low-aspect ratio SC (SC1 through SC4) walls under displacement-controlled cyclic loading. The aspect ratio (height-to-length) of the four walls was 0.5. The height and the length of the wall specimens were 48 in. and 78 in., respectively. The distance between the wall base and the center line of the loading plates was 39 in. The steel faceplates were embedded into the foundation block using shear studs attached to the inside of the steel plates. Holes in the steel faceplates enabled the placement of transverse reinforcement in the foundation block.

The total wall thickness was 11.4 in. for SC1 and SC2 and 7.8 in. for SC3 and SC4. The faceplates were 0.18-in. thick, resulting in reinforcement ratios, ρ, of 3.1% and 4.5% for SC1/SC2 and SC3/SC4, respectively. The diameter of the studs and tie rods was 0.52 in. Studs and tie rods were used in SC1 and SC3 but only tie rods were used in SC2 and SC4. The studs were spaced 3 in. on center in SC1 and SC3. Tie rods were spaced at 6 in. in all four SC walls. A photograph of SC1 is presented in Figure 7-11. More information about the material properties, test setup, loading protocol, and instrumentation are reported in Chen (2016).

The in-plane monotonic response of the SC wall piers was also calculated based on the specifications of Appendix N9 to AISC N690s1 (2014), which assumes response in pure shear and does not consider wall aspect ratio, slenderness ratio, and axial load.

Figure 7-12 presents the predicted monotonic response of the Chen's walls by AISC N690s1 (dashed black line) and the predictive equations of this report (dotted blue line) together with the measured cyclic force-displacement relationship (solid gray line).

Figure 7-11 SC1 specimen before the test [Chen (2016)]

Although the predictive equations proposed here for response under monotonic loading slightly overestimate the cyclic response of the SC walls tested by Chen (2016), a good agreement between the test and analytical results confirms the utility of the proposed equations. The peak shear strength is overestimated by the equation in AISC N690s1 developed by Varma and his co-workers at Purdue University for shear-critical walls typical of labyrinthine nuclear power plants. The ASIC-predicted shear strengths for SC3 and SC4 were not reported in Figure 7-12c and Figure 7-12d because the shear strength equation, $(1.11-5.16\bar{\rho})A_s f_y$, results in negative strengths for these walls ($\bar{\rho}=0.24$ and $V_n=-0.13A_s f_y$ for SC3 and SC4).

7.9 Effective Lateral Stiffness of SC Wall Piers

Building codes and standards of practice recommend reductions in the flexural and shear rigidities of uncracked reinforced concrete shear walls for estimation of effective stiffness for the propose of static and dynamic analysis. For example, ASCE 41-13 (2013) recommends a reduction of 50% in the flexural rigidity and no reduction in the shear rigidity for *cracked* reinforced concrete shear walls. There are no comparable recommendations for SC wall piers. The results of the analysis of 77 SC walls were used to estimate reduction factors for shear and flexural rigidities as a function of the design variables considered in this study.

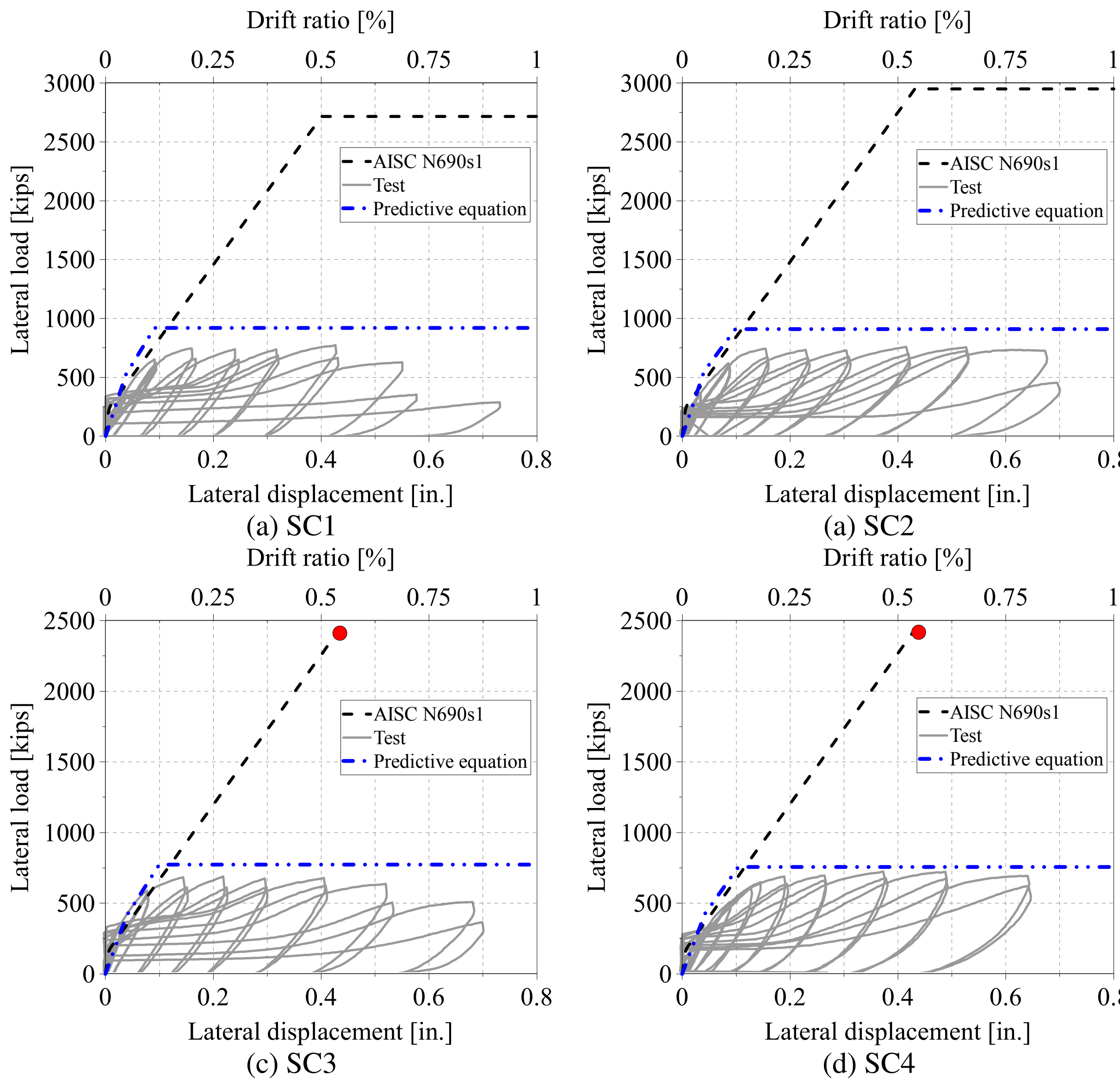

Figure 7-12 Predicted and measured response of SC walls

The effective flexural and shear rigidities of a SC wall pier can be calculated as:

$$EI_{eff} = \eta_f (E_c I_c + E_s I_s) \tag{7-10}$$

$$GA_{eff} = \eta_v (G_c A_c^{eff} + G_s A_s^{eff}) \tag{7-11}$$

where η_f and η_v are the flexure and shear stiffness reduction factors and can be calculated as:

$$\eta_f = \frac{K_f^{DYNA}}{K_{fc} + K_{fs}},\ \eta_v = \frac{K_v^{DYNA}}{K_{vc} + K_{vs}} \tag{7-12}$$

where K_f^{DYNA} and K_v^{DYNA} are the DYNA-predicted secant flexure and shear stiffnesses at the yield point, respectively, and calculated by dividing the DYNA-predicted yield force to the shear and flexural displacements, respectively: similar to the calculation of K_{cr} in Figure 7-9.

The flexural displacement at the top of the SC wall, Δ_f, was calculated as:

$$\Delta_f = \zeta\theta H \tag{7-13}$$

where θ is the rotation at top of the wall, H is the height of the wall, ζ is the distance between the top of the wall and centroid of the curvature diagram, and θ and ζ can be calculated as:

$$\theta = \frac{\Delta_{v1} - \Delta_{v2}}{L} \tag{7-14}$$

$$\zeta = \frac{\int_{y=0}^{y=h} y\Phi(y)dy}{h\int_{y=0}^{y=h} \Phi(y)dy} \tag{7-15}$$

where Δ_{v1} and Δ_{v2} are the vertical displacements on the tension and compression faces at the top of the wall, respectively, L is the length of the wall, and $\Phi(y)$ is the curvature of the wall section at a distance y from the top of the wall.

Each wall was discretized into sub-elements along its height to calculate the flexural displacement. The curvature in the ith sub-element was calculated as:

$$\Phi_i = \frac{\delta_{v1}^i - \delta_{v2}^i}{Lh_{sub}^i} \tag{7-16}$$

where δ_{v1}^i and δ_{v2}^i are the relative vertical displacements on the tension and compression faces of the ith sub-element over its height, h_{sub}^i, respectively. The distance ζ was calculated as:

$$\zeta = \frac{\sum_{k=1}^{m} \Phi_k (k-1/2)}{m\sum_{k=1}^{m} \Phi_k} \tag{7-17}$$

where m is the number of sub-elements along the height of the wall. The height of each sub-element was set to 1 in for these calculations.

The shear displacement, Δ_v, was calculated as the difference between the total lateral displacement and the flexural displacement. The values of ζ, the ratio of the shear and flexure displacements to the yield displacement, yield displacement, and flexure and shear stiffness reduction factors are reported in Table 7-7.

The ratio of Δ_f / Δ_y varies between 0.37 and 0.47 with an average of 0.41 for low aspect ratio SC walls ($H/L = 0.5$) and between 0.88 and 0.94 with an average of 0.91 for the high aspect ratio SC walls ($H/L = 2.0$). The distance between the top of the wall and the centroid of the curvature diagram, ζ, varies between 0.7 and 0.91, with an average of 0.8.

Based on these results, an estimation of the flexural displacement at any drift ratio in a SC panel can be estimated as:

$$\Delta_f = 0.8(\Delta_{v1} - \Delta_{v2})\frac{H}{L} \tag{7-18}$$

where Δ_{v1} and Δ_{v2} are the vertical displacements at the tension and compression toes at the top of the wall, at given drift ratio.

Table 7-7 indicates that the flexure and shear stiffness reduction factors are affected by design variables. The main effect plots of Figure 7-13 shows that the flexure stiffness reduction factor is significantly affected by all design variables. The effects of slenderness ratio and concrete strength on the shear stiffness reduction factor is negligible but the impact of other design variables is significant.

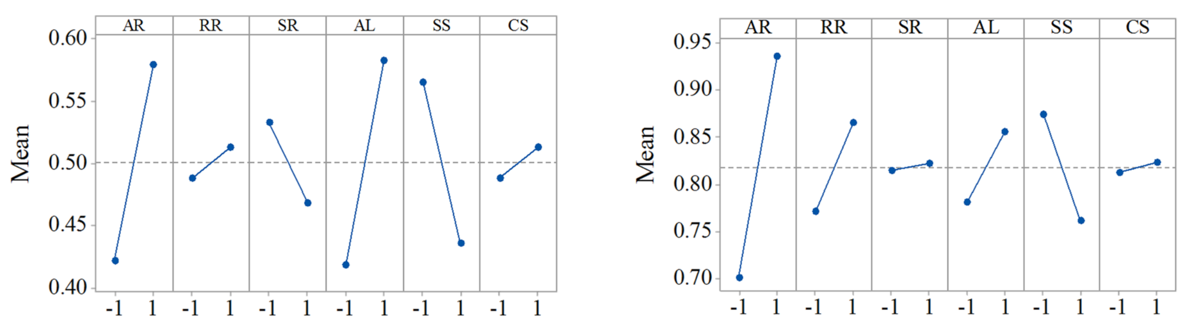

(a) η_f (b) η_v

Figure 7-13 Main effect plots of design variables

Table 7-7 Effective stiffness calculation

Run	ζ	Δ_f/Δ_y	Δ_v/Δ_y	Δ_y	η_f	η_v	Run	ζ	Δ_f/Δ_y	Δ_v/Δ_y	Δ_y	η_f	η_v
1	0.83	42%	58%	0.015	0.43	0.74	40	0.73	90%	10%	0.233	0.68	0.91
2	0.82	43%	57%	0.015	0.43	0.76	41	0.76	92%	8%	0.108	0.49	0.87
3	0.77	39%	61%	0.045	0.28	0.44	42	0.76	92%	8%	0.108	0.48	0.84
4	0.78	42%	58%	0.040	0.27	0.47	43	0.79	94%	6%	0.183	0.34	0.76
5	0.82	38%	62%	0.025	0.56	0.82	44	0.80	94%	6%	0.178	0.32	0.70
6	0.80	38%	62%	0.025	0.62	0.90	45	0.73	90%	10%	0.158	0.70	0.94
7	0.86	37%	63%	0.045	0.42	0.60	46	0.71	89%	11%	0.178	0.76	0.95
8	0.82	38%	62%	0.040	0.52	0.75	47	0.76	92%	8%	0.238	0.54	0.89
9	0.87	45%	55%	0.020	0.34	0.67	48	0.75	91%	9%	0.258	0.59	0.91
10	0.86	46%	54%	0.020	0.34	0.69	49	0.72	91%	9%	0.118	0.63	0.97
11	0.88	45%	55%	0.035	0.26	0.51	50	0.73	91%	9%	0.113	0.61	0.95
12	0.88	47%	53%	0.035	0.25	0.52	51	0.72	92%	8%	0.228	0.53	0.90
13	0.85	39%	61%	0.030	0.49	0.76	52	0.74	92%	8%	0.208	0.48	0.88
14	0.82	39%	61%	0.030	0.56	0.85	53	0.71	89%	11%	0.153	0.76	0.99
15	0.91	39%	61%	0.050	0.37	0.56	54	0.71	89%	11%	0.168	0.80	0.98
16	0.87	38%	62%	0.050	0.44	0.65	55	0.73	91%	9%	0.258	0.63	0.95
17	0.86	42%	58%	0.020	0.44	0.78	56	0.73	90%	10%	0.263	0.66	0.95
18	0.85	43%	57%	0.020	0.42	0.78	57	0.77	93%	7%	0.128	0.53	1.00
19	0.86	41%	59%	0.040	0.37	0.64	58	0.77	93%	7%	0.128	0.50	0.99
20	0.86	43%	57%	0.035	0.35	0.65	59	0.80	94%	6%	0.238	0.44	1.00
21	0.85	39%	61%	0.030	0.52	0.80	60	0.81	94%	6%	0.228	0.39	0.99
22	0.82	38%	62%	0.030	0.57	0.87	61	0.74	91%	9%	0.168	0.68	1.00
23	0.88	38%	62%	0.045	0.45	0.69	62	0.73	90%	10%	0.188	0.72	1.00
24	0.86	38%	62%	0.050	0.47	0.70	63	0.78	93%	7%	0.283	0.55	1.00
25	0.89	44%	56%	0.025	0.38	0.74	64	0.77	92%	8%	0.298	0.58	1.00
26	0.88	45%	55%	0.025	0.36	0.73	65	0.76	80%	20%	0.093	0.54	0.84
27	0.90	44%	56%	0.040	0.34	0.65	66	0.84	39%	61%	0.038	0.42	0.64
28	0.89	45%	55%	0.040	0.31	0.63	67	0.76	93%	7%	0.158	0.45	0.90
29	0.86	39%	61%	0.030	0.50	0.80	68	0.76	80%	20%	0.088	0.54	0.81
30	0.82	39%	61%	0.030	0.56	0.86	69	0.77	81%	19%	0.103	0.52	0.88
31	0.91	39%	61%	0.050	0.41	0.66	70	0.76	80%	20%	0.093	0.55	0.84
32	0.87	39%	61%	0.050	0.46	0.70	71	0.78	81%	19%	0.103	0.49	0.82
33	0.74	91%	9%	0.080	0.62	0.93	72	0.78	83%	17%	0.083	0.42	0.79
34	0.73	90%	10%	0.070	0.67	0.92	73	0.75	79%	21%	0.108	0.61	0.88
35	0.76	93%	7%	0.180	0.38	0.77	74	0.75	79%	21%	0.073	0.62	0.89
36	0.78	93%	7%	0.140	0.42	0.83	75	0.77	81%	19%	0.118	0.48	0.80
37	0.71	89%	11%	0.125	0.82	0.97	76	0.75	80%	20%	0.093	0.53	0.82
38	0.70	88%	12%	0.158	0.84	0.97	77	0.76	80%	20%	0.098	0.54	0.84
39	0.74	92%	8%	0.233	0.43	0.77							

Based on the results of ANOVA, two regression equations are proposed for the calculation of the flexure and shear stiffness reduction factors as a function of the coded design variables (i.e., variables varying between -1 and +1):

$$\begin{aligned}\eta_f = {} & 0.531+0.077(\mathrm{AR})+0.012(\mathrm{RR})-0.032(\mathrm{SR})+0.083(\mathrm{AL})-0.065(\mathrm{SS})+0.012(\mathrm{CS}) \\ & -0.032(\mathrm{AR}^2)-0.017(\mathrm{AR})(\mathrm{SS})-0.012(\mathrm{RR})(\mathrm{AL})+0.017(\mathrm{RR})(\mathrm{SS})-0.011(\mathrm{RR})(\mathrm{CS}) \\ & -0.019(\mathrm{AL})(\mathrm{CS})\end{aligned} \tag{7-19}$$

$$\eta_v = 0.836 + 0.111(\text{AR}) + 0.040(\text{RR}) + 0.038(\text{AL}) - 0.059(\text{SS}) + 0.011(\text{CS})$$
$$-0.026(\text{AR}^2) - 0.011(\text{AR})(\text{AL}) + 0.027(\text{AR})(\text{SS}) + 0.012(\text{RR})(\text{SR}) - 0.017(\text{RR})(\text{AL}) \quad (7\text{-}20)$$
$$+ 0.02(\text{RR})(\text{SS}) + 0.013(\text{AL})(\text{CS})$$

Equations (7-19) and (7-20) are used to calculate the effective flexural and shear rigidities of a SC wall sample in the following section. .

7.10 Calculation of Monotonic Response and Effective Stiffness of a SC Wall Pier

The monotonic response and effective stiffness of a cantilever SC wall pier on a rigid foundation are calculated using the predictive equations presented in Section 7.9. The properties of the SC wall are presented in Table 7-8.

Table 7-8 SC wall properties

Height, H (in.)	157
Length, L (in.)	157
Infill concrete thickness, T (in.)	12
Steel faceplate thickness, t_s (in.)	0.25
Stud spacing, S (in.)	9
Steel strength, f_y (ksi)	50.8
Concrete strength, f_c' (ksi)	6
Axial load, P (kips)	1700

7.10.1 Mechanical Properties of SC Wall

$$E_c = 57000\sqrt{f_c'} = 57000\sqrt{6000} \times 0.001 = 4415 \text{ ksi} \quad (7\text{-}21)$$

$$G_c = E_c / 2(1+\nu_c) = 4415 / 2(1+0.2) = 1840 \text{ ksi} \quad (7\text{-}22)$$

$$I_c = \frac{1}{12}TL^3 = \frac{1}{12} \times 12 \times 157^3 = 3869893 \text{ in}^4 \quad (7\text{-}23)$$

$$A_c = TL = 12 \times 157 = 1884 \text{ in}^2 \quad (7\text{-}24)$$

$$G_s = E_s / 2(1+\nu_s) = 29000 / 2(1+0.3) = 11154 \text{ ksi} \quad (7\text{-}25)$$

$$I_s = \frac{1}{12} 2t_s L^3 = \frac{1}{12} \times 2 \times 0.25 \times 157^3 = 161246 \text{ in}^4 \tag{7-26}$$

$$A_s = 2t_s L = 2 \times 0.25 \times 157 = 78.5 \text{ in}^2 \tag{7-27}$$

The actual and coded values of the design variables are listed in Table 7-9. The coded values of the design variables were calculated using the actual values and Equation (7-9).

Table 7-9 Values of design variables

Design variable	Actual value	Coded value
Aspect ratio, AR= H/L	1.00	-0.33
Reinforcement ratio, $RR = 2t_s / T$	0.042	-0.10
Slenderness ratio, $SR = S / t_s$	36	0.73
Axial load ratio, $AL = P / (A_g f_c')$	0.2	1.00
Steel strength, $SS = f_y$	50.5	0.00
Concrete strength, $CS = f_c'$	6	0.00

The values of the strength and stiffness factors α_c^y, α_s^y, α_c^p, α_s^p, β_y, and β_p together with the values of flexure and shear stiffness reduction factors η_f and η_v are listed in Table 7-10. The strength and stiffness factors were calculated using the values of the coded design variables and coefficients of the regression models listed in Table 7-6. The flexure and shear stiffness reduction factors were calculated using the values of coded design variables and Equations (7-19) and (7-20), respectively.

Table 7-10 Values of strength and stiffness modification coefficients

α_s^y	α_c^y	α_s^p	α_c^p	β_y	β_p	η_f	η_v
0.13	0.10	0.27	0.12	0.64	0.25	0.56	0.83

7.10.2 Yield and Peak Lateral Strengths

The yield load, V_y, and the peak lateral strength, V_p, of the SC wall pier are calculated using the values of the strength factors and Equations (7-2) and (7-3):

$$V_y = \alpha_c^y A_c f_c' + \alpha_s^y A_s f_y = 0.1 \times 1884 \times 6 + 0.13 \times 78.5 \times 50.8 = 1225 \text{ kips} \tag{7-28}$$

$$V_p = \alpha_c^p A_c f_c' + \alpha_s^p A_s f_y = 0.12 \times 1884 \times 6 + 0.27 \times 78.5 \times 50.8 = 1800 \text{ kips} \tag{7-29}$$

7.10.3 Pre- and Post-Yield Stiffness

The pre- and post-yield stiffness of the SC wall pier, K_{cr} and K_y, are calculated using stiffness factors and Equations (7-4) through (7-8).

$$K_{fc} = \frac{3E_c I_c}{h^3} = \frac{3 \times 4415 \times 3869893}{157^3} = 13245 \text{ kips/in} \tag{7-30}$$

$$K_{fs} = \frac{3E_s I_s}{h^3} = \frac{3 \times 29000 \times 161246}{157^3} = 3625 \text{ kips/in} \tag{7-31}$$

$$K_{vc} = \frac{G_c A_c^{eff}}{h} = \frac{1840 \times (1884/1.2)}{157} = 18400 \text{ kips/in} \tag{7-32}$$

$$K_{vs} = \frac{G_s A_s^{eff}}{h} = \frac{11154 \times (78.5/1.2)}{157} = 4648 \text{ kips/in} \tag{7-33}$$

$$K_{el} = K_{el}^c + K_{el}^s = \frac{1}{\frac{1}{K_{fc}} + \frac{1}{K_{vc}}} + \frac{1}{\frac{1}{K_{fs}} + \frac{1}{K_{vs}}} = 7700 + 2040 = 9740 \text{ kips/in} \tag{7-34}$$

$$K_{cr} = \beta_y K_{el} = 0.64 \times 9740 = 6233 \text{ kips/in} \tag{7-35}$$

$$K_y = \beta_p K_{el} = 0.25 \times 9740 = 2435 \text{ kips/in} \tag{7-36}$$

7.10.4 Displacements at Yield and Peak Points

The values of the yield displacement and displacement at the peak strength are calculated using the yield load, peak lateral strength, and pre- and post-yield stiffness.

$$\Delta_y = \frac{V_y}{K_{cr}} = \frac{1225}{6233} = 0.2 \text{ in.} \tag{7-37}$$

$$\Delta_p = \frac{V_p - V_y}{K_y} + \Delta_y = 0.43 \text{ in.} \tag{7-38}$$

7.10.5 Effective Flexural and Shear Rigidities

The values of the effective flexural and shear rigidities are calculated using stiffness reduction factors, elastic flexural and shear rigidities, and Equations (7-10) and (7-11):

$$EI_{eff} = 0.56(E_c I_c + E_s I_s) = 12195 \text{ kips-in}^2 \tag{7-39}$$

$$GA_{eff} = 0.83(G_c A_c^{eff} + G_s A_s^{eff}) = 4530 \text{ kips-in}^2 \tag{7-40}$$

CHAPTER 8

ANALYTICAL MODELING OF RECTANGULAR SC WALL PANELS

8.1 Introduction

A complete family of seismic analysis and design tools for a structural component or system would include micro-models suitable for finite element analysis of individual components, macro-models suitable for analysis of a framing system, and simplified models suitable for preliminary analysis and design upon which macro-models can later be based.

This chapter presents simplified models for stiffness prediction, and monotonic and cyclic analyses of flexure- and flexure-shear-critical rectangular SC walls. Section 8.2 presents a reliable and straightforward method to calculate the monotonic force-displacement response of an SC wall. The proposed analytical model is validated using results of finite element analyses of SC walls with three aspect ratios (= 0.5, 1 and 2), reinforcement ratios ranging from 2% to 5%, wall thicknesses of 10 in. and 20 in., and concrete compressive strengths of 4 ksi and 7 ksi. Section 8.3 presents analytical simulations of the cyclic response of SC walls using the Modified Ibarra-Krawinler Pinching (MIKP) model (2005). Section 8.4 presents an analytical approach to predict the initial stiffness of an SC wall with baseplate connection. A glossary of terms used in this chapter is provided on pages xviii through xxiii.

8.2 Simplified Monotonic Analysis of SC Walls

Xu et al. (2011) calculated the lateral force-displacement relationship for an RC column assuming concentrated hinges and addressing coupling between axial force, shear force and bending moment. Nonlinear response was simulated using flexural and shear springs at the ends of the column. Backbone curves were established in flexure and shear for the nonlinear springs that were assigned to the sub-elements comprising the column. The Modified-Compression-Field-Theory (MCFT), as developed by Vecchio et al. (1986), was used to establish the moment-curvature and shear force-shear strain relationships for each sub-element. The flexural and shear deformations at the top of the column, calculated by integrating the curvature and shear strain in each section along the column height, are used to obtain the moment-rotation and the shear force-shear displacement relationships for the flexural and shear springs, respectively.

This approach is used to establish the in-plane flexure-shear response of rectangular SC walls [Epackachi et al. (2015a)]. Figure 8-1 illustrates the general procedure.

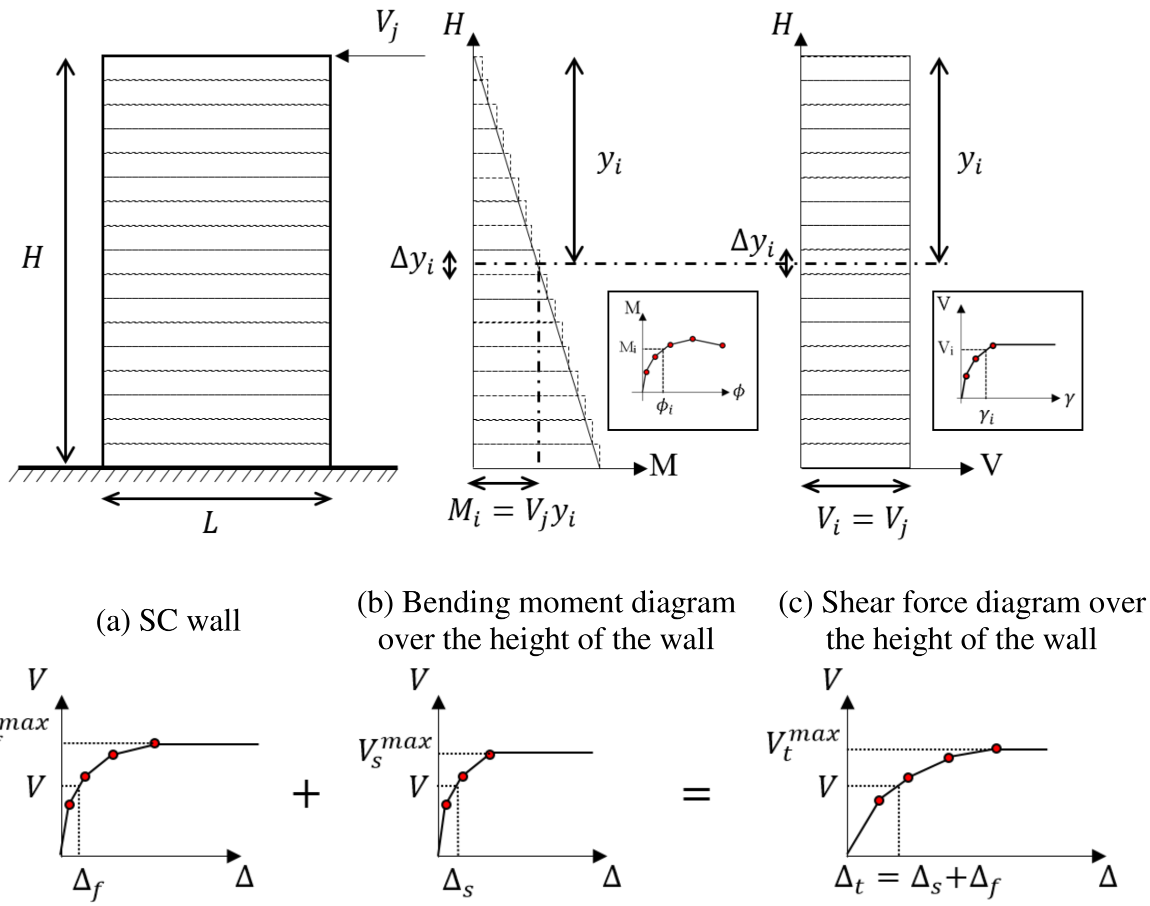

(a) SC wall

(b) Bending moment diagram over the height of the wall

(c) Shear force diagram over the height of the wall

(d) $V-\Delta$ relationship corresponding to flexural behavior of SC wall

(e) $V-\Delta$ relationship corresponding to pure shear behavior of SC wall

(f) $V-\Delta$ relationship of SC wall

Figure 8-1 Simplified monotonic analysis of SC walls

The in-plane flexure-shear response of an SC wall subjected to lateral loading is calculated in eight steps as follows: 1) discretize the wall element into sub-elements along its height and between the points of application of lateral loading (termed a wall panel), 2) calculate the shear force-shear strain relationship for the panel using the equations included in Table 8-1, 3) calculate the moment-curvature relationship for the cross-sections of the SC wall panel using the equations included in either Table 8-2 or Table 8-3, 4) modify the moment-curvature relationships of step 2 to account for flexure-shear interaction in the steel faceplates, 5) set the shear capacity of the panel $(V_t^{\max})$ to the smaller of a) the peak shear force calculated in step 2 ($V_s^{\max}$), and b) the shear force corresponding to the flexural strength calculated in step 4 (V_f^{max}), 6) increment the applied shear force from zero to the shear capacity of the SC wall calculated in step 5 and calculate the incremental moment applied to each sub-element for each increment of the shear force (see Figure 8-1), 7) calculate the values of the curvature and shear strain in each sub-element using the moment-curvature and shear force-shear strain relationships calculated in steps 2 and 4, and 8) calculate the flexural (Δ_f), shear (Δ_s), and total (Δ_t) displacements corresponding to each increment of the shear force as:

$$\Delta_f = \sum_{i=1}^{m} \phi_i \Delta y_i y_i \tag{8-1}$$

$$\Delta_s = \sum_{i=1}^{m} \gamma_i \Delta y_i = \gamma_i \sum_{i=1}^{m} \Delta y_i = \gamma_i H \tag{8-2}$$

$$\Delta_t = \Delta_f + \Delta_s \tag{8-3}$$

The shear force–shear strain and moment–curvature relationships required to make these calculations for an SC wall panel are presented in subsections 8.3.1 and 8.3.2, respectively. The tables identified above are provided in subsections 8.2.1 and 8.2.2.

8.2.1 Shearing Force-Shearing Strain Relationship

Figure 8-2 presents the assumed shear force-shear strain relationship. The coordinates of the three break points (A, B, and C) in Figure 8-2 define the elastic (origin-A), post-concrete cracking (A-B), and post-faceplate yielding (B-C) regions of the response. The calculation of these coordinates is discussed below.

8.2.1.1 Concrete Cracking: Break Point A

In this study, the shear behavior of SC walls proposed by Ozaki et al. (2004) and Varma et al. (2011c) is used to simulate the shear response of SC walls (from points O to B in Figure 8-2).

Varma et al. (2011c) parsed the in-plane response of an SC wall in shear into three regions: 1) elastic, 2) concrete cracking, and 3) steel faceplate yielding. In the elastic range, the infill concrete and the steel faceplates were modeled using isotropic elastic and isotropic elastic plane-stress behaviors, respectively. The shear strength of the SC wall at the onset of concrete cracking was calculated by multiplying the area of the transformed SC wall cross-section, $A_c + nA_s$, by a concrete shear stress equal to $0.063\sqrt{f_c'}$ ksi. The elastic shear stiffness of an SC panel was calculated as the sum of the shear stiffness of the infill concrete ($G_c A_c$) and the steel faceplates ($G_s A_s$). Equations to calculate the coordinates of point A are presented in Table 8-1.

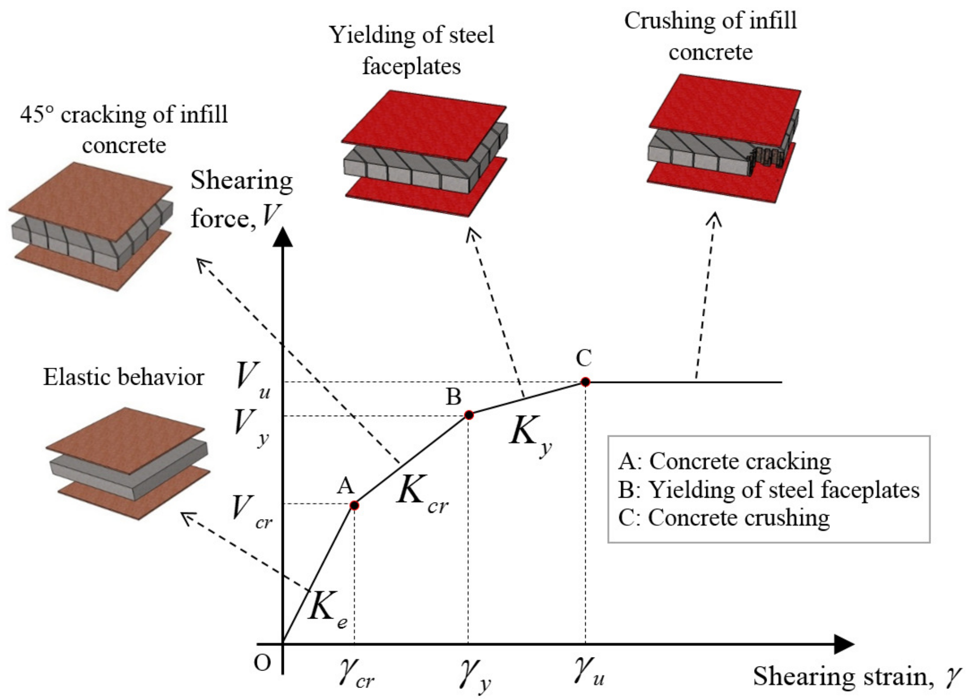

Figure 8-2 In-plane shear response of an SC wall

8.2.1.2 Steel Faceplate Yielding: Break Point B

After concrete cracking, Ozaki et al. (2004) and Varma et al. (2011c) assumed the infill concrete to behave as an orthotropic elastic material with zero stiffness perpendicular to the direction of cracking and 70% of the elastic compression modulus (E_c) in the orthogonal direction. The stiffness of the cracked SC wall was calculated assuming orthotropic behavior of the infill concrete and isotropic elastic plane stress behavior of the steel faceplates. These assumptions are used here to calculate the shear stiffness of a cracked SC wall prior to faceplate yielding. Equations for the post-cracking response of an SC wall panel, derived by Varma et al. (2011c) and Hong et al. (2014), are presented below for completeness. The normal and shear stresses in an SC wall, the steel faceplates, and the infill concrete are defined in Figure 8-3.

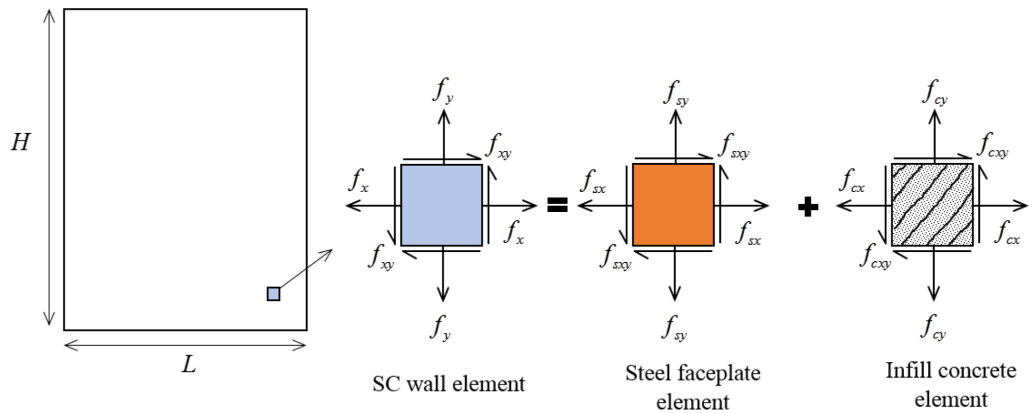

Figure 8-3 Stress definitions

The normal and shear stresses in the cracked infill concrete are calculated assuming orthotropic behavior:

$$\begin{Bmatrix} f_{cx} \\ f_{cy} \\ f_{cxy} \end{Bmatrix} = [T]_\sigma^{-1} [K_c'][T]_\varepsilon \begin{Bmatrix} \varepsilon_x \\ \varepsilon_y \\ \gamma_{xy} \end{Bmatrix} \tag{8-4}$$

where $[K_c']$ is the post-cracking stiffness matrix of the concrete with respect to the principal stress and strain directions; the principal stress directions were assumed to coincide with the principal strain directions; $[T]_\sigma$ is the transformation matrix that relates the principal stresses to the X-Y stresses; and $[T]_\varepsilon$ is the transformation matrix that relates the principal strains to the X-Y strains. Matrices $[K_c']$, $[T]_\sigma$, and $[T]_\varepsilon$ are expressed as:

$$[K_c'] = \begin{bmatrix} 0 & 0 & 0 \\ 0 & E_c^{cr} & 0 \\ 0 & 0 & 0 \end{bmatrix} \tag{8-5}$$

$$[T]_\sigma = \begin{bmatrix} \cos^2\theta^{cr} & \sin^2\theta^{cr} & 2\sin\theta^{cr}\cos\theta^{cr} \\ \sin^2\theta^{cr} & \cos^2\theta^{cr} & -2\sin\theta^{cr}\cos\theta^{cr} \\ -\sin\theta^{cr}\cos\theta^{cr} & \sin\theta\cos\theta^{cr} & \cos^2\theta^{cr} - \sin^2\theta^{cr} \end{bmatrix} \tag{8-6}$$

$$[T]_{\varepsilon} = \begin{bmatrix} \cos^2\theta^{cr} & \sin^2\theta^{cr} & \sin\theta^{cr}\cos\theta^{cr} \\ \sin^2\theta^{cr} & \cos^2\theta^{cr} & -\sin\theta^{cr}\cos\theta^{cr} \\ -2\sin\theta^{cr}\cos\theta^{cr} & 2\sin\theta\cos\theta^{cr} & \cos^2\theta^{cr} - \sin^2\theta^{cr} \end{bmatrix} \tag{8-7}$$

Assuming cracking in the infill concrete at 45°, and substituting (8-5), (8-6), and (8-7) into (8-4), the stress-strain relationship of the cracked infill concrete is calculated as:

$$\begin{Bmatrix} f_{cx} \\ f_{cy} \\ f_{cxy} \end{Bmatrix} = \frac{E_c^{\ cr}}{4} \begin{bmatrix} 1 & 1 & -1 \\ 1 & 1 & -1 \\ -1 & -1 & 1 \end{bmatrix} \begin{Bmatrix} \varepsilon_x \\ \varepsilon_y \\ \gamma_{xy} \end{Bmatrix} \tag{8-8}$$

The normal and shear stresses in the steel faceplates are calculated assuming isotropic elastic plane stress behavior:

$$\begin{Bmatrix} f_{sx} \\ f_{sy} \\ f_{sxy} \end{Bmatrix} = [K_s] \begin{Bmatrix} \varepsilon_x \\ \varepsilon_y \\ \gamma_{xy} \end{Bmatrix} \tag{8-9}$$

where $[K_s]$ is the elastic stiffness matrix of the steel faceplates, and is calculated as:

$$[K_s] = \frac{E_s}{1-\nu_s^{\ 2}} \begin{bmatrix} 1 & \nu_s & 0 \\ \nu_s & 1 & 0 \\ 0 & 0 & \frac{1-\nu_s}{2} \end{bmatrix} \tag{8-10}$$

The equilibrium equations for an SC wall panel subjected to normal forces N_x and N_y, and shear force V, in a matrix form can be expressed as:

$$A_c \begin{Bmatrix} f_{cx} \\ f_{cy} \\ f_{cxy} \end{Bmatrix} + A_s \begin{Bmatrix} f_{sx} \\ f_{sy} \\ f_{sxy} \end{Bmatrix} = \begin{Bmatrix} N_x \\ N_y \\ V \end{Bmatrix} \tag{8-11}$$

Substituting (8-8), (8-9), and (8-10) into (8-11), and assuming that the normal forces are zero:

$$\left(\frac{A_c E_c^{cr}}{4}\begin{bmatrix}1 & 1 & -1\\ 1 & 1 & -1\\ -1 & -1 & 1\end{bmatrix}+\frac{A_s E_s}{1-\nu_s^2}\begin{bmatrix}1 & \nu_s & 0\\ \nu_s & 1 & 0\\ 0 & 0 & \dfrac{1-\nu_s}{2}\end{bmatrix}\right)\begin{Bmatrix}\varepsilon_x\\ \varepsilon_y\\ \gamma_{xy}\end{Bmatrix}=\begin{Bmatrix}0\\ 0\\ V\end{Bmatrix} \tag{8-12}$$

Solving (8-12) yields the normal and shear strains in an SC wall panel as:

$$\varepsilon_x = \varepsilon_y = \frac{\alpha}{2\alpha+(1+\nu_s)\beta}\gamma_{xy} \tag{8-13}$$

$$\gamma_{xy} = \left(\frac{1}{\dfrac{2}{(1+\nu_s)\beta}+\dfrac{1}{\alpha}} + G_s A_s\right)^{-1} V \tag{8-14}$$

where parameters α and β are:

$$\alpha = \frac{A_c E_c^{cr}}{4} \tag{8-15}$$

$$\beta = \frac{A_s E_s}{1-\nu_s^2} \tag{8-16}$$

The in-plane stresses in the infill concrete are calculated by substituting the calculated normal and shear strains of (8-13) and (8-14) into (8-8):

$$\begin{Bmatrix}f_{cx}\\ f_{cy}\\ f_{cxy}\end{Bmatrix}=\frac{E_c^{cr}}{4}\begin{bmatrix}1 & 1 & -1\\ 1 & 1 & -1\\ -1 & -1 & 1\end{bmatrix}\begin{Bmatrix}\varepsilon_x\\ \varepsilon_y\\ \gamma_{xy}\end{Bmatrix}=\frac{\alpha}{A_c}\begin{bmatrix}1 & 1 & -1\\ 1 & 1 & -1\\ -1 & -1 & 1\end{bmatrix}\begin{Bmatrix}\dfrac{\alpha}{2\alpha+(1+\nu_s)\beta}\\ \dfrac{\alpha}{2\alpha+(1+\nu_s)\beta}\\ 1\end{Bmatrix}\gamma_{xy} \tag{8-17}$$

A simpler form of the in-plane stresses in the infill concrete is:

$$\begin{Bmatrix} f_{cx} \\ f_{cy} \\ f_{cxy} \end{Bmatrix} = \frac{V}{A_c} \begin{Bmatrix} -\dfrac{K_\beta}{K_\alpha + K_\beta} \\ -\dfrac{K_\beta}{K_\alpha + K_\beta} \\ \dfrac{K_\beta}{K_\alpha + K_\beta} \end{Bmatrix} \tag{8-18}$$

where the parameters K_α and K_β are calculated as:

$$K_\alpha = G_s A_s \tag{8-19}$$

$$K_\beta = \frac{1}{\dfrac{2}{(1+\nu_s)\beta} + \dfrac{1}{\alpha}} = \frac{1}{\dfrac{2(1-\nu_s)}{A_s E_s} + \dfrac{4}{A_c E_c^{cr}}} \tag{8-20}$$

The in-plane stresses in the steel faceplates are calculated by substituting the calculated normal and shear strains of (8-13) and (8-14) into (8-9) as:

$$\begin{Bmatrix} f_{sx} \\ f_{sy} \\ f_{sxy} \end{Bmatrix} = \frac{E_s}{1-\nu_s^2} \begin{bmatrix} 1 & \nu_s & 0 \\ \nu_s & 1 & 0 \\ 0 & 0 & \dfrac{1-\nu_s}{2} \end{bmatrix} \begin{Bmatrix} \varepsilon_x \\ \varepsilon_y \\ \gamma_{xy} \end{Bmatrix} = \frac{\beta}{A_s} \begin{bmatrix} 1 & \nu_s & 0 \\ \nu_s & 1 & 0 \\ 0 & 0 & \dfrac{1-\nu_s}{2} \end{bmatrix} \begin{Bmatrix} \dfrac{\alpha}{2\alpha + (1+\nu_s)\beta} \\ \dfrac{\alpha}{2\alpha + (1+\nu_s)\beta} \\ 1 \end{Bmatrix} \gamma_{xy} \tag{8-21}$$

A simpler form of the in-plane stresses in the steel faceplates is:

$$\begin{Bmatrix} f_{sx} \\ f_{sy} \\ f_{sxy} \end{Bmatrix} = \frac{V}{A_s} \begin{Bmatrix} \dfrac{K_\beta}{K_\alpha + K_\beta} \\ \dfrac{K_\beta}{K_\alpha + K_\beta} \\ \dfrac{K_\alpha}{K_\alpha + K_\beta} \end{Bmatrix} \tag{8-22}$$

Substituting the in-plane stresses of the steel faceplates into the Von-Mises yield condition, $f_{sx}^2 + f_{sy}^2 - f_{sx} f_{sy} + 3 f_{sxy}^2 \le f_y^2$, produces the yield shear strength and stiffness of an SC panel after concrete cracking (i.e., the slope of the line AB in Figure 8-2) as:

$$V_y = \frac{K_\alpha + K_\beta}{\sqrt{3K^2_\alpha + K_\beta}} A_s f_y \tag{8-23}$$

$$K_{cr} = K_\alpha + K_\beta = G_s A_s + \frac{1}{\frac{2(1-\nu_s)}{A_s E_s} + \frac{4}{A_c E_c^{cr}}} \tag{8-24}$$

Equations to predict the shear force at the onset of faceplate yielding and the shear stiffness of a cracked SC wall panel are provided in Table 8-1.

Table 8-1 Calculation of the shear response of an SC wall panel

Limit state	Shearing force (kips)	Shearing stiffness (kips/rad)
Concrete cracking	$V_{cr} = 0.063\sqrt{f_c'}(A_c + nA_s)$	$K_e = G_s A_s + G_c A_c$
Yielding of the steel faceplates[1,2]	$V_y = \frac{K_\alpha + K_\beta}{\sqrt{3K^2_\alpha + K_\beta}} A_s f_y$	$K_{cr} = K_\alpha + K_\beta$
Concrete crushing[3]	$V_u = \frac{1}{2}\left(\sqrt{1+(\frac{H}{L})^2} + (\eta - 1)\frac{H}{L}\right) A_c f_c'$	$K_y = \frac{V_u - V_y}{0.006 - (\frac{V_{cr}}{K_e} + \frac{V_y - V_{cr}}{K_{cr}})}$

[1] $K_\alpha = G_s A_s$

[2] $K_\beta = 1/(\frac{2(1-\nu_s)}{A_s E_s} + \frac{4}{A_c E_c^{cr}})$

[3] $\eta = A_s f_y / A_c f_c'$

8.2.1.3 Concrete Crushing: Break Point C

Akita et al. (2001) estimated the ultimate shear strain for an SC wall in pure shear to be 6000 micro strain on the basis of test data. Tsuda et al. (2001) and Hong et al. (2014) used this value to characterize the response of SC walls in pure shear.

Hong et al. (2014) used the equations derived by Nielsen et al. (2010) to predict the peak shear capacity of an SC wall. Those equations are available in section 4.9 of [Nielsen et al. (2010)] and are not repeated here.

The post-yield stiffness of an SC wall (i.e., the slope of line BC in Figure 8-2) can be calculated as:

$$K_y = \frac{V_u - V_y}{\gamma_u - \gamma_y} \tag{8-25}$$

where γ_u is 6000 microstrain, as proposed by Akita et al. (2001), and γ_y can be calculated using the elastic and post-cracking shear stiffness and strengths of an SC panel as:

$$\gamma_y = \frac{V_{cr}}{K_e} + \frac{V_y - V_{cr}}{K_{cr}} \tag{8-26}$$

Table 8-1 summarizes the calculation of the shear response of an SC wall panel.

8.2.2 Moment-Curvature Relationship

The moment-curvature relationship for an SC panel was established at the points of 1) concrete cracking, 2) yielding of the steel faceplates at the tension end of the wall, 3) yielding of the steel faceplates at the compression end of the wall, and 4) maximum concrete compressive strain equal to ε_{c0}: the concrete strain at f_c'.

Assumptions were made to calculate flexural strength, consistent with the development of a simplified procedure: (1) plane sections remain plane after bending, (2) flexure-shear interaction is considered in the calculation of the stress in the steel faceplates but its effect on the response of the infill concrete is ignored, (3) the tensile strength of concrete is zero, (4) the flexural strength of the infill concrete is derived using an equivalent rectangular stress block, (5) the steel faceplates and infill concrete are perfectly bonded, and (6) the effects of axial force are ignored.

8.2.2.1 Cracking of the Infill Concrete

Figure 8-4 presents calculations of the flexural strength of an SC wall at the onset of concrete cracking.

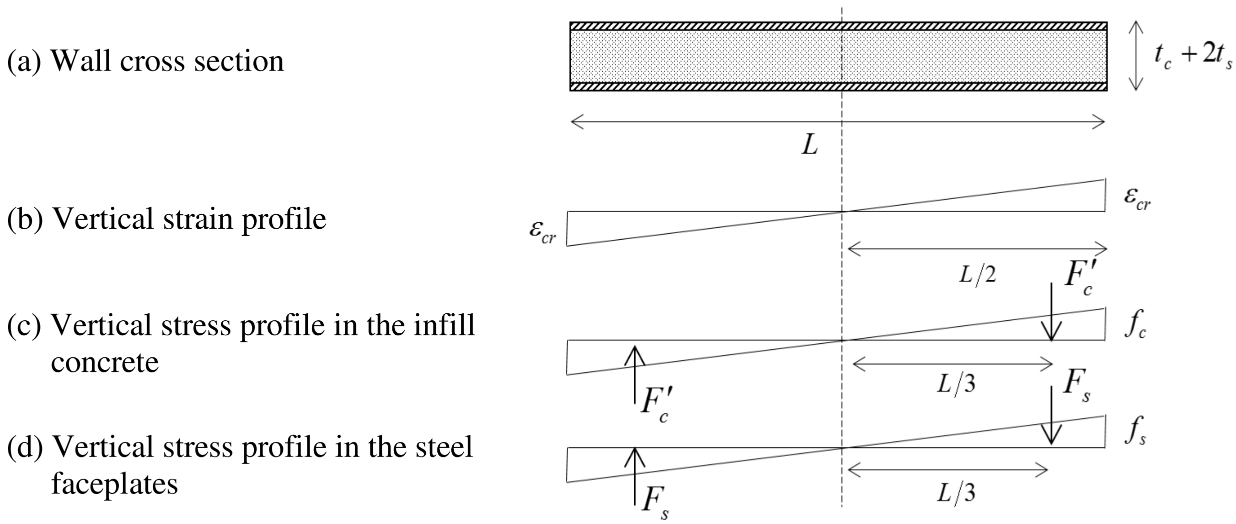

Figure 8-4 Moment-curvature calculation at the onset of concrete cracking

The elastic vertical stresses of the infill concrete and the steel faceplates are:

$$f_c = E_c \varepsilon_{cr} \tag{8-27}$$

$$f_s = E_s \varepsilon_{cr} \tag{8-28}$$

where ε_{cr} is calculated as:

$$\varepsilon_{cr} = \frac{f_r}{E_c} \tag{8-29}$$

The compressive and tensile forces in the infill concrete and the steel faceplates are:

$$F_c' = \frac{1}{2} f_c t_c \, L/2 = \frac{1}{4} E_c \varepsilon_{cr} A_c \tag{8-30}$$

$$F_s = \frac{1}{2} f_s 2t_s \, L/2 = \frac{1}{4} E_s \varepsilon_{cr} A_s \tag{8-31}$$

The flexural strength and curvature of the cross-section of an SC wall panel at the onset of concrete cracking are:

$$M_{cr} = (F_c' + F_s)\, 2L/3 = \frac{1}{6} L \varepsilon_{cr} (E_c A_c + E_s A_s) = \frac{f_r L}{6}(A_c + nA_s) \tag{8-32}$$

$$\phi_{cr} = \frac{\varepsilon_{cr}}{L/2} = \frac{2f_r}{LE_c} \tag{8-33}$$

8.2.2.2 Steel Faceplate Yielding at the Tension End of the Wall Panel

Figure 8-5 presents calculations of the flexural strength of an SC wall panel at the onset of yielding of the steel faceplates at the tension end of the wall.

At the onset of the steel faceplate yielding at the tension end of the wall, the maximum vertical strain in the infill concrete is:

$$\varepsilon_c = \frac{c}{L-c}\varepsilon_y = \frac{\alpha}{1-\alpha}\varepsilon_y \tag{8-34}$$

The compressive force in infill concrete is:

$$F_c' = f_c A_c = f_c t_c c/2 = E_c \varepsilon_c t_c c/2 = E_c \frac{\alpha}{1-\alpha}\varepsilon_y t_c c/2 \tag{8-35}$$

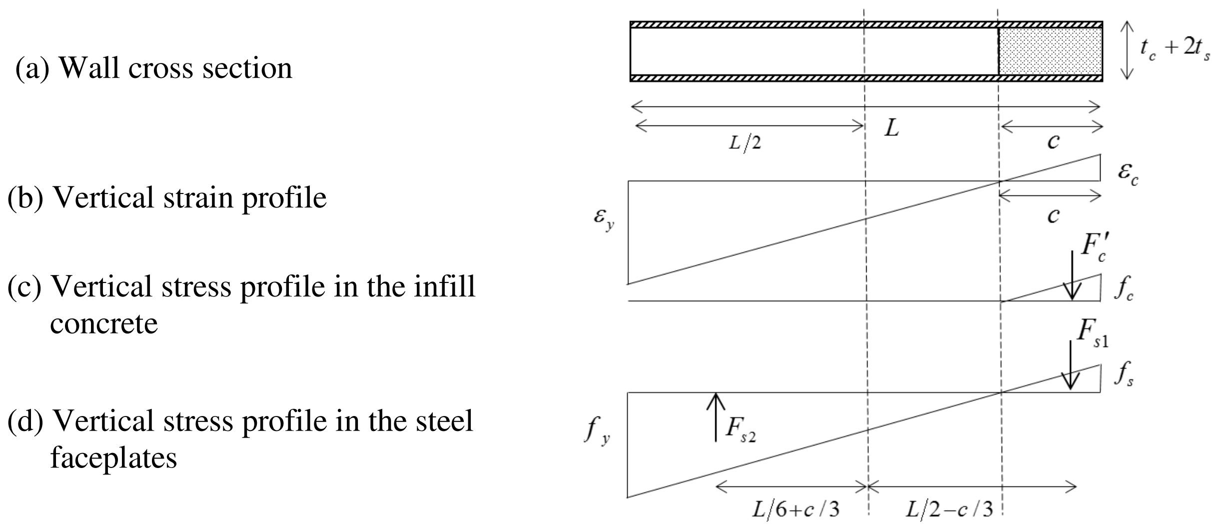

Figure 8-5 Moment-curvature calculation at the onset of steel faceplate yielding at the tension end of the wall

The compressive and tensile forces in the steel faceplates are:

$$F_{s1} = f_s A_s = f_s 2t_s c/2 = E_s \varepsilon_c 2t_s c/2 = E_s \frac{\alpha}{1-\alpha}\varepsilon_y 2t_s c/2 \tag{8-36}$$

$$F_{s2} = f_y 2t_s (L-c)/2 \tag{8-37}$$

Solving the equilibrium equation of the vertical forces, $F_c' + F_{s1} = F_{s2}$, for α :

$$\alpha_y^t = \frac{c}{L} = \frac{\sqrt{\rho'}}{\sqrt{\rho'+1}+\sqrt{\rho'}} \tag{8-38}$$

The flexural strength of an SC panel at the onset of the steel faceplate yielding at the tension end of the wall is:

$$M_y^t = F_{s2}(L/6 + c/3) + (F_c' + F_{s1})(L/2 - c/3) \tag{8-39}$$

Substituting (8-35), (8-36), and (8-37) into (8-39) gives the flexural strength of an SC wall as:

$$M_y^t = f_y A_s L\left(\frac{2\alpha^3 - 3\alpha^2 - \rho'}{12\rho'(\alpha - 1)}\right) \tag{8-40}$$

The curvature of the cross-section at the onset of steel faceplate yielding at the tension end of the wall is:

$$\phi_y^t = \frac{\varepsilon_y}{L - c} = \frac{\varepsilon_y}{L(1-\alpha)} \tag{8-41}$$

8.2.2.3 Steel Faceplate Yielding at the Compression End of the Wall Panel

Figure 8-6 presents calculations of the flexural strength of an SC wall panel at the onset of yielding of the steel faceplates at the compression end of the wall.

(a) Wall cross section

(b) Vertical strain profile

(c) Vertical stress profile in the infill concrete

(d) Vertical stress profile in the steel faceplates

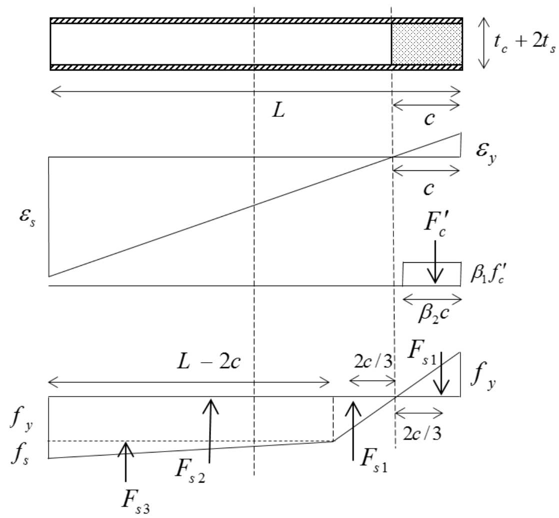

Figure 8-6 Moment-curvature calculation at the onset of the steel faceplate yielding on the compression side of the wall

At the onset of the steel faceplate yielding, the maximum vertical tensile strain in the steel faceplates is:

$$\varepsilon_s = \frac{L-c}{c}\varepsilon_y = \frac{1-\alpha}{\alpha}\varepsilon_y \tag{8-42}$$

The steel stress f_s, identified in Figure 8-6, is:

$$f_s = aE_s(\varepsilon_s - \varepsilon_y) \tag{8-43}$$

The compressive forces in the steel faceplates and the infill concrete are:

$$F'_c = \beta_1\beta_2 f'_c c t_c \tag{8-44}$$

$$F_{s1} = \frac{2t_s f_y c}{2} \tag{8-45}$$

The tensile forces in the steel faceplates are:

$$F_{s2} = 2t_s(L-2c)f_y \tag{8-46}$$

$$F_{s3} = \frac{2t_s(L-2c)f_s}{2} \tag{8-47}$$

Solving the equilibrium equation of the vertical forces, $F_c + F_{s1} = F_{s1} + F_{s2} + F_{s3}$, provides the value of α at the onset of the steel faceplate yielding at the compression end of the wall:

$$\alpha_y^c = \frac{c}{L} = \frac{1}{2}\left(\frac{1-2a+\sqrt{2a\gamma+1}}{-2a+\gamma+2}\right) \tag{8-48}$$

where the γ is calculated as:

$$\gamma = \frac{n\beta_1\beta_2 f'_c}{\rho' f_y} \tag{8-49}$$

The flexural strength of an SC panel at the onset of steel faceplate yielding at the compression end of the wall is:

$$M_y^c = F'_c\left(\frac{L}{2} - \frac{\beta_2 c}{2}\right) + F_{s1}\left(\frac{L}{2} - \frac{c}{3} + c + \frac{2}{3}c - \frac{L}{2}\right) + F_{s2}\left(\frac{L}{2} - \frac{L-2c}{2}\right) + F_{s3}\left(\frac{L}{2} - \frac{L-2c}{3}\right) \tag{8-50}$$

Substituting (8-44), (8-45), (8-46), and (8-47) into (8-50) enables the calculation of the flexural strength of an SC wall panel at the onset of steel faceplate yielding at the compression end of the wall:

$$M_y^c = \beta_1\beta_2 f_c' A_c L\alpha(\frac{1-\beta_2\alpha}{2}) + A_s f_y L((1-a)(\alpha - \frac{4}{3}\alpha^2) + \frac{a}{12\alpha}) \tag{8-51}$$

The curvature at the onset of steel faceplate yielding at the compression end of the wall is:

$$\phi_y^c = \frac{\varepsilon_y}{c} = \frac{\varepsilon_y}{L\alpha} \tag{8-52}$$

If the strain-hardening modulus of the steel is set equal to zero ($a=0$), the normalized neutral axis depth and the flexural strength of the SC panel are simplified to:

$$\alpha_y^c = \frac{1}{\gamma + 2} \tag{8-53}$$

$$M_y^c = \beta_1\beta_2 f_c' A_c \alpha L(\frac{1-\beta_2\alpha}{2}) + A_s f_y^e \alpha L(1 - \frac{4}{3}\alpha) \tag{8-54}$$

8.2.2.4 Peak Compressive Stress in the Infill Concrete

Figure 8-7 presents the calculations of the flexural strength of an SC wall when the maximum concrete compressive strain is equal to ε_{c0}.

(a) Wall cross section

(b) Vertical strain profile

(c) Vertical stress profile in the infill concrete

(d) Vertical stress profile in the steel faceplates

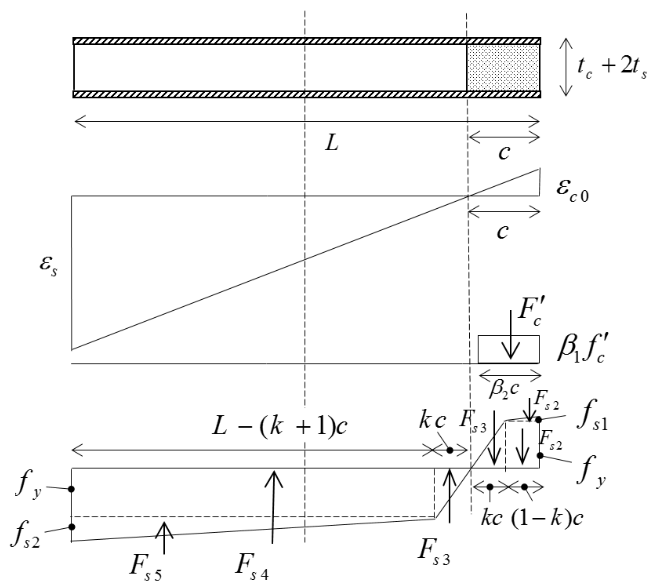

Figure 8-7 Moment-curvature calculation at maximum concrete compressive strain of ε_{c0}

The maximum vertical strain in the steel faceplates when the maximum concrete compressive strain equals ε_{c0} is:

$$\varepsilon_s = \frac{L-c}{c}\varepsilon_{c0} = \frac{1-\alpha}{\alpha}\varepsilon_{c0} \tag{8-55}$$

The parameter k, identified in Figure 8-7, is calculated as:

$$k = \frac{\varepsilon_y}{\varepsilon_{c0}} \tag{8-56}$$

The stresses f_{s1} and f_{s2} in Figure 8-7 are:

$$f_{s1} = aE_s(\varepsilon_{c0} - \varepsilon_y) = aE_s(1-k)\varepsilon_{c0} \tag{8-57}$$

$$f_{s2} = aE_s(\varepsilon_s - \varepsilon_y) = aE_s(\frac{1-\alpha}{\alpha} - k)\varepsilon_{c0} \tag{8-58}$$

The compressive and tensile forces in the steel faceplates and the infill concrete are:

$$F_c' = \beta_1\beta_2 f_c' c t_c \tag{8-59}$$

$$F_{s1} = \frac{1}{2}f_{s1}(1-k)c2t_s = \frac{1}{2}aE_s(1-k)^2\varepsilon_{c0}c2t_s \tag{8-60}$$

$$F_{s2} = f_y(1-k)c2t_s \tag{8-61}$$

$$F_{s3} = \frac{1}{2}f_y kc2t_s \qquad \text{(8-62}$$

$$F_{s4} = f_y 2t_s(L-(k+1)c) \tag{8-63}$$

$$F_{s5} = \frac{1}{2}f_{s2}2t_s(L-(k+1)c) = aE_st_s\varepsilon_{c0}(\frac{1-\alpha}{\alpha} - k)(L-(k+1)c) \tag{8-64}$$

Solving the equilibrium equation of the vertical forces, $F_c' + F_{s1} + F_{s2} + F_{s3} = F_{s3} + F_{s4} + F_{s5}$, produces the value of α when the maximum concrete compressive strain equals ε_{c0}:

$$\alpha_{c0} = \frac{c}{L} = \frac{-\frac{a}{k} - a + 1 + \sqrt{\left(\frac{a}{k} + a - 1\right)^2 + \frac{2a}{k}\left(-2a + \gamma + 2\right)}}{-4a + 2\gamma + 4} \tag{8-65}$$

The flexural strength of an SC panel when the maximum concrete compressive strain equals ε_{c0} is:

$$M_u = F_c'(\frac{L}{2} - \frac{\beta_2 c}{2}) + F_{s1}(\frac{L}{2} - \frac{(1-k)c}{3}) + F_{s2}(\frac{L}{2} - \frac{(1-k)c}{2}) +$$
$$F_{s3}((1-k)c + kc + \frac{2}{3}kc - \left((1-k)c + \frac{kc}{3}\right)) + F_{s4}(\frac{L}{2} - \frac{L-(k+1)c}{2}) + \quad (8\text{-}66)$$
$$F_{s5}(\frac{L}{2} - \frac{L-(k+1)c}{3})$$

and substituting (8-59) through (8-64) into (8-66) gives:

$$M_u = \beta_1 \beta_2 f_c' A_c L\alpha(\frac{1-\beta_2\alpha}{2}) + A_s f_y L((1-a)(-\alpha^2 + \alpha - \frac{(k\alpha)^2}{3}) + \frac{a}{12k\alpha}) \quad (8\text{-}67)$$

The corresponding curvature is:

$$\phi_u = \frac{\varepsilon_{c0}}{c} = \frac{\varepsilon_{c0}}{L\alpha} \quad (8\text{-}68)$$

If the strain-hardening modulus of the steel is set equal to zero ($a = 0$), the normalized neutral axis depth and the flexural strength of an SC panel when the maximum concrete compressive strain is equal to ε_{c0} are simplified to:

$$\alpha_u = \frac{1}{\gamma + 2} \quad (8\text{-}69)$$

$$M_u = \beta_1 \beta_2 f_c' A_c \alpha L(\frac{1-\beta_2\alpha}{2}) + A_s f_y^e \alpha L(1 - \alpha - \frac{\alpha k^2}{3}) \quad (8\text{-}70)$$

The moment-curvature relationship for the cross-section can be represented by the piecewise linear relationship of Figure 8-8.

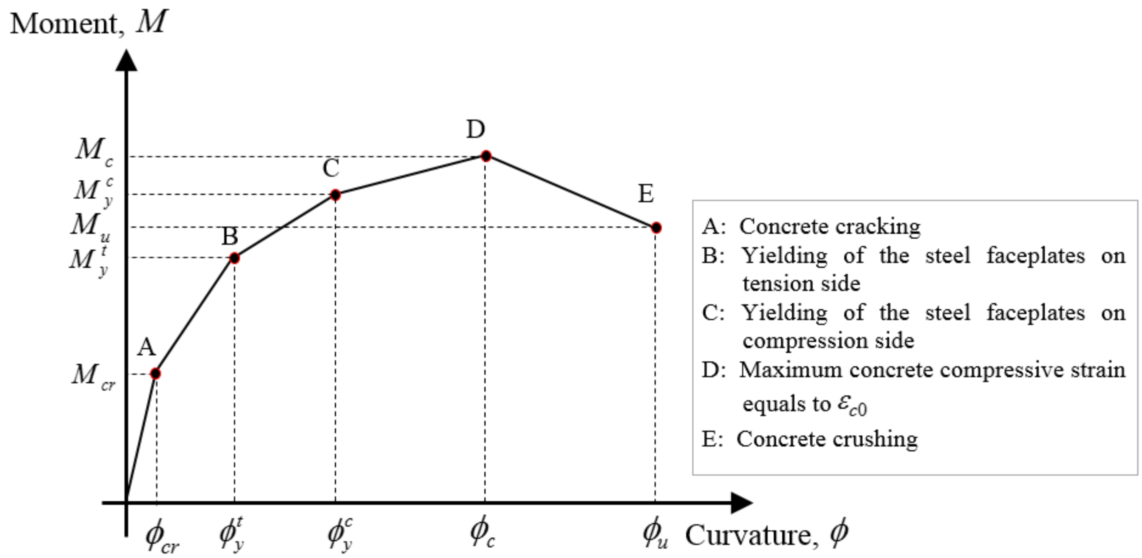

Figure 8-8 Moment-curvature relationship for an SC wall panel

Table 8-2 summarizes the flexural strength calculations for an SC wall panel considering strain-hardening of the steel faceplates. Table 8-3 presents the corresponding equations assuming elastic-perfectly plastic behavior for the steel faceplates. Preliminary analysis showed that hardening had no significant effect on the values of the moments and curvatures, and that the flexural response of an SC wall panel can be reasonably calculated assuming elastic-perfectly plastic behavior for the steel.

8.2.3 Concrete Behavior

The concrete stress-strain relationship proposed by Tsai (1988) is used to describe the behavior of the infill concrete:

$$\frac{f_c}{f_c'} = \frac{n'x}{1 + (n' - \frac{r}{r-1})x + \frac{x^r}{r-1}} \tag{8-71}$$

Chang et al. (1994) proposed (8-72) to calculate the strain corresponding to peak stress, and (8-73) and (8-74) to establish the shape of the stress-strain relationship:

$$\varepsilon_{c0} = \frac{(f_c')^{1/4}}{4000} \tag{8-72}$$

$$n' = \frac{46}{(f_c')^{3/8}} \tag{8-73}$$

$$r = \frac{f_c'}{750} - 1.9 \tag{8-74}$$

Figure 8-9 presents the stress–strain relationships for unconfined uniaxial compressive strengths of 3, 4, 5, 6, and 7 ksi, which is considered a practical range for infill concrete in SC walls, noting that the strain limit for calculations is ε_{c0}.

Figure 8-6 and Figure 8-7 present the calculation of the equivalent rectangular stress block parameters corresponding to two limit states: 1) yielding of the steel faceplates on the compression side of the wall, and 2) maximum concrete compressive strain equal to ε_{c0}. The values of β_1 and β_2 corresponding to these limit states, presented in Table 8-4, are calculated assuming that the equivalent rectangular stress block recovered the area under the stress-strain relationship and the location of its resultant. Values of the two stress block parameters are presented for $3 \le f_c' \le 7$ ksi and faceplate yield strengths of 36, 45, and 60 ksi. Values for other combinations of f_c' and f_y can be interpolated.

Table 8-2 Calculation of the flexural response of an SC wall panel considering steel hardening

Limit state	$\alpha = \frac{c}{L}$	ϕ	M
Concrete cracking	$\alpha_{cr} = \frac{L}{2}$	$\phi_{cr} = \frac{2f_r}{LE_c}$	$M_{cr} = \frac{f_r L}{6}(A_c + nA_s)$
Yielding of the steel faceplates at the tension end of the wall[1]	$\alpha_y^t = \frac{\sqrt{\rho'}}{\sqrt{\rho'+1}+\sqrt{\rho'}}$	$\phi_y^t = \frac{\varepsilon_y}{L(1-\alpha)}$	$M_y^t = A_s f_y^e L_y^t$
	$L_y^t = L(\frac{2\alpha^3 - 3\alpha^2 - \rho'}{12\rho'(\alpha-1)})$		
Yielding of the steel faceplates at the compression end of the wall[2]	$\alpha_y^c = \frac{1}{2}\left(\frac{1-2a+\sqrt{2a\gamma+1}}{-2a+\gamma+2}\right)$	$\phi_y^c = \frac{\varepsilon_y}{L\alpha}$	$M_y^c = \beta_1\beta_2 f_c' A_c L_c' + A_s f_y^e L_s'$
	$L_c' = L\alpha(\frac{1-\beta_2\alpha}{2})$, $L_s' = L((1-a)(\alpha - \frac{4}{3}\alpha^2) + \frac{a}{12\alpha})$		
Maximum concrete compressive strain equal to ε_{c0}	$\alpha_u = \frac{-\frac{a}{k} - a + 1 + \sqrt{\left(\frac{a}{k}+a-1\right)^2 + \frac{2a}{k}(-2a+\gamma+2)}}{-4a+2\gamma+4}$	$\phi_u = \frac{\varepsilon_{c0}}{L\alpha}$	$M_u = \beta_1\beta_2 f_c' A_c L_c'' + A_s f_y^e L_s''$
	$L_c'' = L\alpha(\frac{1-\beta_2\alpha}{2})$, $L_s'' = L((1-a)(-\alpha^2 + \alpha - \frac{(k\alpha)^2}{3}) + \frac{a}{12k\alpha})$		

[1] $\rho' = 2t_s n / t_c$

[2] $\gamma = (n\beta_1\beta_2 f_c')/(\rho' f_y)$

Table 8-3 Calculation of the flexural response of an SC wall panel without steel hardening

Limit state	$\alpha = \frac{c}{L}$	ϕ	M
Concrete cracking	$\alpha_{cr} = \frac{L}{2}$	$\phi_{cr} = \frac{2f_r}{LE_c}$	$M_{cr} = \frac{f_r L}{6}(A_c + nA_s)$
Yielding of the steel faceplates at the tension end of the wall	$\alpha_y^t = \frac{\sqrt{\rho'}}{\sqrt{\rho'+1}+\sqrt{\rho'}}$	$\phi_y^t = \frac{\varepsilon_y}{L(1-\alpha)}$	$M_y^t = A_s f_y^e L_y^t$
	$L_y^t = L(\frac{2\alpha^3 - 3\alpha^2 - \rho'}{12\rho'(\alpha-1)})$		
Yielding of the steel faceplates at the compression end of the wall	$\alpha_y^c = \frac{1}{\gamma+2}$	$\phi_y^c = \frac{\varepsilon_y}{L\alpha}$	$M_y^c = \beta_1\beta_2 f_c' A_c L_c' + A_s f_y^e L_s'$
	$L_c' = \alpha L(\frac{1-\beta_2\alpha}{2})$, $L_s' = \alpha L(1-\frac{4}{3}\alpha)$		
Maximum concrete compressive strain equal to ε_{c0}	$\alpha_u = \frac{1}{\gamma+2}$	$\phi_u = \frac{\varepsilon_{c0}}{L\alpha}$	$M_u = \beta_1\beta_2 f_c' A_c L_c'' + A_s f_y^e L_s''$
	$L_c'' = \alpha L(\frac{1-\beta_2\alpha}{2})$, $L_s'' = \alpha L(1-\alpha-\frac{\alpha k^2}{3})$		

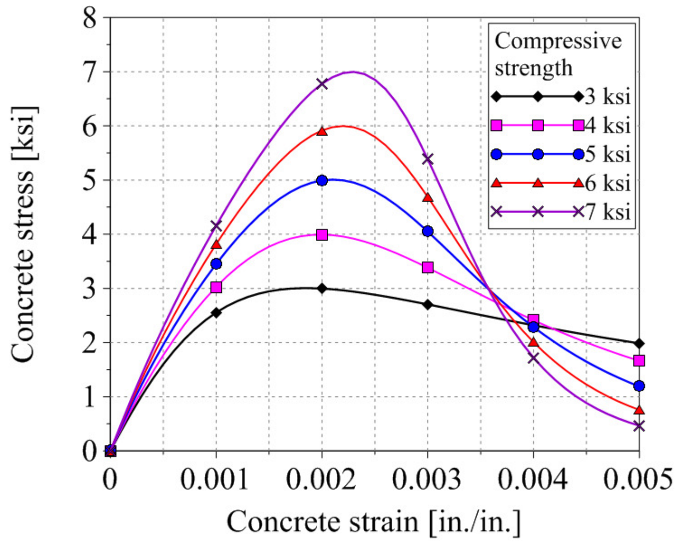

Figure 8-9 Unconfined uniaxial compressive stress-strain relationships for the infill concrete

Table 8-4 Values of the stress block parameters

f_c' (ksi)	Steel faceplate yielding at the compression end of the wall						Maximum concrete compressive strain equal to ε_{c0}	
	$f_y = 36$ ksi		$f_y = 45$ ksi		$f_y = 60$ ksi			
	β_1	β_2	β_1	β_2	β_1	β_2	β_1	β_2
3	0.77	0.73	0.83	0.74	0.92	0.78	0.91	0.77
4	0.68	0.71	0.75	0.72	0.88	0.75	0.88	0.75
5	0.62	0.70	0.69	0.71	0.84	0.73	0.87	0.74
6	0.57	0.70	0.64	0.70	0.80	0.72	0.86	0.73
7	0.54	0.69	0.61	0.70	0.76	0.71	0.83	0.72

8.2.4 Steel Material

Consistent with the development of a simplified procedure, the flexural strength of the faceplates is calculated assuming a steel stress, f_y', equal to the average of the yield and tensile strengths of the steel faceplates.

8.2.5 Flexure-Shear Interaction

The effect of shear force on the moment-curvature relationship is considered by reducing the yield stress of the steel faceplates. The effect of flexure-shear interaction on the response of the infill concrete is ignored. An effective yield stress is:

$$f_y^e = \sqrt{f_y'^2 - 3\tau^2} \tag{8-75}$$

which is based on the Von-Mises yield condition and assumes zero horizontal stress along the length of the steel faceplates.

The equivalent shear stress in the steel faceplates, τ in (8-75), is calculated by dividing the shear force associated with the flexural resistance of the steel faceplates, by the cross-sectional area of the faceplates. The shear force associated with the flexural resistance of the steel faceplates can be calculated by dividing the flexural strength of the steel faceplates, $A_s f'_y L''_s$ in Table 8-3, by the moment-to-shear ratio of the SC wall panel (M/V). Substituting $\tau = f'_y L''_s / (M/V)$ into (8-75):

$$f_y^e = f'_y(\sqrt{1-\zeta^2}) \tag{8-76}$$

where ζ is:

$$\zeta = \sqrt{3}\left(\frac{3\gamma+3-k^2}{3(\gamma+2)^2}\right)\left(\frac{VL}{M}\right) \le 1 \tag{8-77}$$

and γ is calculated using equation included in Table 8-2. The effective yield stress of the steel faceplates is a function of the concrete uniaxial compressive strength, the yield stress of the steel faceplates, the reinforcement ratio, and the normalized moment-to-shear ratio (M/VL)[1]. Note that the normalized moment-to-shear ratio is identical to the wall aspect ratio (H/L) for a single story wall panel of height H and length L. The influence of the normalized moment-to-shear ratio and concrete strength on f_y^e is presented in Figure 8-10.

Results are presented in Figure 8-10 for a wall panel that is 60 in. long, 10 in. thick, and constructed with 0.25- in. thick steel faceplates that have a yield strength of 36 ksi. Figure 8-10 indicates that a) the yield stress is significantly reduced for aspect ratio less than one on account of flexure-shear interaction, and b) the reduction in yield stress diminishes with increasing concrete compressive strength because flexure-shear interaction decreases with an increase in the shear load resisted by the infill concrete.

[1] Equations (8-76) and (8-77) indicate that the effective yield stress of the steel faceplates is a function of γ and the normalized moment-to-shear ratio (M/VL). The parameter γ is calculated using concrete uniaxial compressive strength, yield stress of the steel faceplates, and reinforcement ratio (see Table 8-2).

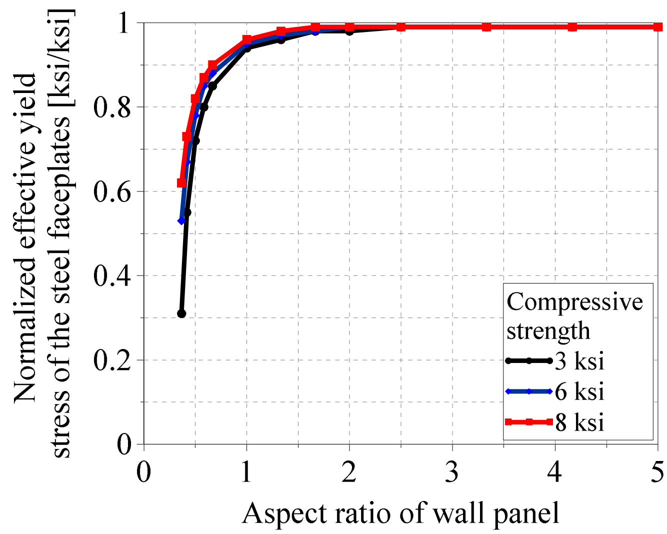

Figure 8-10 Effective yield stress of the steel faceplates

8.2.6 Vertical Discretization of the SC Wall Panel

The vertical discretization of an SC wall panel will affect the calculation of response because the effects of flexure-shear interaction change continuously. Results are presented in Figure 8-11 for wall panels that are 150 in. long, 10 in. thick, with 0.19-in. thick steel faceplates having a yield strength of 36 ksi, and aspect ratios of 0.5, 1.0, and 2.0. The results of Figure 8-11 indicate that the use of 10 sub-elements between points of application of lateral load is sufficient for analysis: increasing the number of sub-elements to 20 and 50 does not measurably change the results.

8.2.7 Validation of the Simplified Procedure

The simplified monotonic analysis procedure is validated using results of finite element analysis of 36 rectangular SC walls. The four design variables considered were 1) aspect ratio (0.5, 1.0 and 2.0), 2) reinforcement ratio (2% to 5%), 3) wall thickness (10, 20 and 30 inches), and 4) concrete compressive strength (4 ksi and 7 ksi). Validation of the baseline model, as presented in Chapter 6, was performed by simulation of the nonlinear cyclic in-plane behavior of four large-scale rectangular SC walls tested at the University at Buffalo.

Table 8-5 summarizes the design parameters for each analysis case used to validate the simplified procedure. Each entry case is identified by aspect ratio (L for low-aspect ratio, 0.5; I for intermediate-aspect ratio, 1.0; and H for high-aspect ratio, 2.0); concrete compressive strength (N for normal-strength concrete and I for intermediate-strength concrete); thickness; and reinforcement ratio. For example, LAN10-4 denotes a 10 in. thick, low-aspect ratio SC wall constructed with normal-strength concrete ($f_c' = 4$ ksi) and a reinforcement ratio of 4% ($= 2t_s / T = 0.04$, where T is the overall thickness of the wall: $t_c + 2t_s$). In Table 8-5, H, L, and T are the height, length, and the overall thickness of the walls, respectively. To speed the simulations but retain a reasonable scale for the modeled walls, the length of the walls was set to 150 inches. The heights of the low-, intermediate- and high-aspect ratio SC walls were selected to achieve the desired aspect ratios of 0.5, 1.0, and 2.0, respectively. The spacing of the studs and tie rods were 5 in. and 20 in., respectively. The diameter of the studs and tie rods was 0.38 in. The spacings and diameter of the studs and tie rods were based on the specifications proposed in AISC N690s1 (2014).

The smeared crack Winfrith model (MAT085) in LS-DYNA was used to model the infill concrete. The uniaxial compressive strength of the concrete was assumed to be 4 ksi and 7 ksi for normal- and intermediate-strength concrete, respectively. The plastic-damage model, Mat-Plasticity-With-Damage (MAT081) in LS-DYNA was used for the steel faceplates and connectors. ASTM A36 steel was assumed for the steel faceplates, with yield and tensile strengths of 38 and 55 ksi, respectively. Table 8-6 summarizes the material properties assumed for the DYNA models. Friction between the infill concrete and the steel faceplates, the infill concrete and the baseplate, and the baseplate and the steel plate embedded in the foundation block were considered using the Contact-Automatic-Surface-To-Surface formulation, with a coefficient of friction 0.5 (see Section 6.4.3). The steel faceplates were tied to the baseplate using the kinematic constraint Contact-Tied-Shell-Edge-To-Surface. The studs and tie rods were coupled to the infill concrete elements using Constrained-Lagrange-In-Solid. Beam elements were used to represent the studs and tie rods. Eight-node solid elements were used to model the infill concrete, and four-node shell elements were used for the steel faceplates. The infill concrete was modeled with 1 in. × 1 in. × 1 in. elements and the steel faceplates were modeled with 1 in. × 1 in. elements. The walls were rigidly connected to an infinitely stiff base.

Figure 8-12 through Figure 8-17 present the DYNA-predicted shear force-displacement relationships together with those predicted using the proposed method calculated using 75 sub-elements over the height of the wall panel. The proposed method accurately predicts the monotonic in-plane response of the SC walls with different aspect ratios, reinforcement ratios, concrete strengths, and wall thicknesses up to the point of maximum shear resistance. The peak shear resistance of the low-aspect ratio walls is slightly over-estimated.

Table 8-5 Properties of the DYNA models

No.	SC wall type	Model	Concrete strength (psi)	Aspect ratio	$H \times L \times T$ (in.×in.×in.)	t_s (in.)	Reinforcement ratio (%)
1	Low-aspect ratio SC walls	LAN10-4	4000	0.50	75 × 150 × 10	3/16	3.8
2		LAH10-4	7000	0.50	75 × 150 × 10	3/16	3.8
3		LAN10-5	4000	0.50	75 × 150 × 10	1/4	5.0
4		LAH10-5	7000	0.50	75 × 150 × 10	1/4	5.0
5		LAN20-2	4000	0.50	75 × 150 × 20	3/16	1.9
6		LAH20-2	7000	0.50	75 × 150 × 20	3/16	1.9
7		LAN20-5	4000	0.50	75 × 150 × 20	1/2	5.0
8		LAH20-5	7000	0.50	75 × 150 × 20	1/2	5.0
9		LAN30-2	4000	0.50	75 × 150 × 30	5/16	2.1
10		LAH30-2	7000	0.50	75 × 150 × 30	5/16	2.1
11		LAN30-5	4000	0.50	75 × 150 × 30	3/4	5.0
12		LAH30-5	7000	0.50	75 × 150 × 30	3/4	5.0
13	Intermediate-aspect ratio SC walls	IAN10-4	4000	1.00	150 × 150 × 10	3/16	3.8
14		IAH10-4	7000	1.00	150 × 150 × 10	3/16	3.8
15		IAN10-5	4000	1.00	150 × 150 × 10	1/4	5.0
16		IAH10-5	7000	1.00	150 × 150 × 10	1/4	5.0
17		IAN20-2	4000	1.00	150 × 150 × 20	3/16	1.9
18		IAH20-2	7000	1.00	150 × 150 × 20	3/16	1.9
19		IAN20-5	4000	1.00	150 × 150 × 20	1/2	5.0
20		IAH20-5	7000	1.00	150 × 150 × 20	1/2	5.0
21		IAN30-2	4000	1.00	150 × 150 × 30	5/16	2.1
22		IAH30-2	7000	1.00	150 × 150 × 30	5/16	2.1
23		IAN30-5	4000	1.00	150 × 150 × 30	3/4	5.0
24		IAH30-5	7000	1.00	150 × 150 × 30	3/4	5.0
25	High-aspect ratio SC walls	HAN10-4	4000	2.00	300 × 150 × 10	3/16	3.8
26		HAH10-4	7000	2.00	300 × 150 × 10	3/16	3.8
27		HAN10-5	4000	2.00	300 × 150 × 10	1/4	5.0
28		HAH10-5	7000	2.00	300 × 150 × 10	1/4	5.0
29		HAN20-2	4000	2.00	300 × 150 × 20	3/16	1.9
30		HAH20-2	7000	2.00	300 × 150 × 20	3/16	1.9
31		HAN20-5	4000	2.00	300 × 150 × 20	1/2	5.0
32		HAH20-5	7000	2.00	300 × 150 × 20	1/2	5.0
33		HAN30-2	4000	2.00	300 × 150 × 30	5/16	2.1
34		HAH30-2	7000	2.00	300 × 150 × 30	5/16	2.1
35		HAN30-5	4000	2.00	300 × 150 × 30	3/4	5.0
36		HAH30-5	7000	2.00	300 × 150 × 30	3/4	5.0

Table 8-6 Material properties for the DYNA analysis

Material		Young's modulus (ksi)	Poison ratio	Uniaxial compressive strength (ksi)	Uniaxial tensile strength (ksi)	Yield strength (ksi)	Ultimate strength (ksi)	Crack width (in.)	Agg. Size (in.)
Infill concrete	Normal strength	3600	0.18	4.0	0.3	-	-	0.0027	0.75
	Intermediate strength	4800	0.18	7.0	0.6	-	-	0.002	0.75
Faceplate		29000	0.30	-	-	36	55	-	-
Connectors		29000	0.30	-	-	50	75	-	-

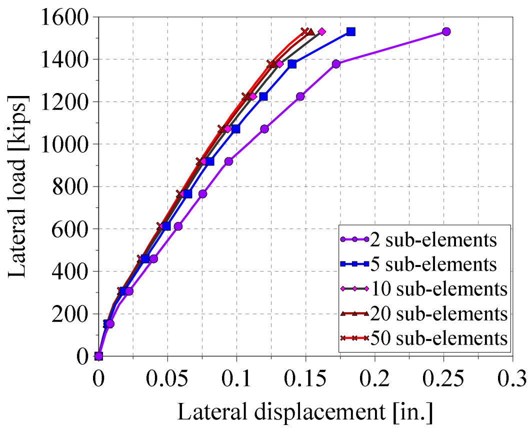

(a) Aspect ratio of 0.5

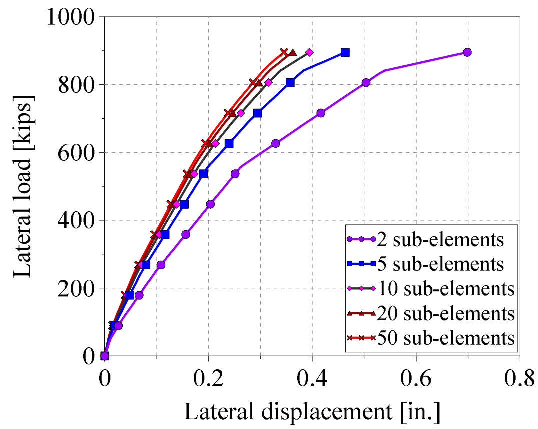

(b) Aspect ratio of 1.0

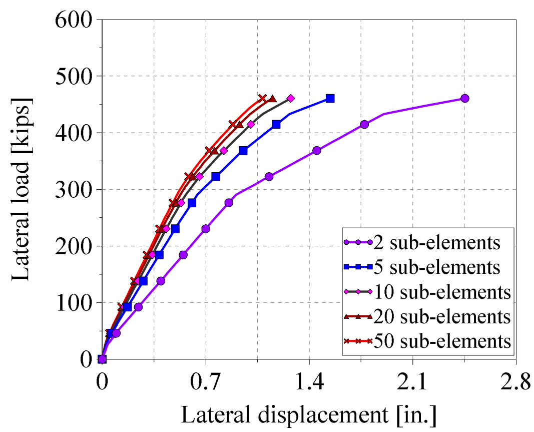

(c) Aspect ratio of 2.0

Figure 8-11 Force-displacement relationships of SC walls with differing numbers of sub-elements

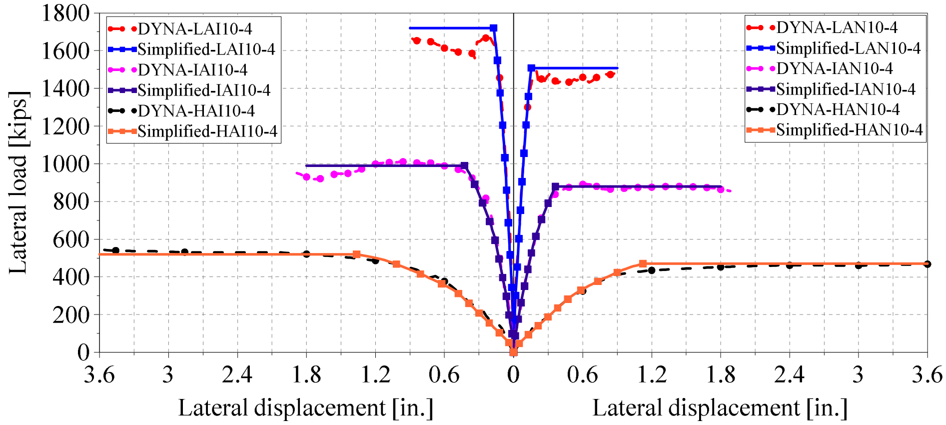

Figure 8-12 Force-displacement relationship for 10-in. thick walls with 3.8% reinforcement ratio

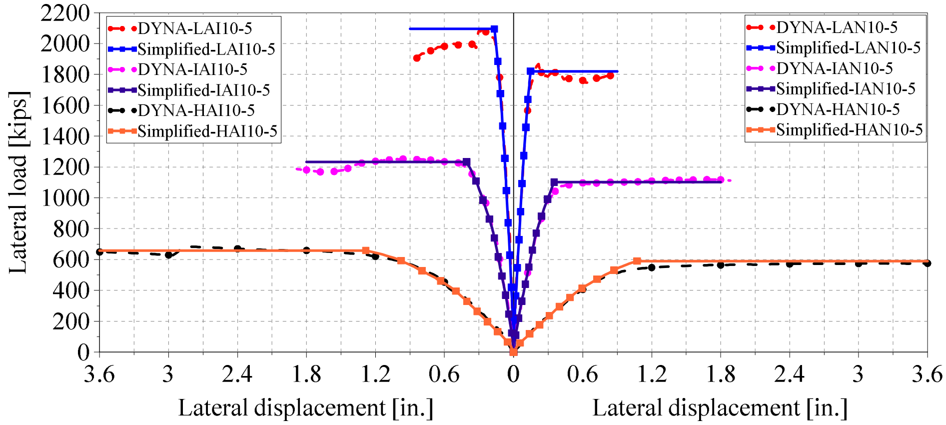

Figure 8-13 Force-displacement relationship for-10 in. thick walls with 5.0% reinforcement ratio

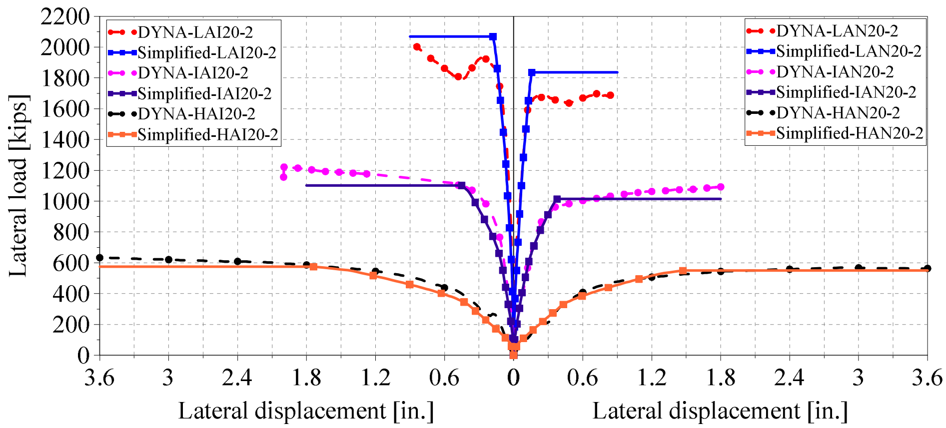

Figure 8-14 Force-displacement relationship for 20-in. thick walls with 1.9% reinforcement ratio

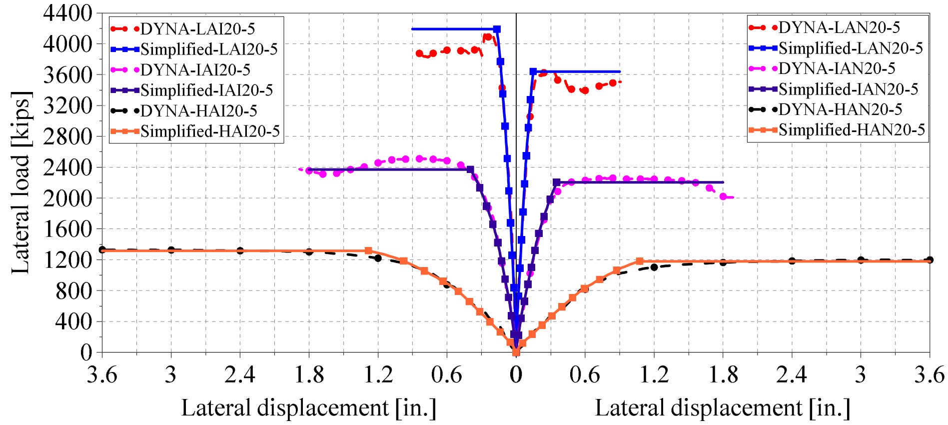

Figure 8-15 Force-displacement relationship for 20-in. thick walls with 5.0% reinforcement ratio

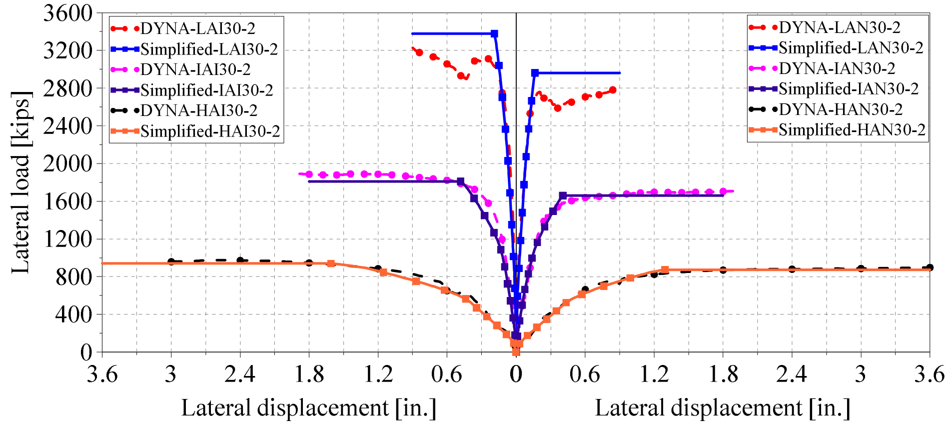

Figure 8-16 Force-displacement relationship for 30-in. thick walls with 2.1% reinforcement ratio

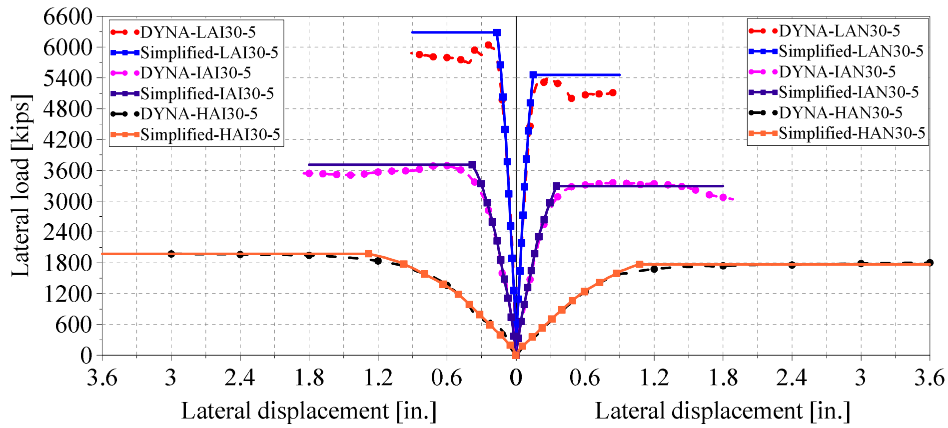

Figure 8-17 Force-displacement relationship for 30-in. thick walls with 5.0% reinforcement ratio

Figure 8-18 presents the components of displacement for the analytically derived and DYNA-predicted force-displacement relationships for the 10-in. thick rectangular SC walls with a reinforcement ratio of 3.8% and aspect ratios of 0.5, 1.0, and 2.0. The shear displacements dominate for an aspect ratio of 0.5 and the flexural displacements dominate for aspect ratios greater than 1.0, which are expected outcomes. The lateral displacement corresponding to shear strength is underestimated because the stiffness reduction due to the out-of-plane buckling of the steel faceplates is not considered in the simplified procedure but is captured in the DYNA analysis. These results further confirmed the utility of the proposed simplified method for the monotonic analysis of rectangular SC wall panels.

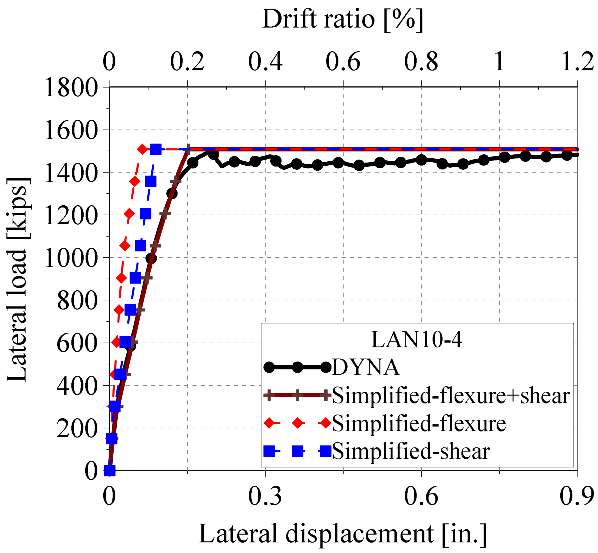

(a) Aspect ratio of 0.5

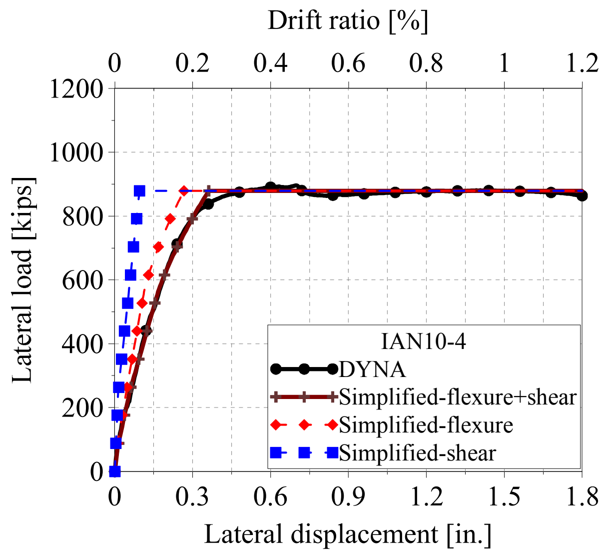

(b) Aspect ratio of 1.0

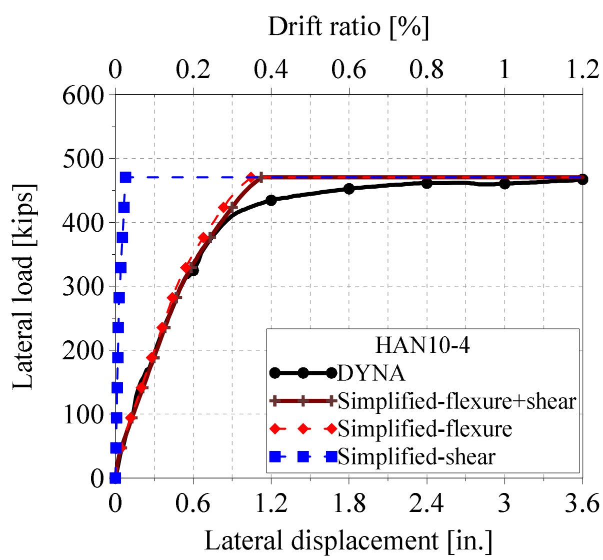

(c) Aspect ratio of 2.0

Figure 8-18 Analytically- and DYNA-predicted force-displacement relationships for 10-in. thick wall with 3.8% reinforcement ratio

8.2.8 Force-Displacement Response of Multi-Story SC Walls

Single story walls are rarely used in practice and so a simplified method must be appropriate for analysis of multi-story SC walls. Small-size walls are analyzed to take advantage of prior work and to minimize the computational expense, without sacrificing rigor. Two three-story walls are analyzed using the proposed method in MATLAB and the finite element method using DYNA, with the same material models, elements, and boundary conditions used previously for the analysis of the 36 rectangular SC walls. The length and height of the walls are 60 in. and 120 in., respectively. The thickness of the walls is 12 in.; the thickness of each steel faceplate is 0.19 in. Beams and columns are not included in the models. The SC walls are subjected to uniform and triangular distributions of lateral loads, as shown in Figure 8-19.

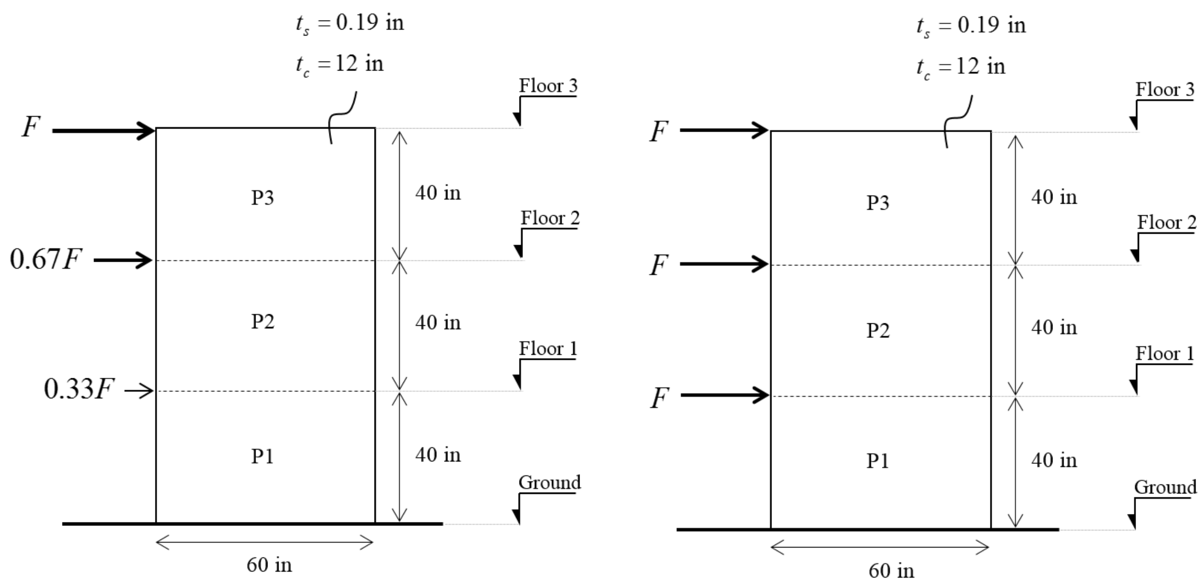

Figure 8-19 Elevation view of three-story SC walls subject to uniform and triangular loadings

The shear force-shear strain relationship for each panel of the three-story walls (P1, P2, and P3 presented in Figure 8-19) is calculated using the equations of Table 8-3. The moment-curvature relationship for each panel is calculated using an effective yield stress [(8-76)] that is a function of the moment-to-shear ratio (M/VL), which in turn depends on the vertical distribution of lateral loads above the panel.

The moment-to-shear ratio for P1 in both SC walls is presented below to illustrate the calculation. The level of the resultant of the lateral loads applied above P1 for the SC walls subjected to uniform and triangular distributions of lateral loads are calculated using (8-78) and (8-79), respectively:

$$h_r = \frac{F \times 3H + F \times 2H + F \times H}{F + F + F} = 2H \tag{8-78}$$

$$h_r = \frac{F \times 3H + 0.67F \times 2H + 0.33F \times H}{F + 0.67F + 0.33F} = 2.34H \tag{8-79}$$

The moment-to-shear ratio for P1 is calculated as $h_r / L = 1.33\ (2H / L)$ and $= 1.56\ \ (2.34H / L)$ for the SC walls subjected to uniform and triangular distributions of lateral loads, respectively.

The flexural displacement at the top of each 40-in. tall panel is calculated using (8-1) with y_i as the distance between the center of ith sub-element of the panel and top of the three-story SC wall. Seventy five sub-elements are used for each of the three panels. The shear displacement at top of each panel is calculated using (8-2). The total displacement at the top of the wall is:

$$\Delta_t = (\Delta_{s1} + \Delta_{f1}) + (\Delta_{s2} + \Delta_{f2}) + (\Delta_{s3} + \Delta_{f3}) \tag{8-80}$$

where the rotation at the top of each wall panel is:

$$\theta_j = \theta_{j-1} + \sum_{i=1}^{m} \phi_i^j \Delta y_i^j \tag{8-81}$$

where i and j denote the sub-element and story numbers, respectively, and $\theta_0 = 0$. The displacement components and rotations at the tops of the panels are defined in Figure 8-20.

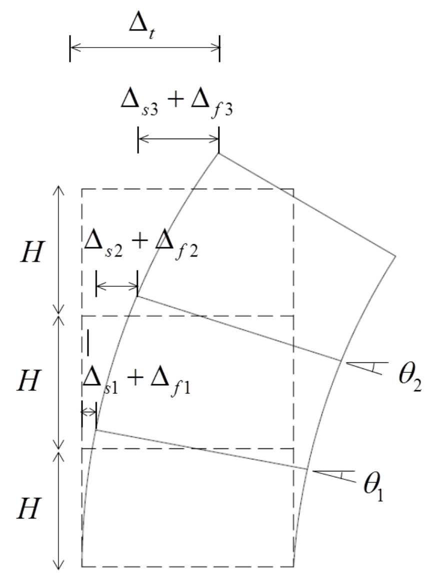

Figure 8-20 Displacement calculation in three-story SC wall

Responses per (8-80) are presented in Figure 8-21. The proposed method reasonably predict the monotonic response of this three-story SC wall subjected to both uniform and triangular loadings. The initial stiffness is accurately predicted and the peak shear strength is estimated with an error of less than 10%.

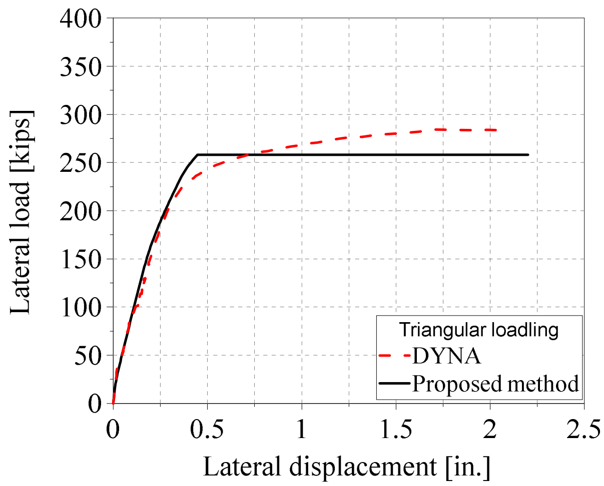

Figure 8-21 Analytically- and numerically-predicted responses of a three-story SC wall

8.3 Simulation of Cyclic Response

The Ibarra-Krawinkler Pinching (IKP) model proposed by Ibarra et al. (2005) is used to simulate the cyclic hysteretic response of SC walls. This model incorporates alternate cyclic deterioration modes (2005). Ibarra et al. successfully simulated the inelastic behavior of two tested RC columns subjected to axial and cyclic lateral loadings using this model. Gulec et al. (2011) used this model to simulate the cyclic behavior of seven low aspect ratio reinforced concrete walls.

8.3.1 Description of the IKP Model

The hysteretic model proposed by Ibarra et al. (2005) is defined using the piece-wise linear backbone curve presented in Figure 8-22(a) and the basic hysteretic rules presented in Figure 8-22(b). The backbone curve consists of a bilinear curve in the pre-peak-strength region and a linear curve in the post-peak-strength response. The unloading branch of the cyclic response is simulated using a linear curve. The reloading branch consists of two segments. The first reloading path (paths 3-4 and 7-8 in Figure 8-22(b)) is directed towards a break point (points 4 and 8) and the second path (paths 4-5 and 8-9) connects the break point to the point corresponding to the maximum displacement of the earlier cycles in the same quadrant (points 2 and 6 in

Figure 8-22(b)). The break point is a function of the maximum force ($F_{\max}$) and residual displacement (δ_{perl}) achieved in the previous cycle in the same quadrant, and is established using displacement and force coordinates equal to $(1-k_d)\delta_{perl}$ and $k_f F_{\max}$, respectively.

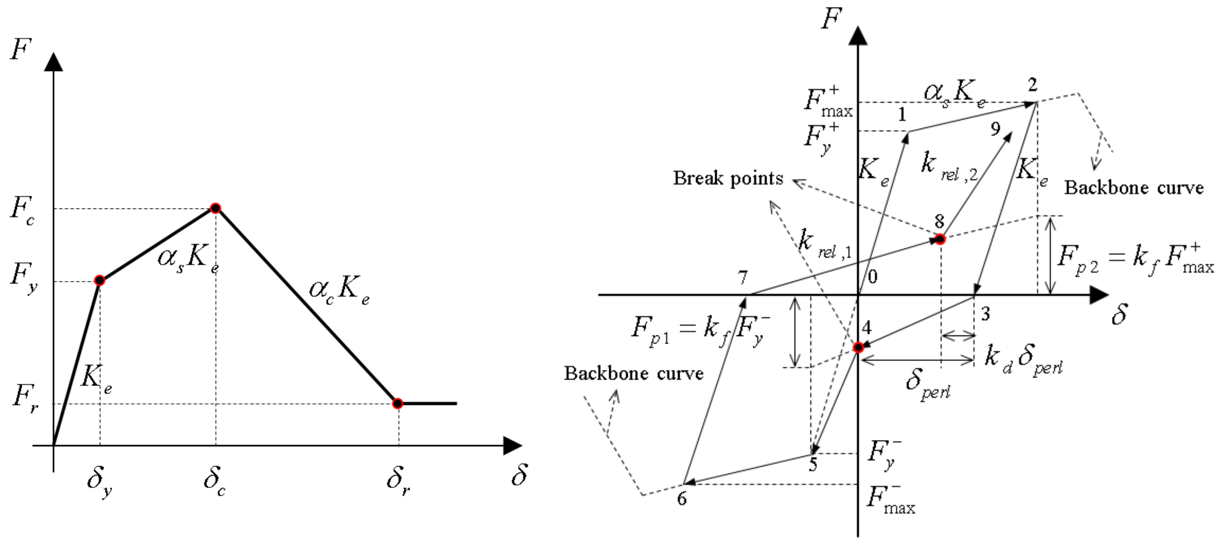

(a) Backbone curve (b) Hysteretic model

Figure 8-22 Pinching model proposed by Ibarra et al. (2005)

Four models of deterioration modes are considered in the IKP model, namely, the basic-strength, post-capping strength, unloading stiffness, and accelerated stiffness, as cartooned in Figure 8-23. Details are available in Ibarra et al. (2005).

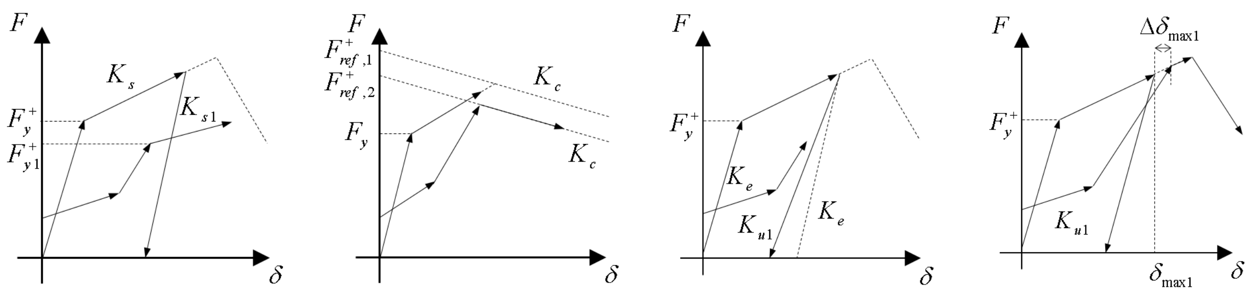

(a) Basic strength (b) Post-capping strength (c) Unloading-stiffness (d) Accelerated stiffness

Figure 8-23 Deterioration modes available with the IKP model

Ibarra et al. used an energy-based deterioration parameter to control deterioration. This parameter is based on the hysteretic energy dissipated in cyclic excursions and is calculated as:

$$\beta = (\frac{E_i}{E_t - \sum_{i=1}^{n} E_j})^d \tag{8-82}$$

8.3.2 Validation of the Cyclic Analysis

The accuracy of the predictions of IKP model is validated using the results of finite element cyclic analysis of 12 DYNA models selected from the 36 models used for monotonic analyses. The models selected for cyclic analyses are LAN10-5, LAI10-5, LAN20-2, LAI20-2, IAN10-5, IAI10-5, IAN20-2, IAI20-2, HAN10-5, HAI10-5, HAN20-2, and HAI20-2. The wall length in the DYNA model used for the cyclic analysis is set equal to 60 in. to reduce the computational effort. The same material models, elements, and boundary condition used for the monotonic analyses are adopted for the cyclic analyses.

Figure 8-24 presents the cyclic force-displacement relationship for LAN10-5. Pinching of the force-displacement response is evident in the post-peak-strength cycles.

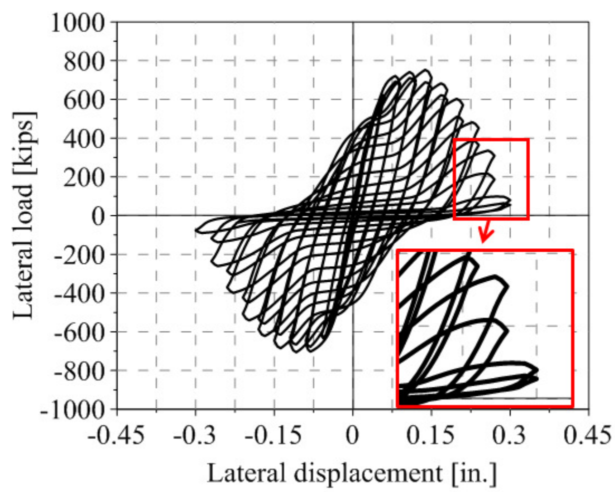

Figure 8-24 Cyclic force-displacement relationship of LAN10-5

The degree of pinching in the response of an SC wall is expected to be less than that of an RC wall having a cross-section with 1) identical dimensions to those of the infill concrete cross-section, and 2) a reinforcement ratio equal to the ratio of the cross-sectional area of the steel faceplates to the total cross-sectional area of the SC wall, since the cyclic response is governed by the hysteretic behavior of the steel faceplates after significant damage occurs in the infill concrete. The cyclic response of SC walls cannot be accurately simulated using the pinching model proposed originally by Ibarra et al. (2005)

A modification to the original IKP model is proposed for SC walls using 1) a tri-linear curve for the pre-peak-strength response that characterized the yielding of the steel faceplates at the tension and compression ends of the wall, and crushing of the infill concrete, 2) a bilinear curve for the unloading branch, and 3) a tri-linear curve for the re-loading branch. These modifications to the backbone curve and hysteretic force-displacement relationship of the IKP model are presented in Figure 8-25. Figure 8-25(a) presents the proposed backbone curve for cyclic simulations. Figure 8-25(b) presents the backbone curve of the IKP model (dotted line), the hysteretic force-displacement relationship proposed by Ibarra et al. (solid line), and the modified hysteretic force-displacement relationship (dashed line).

The unloading and reloading branches of the modified hysteretic force-displacement relationship consisted of two segments with stiffness $k'_{unl,1}$ and $k'_{unl,2}$, and three segments with stiffness $k'_{rel,1}$, $k'_{rel,2}$, and $k'_{rel,3}$, respectively. The first unloading path targets the force equal to a fraction, ξ, of the maximum force, $F_{\max}$, achieved in the same quadrant in the previous cycle. The first control point of the reloading branch (points a and d in Figure 8-25(b)) on the force axis is established using the coordinate of the residual displacement in the previous cycle and the value of stiffness $k'_{rel,1}$. The calculated force corresponding to this point should not exceed $k_f F_{\max}$ (see Figure 8-25(b)). The second part of the reloading branch targets the second control point of the reloading branch (points b and e in Figure 8-25(b)) with the displacement and force coordinates of $(1-k_d)\delta_{perl}$ and $k_f F_{\max}$, respectively. The third part of the reloading branch targets the maximum displacement achieved in the previous cycle.

The Modified IKP (MIKP) model is implemented in MATLAB (2012) and used to simulate the DYNA-predicted cyclic responses of selected SC walls. The MATLAB code is provided in Appendix D. The backbone curve in the pre-peak-strength region is calculated using the approach proposed for the monotonic analysis of SC walls, as described in Section 8.3. The slope of the backbone curve in the post-peak-strength response and pinching, deterioration, and rate parameters are calculated using the results of finite element analysis of the 12 DYNA models. The basic strength and post-capping strength deterioration modes are not considered since these modes simulate the degradation of the backbone curve under cyclic loading. The calculated values of the parameters for the backbone curve are presented in Table 8-7. The cyclic force-displacement relationship of a rectangular SC wall is defined using 1) the displacements and forces in the pre-peak-strength region predicted by the proposed method for monotonic analysis, 2) the slope of the backbone curve in the post-peak-strength region, and 3) the values of the pinching, deterioration, and rate parameters, as described below.

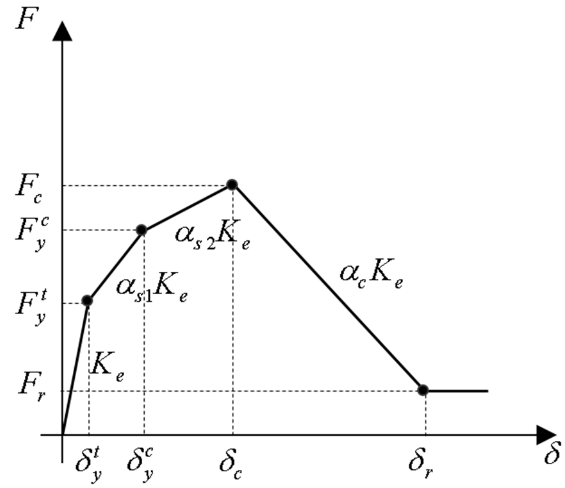

(a) Backbone curve

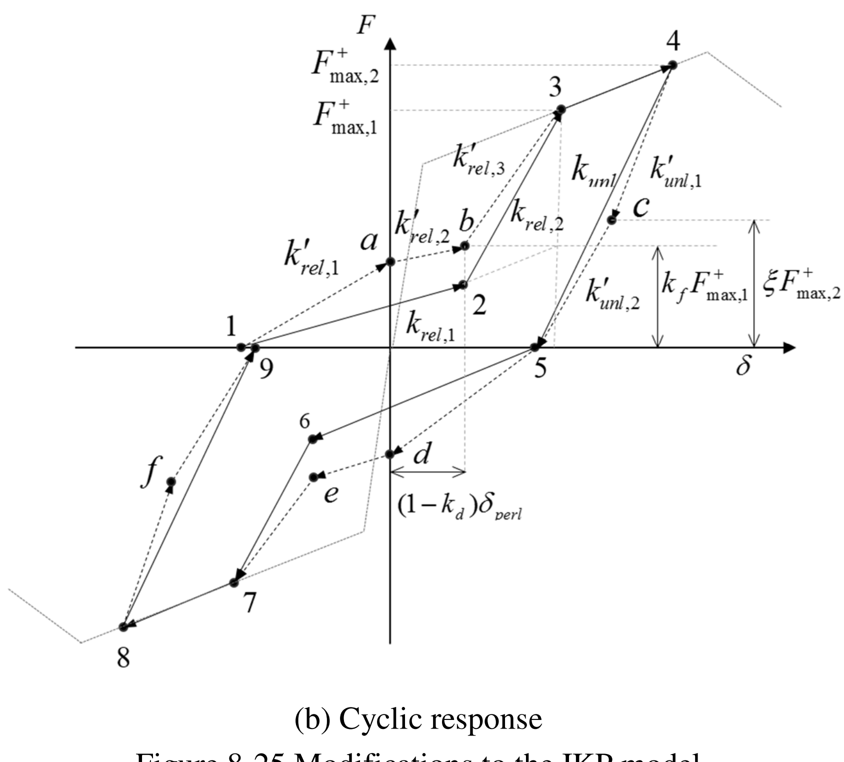

(b) Cyclic response

Figure 8-25 Modifications to the IKP model

In Table 8-7, the effective stiffness, K_e^p, is defined as the ratio of the force associated with the yielding of the steel faceplates on the tension end of the wall to its corresponding displacement. The shear forces and displacements corresponding to flexural strength, F_c and δ_c, are presented in columns three and four of Table 8-7. The backbone curve is fully defined by the displacements and forces corresponding to the pre-peak-strength control points, namely, the yielding of the steel faceplates at the tension and compression ends of the wall (presented in Figure 8-25(a)), and the slope of the backbone curve in the post-peak-strength region. The ratios of the displacement and force at the control points to the displacement and force at peak strength are presented in columns 5 through 8 of Table 8-7, where the forces and displacements are calculated using the method proposed previously for monotonic analysis. The ratio of post-peak stiffness to effective stiffness is presented in column 9.

Table 8-7 Calculated backbone parameters

Specimen (1)	K_e^p $(\frac{\text{kips}}{\text{in.}})$ (2)	F_c (kips) (3)	δ_c (in.) (4)	$\frac{F_y^t}{F_c}$ $(\frac{\text{kips}}{\text{kips}})$ (5)	$\frac{F_y^c}{F_c}$ $(\frac{\text{kips}}{\text{kips}})$ (6)	$\frac{\delta_y^t}{\delta_c}$ $(\frac{\text{in.}}{\text{in.}})$ (7)	$\frac{\delta_y^c}{\delta_c}$ $(\frac{\text{in.}}{\text{in.}})$ (8)	α_c (%) (9)
LAN10-5	15196	751	0.12	0.59	0.87	0.24	0.39	-18
LAI10-5	16743	862	0.11	0.56	0.87	0.26	0.46	-31
LAN20-2	16806	750	0.12	0.58	0.95	0.22	0.48	-16
LAI20-2	19138	846	0.12	0.57	0.94	0.21	0.52	-21
IAN10-5	4018	447	0.20	0.64	0.93	0.35	0.59	-8
IAI10-5	4470	503	0.20	0.59	0.90	0.33	0.63	-12
IAN20-2	4533	415	0.20	0.60	0.96	0.27	0.71	-13
IAI20-2	5430	450	0.20	0.57	0.95	0.24	0.78	-12
HAN10-5	692	230	0.57	0.65	0.93	0.38	0.63	-16
HAI10-5	757	259	0.57	0.60	0.90	0.36	0.68	-17
HAN20-2	722	212	0.57	0.60	0.96	0.31	0.81	-17
HAI20-2	800	229	0.60	0.57	0.95	0.27	0.88	-19

Table 8-8 presents the values of the pinching (k_f, k_d, ξ), deterioration ($\gamma_{unl,1}$, $\gamma_{unl,2}$, $\gamma_{rel,1}$, γ_a), and rate parameters ($d_{unl,1}$, $d_{unl,2}$, $d_{rel,1}$, d_a) calibrated from the DYNA-predicted force-displacement relationships. The hysteretic energy dissipation capacity corresponding to each deterioration mode is calculated by multiplying the calculated deterioration parameters by the product of the peak force and its corresponding displacement ($=F_c\delta_c$). Table 8-8 shows that the pinching parameter,

k_f, is affected by the reinforcement ratio and the moment-to-shear ratio. The other two pinching parameters, k_d and ξ, presented in the third and fourth columns of Table 8-8, are not affected by the design variables considered in this study. The deterioration parameters and rate parameter corresponding to the reloading stiffness ($k'_{rel,1}$ presented in Figure 8-25(b)) deterioration mode are influenced by the moment-to-shear ratio. The analysis results are not substantially affected by the rate parameters corresponding to the unloading stiffness and accelerated stiffness modes and the best results are obtained by setting these parameters equal to 1.0.

Table 8-8 Calculated pinching, deterioration, and rate parameters

Specimen	k_f	k_d	ξ	$\gamma_{unl,1}$	$\gamma_{unl,2}$	$\gamma_{rel,1}$	γ_a	$d_{unl,1}$	$d_{unl,2}$	$d_{rel,1}$	d_a
LAN10-5	0.60	0.30	0.50	25	20	20	20	1	1	0.45	1
LAI10-5	0.60	0.30	0.50	25	20	20	20	1	1	0.45	1
LAN20-2	0.40	0.30	0.50	25	20	20	20	1	1	0.45	1
LAI20-2	0.40	0.30	0.50	25	20	20	20	1	1	0.45	1
IAN10-5	0.40	0.30	0.50	40	35	20	40	1	1	0.35	1
IAI10-5	0.40	0.30	0.50	40	35	20	40	1	1	0.35	1
IAN20-2	0.30	0.30	0.50	40	35	20	40	1	1	0.35	1
IAI20-2	0.30	0.30	0.50	40	35	20	40	1	1	0.35	1
HAN10-5	0.30	0.30	0.50	40	35	20	40	1	1	0.25	1
HAI10-5	0.30	0.30	0.50	40	35	20	40	1	1	0.25	1
HAN20-2	0.30	0.30	0.50	40	35	20	40	1	1	0.25	1
HAI20-2	0.30	0.30	0.50	40	35	20	40	1	1	0.25	1

On the basis of the finite element analyses of the 12 DYNA models selected from the 36 models, the post-peak stiffness of the backbone curve can be considered to be 15% to 20% of the effective stiffness of the rectangular SC wall, as presented in the last column of Table 8-7. The calculated values of the pinching, deterioration, and rate parameters of Table 8-8 can be used to simulate the hysteretic response of rectangular SC walls with an aspect ratio between 0.5 to 2, a reinforcement ratio between 2% and 5%, and low axial loads.

Figure 8-26 presents the analytical- and DYNA-predicted force-displacement relationships for the twelve SC walls: SC walls with aspect ratios of 0.5, 1.0, and 2.0, thickness of 10 in. and 20 in., and reinforcement ratios of 2% and 5%. The MIKP model reasonably simulates the cyclic response of the SC walls: the post-peak pinched behavior, the continuity of the response in the pre- and post-peak-strength regions, and the unloading branch of the cyclic force-displacement relationship are captured well.

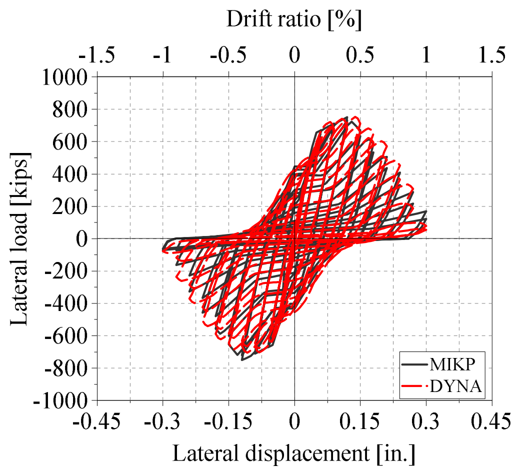

(a) LAN10-5

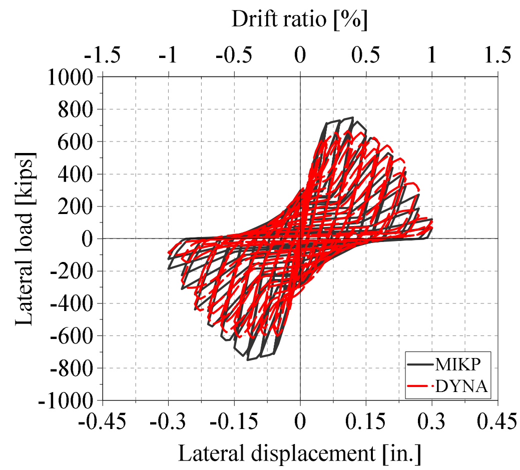

(b) LAN20-2

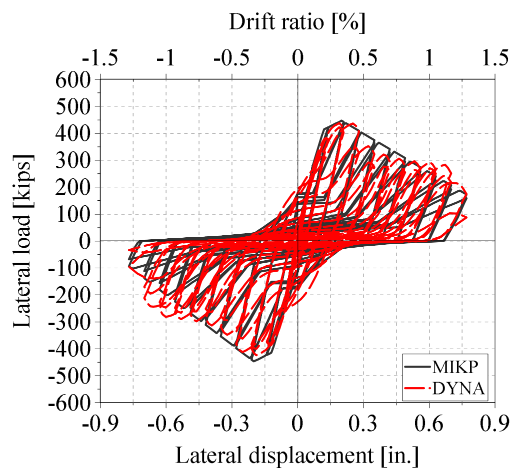

(c) IAN10-5

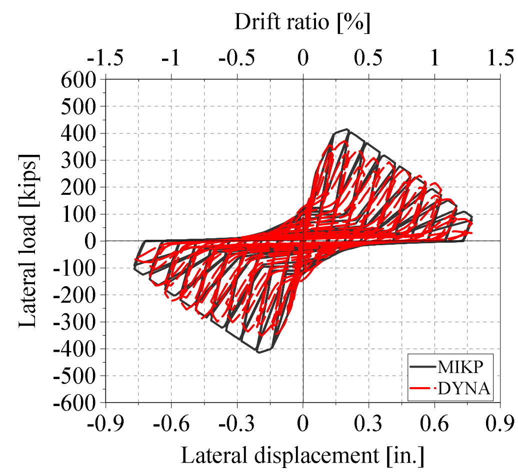

(d) IAN20-2

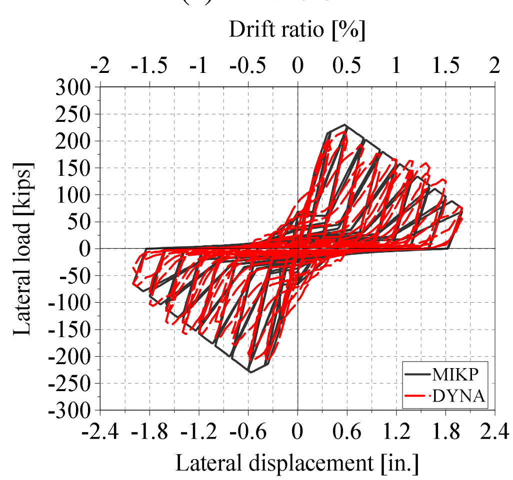

(e) HAN10-5

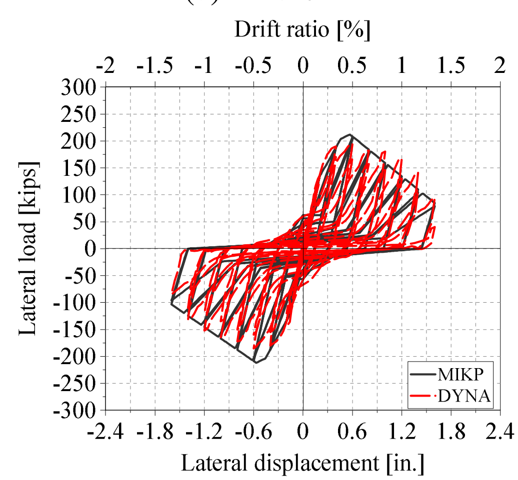

(f) HAN20-2

Figure 8-26 Cyclic modeling of SC walls using the MIKP model

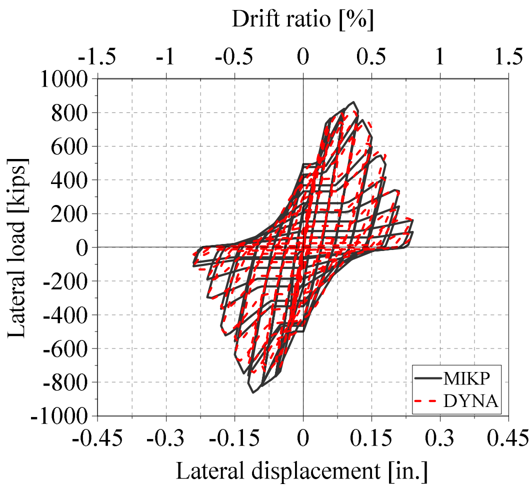

(a) LAH10-5

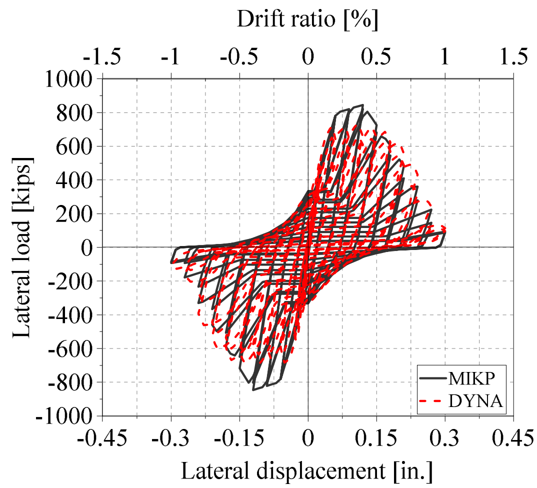

(b) LAH20-2

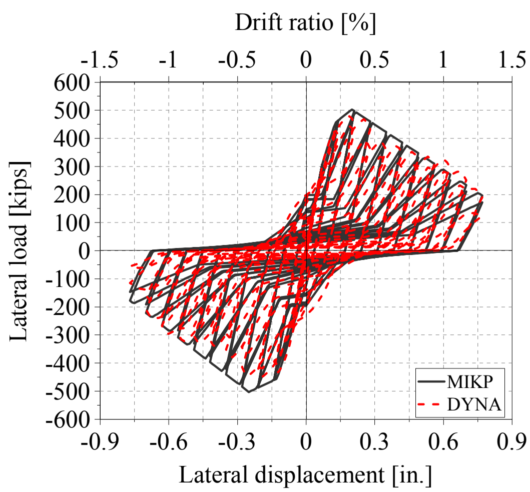

(c) IAH10-5

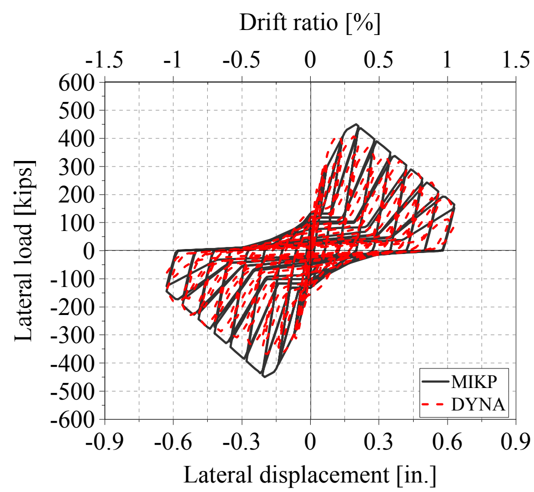

(d) IAH20-2

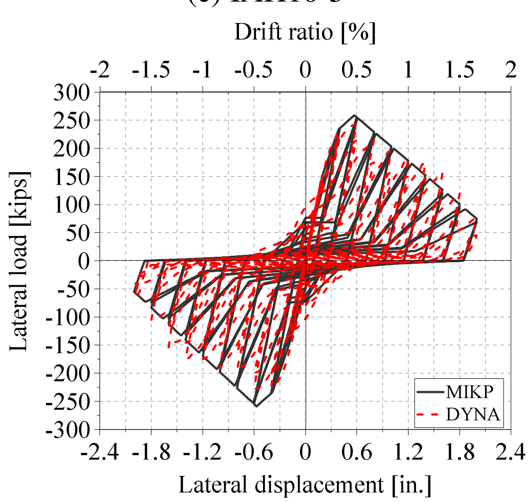

(e) HAH10-5

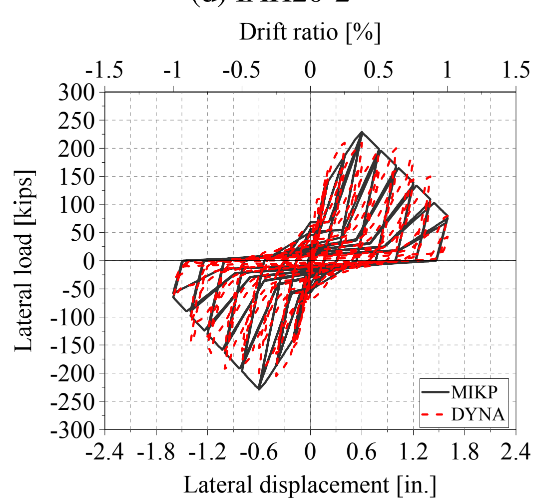

(f) HAH20-2

Figure 8-26 Cyclic modeling of SC walls using the MIKP model (cont.)

8.4 Initial Stiffness of SC Walls with a Baseplate Connection

The experimental study of the four SC walls, described in Chapter 5, indicated that the rotation of the base connection governed their total lateral displacement. This result identifies the importance of characterizing the stiffness of the connection of an SC wall to its foundation.

In this section, an analytical approach is proposed to characterize the rotational flexibility of an SC wall with a baseplate connection [Epackachi et al. (2015c)]. The method is validated using data from the tests presented in Chapter 5.

To calculate the initial stiffness of an SC wall with a baseplate connection, the wall was modeled as a cantilever beam with a rotational spring at its base. A schematic drawing of the model is presented in Figure 8-27.

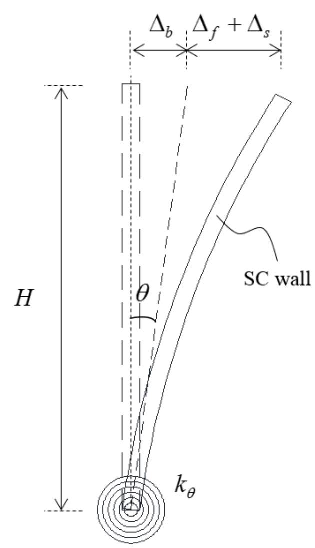

Figure 8-27 SC wall model for initial stiffness calculation

The total lateral displacement at top of the wall, Δ_t, is calculated as:

$$\Delta_t = \Delta_b + \Delta_f + \Delta_s \qquad (8\text{-}83)$$

The initial stiffness of the SC wall can be calculated as:

$$\frac{1}{K_t} = \frac{1}{K_b} + \frac{1}{K_f} + \frac{1}{K_s} \qquad (8\text{-}84)$$

The initial flexural and shear stiffness of the SC wall can be estimated as:

$$K_f = \frac{3EI_g}{H^3} \tag{8-85}$$

$$K_s = \frac{GA_g}{\kappa H} \tag{8-86}$$

where EI_g is the flexural rigidity of the SC wall and is calculated as the sum of the flexural rigidities of the steel faceplates ($E_s I_s$) and the infill concrete ($E_c I_c$), and GA_g is the shear rigidity of the SC wall, calculated as the sum of the shear rigidities of the steel faceplates ($G_s A_s$) and the infill concrete ($G_c A_c$).

Assuming that the moment-rotation relationship of the spring at the wall base is $M = K_\theta \theta$, the lateral stiffness K_b is calculated as:

$$K_b = K_\theta / H^2 \tag{8-87}$$

Substituting (8-85), (8-86), and (8-87) into (8-84), the lateral stiffness of the SC wall is calculated as:

$$K_t = \left(\frac{\kappa}{GA_g} H + \frac{1}{k_\theta} H^2 + \frac{1}{3EI_g} H^3\right)^{-1} \tag{8-88}$$

An analytical method is developed to characterize the rotational stiffness of a baseplate connection of a rectangular SC wall to its foundation block. The following assumptions are made: (1) the SC wall is modeled as a cantilever beam with elastic behavior, (2) the neutral axis is located at the compressive toe of the wall, (3) the effects of axial force are insignificant, (4) the effect of post-tensioning the threaded bars is small[1], and (5) the configuration of the threaded bars in the baseplate connection is that presented in Figure 8-28.

---

[1] The analytical calculations presented later in this section show that the base rotation is signifacntly affected by the out-of-plane deformation of the baseplate and not by the extension of the threaded bars. Accordingly, the post-tensioning of a baseplate to its foundation using threaded bars will have no significant effect on the rotational stiffness of the baseplate connection.

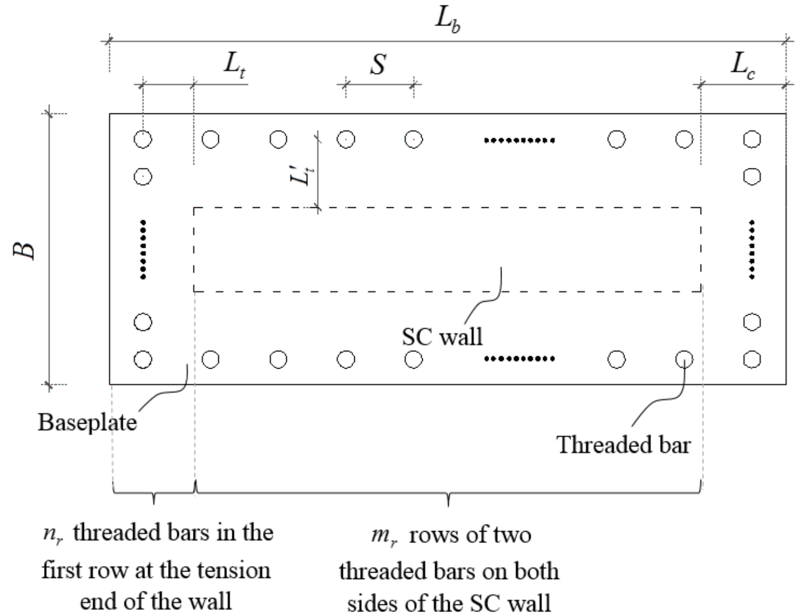

Figure 8-28 Plan view of an SC wall

Figure 8-29 and Figure 8-30 present elevation and cross-section views, respectively. These figures show the deformations of the threaded bars and baseplate, and the distribution of tensile forces in threaded bars and bearing stress on the foundation.

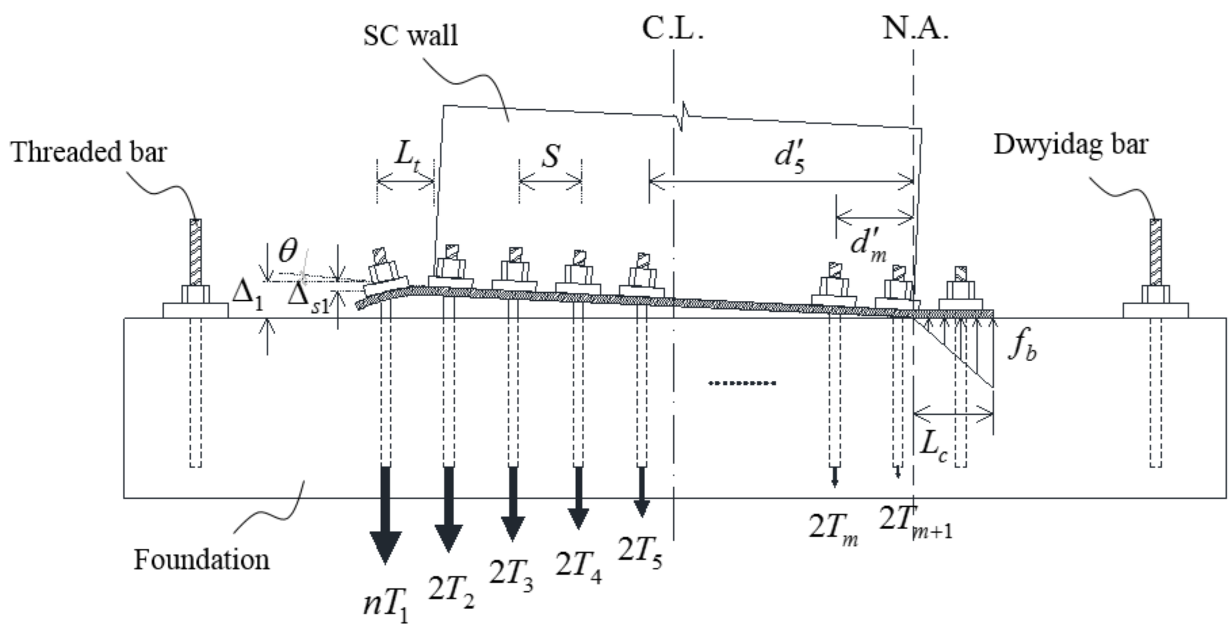

Figure 8-29 Elevation view of an SC wall

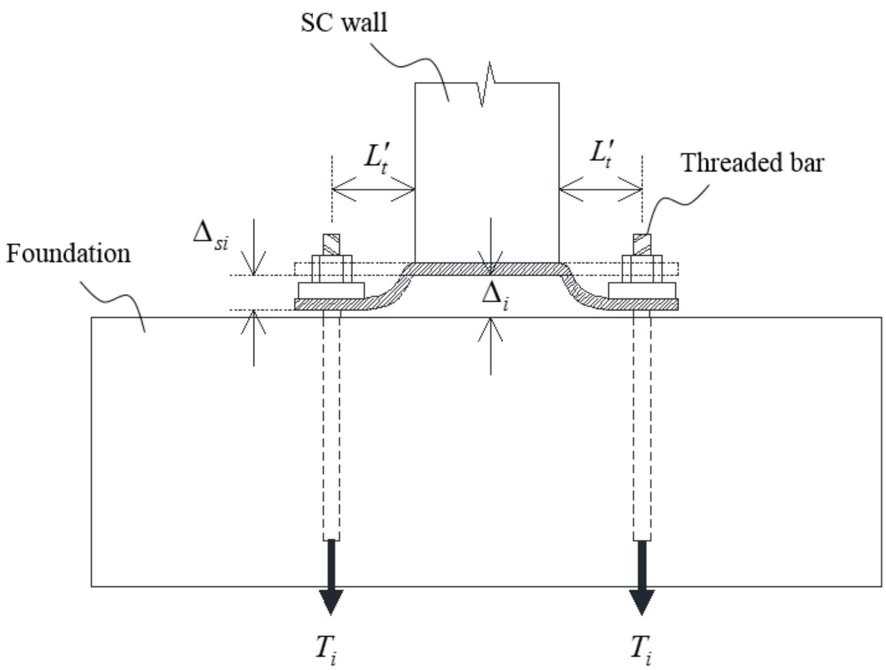

Figure 8-30 Cross-section view of an SC wall

The deflection of the baseplate at the level of the first row of threaded bars, Δ_{s1} (see Figure 8-29), and at the level of the ith row of threaded bars, Δ_{si} (see Figure 8-30), can be calculated using (8-89) and (8-90), respectively.

$$\Delta_{s1} = \frac{n_r T_1}{\frac{3E_s I_{sb}}{L_t^3}} + \frac{n_r T_1}{\frac{G_s A_{sb}}{L_t}} \tag{8-89}$$

$$\Delta_{si} = \frac{T_i}{\frac{3E_s I'_{sb}}{L_t'^3}} + \frac{T_i}{\frac{G_s A'_{sb}}{L'_t}} \tag{8-90}$$

where I_{sb}, A_{sb}, I'_{sb}, and A'_{sb} can be calculated as:

$$I_{sb} = \frac{Bt_p^3}{12} \tag{8-91}$$

$$A_{sb} = \frac{5}{6} Bt_p \tag{8-92}$$

$$I'_{sb} = \frac{St_p^3}{12} \tag{8-93}$$

$$A'_{sb} = \frac{5}{6} St_p \tag{8-94}$$

The tensile force in each threaded bar at the level of the ith row of threaded bars can be calculated as:

$$T_i = (\frac{E_s A_r}{L_r})(\Delta_i - \Delta_{si}) \tag{8-95}$$

where $\Delta_i - \Delta_{si}$ represents the actual elongation of threaded bar (see Figure 8-29 and Figure 8-30) and $E_s A_r / L_r$ is the axial stiffness of the threaded bar. Given the value of Δ_1 for the baseplate, the vertical displacement of the baseplate at the level of the ith row of threaded bars, Δ_i, can be calculated as:

$$\Delta_i = \frac{d'_i}{d'_1} \Delta_1 \tag{8-96}$$

Substituting (8-95) into (8-89) and (8-90) results the equations to calculate baseplate deformation at the levels of the first and ith rows of threaded bars as:

$$\Delta_{s1} = \frac{n_r (\frac{E_s A_r}{L_r})(\Delta_1 - \Delta_{s1})}{\frac{3E_s I_{sb}}{L_t^3}} + \frac{n_r (\frac{E_s A_r}{L_r})(\Delta_1 - \Delta_{s1})}{\frac{G_s A_{sb}}{L_t}} = \psi(\Delta_1 - \Delta_{s1}) \Rightarrow \Delta_{s1} = \frac{\psi}{\psi + 1} \Delta_1 \tag{8-97}$$

$$\Delta_{si} = \frac{(\frac{E_s A_r}{L_r})(\Delta_i - \Delta_{si})}{\frac{3E_s I'_{sb}}{L_t'^3}} + \frac{(\frac{E_s A_r}{L_r})(\Delta_i - \Delta_{si})}{\frac{G_s A'_{sb}}{L'_t}} = \xi(\Delta_i - \Delta_{si}) \Rightarrow \Delta_{si} = \frac{\xi}{\xi + 1} \Delta_i \tag{8-98}$$

where the parameters ψ and ξ can be calculated as:

$$\psi = (\frac{L_t}{L_r}) \left[\frac{n_r A_r L_t^2}{3I_{sb}} + \frac{2n_r A_r (1 + \nu_s)}{A_{sb}} \right] \tag{8-99}$$

$$\xi = (\frac{L'_t}{L_r}) \left[\frac{A_r L_t'^2}{3I'_{sb}} + \frac{2A_r (1 + \nu_s)}{A'_{sb}} \right] \tag{8-100}$$

Substituting (8-98) into (8-95) yeilds the equations to calculate the tensile force in each threaded bar at the levels of the first and ith rows of bars as:

$$T_1 = (\frac{E_s A_r}{L_r})\frac{\Delta_1}{1+\psi} \tag{8-101}$$

$$T_i = (\frac{E_s A_r}{L_r})\frac{\Delta_i}{1+\xi} \tag{8-102}$$

Equilibrium of the vertical forces can be expressed as:

$$\sum F_{ver} = 0 \Rightarrow f_b\left(L_c B/2\right) = n_r T_1 + 2T_2 + \cdots + 2T_m + 2T_{m+1} \tag{8-103}$$

The bending moment of the vertical forces (i.e., tensile forces of the threaded bars and compressive force of the bearing stress) at the wall centerline can be calculated as:

$$M = n_r T_1 d_1 + 2T_2 d_2 + 2T_3 d_3 + \cdots - 2T_m d_m - 2T_{m+1} d_{m+1} + (f_b L_c B/2)(L_b/2 - L_c/3) \tag{8-104}$$

The rotational stiffness of the baseplate connection is:

$$K_\theta = M d_1' / \Delta_1 \tag{8-105}$$

The rotational stiffness of a baseplate connection can be calculated in seven steps using (8-96) through (8-105): 1) set the vertical displacement of the baseplate at the level of the first row of threaded bars at the tension end of the wall, Δ_1 (see Figure 8-29), equal to a small value ($\simeq$ 1% length of the wall), 2) calculate the vertical displacement of the baseplate at the level of the ith row of threaded bars, Δ_i, using (8-96), 3) calculate the values of ψ and ξ using (8-99) and (8-100), respectively, 4) calculate the tensile force in each threaded bar at the levels of the first and ith rows of threaded bars, T_1 and T_i, using (8-101) and (8-102), respectively, 5) calculate the maximum bearing stress, f_b in Figure 8-29, using (8-103), 6) calculate the bending moment of the vertical forces at the wall centerline corresponding to uplift Δ_1, using (8-104), and 7) calculate the rotational stiffness of baseplate connection, k_θ, using (8-105) .

The results of the four SC wall tests are used to validate the proposed method noting that the threaded bars were post-tensioned in the experiments. Figure 8-31 presents a plan view of the constructed SC walls.

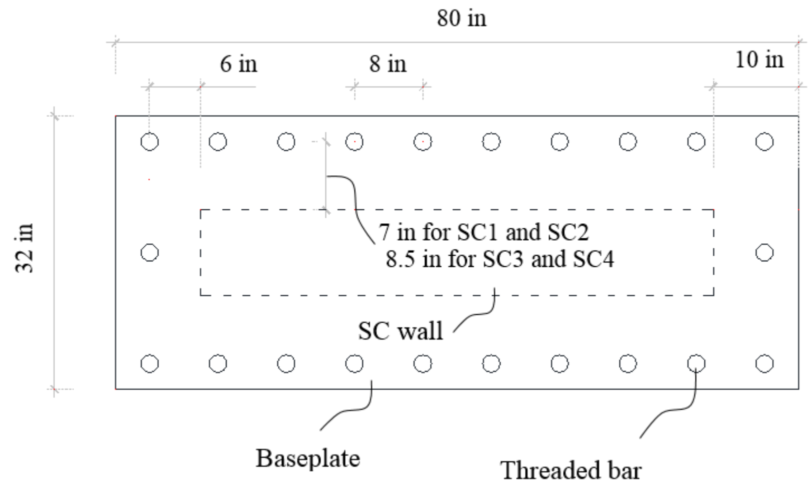

Figure 8-31 Plan view of tested SC walls

Table 8-9 presents the input parameters for the analytical calculation of the initial stiffness of the SC walls. The input parameters were calculated using geometrical and material properties of the four SC walls.

Table 8-9 Input parameters for the stiffness calculation of the baseplate connection

SC wall	n_r	m_r	L_b (in)	B (in)	L_t (in)	L_t' (in)	L_c (in)	L_r (in)	A_r (in^2)	S (in)	t_p (in)	ν_s	E_s (ksi)	E_c (ksi)
SC1/SC2	3	8	80	32	6	7	10	20	1.23	8	1	0.3	29000	3000
SC3/SC4	3	8	80	32	6	8.5	10	20	1.23	8	1	0.3	29000	3300

The parameters I_{sb}, A_{sb}, I_{sb}', and A_{sb}' are:

$$I_{sb} = Bt_p^3/12 = 32\times1^3/12 = 2.7 \text{ in}^4 \tag{8-106}$$

$$A_{sb} = \frac{5}{6}Bt_p = \frac{5}{6}\times32\times1 = 26.7 \text{ in}^2 \tag{8-107}$$

$$I_{sb}' = St_p^3/12 = 8\times1^3/12 = 0.7 \text{ in}^4 \tag{8-108}$$

$$A_{sb}' = \frac{5}{6}St_p = \frac{5}{6}\times8\times1 = 6.7 \text{ in}^2 \tag{8-109}$$

The calculation of the stiffness of the baseplate connection follows the steps below:

Step 1: An uplift Δ_1 is assumed for the baseplate at the level of the first row of the threaded bars at the tension end of the wall.

Step 2: The vertical displacement of the baseplate at the level of the ith row of threaded bars, Δ_i, is:

$$\Delta_i = \frac{d_i'}{66}\Delta_1 \text{ , } (d_1' = 66 \text{ in., } d_2' = 60 \text{ in., } d_3' = 54 \text{ in., ..., } d_9' = 2 \text{ in.}) \tag{8-110}$$

Step 3: The value of ψ for SC1 through SC4 is:

$$\psi = (\frac{L_t}{L_r})\left[\frac{n_r A_r L_t^2}{3I_{sb}} + \frac{2n_r A_r(1+\nu_s)}{A_{sb}}\right] = (\frac{6}{20})\left[\frac{3\times1.23\times6^2}{3\times2.7} + \frac{2\times3\times1.23\times(1+0.3)}{26.7}\right] = 5.1 \tag{8-111}$$

The value of ξ for SC1 and SC2 is:

$$\xi = (\frac{L_t'}{L_r})\left[\frac{A_r L_t'^2}{3I_{sb}'} + \frac{2A_r(1+\nu_s)}{A_{sb}'}\right] = (\frac{7}{20})\left[\frac{1.23\times7^2}{3\times0.7} + \frac{2\times1.23\times(1+0.3)}{6.7}\right] = 10.6 \tag{8-112}$$

The value of ξ for SC3 and SC4 is:

$$\xi = (\frac{L_t'}{L_r})\left[\frac{A_r L_t'^2}{3I_{sb}'} + \frac{2A_r(1+\nu_s)}{A_{sb}'}\right] = (\frac{8.5}{20})\left[\frac{1.23\times8.5^2}{3\times0.7} + \frac{2\times1.23\times(1+0.3)}{6.7}\right] = 18.2 \tag{8-113}$$

The contributions of the axial extension of the threaded bars to Δ_1 per (8-97) is less than 15% for SC1 through SC4 and less than 8% to Δ_i per (8-98) for the remaining bars in the walls. Since the contribution is very small, the fourth assumption on page 8-40 is not substantially violated if the baseplate is post-tensioned to the foundation block.

Step 4: Assuming that the axial stiffness of the threaded bar is K_r, the tensile force in each threaded bar at the level of the first row of threaded bars is:

$$T_1 = K_r \frac{\Delta_1}{1+\psi} = \frac{K_r\Delta_1}{6.1} \tag{8-114}$$

The tensile force in each threaded bar at the level of the ith row of threaded bars in SC1 and SC2 is:

$$T_i = K_r \frac{\Delta_i}{1+\xi} = \frac{K_r \Delta_i}{11.6} \quad (8\text{-}115)$$

The tensile force in each threaded bar at the level of the ith row of threaded bars in SC3 and SC4 is:

$$T_i = K_r \frac{\Delta_i}{1+\xi} = \frac{K_r \Delta_i}{19.2} \quad (8\text{-}116)$$

Step 5: The equilibrium of the vertical forces is:

$$\sum F_{ver} = 0 \Rightarrow 3T_1 + 2T_2 + \cdots + 2T_9 = \frac{f_b L_c B}{2} \quad (8\text{-}117)$$

Substituting (8-114) and (8-115) into (8-117) produces the maximum bearing stress in SC1 and SC2:

$$f_c = 0.007 K_r \Delta_1 \quad (8\text{-}118)$$

The maximum bearing stress in SC3 and SC4 is:

$$f_c = 0.0054 K_r \Delta_1 \quad (8\text{-}119)$$

Step 6: The bending moment of the vertical forces at the wall centerline corresponding to uplift Δ_1 is:

$$M = 3T_1 d_1 + 2T_2 d_2 + \cdots - 2T_6 d_6 - \cdots - 2T_9 d_9 + \left(\frac{f_b L_c B}{2}\right)(L_b / 2 - L_c / 3) \quad (8\text{-}120)$$

Substituting (8-114) and (8-115), and (8-118) into (8-120) produces the bending moment in SC1 and SC2:

$$M = 65.6 K_r \Delta_1 \quad (8\text{-}121)$$

The bending moment in SC3 and SC4 is:

$$M = 53.8 K_r \Delta_1 \quad (8\text{-}122)$$

Step 7: The rotational stiffness of the baseplate connection is calculated by substituting (8-121) into (8-105). The rotational stiffness of the connection in SC1 and SC2 is:

$$K_\theta = Md_1' / \Delta_1 = 65.6K_r d_1' \tag{8-123}$$

The rotational stiffness of the connection in SC3 and SC4 is:

$$K_\theta = Md_1' / \Delta_1 = 53.8K_r d_1' \tag{8-124}$$

The axial stiffness of the threaded bar is:

$$K_r = \frac{E_s A_r}{L_r} = \frac{29000 \times 1.23}{20} = 1780 \text{ kips/in.} \tag{8-125}$$

Substituting (8-125) into (8-123) produces the rotational stiffness of the baseplate connection equals to 7704167 kip-in/rad and 6331440 kip-in/rad for SC1/SC2 and SC3/SC4, respectively.

The flexural rigidities of the walls are:

$$EI_g = E_s I_s + E_c I_c = \frac{1}{12}(E_s 2t_s L^3 + E_c t_c L^3) = 843750000 \text{ kips.in}^2 \text{ for SC1 and SC2} \tag{8-126}$$

$$EI_g = E_s I_s + E_c I_c = \frac{1}{12}(E_s 2t_s L^3 + E_c t_c L^3) = 730350000 \text{ kips.in}^2 \text{ for SC3 and SC4} \tag{8-127}$$

The shear rigidities of the walls are:

$$GA_g = G_s A_s + G_c A_c = G_s 2t_s L + G_c t_c L) = 1150962 \text{ kips for SC1 and SC2} \tag{8-128}$$

$$GA_g = G_s A_s + G_c A_c = G_s 2t_s L + G_c t_c L) = 993462 \text{ kips for SC3 and SC4} \tag{8-129}$$

Table 8-10 presents the lateral stiffness calculation for the SC walls. The second, third, and fourth columns of the table present the theoretical flexural and shear stiffness and lateral stiffness of the baseplate connection, respectively. The fifth and sixth columns present the theoretical and measured initial stiffness of the SC walls, where the theoretical initial stiffness of the SC walls is calculated using (8-88). The ratio of the measured to the predicted initial stiffness of the SC walls is presented in the last column. Good agreement was obtained between the analytical and test results, confirming the utility of the proposed method for calculating the initial stiffness of an SC wall with baseplate connection.

Table 8-10 Values of measured and predicted initial stiffness of the SC walls

Wall	$\frac{3EI_g}{H^3}$ (kip/in)	$\frac{GA_g}{\kappa H}$ (kip/in)	$\frac{K_\theta}{H^2}$ (kip/in)	K_t (kip/in)	$K_{\exp}$ (kip/in)	$\frac{K_{\exp}}{K_t}$
SC1	11719	15986	2140	1625	1680	1.03
SC2	11719	15986	2140	1625	1420	0.88
SC3	10144	13798	1758	1350	1380	1.02
SC4	10144	13798	1758	1350	1310	0.97

CHAPTER 9

SUMMARY AND CONCLUSIONS

9.1 Summary

The seismic behavior of intermediate-to-low aspect ratio, rectangular steel-plate concrete (SC) composite shear walls was investigated as part of a NSF-funded NEESR project on conventional and composite structural walls. The SC wall piers studied here were composed of steel faceplates, infill concrete, headed steel studs anchoring the faceplates to the infill, and tie rods connecting the two faceplates through the infill. The focus was the in-plane behavior of flexure- and flexure-shear critical SC walls. Composite walls with boundary columns and flanges, and wall piers with very low-aspect ratios (height-to-length less than 0.5), were not studied. The research project included experimental, numerical and analytical studies.

The experimental study investigated the cyclic inelastic behavior of SC walls. Four large walls, SC1 through SC4, were constructed in the Bowen Laboratory at Purdue University and the NEES laboratory at the University at Buffalo. The aspect ratio (height-to-length, *H*/*L*) of all four walls was 1.0. The specimens were anchored to a concrete basemat with a pre-tensioned bolted connection that was designed to be stronger than the walls. The connection consisted of a steel plate embedded in the foundation block, a baseplate attached to the steel faceplates, threaded bars securing the baseplate to the foundation block, headed studs attached to the baseplate, shear lugs attached to the steel plate embedded in the foundation block, and a steel anchorage securing the threaded bars to the foundation block. Post-tensioned Dwyidag bars were used to anchor the foundation block to the strong floor. The design parameters considered in the experimental investigation were wall thickness (9 in. and 12 in.), reinforcement ratio (3.1% and 4.2%), and faceplate slenderness ratio (21, 24, and 32). Studs and tie rods were used as shear connectors in SC1 and SC3. Only tie rods were used in SC2 and SC4. Trial designs for the walls and the re-usable foundation block were prepared and analyzed by hand, using XTRACT for detailed cross-section analysis, and using ABAQUS to explore design alternatives and develop force-displacement relationships.

The progression of damage with increasing cyclic lateral displacements in the four walls was similar: tensile cracking of concrete, tensile yielding of the steel faceplates, crushing of concrete at the toes of the wall, outward local buckling of the steel faceplates, and fracture of the steel faceplates. The test results were used to characterize cyclic force-displacement relationships; post-peak response focusing on the influence of the stud spacing; energy dissipation and equivalent viscous damping ratios; strain and stress fields in the steel faceplates; the contribution of the steel faceplates to the total lateral load; contributions of shear, flexure, and base rotation to the total lateral displacement; and displacement ductility.

A finite element model for the nonlinear cyclic analysis of flexure- and flexure-shear-critical SC walls was developed and validated using the test data. The finite element codes ABAQUS, VecTor2, and LS-DYNA were evaluated. Only DYNA recovered the measured cyclic responses well. Measured global and local responses of the walls were used to validate the DYNA model. The validated model was used to investigate the influence of interface friction between the steel faceplates and the infill concrete, and the distribution of the shear studs attached to baseplate, on the cyclic response of SC walls.

A parametric study on the in-plane monotonic response of SC walls was conducted using the validated and benchmarked DYNA model. The results of finite element analysis of 77 SC wall piers were used to investigate the effects of wall aspect ratio, reinforcement ratio, slenderness ratio, axial load, yield strength of the steel faceplates, and uniaxial compressive strength of concrete on the in-plane response of SC walls. The baseline model was validated and benchmarked using data from tests of large-scale SC wall piers at the University at Buffalo. The interaction effects of the design variables on the shear force resisted by the infill concrete and steel faceplates and on the pre- and post-yield stiffness of SC walls were investigated using a three-level six-factor fractional factorial design. The analysis results were used to develop a predictive model for the monotonic response of SC walls up to peak strength considering the effects of various design parameters. The predictive model was validated using data from tests of four SC wall piers with an aspect ratio (height-to-length) of 0.5. Equations were proposed to estimate the effective shear and flexural rigidities of SC wall piers for dynamic analysis. Sample calculations of the monotonic response and effective stiffness were provided.

Analytical models for calculating the monotonic and cyclic responses of single and multi-story SC wall panels were developed, verified and validated. These models could be used for preliminary analysis and design of structures including SC walls. The analytical models were verified using the results of the parametric DYNA study. The Ibarra-Krawinkler Pinching model was modified to predict the cyclic response of SC walls, and the results of cyclic finite element analysis of 12 models of SC walls were used to establish backbone curve, pinching, deterioration, and rate parameters for the modified IKP model. An analytical model for predicting the rotational stiffness of a baseplate connection was developed and validated using test data.

9.2 Conclusions

This section presents the key conclusions of the experimental, numerical, and analytical studies.

9.2.1 Experimental Study

1. The four walls sustained peak lateral loads close to those predicted by pre-test calculations using commercially available software.
2. Faceplate slenderness ratio did not influence the peak resistance of SC walls in range of slenderness ratio studied (21 to 32). The rate of strength deterioration was affected by the faceplate slenderness ratio, with slightly better performance observed for values of the ratio less than the limit proposed in the draft appendix to AISC N690.
3. Damage to flexure-critical SC walls in the pre-peak-strength region included concrete cracking at toes of the wall at drift ratios less than 0.15% and steel faceplate buckling at 0.5% drift ratio. Concrete crushing occurred at peak load. Tearing of the steel faceplates occurred in the post-peak-strength region of the SC wall response.
4. Pinched hysteresis and loss of stiffness and strength were observed in all four walls at lateral displacements greater than those corresponding to peak load. Pinching in the hysteretic response of the SC walls was attributed to the cracking and crushing of the infill concrete, tearing of the steel faceplates, and flexibility at the base of the wall due to the baseplate connection.
5. The damage to the infill concrete was concentrated around the level of the first row of connectors in all four walls.
6. The distance between the first row of connectors and the base of an SC wall has a significant influence on the post-peak behavior. The use of a smaller distance between the first row of connectors and the baseplate forced the buckling of the faceplates away from the CJP welded connection of the faceplates to the baseplate and avoided premature fracture of the welded connection.

7. Tie rods instead of shear studs are recommended near the base of an SC wall to improve seismic response, where the faceplates are likely to buckle and high tensile forces are imposed on the connectors.
8. The equivalent viscous damping for flexure-critical SC walls can be assumed to be 5% at displacements less than that at peak strength and 10% for greater displacements.
9. The displacement due to the base rotation governed the total lateral displacement for the SC walls with a bolted baseplate to RC foundation connection, indicating the importance of addressing foundation flexibility in design and analysis of SC walls.

9.2.2 Numerical and Analytical Studies

1. Models of SC walls can be prepared in LS-DYNA to reliably compute monotonic and cyclic responses that are flexure- or flexure-shear-critical. For this purpose: 1) the smeared crack Winfrith model, MAT085, can be used for the infill concrete; in the absence of experimental data, the specific fracture energy can be estimated for a given aggregate size using CEB-FIP Model Code (1993); 2) the plastic-damage model, MAT081, can be used for the faceplates; 3) beam, shell, and solid elements can be used to model connectors, steel faceplates, and infill concrete, respectively, and a mesh size of 1 in. is appropriate for the solids and shells; and 4) the tie constraint can be used to attach the studs and tie rods to the steel faceplates and the baseplate and the Lagrange-In-Solid constraint can be used to attach the connectors to the infill concrete elements.
2. The DYNA model can be used to predict damage to the infill concrete and the steel faceplates and thus can be used to develop robust fragility functions for seismic probabilistic risk assessment.
3. The assumption of perfect bond between the steel faceplates and the infill concrete does not significantly affect the pre-peak-strength response of the SC walls in the range of faceplate slenderness studied here. The post-peak resistance of SC walls is underpredicted if perfect bond is assumed due to premature fracture of the faceplates. Perfect bond should not be assumed for finite element analysis.
4. In-plane cyclic response of SC wall is not affected by the choice of the coefficient of friction between the infill concrete and the steel faceplates.

5. The initial stiffness of SC walls constructed with a baseplate connection to an RC foundation may be substantially affected by the flexibility of the connection, with a potential significant impact on the dynamic response of the supported structure.
6. Of the design parameters considered in the parametric study (aspect ratio, reinforcement ratio, slenderness ratio, axial load, yield strength of the steel faceplates, and uniaxial compressive strength of concrete), aspect ratio has the greatest effect on the shear strength and lateral stiffness of SC walls. The aspect ratio also affects the impact of the other design variables on global response. Of all the variables considered, the slenderness ratio had the smallest effect on strength and stiffness.
7. The in-plane monotonic response up to peak load of the tested SC walls was successfully predicted using the proposed empirical equations. The proposed empirical equations for the monotonic strength and stiffness of SC wall piers are applicable for the range of design variables considered in this study and any extrapolation beyond the scope of the variables require additional analysis or testing.
8. The results of analysis of 77 SC wall piers were used to investigate the effects of design variables including aspect ratio, reinforcement ratio, slenderness ratio, axial load, yield strength of the steel faceplates, and uniaxial compressive strength of concrete on the effective stiffness of SC walls. Equations to calculate reduction factors for shear and flexural stiffness were formulated as a function of key design variables, and these can be used for elastic analysis of structures including SC wall piers.

CHAPTER 10

REFERENCES

ACI 374 Committee. (2005). "Acceptance criteria for moment frames based on structural testing and commentary." American Concrete Institute, Farmington Hills, MI.

ACI 349 Committee. (2006). "Code requirements for nuclear safety-related concrete structures (ACI 349-06) and commentary." American Concrete Institute, Farmington Hills, MI.

ACI 318 Committee. (2011). "Building code requirements for structural concrete (ACI 318-11) and commentary." American Concrete Institute, Farmington Hills, MI.

ACI 318 Committee. (2014). "Building code requirements for structural concrete (ACI 318-14) and commentary." American Concrete Institute, Farmington Hills, MI.

American Institute of Steel Construction. (2005). "Seismic provisions for structural steel buildings." American Institute of Steel Construction, Chicago, IL.

American Institute of Steel Construction. (2014) "Specification for safety-related steel structures for nuclear facilities, Supplement No. 1." N690s1, American Institute of Steel Construction, Chicago, IL.

Akita, S., Ozaki, M., Niwa, N., Matsuo, I., and Hara, K. (2001). "Study on steel plate reinforced concrete bearing wall for nuclear power plants (part #2): analytical method to evaluate response of SC walls." 16th International Conference on Structural Mechanics in Reactor Technology (SMiRT16), International Association for Structural Mechanics in Reactor Technology (IASMiRT), Washington DC, USA.

Akiyama, H., Sekimoto, H., Tanaka, M., Inoue, K., Fukihara, M., and Okuda, Y. (1989). "1/10th scale model test of inner concrete structure composed of concrete filled steel bearing wall." 10th International Conference on Structural Mechanics in Reactor Technology (SMiRT10), International Association for Structural Mechanics in Reactor Technology (IASMiRT), Anaheim, California, USA, 73-78.

Ali, A., Kim, D., and Cho, S. G. (2013). "Modeling of nonlinear cyclic load behavior of I-shaped composite steel-concrete shear walls of nuclear power plants." Nuclear Engineering and Technology, 45(1), 89-98.

American Society of Civil Engineers. (2013). "Seismic evaluation and retrofit of existing buildings (ASCE/SEI 41-13)." ASCE, Reston, VA.

ASTM A370 (1997). "Standard test methods and definitions for mechanical testing of steel products." American Society for Testing and Materials, West Conshohocken, PA.

ASTM C39 (2002). "Standard test method for compressive strength of cylindrical concrete specimens." American Society for Testing and Materials, West Conshohocken, PA.

Balmer, G. G. (1949). "Shearing strength of concrete under high triaxial stress - computation of Mohr's envelope as a curve." Structural Research Laboratory Report SP-23, Denver, Colorado.

Bathe, K. J. (1982). "Finite element procedures in engineering analysis." Prentice Hall, Engle Wood Cliffs, New Jersey.

Bessason, B., and Sigfusson, T. (2001). "Capacity and earthquake response analysis of RC-shear walls." Nordic Concrete Research, 27, 1-14.

Booth, P. N., Varma, A. H., Malushte, S. R., and Johnson, W. H. (2007). "Response of modular composite walls to combined thermal and mechanical load." 19th International Conference on Structural Mechanics in Reactor Technology (SMiRT19), International Association for Structural Mechanics in Reactor Technology (IASMiRT), Toronto, Canada.

Bowerman, H., Coyle, N., and Chapman, J. C. (2002). "An innovative steel/concrete construction system." The Structural Engineer, 80(20), 33-38.

Broadhouse, B. J. (1986). "DRASTIC-A compute code for dynamic analysis of stress transients in reinforced concrete." Safety and Engineering Science Division, AEE, Winfrith, AEEW – R2124.

Brockenbrough, R. L., and Merritt, F. S. (1999). "Structural steel designer's handbook." McGraw-Hill, New York.

Comité Euro-International du Béton (CEB-FIP). (1993). "CEB-FIP model code 1990." Thomas Telford, London.

Chadwell, C. B., and Imbsen, R. A. (2002). "XTRACT-cross section analysis software for structural and earthquake engineering." TRC, Rancho Cordova, CA.

Chang, G. A., and Mander, J. B. (1994). "Seismic energy based fatigue damage analysis of bridge columns: part I-evaluation of seismic capacity." Report No. NCEER-94-0006, National Center for Earthquake Engineering Research, Buffalo, NY.

Chang, C.C., Huang, Y.N., Chen, B.A., Epackachi, S., and Whittaker, A. S. (2015). "An experimental study for in-plane cyclic behavior of low aspect-ratio SC wall piers." 23rd International Conference on Structural Mechanics in Reactor Technology (SMiRT23), International Association for Structural Mechanics in Reactor Technology (IASMiRT), Manchester, UK.

Chaudhary, S., Ali, A., Kim, D., and Cho, S. G. (2011). "Seismic analysis of steel concrete composite walls of nuclear power plant structures." 21th International Conference on Structural Mechanics in Reactor Technology (SMiRT21), International Association for Structural Mechanics in Reactor Technology (IASMiRT), New Delhi, India.

Chen, B.A. (2016). "Seismic response of steel-plate concrete (SC) composite shear walls." PhD dissertation in preparation, Department of Civil Engineering, National Taiwan University, Taiwan.

Chen, W. F., and Han, D. J. (2007). "Plasticity for structural engineers." J. Ross Publishing, New York.

Chopra, A. K. (2012). "Dynamics of structures: theory and applications to earthquake engineering (4th Edition)." Prentice Hall, Englewood Cliffs, New Jersey.

Collins, M. P., and Mitchell, D. (1991). "Prestressed concrete structures." Prentice Hall, College Division.

Danay, A. (2012). "Response of steel-concrete composite panels to in-plane loading." Nuclear Engineering and Design, 242, 52-62.

Emori, K. (2002). "Compressive and shear strength of concrete filled steel box wall." Steel Structures (Korean Journal), 2(1), 29-40.

Eom, T. S., Park, H. G., Lee, C. H., Kim, J. H., and Chang, I. H. (2009). "Behavior of double skin composite wall subjected to in-plane cyclic loading." Journal of Structural Engineering, 135(10), 1239-1249.

Epackachi, S., Nguyen, N. H., Kurt, E. G., Whittaker, A. S. and Varma, A.H. (2013a). "An experimental study of the in-plane shear response of steel concrete composite walls." 22nd International Conference on Structural Mechanics in Reactor Technology (SMiRT22), International Association for Structural Mechanics in Reactor Technology (IASMiRT), San Francisco, California, US.

Epackachi, S., Nguyen, N.H., Kurt, E.G., Whittaker, A.S, and Varma, A.H. (2013b). "In-plane seismic behavior of rectangular steel-plate composite wall piers." Journal of Structural Engineering (ASCE), DOI: 10.1061/(ASCE)ST.1943-541X.0001148.

Epackachi, S., Nguyen, H. N., Kurt, E. G., Pitman, M., Weinreber, S., Whittaker, A. S. and Varma, A. (2014a). "Steel-plate composite shear wall - specimen No. 1 (SC1)." Network for Earthquake Engineering Simulation (distributor), Dataset, DOI: 10.4231/D3BG2H97F.

Epackachi, S., Nguyen, H. N., Kurt, E. G., Pitman, M., Weinreber, S., Whittaker, A. S. and Varma, A. (2014b). "Steel-plate composite shear wall - specimen No. 2 (SC2)." Network for Earthquake Engineering Simulation (distributor), Dataset, DOI: 10.4231/D36T0GW54.

Epackachi, S., Nguyen, H. N., Kurt, E. G., Pitman, M., Weinreber, S., Whittaker, A. S. and Varma, A. (2014c). "Steel-plate composite shear wall - specimen No. 3 (SC3)." Network for Earthquake Engineering Simulation (distributor), Dataset, DOI: 10.4231/D3319S315.

Epackachi, S., Nguyen, H. N., Kurt, E. G., Pitman, M., Weinreber, S., Whittaker, A. S. and Varma, A. (2014d). "Steel-plate composite shear wall - specimen No. 4 (SC4)." Network for Earthquake Engineering Simulation (distributor), Dataset, DOI: 10.4231/D3Z892F6J.

Epackachi, S., Whittaker, A.S., and Varma, A.H. (2014e). "Numerical and experimental investigation on in-plane behavior of steel-concrete composite walls." Transactions of 2014 Structures Congress (ASCE), Boston, MA, USA.

Epackachi, S., Whittaker, A.S, and Huang, Y.N. (2015a). "Analytical modeling of rectangular SC wall panels." Journal of Construction Steel Research, DOI:10.1016/j.jcsr.2014.10.016.

Epackachi, S., Whittaker, A.S, Varma, A.H., and Kurt, E.G. (2015b). "Finite element modeling of steel-plate concrete composite wall piers." Engineering Structures, DOI: 10.1016/j.engstruct.2015.06.02.

Epackachi, S., Whittaker, A. S., and Varma, A.H. (2015c). "An analytical model for a baseplate connection of an SC wall to an RC foundation." 8th International Conference on Steel Structures, Jeju, South Korea.

Epackachi, S., Whittaker, A. S. and Varma, A.H. (2015d). "Experimental behavior of flexure critical steel-Plate composite SC shear walls." 23rd International Conference on Structural Mechanics in Reactor Technology (SMiRT23), International Association for Structural Mechanics in Reactor Technology (IASMiRT), Manchester, UK.

Farhidzadeh, A., Epackachi, S., Salamone, S., and Whittaker, A.S. (2015). "Bayesian decision and mixture models for AE monitoring of steel–concrete composite shear walls." Smart Materials and Structures, DOI: 10.1088/0964-1726/24/11/115028.

Fukumoto, T., Kato, B., and Sato, K. (1987). "Concrete filled steel bearing walls." IABSE Symposium, Paris-Versailles.

Gulec, C. K., and Whittaker, A. S. (2011). "Hysteretic modeling of squat reinforced concrete shear walls." 21th International Conference on Structural Mechanics in Reactor Technology (SMiRT21), International Association for Structural Mechanics in Reactor Technology (IASMiRT), New Delhi, India.

Hassinen, P., Kouhi, J., Zimmerman, T. J. E., and Stephens, M. J. (1989). "Static and cyclic load tests of a composite ice-resisting wall." Rep. No. 965, Technical Research Center of Finland, Helsinki, Finland.

Hong, S. G., Kim, W., Lee, K. J., Hong, N. K., and Lee, D. H. (2010). "Out-of-plane shear strength of steel-plate-reinforced concrete walls dependent on bond behavior." Journal of Disaster Research, 5(4), 385-394.

Hong, S. G., Lee, S. J., and Lee, M. J. (2014). "Steel plate concrete walls for containment structures in Korea: in-plane shear behavior." Infrastructure Systems for Nuclear Energy, 237-257.

Hristovski, V. T., and Noguchi, H. (2002). "Finite element modeling of RC members subjected to shear." Third DIANA World Conference, Tokyo, Japan, 175-183.

Hu, H. T., and Schnobrich, W. C. (1990). "Nonlinear analysis of cracked reinforced concrete." ACI Structural Journal, 87(2), 199-207.

Ibarra, L. F., Medina, R. A., and Krawinkler, H. (2005). "Hysteretic models that incorporate strength and stiffness deterioration." Earthquake Engineering and Structural Dynamics, 34(12), 1489-1511.

JEAC 4618 (2009). "Technical code for seismic design of steel plate reinforced concrete structures: buildings and structures." Japanese Electric Association Nuclear Standards Committee, Tokyo, Japan.

Kupfer, H. B., Hubert, K. H., and Hubert, R. (1969). "Behavior of concrete under biaxial stresses." ACI Structural Journal, 66(8), 656-666.

Kurt, E.G. (2015). "Seismic assessment of steel-plate concrete composite walls." Ph.D. dissertation, Purdue University, West Lafayette, IN.

Kurt, E.G., Varma, A. H., Booth, P., and Whittaker, A. S. (2013). "SC wall piers and basemat connections: numerical investigation of behavior and design." 22nd International Conference on Structural Mechanics in Reactor Technology (SMiRT22), International Association for Structural Mechanics in Reactor Technology (IASMiRT), San Francisco, California, US.

Kurt, E.G., Varma, A.H., Epackachi, S., Whittaker, A.S. (2015). “Rectangular SC wall piers: summary of seismic behavior and design.” Transaction 2015 Structures Congress (ASCE), Portland, Oregon, USA, DOI: 10.1061/9780784479117.089.

Lee, J., and Fenves, G. L. (1998). "Plastic-damage model for cyclic loading of concrete structures." Journal of Engineering Mechanics, 124(8), 892-900.

Link, R. A., and Elwi, A. E. (1995). "Composite concrete-steel plate walls: analysis and behavior." Journal of Structural Engineering, 121(2), 260-271.

LS-DYNA (2012a). "Keyword User's Manual, Volume I." Version 971 R6.0.0, Livermore, CA, USA.

LS-DYNA (2012b). "Keyword User's Manual, Volume II." Version 971 R6.0.0, Livermore, CA, USA.

Lubliner, J., Oliver, J., Oller, S., and Onate, E. (1989). "A plastic-damage model for concrete." International Journal of Solids and Structures, 25(3), 299-326.

Mander, J. B., Priestley, M. J. N., and Park, R. (1988). "Observed stress-strain behavior of confined concrete." Journal of Structural Engineering, 114(8), 1827-1849.

Mansour, M., and Hsu, T. T. C. (2005a). "Behavior of reinforced concrete elements under cyclic shear. I: experiments." Journal of Structural Engineering, 131(1), 44-53.

Mansour, M., and Hsu, T. T. C. (2005b). "Behavior of reinforced concrete elements under cyclic shear. II: theoretical model." Journal of Structural Engineering, 131(1), 54-65.

MATLAB (2012). "Version 7.13.0.564." MathWorks Inc., Natick, MA.

Minitab (2013). "Minitab Manual." Minitab Inc., State College, PA, USA.

Montgomery, D. C. (1982). "Design and analysis of experiments." Wiley, New York.

Nguyen, N.H., Epackachi, S., Kurt, E.G., Whittaker, A.S., and Varma, A.H., (2013). "In-plane shear response of steel-concrete composite shear walls: results of experiments." Transactions of Australian Earthquake Engineering Society 2013 Conference, Hobart, Tasmania, Australia.

Nguyen, N. H. (2016). "Seismic response of steel-plate concrete composite shear wall piers." Ph.D. dissertation, University at Buffalo, Buffalo, NY.

Nie, J.G., Hu, H.S., Fan, J.S., Tao, M.X., Li, S.T., and Liu, F.J. (2013). "Experimental study on seismic behavior of high-strength concrete filled double-steel-plate composite walls." Journal of Constructional Steel Research, 88, 206-219.

Nie, J. G., Ma, X. W., Tao, M. X., Fan, J. S., and Bu, F. M. (2014). "Effective stiffness of composite shear wall with double plates and filled concrete." Journal of Constructional Steel Research, 99, 140-148.

Nielsen, M. P., and Hoang, L. C. (2010). "Limit analysis and concrete plasticity." CRC Press, Boca Raton, FL.

Nuclear Power Engineering Corporation. (1994). "Specification report of seismic shear wall ISP on NUPEC'S seismic ultimate dynamic response test." NU-SSWIP-D009, Tokyo, Japan.

Orakcal, K., Ulugtekin, D., and Massone, L. M. (2012). "Constitutive modeling of reinforced concrete panel behavior under cyclic loading." 15th World Conference on Earthquake Engineering, Lisbon, Portugal.

Ottosen, N. S. (1977). "A failure criterion for concrete." Journal of the Engineering Mechanics Division, 103(4), 527-535.

Ozaki, M., Akita, S., Niwa, N., Matsuo, I., and Usami, S. (2001a). "Study on steel-plate reinforced concrete bearing wall for nuclear power plants part 1: shear and bending loading tests of SC walls." 16th International Conference on Structural Mechanics in Reactor Technology (SMiRT16), International Association for Structural Mechanics in Reactor Technology (IASMiRT), Washington DC, USA.

Ozaki, M., Osuga, H., Nakayama, T., and Adachi, N. (2001b). "Study on steel plate reinforced concrete panels having an opening subjected to cyclic in-plane shear." 16th International Conference on Structural Mechanics in Reactor Technology (SMiRT16), International Association for Structural Mechanics in Reactor Technology (IASMiRT), Washington DC, USA.

Ozaki, M., Akita, S., Osuga, H., Nakayama, T., and Adachi, N. (2004). "Study on steel plate reinforced concrete panels subjected to cyclic in-plane shear." Nuclear Engineering and Design, 228(1-3), 225-244.

Park, R. (1988). "Ductility evaluation from laboratory and analytical testing." 9th World Conference on Earthquake Engineering, 8, pp. 605-616, Tokyo-Kyoto, Japan.

Park, R., Priestley, M. J. N., and Gill, W. D. (1982). "Ductility of square-confined concrete columns." 108 (ST4), 929-950.

Rabbat, B. G., and Russell, H. G. (1985). "Friction coefficient of steel on concrete or grout." Journal of Structural Engineering, 111(3), 505-515.

Richart, F. E., Braendtzaeg, A., and Brown, R. L. (1928). "A study of the failure of concrete under combined compressive stress." University of Illinois, Engineering Experimental Station Bulletin, 185, 103.

Saenz, L. P. (1964). "Discussion of equation for the stress-strain curve of concrete, by P. Desay and S. Krishan." ACI Journal, 61(9), 1229-1235.

Sasaki, N., Akiyama, H., Narikawa, M., Hara, K., Takeuchi, M., and Usami, S. (1995). "Study on a concrete filled steel structure for nuclear power plants (part #2): shear and bending loading tests on wall member." 13th International Conference on Structural Mechanics in Reactor Technology (SMiRT13), International Association for Structural Mechanics in Reactor Technology (IASMiRT), Porto Alegre, Brazil, 27-32.

Schwer, L. (2011). "The Winfrith concrete model: beauty or beast? Insights into the Winfrith concrete model." 8th European LS-DYNA Users Conference, Strasbourg, France.

SEESL (2008). "Online lab manual of the structural engineering and earthquake simulation laboratory." University at Buffalo.

Sener, K., Varma, A. H., Malushte, S. R., and Coogler, K. (2013). "Experimental database of SC composite specimens tested under out-of-plane shear loading." 22nd International Conference on Structural Mechanics in Reactor Technology (SMiRT22), International Association for Structural Mechanics in Reactor Technology (IASMiRT), San Francisco, California, US.

Sener, K. C., and Varma, A. H. (2014). "Steel-plate composite walls: experimental database and design for out-of-plane shear." Journal of Constructional Steel Research, 100, 197-210.

SIMULIA (2012a). "ABAQUS analysis user's manual." Version 6.12, Dassault Systèmes Simulia Corp., Providence, Rhode Island, USA.

SIMULIA (2012b). "ABAQUS theory manual." Version 6.12, Dassault Systèmes Simulia Corp., Providence, Rhode Island, USA.

Sittipunt, C., and Wood, S. L. (1995). "Influence of web reinforcement on the cyclic response of structural walls." ACI Structural Journal, 92(6), 745-756.

SNG, K. (2010). "SNG steel plate concrete structures." Board of KEPIC Policy Structural Committee, Seoul, Korea.

Stephens, M. J., and Zimmerman, T. J. E. (1990). "The strength of composite ice-resisting walls subjected to combined loads." The First ISOPE European Offshore Mechanics Symposium. International Society of Offshore and Polar Engineers, Trondheim, Norway.

Suzuki, H., and Kato, B. (1984). "Shear strengths of concrete-filled steel box elements." Composite and Mixed Construction (ASCE), Seattle, Washington, US, 254-266.

Suzuki, N., Akiyama, H., Narikawa, M., Hara, K., Takeuchi, M., and Matsuo, I. (1995). "Study on a concrete filled steel structure for nuclear power plants (part #4): analytical method to estimate shear strength." 13th International Conference on Structural Mechanics in Reactor Technology (SMiRT13), International Association for Structural Mechanics in Reactor Technology (IASMiRT), Porto Alegre, Brazil, 33-38.

Takeda, T., Yamaguchi, T., Nakayama, T., Akiyama, K., and Kato, Y. (1995). "Experimental study on shear characteristics of concrete filled steel plate wall." 13th International Conference on Structural Mechanics in Reactor Technology (SMiRT13), International Association for Structural Mechanics in Reactor Technology (IASMiRT), Porto Alegre, Brazil, 3-14.

Takeuchi, M., Akiyama, H., Narikawa, M., Hara, K., Tsubota, H., and Matsuo, I. (1995). "Study on a concrete filled steel structure for nuclear power plants (part #1): outline of the structure and the mock-up test." 13th International Conference on Structural Mechanics in Reactor Technology (SMiRT13), International Association for Structural Mechanics in Reactor Technology (IASMiRT), Porto Alegre, Brazil.

Takeuchi, M., Narikawa, M., Matsuo, I., Hara, K., and Usami, S. (1998). "Study on a concrete filled structure for nuclear power plants." Nuclear Engineering and Design, 179(2), 209-223.

Tata Steel Inc., Netherlands, www.tatasteelconstruction.com.

Tomlinson, M., Chapman, M., and Wright, H. D. (1989). "Shell composite construction for shallow draft immersed tube tunnels." ICE International Conference on Immersed Tube Tunnels Techniques, Manchester, UK.

Tsai, W. T. (1988). "Uniaxial compressional stress-strain relation of concrete." Journal of Structural Engineering, 114(9), 2133–2136.

Tsuda, K., Tatsuo, N., Eto, H., Akiayama, K., Shimizu, A., Tanouchi, K., and Aoyama, H. (2001). "Experimental study on steel plate reinforced concrete shear walls with joint bars." 16th International Conference on Structural Mechanics in Reactor Technology (SMiRT16), International Association for Structural Mechanics in Reactor Technology (IASMiRT), Washington DC, USA.

Usami, S., Akiyama, H., Narikawa, M., Hara, K., Takeuchi, M., and Sasaki, N. (1995). "Study on a concrete filled steel structure for nuclear power plants (part #2): compressive loading tests on wall members." 13th International Conference on Structural Mechanics in Reactor Technology (SMiRT13), International Association for Structural Mechanics in Reactor Technology (IASMiRT), Porto Alegre, Brazil.

Uy, B., and Bradford, M. A. (1996). "Elastic local buckling of steel plates in composite steel-concrete members." Engineering Structures, 18(3), 193-200.

Varma, A. H., Malushte, S. R., Sener, K. C., and Booth, P. N. (2009). "Analysis and design of modular composite walls for combined thermal and mechanical loading." 20th International Conference on Structural Mechanics in Reactor Technology (SMiRT19), International Association for Structural Mechanics in Reactor Technology (IASMiRT), Espoo, Finland.

Varma, A. H., Malushte, S., Sener, K., Booth, P. N., and Coogler, K. (2011a). "Steel-plate composite (SC) walls: analysis and design including thermal effects." 21th International

Conference on Structural Mechanics in Reactor Technology (SMiRT21), International Association for Structural Mechanics in Reactor Technology (IASMiRT), New Delhi, India.

Varma, A. H., Sener, K., Zhang, K., Coogler, K., and Malushte, S. (2011b). "Out-of-plane shear behavior of SC composite structures." 21th International Conference on Structural Mechanics in Reactor Technology (SMiRT21), International Association for Structural Mechanics in Reactor Technology (IASMiRT), New Delhi, India.

Varma, A. H., Zhang, K., Chi, H., Booth, P. N., and Baker, T. (2011c). "In-plane shear behavior of SC composite walls: theory vs. experiment." 21th International Conference on Structural Mechanics in Reactor Technology (SMiRT21), International Association for Structural Mechanics in Reactor Technology (IASMiRT), New Delhi, India.

Varma, A. H., Malushte, S. R., Sener, K. C., and Booth, P. N. (2012). "Analysis recommendations for steel-composite (SC) walls of safety-related nuclear facilities." Structures Congress 2012, ASCE, 1871-1880.

Varma, A. H., Sener, K., and Inductries, M. H. (2013a). "Lateral load behavior of a containment internal structure consisting of composite SC walls." 22nd International Conference on Structural Mechanics in Reactor Technology (SMiRT22), International Association for Structural Mechanics in Reactor Technology (IASMiRT), San Francisco, California, US.

Varma, A. H., Zhang, K., and Malushte, S. R. (2013b). "Local buckling of SC composite walls at ambient and elevated temperatures." 22nd International Conference on Structural Mechanics in Reactor Technology (SMiRT22), International Association for Structural Mechanics in Reactor Technology (IASMiRT), San Francisco, California, US.

Varma, A. H., Malushte, S. R., Sener, K. C., and Lai, Z. (2014). "Steel-plate composite (SC) walls for safety related nuclear facilities: Design for in-plane forces and out-of-plane moments." Nuclear Engineering and Design, 269(1), 240-249.

Vecchio, F. J. (2000). "Disturbed stress field model for reinforced concrete: formulation." Journal of Structural Engineering, 126(9), 1070-1077.

Vecchio, F. J. (1992). "Finite element modeling of concrete expansion and confinement." Journal of Structural Engineering, 118(9), 2390-2406.

Vecchio, F. J. (1989). "Nonlinear finite element analysis of reinforced concrete membranes." ACI Structural Journal, 86(1), 26-35.

Vecchio, F. J. (1990). "Reinforced concrete membrane element formulations." Journal of Structural Engineering, 116(3), 730-750.

Vecchio, F. J. (1999). "Towards cyclic load modeling of reinforced concrete." ACI Structural Journal, 96(2), 193-202.

Vecchio, F. J., and Collins, M. P. (1993). "Compression response of cracked reinforced concrete." Journal of Structural Engineering, 119(12), 3590-3610.

Vecchio, F. J., and DeRoo, A. (1995). "Smeared crack modelling of concrete tension splitting." Journal of Engineering Mechanics, 121(6), 702-708.

Vecchio, F. J., and McQuade, I. (2011). "Towards improved modeling of steel-concrete composite wall elements." Nuclear Engineering and Design, 241(8), 2629-2642.

Vecchio, F. J., and Collins, M. P. (1986). "Modified compression-field theory for reinforced concrete elements subjected to shear." ACI Structural Journal, 83(2), 219-231.

Vishay Precision Group. (2010). "General purpose strain gages-rectangular rosette." Document Number: 11095Raleigh, NC.

Walraven, J. C. (1981). "Fundamental analysis of aggregate interlock." Journal of the Structural Division, 107(11), 2245-2270.

Wittmann, F. H., Rokugo, K., Bruehwiler, E., Mihashi, H., and Simonin, P. (1988). "Fracture energy and strain softening of concrete as determined by means of compact tension specimens." Materials and Structures, 21(121), 21-32.

Wong, P. S., Vecchio, F. J., and Trommels, H. (2013). "VecTor2 and Formworks User's Manual, Second Edition." University of Toronto, Toronto, Canada.

Wright, H. D. (1995). "The behavior of composite walling under construction and service loading." Journal of Constructional Steel Research, 35(3), 257-273.

Wright, H. D., Evans, H. R., and Gallocher, S. C. (1992). "Composite walling." Engineering Foundation Conference, Missouri, USA.

Wright, H. D., Hossain, K. M. A., and Gallocher, S. C. (1994). "Composite walls as shear elements in tall structures." ASCE Structures Congress XII, Atlanta, GA, USA, 140-145.

Wright, H. D., Oduyemi, T. O. S., and Evans, H. R. (1991a). "The design of double skin composite elements." Journal of Constructional Steel Research, 19(2), 111-132.

Wright, H. D., Oduyemi, T. O. S., and Evans, H. R. (1991b). "The experimental behavior of double skin composite elements." Journal of Constructional Steel Research, 19(2), 97-110.

Xiaowei, M., Jianguo, N., and Muxuan, T. (2013). "Nonlinear finite-element analysis of double-skin steel-concrete composite shear wall structures." IACSIT International Journal of Engineering and Technology, 5(6), 648-652.

Xu, S. Y., and Zhang, J. (2011). "Hysteretic shear-flexure interaction model of reinforced concrete columns for seismic response assessment of bridges." Earthquake Engineering and Structural Dynamics, 40(3), 315-337.

Zhang, K., Varma, A., and Gallocher, S. (2013). "Partial composite action in SC composite walls for nuclear structures." 22nd International Conference on Structural Mechanics in Reactor Technology (SMiRT22), International Association for Structural Mechanics in Reactor Technology (IASMiRT), San Francisco, California, US.

Zhang, K., Varma, A. H., Malushte, S. R., and Gallocher, S. (2014). "Effect of shear connectors on local buckling and composite action in steel concrete composite walls." Nuclear Engineering and Design, 269, 231-239.

Zhao, Q., and Astaneh-Asl, A. (2004). "Cyclic behavior of traditional and innovative composite shear walls." Journal of Structural Engineering, 130(2), 271-284.

Zhong, J. X. (2005). "Model-based simulation of reinforced concrete plane stress structures." Ph.D. dissertation, University of Houston, Houston, TX.

Zhou, J., Mo, Y. L., Sun, X., and Li, J. (2010). "Seismic performance of composite steel plate reinforce concrete shear wall." 12th International Conference on Engineering, Science, Construction, and Operations in Challenging Environments-Earth and Space 2010, American Society of Civil Engineers, 3002-3010.

APPENDIX A. CAD DRAWINGS OF THE SPECIMENS AND FOUNDATION BLOCK

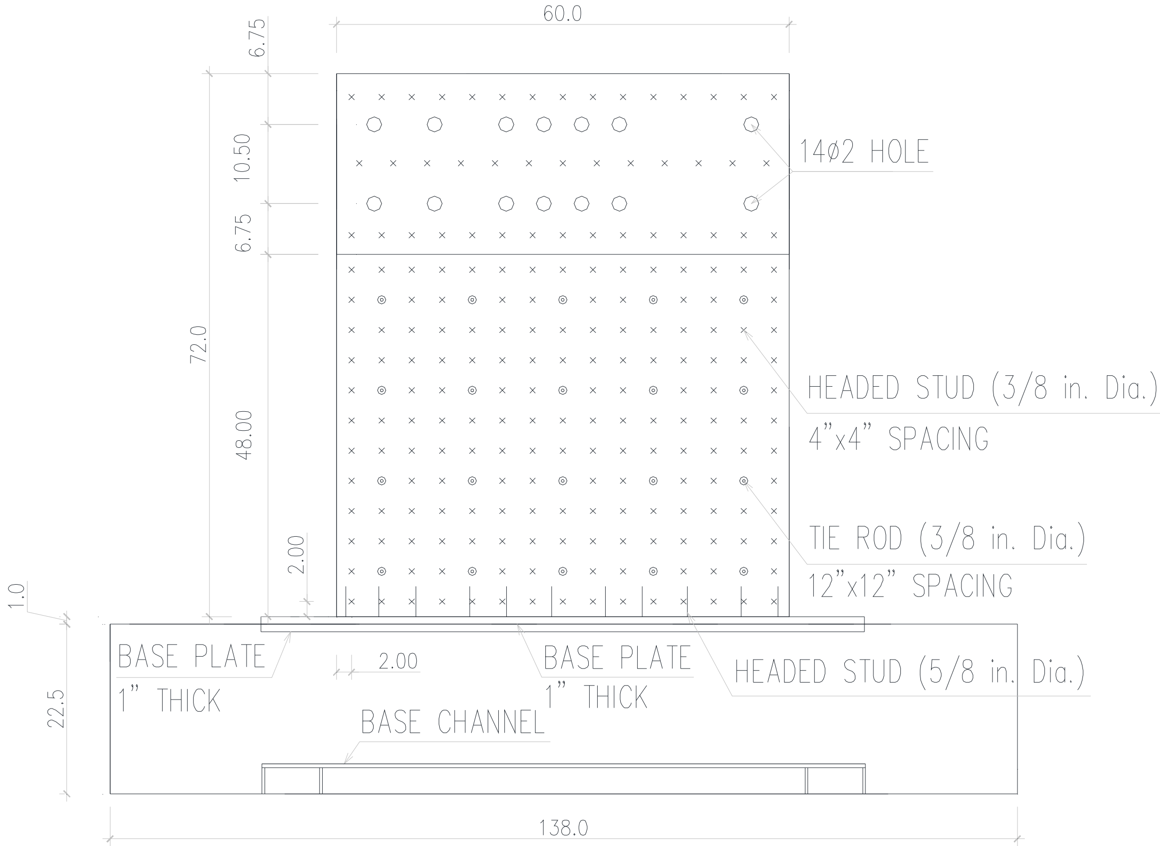

Figure A-1 Elevation view of specimen SC1

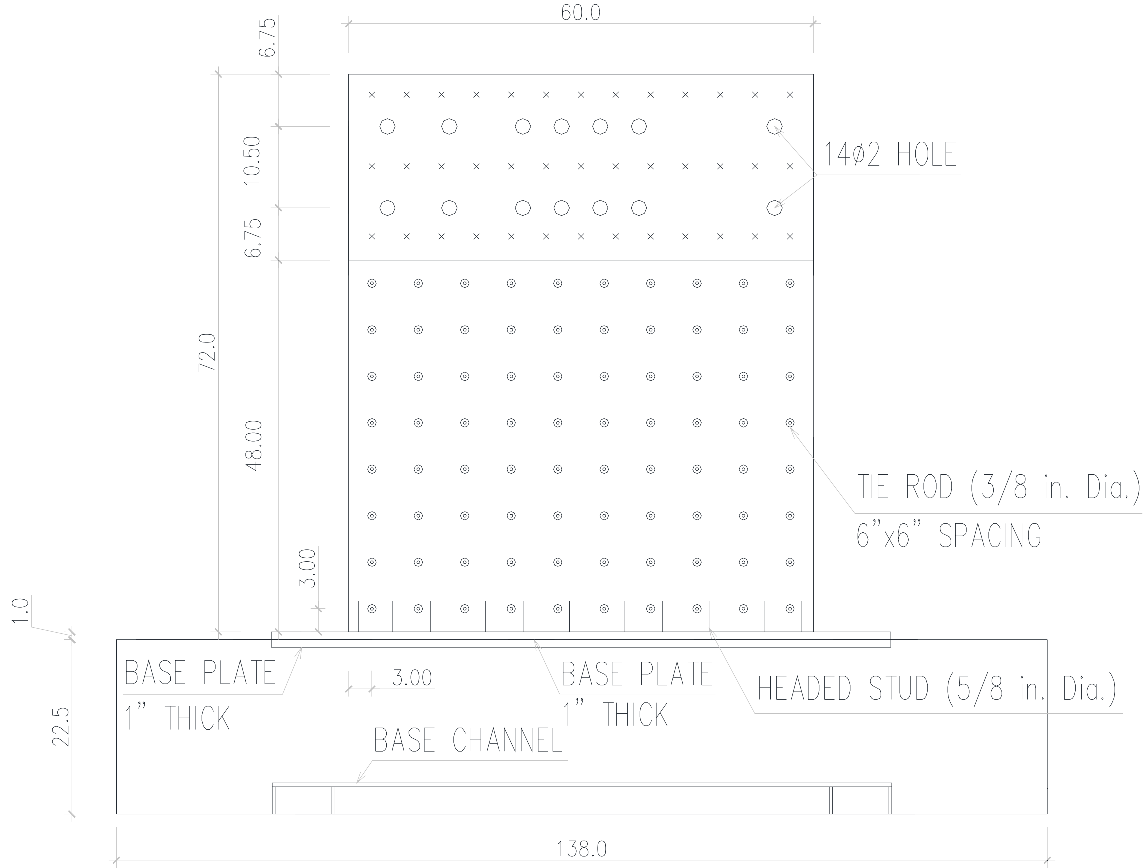

Figure A-2 Elevation view of specimen SC2

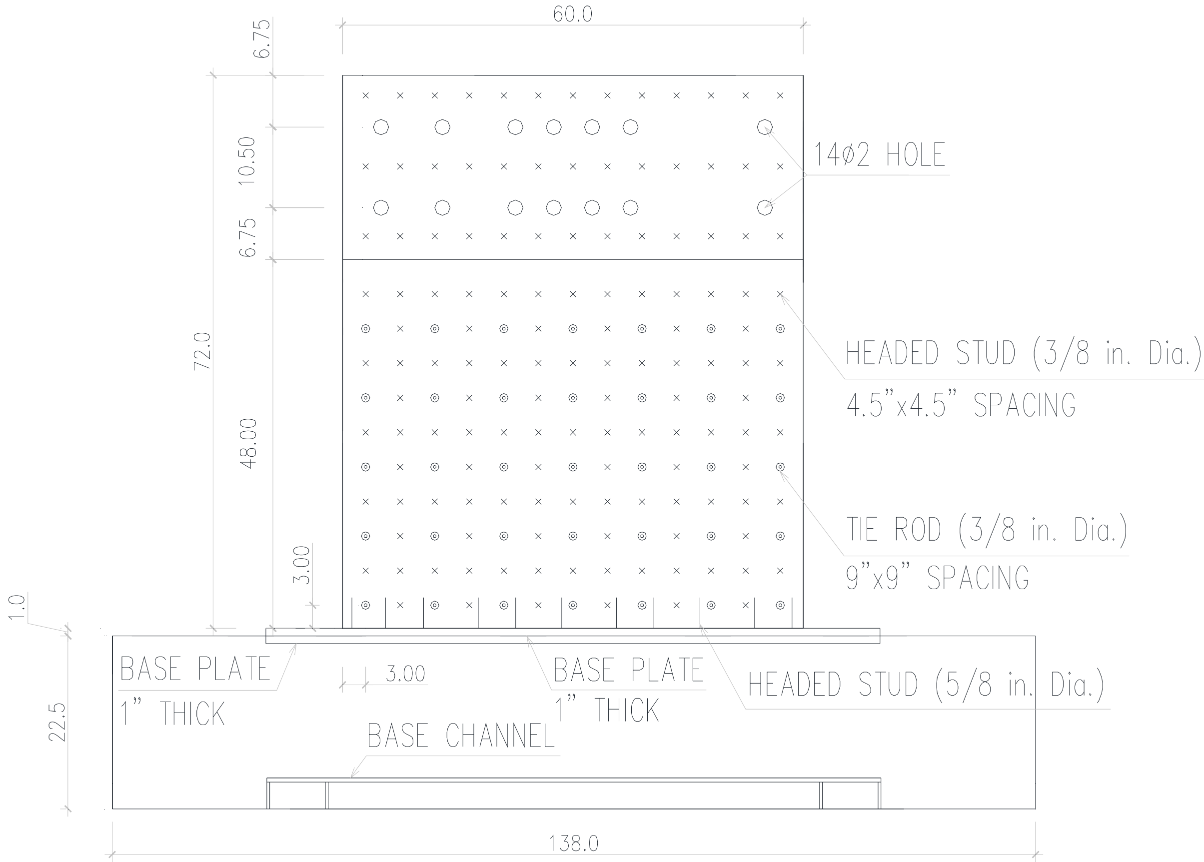

Figure A-3 Elevation view of specimen SC3

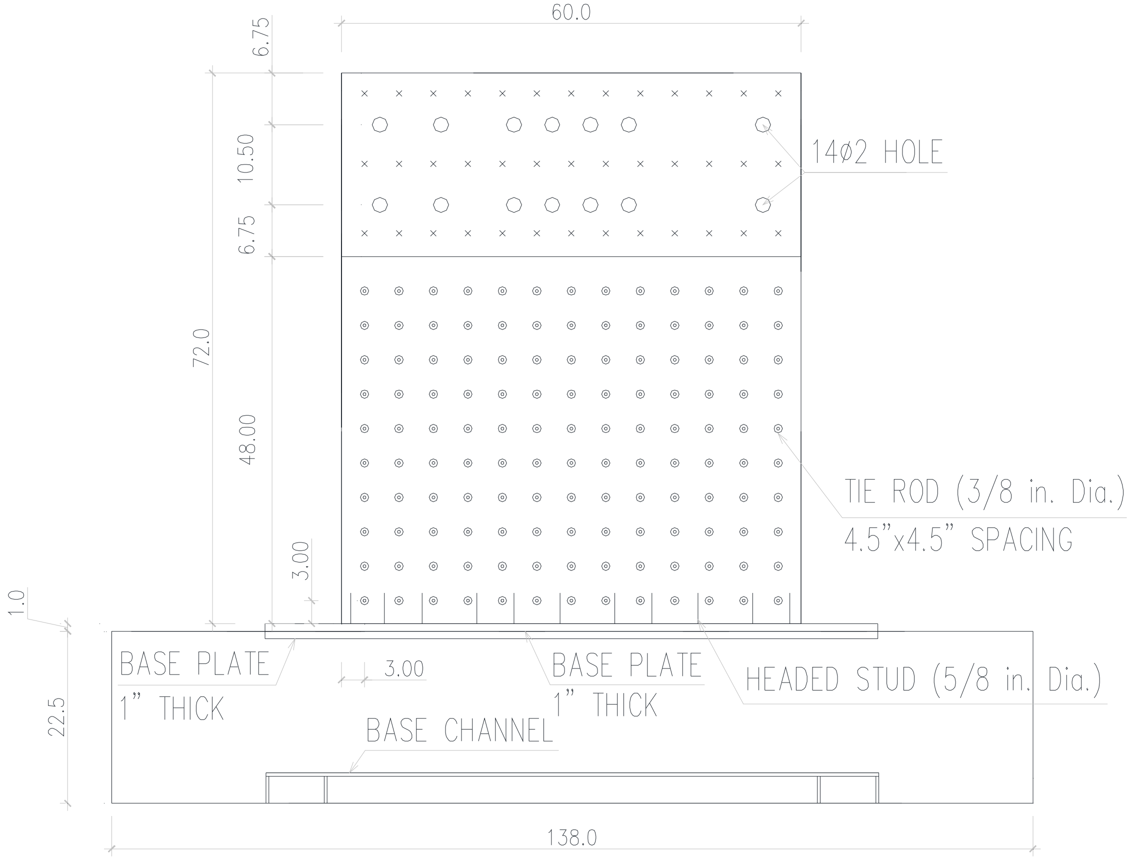

Figure A-4 Elevation view of specimen SC4

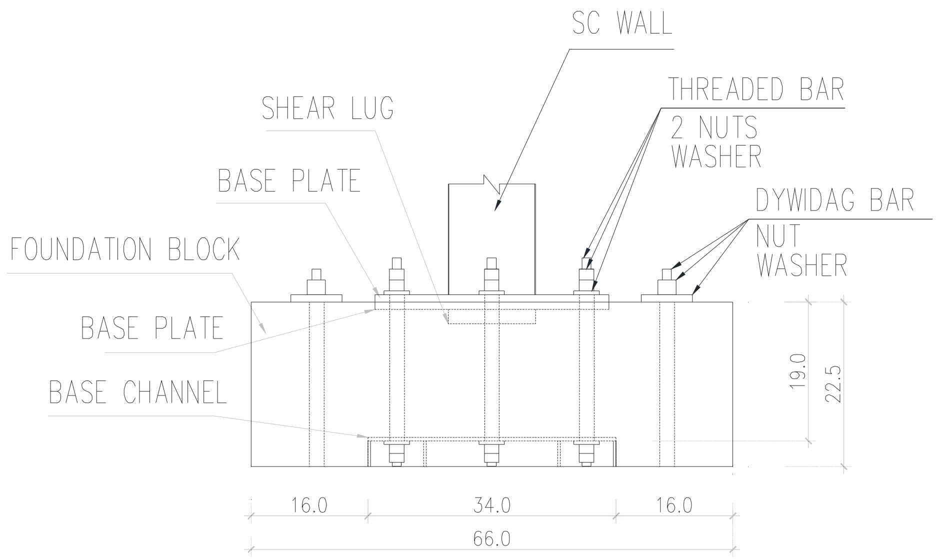

Figure A-5 Cross-section through the foundation block

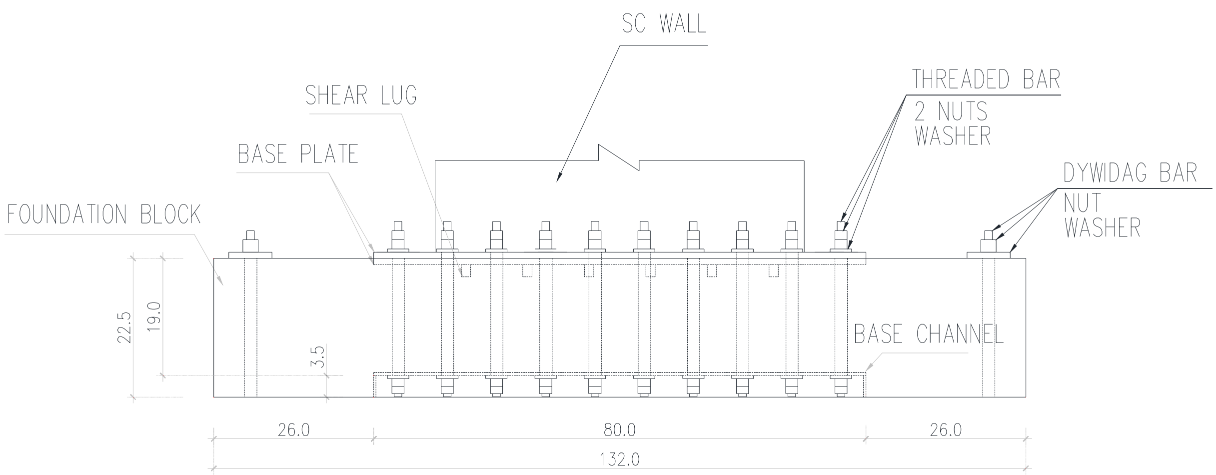

Figure A-6 Cross-section through the foundation block

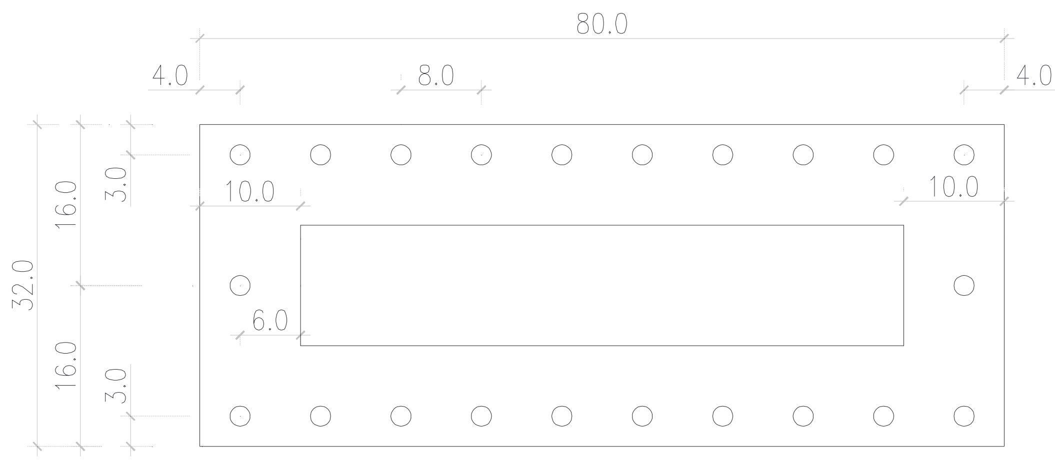

Figure A-7 Plan view of the baseplate

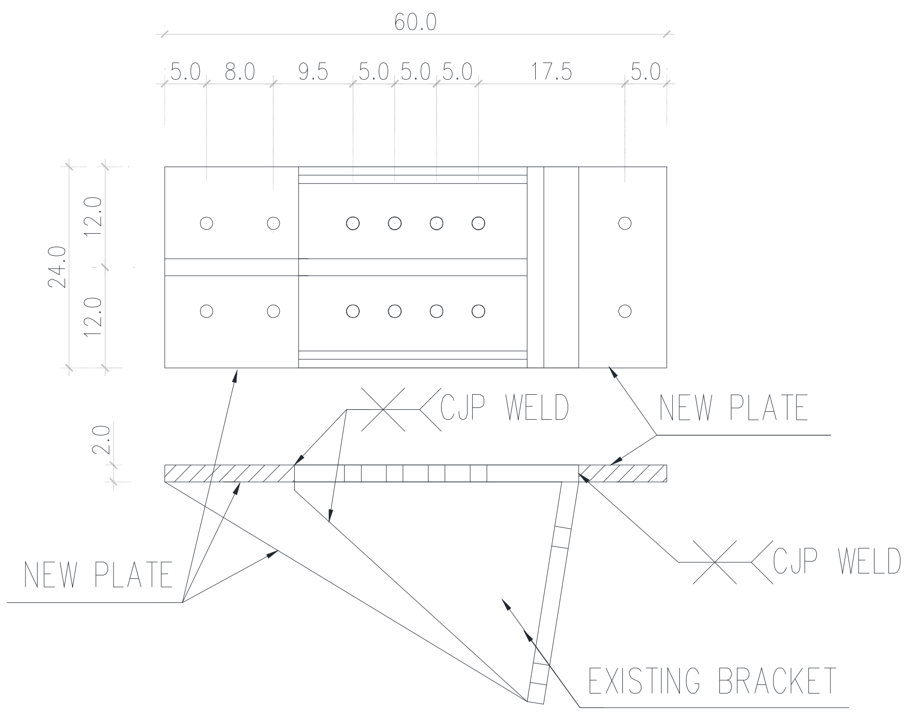

Figure A-8 Loading plate and loading bracket

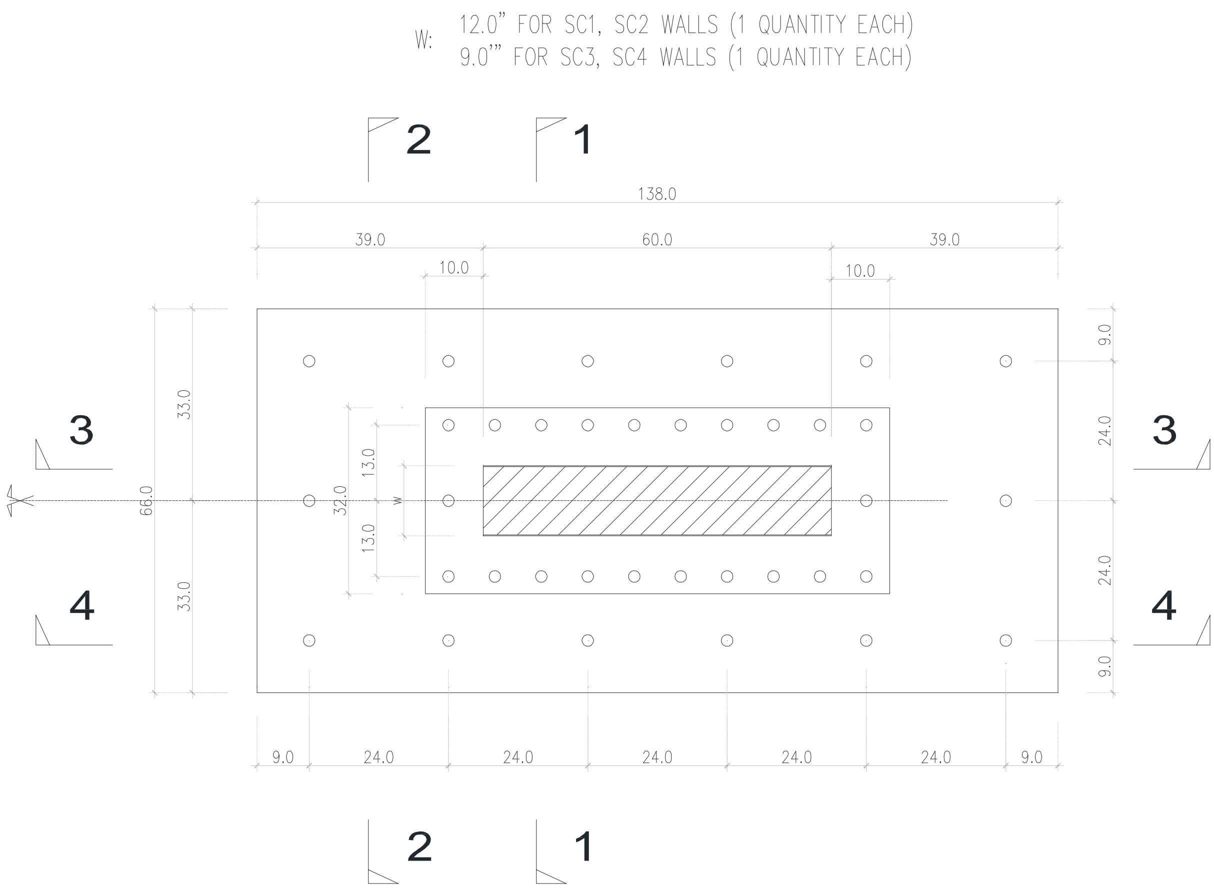

Figure A-9 Plan view of baseplate and top of the foundation block

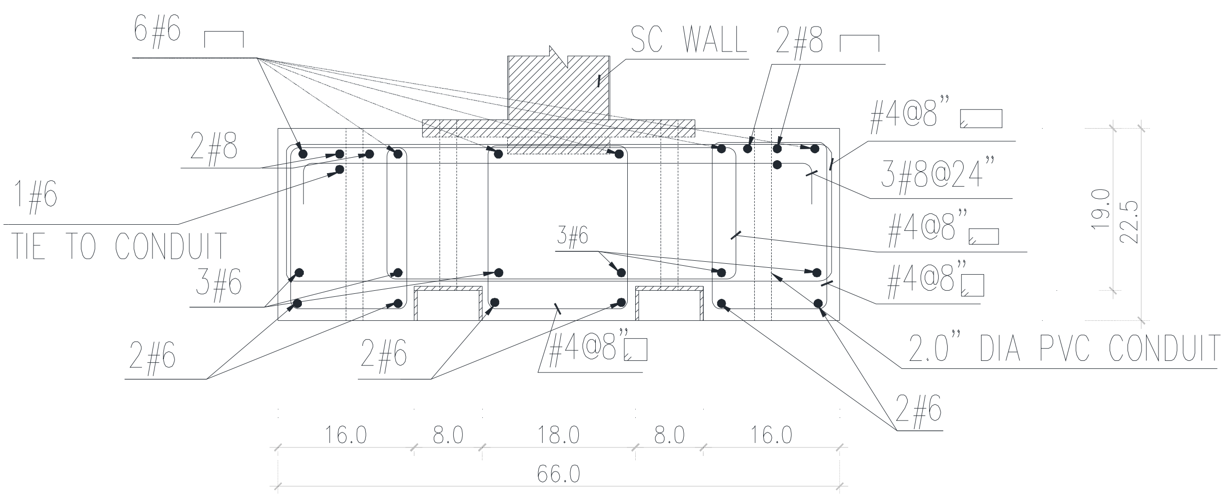

Figure A-10 Section 1-1 per Figure A-9

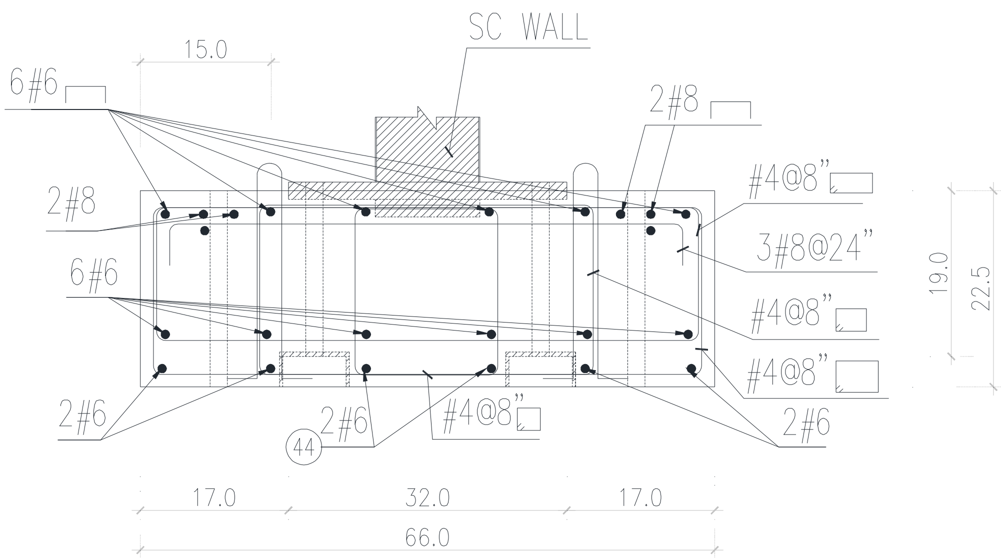

Figure A-11 Section 2-2 per Figure A-9

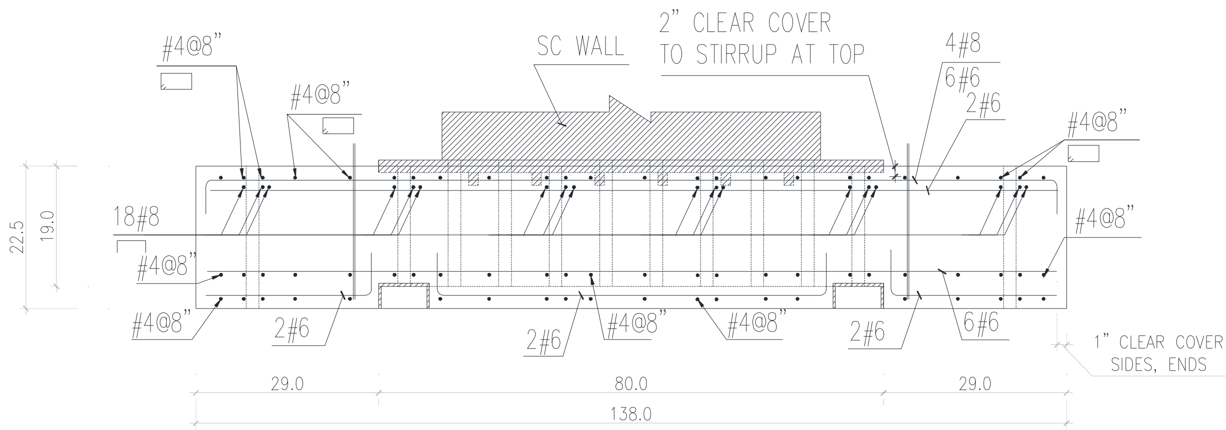

Figure A-12 Section 3-3 per Figure A-9

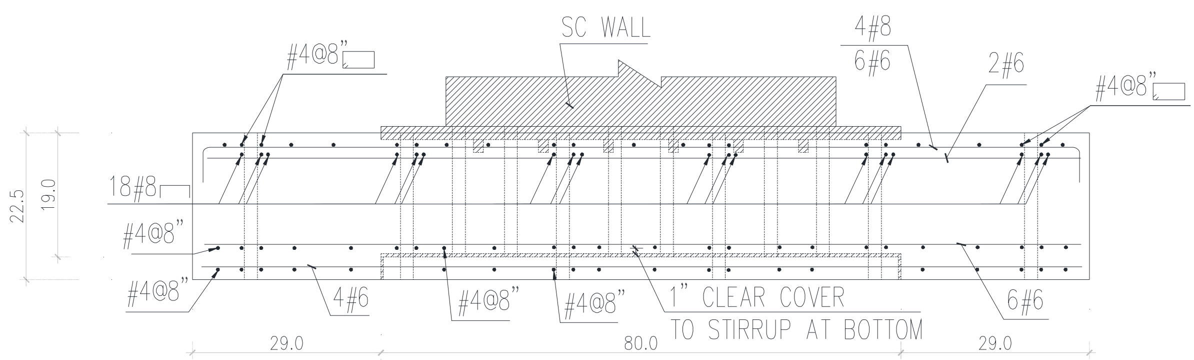

Figure A-13 Section 4-4 per Figure A-9

APPENDIX B. PHOTOGRAPHS OF TEST SPECIMENS

B.1 SC1

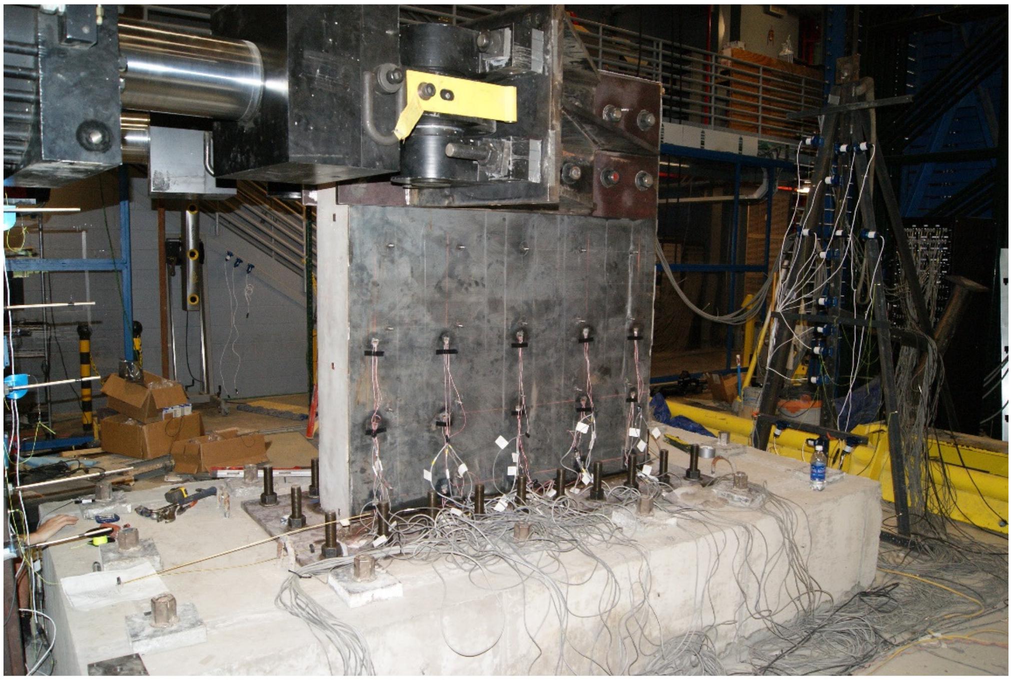

Figure B-1 SC1 before testing

Figure B-2 SC1 before testing

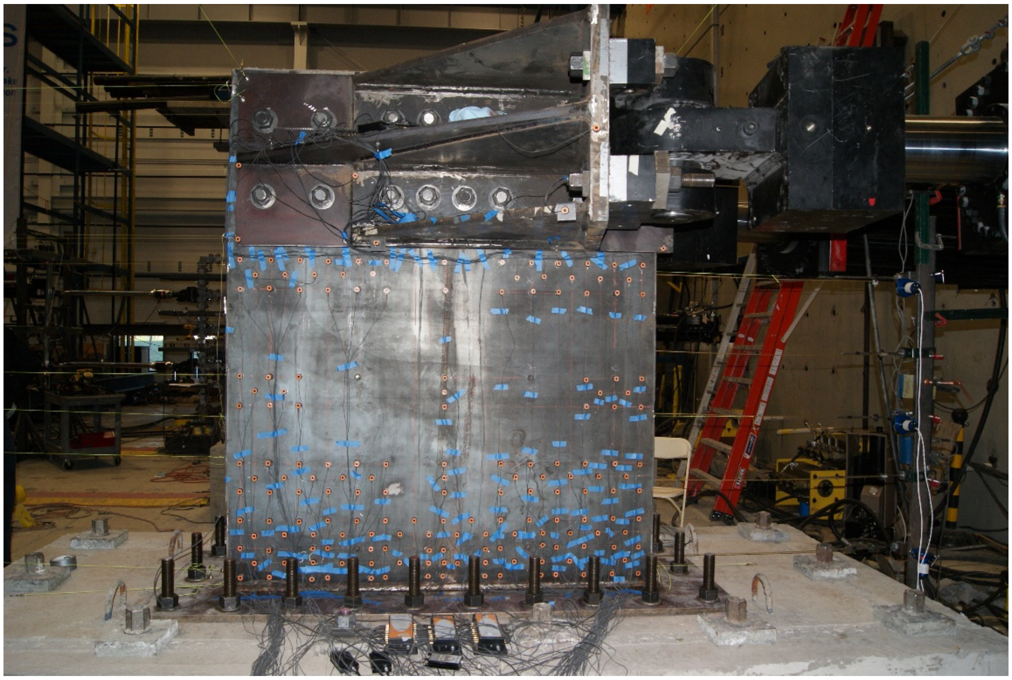

Figure B-3 SC1 before testing

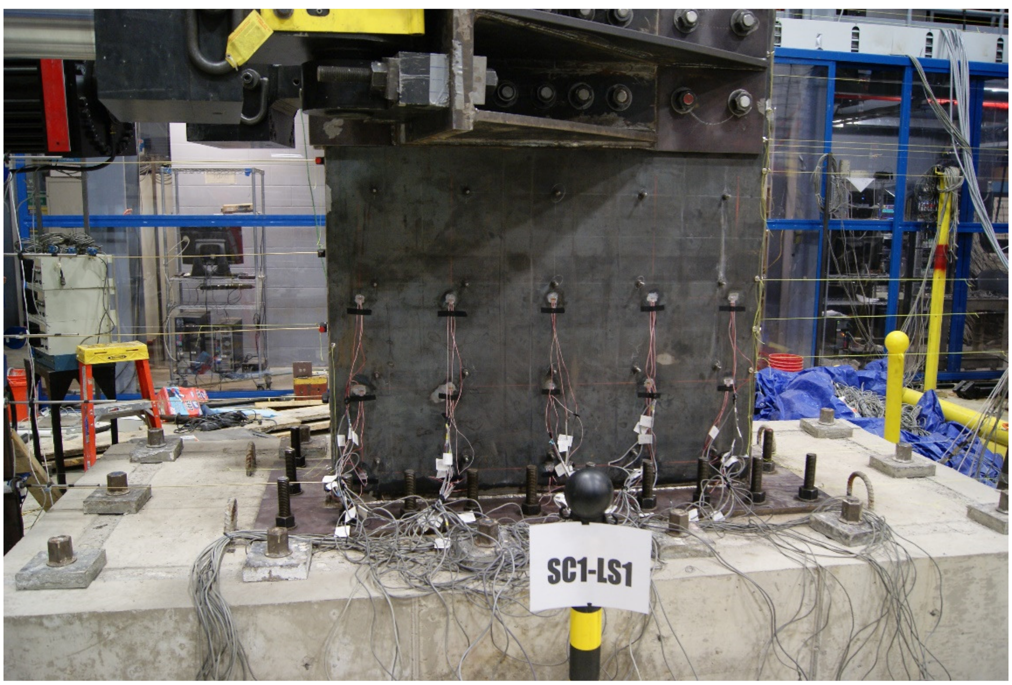

Figure B-4 SC1 before testing

Figure B-5 Damage to SC1 at 0.47% drift ratio

Figure B-6 Damage to SC1 at 0.47% drift ratio

Figure B-7 Damage to SC1 at 0.7% drift ratio

Figure B-8 Damage to SC1 at 0.7% drift ratio

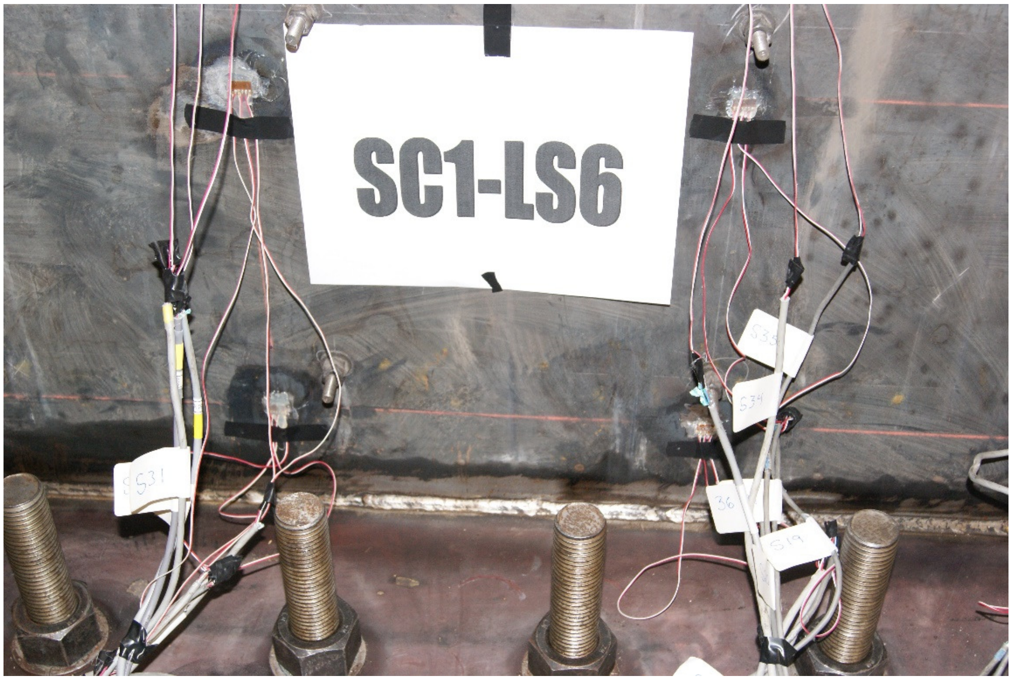

Figure B-9 Damage to SC1 at 0.7% drift ratio


Figure B-10 Damage to SC1 at 0.7% drift ratio

Figure B-11 Damage to SC1 at 0.93% drift ratio

Figure B-12 Damage to SC1 at 0.93% drift ratio

Figure B-13 Damage to SC1 at 1.17% drift ratio

Figure B-14 Damage to SC1 at 1.17% drift ratio

Figure B-15 Damage to SC1 at 1.40% drift ratio

Figure B-16 Damage to SC1 at 1.40% drift ratio

Figure B-17 Damage to SC1 at 1.63% drift ratio

Figure B-18 Damage to SC1 at 1.63% drift ratio

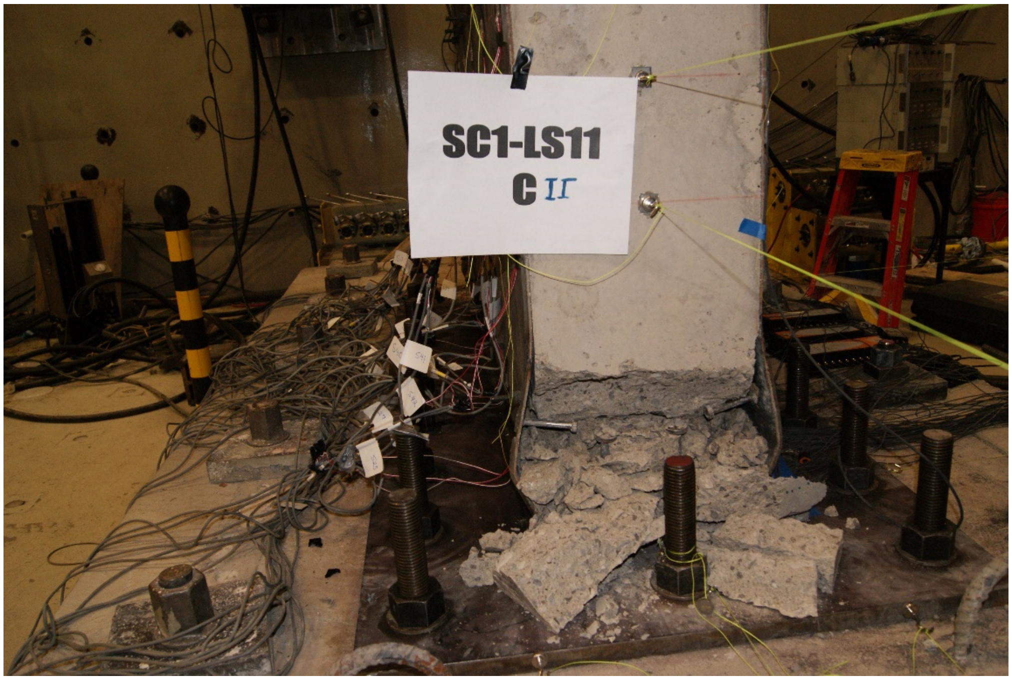

Figure B-19 Damage to SC1 at 1.87% drift ratio

Figure B-20 Damage to SC1 at 1.87% drift ratio

Figure B-21 Damage to SC1 at 2.10% drift ratio

Figure B-22 Damage to SC1 at 2.10% drift ratio

Figure B-23 Damage to SC1 at 2.33% drift ratio


Figure B-24 Damage to SC1 at 2.33% drift ratio

Figure B-25 Damage to SC1 at 2.33% drift ratio

Figure B-26 Damage to SC1 at 2.33% drift ratio

Figure B-27 Damage to SC1 at 2.8% drift ratio

Figure B-28 Damage to SC1 at 2.8% drift ratio

Figure B-29 Damage to SC1 at 2.8% drift ratio

Figure B-30 Damage to SC1 at 2.8% drift ratio

Figure B-31 Damage to SC1 at 2.8% drift ratio

Figure B-32 Damage to SC1 at 2.8% drift ratio

Figure B-33 Damage to SC1 at 3.3% drift ratio

Figure B-34 Damage to SC1 at 3.3% drift ratio

Figure B-35 Damage to SC1 at 3.3% drift ratio

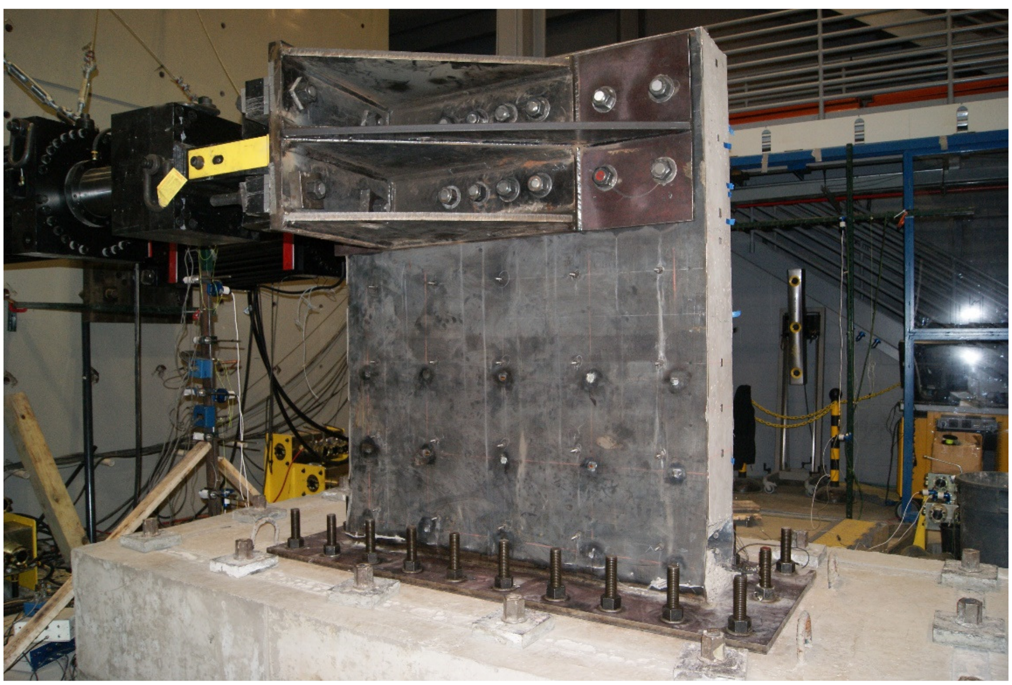

Figure B-36 Damage to SC1 at the end of testing

Figure B-37 Damage to SC1 at the end of testing

Figure B-38 Damage to SC1 at the end of testing

Figure B-39 Damage to SC1 at the end of testing

Figure B-40 Damage to SC1 at the end of testing

B.2 SC2

Figure B-41 Damage to SC2 at 0.47% drift ratio

Figure B-42 Damage to SC2 at 0.47% drift ratio

Figure B-43 Damage to SC2 at 0.70% drift ratio

Figure B-44 Damage to SC2 at 0.70% drift ratio

Figure B-45 Damage to SC2 at 0.93% drift ratio

Figure B-46 Damage to SC2 at 0.93% drift ratio

Figure B-47 Damage to SC2 at 1.17% drift ratio

Figure B-48 Damage to SC2 at 1.17% drift ratio

Figure B-49 Damage to SC2 at 1.40% drift ratio

Figure B-50 Damage to SC2 at 1.40% drift ratio

Figure B-51 Damage to SC2 at 1.63% drift ratio

Figure B-52 Damage to SC2 at 1.63% drift ratio

Figure B-53 Damage to SC2 at 1.63% drift ratio

Figure B-54 Damage to SC2 at 1.63% drift ratio

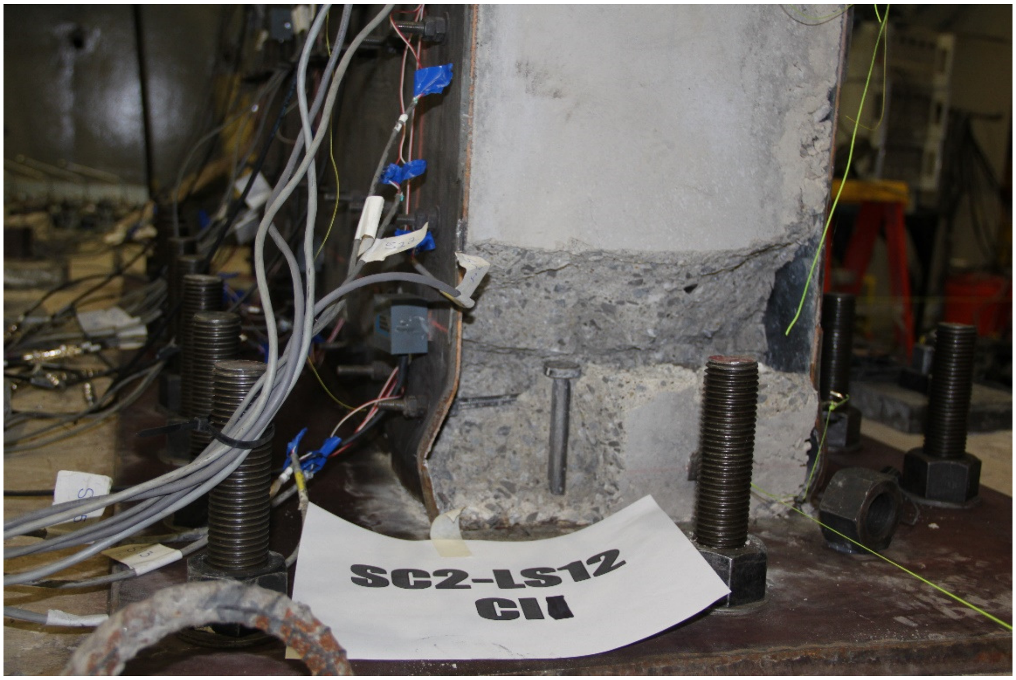

Figure B-55 Damage to SC2 at 2.10% drift ratio

Figure B-56 Damage to SC2 at 2.10% drift ratio

Figure B-57 Damage to SC2 at 2.33% drift ratio

Figure B-58 Damage to SC2 at 2.33% drift ratio

Figure B-59 Damage to SC2 at 2.80% drift ratio

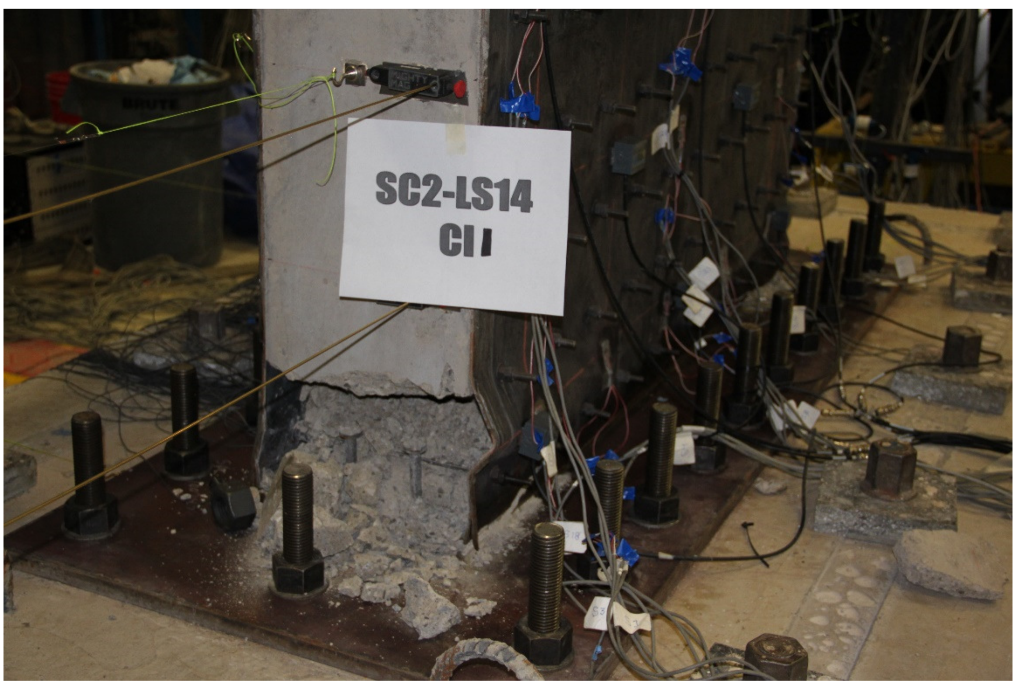

Figure B-60 Damage to SC2 at 2.80% drift ratio

Figure B-61 Damage to SC2 at 3.27% drift ratio

Figure B-62 Damage to SC2 at 3.27% drift ratio

Figure B-63 Damage to SC2 at the end of testing

Figure B-64 Damage to SC2 at the end of testing

Figure B-65 Damage to SC2 at the end of testing

Figure B-66 Damage to SC2 at the end of testing

B.3 SC3

Figure B-67 Damage to SC3 at 0.47% drift ratio

Figure B-68 Damage to SC3 at 0.47% drift ratio

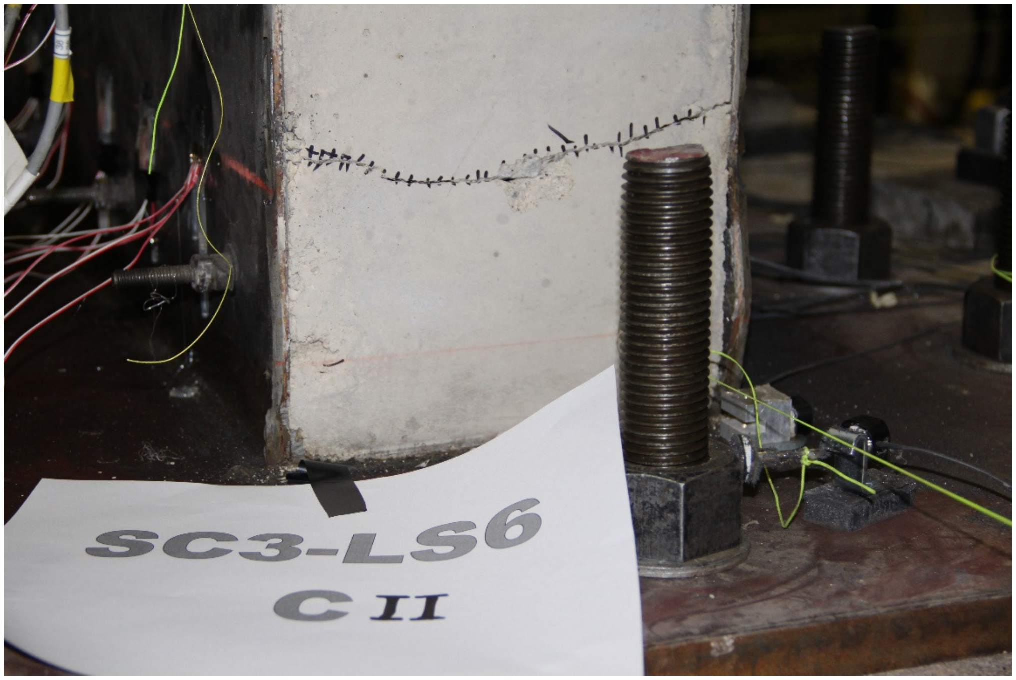

Figure B-69 Damage to SC3 at 0.70% drift ratio

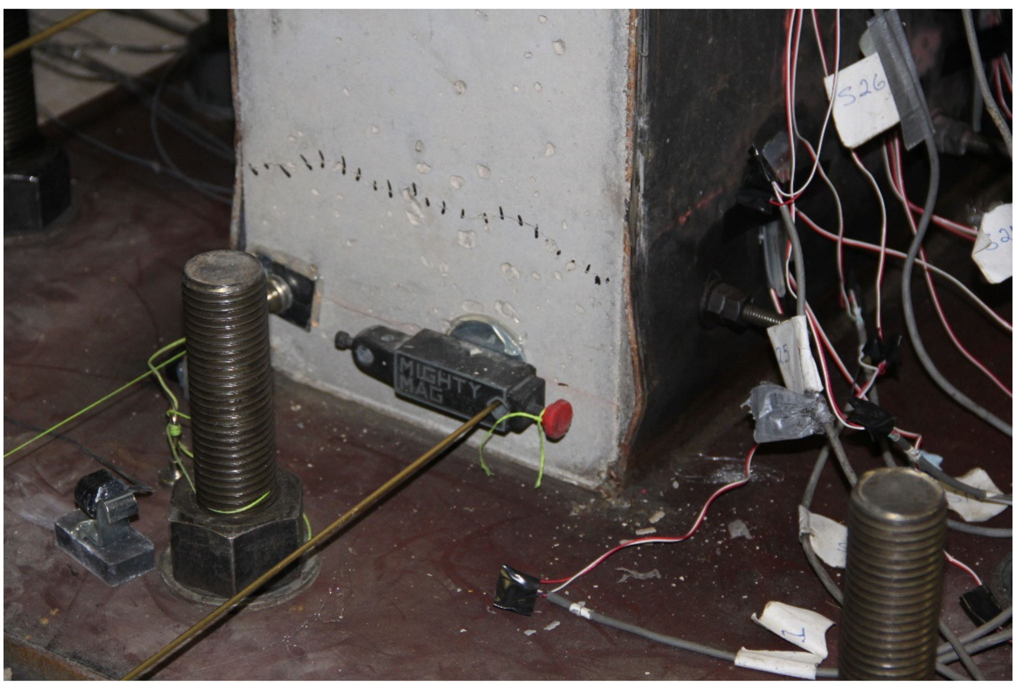

Figure B-70 Damage to SC3 at 0.70% drift ratio

Figure B-71 Damage to SC3 at 0.93% drift ratio

Figure B-72 Damage to SC3 at 0.93% drift ratio

Figure B-73 Damage to SC3 at 1.17% drift ratio

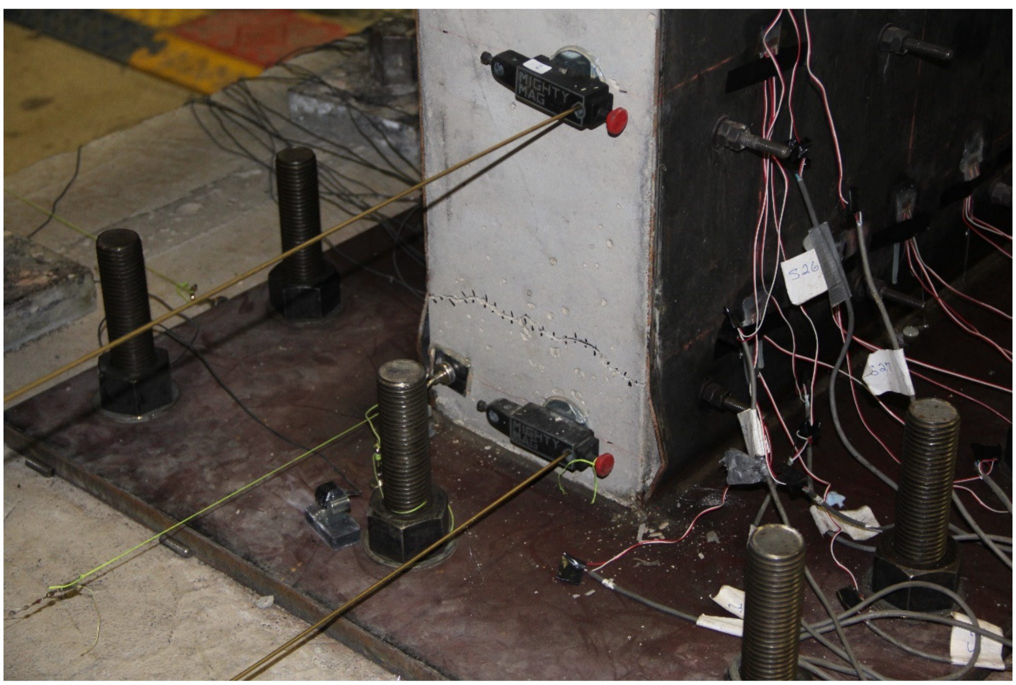

Figure B-74 Damage to SC3 at 1.17% drift ratio

Figure B-75 Damage to SC3 at 1.40% drift ratio

Figure B-76 Damage to SC3 at 1.40% drift ratio

Figure B-77 Damage to SC3 at 1.63% drift ratio

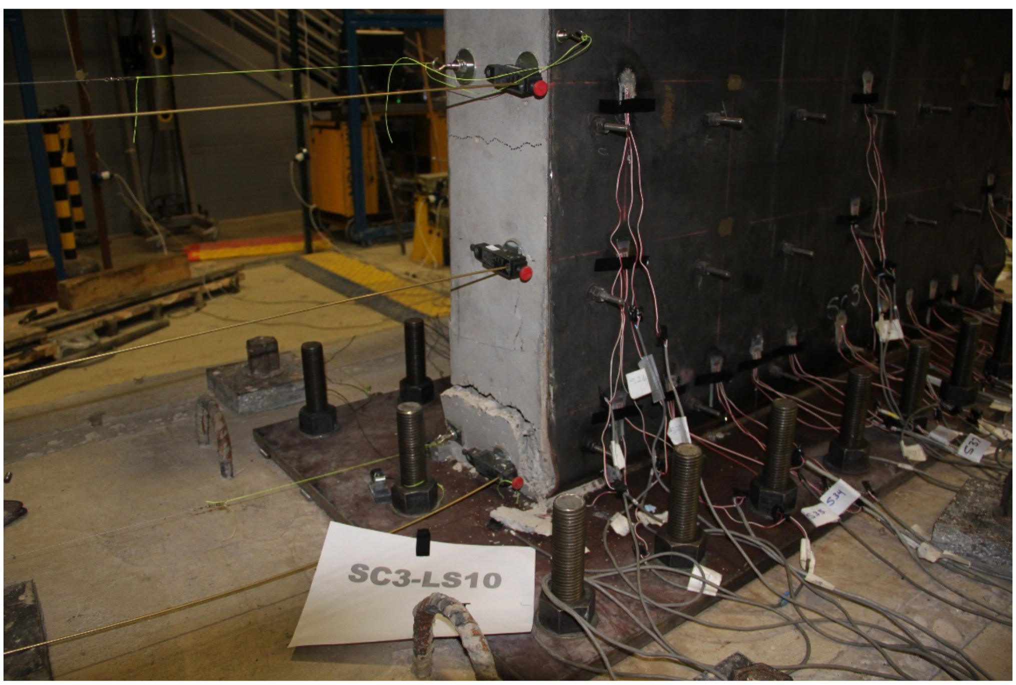

Figure B-78 Damage to SC3 at 1.63% drift ratio

Figure B-79 Damage to SC3 at 1.87% drift ratio

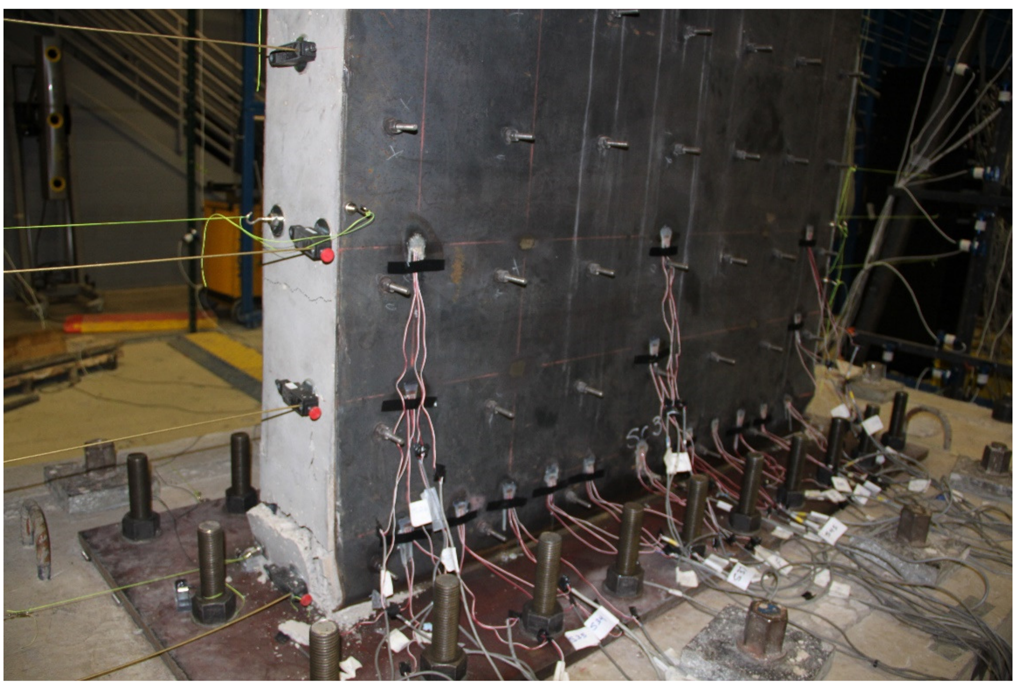

Figure B-80 Damage to SC3 at 1.87% drift ratio

Figure B-81 Damage to SC3 at 2.10% drift ratio

Figure B-82 Damage to SC3 at 2.10% drift ratio

Figure B-83 Damage to SC3 at 2.33% drift ratio

Figure B-84 Damage to SC3 at 2.33% drift ratio

Figure B-85 Damage to SC3 at 2.80% drift ratio

Figure B-86 Damage to SC3 at 2.80% drift ratio

Figure B-87 Damage to SC3 at 3.27% drift ratio

Figure B-88 Damage to SC3 at 3.27% drift ratio

Figure B-89 Damage to SC3 at the end of testing

Figure B-90 Damage to SC3 at the end of testing

Figure B-91 Damage to SC3 at the end of testing

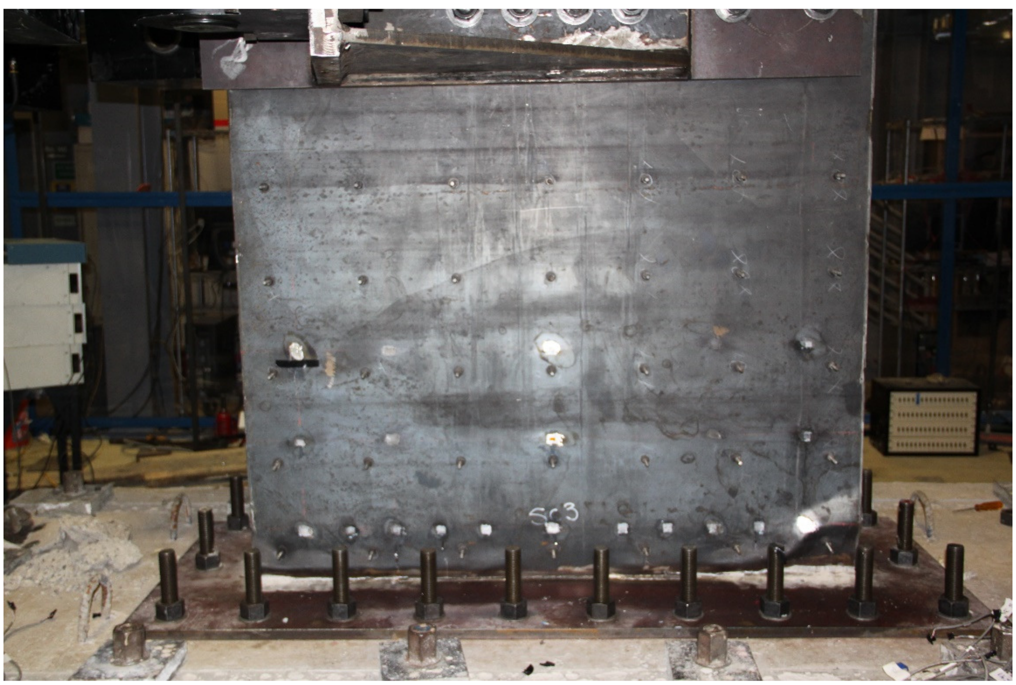

Figure B-92 Damage to SC3 at the end of testing

B.4 SC4

Figure B-93 Damage to SC4 at 0.47% drift ratio

Figure B-94 Damage to SC4 at 0.47% drift ratio

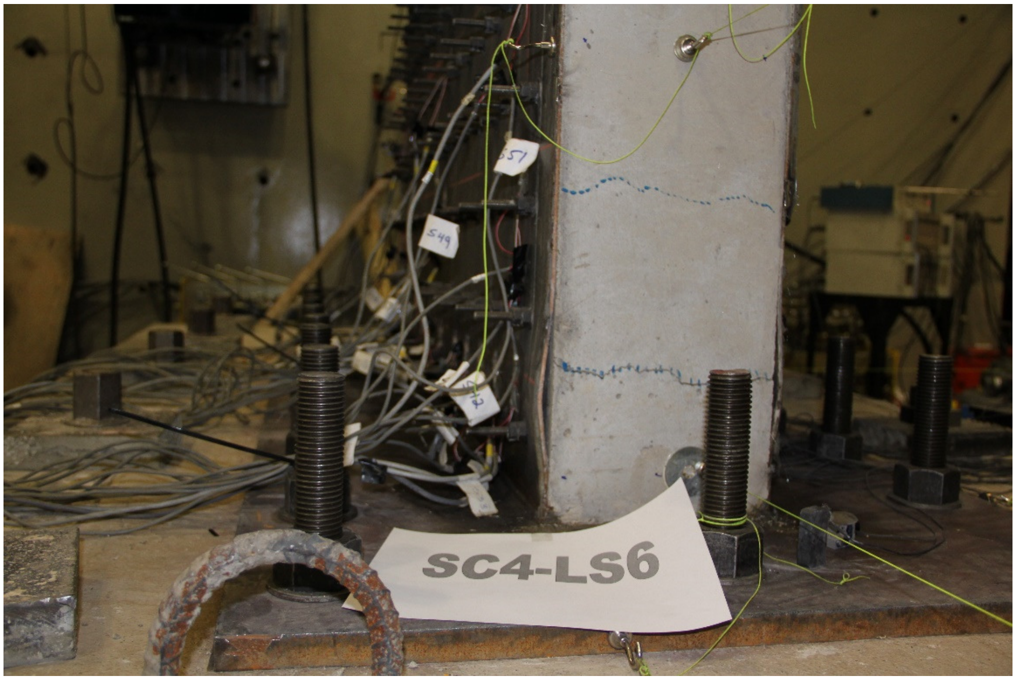

Figure B-95 Damage to SC4 at 0.70% drift ratio

Figure B-96 Damage to SC4 at 0.70% drift ratio

Figure B-97 Damage to SC4 at 0.93% drift ratio

Figure B-98 Damage to SC4 at 0.93% drift ratio

Figure B-99 Damage to SC4 at 1.17% drift ratio

Figure B-100 Damage to SC4 at 1.17% drift ratio

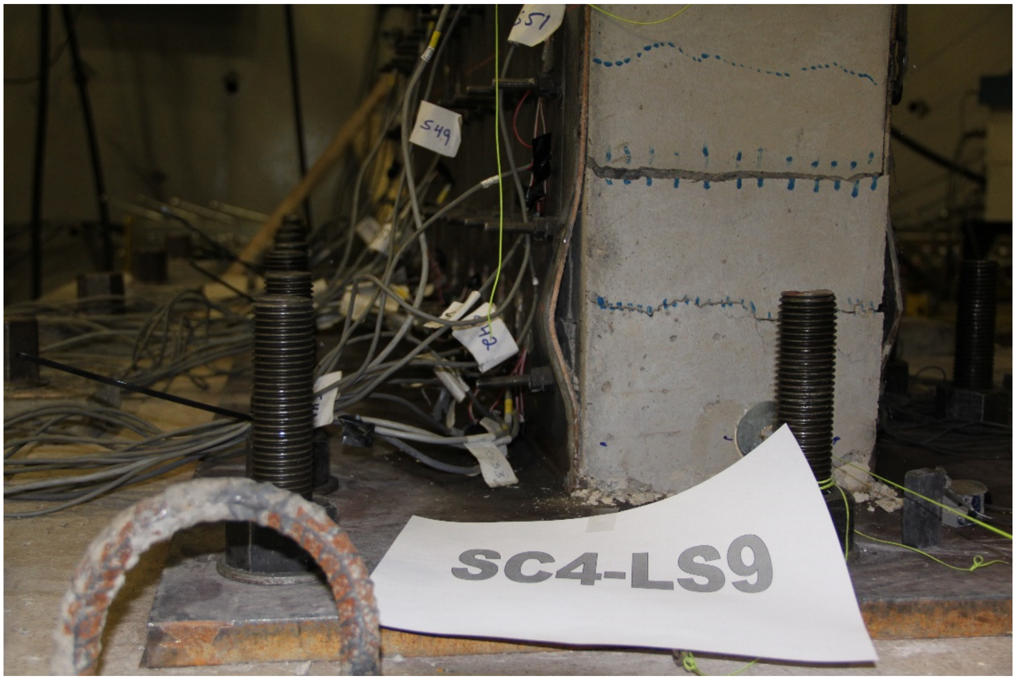

Figure B-101 Damage to SC4 at 1.40% drift ratio

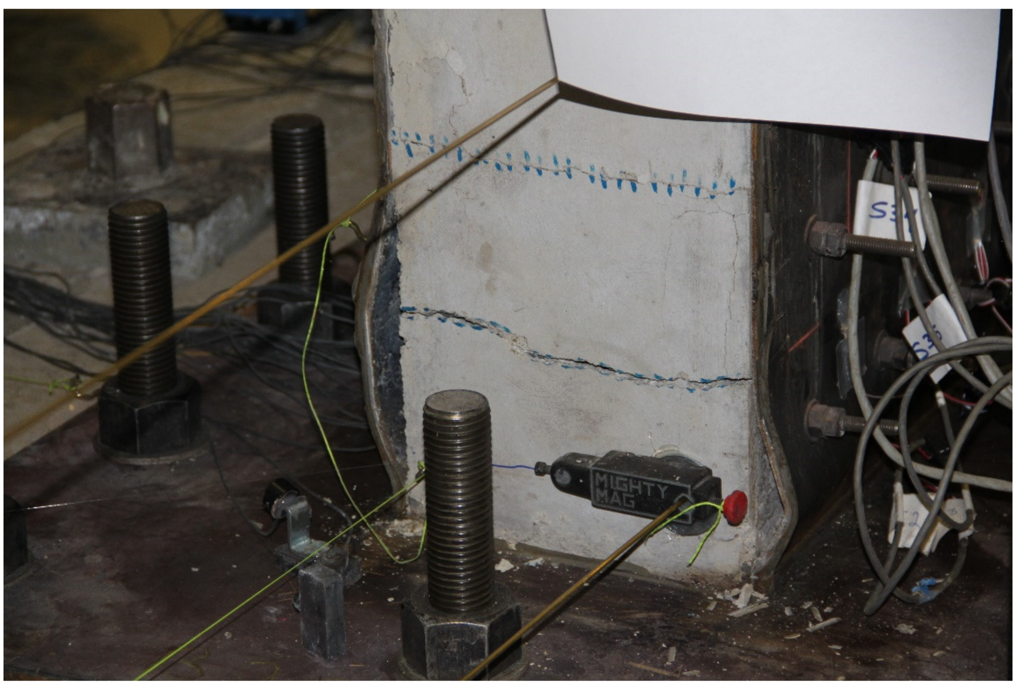

Figure B-102 Damage to SC4 at 1.40% drift ratio

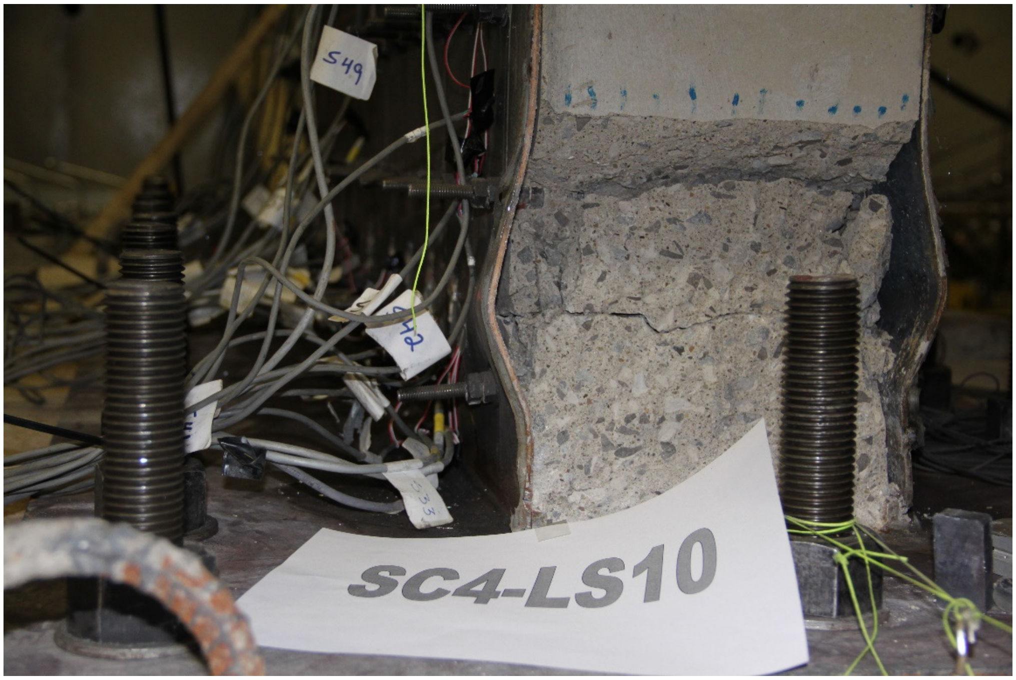

Figure B-103 Damage to SC4 at 1.63% drift ratio

Figure B-104 Damage to SC4 at 1.63% drift ratio

Figure B-105 Damage to SC4 at 1.87% drift ratio

Figure B-106 Damage to SC4 at 1.87% drift ratio

Figure B-107 Damage to SC4 at 2.10% drift ratio

Figure B-108 Damage to SC4 at 2.10% drift ratio

Figure B-109 Damage to SC4 at 2.33% drift ratio

Figure B-110 Damage to SC4 at 2.33% drift ratio

Figure B-111 Damage to SC4 at 2.80% drift ratio

Figure B-112 Damage to SC4 at 2.80% drift ratio

Figure B-113 Damage to SC4 at 3.27% drift ratio

Figure B-114 Damage to SC4 at 3.27% drift ratio

Figure B-115 Damage to SC4 at the end of testing

Figure B-116 Damage to SC4 at the end of testing

Figure B-117 Damage to SC4 at the end of testing

Figure B-118 Damage to SC4 at the end of testing

B.5 Damage to the Infill Concrete of SC2

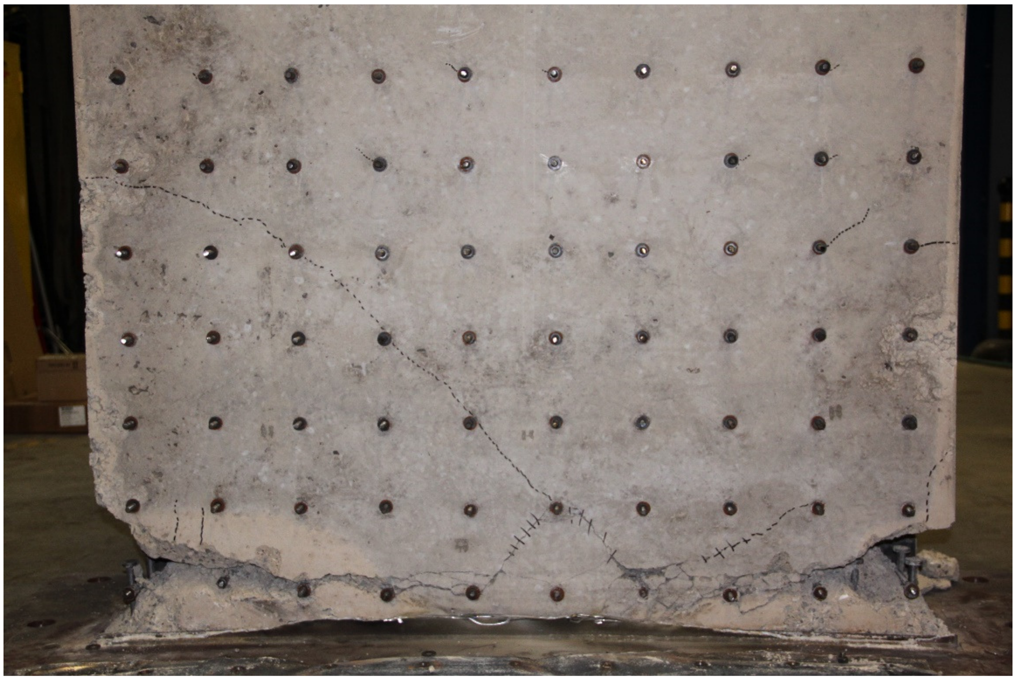

Figure B-119 Damage to the infill concrete of SC2 at the end of testing

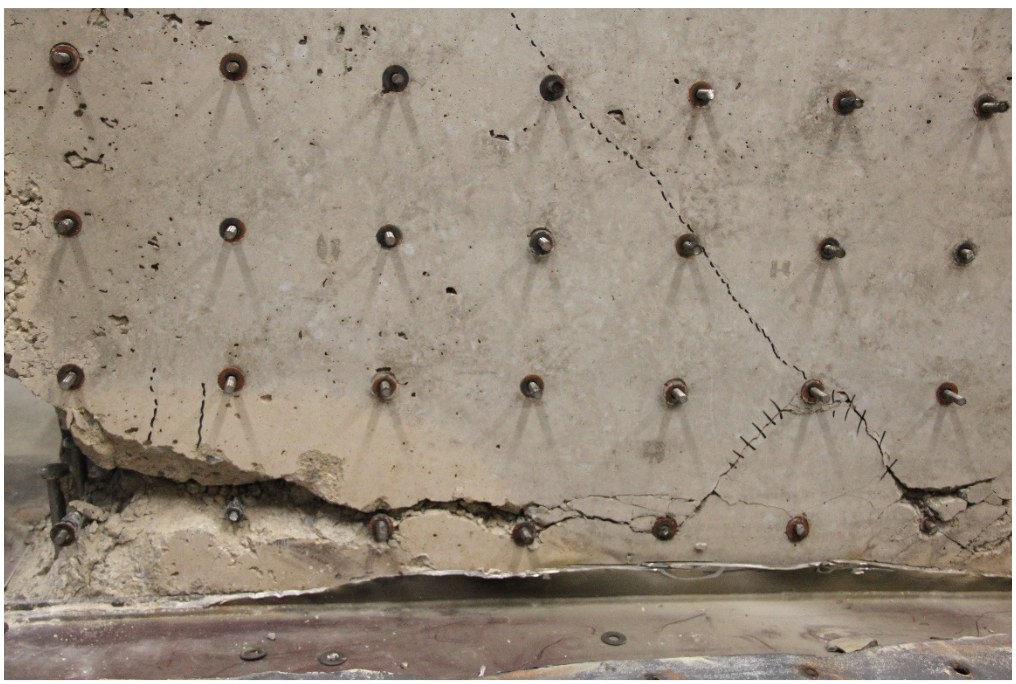

Figure B-120 Damage to the infill concrete of SC2 at the end of testing

Figure B-121 Damage to the infill concrete of SC2 at the end of testing

Figure B-122 Damage to the infill concrete of SC2 at the end of testing

B.6 Damage to the Infill Concrete of SC4

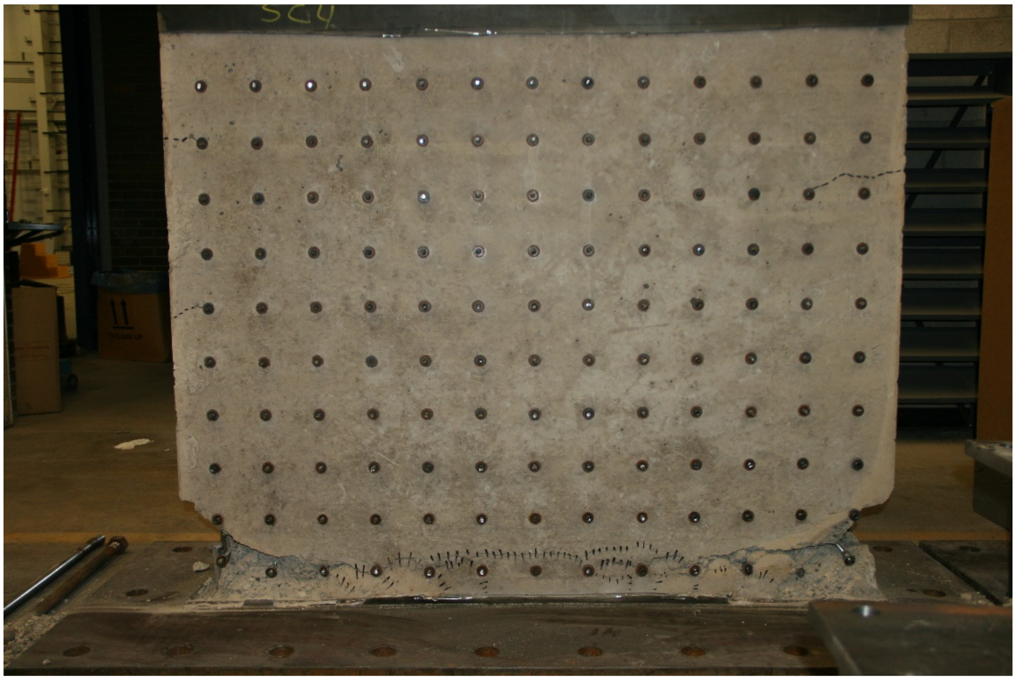

Figure B-123 Damage to the infill concrete of SC4 at the end of testing

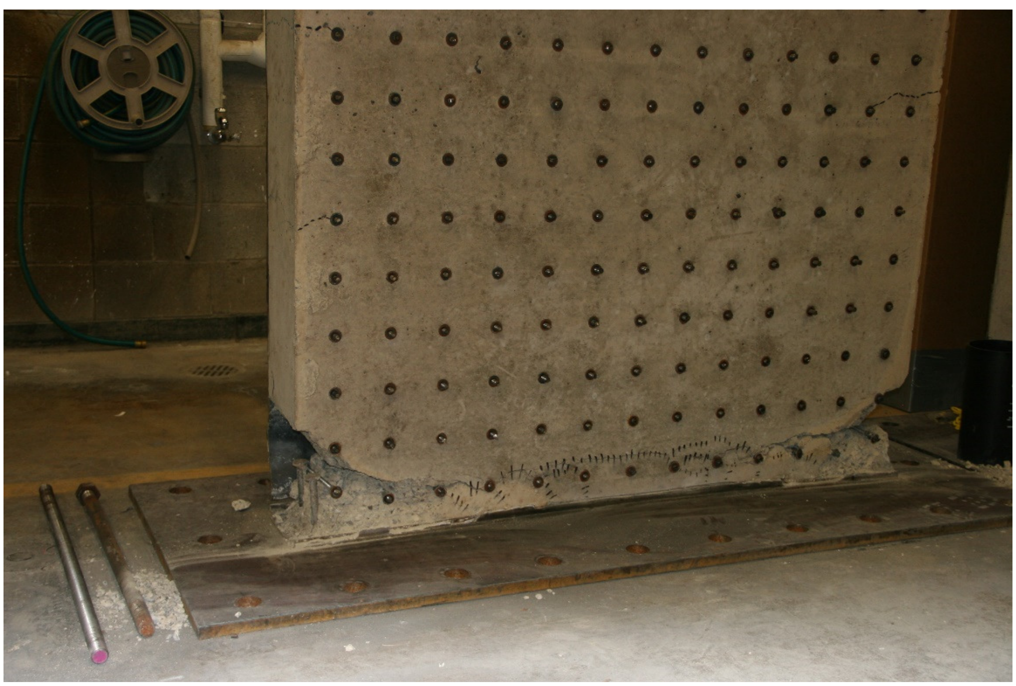

Figure B-124 Damage to the infill concrete of SC4 at the end of testing

Figure B-125 Damage to the infill concrete of SC4 at the end of testing

Figure B-126 Damage to the infill concrete of SC4 at the end of testing

APPENDIX C. ROSETTE GAGE SPECIFICATIONS

062UR

Micro-Measurements

VISHAY PRECISION GROUP

General Purpose Strain Gages - Rectangular Rosette

GAGE PATTERN DATA

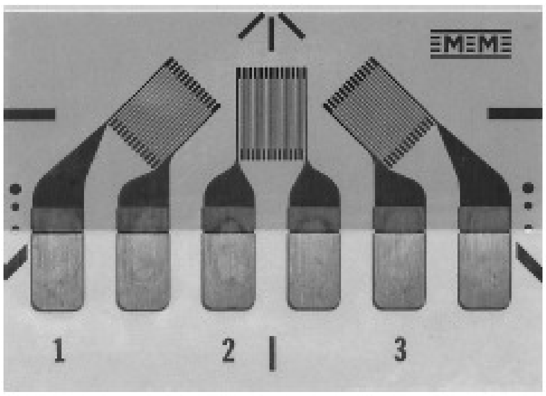

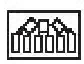

actual size

GAGE DESIGNATION See Note 1	RESISTANCE (OHMS)	OPTIONS AVAILABLE See Note 2
CEA-XX-062UR-120	120 ± 0.4%	P2
CEA-XX-062UR-350	350 ± 0.4%	P2

DESCRIPTION

Small 45° rectangular single-plane rosette in a compact geometry. Exposed solder tab area 0.07 x 0.04 in [1.8 x 1.0 mm]

GAGE DIMENSIONS

Legend: ES = Each Section; S = Section (S1 = Sec 1); CP = Complete Pattern; M = Matrix

inch / millimeter

Gage Length	Overall Length	Grid Width	Overall Width	Matrix Length	Matrix Width
0.062 ES	0.222 CP	0.062 ES	0.420 CP	0.32	0.48
1.57 ES	5.64 CP	1.57 ES	10.67 CP	8.1	12.2

GAGE SERIES DATA See Gage Series data sheet for complete specifications.

Series	Description	Strain Range	Temperature Range
CEA	Universal general-purpose strain gages.	±3%	−100° to +350°F [−75° to +175°C]

Note 1: Insert desired S-T-C number in spaces marked XX.

Note 2: Products with designations and options shown in bold are not RoHS compliant.

APPENDIX D. MATLAB CODE FOR CYCLIC ANALYSIS OF SC WALLS

```
%-----------------------------------------------------------------------------
% University at Buffalo
% Department of Civil, Structural and Environmental Engineering
% MACRO MODEL FOR CYCLIC SIMULATION OF RC and SC WALLS
% Modified-Ibarra-Krawinkler Pinching (MIKP) model
% DEVELOPED BY SIAMAK EPACKACHI - 2014
% UNITS: SI UNITS (kips, inch, s)
%
%-----------------------------------------------------------------------------

clc;
clear;

% ******************************OUTPUT************************************

% F matrix
% first column: total time
% second column: displacement
% third column: force

% ******************************INPUT*************************************

%-----------------------------------------------------------------------------
% info matrix:
% First column presents the values of the displacements of the critical
% points on the backbone curve (first quadrant)
% Second column presents the values of the forces of the critical
% points on the backbone curve (first quadrant)
% First column presents the values of the displacements of the critical
% points on the backbone curve (third quadrant)
% Second column presents the values of the forces of the critical
% points on the backbone curve (third quadrant)
%
%-----------------------------------------------------------------------------

info=[ ...;
0.16    126 0.12    123
0.95    252 0.79    246
1.47    252 1.44    246
2.37    197 1.96    239
];

%-----------------------------------------------------------------------------
% info2 matrix:
% Values of the pinching and deterioration parameters.
%-----------------------------------------------------------------------------

info2=[ ...;
0.5 ...  kf
0.1 ...  kd
0.5 ...  kisi
```

```
1000 ... deterioration parameter for basec strength
1000 ... deterioration parameter for post capping
30 ...   deterioration parameter for unloading 1
20 ...   deterioration parameter for unloading 2
1000 ... deterioration parameter for reloading
20 ...   deterioration parameter for accelerated stiffness
];


%---------------------------------------------------------------------------
% info3 matrix:
% Values of rate parameters.
%---------------------------------------------------------------------------

info3=[ ...
1 ...    rate parameter for basec strength
1 ...    rate parameter for post capping
1 ...    rate parameter for unloading 1
1 ...    rate parameter for unloading 2
1 ...    rate parameter for reloading
1 ...    rate parameter for accelerated stiffness
];

%---------------------------------------------------------------------------
% a matrix is the loading matrix
% first column: load step number
% second column: maximum displacement for each load step
% third column: total time for each load step
% fourth column: displacement increment for each load step
% fifth column: number of cycles per load step
%---------------------------------------------------------------------------

a=[...;
1   0.064     0.12    0.01    3
2   0.13     0.24    0.01    2
3   0.2     0.48    0.01    2
4   0.27     0.72    0.01    2
5   0.36     0.96    0.01    2
6   0.45       1.2     0.01    2
7   0.70    1.44    0.01    2
8   0.95    1.68    0.01    2
9   1.45    1.92    0.01    2
10  2       2.16    0.01    2
];

%----CYCLIC DETERIORATION RULE-----------------------
% RAHNAMA AND KRAWINKLER detflag=0
% EPACKACHI detflag=1
detflag=1;

%----RELOADING PARAMETER-----------------------------
% BILINEAR RELOADING flagl=0
% TRILINEAR RELOADING flagl=1
flagl=0;
```

```
% *******************END OF INPUT PARAMETERS**************************

%----Displacements and forces of the critical points of the backbone curve

xypos=info(1,1);
fypos=info(1,2);
xyneg=info(1,3);
fyneg=info(1,4);

xccpos=info(2,1);
fyypos=info(2,2);
xccneg=info(2,3);
fyyneg=info(2,4);

xcpos=info(3,1);
fupos=info(3,2);
xcneg=info(3,3);
funeg=info(3,4);

xsspos=info(4,1);
frrpos=info(4,2);
xssneg=info(4,3);
frrneg=info(4,4);

frpos=0.2*fypos;
frneg=0.2*fyneg;

mmpos=(info(4,2)-info(3,2))/(info(4,1)-info(3,1));
mmneg=(info(4,4)-info(3,4))/(info(4,3)-info(3,3));
xspos=(frpos-info(3,2))/mmpos+info(3,1);
xsneg=(frneg-info(3,4))/mmneg+info(3,3);

%----PINCHING MODEL-----------------------------

kf=info2(1,1);
kd=info2(1,2);
facfp=info2(1,3);

%--inherent hysteretic energy dissipation -----------------
% BASIC STRENGTH
etots=info2(1,4)*fupos*xcpos;
erates=info3(1,1);
% POST CAPPING
etotc=info2(1,5)*fupos*xcpos;
eratec=info3(1,2);
% UNLOADING STIFFNESS 1
etotk=info2(1,6)*fupos*xcpos;
eratek=info3(1,3);
% UNLOADING STIFFNESS 2
etotkk=info2(1,7)*fupos*xcpos;
eratekk=info3(1,4);
% RELOADING STIFFNESS
etotkkk=info2(1,8)*fupos*xcpos;
eratekkk=info3(1,5);
% ACCELERATED STIFFNESS
```

```
etota=info2(1,9)*fupos*xcpos;
eratea=info3(1,6);

%----STIFFNESS VALUES-----------------------------

kepos=fypos/xypos;
keneg=fyneg/xyneg;
kcpos=(fyypos-fypos)/(xccpos-xypos);
kcneg=(fyyneg-fyneg)/(xccneg-xyneg);
kccpos=(fupos-fyypos)/(xcpos-xccpos);
kccneg=(funeg-fyyneg)/(xcneg-xccneg);
kspos=(frrpos-fupos)/(xsspos-xcpos);
ksneg=(frrneg-funeg)/(xssneg-xcneg);
ksspos=(frpos-frrpos)/(xspos-xsspos);
kssneg=(frneg-frrneg)/(xsneg-xssneg);
krpos=0;
krneg=0;
kunl=0.5*(kepos+keneg);
kunll=kunl;
krelp=kunl;
kreln=kunl;

%----REFERNCE POINT VALUES-----------------------------

sloppos=(frrpos-fupos)/(xsspos-xcpos);
frefpos=fupos-sloppos*xcpos;
slopneg=(frrneg-funeg)/(xssneg-xcneg);
frefneg=funeg-slopneg*xcneg;

%-------------------------------------------------------

[x,y]=size(a);
b(1,1)=0;
b(1,2)=0;
b(1,3)=0;

ind=1;

for i=1:x
    stepc=1/(4*a(i,2)/a(i,4));
    step=a(i,3)/(4*a(i,2)/a(i,4))/a(i,5);
    for j=1:a(i,5)
        for k=a(i,4):a(i,4):a(i,2)
            ind=ind+1;
            b(ind,1)=b(ind-1,1)+stepc;
            b(ind,2)=b(ind-1,2)+step;
            b(ind,3)=k;
        end
        for k=a(i,2)-a(i,4):-a(i,4):-a(i,2)
            ind=ind+1;
            b(ind,1)=b(ind-1,1)+stepc;
            b(ind,2)=b(ind-1,2)+step;
            b(ind,3)=k;
        end
        for k=-a(i,2)+a(i,4):a(i,4):0
```

```
            ind=ind+1;
            b(ind,1)=b(ind-1,1)+stepc;
            b(ind,2)=b(ind-1,2)+step;
            b(ind,3)=k;
        end
    end
end

[x,y]=size(b);

%----INITIALIZATION--------------------------------
stat=1;
ind=1;
F(1,1:13)=0;

fneg=-fyneg;
fpos=fypos;
delneg=-xyneg;
delpos=xypos;
delresneg=0;
delrespos=0;
sume=0;
epos=0;
eneg=0;
betaposs=0;
betanegs=0;
betaposc=0;
betanegc=0;
betaposk=0;
betanegk=0;
betaposkk=0;
betanegkk=0;
betaposkkk=0;
betanegkkk=0;
betaposa=0;
betanega=0;
% Increment of dissipated ennergy at positive side
einc0=0;
% Increment of dissipated ennergy at negative side
einc1=0;
%----------------------------------------------------------
coind=0;
for i=2:x

    coind=coind+1;

    F(i,1)=b(i,2);
    F(i,2)=b(i,3);

    XOLD=b(i-1,3);
    X=b(i,3);
    FOLD=F(i-1,3);

if((stat~=5)&&(stat~=25)&&(stat~=6)&&(stat~=26)&&(stat~=7)&&(stat~=27))
    if(abs(X)>=abs(XOLD))
```

```
if((stat==1)&&(X>0))
    XLB=0;
    XUB=xypos;
    FLB=0;
    FUB=fypos;
    KLB=kepos;
    KUP=kcpos;
    statLB=1;
    statUB=2;
elseif((stat==1)&&(X<0))
    XLB=0;
    XUB=-xyneg;
    FLB=0;
    FUB=-fyneg;
    KLB=keneg;
    KUP=kcneg;
    statLB=21;
    statUB=22;
elseif((stat==21)&&(X<0))
    XLB=0;
    XUB=-xyneg;
    FLB=0;
    FUB=-fyneg;
    KLB=keneg;
    KUP=kcneg;
    statLB=21;
    statUB=22;
elseif((stat==21)&&(X>0))
    XLB=0;
    XUB=xypos;
    FLB=0;
    FUB=fypos;
    KLB=kepos;
    KUP=kcpos;
    statLB=1;
    statUB=2;
elseif(stat==2)
    XLB=xypos;
    XUB=xccpos;
    FLB=fypos;
    FUB=fyypos;
    KLB=kcpos;
    KUP=kccpos;
    statLB=2;
    statUB=200;
elseif(stat==22)
    XLB=-xyneg;
    XUB=-xccneg;
    FLB=-fyneg;
    FUB=-fyyneg;
    KLB=kcneg;
    KUP=kccneg;
    statLB=22;
    statUB=2200;
elseif(stat==200)
    XLB=xccpos;
    XUB=xcpos;
```

```
    FLB=fyypos;
    FUB=fupos;
    KLB=kccpos;
    KUP=kspos;
    statLB=200;
    statUB=3;
elseif(stat==2200)
    XLB=-xccneg;
    XUB=-xcneg;
    FLB=-fyyneg;
    FUB=-funeg;
    KLB=kccneg;
    KUP=ksneg;
    statLB=2200;
    statUB=23;
elseif(stat==3)
    XLB=xcpos;
    XUB=xsspos;
    FLB=fupos;
    FUB=frrpos;
    KLB=kspos;
    KUP=ksspos;
    statLB=3;
    statUB=300;
elseif(stat==23)
    XLB=-xcneg;
    XUB=-xssneg;
    FLB=-funeg;
    FUB=-frrneg;
    KLB=ksneg;
    KUP=kssneg;
    statLB=23;
    statUB=2300;
elseif(stat==300)
    XLB=xsspos;
    XUB=xspos;
    FLB=frrpos;
    FUB=frpos;
    KLB=ksspos;
    KUP=krpos;
    statLB=300;
    statUB=4;
elseif(stat==2300)
    XLB=-xssneg;
    XUB=-xsneg;
    FLB=-frrneg;
    FUB=-frneg;
    KLB=kssneg;
    KUP=krneg;
    statLB=2300;
    statUB=24;
elseif(stat==4)
    XLB=xspos;
    XUB=100*xspos;
    FLB=frpos;
    FUB=frpos;
    KLB=krpos;
```

```
            KUP=krpos;
            statLB=4;
            statUB=4;
        elseif(stat==24)
            XLB=-xsneg;
            XUB=-100*xsneg;
            FLB=-frneg;
            FUB=-frneg;
            KLB=krneg;
            KUP=krneg;
            statLB=24;
            statUB=24;
        end
        if (abs(X)<=abs(XUB))
            F(i,3)=(X-XLB)*KLB+FLB;
            stat=statLB;
%---------------Hysteretic Energy--------------------------
            if(F(i,3)>=0)
                efalg=0;
                einc0=0.5*(F(i,3)+FOLD)*(X-XOLD);
            else
                efalg=1;
                einc1=0.5*(F(i,3)+FOLD)*(X-XOLD);
            end
%----------------------------------------------------------
        else
            F(i,3)=(X-XUB)*KUP+FUB;
            stat=statUB;
%---------------Hysteretic Energy--------------------------
            if(F(i,3)>=0)
                efalg=0;
                einc0=0.5*(F(i,3)+FUB)*(X-XUB)+0.5*(FUB+FOLD)*(XUB-XOLD);
            else
                efalg=1;
                einc1=0.5*(F(i,3)+FUB)*(X-XUB)+0.5*(FUB+FOLD)*(XUB-XOLD);
            end
%----------------------------------------------------------
        end
    else
        if (stat==1)
            if(X>=0)
                F(i,3)=kepos*X;
                stat=1;
%---------------Hysteretic Energy--------------------------
                efalg=0;
                einc0=0.5*(F(i,3)+FOLD)*(X-XOLD);
%----------------------------------------------------------
            else
                F(i,3)=keneg*X;
                stat=21;
%---------------Hysteretic Energy--------------------------
                efalg=2;
                einc0=-0.5*FOLD*XOLD;
                einc1=0.5*F(i,3)*X;
%----------------------------------------------------------
            end
        elseif (stat==21)
```

```
            if(X<=0)
                F(i,3)=keneg*X;
                stat=21;
%---------------Hysteretic Energy--------------------------
                efalg=1;
                eincl=0.5*(F(i,3)+FOLD)*(X-XOLD);
%------------------------------------------------------------
            else
                F(i,3)=kepos*X;
                stat=1;
%---------------Hysteretic Energy--------------------------
                efalg=3;
                eincl=-0.5*FOLD*XOLD;
                einc0=0.5*F(i,3)*X;
%------------------------------------------------------------
            end
        else
            if(FOLD>=0)
                F(i,3)=FOLD+(X-XOLD)*kunl;
                stat=5;
                delpos=XOLD;
                fpos=FOLD;
                del5m=XOLD;
                f5m=FOLD;
%---------------Hysteretic Energy--------------------------
                efalg=0;
                einc0=0.5*(F(i,3)+FOLD)*(X-XOLD);
%------------------------------------------------------------
            else
                F(i,3)=FOLD+(X-XOLD)*kunl;
                stat=25;
                delneg=XOLD;
                fneg=FOLD;
                del25m=XOLD;
                f25m=FOLD;
%---------------Hysteretic Energy--------------------------
                efalg=1;
                eincl=0.5*(F(i,3)+FOLD)*(X-XOLD);
%------------------------------------------------------------
            end
        end
    end
elseif (stat==5)
    del5=delpos;
    f5=fpos;
    if(X<=del5)
        F(i,3)=FOLD+(X-XOLD)*kunl;
            if (F(i,3)>=facfp*f5m)
                stat=5;
%---------------Hysteretic Energy--------------------------
                efalg=0;
                einc0=0.5*(F(i,3)+FOLD)*(X-XOLD);
%------------------------------------------------------------
            else
                XPOSM=del5m-f5m*(1-facfp)/kunl;
                slopu=max(facfp*f5m/XPOSM,kunll);
                F(i,3)=facfp*f5m+(X-XPOSM)*slopu;
```

```
                if (F(i,3)>=0)
                    stat=5;
%---------------Hysteretic Energy--------------------------
                efalg=0;
                einc0=0.5*(F(i,3)+FOLD)*(X-XOLD);
%------------------------------------------------------------
                else
%---FIRST AND SECOND DET:BASIC AND POST CAPPING STRENGTH---
                frefneg=(1-betaposc)*frefneg;
                fynegold=fyneg;
                fyneg=(1-betaposs)*fyneg;
                fyyneg=fyyneg-(fyneg-fynegold);

                if(fyyneg<=frneg)
                    fyyneg=frneg;
                    kcneg=(fyyneg-fyneg)/(xccneg-xyneg);
                    kccneg=0;
                else
                    kcneg=(1-betaposs)*kcneg;
                    kccneg=(1-betaposs)*kccneg;
                    if(kccneg<=0)
                        kccneg=0;
                    end
                    if(kcneg<=0)
                        kcneg=0;
                    end
                    if(kcneg<=kccneg)
                        kcneg=kccneg;
                    end
                end
                xyneg=fyneg/keneg;
                xccneg=(fyyneg-fyneg)/kcneg+xyneg;
                xcneg=(frefneg-fyyneg+kccneg*xccneg)/(kccneg-slopneg);
                frrneg=frefneg+slopneg*xssneg;
                if(frrneg<frneg)
                    frrneg=frneg;
                    xssneg=(frneg-frefneg)/slopneg;
                    kssneg=0;
                    xsneg=xssneg;
                else
                    xsneg=xssneg+(frneg-frrneg)/kssneg;
                end
                funeg=fyyneg+kccneg*(xcneg-xccneg);

                if((abs(delneg)>=xyneg)&&(abs(delneg)<=xccneg))
                    fneg=-(fyneg+kcneg*(abs(delneg)-xyneg));
                elseif((abs(delneg)>xccneg)&&(abs(delneg)<=xcneg))
                    fneg=-(fyyneg+kccneg*(abs(delneg)-xccneg));
                elseif((abs(delneg)>xcneg)&&(abs(delneg)<=xssneg))
                    fneg=-(funeg+ksneg*(abs(delneg)-xcneg));
                elseif((abs(delneg)>xssneg)&&(abs(delneg)<=xsneg))
                    fneg=-(frrneg+kssneg*(abs(delneg)-xssneg));
                else
                    fneg=-((abs(delneg)-xsneg)*krneg+frneg);
                end
%---THIRD DET: UNLOADING STIFFNESS-----------------------
```

```
                kunl=(1-betaposk)*kunl;
%---FOURTH DET: ACCELERATED STIFF-------------------------
                delneg=(1+betaposa)*delneg;
                if((abs(delneg)>=xyneg)&&(abs(delneg)<=xccneg))
                    fneg=-(fyneg+kcneg*(abs(delneg)-xyneg));
                elseif((abs(delneg)>=xccneg)&&(abs(delneg)<=xcneg))
                    fneg=-(fyyneg+kccneg*(abs(delneg)-xccneg));
                elseif((abs(delneg)>xcneg)&&(abs(delneg)<=xssneg))
                    fneg=-(funeg+ksneg*(abs(delneg)-xcneg));
                elseif((abs(delneg)>xssneg)&&(abs(delneg)<=xsneg))
                    fneg=-(frrneg+kssneg*(abs(delneg)-xssneg));
                else
                    fneg=-((abs(delneg)-xsneg)*krneg+frneg);
                end
%---FIFTH DET: UNLOADING STIFFNESS-------------------------
                kunll=(1-betaposkk)*kunll;
%---SIXTH DET: RELOADING STIFFNESS-------------------------
                krelp=(1-betaposkkk)*krelp;
%------------------------------------------------------------
                delrespos=XOLD-FOLD/kunll;
                if (delrespos<0)
                    delrespos=0;
                end
                stat=26;
                if(flagl==0)
%----BILINEAR RELOADING-----------------------------------
                    m26=kf*abs(fneg)/(delrespos-delneg);
                    F(i,3)=(X-delrespos)*m26;
                else
%----TRLINEAR RELOADING-----------------------------------
                    m26=kf*abs(fneg)/(delrespos-delneg);
                    if(krelp<m26)
                        m266=m26;
                    else
                        y0=-krelp*delrespos;
                        if(abs(y0)>abs(kf*fneg))
                            m266=abs(kf*fneg)/delrespos;
                            m26=0;
                        else
                            m266=krelp;
                            m26=(abs(kf*fneg)-abs(y0))/(-delneg);
                        end
                    end
                    y0n=-m266*delrespos;
                    F(i,3)=(X-delrespos)*m266;
                end
%---------------Hysteretic Energy--------------------------
                efalg=2;
                einc0=-0.5*FOLD*(XOLD-delrespos);
                einc1=0.5*F(i,3)*(X-delrespos);
%------------------------------------------------------------
                end
            end
    else
        if(del5<=xccpos)
            if(X<=xccpos)
                F(i,3)=f5+kcpos*(X-del5);
```

```
                stat=2;
%---------------Hysteretic Energy--------------------------
                efalg=0;
                einc0=0.5*(F(i,3)+f5)*(X-del5)+0.5*(f5+FOLD)*(del5-XOLD);
%----------------------------------------------------------
            else
                F(i,3)=fyypos+kccpos*(X-xccpos);
                stat=200;
%---------------Hysteretic Energy--------------------------
                efalg=0;
                einc0=0.5*(F(i,3)+fyypos)*(X-xccpos)+0.5*(fyypos+f5)*(xccpos-
del5)+0.5*(f5+FOLD)*(del5-XOLD);
%----------------------------------------------------------
            end
        elseif(del5<=xcpos)
            if(X<=xcpos)
                F(i,3)=f5+kccpos*(X-del5);
                stat=200;
%---------------Hysteretic Energy--------------------------
                efalg=0;
                einc0=0.5*(F(i,3)+f5)*(X-del5)+0.5*(f5+FOLD)*(del5-XOLD);
%----------------------------------------------------------
            else
                F(i,3)=fupos+kspos*(X-xcpos);
                stat=3;
%---------------Hysteretic Energy--------------------------
                efalg=0;
                einc0=0.5*(F(i,3)+fupos)*(X-xcpos)+0.5*(fupos+f5)*(xcpos-
del5)+0.5*(f5+FOLD)*(del5-XOLD);
%----------------------------------------------------------
            end
        elseif(del5<=xsspos)
            if(X<=xsspos)
                F(i,3)=f5+kspos*(X-del5);
                stat=3;
%---------------Hysteretic Energy--------------------------
                efalg=0;
                einc0=0.5*(F(i,3)+f5)*(X-del5)+0.5*(f5+FOLD)*(del5-XOLD);
%----------------------------------------------------------
            else
                F(i,3)=frrpos+ksspos*(X-xsspos);
                stat=300;
%---------------Hysteretic Energy--------------------------
                efalg=0;
                einc0=0.5*(F(i,3)+frrpos)*(X-xsspos)+0.5*(frrpos+f5)*(xsspos-
del5)+0.5*(f5+FOLD)*(del5-XOLD);
%----------------------------------------------------------
            end
        elseif(del5<=xspos)
            if(X<=xspos)
                F(i,3)=f5+ksspos*(X-del5);
                stat=300;
%---------------Hysteretic Energy--------------------------
                efalg=0;
                einc0=0.5*(F(i,3)+f5)*(X-del5)+0.5*(f5+FOLD)*(del5-XOLD);
%----------------------------------------------------------
            else
```

```
                F(i,3)=frpos+krpos*(X-xspos);
                stat=4;
%---------------Hysteretic Energy--------------------------
                efalg=0;
                einc0=0.5*(F(i,3)+frpos)*(X-xspos)+0.5*(frpos+f5)*(xspos-
del5)+0.5*(f5+FOLD)*(del5-XOLD);
%----------------------------------------------------------
            end
        else
            F(i,3)=f5+krpos*(X-del5);
            stat=4;
%---------------Hysteretic Energy--------------------------
                efalg=0;
                einc0=0.5*(F(i,3)+f5)*(X-del5)+0.5*(f5+FOLD)*(del5-XOLD);
%----------------------------------------------------------
        end
    end
elseif (stat==25)
    del25=delneg;
    f25=fneg;
    if(X>=del25)
        F(i,3)=FOLD+(X-XOLD)*kunl;
        if (F(i,3)<=facfp*f25m)
            stat=25;
 %---------------Hysteretic Energy--------------------------
                efalg=1;
                einc1=0.5*(F(i,3)+FOLD)*(X-XOLD);
%----------------------------------------------------------
        else
            XNEGM=del25m-f25m*(1-facfp)/kunl;
            slopu=max(facfp*f25m/XNEGM,kunll);
            F(i,3)=facfp*f25m+(X-XNEGM)*slopu;
            if (F(i,3)<=0)
                stat=25;
%---------------Hysteretic Energy--------------------------
                efalg=1;
                einc1=0.5*(F(i,3)+FOLD)*(X-XOLD);
%----------------------------------------------------------
            else
%---FIRST AND SECOND DET:BASIC AND POST CAPPING STRENGTH---
                frefpos=(1-betanegc)*frefpos;
                fyposold=fypos;
                fypos=(1-betanegs)*fypos;
                fyypos=fyypos-(fypos-fyposold);
                if(fyypos<=frpos)
                    fyypos=frpos;
                    kcpos=(fyypos-fypos)/(xccpos-xypos);
                    kccpos=0;
                else
                    kcpos=(1-betanegs)*kcpos;
                    kccpos=(1-betanegs)*kccpos;
                    if(kccpos<=0)
                        kccpos=0;
                    end
                    if(kcpos<=0)
                        kcpos=0;
                    end
```

```
                if(kcpos<=kccpos)
                    kcpos=kccpos;
                end
            end
            xypos=fypos/kepos;
            xccpos=(fyypos-fypos)/kcpos+xypos;
            xcpos=(frefpos-fyypos+kccpos*xccpos)/(kccpos-sloppos);
            frrpos=frefpos+sloppos*xsspos;
            if(frrpos<frpos)
                frrpos=frpos;
                xsspos=(frpos-frefpos)/sloppos;
                ksspos=0;
                xspos=xsspos;
            else
                xspos=xsspos+(frpos-frrpos)/ksspos;
            end
            fupos=fyypos+kccpos*(xcpos-xccpos);

            if((delpos>=xypos)&&(delpos<=xccpos))
                fpos=fypos+kcpos*(delpos-xypos);
            elseif((delpos>xccpos)&&(delpos<=xcpos))
                fpos=fyypos+kccpos*(delpos-xccpos);
            elseif((delpos>xcpos)&&(delpos<=xsspos))
                fpos=fupos+kspos*(delpos-xcpos);
            elseif((delpos>xsspos)&&(delpos<=xspos))
                fpos=frrpos+ksspos*(delpos-xsspos);
            else
                fpos=(delpos-xspos)*krpos+frpos;
            end
%---THIRD DET: UNLOADING STIFFNESS------------------------
            kunl=(1-betanegk)*kunl;
%---FOURTH DET: ACCELERATED STIFF------------------------
            delpos=(1+betanega)*delpos;
            if((delpos>=xypos)&&(delpos<=xccpos))
                fpos=fypos+kcpos*(delpos-xypos);
            elseif((delpos>=xccpos)&&(delpos<=xcpos))
                fpos=fyypos+kccpos*(delpos-xccpos);
            elseif((delpos>xcpos)&&(delpos<=xsspos))
                fpos=fupos+kspos*(delpos-xcpos);
            elseif((delpos>xsspos)&&(delpos<=xspos))
                fpos=frrpos+ksspos*(delpos-xsspos);
            else
                fpos=(delpos-xspos)*krpos+frpos;
            end
%---FIFTH DET: UNLOADING STIFFNESS-------------------------
            kunll=(1-betanegkk)*kunll;
%---SIXTH DET: RELOADING STIFFNESS-------------------------
            kreln=(1-betanegkkk)*kreln;
%------------------------------------------------------------
            delresneg=XOLD-FOLD/kunll;
            if (delresneg>0)
                delresneg=0;
            end
            stat=6;
            if(flagl==0)
%----BILINEAR RELOADING----------------------------------
                m6=kf*fpos/(delpos-delresneg);
```

```
                    F(i,3)=(X-delresneg)*m6;
                else
%----TRILINEAR RELOADING----------------------------------
                    m6=kf*fpos/(delpos-delresneg);
                    if(kreln<m6)
                        m66=m6;
                    else
                        y0=-kreln*delresneg;
                        if(y0>kf*fpos)
                            m66=-kf*fpos/delresneg;
                            m6=0;
                        else
                            m66=kreln;
                            m6=(kf*fpos-y0)/delpos;
                        end
                    end
                    y0p=-m66*delresneg;
                    F(i,3)=(X-delresneg)*m66;
                end

%---------------Hysteretic Energy--------------------------
                efalg=3;
                eincl=-0.5*FOLD*(XOLD-delresneg);
                einc0=0.5*F(i,3)*(X-delresneg);
%-----------------------------------------------------------
            end
        end
    else
        if(del25>=-xccneg)
            if(X>=-xccneg)
                F(i,3)=f25+kcneg*(X-del25);
                stat=22;
%---------------Hysteretic Energy--------------------------
                efalg=1;
                eincl=0.5*(F(i,3)+f25)*(X-del25)+0.5*(f25+FOLD)*(del25-XOLD);
%-----------------------------------------------------------
            else
                F(i,3)=fyyneg+kccneg*(X-xccneg);
                stat=2200;
%---------------Hysteretic Energy--------------------------
                efalg=1;
                eincl=0.5*(F(i,3)+fyyneg)*(X-
xccneg)+0.5*(fyyneg+f25)*(xccneg-del25)+0.5*(f25+FOLD)*(del25-XOLD);
%-----------------------------------------------------------
            end
        elseif(del25>=-xcneg)
            if(X>=-xcneg)
                F(i,3)=f25+kccneg*(X-del25);
                stat=2200;
%---------------Hysteretic Energy--------------------------
                efalg=1;
                eincl=0.5*(F(i,3)+f25)*(X-del25)+0.5*(f25+FOLD)*(del25-XOLD);
%-----------------------------------------------------------
            else
                F(i,3)=funeg+ksneg*(X-xcneg);
                stat=23;
%---------------Hysteretic Energy--------------------------
```

```
                efalg=1;
                eincl=0.5*(F(i,3)+funeg)*(X-xcneg)+0.5*(funeg+f25)*(xcneg-
del25)+0.5*(f25+FOLD)*(del25-XOLD);
%------------------------------------------------------------
            end
        elseif(del25>=-xssneg)
            if(X>=-xssneg)
                F(i,3)=f25+ksneg*(X-del25);
                stat=23;
%---------------Hysteretic Energy--------------------------
                efalg=1;
                eincl=0.5*(F(i,3)+f25)*(X-del25)+0.5*(f25+FOLD)*(del25-XOLD);
%------------------------------------------------------------
            else
                F(i,3)=frrneg+kssneg*(X-xssneg);
                stat=2300;
%---------------Hysteretic Energy--------------------------
                efalg=1;
                eincl=0.5*(F(i,3)+frrneg)*(X-
xssneg)+0.5*(frrneg+f25)*(xssneg-del25)+0.5*(f25+FOLD)*(del25-XOLD);
%------------------------------------------------------------
            end
        elseif(del25>=-xsneg)
            if(X>=-xsneg)
                F(i,3)=f25+kssneg*(X-del25);
                stat=2300;
%---------------Hysteretic Energy--------------------------
                efalg=1;
                eincl=0.5*(F(i,3)+f25)*(X-del25)+0.5*(f25+FOLD)*(del25-XOLD);
%------------------------------------------------------------
            else
                F(i,3)=frneg+krneg*(X-xsneg);
                stat=24;
%---------------Hysteretic Energy--------------------------
                efalg=1;
                eincl=0.5*(F(i,3)+frneg)*(X-xsneg)+0.5*(frneg+f25)*(xsneg-
del25)+0.5*(f25+FOLD)*(del25-XOLD);
%------------------------------------------------------------
            end
        else
            F(i,3)=f25+krneg*(X-del25);
            stat=24;
%---------------Hysteretic Energy--------------------------
                efalg=1;
                eincl=0.5*(F(i,3)+f25)*(X-del25)+0.5*(f25+FOLD)*(del25-XOLD);
%------------------------------------------------------------
        end
    end
elseif (stat==26)
    if(X<(1-kd)*delresneg)
        m27=((1-kf)*fneg+(delneg-(1-kd)*delresneg)*m26)/(delneg-(1-
kd)*delresneg);
        if(flagl==0)
            facx=((delrespos-(1-kd)*delresneg)/(delrespos-delneg))*kf*fneg;
        else
            facx=y0n+(1-kd)*delresneg*m26;
        end
```

```
        F(i,3)=m27*(X-(1-kd)*delresneg)+facx;
        stat=27;
%---------------Hysteretic Energy--------------------------
                efalg=1;
                eincl=0.5*(F(i,3)+facx)*(X-(1-
kd)*delresneg)+0.5*(facx+FOLD)*((1-kd)*delresneg-XOLD);
%----------------------------------------------------------
    else
        if(X<=XOLD)
            stat=26;
            if(flagl==0)
                F(i,3)=m26*(X-XOLD)+FOLD;
            else
                if(X>=-1e-6)
                    F(i,3)=m266*(X-XOLD)+FOLD;
                else
                    F(i,3)=m26*(X-XOLD)+FOLD;
                end
            end
%---------------Hysteretic Energy--------------------------
                efalg=1;
                eincl=0.5*(F(i,3)+FOLD)*(X-XOLD);
%----------------------------------------------------------
        else
            F(i,3)=FOLD+(X-XOLD)*kunl;
            stat=25;
            del25m=XOLD;
            f25m=FOLD;
%---------------Hysteretic Energy--------------------------
                efalg=1;
                eincl=0.5*(F(i,3)+FOLD)*(X-XOLD);
%---------------------------------------------------------
        end
    end
elseif (stat==27)
    if(X<=delneg)
        if(X>=-xccneg)
            F(i,3)=-fyneg+kcneg*(X+xyneg);
            stat=22;
 %---------------Hysteretic Energy--------------------------
                efalg=1;
                eincl=0.5*(F(i,3)+fneg)*(X-delneg)+0.5*(fneg+FOLD)*(delneg-
XOLD);
%----------------------------------------------------------
        elseif(X>=-xcneg)
            F(i,3)=-fyyneg+kccneg*(X+xccneg);
            stat=2200;
 %---------------Hysteretic Energy--------------------------
                efalg=1;
                eincl=0.5*(F(i,3)+fneg)*(X-delneg)+0.5*(fneg+FOLD)*(delneg-
XOLD);
%----------------------------------------------------------
        elseif(X>=-xssneg)
            F(i,3)=-funeg+ksneg*(X+xcneg);
            stat=23;
%---------------Hysteretic Energy--------------------------
                efalg=1;
```

```
                eincl=0.5*(F(i,3)+fneg)*(X-delneg)+0.5*(fneg+FOLD)*(delneg-
XOLD);
%-----------------------------------------------------------
        elseif(X>=-xsneg)
            F(i,3)=-frrneg+kssneg*(X+xssneg);
            stat=2300;
%---------------Hysteretic Energy--------------------------
                efalg=1;
                eincl=0.5*(F(i,3)+fneg)*(X-delneg)+0.5*(fneg+FOLD)*(delneg-
XOLD);
%-----------------------------------------------------------
        else
            F(i,3)=-frneg+krneg*(X+xsneg);
            stat=24;
%---------------Hysteretic Energy--------------------------
                efalg=1;
                eincl=0.5*(F(i,3)+fneg)*(X-delneg)+0.5*(fneg+FOLD)*(delneg-
XOLD);
%-----------------------------------------------------------
        end
    else
        if(X<=XOLD)
            F(i,3)=m27*(X-XOLD)+FOLD;
            stat=27;
%---------------Hysteretic Energy--------------------------
                efalg=1;
                eincl=0.5*(F(i,3)+FOLD)*(X-XOLD);
%-----------------------------------------------------------
        else
             F(i,3)=FOLD+(X-XOLD)*kunl;
             stat=25;
             del25m=XOLD;
             f25m=FOLD;
%---------------Hysteretic Energy--------------------------
                efalg=1;
                eincl=0.5*(F(i,3)+FOLD)*(X-XOLD);
%----------------------------------------------------------
        end
    end
elseif (stat==6)
    if(X>(1-kd)*delrespos)
        m7=((1-kf)*fpos+(delpos-(1-kd)*delrespos)*m6)/(delpos-(1-
kd)*delrespos);
        if(flagl==0)
            facx=((-delresneg+(1-kd)*delrespos)/(-delresneg+delpos))*kf*fpos;
        else
            facx=y0p+(1-kd)*delrespos*m6;
        end
        F(i,3)=m7*(X-(1-kd)*delrespos)+facx;
        stat=7;
%---------------Hysteretic Energy--------------------------
                efalg=0;
                einc0=0.5*(F(i,3)+facx)*(X-(1-
kd)*delrespos)+0.5*(facx+FOLD)*((1-kd)*delrespos-XOLD);
%-----------------------------------------------------------
    else
        if(X>=XOLD)
```

```
            stat=6;
            if(flagl==0)
                F(i,3)=m6*(X-XOLD)+FOLD;
            else
                if(X<=1e-6)
                    F(i,3)=m66*(X-XOLD)+FOLD;
                else
                    F(i,3)=m6*(X-XOLD)+FOLD;
                end
            end
%---------------Hysteretic Energy--------------------------
                efalg=0;
                einc0=0.5*(F(i,3)+FOLD)*(X-XOLD);
%----------------------------------------------------------
        else
            F(i,3)=FOLD+(X-XOLD)*kunl;
            stat=5;
            del5m=XOLD;
            f5m=FOLD;
%---------------Hysteretic Energy--------------------------
                efalg=0;
                einc0=0.5*(F(i,3)+FOLD)*(X-XOLD);
%---------------------------------------------------------
        end
    end
elseif (stat==7)
    if(X>delpos)
        if(X<=xccpos)
            F(i,3)=fypos+kcpos*(X-xypos);
            stat=2;
 %--------------Hysteretic Energy--------------------------
                efalg=0;
                einc0=0.5*(F(i,3)+fpos)*(X-delpos)+0.5*(fpos+FOLD)*(delpos-
XOLD);
%----------------------------------------------------------
        elseif(X<=xcpos)
            F(i,3)=fyypos+kccpos*(X-xccpos);
            stat=200;
 %--------------Hysteretic Energy--------------------------
                efalg=0;
                einc0=0.5*(F(i,3)+fpos)*(X-delpos)+0.5*(fpos+FOLD)*(delpos-
XOLD);
%----------------------------------------------------------
        elseif(X<=xsspos)
            F(i,3)=fupos+kspos*(X-xcpos);
            stat=3;
 %--------------Hysteretic Energy--------------------------
                efalg=0;
                einc0=0.5*(F(i,3)+fpos)*(X-delpos)+0.5*(fpos+FOLD)*(delpos-
XOLD);
%----------------------------------------------------------
        elseif(X<=xspos)
            F(i,3)=frrpos+ksspos*(X-xsspos);
            stat=300;
 %--------------Hysteretic Energy--------------------------
                efalg=0;
```

```
                einc0=0.5*(F(i,3)+fpos)*(X-delpos)+0.5*(fpos+FOLD)*(delpos-
XOLD);
%-----------------------------------------------------------
        else
            F(i,3)=frpos+krpos*(X-xspos);
            stat=4;
 %---------------Hysteretic Energy--------------------------
                efalg=0;
                einc0=0.5*(F(i,3)+fpos)*(X-delpos)+0.5*(fpos+FOLD)*(delpos-
XOLD);
%-----------------------------------------------------------
        end
    else
        if(X>=XOLD)
            F(i,3)=m7*(X-XOLD)+FOLD;
            stat=7;
%---------------Hysteretic Energy--------------------------
                efalg=0;
                einc0=0.5*(F(i,3)+FOLD)*(X-XOLD);
%-----------------------------------------------------------
        else
            F(i,3)=FOLD+(X-XOLD)*kunl;
            stat=5;
            del5m=XOLD;
            f5m=FOLD;
%---------------Hysteretic Energy--------------------------
                efalg=0;
                einc0=0.5*(F(i,3)+FOLD)*(X-XOLD);
%----------------------------------------------------------
        end
    end
end

    if(einc0<0)
        tt=1;
    elseif (einc1<0)
        tt=1;
    end

    if (efalg==0)
        sume=sume+einc0;
        epos=epos+einc0;
        if(epos<0)
            epos=0;
        end
    elseif(efalg==1)
        sume=sume+einc1;
        eneg=eneg+einc1;
        if(eneg<0)
            eneg=0;
        end
    elseif(efalg==2)
        sume=sume+einc0;
        epos=epos+einc0;
        if(epos<0)
            epos=0;
```

```
    end

if (detflag==1)
    betaposs=(sume/etots)^erates;
    betaposc=(sume/etotc)^eratec;
    betaposa=(sume/etota)^eratea;
    betaposk=(sume/etotk)^eratek;
    betaposkk=(sume/etotkk)^eratekk;
    betaposkkk=(sume/etotkkk)^eratekkk;
    if(betaposs<=0)
        betaposs=0;
    elseif(betaposs>=1)
        betaposs=1;
    end
    if(betaposc<=0)
        betaposc=0;
    elseif(betaposc>=1)
        betaposc=1;
    end
    if(betaposa<=0)
        betaposa=0;
    elseif(betaposa>=1)
        betaposa=1;
    end
    if(betaposk<=0)
        betaposk=0;
    elseif(betaposk>=1)
        betaposk=1;
    end
    if(betaposkk<=0)
        betaposkk=0;
    elseif(betaposkk>=1)
        betaposkk=1;
    end
    if(betaposkkk<=0)
        betaposkkk=0;
    elseif(betaposkkk>=1)
        betaposkkk=1;
    end
else
    if(sume>=etots)
        betaposs=1;
    elseif((epos)/(etots-sume)>=1)
        betaposs=1;
    else
        betaposs=((epos)/(etots-sume))^erates;
    end
    if(sume>=etotc)
        betaposc=1;
    elseif((epos)/(etotc-sume)>=1)
        betaposc=1;
    else
        betaposc=((epos)/(etotc-sume))^eratec;
    end
    if(sume>=etota)
        betaposa=1;
    elseif((epos)/(etota-sume)>=1)
```

```
        betaposa=1;
    else
        betaposa=((epos)/(etota-sume))^eratea;
    end
    if(sume>=etotk)
        betaposk=1;
    elseif((epos)/(etotk-sume)>=1)
        betaposk=1;
    else
        betaposk=((epos)/(etotk-sume))^eratek;
    end
    if(sume>=etotkk)
        betaposkk=1;
    elseif((epos)/(etotkk-sume)>=1)
        betaposkk=1;
    else
        betaposkk=((epos)/(etotkk-sume))^eratekk;
    end
    if(sume>=etotkkk)
        betaposkkk=1;
    elseif((epos)/(etotkkk-sume)>=1)
        betaposkkk=1;
    else
        betaposkkk=((epos)/(etotkkk-sume))^eratekkk;
    end
end

epos=0;
eneg=einc1;
sume=sume+einc1;

elseif(efalg==3)
    sume=sume+einc1;
    eneg=eneg+einc1;
    if(eneg<0)
        eneg=0;
    end

if (detflag==1)
    betanegs=(sume/etots)^erates;
    betanegc=(sume/etotc)^eratec;
    betanega=(sume/etota)^eratea;
    betanegk=(sume/etotk)^eratek;
    betanegkk=(sume/etotkk)^eratekk;
    betanegkkk=(sume/etotkkk)^eratekkk;
    if(betanegs<=0)
        betanegs=0;
    elseif(betanegs>=1)
        betanegs=1;
    end
    if(betanegc<=0)
        betanegc=0;
    elseif(betanegc>=1)
        betanegc=1;
    end
    if(betanega<=0)
```

```
            betanega=0;
        elseif(betanega>=1)
            betanega=1;
        end
        if(betanegk<=0)
            betanegk=0;
        elseif(betanegk>=1)
            betanegk=1;
        end
        if(betanegkk<=0)
            betanegkk=0;
        elseif(betanegkk>=1)
            betanegkk=1;
        end
        if(betanegkkk<=0)
            betanegkkk=0;
        elseif(betanegkkk>=1)
            betanegkkk=1;
        end
    else
        if(sume>=etots)
            betanegs=1;
        elseif((eneg)/(etots-sume)>=1)
            betanegs=1;
        else
            betanegs=((eneg)/(etots-sume))^erates;
        end
        if(sume>=etotc)
            betanegc=1;
        elseif((eneg)/(etotc-sume)>=1)
            betanegc=1;
        else
            betanegc=((eneg)/(etotc-sume))^eratec;
        end
        if(sume>=etota)
            betanega=1;
        elseif((eneg)/(etota-sume)>=1)
            betanega=1;
        else
            betanega=((eneg)/(etota-sume))^eratea;
        end
        if(sume>=etotk)
            betanegk=1;
        elseif((eneg)/(etotk-sume)>=1)
            betanegk=1;
        else
            betanegk=((eneg)/(etotk-sume))^eratek;
        end
        if(sume>=etotkk)
            betanegkk=1;
        elseif((eneg)/(etotkk-sume)>=1)
            betanegkk=1;
        else
            betanegkk=((eneg)/(etotkk-sume))^eratekk;
        end
        if(sume>=etotkkk)
            betanegkkk=1;
```

```
        elseif((eneg)/(etotkkk-sume)>=1)
            betanegkkk=1;
        else
            betanegkkk=((eneg)/(etotkkk-sume))^eratekkk;
        end
    end

    epos=einc0;
    eneg=0;
    sume=sume+einc0;
    end

    F(i,4)=stat;
    F(i,5)=sume;
    F(i,6)=betaposk;
    F(i,7)=betanegk;
    F(i,8)=betaposkk;
    F(i,9)=betanegkk;
    F(i,10)=betaposa;
    F(i,11)=betanega;
%}


end

plot(F(:,2),F(:,3));
```

MCEER Technical Reports

MCEER publishes technical reports on a variety of subjects written by authors funded through MCEER. These reports are available from both MCEER Publications and the National Technical Information Service (NTIS). Requests for reports should be directed to MCEER Publications, MCEER, University at Buffalo, State University of New York, 133A Ketter Hall, Buffalo, New York 14260. Reports can also be requested through NTIS, P.O. Box 1425, Springfield, Virginia 22151. NTIS accession numbers are shown in parenthesis, if available.

NCEER-87-0001 "First-Year Program in Research, Education and Technology Transfer," 3/5/87, (PB88-134275, A04, MF-A01).

NCEER-87-0002 "Experimental Evaluation of Instantaneous Optimal Algorithms for Structural Control," by R.C. Lin, T.T. Soong and A.M. Reinhorn, 4/20/87, (PB88-134341, A04, MF-A01).

NCEER-87-0003 "Experimentation Using the Earthquake Simulation Facilities at University at Buffalo," by A.M. Reinhorn and R.L. Ketter, not available.

NCEER-87-0004 "The System Characteristics and Performance of a Shaking Table," by J.S. Hwang, K.C. Chang and G.C. Lee, 6/1/87, (PB88-134259, A03, MF-A01). This report is available only through NTIS (see address given above).

NCEER-87-0005 "A Finite Element Formulation for Nonlinear Viscoplastic Material Using a Q Model," by O. Gyebi and G. Dasgupta, 11/2/87, (PB88-213764, A08, MF-A01).

NCEER-87-0006 "Symbolic Manipulation Program (SMP) - Algebraic Codes for Two and Three Dimensional Finite Element Formulations," by X. Lee and G. Dasgupta, 11/9/87, (PB88-218522, A05, MF-A01).

NCEER-87-0007 "Instantaneous Optimal Control Laws for Tall Buildings Under Seismic Excitations," by J.N. Yang, A. Akbarpour and P. Ghaemmaghami, 6/10/87, (PB88-134333, A06, MF-A01). This report is only available through NTIS (see address given above).

NCEER-87-0008 "IDARC: Inelastic Damage Analysis of Reinforced Concrete Frame - Shear-Wall Structures," by Y.J. Park, A.M. Reinhorn and S.K. Kunnath, 7/20/87, (PB88-134325, A09, MF-A01). This report is only available through NTIS (see address given above).

NCEER-87-0009 "Liquefaction Potential for New York State: A Preliminary Report on Sites in Manhattan and Buffalo," by M. Budhu, V. Vijayakumar, R.F. Giese and L. Baumgras, 8/31/87, (PB88-163704, A03, MF-A01). This report is available only through NTIS (see address given above).

NCEER-87-0010 "Vertical and Torsional Vibration of Foundations in Inhomogeneous Media," by A.S. Veletsos and K.W. Dotson, 6/1/87, (PB88-134291, A03, MF-A01). This report is only available through NTIS (see address given above).

NCEER-87-0011 "Seismic Probabilistic Risk Assessment and Seismic Margins Studies for Nuclear Power Plants," by Howard H.M. Hwang, 6/15/87, (PB88-134267, A03, MF-A01). This report is only available through NTIS (see address given above).

NCEER-87-0012 "Parametric Studies of Frequency Response of Secondary Systems Under Ground-Acceleration Excitations," by Y. Yong and Y.K. Lin, 6/10/87, (PB88-134309, A03, MF-A01). This report is only available through NTIS (see address given above).

NCEER-87-0013 "Frequency Response of Secondary Systems Under Seismic Excitation," by J.A. HoLung, J. Cai and Y.K. Lin, 7/31/87, (PB88-134317, A05, MF-A01). This report is only available through NTIS (see address given above).

NCEER-87-0014 "Modelling Earthquake Ground Motions in Seismically Active Regions Using Parametric Time Series Methods," by G.W. Ellis and A.S. Cakmak, 8/25/87, (PB88-134283, A08, MF-A01). This report is only available through NTIS (see address given above).

NCEER-87-0015 "Detection and Assessment of Seismic Structural Damage," by E. DiPasquale and A.S. Cakmak, 8/25/87, (PB88-163712, A05, MF-A01). This report is only available through NTIS (see address given above).

NCEER-87-0016 "Pipeline Experiment at Parkfield, California," by J. Isenberg and E. Richardson, 9/15/87, (PB88-163720, A03, MF-A01). This report is available only through NTIS (see address given above).

NCEER-87-0017 "Digital Simulation of Seismic Ground Motion," by M. Shinozuka, G. Deodatis and T. Harada, 8/31/87, (PB88-155197, A04, MF-A01). This report is available only through NTIS (see address given above).

NCEER-87-0018 "Practical Considerations for Structural Control: System Uncertainty, System Time Delay and Truncation of Small Control Forces," J.N. Yang and A. Akbarpour, 8/10/87, (PB88-163738, A08, MF-A01). This report is only available through NTIS (see address given above).

NCEER-87-0019 "Modal Analysis of Nonclassically Damped Structural Systems Using Canonical Transformation," by J.N. Yang, S. Sarkani and F.X. Long, 9/27/87, (PB88-187851, A04, MF-A01).

NCEER-87-0020 "A Nonstationary Solution in Random Vibration Theory," by J.R. Red-Horse and P.D. Spanos, 11/3/87, (PB88-163746, A03, MF-A01).

NCEER-87-0021 "Horizontal Impedances for Radially Inhomogeneous Viscoelastic Soil Layers," by A.S. Veletsos and K.W. Dotson, 10/15/87, (PB88-150859, A04, MF-A01).

NCEER-87-0022 "Seismic Damage Assessment of Reinforced Concrete Members," by Y.S. Chung, C. Meyer and M. Shinozuka, 10/9/87, (PB88-150867, A05, MF-A01). This report is available only through NTIS (see address given above).

NCEER-87-0023 "Active Structural Control in Civil Engineering," by T.T. Soong, 11/11/87, (PB88-187778, A03, MF-A01).

NCEER-87-0024 "Vertical and Torsional Impedances for Radially Inhomogeneous Viscoelastic Soil Layers," by K.W. Dotson and A.S. Veletsos, 12/87, (PB88-187786, A03, MF-A01).

NCEER-87-0025 "Proceedings from the Symposium on Seismic Hazards, Ground Motions, Soil-Liquefaction and Engineering Practice in Eastern North America," October 20-22, 1987, edited by K.H. Jacob, 12/87, (PB88-188115, A23, MF-A01). This report is available only through NTIS (see address given above).

NCEER-87-0026 "Report on the Whittier-Narrows, California, Earthquake of October 1, 1987," by J. Pantelic and A. Reinhorn, 11/87, (PB88-187752, A03, MF-A01). This report is available only through NTIS (see address given above).

NCEER-87-0027 "Design of a Modular Program for Transient Nonlinear Analysis of Large 3-D Building Structures," by S. Srivastav and J.F. Abel, 12/30/87, (PB88-187950, A05, MF-A01). This report is only available through NTIS (see address given above).

NCEER-87-0028 "Second-Year Program in Research, Education and Technology Transfer," 3/8/88, (PB88-219480, A04, MF-A01).

NCEER-88-0001 "Workshop on Seismic Computer Analysis and Design of Buildings With Interactive Graphics," by W. McGuire, J.F. Abel and C.H. Conley, 1/18/88, (PB88-187760, A03, MF-A01). This report is only available through NTIS (see address given above).

NCEER-88-0002 "Optimal Control of Nonlinear Flexible Structures," by J.N. Yang, F.X. Long and D. Wong, 1/22/88, (PB88-213772, A06, MF-A01).

NCEER-88-0003 "Substructuring Techniques in the Time Domain for Primary-Secondary Structural Systems," by G.D. Manolis and G. Juhn, 2/10/88, (PB88-213780, A04, MF-A01).

NCEER-88-0004 "Iterative Seismic Analysis of Primary-Secondary Systems," by A. Singhal, L.D. Lutes and P.D. Spanos, 2/23/88, (PB88-213798, A04, MF-A01).

NCEER-88-0005 "Stochastic Finite Element Expansion for Random Media," by P.D. Spanos and R. Ghanem, 3/14/88, (PB88-213806, A03, MF-A01).

NCEER-88-0006 "Combining Structural Optimization and Structural Control," by F.Y. Cheng and C.P. Pantelides, 1/10/88, (PB88-213814, A05, MF-A01).

NCEER-88-0007 "Seismic Performance Assessment of Code-Designed Structures," by H.H-M. Hwang, J-W. Jaw and H-J. Shau, 3/20/88, (PB88-219423, A04, MF-A01). This report is only available through NTIS (see address given above).

NCEER-88-0008 "Reliability Analysis of Code-Designed Structures Under Natural Hazards," by H.H-M. Hwang, H. Ushiba and M. Shinozuka, 2/29/88, (PB88-229471, A07, MF-A01). This report is only available through NTIS (see address given above).

NCEER-88-0009 "Seismic Fragility Analysis of Shear Wall Structures," by J-W Jaw and H.H-M. Hwang, 4/30/88, (PB89-102867, A04, MF-A01).

NCEER-88-0010 "Base Isolation of a Multi-Story Building Under a Harmonic Ground Motion - A Comparison of Performances of Various Systems," by F-G Fan, G. Ahmadi and I.G. Tadjbakhsh, 5/18/88, (PB89-122238, A06, MF-A01). This report is only available through NTIS (see address given above).

NCEER-88-0011 "Seismic Floor Response Spectra for a Combined System by Green's Functions," by F.M. Lavelle, L.A. Bergman and P.D. Spanos, 5/1/88, (PB89-102875, A03, MF-A01).

NCEER-88-0012 "A New Solution Technique for Randomly Excited Hysteretic Structures," by G.Q. Cai and Y.K. Lin, 5/16/88, (PB89-102883, A03, MF-A01).

NCEER-88-0013 "A Study of Radiation Damping and Soil-Structure Interaction Effects in the Centrifuge," by K. Weissman, supervised by J.H. Prevost, 5/24/88, (PB89-144703, A06, MF-A01).

NCEER-88-0014 "Parameter Identification and Implementation of a Kinematic Plasticity Model for Frictional Soils," by J.H. Prevost and D.V. Griffiths, not available.

NCEER-88-0015 "Two- and Three- Dimensional Dynamic Finite Element Analyses of the Long Valley Dam," by D.V. Griffiths and J.H. Prevost, 6/17/88, (PB89-144711, A04, MF-A01).

NCEER-88-0016 "Damage Assessment of Reinforced Concrete Structures in Eastern United States," by A.M. Reinhorn, M.J. Seidel, S.K. Kunnath and Y.J. Park, 6/15/88, (PB89-122220, A04, MF-A01). This report is only available through NTIS (see address given above).

NCEER-88-0017 "Dynamic Compliance of Vertically Loaded Strip Foundations in Multilayered Viscoelastic Soils," by S. Ahmad and A.S.M. Israil, 6/17/88, (PB89-102891, A04, MF-A01).

NCEER-88-0018 "An Experimental Study of Seismic Structural Response With Added Viscoelastic Dampers," by R.C. Lin, Z. Liang, T.T. Soong and R.H. Zhang, 6/30/88, (PB89-122212, A05, MF-A01). This report is available only through NTIS (see address given above).

NCEER-88-0019 "Experimental Investigation of Primary - Secondary System Interaction," by G.D. Manolis, G. Juhn and A.M. Reinhorn, 5/27/88, (PB89-122204, A04, MF-A01).

NCEER-88-0020 "A Response Spectrum Approach For Analysis of Nonclassically Damped Structures," by J.N. Yang, S. Sarkani and F.X. Long, 4/22/88, (PB89-102909, A04, MF-A01).

NCEER-88-0021 "Seismic Interaction of Structures and Soils: Stochastic Approach," by A.S. Veletsos and A.M. Prasad, 7/21/88, (PB89-122196, A04, MF-A01). This report is only available through NTIS (see address given above).

NCEER-88-0022 "Identification of the Serviceability Limit State and Detection of Seismic Structural Damage," by E. DiPasquale and A.S. Cakmak, 6/15/88, (PB89-122188, A05, MF-A01). This report is available only through NTIS (see address given above).

NCEER-88-0023 "Multi-Hazard Risk Analysis: Case of a Simple Offshore Structure," by B.K. Bhartia and E.H. Vanmarcke, 7/21/88, (PB89-145213, A05, MF-A01).

NCEER-88-0024 "Automated Seismic Design of Reinforced Concrete Buildings," by Y.S. Chung, C. Meyer and M. Shinozuka, 7/5/88, (PB89-122170, A06, MF-A01). This report is available only through NTIS (see address given above).

NCEER-88-0025 "Experimental Study of Active Control of MDOF Structures Under Seismic Excitations," by L.L. Chung, R.C. Lin, T.T. Soong and A.M. Reinhorn, 7/10/88, (PB89-122600, A04, MF-A01).

NCEER-88-0026 "Earthquake Simulation Tests of a Low-Rise Metal Structure," by J.S. Hwang, K.C. Chang, G.C. Lee and R.L. Ketter, 8/1/88, (PB89-102917, A04, MF-A01).

NCEER-88-0027 "Systems Study of Urban Response and Reconstruction Due to Catastrophic Earthquakes," by F. Kozin and H.K. Zhou, 9/22/88, (PB90-162348, A04, MF-A01).

NCEER-88-0028 "Seismic Fragility Analysis of Plane Frame Structures," by H.H-M. Hwang and Y.K. Low, 7/31/88, (PB89-131445, A06, MF-A01).

NCEER-88-0029 "Response Analysis of Stochastic Structures," by A. Kardara, C. Bucher and M. Shinozuka, 9/22/88, (PB89-174429, A04, MF-A01).

NCEER-88-0030 "Nonnormal Accelerations Due to Yielding in a Primary Structure," by D.C.K. Chen and L.D. Lutes, 9/19/88, (PB89-131437, A04, MF-A01).

NCEER-88-0031 "Design Approaches for Soil-Structure Interaction," by A.S. Veletsos, A.M. Prasad and Y. Tang, 12/30/88, (PB89-174437, A03, MF-A01). This report is available only through NTIS (see address given above).

NCEER-88-0032 "A Re-evaluation of Design Spectra for Seismic Damage Control," by C.J. Turkstra and A.G. Tallin, 11/7/88, (PB89-145221, A05, MF-A01).

NCEER-88-0033 "The Behavior and Design of Noncontact Lap Splices Subjected to Repeated Inelastic Tensile Loading," by V.E. Sagan, P. Gergely and R.N. White, 12/8/88, (PB89-163737, A08, MF-A01).

NCEER-88-0034 "Seismic Response of Pile Foundations," by S.M. Mamoon, P.K. Banerjee and S. Ahmad, 11/1/88, (PB89-145239, A04, MF-A01).

NCEER-88-0035 "Modeling of R/C Building Structures With Flexible Floor Diaphragms (IDARC2)," by A.M. Reinhorn, S.K. Kunnath and N. Panahshahi, 9/7/88, (PB89-207153, A07, MF-A01).

NCEER-88-0036 "Solution of the Dam-Reservoir Interaction Problem Using a Combination of FEM, BEM with Particular Integrals, Modal Analysis, and Substructuring," by C-S. Tsai, G.C. Lee and R.L. Ketter, 12/31/88, (PB89-207146, A04, MF-A01).

NCEER-88-0037 "Optimal Placement of Actuators for Structural Control," by F.Y. Cheng and C.P. Pantelides, 8/15/88, (PB89-162846, A05, MF-A01).

NCEER-88-0038 "Teflon Bearings in Aseismic Base Isolation: Experimental Studies and Mathematical Modeling," by A. Mokha, M.C. Constantinou and A.M. Reinhorn, 12/5/88, (PB89-218457, A10, MF-A01). This report is available only through NTIS (see address given above).

NCEER-88-0039 "Seismic Behavior of Flat Slab High-Rise Buildings in the New York City Area," by P. Weidlinger and M. Ettouney, 10/15/88, (PB90-145681, A04, MF-A01).

NCEER-88-0040 "Evaluation of the Earthquake Resistance of Existing Buildings in New York City," by P. Weidlinger and M. Ettouney, 10/15/88, not available.

NCEER-88-0041 "Small-Scale Modeling Techniques for Reinforced Concrete Structures Subjected to Seismic Loads," by W. Kim, A. El-Attar and R.N. White, 11/22/88, (PB89-189625, A05, MF-A01).

NCEER-88-0042 "Modeling Strong Ground Motion from Multiple Event Earthquakes," by G.W. Ellis and A.S. Cakmak, 10/15/88, (PB89-174445, A03, MF-A01).

NCEER-88-0043 "Nonstationary Models of Seismic Ground Acceleration," by M. Grigoriu, S.E. Ruiz and E. Rosenblueth, 7/15/88, (PB89-189617, A04, MF-A01).

NCEER-88-0044 "SARCF User's Guide: Seismic Analysis of Reinforced Concrete Frames," by Y.S. Chung, C. Meyer and M. Shinozuka, 11/9/88, (PB89-174452, A08, MF-A01).

NCEER-88-0045 "First Expert Panel Meeting on Disaster Research and Planning," edited by J. Pantelic and J. Stoyle, 9/15/88, (PB89-174460, A05, MF-A01).

NCEER-88-0046 "Preliminary Studies of the Effect of Degrading Infill Walls on the Nonlinear Seismic Response of Steel Frames," by C.Z. Chrysostomou, P. Gergely and J.F. Abel, 12/19/88, (PB89-208383, A05, MF-A01).

NCEER-88-0047 "Reinforced Concrete Frame Component Testing Facility - Design, Construction, Instrumentation and Operation," by S.P. Pessiki, C. Conley, T. Bond, P. Gergely and R.N. White, 12/16/88, (PB89-174478, A04, MF-A01).

NCEER-89-0001 "Effects of Protective Cushion and Soil Compliancy on the Response of Equipment Within a Seismically Excited Building," by J.A. HoLung, 2/16/89, (PB89-207179, A04, MF-A01).

NCEER-89-0002 "Statistical Evaluation of Response Modification Factors for Reinforced Concrete Structures," by H.H-M. Hwang and J-W. Jaw, 2/17/89, (PB89-207187, A05, MF-A01).

NCEER-89-0003 "Hysteretic Columns Under Random Excitation," by G-Q. Cai and Y.K. Lin, 1/9/89, (PB89-196513, A03, MF-A01).

NCEER-89-0004 "Experimental Study of `Elephant Foot Bulge' Instability of Thin-Walled Metal Tanks," by Z-H. Jia and R.L. Ketter, 2/22/89, (PB89-207195, A03, MF-A01).

NCEER-89-0005 "Experiment on Performance of Buried Pipelines Across San Andreas Fault," by J. Isenberg, E. Richardson and T.D. O'Rourke, 3/10/89, (PB89-218440, A04, MF-A01). This report is available only through NTIS (see address given above).

NCEER-89-0006 "A Knowledge-Based Approach to Structural Design of Earthquake-Resistant Buildings," by M. Subramani, P. Gergely, C.H. Conley, J.F. Abel and A.H. Zaghw, 1/15/89, (PB89-218465, A06, MF-A01).

NCEER-89-0007 "Liquefaction Hazards and Their Effects on Buried Pipelines," by T.D. O'Rourke and P.A. Lane, 2/1/89, (PB89-218481, A09, MF-A01).

NCEER-89-0008 "Fundamentals of System Identification in Structural Dynamics," by H. Imai, C-B. Yun, O. Maruyama and M. Shinozuka, 1/26/89, (PB89-207211, A04, MF-A01).

NCEER-89-0009 "Effects of the 1985 Michoacan Earthquake on Water Systems and Other Buried Lifelines in Mexico," by A.G. Ayala and M.J. O'Rourke, 3/8/89, (PB89-207229, A06, MF-A01).

NCEER-89-R010 "NCEER Bibliography of Earthquake Education Materials," by K.E.K. Ross, Second Revision, 9/1/89, (PB90-125352, A05, MF-A01). This report is replaced by NCEER-92-0018.

NCEER-89-0011 "Inelastic Three-Dimensional Response Analysis of Reinforced Concrete Building Structures (IDARC-3D), Part I - Modeling," by S.K. Kunnath and A.M. Reinhorn, 4/17/89, (PB90-114612, A07, MF-A01). This report is available only through NTIS (see address given above).

NCEER-89-0012 "Recommended Modifications to ATC-14," by C.D. Poland and J.O. Malley, 4/12/89, (PB90-108648, A15, MF-A01).

NCEER-89-0013 "Repair and Strengthening of Beam-to-Column Connections Subjected to Earthquake Loading," by M. Corazao and A.J. Durrani, 2/28/89, (PB90-109885, A06, MF-A01).

NCEER-89-0014 "Program EXKAL2 for Identification of Structural Dynamic Systems," by O. Maruyama, C-B. Yun, M. Hoshiya and M. Shinozuka, 5/19/89, (PB90-109877, A09, MF-A01).

NCEER-89-0015 "Response of Frames With Bolted Semi-Rigid Connections, Part I - Experimental Study and Analytical Predictions," by P.J. DiCorso, A.M. Reinhorn, J.R. Dickerson, J.B. Radziminski and W.L. Harper, 6/1/89, not available.

NCEER-89-0016 "ARMA Monte Carlo Simulation in Probabilistic Structural Analysis," by P.D. Spanos and M.P. Mignolet, 7/10/89, (PB90-109893, A03, MF-A01).

NCEER-89-P017 "Preliminary Proceedings from the Conference on Disaster Preparedness - The Place of Earthquake Education in Our Schools," Edited by K.E.K. Ross, 6/23/89, (PB90-108606, A03, MF-A01).

NCEER-89-0017 "Proceedings from the Conference on Disaster Preparedness - The Place of Earthquake Education in Our Schools," Edited by K.E.K. Ross, 12/31/89, (PB90-207895, A012, MF-A02). This report is available only through NTIS (see address given above).

NCEER-89-0018 "Multidimensional Models of Hysteretic Material Behavior for Vibration Analysis of Shape Memory Energy Absorbing Devices, by E.J. Graesser and F.A. Cozzarelli, 6/7/89, (PB90-164146, A04, MF-A01).

NCEER-89-0019 "Nonlinear Dynamic Analysis of Three-Dimensional Base Isolated Structures (3D-BASIS)," by S. Nagarajaiah, A.M. Reinhorn and M.C. Constantinou, 8/3/89, (PB90-161936, A06, MF-A01). This report has been replaced by NCEER-93-0011.

NCEER-89-0020 "Structural Control Considering Time-Rate of Control Forces and Control Rate Constraints," by F.Y. Cheng and C.P. Pantelides, 8/3/89, (PB90-120445, A04, MF-A01).

NCEER-89-0021 "Subsurface Conditions of Memphis and Shelby County," by K.W. Ng, T-S. Chang and H-H.M. Hwang, 7/26/89, (PB90-120437, A03, MF-A01).

NCEER-89-0022 "Seismic Wave Propagation Effects on Straight Jointed Buried Pipelines," by K. Elhmadi and M.J. O'Rourke, 8/24/89, (PB90-162322, A10, MF-A02).

NCEER-89-0023 "Workshop on Serviceability Analysis of Water Delivery Systems," edited by M. Grigoriu, 3/6/89, (PB90-127424, A03, MF-A01).

NCEER-89-0024 "Shaking Table Study of a 1/5 Scale Steel Frame Composed of Tapered Members," by K.C. Chang, J.S. Hwang and G.C. Lee, 9/18/89, (PB90-160169, A04, MF-A01).

NCEER-89-0025 "DYNA1D: A Computer Program for Nonlinear Seismic Site Response Analysis - Technical Documentation," by Jean H. Prevost, 9/14/89, (PB90-161944, A07, MF-A01). This report is available only through NTIS (see address given above).

NCEER-89-0026 "1:4 Scale Model Studies of Active Tendon Systems and Active Mass Dampers for Aseismic Protection," by A.M. Reinhorn, T.T. Soong, R.C. Lin, Y.P. Yang, Y. Fukao, H. Abe and M. Nakai, 9/15/89, (PB90-173246, A10, MF-A02). This report is available only through NTIS (see address given above).

NCEER-89-0027 "Scattering of Waves by Inclusions in a Nonhomogeneous Elastic Half Space Solved by Boundary Element Methods," by P.K. Hadley, A. Askar and A.S. Cakmak, 6/15/89, (PB90-145699, A07, MF-A01).

NCEER-89-0028 "Statistical Evaluation of Deflection Amplification Factors for Reinforced Concrete Structures," by H.H.M. Hwang, J-W. Jaw and A.L. Ch'ng, 8/31/89, (PB90-164633, A05, MF-A01).

NCEER-89-0029 "Bedrock Accelerations in Memphis Area Due to Large New Madrid Earthquakes," by H.H.M. Hwang, C.H.S. Chen and G. Yu, 11/7/89, (PB90-162330, A04, MF-A01).

NCEER-89-0030 "Seismic Behavior and Response Sensitivity of Secondary Structural Systems," by Y.Q. Chen and T.T. Soong, 10/23/89, (PB90-164658, A08, MF-A01).

NCEER-89-0031 "Random Vibration and Reliability Analysis of Primary-Secondary Structural Systems," by Y. Ibrahim, M. Grigoriu and T.T. Soong, 11/10/89, (PB90-161951, A04, MF-A01).

NCEER-89-0032 "Proceedings from the Second U.S. - Japan Workshop on Liquefaction, Large Ground Deformation and Their Effects on Lifelines, September 26-29, 1989," Edited by T.D. O'Rourke and M. Hamada, 12/1/89, (PB90-209388, A22, MF-A03).

NCEER-89-0033 "Deterministic Model for Seismic Damage Evaluation of Reinforced Concrete Structures," by J.M. Bracci, A.M. Reinhorn, J.B. Mander and S.K. Kunnath, 9/27/89, (PB91-108803, A06, MF-A01).

NCEER-89-0034 "On the Relation Between Local and Global Damage Indices," by E. DiPasquale and A.S. Cakmak, 8/15/89, (PB90-173865, A05, MF-A01).

NCEER-89-0035 "Cyclic Undrained Behavior of Nonplastic and Low Plasticity Silts," by A.J. Walker and H.E. Stewart, 7/26/89, (PB90-183518, A10, MF-A01).

NCEER-89-0036 "Liquefaction Potential of Surficial Deposits in the City of Buffalo, New York," by M. Budhu, R. Giese and L. Baumgrass, 1/17/89, (PB90-208455, A04, MF-A01).

NCEER-89-0037 "A Deterministic Assessment of Effects of Ground Motion Incoherence," by A.S. Veletsos and Y. Tang, 7/15/89, (PB90-164294, A03, MF-A01).

NCEER-89-0038 "Workshop on Ground Motion Parameters for Seismic Hazard Mapping," July 17-18, 1989, edited by R.V. Whitman, 12/1/89, (PB90-173923, A04, MF-A01).

NCEER-89-0039 "Seismic Effects on Elevated Transit Lines of the New York City Transit Authority," by C.J. Costantino, C.A. Miller and E. Heymsfield, 12/26/89, (PB90-207887, A06, MF-A01).

NCEER-89-0040 "Centrifugal Modeling of Dynamic Soil-Structure Interaction," by K. Weissman, Supervised by J.H. Prevost, 5/10/89, (PB90-207879, A07, MF-A01).

NCEER-89-0041 "Linearized Identification of Buildings With Cores for Seismic Vulnerability Assessment," by I-K. Ho and A.E. Aktan, 11/1/89, (PB90-251943, A07, MF-A01).

NCEER-90-0001 "Geotechnical and Lifeline Aspects of the October 17, 1989 Loma Prieta Earthquake in San Francisco," by T.D. O'Rourke, H.E. Stewart, F.T. Blackburn and T.S. Dickerman, 1/90, (PB90-208596, A05, MF-A01).

NCEER-90-0002 "Nonnormal Secondary Response Due to Yielding in a Primary Structure," by D.C.K. Chen and L.D. Lutes, 2/28/90, (PB90-251976, A07, MF-A01).

NCEER-90-0003 "Earthquake Education Materials for Grades K-12," by K.E.K. Ross, 4/16/90, (PB91-251984, A05, MF-A05). This report has been replaced by NCEER-92-0018.

NCEER-90-0004 "Catalog of Strong Motion Stations in Eastern North America," by R.W. Busby, 4/3/90, (PB90-251984, A05, MF-A01).

NCEER-90-0005 "NCEER Strong-Motion Data Base: A User Manual for the GeoBase Release (Version 1.0 for the Sun3)," by P. Friberg and K. Jacob, 3/31/90 (PB90-258062, A04, MF-A01).

NCEER-90-0006 "Seismic Hazard Along a Crude Oil Pipeline in the Event of an 1811-1812 Type New Madrid Earthquake," by H.H.M. Hwang and C-H.S. Chen, 4/16/90, (PB90-258054, A04, MF-A01).

NCEER-90-0007 "Site-Specific Response Spectra for Memphis Sheahan Pumping Station," by H.H.M. Hwang and C.S. Lee, 5/15/90, (PB91-108811, A05, MF-A01).

NCEER-90-0008 "Pilot Study on Seismic Vulnerability of Crude Oil Transmission Systems," by T. Ariman, R. Dobry, M. Grigoriu, F. Kozin, M. O'Rourke, T. O'Rourke and M. Shinozuka, 5/25/90, (PB91-108837, A06, MF-A01).

NCEER-90-0009 "A Program to Generate Site Dependent Time Histories: EQGEN," by G.W. Ellis, M. Srinivasan and A.S. Cakmak, 1/30/90, (PB91-108829, A04, MF-A01).

NCEER-90-0010 "Active Isolation for Seismic Protection of Operating Rooms," by M.E. Talbott, Supervised by M. Shinozuka, 6/8/9, (PB91-110205, A05, MF-A01).

NCEER-90-0011 "Program LINEARID for Identification of Linear Structural Dynamic Systems," by C-B. Yun and M. Shinozuka, 6/25/90, (PB91-110312, A08, MF-A01).

NCEER-90-0012 "Two-Dimensional Two-Phase Elasto-Plastic Seismic Response of Earth Dams," by A.N. Yiagos, Supervised by J.H. Prevost, 6/20/90, (PB91-110197, A13, MF-A02).

NCEER-90-0013 "Secondary Systems in Base-Isolated Structures: Experimental Investigation, Stochastic Response and Stochastic Sensitivity," by G.D. Manolis, G. Juhn, M.C. Constantinou and A.M. Reinhorn, 7/1/90, (PB91-110320, A08, MF-A01).

NCEER-90-0014 "Seismic Behavior of Lightly-Reinforced Concrete Column and Beam-Column Joint Details," by S.P. Pessiki, C.H. Conley, P. Gergely and R.N. White, 8/22/90, (PB91-108795, A11, MF-A02).

NCEER-90-0015 "Two Hybrid Control Systems for Building Structures Under Strong Earthquakes," by J.N. Yang and A. Danielians, 6/29/90, (PB91-125393, A04, MF-A01).

NCEER-90-0016 "Instantaneous Optimal Control with Acceleration and Velocity Feedback," by J.N. Yang and Z. Li, 6/29/90, (PB91-125401, A03, MF-A01).

NCEER-90-0017 "Reconnaissance Report on the Northern Iran Earthquake of June 21, 1990," by M. Mehrain, 10/4/90, (PB91-125377, A03, MF-A01).

NCEER-90-0018 "Evaluation of Liquefaction Potential in Memphis and Shelby County," by T.S. Chang, P.S. Tang, C.S. Lee and H. Hwang, 8/10/90, (PB91-125427, A09, MF-A01).

NCEER-90-0019 "Experimental and Analytical Study of a Combined Sliding Disc Bearing and Helical Steel Spring Isolation System," by M.C. Constantinou, A.S. Mokha and A.M. Reinhorn, 10/4/90, (PB91-125385, A06, MF-A01). This report is available only through NTIS (see address given above).

NCEER-90-0020 "Experimental Study and Analytical Prediction of Earthquake Response of a Sliding Isolation System with a Spherical Surface," by A.S. Mokha, M.C. Constantinou and A.M. Reinhorn, 10/11/90, (PB91-125419, A05, MF-A01).

NCEER-90-0021 "Dynamic Interaction Factors for Floating Pile Groups," by G. Gazetas, K. Fan, A. Kaynia and E. Kausel, 9/10/90, (PB91-170381, A05, MF-A01).

NCEER-90-0022 "Evaluation of Seismic Damage Indices for Reinforced Concrete Structures," by S. Rodriguez-Gomez and A.S. Cakmak, 9/30/90, PB91-171322, A06, MF-A01).

NCEER-90-0023 "Study of Site Response at a Selected Memphis Site," by H. Desai, S. Ahmad, E.S. Gazetas and M.R. Oh, 10/11/90, (PB91-196857, A03, MF-A01).

NCEER-90-0024 "A User's Guide to Strongmo: Version 1.0 of NCEER's Strong-Motion Data Access Tool for PCs and Terminals," by P.A. Friberg and C.A.T. Susch, 11/15/90, (PB91-171272, A03, MF-A01).

NCEER-90-0025 "A Three-Dimensional Analytical Study of Spatial Variability of Seismic Ground Motions," by L-L. Hong and A.H.-S. Ang, 10/30/90, (PB91-170399, A09, MF-A01).

NCEER-90-0026 "MUMOID User's Guide - A Program for the Identification of Modal Parameters," by S. Rodriguez-Gomez and E. DiPasquale, 9/30/90, (PB91-171298, A04, MF-A01).

NCEER-90-0027 "SARCF-II User's Guide - Seismic Analysis of Reinforced Concrete Frames," by S. Rodriguez-Gomez, Y.S. Chung and C. Meyer, 9/30/90, (PB91-171280, A05, MF-A01).

NCEER-90-0028 "Viscous Dampers: Testing, Modeling and Application in Vibration and Seismic Isolation," by N. Makris and M.C. Constantinou, 12/20/90 (PB91-190561, A06, MF-A01).

NCEER-90-0029 "Soil Effects on Earthquake Ground Motions in the Memphis Area," by H. Hwang, C.S. Lee, K.W. Ng and T.S. Chang, 8/2/90, (PB91-190751, A05, MF-A01).

NCEER-91-0001 "Proceedings from the Third Japan-U.S. Workshop on Earthquake Resistant Design of Lifeline Facilities and Countermeasures for Soil Liquefaction, December 17-19, 1990," edited by T.D. O'Rourke and M. Hamada, 2/1/91, (PB91-179259, A99, MF-A04).

NCEER-91-0002 "Physical Space Solutions of Non-Proportionally Damped Systems," by M. Tong, Z. Liang and G.C. Lee, 1/15/91, (PB91-179242, A04, MF-A01).

NCEER-91-0003 "Seismic Response of Single Piles and Pile Groups," by K. Fan and G. Gazetas, 1/10/91, (PB92-174994, A04, MF-A01).

NCEER-91-0004 "Damping of Structures: Part 1 - Theory of Complex Damping," by Z. Liang and G. Lee, 10/10/91, (PB92-197235, A12, MF-A03).

NCEER-91-0005 "3D-BASIS - Nonlinear Dynamic Analysis of Three Dimensional Base Isolated Structures: Part II," by S. Nagarajaiah, A.M. Reinhorn and M.C. Constantinou, 2/28/91, (PB91-190553, A07, MF-A01). This report has been replaced by NCEER-93-0011.

NCEER-91-0006 "A Multidimensional Hysteretic Model for Plasticity Deforming Metals in Energy Absorbing Devices," by E.J. Graesser and F.A. Cozzarelli, 4/9/91, (PB92-108364, A04, MF-A01).

NCEER-91-0007 "A Framework for Customizable Knowledge-Based Expert Systems with an Application to a KBES for Evaluating the Seismic Resistance of Existing Buildings," by E.G. Ibarra-Anaya and S.J. Fenves, 4/9/91, (PB91-210930, A08, MF-A01).

NCEER-91-0008 "Nonlinear Analysis of Steel Frames with Semi-Rigid Connections Using the Capacity Spectrum Method," by G.G. Deierlein, S-H. Hsieh, Y-J. Shen and J.F. Abel, 7/2/91, (PB92-113828, A05, MF-A01).

NCEER-91-0009 "Earthquake Education Materials for Grades K-12," by K.E.K. Ross, 4/30/91, (PB91-212142, A06, MF-A01). This report has been replaced by NCEER-92-0018.

NCEER-91-0010 "Phase Wave Velocities and Displacement Phase Differences in a Harmonically Oscillating Pile," by N. Makris and G. Gazetas, 7/8/91, (PB92-108356, A04, MF-A01).

NCEER-91-0011 "Dynamic Characteristics of a Full-Size Five-Story Steel Structure and a 2/5 Scale Model," by K.C. Chang, G.C. Yao, G.C. Lee, D.S. Hao and Y.C. Yeh," 7/2/91, (PB93-116648, A06, MF-A02).

NCEER-91-0012 "Seismic Response of a 2/5 Scale Steel Structure with Added Viscoelastic Dampers," by K.C. Chang, T.T. Soong, S-T. Oh and M.L. Lai, 5/17/91, (PB92-110816, A05, MF-A01).

NCEER-91-0013 "Earthquake Response of Retaining Walls; Full-Scale Testing and Computational Modeling," by S. Alampalli and A-W.M. Elgamal, 6/20/91, not available.

NCEER-91-0014 "3D-BASIS-M: Nonlinear Dynamic Analysis of Multiple Building Base Isolated Structures," by P.C. Tsopelas, S. Nagarajaiah, M.C. Constantinou and A.M. Reinhorn, 5/28/91, (PB92-113885, A09, MF-A02).

NCEER-91-0015 "Evaluation of SEAOC Design Requirements for Sliding Isolated Structures," by D. Theodossiou and M.C. Constantinou, 6/10/91, (PB92-114602, A11, MF-A03).

NCEER-91-0016 "Closed-Loop Modal Testing of a 27-Story Reinforced Concrete Flat Plate-Core Building," by H.R. Somaprasad, T. Toksoy, H. Yoshiyuki and A.E. Aktan, 7/15/91, (PB92-129980, A07, MF-A02).

NCEER-91-0017 "Shake Table Test of a 1/6 Scale Two-Story Lightly Reinforced Concrete Building," by A.G. El-Attar, R.N. White and P. Gergely, 2/28/91, (PB92-222447, A06, MF-A02).

NCEER-91-0018 "Shake Table Test of a 1/8 Scale Three-Story Lightly Reinforced Concrete Building," by A.G. El-Attar, R.N. White and P. Gergely, 2/28/91, (PB93-116630, A08, MF-A02).

NCEER-91-0019 "Transfer Functions for Rigid Rectangular Foundations," by A.S. Veletsos, A.M. Prasad and W.H. Wu, 7/31/91, not available.

NCEER-91-0020 "Hybrid Control of Seismic-Excited Nonlinear and Inelastic Structural Systems," by J.N. Yang, Z. Li and A. Danielians, 8/1/91, (PB92-143171, A06, MF-A02).

NCEER-91-0021 "The NCEER-91 Earthquake Catalog: Improved Intensity-Based Magnitudes and Recurrence Relations for U.S. Earthquakes East of New Madrid," by L. Seeber and J.G. Armbruster, 8/28/91, (PB92-176742, A06, MF-A02).

NCEER-91-0022 "Proceedings from the Implementation of Earthquake Planning and Education in Schools: The Need for Change - The Roles of the Changemakers," by K.E.K. Ross and F. Winslow, 7/23/91, (PB92-129998, A12, MF-A03).

NCEER-91-0023 "A Study of Reliability-Based Criteria for Seismic Design of Reinforced Concrete Frame Buildings," by H.H.M. Hwang and H-M. Hsu, 8/10/91, (PB92-140235, A09, MF-A02).

NCEER-91-0024 "Experimental Verification of a Number of Structural System Identification Algorithms," by R.G. Ghanem, H. Gavin and M. Shinozuka, 9/18/91, (PB92-176577, A18, MF-A04).

NCEER-91-0025 "Probabilistic Evaluation of Liquefaction Potential," by H.H.M. Hwang and C.S. Lee," 11/25/91, (PB92-143429, A05, MF-A01).

NCEER-91-0026 "Instantaneous Optimal Control for Linear, Nonlinear and Hysteretic Structures - Stable Controllers," by J.N. Yang and Z. Li, 11/15/91, (PB92-163807, A04, MF-A01).

NCEER-91-0027 "Experimental and Theoretical Study of a Sliding Isolation System for Bridges," by M.C. Constantinou, A. Kartoum, A.M. Reinhorn and P. Bradford, 11/15/91, (PB92-176973, A10, MF-A03).

NCEER-92-0001 "Case Studies of Liquefaction and Lifeline Performance During Past Earthquakes, Volume 1: Japanese Case Studies," Edited by M. Hamada and T. O'Rourke, 2/17/92, (PB92-197243, A18, MF-A04).

NCEER-92-0002 "Case Studies of Liquefaction and Lifeline Performance During Past Earthquakes, Volume 2: United States Case Studies," Edited by T. O'Rourke and M. Hamada, 2/17/92, (PB92-197250, A20, MF-A04).

NCEER-92-0003 "Issues in Earthquake Education," Edited by K. Ross, 2/3/92, (PB92-222389, A07, MF-A02).

NCEER-92-0004 "Proceedings from the First U.S. - Japan Workshop on Earthquake Protective Systems for Bridges," Edited by I.G. Buckle, 2/4/92, (PB94-142239, A99, MF-A06).

NCEER-92-0005 "Seismic Ground Motion from a Haskell-Type Source in a Multiple-Layered Half-Space," A.P. Theoharis, G. Deodatis and M. Shinozuka, 1/2/92, not available.

NCEER-92-0006 "Proceedings from the Site Effects Workshop," Edited by R. Whitman, 2/29/92, (PB92-197201, A04, MF-A01).

NCEER-92-0007 "Engineering Evaluation of Permanent Ground Deformations Due to Seismically-Induced Liquefaction," by M.H. Baziar, R. Dobry and A-W.M. Elgamal, 3/24/92, (PB92-222421, A13, MF-A03).

NCEER-92-0008 "A Procedure for the Seismic Evaluation of Buildings in the Central and Eastern United States," by C.D. Poland and J.O. Malley, 4/2/92, (PB92-222439, A20, MF-A04).

NCEER-92-0009 "Experimental and Analytical Study of a Hybrid Isolation System Using Friction Controllable Sliding Bearings," by M.Q. Feng, S. Fujii and M. Shinozuka, 5/15/92, (PB93-150282, A06, MF-A02).

NCEER-92-0010 "Seismic Resistance of Slab-Column Connections in Existing Non-Ductile Flat-Plate Buildings," by A.J. Durrani and Y. Du, 5/18/92, (PB93-116812, A06, MF-A02).

NCEER-92-0011 "The Hysteretic and Dynamic Behavior of Brick Masonry Walls Upgraded by Ferrocement Coatings Under Cyclic Loading and Strong Simulated Ground Motion," by H. Lee and S.P. Prawel, 5/11/92, not available.

NCEER-92-0012 "Study of Wire Rope Systems for Seismic Protection of Equipment in Buildings," by G.F. Demetriades, M.C. Constantinou and A.M. Reinhorn, 5/20/92, (PB93-116655, A08, MF-A02).

NCEER-92-0013 "Shape Memory Structural Dampers: Material Properties, Design and Seismic Testing," by P.R. Witting and F.A. Cozzarelli, 5/26/92, (PB93-116663, A05, MF-A01).

NCEER-92-0014 "Longitudinal Permanent Ground Deformation Effects on Buried Continuous Pipelines," by M.J. O'Rourke, and C. Nordberg, 6/15/92, (PB93-116671, A08, MF-A02).

NCEER-92-0015 "A Simulation Method for Stationary Gaussian Random Functions Based on the Sampling Theorem," by M. Grigoriu and S. Balopoulou, 6/11/92, (PB93-127496, A05, MF-A01).

NCEER-92-0016 "Gravity-Load-Designed Reinforced Concrete Buildings: Seismic Evaluation of Existing Construction and Detailing Strategies for Improved Seismic Resistance," by G.W. Hoffmann, S.K. Kunnath, A.M. Reinhorn and J.B. Mander, 7/15/92, (PB94-142007, A08, MF-A02).

NCEER-92-0017 "Observations on Water System and Pipeline Performance in the Limón Area of Costa Rica Due to the April 22, 1991 Earthquake," by M. O'Rourke and D. Ballantyne, 6/30/92, (PB93-126811, A06, MF-A02).

NCEER-92-0018 "Fourth Edition of Earthquake Education Materials for Grades K-12," Edited by K.E.K. Ross, 8/10/92, (PB93-114023, A07, MF-A02).

NCEER-92-0019 "Proceedings from the Fourth Japan-U.S. Workshop on Earthquake Resistant Design of Lifeline Facilities and Countermeasures for Soil Liquefaction," Edited by M. Hamada and T.D. O'Rourke, 8/12/92, (PB93-163939, A99, MF-E11).

NCEER-92-0020 "Active Bracing System: A Full Scale Implementation of Active Control," by A.M. Reinhorn, T.T. Soong, R.C. Lin, M.A. Riley, Y.P. Wang, S. Aizawa and M. Higashino, 8/14/92, (PB93-127512, A06, MF-A02).

NCEER-92-0021 "Empirical Analysis of Horizontal Ground Displacement Generated by Liquefaction-Induced Lateral Spreads," by S.F. Bartlett and T.L. Youd, 8/17/92, (PB93-188241, A06, MF-A02).

NCEER-92-0022 "IDARC Version 3.0: Inelastic Damage Analysis of Reinforced Concrete Structures," by S.K. Kunnath, A.M. Reinhorn and R.F. Lobo, 8/31/92, (PB93-227502, A07, MF-A02).

NCEER-92-0023 "A Semi-Empirical Analysis of Strong-Motion Peaks in Terms of Seismic Source, Propagation Path and Local Site Conditions, by M. Kamiyama, M.J. O'Rourke and R. Flores-Berrones, 9/9/92, (PB93-150266, A08, MF-A02).

NCEER-92-0024 "Seismic Behavior of Reinforced Concrete Frame Structures with Nonductile Details, Part I: Summary of Experimental Findings of Full Scale Beam-Column Joint Tests," by A. Beres, R.N. White and P. Gergely, 9/30/92, (PB93-227783, A05, MF-A01).

NCEER-92-0025 "Experimental Results of Repaired and Retrofitted Beam-Column Joint Tests in Lightly Reinforced Concrete Frame Buildings," by A. Beres, S. El-Borgi, R.N. White and P. Gergely, 10/29/92, (PB93-227791, A05, MF-A01).

NCEER-92-0026 "A Generalization of Optimal Control Theory: Linear and Nonlinear Structures," by J.N. Yang, Z. Li and S. Vongchavalitkul, 11/2/92, (PB93-188621, A05, MF-A01).

NCEER-92-0027 "Seismic Resistance of Reinforced Concrete Frame Structures Designed Only for Gravity Loads: Part I - Design and Properties of a One-Third Scale Model Structure," by J.M. Bracci, A.M. Reinhorn and J.B. Mander, 12/1/92, (PB94-104502, A08, MF-A02).

NCEER-92-0028 "Seismic Resistance of Reinforced Concrete Frame Structures Designed Only for Gravity Loads: Part II - Experimental Performance of Subassemblages," by L.E. Aycardi, J.B. Mander and A.M. Reinhorn, 12/1/92, (PB94-104510, A08, MF-A02).

NCEER-92-0029 "Seismic Resistance of Reinforced Concrete Frame Structures Designed Only for Gravity Loads: Part III - Experimental Performance and Analytical Study of a Structural Model," by J.M. Bracci, A.M. Reinhorn and J.B. Mander, 12/1/92, (PB93-227528, A09, MF-A01).

NCEER-92-0030 "Evaluation of Seismic Retrofit of Reinforced Concrete Frame Structures: Part I - Experimental Performance of Retrofitted Subassemblages," by D. Choudhuri, J.B. Mander and A.M. Reinhorn, 12/8/92, (PB93-198307, A07, MF-A02).

NCEER-92-0031 "Evaluation of Seismic Retrofit of Reinforced Concrete Frame Structures: Part II - Experimental Performance and Analytical Study of a Retrofitted Structural Model," by J.M. Bracci, A.M. Reinhorn and J.B. Mander, 12/8/92, (PB93-198315, A09, MF-A03).

NCEER-92-0032 "Experimental and Analytical Investigation of Seismic Response of Structures with Supplemental Fluid Viscous Dampers," by M.C. Constantinou and M.D. Symans, 12/21/92, (PB93-191435, A10, MF-A03). This report is available only through NTIS (see address given above).

NCEER-92-0033 "Reconnaissance Report on the Cairo, Egypt Earthquake of October 12, 1992," by M. Khater, 12/23/92, (PB93-188621, A03, MF-A01).

NCEER-92-0034 "Low-Level Dynamic Characteristics of Four Tall Flat-Plate Buildings in New York City," by H. Gavin, S. Yuan, J. Grossman, E. Pekelis and K. Jacob, 12/28/92, (PB93-188217, A07, MF-A02).

NCEER-93-0001 "An Experimental Study on the Seismic Performance of Brick-Infilled Steel Frames With and Without Retrofit," by J.B. Mander, B. Nair, K. Wojtkowski and J. Ma, 1/29/93, (PB93-227510, A07, MF-A02).

NCEER-93-0002 "Social Accounting for Disaster Preparedness and Recovery Planning," by S. Cole, E. Pantoja and V. Razak, 2/22/93, (PB94-142114, A12, MF-A03).

NCEER-93-0003 "Assessment of 1991 NEHRP Provisions for Nonstructural Components and Recommended Revisions," by T.T. Soong, G. Chen, Z. Wu, R-H. Zhang and M. Grigoriu, 3/1/93, (PB93-188639, A06, MF-A02).

NCEER-93-0004 "Evaluation of Static and Response Spectrum Analysis Procedures of SEAOC/UBC for Seismic Isolated Structures," by C.W. Winters and M.C. Constantinou, 3/23/93, (PB93-198299, A10, MF-A03).

NCEER-93-0005 "Earthquakes in the Northeast - Are We Ignoring the Hazard? A Workshop on Earthquake Science and Safety for Educators," edited by K.E.K. Ross, 4/2/93, (PB94-103066, A09, MF-A02).

NCEER-93-0006 "Inelastic Response of Reinforced Concrete Structures with Viscoelastic Braces," by R.F. Lobo, J.M. Bracci, K.L. Shen, A.M. Reinhorn and T.T. Soong, 4/5/93, (PB93-227486, A05, MF-A02).

NCEER-93-0007 "Seismic Testing of Installation Methods for Computers and Data Processing Equipment," by K. Kosar, T.T. Soong, K.L. Shen, J.A. HoLung and Y.K. Lin, 4/12/93, (PB93-198299, A07, MF-A02).

NCEER-93-0008 "Retrofit of Reinforced Concrete Frames Using Added Dampers," by A. Reinhorn, M. Constantinou and C. Li, not available.

NCEER-93-0009 "Seismic Behavior and Design Guidelines for Steel Frame Structures with Added Viscoelastic Dampers," by K.C. Chang, M.L. Lai, T.T. Soong, D.S. Hao and Y.C. Yeh, 5/1/93, (PB94-141959, A07, MF-A02).

NCEER-93-0010 "Seismic Performance of Shear-Critical Reinforced Concrete Bridge Piers," by J.B. Mander, S.M. Waheed, M.T.A. Chaudhary and S.S. Chen, 5/12/93, (PB93-227494, A08, MF-A02).

NCEER-93-0011 "3D-BASIS-TABS: Computer Program for Nonlinear Dynamic Analysis of Three Dimensional Base Isolated Structures," by S. Nagarajaiah, C. Li, A.M. Reinhorn and M.C. Constantinou, 8/2/93, (PB94-141819, A09, MF-A02).

NCEER-93-0012 "Effects of Hydrocarbon Spills from an Oil Pipeline Break on Ground Water," by O.J. Helweg and H.H.M. Hwang, 8/3/93, (PB94-141942, A06, MF-A02).

NCEER-93-0013 "Simplified Procedures for Seismic Design of Nonstructural Components and Assessment of Current Code Provisions," by M.P. Singh, L.E. Suarez, E.E. Matheu and G.O. Maldonado, 8/4/93, (PB94-141827, A09, MF-A02).

NCEER-93-0014 "An Energy Approach to Seismic Analysis and Design of Secondary Systems," by G. Chen and T.T. Soong, 8/6/93, (PB94-142767, A11, MF-A03).

NCEER-93-0015 "Proceedings from School Sites: Becoming Prepared for Earthquakes - Commemorating the Third Anniversary of the Loma Prieta Earthquake," Edited by F.E. Winslow and K.E.K. Ross, 8/16/93, (PB94-154275, A16, MF-A02).

NCEER-93-0016 "Reconnaissance Report of Damage to Historic Monuments in Cairo, Egypt Following the October 12, 1992 Dahshur Earthquake," by D. Sykora, D. Look, G. Croci, E. Karaesmen and E. Karaesmen, 8/19/93, (PB94-142221, A08, MF-A02).

NCEER-93-0017 "The Island of Guam Earthquake of August 8, 1993," by S.W. Swan and S.K. Harris, 9/30/93, (PB94-141843, A04, MF-A01).

NCEER-93-0018 "Engineering Aspects of the October 12, 1992 Egyptian Earthquake," by A.W. Elgamal, M. Amer, K. Adalier and A. Abul-Fadl, 10/7/93, (PB94-141983, A05, MF-A01).

NCEER-93-0019 "Development of an Earthquake Motion Simulator and its Application in Dynamic Centrifuge Testing," by I. Krstelj, Supervised by J.H. Prevost, 10/23/93, (PB94-181773, A-10, MF-A03).

NCEER-93-0020 "NCEER-Taisei Corporation Research Program on Sliding Seismic Isolation Systems for Bridges: Experimental and Analytical Study of a Friction Pendulum System (FPS)," by M.C. Constantinou, P. Tsopelas, Y-S. Kim and S. Okamoto, 11/1/93, (PB94-142775, A08, MF-A02).

NCEER-93-0021 "Finite Element Modeling of Elastomeric Seismic Isolation Bearings," by L.J. Billings, Supervised by R. Shepherd, 11/8/93, not available.

NCEER-93-0022 "Seismic Vulnerability of Equipment in Critical Facilities: Life-Safety and Operational Consequences," by K. Porter, G.S. Johnson, M.M. Zadeh, C. Scawthorn and S. Eder, 11/24/93, (PB94-181765, A16, MF-A03).

NCEER-93-0023 "Hokkaido Nansei-oki, Japan Earthquake of July 12, 1993, by P.I. Yanev and C.R. Scawthorn, 12/23/93, (PB94-181500, A07, MF-A01).

NCEER-94-0001 "An Evaluation of Seismic Serviceability of Water Supply Networks with Application to the San Francisco Auxiliary Water Supply System," by I. Markov, Supervised by M. Grigoriu and T. O'Rourke, 1/21/94, (PB94-204013, A07, MF-A02).

NCEER-94-0002 "NCEER-Taisei Corporation Research Program on Sliding Seismic Isolation Systems for Bridges: Experimental and Analytical Study of Systems Consisting of Sliding Bearings, Rubber Restoring Force Devices and Fluid Dampers," Volumes I and II, by P. Tsopelas, S. Okamoto, M.C. Constantinou, D. Ozaki and S. Fujii, 2/4/94, (PB94-181740, A09, MF-A02 and PB94-181757, A12, MF-A03).

NCEER-94-0003 "A Markov Model for Local and Global Damage Indices in Seismic Analysis," by S. Rahman and M. Grigoriu, 2/18/94, (PB94-206000, A12, MF-A03).

NCEER-94-0004 "Proceedings from the NCEER Workshop on Seismic Response of Masonry Infills," edited by D.P. Abrams, 3/1/94, (PB94-180783, A07, MF-A02).

NCEER-94-0005 "The Northridge, California Earthquake of January 17, 1994: General Reconnaissance Report," edited by J.D. Goltz, 3/11/94, (PB94-193943, A10, MF-A03).

NCEER-94-0006 "Seismic Energy Based Fatigue Damage Analysis of Bridge Columns: Part I - Evaluation of Seismic Capacity," by G.A. Chang and J.B. Mander, 3/14/94, (PB94-219185, A11, MF-A03).

NCEER-94-0007 "Seismic Isolation of Multi-Story Frame Structures Using Spherical Sliding Isolation Systems," by T.M. Al-Hussaini, V.A. Zayas and M.C. Constantinou, 3/17/94, (PB94-193745, A09, MF-A02).

NCEER-94-0008 "The Northridge, California Earthquake of January 17, 1994: Performance of Highway Bridges," edited by I.G. Buckle, 3/24/94, (PB94-193851, A06, MF-A02).

NCEER-94-0009 "Proceedings of the Third U.S.-Japan Workshop on Earthquake Protective Systems for Bridges," edited by I.G. Buckle and I. Friedland, 3/31/94, (PB94-195815, A99, MF-A06).

NCEER-94-0010 "3D-BASIS-ME: Computer Program for Nonlinear Dynamic Analysis of Seismically Isolated Single and Multiple Structures and Liquid Storage Tanks," by P.C. Tsopelas, M.C. Constantinou and A.M. Reinhorn, 4/12/94, (PB94-204922, A09, MF-A02).

NCEER-94-0011 "The Northridge, California Earthquake of January 17, 1994: Performance of Gas Transmission Pipelines," by T.D. O'Rourke and M.C. Palmer, 5/16/94, (PB94-204989, A05, MF-A01).

NCEER-94-0012 "Feasibility Study of Replacement Procedures and Earthquake Performance Related to Gas Transmission Pipelines," by T.D. O'Rourke and M.C. Palmer, 5/25/94, (PB94-206638, A09, MF-A02).

NCEER-94-0013 "Seismic Energy Based Fatigue Damage Analysis of Bridge Columns: Part II - Evaluation of Seismic Demand," by G.A. Chang and J.B. Mander, 6/1/94, (PB95-18106, A08, MF-A02).

NCEER-94-0014 "NCEER-Taisei Corporation Research Program on Sliding Seismic Isolation Systems for Bridges: Experimental and Analytical Study of a System Consisting of Sliding Bearings and Fluid Restoring Force/Damping Devices," by P. Tsopelas and M.C. Constantinou, 6/13/94, (PB94-219144, A10, MF-A03).

NCEER-94-0015 "Generation of Hazard-Consistent Fragility Curves for Seismic Loss Estimation Studies," by H. Hwang and J-R. Huo, 6/14/94, (PB95-181996, A09, MF-A02).

NCEER-94-0016 "Seismic Study of Building Frames with Added Energy-Absorbing Devices," by W.S. Pong, C.S. Tsai and G.C. Lee, 6/20/94, (PB94-219136, A10, A03).

NCEER-94-0017 "Sliding Mode Control for Seismic-Excited Linear and Nonlinear Civil Engineering Structures," by J. Yang, J. Wu, A. Agrawal and Z. Li, 6/21/94, (PB95-138483, A06, MF-A02).

NCEER-94-0018 "3D-BASIS-TABS Version 2.0: Computer Program for Nonlinear Dynamic Analysis of Three Dimensional Base Isolated Structures," by A.M. Reinhorn, S. Nagarajaiah, M.C. Constantinou, P. Tsopelas and R. Li, 6/22/94, (PB95-182176, A08, MF-A02).

NCEER-94-0019 "Proceedings of the International Workshop on Civil Infrastructure Systems: Application of Intelligent Systems and Advanced Materials on Bridge Systems," Edited by G.C. Lee and K.C. Chang, 7/18/94, (PB95-252474, A20, MF-A04).

NCEER-94-0020 "Study of Seismic Isolation Systems for Computer Floors," by V. Lambrou and M.C. Constantinou, 7/19/94, (PB95-138533, A10, MF-A03).

NCEER-94-0021 "Proceedings of the U.S.-Italian Workshop on Guidelines for Seismic Evaluation and Rehabilitation of Unreinforced Masonry Buildings," Edited by D.P. Abrams and G.M. Calvi, 7/20/94, (PB95-138749, A13, MF-A03).

NCEER-94-0022 "NCEER-Taisei Corporation Research Program on Sliding Seismic Isolation Systems for Bridges: Experimental and Analytical Study of a System Consisting of Lubricated PTFE Sliding Bearings and Mild Steel Dampers," by P. Tsopelas and M.C. Constantinou, 7/22/94, (PB95-182184, A08, MF-A02).

NCEER-94-0023 “Development of Reliability-Based Design Criteria for Buildings Under Seismic Load,” by Y.K. Wen, H. Hwang and M. Shinozuka, 8/1/94, (PB95-211934, A08, MF-A02).

NCEER-94-0024 “Experimental Verification of Acceleration Feedback Control Strategies for an Active Tendon System,” by S.J. Dyke, B.F. Spencer, Jr., P. Quast, M.K. Sain, D.C. Kaspari, Jr. and T.T. Soong, 8/29/94, (PB95-212320, A05, MF-A01).

NCEER-94-0025 “Seismic Retrofitting Manual for Highway Bridges,” Edited by I.G. Buckle and I.F. Friedland, published by the Federal Highway Administration (PB95-212676, A15, MF-A03).

NCEER-94-0026 “Proceedings from the Fifth U.S.-Japan Workshop on Earthquake Resistant Design of Lifeline Facilities and Countermeasures Against Soil Liquefaction,” Edited by T.D. O’Rourke and M. Hamada, 11/7/94, (PB95-220802, A99, MF-E08).

NCEER-95-0001 "Experimental and Analytical Investigation of Seismic Retrofit of Structures with Supplemental Damping: Part 1 - Fluid Viscous Damping Devices," by A.M. Reinhorn, C. Li and M.C. Constantinou, 1/3/95, (PB95-266599, A09, MF-A02).

NCEER-95-0002 "Experimental and Analytical Study of Low-Cycle Fatigue Behavior of Semi-Rigid Top-And-Seat Angle Connections," by G. Pekcan, J.B. Mander and S.S. Chen, 1/5/95, (PB95-220042, A07, MF-A02).

NCEER-95-0003 "NCEER-ATC Joint Study on Fragility of Buildings," by T. Anagnos, C. Rojahn and A.S. Kiremidjian, 1/20/95, (PB95-220026, A06, MF-A02).

NCEER-95-0004 "Nonlinear Control Algorithms for Peak Response Reduction," by Z. Wu, T.T. Soong, V. Gattulli and R.C. Lin, 2/16/95, (PB95-220349, A05, MF-A01).

NCEER-95-0005 "Pipeline Replacement Feasibility Study: A Methodology for Minimizing Seismic and Corrosion Risks to Underground Natural Gas Pipelines," by R.T. Eguchi, H.A. Seligson and D.G. Honegger, 3/2/95, (PB95-252326, A06, MF-A02).

NCEER-95-0006 "Evaluation of Seismic Performance of an 11-Story Frame Building During the 1994 Northridge Earthquake," by F. Naeim, R. DiSulio, K. Benuska, A. Reinhorn and C. Li, not available.

NCEER-95-0007 "Prioritization of Bridges for Seismic Retrofitting," by N. Basöz and A.S. Kiremidjian, 4/24/95, (PB95-252300, A08, MF-A02).

NCEER-95-0008 "Method for Developing Motion Damage Relationships for Reinforced Concrete Frames," by A. Singhal and A.S. Kiremidjian, 5/11/95, (PB95-266607, A06, MF-A02).

NCEER-95-0009 "Experimental and Analytical Investigation of Seismic Retrofit of Structures with Supplemental Damping: Part II - Friction Devices," by C. Li and A.M. Reinhorn, 7/6/95, (PB96-128087, A11, MF-A03).

NCEER-95-0010 "Experimental Performance and Analytical Study of a Non-Ductile Reinforced Concrete Frame Structure Retrofitted with Elastomeric Spring Dampers," by G. Pekcan, J.B. Mander and S.S. Chen, 7/14/95, (PB96-137161, A08, MF-A02).

NCEER-95-0011 "Development and Experimental Study of Semi-Active Fluid Damping Devices for Seismic Protection of Structures," by M.D. Symans and M.C. Constantinou, 8/3/95, (PB96-136940, A23, MF-A04).

NCEER-95-0012 "Real-Time Structural Parameter Modification (RSPM): Development of Innervated Structures," by Z. Liang, M. Tong and G.C. Lee, 4/11/95, (PB96-137153, A06, MF-A01).

NCEER-95-0013 "Experimental and Analytical Investigation of Seismic Retrofit of Structures with Supplemental Damping: Part III - Viscous Damping Walls," by A.M. Reinhorn and C. Li, 10/1/95, (PB96-176409, A11, MF-A03).

NCEER-95-0014 "Seismic Fragility Analysis of Equipment and Structures in a Memphis Electric Substation," by J-R. Huo and H.H.M. Hwang, 8/10/95, (PB96-128087, A09, MF-A02).

NCEER-95-0015 "The Hanshin-Awaji Earthquake of January 17, 1995: Performance of Lifelines," Edited by M. Shinozuka, 11/3/95, (PB96-176383, A15, MF-A03).

NCEER-95-0016 "Highway Culvert Performance During Earthquakes," by T.L. Youd and C.J. Beckman, available as NCEER-96-0015.

NCEER-95-0017 "The Hanshin-Awaji Earthquake of January 17, 1995: Performance of Highway Bridges," Edited by I.G. Buckle, 12/1/95, not available.

NCEER-95-0018 "Modeling of Masonry Infill Panels for Structural Analysis," by A.M. Reinhorn, A. Madan, R.E. Valles, Y. Reichmann and J.B. Mander, 12/8/95, (PB97-110886, MF-A01, A06).

NCEER-95-0019 "Optimal Polynomial Control for Linear and Nonlinear Structures," by A.K. Agrawal and J.N. Yang, 12/11/95, (PB96-168737, A07, MF-A02).

NCEER-95-0020 "Retrofit of Non-Ductile Reinforced Concrete Frames Using Friction Dampers," by R.S. Rao, P. Gergely and R.N. White, 12/22/95, (PB97-133508, A10, MF-A02).

NCEER-95-0021 "Parametric Results for Seismic Response of Pile-Supported Bridge Bents," by G. Mylonakis, A. Nikolaou and G. Gazetas, 12/22/95, (PB97-100242, A12, MF-A03).

NCEER-95-0022 "Kinematic Bending Moments in Seismically Stressed Piles," by A. Nikolaou, G. Mylonakis and G. Gazetas, 12/23/95, (PB97-113914, MF-A03, A13).

NCEER-96-0001 "Dynamic Response of Unreinforced Masonry Buildings with Flexible Diaphragms," by A.C. Costley and D.P. Abrams," 10/10/96, (PB97-133573, MF-A03, A15).

NCEER-96-0002 "State of the Art Review: Foundations and Retaining Structures," by I. Po Lam, not available.

NCEER-96-0003 "Ductility of Rectangular Reinforced Concrete Bridge Columns with Moderate Confinement," by N. Wehbe, M. Saiidi, D. Sanders and B. Douglas, 11/7/96, (PB97-133557, A06, MF-A02).

NCEER-96-0004 "Proceedings of the Long-Span Bridge Seismic Research Workshop," edited by I.G. Buckle and I.M. Friedland, not available.

NCEER-96-0005 "Establish Representative Pier Types for Comprehensive Study: Eastern United States," by J. Kulicki and Z. Prucz, 5/28/96, (PB98-119217, A07, MF-A02).

NCEER-96-0006 "Establish Representative Pier Types for Comprehensive Study: Western United States," by R. Imbsen, R.A. Schamber and T.A. Osterkamp, 5/28/96, (PB98-118607, A07, MF-A02).

NCEER-96-0007 "Nonlinear Control Techniques for Dynamical Systems with Uncertain Parameters," by R.G. Ghanem and M.I. Bujakov, 5/27/96, (PB97-100259, A17, MF-A03).

NCEER-96-0008 "Seismic Evaluation of a 30-Year Old Non-Ductile Highway Bridge Pier and Its Retrofit," by J.B. Mander, B. Mahmoodzadegan, S. Bhadra and S.S. Chen, 5/31/96, (PB97-110902, MF-A03, A10).

NCEER-96-0009 "Seismic Performance of a Model Reinforced Concrete Bridge Pier Before and After Retrofit," by J.B. Mander, J.H. Kim and C.A. Ligozio, 5/31/96, (PB97-110910, MF-A02, A10).

NCEER-96-0010 "IDARC2D Version 4.0: A Computer Program for the Inelastic Damage Analysis of Buildings," by R.E. Valles, A.M. Reinhorn, S.K. Kunnath, C. Li and A. Madan, 6/3/96, (PB97-100234, A17, MF-A03).

NCEER-96-0011 "Estimation of the Economic Impact of Multiple Lifeline Disruption: Memphis Light, Gas and Water Division Case Study," by S.E. Chang, H.A. Seligson and R.T. Eguchi, 8/16/96, (PB97-133490, A11, MF-A03).

NCEER-96-0012 "Proceedings from the Sixth Japan-U.S. Workshop on Earthquake Resistant Design of Lifeline Facilities and Countermeasures Against Soil Liquefaction, Edited by M. Hamada and T. O'Rourke, 9/11/96, (PB97-133581, A99, MF-A06).

NCEER-96-0013 "Chemical Hazards, Mitigation and Preparedness in Areas of High Seismic Risk: A Methodology for Estimating the Risk of Post-Earthquake Hazardous Materials Release," by H.A. Seligson, R.T. Eguchi, K.J. Tierney and K. Richmond, 11/7/96, (PB97-133565, MF-A02, A08).

NCEER-96-0014 "Response of Steel Bridge Bearings to Reversed Cyclic Loading," by J.B. Mander, D-K. Kim, S.S. Chen and G.J. Premus, 11/13/96, (PB97-140735, A12, MF-A03).

NCEER-96-0015 "Highway Culvert Performance During Past Earthquakes," by T.L. Youd and C.J. Beckman, 11/25/96, (PB97-133532, A06, MF-A01).

NCEER-97-0001 "Evaluation, Prevention and Mitigation of Pounding Effects in Building Structures," by R.E. Valles and A.M. Reinhorn, 2/20/97, (PB97-159552, A14, MF-A03).

NCEER-97-0002 "Seismic Design Criteria for Bridges and Other Highway Structures," by C. Rojahn, R. Mayes, D.G. Anderson, J. Clark, J.H. Hom, R.V. Nutt and M.J. O'Rourke, 4/30/97, (PB97-194658, A06, MF-A03).

NCEER-97-0003 "Proceedings of the U.S.-Italian Workshop on Seismic Evaluation and Retrofit," Edited by D.P. Abrams and G.M. Calvi, 3/19/97, (PB97-194666, A13, MF-A03).

NCEER-97-0004 "Investigation of Seismic Response of Buildings with Linear and Nonlinear Fluid Viscous Dampers," by A.A. Seleemah and M.C. Constantinou, 5/21/97, (PB98-109002, A15, MF-A03).

NCEER-97-0005 "Proceedings of the Workshop on Earthquake Engineering Frontiers in Transportation Facilities," edited by G.C. Lee and I.M. Friedland, 8/29/97, (PB98-128911, A25, MR-A04).

NCEER-97-0006 "Cumulative Seismic Damage of Reinforced Concrete Bridge Piers," by S.K. Kunnath, A. El-Bahy, A. Taylor and W. Stone, 9/2/97, (PB98-108814, A11, MF-A03).

NCEER-97-0007 "Structural Details to Accommodate Seismic Movements of Highway Bridges and Retaining Walls," by R.A. Imbsen, R.A. Schamber, E. Thorkildsen, A. Kartoum, B.T. Martin, T.N. Rosser and J.M. Kulicki, 9/3/97, (PB98-108996, A09, MF-A02).

NCEER-97-0008 "A Method for Earthquake Motion-Damage Relationships with Application to Reinforced Concrete Frames," by A. Singhal and A.S. Kiremidjian, 9/10/97, (PB98-108988, A13, MF-A03).

NCEER-97-0009 "Seismic Analysis and Design of Bridge Abutments Considering Sliding and Rotation," by K. Fishman and R. Richards, Jr., 9/15/97, (PB98-108897, A06, MF-A02).

NCEER-97-0010 "Proceedings of the FHWA/NCEER Workshop on the National Representation of Seismic Ground Motion for New and Existing Highway Facilities," edited by I.M. Friedland, M.S. Power and R.L. Mayes, 9/22/97, (PB98-128903, A21, MF-A04).

NCEER-97-0011 "Seismic Analysis for Design or Retrofit of Gravity Bridge Abutments," by K.L. Fishman, R. Richards, Jr. and R.C. Divito, 10/2/97, (PB98-128937, A08, MF-A02).

NCEER-97-0012 "Evaluation of Simplified Methods of Analysis for Yielding Structures," by P. Tsopelas, M.C. Constantinou, C.A. Kircher and A.S. Whittaker, 10/31/97, (PB98-128929, A10, MF-A03).

NCEER-97-0013 "Seismic Design of Bridge Columns Based on Control and Repairability of Damage," by C-T. Cheng and J.B. Mander, 12/8/97, (PB98-144249, A11, MF-A03).

NCEER-97-0014 "Seismic Resistance of Bridge Piers Based on Damage Avoidance Design," by J.B. Mander and C-T. Cheng, 12/10/97, (PB98-144223, A09, MF-A02).

NCEER-97-0015 "Seismic Response of Nominally Symmetric Systems with Strength Uncertainty," by S. Balopoulou and M. Grigoriu, 12/23/97, (PB98-153422, A11, MF-A03).

NCEER-97-0016 "Evaluation of Seismic Retrofit Methods for Reinforced Concrete Bridge Columns," by T.J. Wipf, F.W. Klaiber and F.M. Russo, 12/28/97, (PB98-144215, A12, MF-A03).

NCEER-97-0017 "Seismic Fragility of Existing Conventional Reinforced Concrete Highway Bridges," by C.L. Mullen and A.S. Cakmak, 12/30/97, (PB98-153406, A08, MF-A02).

NCEER-97-0018 "Loss Asssessment of Memphis Buildings," edited by D.P. Abrams and M. Shinozuka, 12/31/97, (PB98-144231, A13, MF-A03).

NCEER-97-0019 "Seismic Evaluation of Frames with Infill Walls Using Quasi-static Experiments," by K.M. Mosalam, R.N. White and P. Gergely, 12/31/97, (PB98-153455, A07, MF-A02).

NCEER-97-0020 "Seismic Evaluation of Frames with Infill Walls Using Pseudo-dynamic Experiments," by K.M. Mosalam, R.N. White and P. Gergely, 12/31/97, (PB98-153430, A07, MF-A02).

NCEER-97-0021 "Computational Strategies for Frames with Infill Walls: Discrete and Smeared Crack Analyses and Seismic Fragility," by K.M. Mosalam, R.N. White and P. Gergely, 12/31/97, (PB98-153414, A10, MF-A02).

NCEER-97-0022 "Proceedings of the NCEER Workshop on Evaluation of Liquefaction Resistance of Soils," edited by T.L. Youd and I.M. Idriss, 12/31/97, (PB98-155617, A15, MF-A03).

MCEER-98-0001 "Extraction of Nonlinear Hysteretic Properties of Seismically Isolated Bridges from Quick-Release Field Tests," by Q. Chen, B.M. Douglas, E.M. Maragakis and I.G. Buckle, 5/26/98, (PB99-118838, A06, MF-A01).

MCEER-98-0002 "Methodologies for Evaluating the Importance of Highway Bridges," by A. Thomas, S. Eshenaur and J. Kulicki, 5/29/98, (PB99-118846, A10, MF-A02).

MCEER-98-0003 "Capacity Design of Bridge Piers and the Analysis of Overstrength," by J.B. Mander, A. Dutta and P. Goel, 6/1/98, (PB99-118853, A09, MF-A02).

MCEER-98-0004 "Evaluation of Bridge Damage Data from the Loma Prieta and Northridge, California Earthquakes," by N. Basoz and A. Kiremidjian, 6/2/98, (PB99-118861, A15, MF-A03).

MCEER-98-0005 "Screening Guide for Rapid Assessment of Liquefaction Hazard at Highway Bridge Sites," by T. L. Youd, 6/16/98, (PB99-118879, A06, not available on microfiche).

MCEER-98-0006 "Structural Steel and Steel/Concrete Interface Details for Bridges," by P. Ritchie, N. Kauhl and J. Kulicki, 7/13/98, (PB99-118945, A06, MF-A01).

MCEER-98-0007 "Capacity Design and Fatigue Analysis of Confined Concrete Columns," by A. Dutta and J.B. Mander, 7/14/98, (PB99-118960, A14, MF-A03).

MCEER-98-0008 "Proceedings of the Workshop on Performance Criteria for Telecommunication Services Under Earthquake Conditions," edited by A.J. Schiff, 7/15/98, (PB99-118952, A08, MF-A02).

MCEER-98-0009 "Fatigue Analysis of Unconfined Concrete Columns," by J.B. Mander, A. Dutta and J.H. Kim, 9/12/98, (PB99-123655, A10, MF-A02).

MCEER-98-0010 "Centrifuge Modeling of Cyclic Lateral Response of Pile-Cap Systems and Seat-Type Abutments in Dry Sands," by A.D. Gadre and R. Dobry, 10/2/98, (PB99-123606, A13, MF-A03).

MCEER-98-0011 "IDARC-BRIDGE: A Computational Platform for Seismic Damage Assessment of Bridge Structures," by A.M. Reinhorn, V. Simeonov, G. Mylonakis and Y. Reichman, 10/2/98, (PB99-162919, A15, MF-A03).

MCEER-98-0012 "Experimental Investigation of the Dynamic Response of Two Bridges Before and After Retrofitting with Elastomeric Bearings," by D.A. Wendichansky, S.S. Chen and J.B. Mander, 10/2/98, (PB99-162927, A15, MF-A03).

MCEER-98-0013 "Design Procedures for Hinge Restrainers and Hinge Sear Width for Multiple-Frame Bridges," by R. Des Roches and G.L. Fenves, 11/3/98, (PB99-140477, A13, MF-A03).

MCEER-98-0014 "Response Modification Factors for Seismically Isolated Bridges," by M.C. Constantinou and J.K. Quarshie, 11/3/98, (PB99-140485, A14, MF-A03).

MCEER-98-0015 "Proceedings of the U.S.-Italy Workshop on Seismic Protective Systems for Bridges," edited by I.M. Friedland and M.C. Constantinou, 11/3/98, (PB2000-101711, A22, MF-A04).

MCEER-98-0016 "Appropriate Seismic Reliability for Critical Equipment Systems: Recommendations Based on Regional Analysis of Financial and Life Loss," by K. Porter, C. Scawthorn, C. Taylor and N. Blais, 11/10/98, (PB99-157265, A08, MF-A02).

MCEER-98-0017 "Proceedings of the U.S. Japan Joint Seminar on Civil Infrastructure Systems Research," edited by M. Shinozuka and A. Rose, 11/12/98, (PB99-156713, A16, MF-A03).

MCEER-98-0018 "Modeling of Pile Footings and Drilled Shafts for Seismic Design," by I. PoLam, M. Kapuskar and D. Chaudhuri, 12/21/98, (PB99-157257, A09, MF-A02).

MCEER-99-0001 "Seismic Evaluation of a Masonry Infilled Reinforced Concrete Frame by Pseudodynamic Testing," by S.G. Buonopane and R.N. White, 2/16/99, (PB99-162851, A09, MF-A02).

MCEER-99-0002 "Response History Analysis of Structures with Seismic Isolation and Energy Dissipation Systems: Verification Examples for Program SAP2000," by J. Scheller and M.C. Constantinou, 2/22/99, (PB99-162869, A08, MF-A02).

MCEER-99-0003 "Experimental Study on the Seismic Design and Retrofit of Bridge Columns Including Axial Load Effects," by A. Dutta, T. Kokorina and J.B. Mander, 2/22/99, (PB99-162877, A09, MF-A02).

MCEER-99-0004 "Experimental Study of Bridge Elastomeric and Other Isolation and Energy Dissipation Systems with Emphasis on Uplift Prevention and High Velocity Near-source Seismic Excitation," by A. Kasalanati and M. C. Constantinou, 2/26/99, (PB99-162885, A12, MF-A03).

MCEER-99-0005 "Truss Modeling of Reinforced Concrete Shear-flexure Behavior," by J.H. Kim and J.B. Mander, 3/8/99, (PB99-163693, A12, MF-A03).

MCEER-99-0006 "Experimental Investigation and Computational Modeling of Seismic Response of a 1:4 Scale Model Steel Structure with a Load Balancing Supplemental Damping System," by G. Pekcan, J.B. Mander and S.S. Chen, 4/2/99, (PB99-162893, A11, MF-A03).

MCEER-99-0007 "Effect of Vertical Ground Motions on the Structural Response of Highway Bridges," by M.R. Button, C.J. Cronin and R.L. Mayes, 4/10/99, (PB2000-101411, A10, MF-A03).

MCEER-99-0008 "Seismic Reliability Assessment of Critical Facilities: A Handbook, Supporting Documentation, and Model Code Provisions," by G.S. Johnson, R.E. Sheppard, M.D. Quilici, S.J. Eder and C.R. Scawthorn, 4/12/99, (PB2000-101701, A18, MF-A04).

MCEER-99-0009 "Impact Assessment of Selected MCEER Highway Project Research on the Seismic Design of Highway Structures," by C. Rojahn, R. Mayes, D.G. Anderson, J.H. Clark, D'Appolonia Engineering, S. Gloyd and R.V. Nutt, 4/14/99, (PB99-162901, A10, MF-A02).

MCEER-99-0010 "Site Factors and Site Categories in Seismic Codes," by R. Dobry, R. Ramos and M.S. Power, 7/19/99, (PB2000-101705, A08, MF-A02).

MCEER-99-0011 "Restrainer Design Procedures for Multi-Span Simply-Supported Bridges," by M.J. Randall, M. Saiidi, E. Maragakis and T. Isakovic, 7/20/99, (PB2000-101702, A10, MF-A02).

MCEER-99-0012 "Property Modification Factors for Seismic Isolation Bearings," by M.C. Constantinou, P. Tsopelas, A. Kasalanati and E. Wolff, 7/20/99, (PB2000-103387, A11, MF-A03).

MCEER-99-0013 "Critical Seismic Issues for Existing Steel Bridges," by P. Ritchie, N. Kauhl and J. Kulicki, 7/20/99, (PB2000-101697, A09, MF-A02).

MCEER-99-0014 "Nonstructural Damage Database," by A. Kao, T.T. Soong and A. Vender, 7/24/99, (PB2000-101407, A06, MF-A01).

MCEER-99-0015 "Guide to Remedial Measures for Liquefaction Mitigation at Existing Highway Bridge Sites," by H.G. Cooke and J. K. Mitchell, 7/26/99, (PB2000-101703, A11, MF-A03).

MCEER-99-0016 "Proceedings of the MCEER Workshop on Ground Motion Methodologies for the Eastern United States," edited by N. Abrahamson and A. Becker, 8/11/99, (PB2000-103385, A07, MF-A02).

MCEER-99-0017 "Quindío, Colombia Earthquake of January 25, 1999: Reconnaissance Report," by A.P. Asfura and P.J. Flores, 10/4/99, (PB2000-106893, A06, MF-A01).

MCEER-99-0018 "Hysteretic Models for Cyclic Behavior of Deteriorating Inelastic Structures," by M.V. Sivaselvan and A.M. Reinhorn, 11/5/99, (PB2000-103386, A08, MF-A02).

MCEER-99-0019 "Proceedings of the 7th U.S.- Japan Workshop on Earthquake Resistant Design of Lifeline Facilities and Countermeasures Against Soil Liquefaction," edited by T.D. O'Rourke, J.P. Bardet and M. Hamada, 11/19/99, (PB2000-103354, A99, MF-A06).

MCEER-99-0020 "Development of Measurement Capability for Micro-Vibration Evaluations with Application to Chip Fabrication Facilities," by G.C. Lee, Z. Liang, J.W. Song, J.D. Shen and W.C. Liu, 12/1/99, (PB2000-105993, A08, MF-A02).

MCEER-99-0021 "Design and Retrofit Methodology for Building Structures with Supplemental Energy Dissipating Systems," by G. Pekcan, J.B. Mander and S.S. Chen, 12/31/99, (PB2000-105994, A11, MF-A03).

MCEER-00-0001 "The Marmara, Turkey Earthquake of August 17, 1999: Reconnaissance Report," edited by C. Scawthorn; with major contributions by M. Bruneau, R. Eguchi, T. Holzer, G. Johnson, J. Mander, J. Mitchell, W. Mitchell, A. Papageorgiou, C. Scaethorn, and G. Webb, 3/23/00, (PB2000-106200, A11, MF-A03).

MCEER-00-0002 "Proceedings of the MCEER Workshop for Seismic Hazard Mitigation of Health Care Facilities," edited by G.C. Lee, M. Ettouney, M. Grigoriu, J. Hauer and J. Nigg, 3/29/00, (PB2000-106892, A08, MF-A02).

MCEER-00-0003 "The Chi-Chi, Taiwan Earthquake of September 21, 1999: Reconnaissance Report," edited by G.C. Lee and C.H. Loh, with major contributions by G.C. Lee, M. Bruneau, I.G. Buckle, S.E. Chang, P.J. Flores, T.D. O'Rourke, M. Shinozuka, T.T. Soong, C-H. Loh, K-C. Chang, Z-J. Chen, J-S. Hwang, M-L. Lin, G-Y. Liu, K-C. Tsai, G.C. Yao and C-L. Yen, 4/30/00, (PB2001-100980, A10, MF-A02).

MCEER-00-0004 "Seismic Retrofit of End-Sway Frames of Steel Deck-Truss Bridges with a Supplemental Tendon System: Experimental and Analytical Investigation," by G. Pekcan, J.B. Mander and S.S. Chen, 7/1/00, (PB2001-100982, A10, MF-A02).

MCEER-00-0005 "Sliding Fragility of Unrestrained Equipment in Critical Facilities," by W.H. Chong and T.T. Soong, 7/5/00, (PB2001-100983, A08, MF-A02).

MCEER-00-0006 "Seismic Response of Reinforced Concrete Bridge Pier Walls in the Weak Direction," by N. Abo-Shadi, M. Saiidi and D. Sanders, 7/17/00, (PB2001-100981, A17, MF-A03).

MCEER-00-0007 "Low-Cycle Fatigue Behavior of Longitudinal Reinforcement in Reinforced Concrete Bridge Columns," by J. Brown and S.K. Kunnath, 7/23/00, (PB2001-104392, A08, MF-A02).

MCEER-00-0008 "Soil Structure Interaction of Bridges for Seismic Analysis," I. PoLam and H. Law, 9/25/00, (PB2001-105397, A08, MF-A02).

MCEER-00-0009 "Proceedings of the First MCEER Workshop on Mitigation of Earthquake Disaster by Advanced Technologies (MEDAT-1), edited by M. Shinozuka, D.J. Inman and T.D. O'Rourke, 11/10/00, (PB2001-105399, A14, MF-A03).

MCEER-00-0010 "Development and Evaluation of Simplified Procedures for Analysis and Design of Buildings with Passive Energy Dissipation Systems, Revision 01," by O.M. Ramirez, M.C. Constantinou, C.A. Kircher, A.S. Whittaker, M.W. Johnson, J.D. Gomez and C. Chrysostomou, 11/16/01, (PB2001-105523, A23, MF-A04).

MCEER-00-0011 "Dynamic Soil-Foundation-Structure Interaction Analyses of Large Caissons," by C-Y. Chang, C-M. Mok, Z-L. Wang, R. Settgast, F. Waggoner, M.A. Ketchum, H.M. Gonnermann and C-C. Chin, 12/30/00, (PB2001-104373, A07, MF-A02).

MCEER-00-0012 "Experimental Evaluation of Seismic Performance of Bridge Restrainers," by A.G. Vlassis, E.M. Maragakis and M. Saiid Saiidi, 12/30/00, (PB2001-104354, A09, MF-A02).

MCEER-00-0013 "Effect of Spatial Variation of Ground Motion on Highway Structures," by M. Shinozuka, V. Saxena and G. Deodatis, 12/31/00, (PB2001-108755, A13, MF-A03).

MCEER-00-0014 "A Risk-Based Methodology for Assessing the Seismic Performance of Highway Systems," by S.D. Werner, C.E. Taylor, J.E. Moore, II, J.S. Walton and S. Cho, 12/31/00, (PB2001-108756, A14, MF-A03).

MCEER-01-0001 "Experimental Investigation of P-Delta Effects to Collapse During Earthquakes," by D. Vian and M. Bruneau, 6/25/01, (PB2002-100534, A17, MF-A03).

MCEER-01-0002 "Proceedings of the Second MCEER Workshop on Mitigation of Earthquake Disaster by Advanced Technologies (MEDAT-2)," edited by M. Bruneau and D.J. Inman, 7/23/01, (PB2002-100434, A16, MF-A03).

MCEER-01-0003 "Sensitivity Analysis of Dynamic Systems Subjected to Seismic Loads," by C. Roth and M. Grigoriu, 9/18/01, (PB2003-100884, A12, MF-A03).

MCEER-01-0004 "Overcoming Obstacles to Implementing Earthquake Hazard Mitigation Policies: Stage 1 Report," by D.J. Alesch and W.J. Petak, 12/17/01, (PB2002-107949, A07, MF-A02).

MCEER-01-0005 "Updating Real-Time Earthquake Loss Estimates: Methods, Problems and Insights," by C.E. Taylor, S.E. Chang and R.T. Eguchi, 12/17/01, (PB2002-107948, A05, MF-A01).

MCEER-01-0006 "Experimental Investigation and Retrofit of Steel Pile Foundations and Pile Bents Under Cyclic Lateral Loadings," by A. Shama, J. Mander, B. Blabac and S. Chen, 12/31/01, (PB2002-107950, A13, MF-A03).

MCEER-02-0001 "Assessment of Performance of Bolu Viaduct in the 1999 Duzce Earthquake in Turkey" by P.C. Roussis, M.C. Constantinou, M. Erdik, E. Durukal and M. Dicleli, 5/8/02, (PB2003-100883, A08, MF-A02).

MCEER-02-0002 "Seismic Behavior of Rail Counterweight Systems of Elevators in Buildings," by M.P. Singh, Rildova and L.E. Suarez, 5/27/02. (PB2003-100882, A11, MF-A03).

MCEER-02-0003 "Development of Analysis and Design Procedures for Spread Footings," by G. Mylonakis, G. Gazetas, S. Nikolaou and A. Chauncey, 10/02/02, (PB2004-101636, A13, MF-A03, CD-A13).

MCEER-02-0004 "Bare-Earth Algorithms for Use with SAR and LIDAR Digital Elevation Models," by C.K. Huyck, R.T. Eguchi and B. Houshmand, 10/16/02, (PB2004-101637, A07, CD-A07).

MCEER-02-0005 "Review of Energy Dissipation of Compression Members in Concentrically Braced Frames," by K.Lee and M. Bruneau, 10/18/02, (PB2004-101638, A10, CD-A10).

MCEER-03-0001 "Experimental Investigation of Light-Gauge Steel Plate Shear Walls for the Seismic Retrofit of Buildings" by J. Berman and M. Bruneau, 5/2/03, (PB2004-101622, A10, MF-A03, CD-A10).

MCEER-03-0002 "Statistical Analysis of Fragility Curves," by M. Shinozuka, M.Q. Feng, H. Kim, T. Uzawa and T. Ueda, 6/16/03, (PB2004-101849, A09, CD-A09).

MCEER-03-0003 "Proceedings of the Eighth U.S.-Japan Workshop on Earthquake Resistant Design f Lifeline Facilities and Countermeasures Against Liquefaction," edited by M. Hamada, J.P. Bardet and T.D. O'Rourke, 6/30/03, (PB2004-104386, A99, CD-A99).

MCEER-03-0004 "Proceedings of the PRC-US Workshop on Seismic Analysis and Design of Special Bridges," edited by L.C. Fan and G.C. Lee, 7/15/03, (PB2004-104387, A14, CD-A14).

MCEER-03-0005 "Urban Disaster Recovery: A Framework and Simulation Model," by S.B. Miles and S.E. Chang, 7/25/03, (PB2004-104388, A07, CD-A07).

MCEER-03-0006 "Behavior of Underground Piping Joints Due to Static and Dynamic Loading," by R.D. Meis, M. Maragakis and R. Siddharthan, 11/17/03, (PB2005-102194, A13, MF-A03, CD-A00).

MCEER-04-0001 "Experimental Study of Seismic Isolation Systems with Emphasis on Secondary System Response and Verification of Accuracy of Dynamic Response History Analysis Methods," by E. Wolff and M. Constantinou, 1/16/04 (PB2005-102195, A99, MF-E08, CD-A00).

MCEER-04-0002 "Tension, Compression and Cyclic Testing of Engineered Cementitious Composite Materials," by K. Kesner and S.L. Billington, 3/1/04, (PB2005-102196, A08, CD-A08).

MCEER-04-0003 "Cyclic Testing of Braces Laterally Restrained by Steel Studs to Enhance Performance During Earthquakes," by O.C. Celik, J.W. Berman and M. Bruneau, 3/16/04, (PB2005-102197, A13, MF-A03, CD-A00).

MCEER-04-0004 "Methodologies for Post Earthquake Building Damage Detection Using SAR and Optical Remote Sensing: Application to the August 17, 1999 Marmara, Turkey Earthquake," by C.K. Huyck, B.J. Adams, S. Cho, R.T. Eguchi, B. Mansouri and B. Houshmand, 6/15/04, (PB2005-104888, A10, CD-A00).

MCEER-04-0005 "Nonlinear Structural Analysis Towards Collapse Simulation: A Dynamical Systems Approach," by M.V. Sivaselvan and A.M. Reinhorn, 6/16/04, (PB2005-104889, A11, MF-A03, CD-A00).

MCEER-04-0006 "Proceedings of the Second PRC-US Workshop on Seismic Analysis and Design of Special Bridges," edited by G.C. Lee and L.C. Fan, 6/25/04, (PB2005-104890, A16, CD-A00).

MCEER-04-0007 "Seismic Vulnerability Evaluation of Axially Loaded Steel Built-up Laced Members," by K. Lee and M. Bruneau, 6/30/04, (PB2005-104891, A16, CD-A00).

MCEER-04-0008 "Evaluation of Accuracy of Simplified Methods of Analysis and Design of Buildings with Damping Systems for Near-Fault and for Soft-Soil Seismic Motions," by E.A. Pavlou and M.C. Constantinou, 8/16/04, (PB2005-104892, A08, MF-A02, CD-A00).

MCEER-04-0009 "Assessment of Geotechnical Issues in Acute Care Facilities in California," by M. Lew, T.D. O'Rourke, R. Dobry and M. Koch, 9/15/04, (PB2005-104893, A08, CD-A00).

MCEER-04-0010 "Scissor-Jack-Damper Energy Dissipation System," by A.N. Sigaher-Boyle and M.C. Constantinou, 12/1/04 (PB2005-108221).

MCEER-04-0011 "Seismic Retrofit of Bridge Steel Truss Piers Using a Controlled Rocking Approach," by M. Pollino and M. Bruneau, 12/20/04 (PB2006-105795).

MCEER-05-0001 "Experimental and Analytical Studies of Structures Seismically Isolated with an Uplift-Restraint Isolation System," by P.C. Roussis and M.C. Constantinou, 1/10/05 (PB2005-108222).

MCEER-05-0002 "A Versatile Experimentation Model for Study of Structures Near Collapse Applied to Seismic Evaluation of Irregular Structures," by D. Kusumastuti, A.M. Reinhorn and A. Rutenberg, 3/31/05 (PB2006-101523).

MCEER-05-0003 "Proceedings of the Third PRC-US Workshop on Seismic Analysis and Design of Special Bridges," edited by L.C. Fan and G.C. Lee, 4/20/05, (PB2006-105796).

MCEER-05-0004 "Approaches for the Seismic Retrofit of Braced Steel Bridge Piers and Proof-of-Concept Testing of an Eccentrically Braced Frame with Tubular Link," by J.W. Berman and M. Bruneau, 4/21/05 (PB2006-101524).

MCEER-05-0005 "Simulation of Strong Ground Motions for Seismic Fragility Evaluation of Nonstructural Components in Hospitals," by A. Wanitkorkul and A. Filiatrault, 5/26/05 (PB2006-500027).

MCEER-05-0006 "Seismic Safety in California Hospitals: Assessing an Attempt to Accelerate the Replacement or Seismic Retrofit of Older Hospital Facilities," by D.J. Alesch, L.A. Arendt and W.J. Petak, 6/6/05 (PB2006-105794).

MCEER-05-0007 "Development of Seismic Strengthening and Retrofit Strategies for Critical Facilities Using Engineered Cementitious Composite Materials," by K. Kesner and S.L. Billington, 8/29/05 (PB2006-111701).

MCEER-05-0008 "Experimental and Analytical Studies of Base Isolation Systems for Seismic Protection of Power Transformers," by N. Murota, M.Q. Feng and G-Y. Liu, 9/30/05 (PB2006-111702).

MCEER-05-0009 "3D-BASIS-ME-MB: Computer Program for Nonlinear Dynamic Analysis of Seismically Isolated Structures," by P.C. Tsopelas, P.C. Roussis, M.C. Constantinou, R. Buchanan and A.M. Reinhorn, 10/3/05 (PB2006-111703).

MCEER-05-0010 "Steel Plate Shear Walls for Seismic Design and Retrofit of Building Structures," by D. Vian and M. Bruneau, 12/15/05 (PB2006-111704).

MCEER-05-0011 "The Performance-Based Design Paradigm," by M.J. Astrella and A. Whittaker, 12/15/05 (PB2006-111705).

MCEER-06-0001 "Seismic Fragility of Suspended Ceiling Systems," H. Badillo-Almaraz, A.S. Whittaker, A.M. Reinhorn and G.P. Cimellaro, 2/4/06 (PB2006-111706).

MCEER-06-0002 "Multi-Dimensional Fragility of Structures," by G.P. Cimellaro, A.M. Reinhorn and M. Bruneau, 3/1/06 (PB2007-106974, A09, MF-A02, CD A00).

MCEER-06-0003 "Built-Up Shear Links as Energy Dissipators for Seismic Protection of Bridges," by P. Dusicka, A.M. Itani and I.G. Buckle, 3/15/06 (PB2006-111708).

MCEER-06-0004 "Analytical Investigation of the Structural Fuse Concept," by R.E. Vargas and M. Bruneau, 3/16/06 (PB2006-111709).

MCEER-06-0005 "Experimental Investigation of the Structural Fuse Concept," by R.E. Vargas and M. Bruneau, 3/17/06 (PB2006-111710).

MCEER-06-0006 "Further Development of Tubular Eccentrically Braced Frame Links for the Seismic Retrofit of Braced Steel Truss Bridge Piers," by J.W. Berman and M. Bruneau, 3/27/06 (PB2007-105147).

MCEER-06-0007 "REDARS Validation Report," by S. Cho, C.K. Huyck, S. Ghosh and R.T. Eguchi, 8/8/06 (PB2007-106983).

MCEER-06-0008 "Review of Current NDE Technologies for Post-Earthquake Assessment of Retrofitted Bridge Columns," by J.W. Song, Z. Liang and G.C. Lee, 8/21/06 (PB2007-106984).

MCEER-06-0009 "Liquefaction Remediation in Silty Soils Using Dynamic Compaction and Stone Columns," by S. Thevanayagam, G.R. Martin, R. Nashed, T. Shenthan, T. Kanagalingam and N. Ecemis, 8/28/06 (PB2007-106985).

MCEER-06-0010 "Conceptual Design and Experimental Investigation of Polymer Matrix Composite Infill Panels for Seismic Retrofitting," by W. Jung, M. Chiewanichakorn and A.J. Aref, 9/21/06 (PB2007-106986).

MCEER-06-0011 "A Study of the Coupled Horizontal-Vertical Behavior of Elastomeric and Lead-Rubber Seismic Isolation Bearings," by G.P. Warn and A.S. Whittaker, 9/22/06 (PB2007-108679).

MCEER-06-0012 "Proceedings of the Fourth PRC-US Workshop on Seismic Analysis and Design of Special Bridges: Advancing Bridge Technologies in Research, Design, Construction and Preservation," Edited by L.C. Fan, G.C. Lee and L. Ziang, 10/12/06 (PB2007-109042).

MCEER-06-0013 "Cyclic Response and Low Cycle Fatigue Characteristics of Plate Steels," by P. Dusicka, A.M. Itani and I.G. Buckle, 11/1/06 06 (PB2007-106987).

MCEER-06-0014 "Proceedings of the Second US-Taiwan Bridge Engineering Workshop," edited by W.P. Yen, J. Shen, J-Y. Chen and M. Wang, 11/15/06 (PB2008-500041).

MCEER-06-0015 "User Manual and Technical Documentation for the REDARS™ Import Wizard," by S. Cho, S. Ghosh, C.K. Huyck and S.D. Werner, 11/30/06 (PB2007-114766).

MCEER-06-0016 "Hazard Mitigation Strategy and Monitoring Technologies for Urban and Infrastructure Public Buildings: Proceedings of the China-US Workshops," edited by X.Y. Zhou, A.L. Zhang, G.C. Lee and M. Tong, 12/12/06 (PB2008-500018).

MCEER-07-0001 "Static and Kinetic Coefficients of Friction for Rigid Blocks," by C. Kafali, S. Fathali, M. Grigoriu and A.S. Whittaker, 3/20/07 (PB2007-114767).

MCEER-07-0002 "Hazard Mitigation Investment Decision Making: Organizational Response to Legislative Mandate," by L.A. Arendt, D.J. Alesch and W.J. Petak, 4/9/07 (PB2007-114768).

MCEER-07-0003 "Seismic Behavior of Bidirectional-Resistant Ductile End Diaphragms with Unbonded Braces in Straight or Skewed Steel Bridges," by O. Celik and M. Bruneau, 4/11/07 (PB2008-105141).

MCEER-07-0004 “Modeling Pile Behavior in Large Pile Groups Under Lateral Loading,” by A.M. Dodds and G.R. Martin, 4/16/07(PB2008-105142).

MCEER-07-0005 “Experimental Investigation of Blast Performance of Seismically Resistant Concrete-Filled Steel Tube Bridge Piers,” by S. Fujikura, M. Bruneau and D. Lopez-Garcia, 4/20/07 (PB2008-105143).

MCEER-07-0006 “Seismic Analysis of Conventional and Isolated Liquefied Natural Gas Tanks Using Mechanical Analogs,” by I.P. Christovasilis and A.S. Whittaker, 5/1/07, not available.

MCEER-07-0007 “Experimental Seismic Performance Evaluation of Isolation/Restraint Systems for Mechanical Equipment – Part 1: Heavy Equipment Study,” by S. Fathali and A. Filiatrault, 6/6/07 (PB2008-105144).

MCEER-07-0008 “Seismic Vulnerability of Timber Bridges and Timber Substructures,” by A.A. Sharma, J.B. Mander, I.M. Friedland and D.R. Allicock, 6/7/07 (PB2008-105145).

MCEER-07-0009 “Experimental and Analytical Study of the XY-Friction Pendulum (XY-FP) Bearing for Bridge Applications,” by C.C. Marin-Artieda, A.S. Whittaker and M.C. Constantinou, 6/7/07 (PB2008-105191).

MCEER-07-0010 “Proceedings of the PRC-US Earthquake Engineering Forum for Young Researchers,” Edited by G.C. Lee and X.Z. Qi, 6/8/07 (PB2008-500058).

MCEER-07-0011 “Design Recommendations for Perforated Steel Plate Shear Walls,” by R. Purba and M. Bruneau, 6/18/07, (PB2008-105192).

MCEER-07-0012 “Performance of Seismic Isolation Hardware Under Service and Seismic Loading,” by M.C. Constantinou, A.S. Whittaker, Y. Kalpakidis, D.M. Fenz and G.P. Warn, 8/27/07, (PB2008-105193).

MCEER-07-0013 “Experimental Evaluation of the Seismic Performance of Hospital Piping Subassemblies,” by E.R. Goodwin, E. Maragakis and A.M. Itani, 9/4/07, (PB2008-105194).

MCEER-07-0014 “A Simulation Model of Urban Disaster Recovery and Resilience: Implementation for the 1994 Northridge Earthquake,” by S. Miles and S.E. Chang, 9/7/07, (PB2008-106426).

MCEER-07-0015 “Statistical and Mechanistic Fragility Analysis of Concrete Bridges,” by M. Shinozuka, S. Banerjee and S-H. Kim, 9/10/07, (PB2008-106427).

MCEER-07-0016 “Three-Dimensional Modeling of Inelastic Buckling in Frame Structures,” by M. Schachter and AM. Reinhorn, 9/13/07, (PB2008-108125).

MCEER-07-0017 “Modeling of Seismic Wave Scattering on Pile Groups and Caissons,” by I. Po Lam, H. Law and C.T. Yang, 9/17/07 (PB2008-108150).

MCEER-07-0018 “Bridge Foundations: Modeling Large Pile Groups and Caissons for Seismic Design,” by I. Po Lam, H. Law and G.R. Martin (Coordinating Author), 12/1/07 (PB2008-111190).

MCEER-07-0019 “Principles and Performance of Roller Seismic Isolation Bearings for Highway Bridges,” by G.C. Lee, Y.C. Ou, Z. Liang, T.C. Niu and J. Song, 12/10/07 (PB2009-110466).

MCEER-07-0020 “Centrifuge Modeling of Permeability and Pinning Reinforcement Effects on Pile Response to Lateral Spreading,” by L.L Gonzalez-Lagos, T. Abdoun and R. Dobry, 12/10/07 (PB2008-111191).

MCEER-07-0021 “Damage to the Highway System from the Pisco, Perú Earthquake of August 15, 2007,” by J.S. O’Connor, L. Mesa and M. Nykamp, 12/10/07, (PB2008-108126).

MCEER-07-0022 “Experimental Seismic Performance Evaluation of Isolation/Restraint Systems for Mechanical Equipment – Part 2: Light Equipment Study,” by S. Fathali and A. Filiatrault, 12/13/07 (PB2008-111192).

MCEER-07-0023 “Fragility Considerations in Highway Bridge Design,” by M. Shinozuka, S. Banerjee and S.H. Kim, 12/14/07 (PB2008-111193).

MCEER-07-0024 “Performance Estimates for Seismically Isolated Bridges,” by G.P. Warn and A.S. Whittaker, 12/30/07 (PB2008-112230).

MCEER-08-0001 “Seismic Performance of Steel Girder Bridge Superstructures with Conventional Cross Frames,” by L.P. Carden, A.M. Itani and I.G. Buckle, 1/7/08, (PB2008-112231).

MCEER-08-0002 “Seismic Performance of Steel Girder Bridge Superstructures with Ductile End Cross Frames with Seismic Isolators,” by L.P. Carden, A.M. Itani and I.G. Buckle, 1/7/08 (PB2008-112232).

MCEER-08-0003 “Analytical and Experimental Investigation of a Controlled Rocking Approach for Seismic Protection of Bridge Steel Truss Piers,” by M. Pollino and M. Bruneau, 1/21/08 (PB2008-112233).

MCEER-08-0004 “Linking Lifeline Infrastructure Performance and Community Disaster Resilience: Models and Multi-Stakeholder Processes,” by S.E. Chang, C. Pasion, K. Tatebe and R. Ahmad, 3/3/08 (PB2008-112234).

MCEER-08-0005 “Modal Analysis of Generally Damped Linear Structures Subjected to Seismic Excitations,” by J. Song, Y-L. Chu, Z. Liang and G.C. Lee, 3/4/08 (PB2009-102311).

MCEER-08-0006 “System Performance Under Multi-Hazard Environments,” by C. Kafali and M. Grigoriu, 3/4/08 (PB2008-112235).

MCEER-08-0007 “Mechanical Behavior of Multi-Spherical Sliding Bearings,” by D.M. Fenz and M.C. Constantinou, 3/6/08 (PB2008-112236).

MCEER-08-0008 “Post-Earthquake Restoration of the Los Angeles Water Supply System,” by T.H.P. Tabucchi and R.A. Davidson, 3/7/08 (PB2008-112237).

MCEER-08-0009 “Fragility Analysis of Water Supply Systems,” by A. Jacobson and M. Grigoriu, 3/10/08 (PB2009-105545).

MCEER-08-0010 “Experimental Investigation of Full-Scale Two-Story Steel Plate Shear Walls with Reduced Beam Section Connections,” by B. Qu, M. Bruneau, C-H. Lin and K-C. Tsai, 3/17/08 (PB2009-106368).

MCEER-08-0011 “Seismic Evaluation and Rehabilitation of Critical Components of Electrical Power Systems,” S. Ersoy, B. Feizi, A. Ashrafi and M. Ala Saadeghvaziri, 3/17/08 (PB2009-105546).

MCEER-08-0012 “Seismic Behavior and Design of Boundary Frame Members of Steel Plate Shear Walls,” by B. Qu and M. Bruneau, 4/26/08 . (PB2009-106744).

MCEER-08-0013 “Development and Appraisal of a Numerical Cyclic Loading Protocol for Quantifying Building System Performance,” by A. Filiatrault, A. Wanitkorkul and M. Constantinou, 4/27/08 (PB2009-107906).

MCEER-08-0014 “Structural and Nonstructural Earthquake Design: The Challenge of Integrating Specialty Areas in Designing Complex, Critical Facilities,” by W.J. Petak and D.J. Alesch, 4/30/08 (PB2009-107907).

MCEER-08-0015 “Seismic Performance Evaluation of Water Systems,” by Y. Wang and T.D. O’Rourke, 5/5/08 (PB2009-107908).

MCEER-08-0016 “Seismic Response Modeling of Water Supply Systems,” by P. Shi and T.D. O’Rourke, 5/5/08 (PB2009-107910).

MCEER-08-0017 “Numerical and Experimental Studies of Self-Centering Post-Tensioned Steel Frames,” by D. Wang and A. Filiatrault, 5/12/08 (PB2009-110479).

MCEER-08-0018 “Development, Implementation and Verification of Dynamic Analysis Models for Multi-Spherical Sliding Bearings,” by D.M. Fenz and M.C. Constantinou, 8/15/08 (PB2009-107911).

MCEER-08-0019 “Performance Assessment of Conventional and Base Isolated Nuclear Power Plants for Earthquake Blast Loadings,” by Y.N. Huang, A.S. Whittaker and N. Luco, 10/28/08 (PB2009-107912).

MCEER-08-0020 "Remote Sensing for Resilient Multi-Hazard Disaster Response – Volume I: Introduction to Damage Assessment Methodologies," by B.J. Adams and R.T. Eguchi, 11/17/08 (PB2010-102695).

MCEER-08-0021 "Remote Sensing for Resilient Multi-Hazard Disaster Response – Volume II: Counting the Number of Collapsed Buildings Using an Object-Oriented Analysis: Case Study of the 2003 Bam Earthquake," by L. Gusella, C.K. Huyck and B.J. Adams, 11/17/08 (PB2010-100925).

MCEER-08-0022 "Remote Sensing for Resilient Multi-Hazard Disaster Response – Volume III: Multi-Sensor Image Fusion Techniques for Robust Neighborhood-Scale Urban Damage Assessment," by B.J. Adams and A. McMillan, 11/17/08 (PB2010-100926).

MCEER-08-0023 "Remote Sensing for Resilient Multi-Hazard Disaster Response – Volume IV: A Study of Multi-Temporal and Multi-Resolution SAR Imagery for Post-Katrina Flood Monitoring in New Orleans," by A. McMillan, J.G. Morley, B.J. Adams and S. Chesworth, 11/17/08 (PB2010-100927).

MCEER-08-0024 "Remote Sensing for Resilient Multi-Hazard Disaster Response – Volume V: Integration of Remote Sensing Imagery and VIEWS^{TM} Field Data for Post-Hurricane Charley Building Damage Assessment," by J.A. Womble, K. Mehta and B.J. Adams, 11/17/08 (PB2009-115532).

MCEER-08-0025 "Building Inventory Compilation for Disaster Management: Application of Remote Sensing and Statistical Modeling," by P. Sarabandi, A.S. Kiremidjian, R.T. Eguchi and B. J. Adams, 11/20/08 (PB2009-110484).

MCEER-08-0026 "New Experimental Capabilities and Loading Protocols for Seismic Qualification and Fragility Assessment of Nonstructural Systems," by R. Retamales, G. Mosqueda, A. Filiatrault and A. Reinhorn, 11/24/08 (PB2009-110485).

MCEER-08-0027 "Effects of Heating and Load History on the Behavior of Lead-Rubber Bearings," by I.V. Kalpakidis and M.C. Constantinou, 12/1/08 (PB2009-115533).

MCEER-08-0028 "Experimental and Analytical Investigation of Blast Performance of Seismically Resistant Bridge Piers," by S.Fujikura and M. Bruneau, 12/8/08 (PB2009-115534).

MCEER-08-0029 "Evolutionary Methodology for Aseismic Decision Support," by Y. Hu and G. Dargush, 12/15/08.

MCEER-08-0030 "Development of a Steel Plate Shear Wall Bridge Pier System Conceived from a Multi-Hazard Perspective," by D. Keller and M. Bruneau, 12/19/08 (PB2010-102696).

MCEER-09-0001 "Modal Analysis of Arbitrarily Damped Three-Dimensional Linear Structures Subjected to Seismic Excitations," by Y.L. Chu, J. Song and G.C. Lee, 1/31/09 (PB2010-100922).

MCEER-09-0002 "Air-Blast Effects on Structural Shapes," by G. Ballantyne, A.S. Whittaker, A.J. Aref and G.F. Dargush, 2/2/09 (PB2010-102697).

MCEER-09-0003 "Water Supply Performance During Earthquakes and Extreme Events," by A.L. Bonneau and T.D. O'Rourke, 2/16/09 (PB2010-100923).

MCEER-09-0004 "Generalized Linear (Mixed) Models of Post-Earthquake Ignitions," by R.A. Davidson, 7/20/09 (PB2010-102698).

MCEER-09-0005 "Seismic Testing of a Full-Scale Two-Story Light-Frame Wood Building: NEESWood Benchmark Test," by I.P. Christovasilis, A. Filiatrault and A. Wanitkorkul, 7/22/09 (PB2012-102401).

MCEER-09-0006 "IDARC2D Version 7.0: A Program for the Inelastic Damage Analysis of Structures," by A.M. Reinhorn, H. Roh, M. Sivaselvan, S.K. Kunnath, R.E. Valles, A. Madan, C. Li, R. Lobo and Y.J. Park, 7/28/09 (PB2010-103199).

MCEER-09-0007 "Enhancements to Hospital Resiliency: Improving Emergency Planning for and Response to Hurricanes," by D.B. Hess and L.A. Arendt, 7/30/09 (PB2010-100924).

MCEER-09-0008 "Assessment of Base-Isolated Nuclear Structures for Design and Beyond-Design Basis Earthquake Shaking," by Y.N. Huang, A.S. Whittaker, R.P. Kennedy and R.L. Mayes, 8/20/09 (PB2010-102699).

MCEER-09-0009 "Quantification of Disaster Resilience of Health Care Facilities," by G.P. Cimellaro, C. Fumo, A.M Reinhorn and M. Bruneau, 9/14/09 (PB2010-105384).

MCEER-09-0010 "Performance-Based Assessment and Design of Squat Reinforced Concrete Shear Walls," by C.K. Gulec and A.S. Whittaker, 9/15/09 (PB2010-102700).

MCEER-09-0011 "Proceedings of the Fourth US-Taiwan Bridge Engineering Workshop," edited by W.P. Yen, J.J. Shen, T.M. Lee and R.B. Zheng, 10/27/09 (PB2010-500009).

MCEER-09-0012 "Proceedings of the Special International Workshop on Seismic Connection Details for Segmental Bridge Construction," edited by W. Phillip Yen and George C. Lee, 12/21/09 (PB2012-102402).

MCEER-10-0001 "Direct Displacement Procedure for Performance-Based Seismic Design of Multistory Woodframe Structures," by W. Pang and D. Rosowsky, 4/26/10 (PB2012-102403).

MCEER-10-0002 "Simplified Direct Displacement Design of Six-Story NEESWood Capstone Building and Pre-Test Seismic Performance Assessment," by W. Pang, D. Rosowsky, J. van de Lindt and S. Pei, 5/28/10 (PB2012-102404).

MCEER-10-0003 "Integration of Seismic Protection Systems in Performance-Based Seismic Design of Woodframed Structures," by J.K. Shinde and M.D. Symans, 6/18/10 (PB2012-102405).

MCEER-10-0004 "Modeling and Seismic Evaluation of Nonstructural Components: Testing Frame for Experimental Evaluation of Suspended Ceiling Systems," by A.M. Reinhorn, K.P. Ryu and G. Maddaloni, 6/30/10 (PB2012-102406).

MCEER-10-0005 "Analytical Development and Experimental Validation of a Structural-Fuse Bridge Pier Concept," by S. El-Bahey and M. Bruneau, 10/1/10 (PB2012-102407).

MCEER-10-0006 "A Framework for Defining and Measuring Resilience at the Community Scale: The PEOPLES Resilience Framework," by C.S. Renschler, A.E. Frazier, L.A. Arendt, G.P. Cimellaro, A.M. Reinhorn and M. Bruneau, 10/8/10 (PB2012-102408).

MCEER-10-0007 "Impact of Horizontal Boundary Elements Design on Seismic Behavior of Steel Plate Shear Walls," by R. Purba and M. Bruneau, 11/14/10 (PB2012-102409).

MCEER-10-0008 "Seismic Testing of a Full-Scale Mid-Rise Building: The NEESWood Capstone Test," by S. Pei, J.W. van de Lindt, S.E. Pryor, H. Shimizu, H. Isoda and D.R. Rammer, 12/1/10 (PB2012-102410).

MCEER-10-0009 "Modeling the Effects of Detonations of High Explosives to Inform Blast-Resistant Design," by P. Sherkar, A.S. Whittaker and A.J. Aref, 12/1/10 (PB2012-102411).

MCEER-10-0010 "L'Aquila Earthquake of April 6, 2009 in Italy: Rebuilding a Resilient City to Withstand Multiple Hazards," by G.P. Cimellaro, I.P. Christovasilis, A.M. Reinhorn, A. De Stefano and T. Kirova, 12/29/10.

MCEER-11-0001 "Numerical and Experimental Investigation of the Seismic Response of Light-Frame Wood Structures," by I.P. Christovasilis and A. Filiatrault, 8/8/11 (PB2012-102412).

MCEER-11-0002 "Seismic Design and Analysis of a Precast Segmental Concrete Bridge Model," by M. Anagnostopoulou, A. Filiatrault and A. Aref, 9/15/11.

MCEER-11-0003 'Proceedings of the Workshop on Improving Earthquake Response of Substation Equipment," Edited by A.M. Reinhorn, 9/19/11 (PB2012-102413).

MCEER-11-0004 "LRFD-Based Analysis and Design Procedures for Bridge Bearings and Seismic Isolators," by M.C. Constantinou, I. Kalpakidis, A. Filiatrault and R.A. Ecker Lay, 9/26/11.

MCEER-11-0005 "Experimental Seismic Evaluation, Model Parameterization, and Effects of Cold-Formed Steel-Framed Gypsum Partition Walls on the Seismic Performance of an Essential Facility," by R. Davies, R. Retamales, G. Mosqueda and A. Filiatrault, 10/12/11.

MCEER-11-0006 "Modeling and Seismic Performance Evaluation of High Voltage Transformers and Bushings," by A.M. Reinhorn, K. Oikonomou, H. Roh, A. Schiff and L. Kempner, Jr., 10/3/11.

MCEER-11-0007 "Extreme Load Combinations: A Survey of State Bridge Engineers," by G.C. Lee, Z. Liang, J.J. Shen and J.S. O'Connor, 10/14/11.

MCEER-12-0001 "Simplified Analysis Procedures in Support of Performance Based Seismic Design," by Y.N. Huang and A.S. Whittaker.

MCEER-12-0002 "Seismic Protection of Electrical Transformer Bushing Systems by Stiffening Techniques," by M. Koliou, A. Filiatrault, A.M. Reinhorn and N. Oliveto, 6/1/12.

MCEER-12-0003 "Post-Earthquake Bridge Inspection Guidelines," by J.S. O'Connor and S. Alampalli, 6/8/12.

MCEER-12-0004 "Integrated Design Methodology for Isolated Floor Systems in Single-Degree-of-Freedom Structural Fuse Systems," by S. Cui, M. Bruneau and M.C. Constantinou, 6/13/12.

MCEER-12-0005 "Characterizing the Rotational Components of Earthquake Ground Motion," by D. Basu, A.S. Whittaker and M.C. Constantinou, 6/15/12.

MCEER-12-0006 "Bayesian Fragility for Nonstructural Systems," by C.H. Lee and M.D. Grigoriu, 9/12/12.

MCEER-12-0007 "A Numerical Model for Capturing the In-Plane Seismic Response of Interior Metal Stud Partition Walls," by R.L. Wood and T.C. Hutchinson, 9/12/12.

MCEER-12-0008 "Assessment of Floor Accelerations in Yielding Buildings," by J.D. Wieser, G. Pekcan, A.E. Zaghi, A.M. Itani and E. Maragakis, 10/5/12.

MCEER-13-0001 "Experimental Seismic Study of Pressurized Fire Sprinkler Piping Systems," by Y. Tian, A. Filiatrault and G. Mosqueda, 4/8/13.

MCEER-13-0002 "Enhancing Resource Coordination for Multi-Modal Evacuation Planning," by D.B. Hess, B.W. Conley and C.M. Farrell, 2/8/13.

MCEER-13-0003 "Seismic Response of Base Isolated Buildings Considering Pounding to Moat Walls," by A. Masroor and G. Mosqueda, 2/26/13.

MCEER-13-0004 "Seismic Response Control of Structures Using a Novel Adaptive Passive Negative Stiffness Device," by D.T.R. Pasala, A.A. Sarlis, S. Nagarajaiah, A.M. Reinhorn, M.C. Constantinou and D.P. Taylor, 6/10/13.

MCEER-13-0005 "Negative Stiffness Device for Seismic Protection of Structures," by A.A. Sarlis, D.T.R. Pasala, M.C. Constantinou, A.M. Reinhorn, S. Nagarajaiah and D.P. Taylor, 6/12/13.

MCEER-13-0006 "Emilia Earthquake of May 20, 2012 in Northern Italy: Rebuilding a Resilient Community to Withstand Multiple Hazards," by G.P. Cimellaro, M. Chiriatti, A.M. Reinhorn and L. Tirca, June 30, 2013.

MCEER-13-0007 "Precast Concrete Segmental Components and Systems for Accelerated Bridge Construction in Seismic Regions," by A.J. Aref, G.C. Lee, Y.C. Ou and P. Sideris, with contributions from K.C. Chang, S. Chen, A. Filiatrault and Y. Zhou, June 13, 2013.

MCEER-13-0008 "A Study of U.S. Bridge Failures (1980-2012)," by G.C. Lee, S.B. Mohan, C. Huang and B.N. Fard, June 15, 2013.

MCEER-13-0009 "Development of a Database Framework for Modeling Damaged Bridges," by G.C. Lee, J.C. Qi and C. Huang, June 16, 2013.

MCEER-13-0010 "Model of Triple Friction Pendulum Bearing for General Geometric and Frictional Parameters and for Uplift Conditions," by A.A. Sarlis and M.C. Constantinou, July 1, 2013.

MCEER-13-0011 "Shake Table Testing of Triple Friction Pendulum Isolators under Extreme Conditions," by A.A. Sarlis, M.C. Constantinou and A.M. Reinhorn, July 2, 2013.

MCEER-13-0012 "Theoretical Framework for the Development of MH-LRFD," by G.C. Lee (coordinating author), H.A Capers, Jr., C. Huang, J.M. Kulicki, Z. Liang, T. Murphy, J.J.D. Shen, M. Shinozuka and P.W.H. Yen, July 31, 2013.

MCEER-13-0013 "Seismic Protection of Highway Bridges with Negative Stiffness Devices," by N.K.A. Attary, M.D. Symans, S. Nagarajaiah, A.M. Reinhorn, M.C. Constantinou, A.A. Sarlis, D.T.R. Pasala, and D.P. Taylor, September 3, 2014.

MCEER-14-0001 "Simplified Seismic Collapse Capacity-Based Evaluation and Design of Frame Buildings with and without Supplemental Damping Systems," by M. Hamidia, A. Filiatrault, and A. Aref, May 19, 2014.

MCEER-14-0002 "Comprehensive Analytical Seismic Fragility of Fire Sprinkler Piping Systems," by Siavash Soroushian, Emmanuel "Manos" Maragakis, Arash E. Zaghi, Alicia Echevarria, Yuan Tian and Andre Filiatrault, August 26, 2014.

MCEER-14-0003 "Hybrid Simulation of the Seismic Response of a Steel Moment Frame Building Structure through Collapse," by M. Del Carpio Ramos, G. Mosqueda and D.G. Lignos, October 30, 2014.

MCEER-14-0004 "Blast and Seismic Resistant Concrete-Filled Double Skin Tubes and Modified Steel Jacketed Bridge Columns," by P.P. Fouche and M. Bruneau, June 30, 2015.

MCEER-14-0005 "Seismic Performance of Steel Plate Shear Walls Considering Various Design Approaches," by R. Purba and M. Bruneau, October 31, 2014.

MCEER-14-0006 "Air-Blast Effects on Civil Structures," by Jinwon Shin, Andrew S. Whittaker, Amjad J. Aref and David Cormie, October 30, 2014.

MCEER-14-0007 "Seismic Performance Evaluation of Precast Girders with Field-Cast Ultra High Performance Concrete (UHPC) Connections," by G.C. Lee, C. Huang, J. Song, and J. S. O'Connor, July 31, 2014.

MCEER-14-0008 "Post-Earthquake Fire Resistance of Ductile Concrete-Filled Double-Skin Tube Columns," by Reza Imani, Gilberto Mosqueda and Michel Bruneau, December 1, 2014.

MCEER-14-0009 "Cyclic Inelastic Behavior of Concrete Filled Sandwich Panel Walls Subjected to In-Plane Flexure," by Y. Alzeni and M. Bruneau, December 19, 2014.

MCEER-14-0010 "Analytical and Experimental Investigation of Self-Centering Steel Plate Shear Walls," by D.M. Dowden and M. Bruneau, December 19, 2014.

MCEER-15-0001 "Seismic Analysis of Multi-story Unreinforced Masonry Buildings with Flexible Diaphragms," by J. Aleman, G. Mosqueda and A.S. Whittaker, June 12, 2015.

MCEER-15-0002 "Site Response, Soil-Structure Interaction and Structure-Soil-Structure Interaction for Performance Assessment of Buildings and Nuclear Structures," by C. Bolisetti and A.S. Whittaker, June 15, 2015.

MCEER-15-0003 "Stress Wave Attenuation in Solids for Mitigating Impulsive Loadings," by R. Rafiee-Dehkharghani, A.J. Aref and G. Dargush, August 15, 2015.

MCEER-15-0004 "Computational, Analytical, and Experimental Modeling of Masonry Structures," by K.M. Dolatshahi and A.J. Aref, November 16, 2015.

MCEER-15-0005 "Property Modification Factors for Seismic Isolators: Design Guidance for Buildings," by W.J. McVitty and M.C. Constantinou, June 30, 2015.

MCEER-15-0006 "Seismic Isolation of Nuclear Power Plants using Sliding Bearings," by Manish Kumar, Andrew S. Whittaker and Michael C. Constantinou, December 27, 2015.

MCEER-15-0007 "Quintuple Friction Pendulum Isolator Behavior, Modeling and Validation," by Donghun Lee and Michael C. Constantinou, December 28, 2015.

MCEER-15-0008 "Seismic Isolation of Nuclear Power Plants using Elastomeric Bearings," by Manish Kumar, Andrew S. Whittaker and Michael C. Constantinou, December 29, 2015.

MCEER-16-0001 "Experimental, Numerical and Analytical Studies on the Seismic Response of Steel-Plate Concrete (SC) Composite Shear Walls," by Siamak Epackachi and Andrew S. Whittaker, June 15, 2016.

MCEER
EARTHQUAKE ENGINEERING TO EXTREME EVENTS
University at Buffalo, The State University of New York
133A Ketter Hall ▪ Buffalo, New York 14260-4300
Phone: (716) 645-3391 ▪ Fax: (716) 645-3399
Email: *mceer@buffalo.edu* ▪ Web: *http://mceer.buffalo.edu*
University at Buffalo *The State University of New York*

ISSN 1520-295X